

University of Alberta  
Department of Civil &  
Environmental Engineering



Structural Engineering Report No. 242

# **Behaviour of Concrete Slabs With Fibre-Reinforced Polymer Reinforcement**

by

Carlos E. Ospina

Scott D. B. Alexander

and

J. J. Cheng

October 2001

**Structural Engineering Report No. 242**

**BEHAVIOUR OF CONCRETE SLABS WITH  
FIBRE-REINFORCED POLYMER REINFORCEMENT**

**by**

**Carlos E. Ospina,  
Scott D. B. Alexander,  
and  
J. J. Roger Cheng**

**Department of Civil and Environmental Engineering**

**University of Alberta**

**Edmonton, Alberta, Canada**

**October, 2001**

## ACKNOWLEDGEMENTS

This report is based on a thesis titled “Slabs with Fibre-reinforced Polymers”, written by the first author under the supervision of the senior authors, leading towards a Ph.D. degree in Structural Engineering.

The study was conducted with the financial assistance provided by the Federal Government of Canada through its Network of Centres of Excellence on Intelligent Sensing for Innovative Structures (ISIS Canada), the National Science and Engineering Research Council (NSERC) of Canada, the Provincial Government of Alberta through its Graduate Fellowship Program, and both the Department of Civil and Environmental Engineering and the Faculty of Graduate Studies and Research of the University of Alberta through diverse scholarships. This support is warmly appreciated.

The donation of GFRP C-bars by Marshall Industries Ltd., a GFRP NEFMAC grid by Autocon Inc., and CFRP sheets by the Industrial Technology Research Institute, ITRI, Taiwan, is deeply appreciated.

The technical assistance of R. Helfrich and L. Burden at the I. F. Morrison Structural Laboratory and the help from many graduate students in the casting of the concrete slabs is warmly acknowledged.

The authors would also like to thank Professor Neil M. Hawkins, head of the Department of Civil and Environmental Engineering at the University of Illinois at Urbana-Champaign, USA, who thoroughly reviewed the first author’s Ph.D. thesis as external examiner. The observations and modifications suggested by Ph.D. examining committee members Dr. Alaa Elwi, Dr. Gary Faulkner and Dr. Hamid Soleymani are also appreciated.

## **ABSTRACT**

Recent concerns on the adverse effects of steel corrosion have prompted the use of non-corroding materials, such as Fibre-Reinforced Polymers (FRPs), as alternative to reinforce concrete slabs. To successfully implement FRP reinforcement in slab construction, it is necessary to understand the advantages and limitations of FRP as well as which materials work and which shapes or forms suit best a given application. Compared to ordinary steel reinforcement, FRP reinforcements display a lower stiffness, usually have a lower bond strength, and rupture in brittle fashion. Some FRP products even have a tendency to creep rupture. The effect of these distinctive features on the structural behaviour of concrete slabs have been just partially identified: the effect of the reduced stiffness and bond strength of FRP rebars and grids on the evaluation of average curvatures and average strains to calculate deflections in slabs is relatively well understood; however, the effects of these properties on the interactive relationship between crack widths and FRP strains at cracks have not been examined in detail. As far as shear design of one- and two-way slabs with FRP rebars and grids is concerned, existing design guidelines are mostly empirical and tests scarce. In regards to slab strengthening with FRP sheets, there is a need to study the feasibility of bonding FRP sheets to the slab surface as a rehabilitation vehicle.

This study examines numerous aspects of the flexural, shear and deformation behaviour of one-way and column-supported two-way concrete slabs reinforced with FRP bars, grids and sheets. The study identifies the conditions under which FRP deformed bars, 2-D grids and sheets are either beneficial or detrimental when used either as internal or external slab reinforcement. Design provisions are proposed to control cracks and deflections in one-way slabs with internal FRP rebars or grids, and to evaluate the punching shear capacity of column-supported slabs reinforced with FRP rebars, grids or sheets.



## RÉSUMÉ

Les inquiétudes récentes sur les effets défavorables de la corrosion de l'acier ont promu l'utilisation des matériaux non-corrosifs, les polymères renforcés de fibres (FRP) par exemple, comme moyens alternatifs pour renforcer les dalles de béton. Afin d'intégrer avec succès les renforcements de FRP dans la construction des dalles, il est nécessaire de comprendre les avantages et les limites des FRP et également quels matériaux et quelles formes s'adaptent le mieux à une application donnée. Les matériaux en FRP possèdent généralement une plus faible rigidité, une résistance à l'adhérence plus faible, et une rupture fragile par rapport à l'acier courant. Certains produits en FRP ont même tendance à se rompre par fluage. Les effets de ces caractéristiques distinctes sur le comportement structural des dalles en béton ont partiellement été identifiés. Les effets d'une rigidité réduite, de la résistance à l'adhérence des barres et des grillages en FRP sur le calcul des déformations dans les dalles sont relativement bien compris dans l'évaluation des courbures et des dilatations moyennes. Cependant, les effets de ces propriétés dans les relations entre la largeur des fissures et la dilatation des FRP sous-jacents n'ont pas encore été étudiés en détail. Pour le calcul des dalles uni-directionnelles ou bi-directionnelles avec des barres et des grillages en FRP, les recommandations existantes sont surtout empiriques et les essais sont rares. Il est donc nécessaire d'étudier l'efficacité de l'adhérence des plaques en FRP collées à la surface des dalles comme moyen de réhabilitation.

Cette recherche identifie les conditions où les barres, les grillages et les plaques en FRP ont, ou n'ont pas, d'effets bénéfiques lorsqu'ils sont utilisés comme renforcement interne ou externe. Des recommandations pour le calcul sont proposées pour contrôler les fissures et les déformations des dalles uni-directionnelles avec des barres et des grillages internes en FRP, et pour évaluer la capacité en cisaillement au poinçonnement des dalles supportées par des poteaux et renforcées par des barres, grillages ou plaques en FRP.

## RESUMEN

Recientemente, debido a los considerables problemas acarreados por la corrosión del acero de refuerzo, el uso de materiales anticorrosivos como los polímeros reforzados con fibras (FRP) ha aumentado como una alternativa para reforzar losas de concreto. Para implementar exitosamente este tipo de refuerzo en la construcción de este tipo de estructuras, es necesario evaluar sus ventajas y desventajas, así como también identificar cuáles materiales o formas son los que mejor cumplen una determinada función. Comparados con el acero de refuerzo ordinario, los refuerzos FRP poseen usualmente una menor rigidez, una menor adherencia al concreto y se fracturan frágilmente. Algunos productos, incluso, tienden a ceder y fracturarse con el tiempo ante una carga constante. Los efectos que estas propiedades tienen en el comportamiento estructural de losas reforzadas con estos elementos no han sido del todo examinados: los efectos que tanto la reducida rigidez como la baja adherencia de las varillas o mallas FRP tienen en la evaluación de curvaturas y deformaciones unitarias promedio para calcular deflexiones han sido estudiados en el pasado; sin embargo, los efectos de dichas variables en la interdependencia entre el ancho de las grietas en el concreto y la deformación en el refuerzo FRP no han recibido la atención que deberían. En lo que respecta al diseño a cortante de losas de concreto armadas en una ó dos direcciones con varillas o mallas FRP, las guías de diseño son netamente empíricas y la evidencia experimental escasa. En lo que respecta al uso de hojas FRP como elementos de refuerzo externo, las condiciones son igual de desalentadoras.

El presente estudio examina numerosos aspectos relacionados con el diseño a la flexión y al cortante por punzonamiento de losas de concreto reforzadas con varillas, mallas u hojas del tipo FRP. El estudio identifica las condiciones bajo las cuales dichos productos constituyen o no un apropiado vehículo para reforzar losas de concreto. Igualmente, se reportan guías de diseño encaminadas a controlar el agrietamiento y la deflexión de losas de concreto armadas con varillas o mallas de FRP en una dirección, y a predecir la capacidad ante el punzonamiento de losas soportadas por columnas, reforzadas en dos direcciones con varillas, mallas, u hojas FRP.

# TABLE OF CONTENTS

	<b>Page</b>
1 Introduction	1
1.1 Description of the Problem	1
1.2 Objective, Scope and Limitations	2
1.3 Organization	4
2 Observed Flexural and Shear Behaviour of Concrete Beams and Slabs with FRP Reinforcement	7
2.1 General	7
2.2 Flexural Tests on Concrete Beams and One-way Slabs Reinforced with Internal FRP Reinforcement	7
2.3 Flexural Tests on Two-way Slabs with Internal FRP Reinforcement	12
2.4 Punching Shear Tests on Two-way Slabs Reinforced with FRP	12
2.4.1 Two-way Slabs with Internal FRP Reinforcement	12
2.4.2 Two-way Slabs Rehabilitated with FRP Sheets	15
3 Background on Serviceability Flexural Behaviour of One-way Concrete Slabs With Internal FRP Reinforcement	17
3.1 General	17
3.2 Implications of Using FRP in the Flexural Design of One-way Concrete Slabs	17
3.3 Cracking in Steel-Reinforced Concrete Slabs	18
3.3.1 Mechanics of Crack Formation	19
3.3.2 Bond between Steel and Concrete	20
3.3.3 Concrete's Tension Stiffening Effect in Steel-reinforced Concrete Members	21
3.3.4 Crack Width and Crack Spacing Calculation Procedures	22
3.3.4.1 The Tension Chord Model	22
3.3.4.2 The CIRIA Model	25
3.3.4.3 The Gergely-Lutz Equation	26

3.3.4.4	ACI 318-99	26
3.4	Cracking in FRP-reinforced One-way Concrete Slabs	27
3.4.1	Bond Between FRP Bars or Grids and Concrete	27
3.4.1.1	Influential Parameters	27
3.4.1.2	Bond Tests of FRP-reinforced Concrete Specimens	29
3.4.1.3	Bond of FRP Relative to Steel	30
3.4.1.4	Bond of Grid-type FRP	31
3.4.2	Concrete's Tension Stiffening Effect in FRP-reinforced Concrete Members	32
3.4.3	Crack Width Calculations in Members with FRP	32
3.4.3.1	Empirical Approaches	32
3.4.3.2	Crack Width Calculation Using the Finite Difference Method	34
3.5	Serviceability Limit State of Deflections	34
3.5.1	Deflection Control Approaches in Steel-reinforced Concrete Slabs	35
3.5.1.1	Allowable Deflections	35
3.5.1.2	Direct Calculation of Deflections: Branson's Method	36
3.5.1.3	Deflection Calculation by Curvature Integration	36
3.5.1.4	Indirect Deflection Control	38
3.5.2	Direct Deflection Control in FRP-reinforced Concrete Slabs	38
3.5.3	Indirect Deflection Control in FRP-reinforced Concrete Slabs	41
4	Background on Punching of FRP-reinforced Concrete Slabs	51
4.1	General	51
4.2	Implications of Using FRP on Slab Punching Capacity	51
4.3	Methods for Estimating Punching Capacities in Steel-reinforced Slabs	52
4.3.1	The Control Surface Method	52
4.3.2	Yield Line Approach for Punching	54
4.3.3	Kinnunen and Nylander's Approach	54

4.3.4	Strip Model for Punching Shear	56
4.3.4.1	Fundamentals	56
4.3.4.2	Simplified Mathematical Formulation of the Strip Model	57
4.4	Existing Punching Shear Design Recommendations for Two-way Slabs Reinforced with FRP	59
4.4.1	Punching of Two-way Slabs with Internal FRP reinforcement	59
4.4.2	Punching of Two-way Slabs Rehabilitated with FRP Sheets	60
4.5	Other Strengthening and Repair Schemes for Slab-Column Connections	61
4.6	Observations	61
5	Experimental Program	67
5.1	Objectives	67
5.2	Series I Tests : Punching Shear Tests of Slabs with Internal FRP	67
5.2.1	Description of Test Specimens	67
5.2.2	Specimen Fabrication	68
5.2.3	Test Set-up	69
5.2.4	Instrumentation	69
5.2.5	Test Procedure	70
5.2.6	Ancillary Tests	70
5.2.6.1	Concrete	70
5.2.6.2	Steel Reinforcement	71
5.2.6.3	GFRP Reinforcement	71
5.3	Series II Tests : Punching Shear Strengthening and Rehabilitating Tests of Interior Slab-column Connections	73
5.3.1	Virgin Slab Design	74
5.3.2	Slab Formwork and Additional Slab Detailing	78
5.3.3	Specimen Fabrication	78
5.3.4	Test Apparatus	79
5.3.4.1	Supports	79

5.3.4.2	Loading Assembly	79
5.3.4.3	Edge Restraint System	80
5.3.5	Instrumentation	81
5.3.5.1	Load Measurement	81
5.3.5.2	Deflection Measurements	81
5.3.5.3	Rotation Measurements	82
5.3.5.4	Crack Measurements	82
5.3.5.5	Strain Measurements on Steel Reinforcement	83
5.3.5.6	Through-Slab Thickness Strains	83
5.3.5.7	Data Acquisition	84
5.3.6	Rehabilitation Techniques	84
5.3.6.1	General	84
5.3.7	Slab-Column Connection Strengthening with CFRP Sheets	84
5.3.7.1	Material Description	84
5.3.7.2	Test ER2-CS1: Rehabilitation Procedure	85
5.3.7.3	Test ER3-CS2: Rehabilitation Procedure	86
5.3.8	Slab-Column Connection Repair by Concrete Patching	86
5.3.9	FRP Sheet Instrumentation	88
5.3.9.1	FRP Sheet Strains	88
5.3.10	Loading Procedure	88
5.3.11	Ancillary Tests	89
5.3.11.1	Concrete for Virgin Slabs	89
5.3.11.2	Steel Reinforcement	89
5.3.11.3	FRP Sheets	89
6	Series I Test: Results, Observations and Evaluation	125
6.1	Load-deflection Response	125
6.2	Crack Widths	127
6.3	Strains in Slab Reinforcement	128
6.3.1	Notation	128
6.3.2	Validation of Strain Gauge Readings	128

6.3.3	Circumferential Strains	129
6.3.4	Forces in Slab Reinforcement	130
6.3.5	Bar Force Gradients	130
6.4	Internal Shears	132
6.5	Influence of Test Variables	133
6.5.1	Top Mat Stiffness Effect	133
6.5.2	Reinforcement Type Effect	134
6.6	Flexural Bond in Slabs with Internal FRP Reinforcement	134
6.6.1	Flexural Bond in GFRP C-bars	134
6.6.2	Flexural Bond in GFRP NEFMAC Grids	135
6.7	Failure Cause of Series I Slabs	136
6.7.1	Governing Failure Mechanism	136
6.7.2	Failure Mechanism in Slabs with GFRP NEFMAC Grids	138
7	Series II Tests: Results, Observations and Evaluation	157
7.1	Objectives	157
7.2	Overall Description of Structural Response	157
7.2.1	Response of Virgin Slabs	157
7.2.2	Response of Slabs Strengthened with CFRP Sheets	159
7.2.3	Response of Slabs Repaired with Concrete Patches	160
7.3	Measurements	161
7.3.1	Force and Moment Resultants	161
7.3.2	Slab Rotations	166
7.3.2.1	Edge Slab Rotations	166
7.3.2.2	Inner Slab Rotations	167
7.3.3	Crack Widths	167
7.3.3.1	Slab Surface Crack Widths	167
7.3.3.2	Through-thickness Crack Measurements	169
7.3.4	Strains in Internal Slab Reinforcing Bars	169
7.3.4.1	Circumferential Bar Force Profiles	170
7.3.4.2	Force Variation Along Perimeter Bars	170

7.3.5	Strains in CFRP Bands	172
7.3.6	Force Gradients in Internal Slab Reinforcement	172
7.3.7	Force Gradients in CFRP Bands	174
7.3.8	Internal Shears	174
7.3.9	Influence of CFRP Sheets	175
7.4	Behavioural Assessment of CFRP-Strengthened Slabs	176
7.4.1	Observations	176
7.4.2	The Role of the CFRP Sheets on the Failure of Rehabilitated Slabs	177
7.4.3	Behavioural Assessment of Slabs Repaired with Concrete Patches	181
8	Evaluation of the Serviceability Flexural Behaviour of Concrete Slabs with Internal FRP Reinforcement	215
8.1	Objectives	215
8.2	Flexural Bond in FRP-reinforced Concrete Members	216
8.3	Concrete's Tension Stiffening Effect in Members with FRP	218
8.4	Prediction of the Overall Flexural Response of Slabs with FRP	221
8.4.1	Application of the Overall Response Flexural Model	227
8.5	Cracking Model for Concrete Slabs Reinforced with FRP	229
8.5.1	Bond-induced Crack Spacing	229
8.5.2	Crack Spacing not Induced by Bond	231
8.5.3	Application of Cracking Model for FRP-reinforced Concrete Members in Flexure	232
8.5.3.1	Beams Reinforced with GFRP C-bars	233
8.5.3.2	One-way Members Reinforced with FRP Grids	234
8.5.3.3	Two-way Slabs Reinforced with GFRP C-bars	234
8.6	Parametric Study	235
8.6.1	Members in Direct Tension	235
8.6.2	Slabs in Flexure	236
8.7	Concluding Statements	239



8.7.1	Deflection Calculations	239
8.7.2	Crack Control in Slabs with FRP	240
8.7.2.1	Conclusions Based on Crack Width Estimates	240
8.7.2.2	Conclusions Based on Estimates of FRP Strains at Cracks	241
9	Deflection Control in One-way Concrete Slabs with Internal FRP Reinforcement	257
9.1	Objective	257
9.2	Indirect Deflection Control Procedures	257
9.2.1	Simplified Procedure Disregarding Concrete's Tension Stiffening Effect	257
9.2.2	Simplified Procedure Accounting for Concrete's Tension Stiffening Effect	260
9.2.3	Procedure Based on $I_e$ Concept	263
9.2.4	Simplified Procedure based on Curvature Integration	268
9.3	Concluding Statements	270
10	Punching of Column-supported Two-way Concrete Slabs Reinforced or Strengthened with FRP	277
10.1	Objectives	277
10.2	Punching of Concrete Two-way Flat Plates with Internal FRP Reinforcement	277
10.2.1	Evaluation of Existing Design Procedures	277
10.2.2	Proposed Empirical Model	282
10.2.3	Comparison of the Existing and Proposed Empirical Models	283
10.2.4	Proposed Mechanical Model	284
10.2.4.1	Fundamentals	284
10.2.4.2	Calculation of the $M_s$ Term in Slabs with FRP Reinforcement	285
10.2.4.3	Calculation of the $w$ Term in Slabs with	

FRP Reinforcement	287
10.2.5 Evaluation of Modified Strip Model for Punching of Slabs with Internal FRP Reinforcement	288
10.3 Punching Shear of Concrete Flat Plates Strengthened with FRP Sheets	289
10.3.1 Proposed Model	289
11 Conclusions and Recommendations	301
11.1 General	301
11.2 Flexural Behaviour	301
11.2.1 Slabs with Internal FRP Reinforcement	301
11.3 Punching Shear Behaviour	303
11.3.1 Slabs with Internal FRP Reinforcement	303
11.3.2 Slabs with External FRP Reinforcement	303
11.3.3 Miscellaneous Rehabilitation Techniques	304
11.4 Design Recommendations	304
11.4.1 Slabs with Internal FRP Reinforcement	304
11.5 Recommendations for Future Research	305
List of References	307
Appendix A Fibre Reinforced Polymer (FRP) Reinforcement: Description, History, Properties, Landmark Applications	323
Appendix B Derivation of the Bond-slip Differential Equation and Formulation of the Tension Chord Model for Linear-Elastic Reinforcement	335
Appendix C Selected Pictures of Experimental Program	345
Appendix D Properties of Flexural Test Specimens Examined	351
Appendix E Derivation of Indirect Deflection Control Procedure for Concrete Beams and One-way Concrete Slabs with Internal FRP Reinforcement Using Branson's Concept, According with Thériault's Definition of $I_e$	353
Appendix F Properties of Punching Test Two-way Slab Specimens with Internal FRP Bars and Grids	355

# LIST OF TABLES

		Page
Table 3.1	Maximum Permissible Computed Deflections (CSA A23.3-94)	42
Table 3.2	Recommended Tension Steel Reinforcement Ratios for Non-prestressed One-way Members to Render Acceptable Deflections (ACI Com. 435, 1978)	42
Table 3.3	Thickness below which deflections must be computed for non- prestressed beams or one-way slabs <u>not</u> supporting or attached to partitions or other construction likely to be damaged by large deflections	43
Table 5.1	Series I Slabs : Properties	91
Table 5.2	Series II Slabs : List of Tests	91
Table 5.3	Mechanical Properties of CFRP Sheets	92
Table 5.4	Series II Slabs : Ancillary Test Results	92
Table 6.1	Series I Slabs : Test Results	139
Table 7.1	Series II Slabs : Test Results	183
Table 8.1	Comparison of Deflection Calculations for $M = 2M_{cr,exp}$	243
Table 10.1	Test to Predicted Ratios : Punching Tests on Slabs with Internal FRP Reinforcement	294
Table 10.2	Test to Predicted Ratios : Series II Slab Tests	295
Table A.1	Classification of FRP Reinforcement (After Fukuyama, 1999)	331
Table A.2	Typical Mechanical Properties of Some Commercially Available FRP Reinforcing Bars and Grids (After ISIS M04-00)	332
Table A.3	Mechanical Properties of Some Commercial FRP Sheet Systems (After ISIS M04-00)	332
Table D.1	Properties of Flexural Test Beam Specimens with Internal FRP Bars or Grids	351
Table F.1	Properties of Punching Test Two-way Slab Specimens with Internal FRP Bars or Grids	355

## LIST OF FIGURES

	<b>Page</b>
Figure 3.1	Flexural Response of Members with FRP 43
Figure 3.2	Stresses in Concrete Prism Subjected to Axial Tension After First and Second Crack Formation 44
Figure 3.3	Splitting Effect on Bond-slip Response 45
Figure 3.4	Concrete's Tension Stiffening Effect 45
Figure 3.5	Stress-strain Response of Tension Chord 46
Figure 3.6	Effective Concrete Area in Tension (CEB/FIP MC90) 46
Figure 3.7	Concrete and Steel Stress Distributions in Terms of Crack Spacing According to Tension Chord Model (After Alvarez, 1998) 47
Figure 3.8	Typical Bond-slip Response of FRP (Pull-out Tests) 48
Figure 3.9	Tension Stiffening in ACI, CSA and CEB/FIP Codes 48
Figure 3.10	Deflections using Curvature Integration 49
Figure 3.11	Idealised Moment-Curvature Response for Members with FRP (Razaqpur <i>et al</i> , 2000) 49
Figure 3.12	Deflection Calculations for Members with FRP According to CSA S806-00 50
Figure 4.1	Effect of $\rho_s$ on Punching Capacity (After Criswell, 1974) 63
Figure 4.2	Control Surfaces for Punching Capacity Evaluation in ACI, CSA and BS Codes 63
Figure 4.3	Fundamental Concepts of Strip Model for Punching (After Alexander and Simmonds, 1991) 64
Figure 4.4	Free Body Diagram of Radial Strip According to Strip Model 65
Figure 5.1	Geometry of Series I Test Specimens 93
Figure 5.2	Types of Reinforcement : Series I Slabs 93
Figure 5.3	Reinforcement Details : Series I Slabs 94
Figure 5.4	Top Reinforcement and Gauge Layout : Slab SR-1 95
Figure 5.5	Top Reinforcement and Gauge Layout : Slab GFR-1 96
Figure 5.6	Top Reinforcement and Gauge Layout : Slab GFR-2 97

Figure 5.7	Top Reinforcement and Gauge Layout : Slab NEF-1	98
Figure 5.8	Anchor Detail : Slabs GFR-1 and GFR-2	99
Figure 5.9	NEFMAC Grid Handling	99
Figure 5.10	Reinforcing Mat : SR-1	100
Figure 5.11	Reinforcing Mat : GFR-1	100
Figure 5.12	Reinforcing Mat : GFR-2	101
Figure 5.13	Reinforcing Grid : NEF-1	101
Figure 5.14	Test Set-up : Series I Slabs	102
Figure 5.15	Test Set-up : Series I Slabs	103
Figure 5.16	LVDT Location : Series I Slabs	103
Figure 5.17	Detail of GFRP Tension Coupons	104
Figure 5.18	Stress-Strain Curves : Series I Slab Reinforcement	104
Figure 5.19	Slab Dimensions : Series II Slabs	105
Figure 5.20	Top Slab Reinforcement and Gauge Layout - Series II Slabs -	106
Figure 5.21	Bottom Slab Reinforcement and Gauge Layout - Series II Slabs -	107
Figure 5.22	Typical Reinforcing Cage : Series II Slabs	108
Figure 5.23	Slab Concreting : Series II Slabs	108
Figure 5.24	Slab Lifting Procedure : Series II Slabs	109
Figure 5.25	Test Set-up Process : Series II Slabs	109
Figure 5.26	Typical Test Set-up : Series II Slabs	110
Figure 5.27	Test Set-up View from SW Corner : Series II Slabs	111
Figure 5.28	Lower Column Support : Series II Slabs	111
Figure 5.29	Edge Restraint System and Loading Set-up Details : Series II Slabs	112
Figure 5.30	Cable Transducer Locations : Series II Slabs	113
Figure 5.31	Horizontal LVDT Array for Slab Rotations : Series II Slabs	114
Figure 5.32	Top Crack Width Measurement Stations	114
Figure 5.33	Strengthening Layout on Test ER2-CS1	115
Figure 5.34	Strengthening Layout on Test ER3-CS2	116
Figure 5.35	FRP Installation : Surface Finishing (ER2-CS1)	117
Figure 5.36	FRP Installation : Finished Surface (ER2-CS1)	117
Figure 5.37	FRP Installation : Sheet Bonding (ER2-CS1)	118

Figure 5.38	FRP Installation : Final Result (ER2-CS1)	118
Figure 5.39	Concrete Patching Technique : Test ER1-CP1	118
Figure 5.40	Concrete Patching Technique : Test ER3-CP2	120
Figure 5.41	Concrete Patching : Jack Hammering	121
Figure 5.42	Concrete Patching : Formwork Detail (ER1-CP1)	121
Figure 5.43	Concrete Patch : Top View (ER1-CP1)	122
Figure 5.44	Concrete Patch : Bottom View (ER1-CP1)	122
Figure 5.45	Response of Steel Rebar and CFRP in Tension	123
Figure 6.1	Response of Series I Slabs	140
Figure 6.2	Crack Pattern : SR-1	140
Figure 6.3	Crack Pattern : GFR-1	141
Figure 6.4	Crack Pattern : GFR-2	141
Figure 6.5	Crack Pattern : NEF-1	142
Figure 6.6	Underside N-S Slab Deflections : SR-1 & NEF-1	142
Figure 6.7	Underside Slab Rotations : Series I Slabs	143
Figure 6.8	Ave. Crack Widths : Series I Slabs	143
Figure 6.9	Ave. Crack Widths : Series I Slabs	144
Figure 6.10	Strain Gauge Layout Plans : Series I Slabs	144
Figure 6.11	Moment Equilibrium Check : GFR-1	145
Figure 6.12	Moment Equilibrium Check : NEF-1	145
Figure 6.13	Ave. Circumferential Top Mat Strains : SR-1	146
Figure 6.14	Ave. Circumferential Top Mat Strains : GFR-1	146
Figure 6.15	Ave. Circumferential Top Mat Strains : GFR-2	147
Figure 6.16	Ave. Circumferential Top Mat Strains : NEF-1	147
Figure 6.17	Force Along Bar C : SR-1	148
Figure 6.18	Force Along Bar C : GFR-1	148
Figure 6.19	Force Along Bar C : GFR-2	149
Figure 6.20	Force Along Rib C : NEF-1	149
Figure 6.21	Bar Force Gradients - Bar A : SR-1	150
Figure 6.22	Bar Force Gradients - Bar A : GFR-1	150
Figure 6.23	Bar Force Gradients - Rib A : NEF-1	151

Figure 6.24	Bar Force Gradients - Perimeter Bars : SR-1	151
Figure 6.25	Bar Force Gradients - Perimeter Bars : GFR-1	152
Figure 6.26	Rib Force Gradients - Perimeter Ribs : NEF-1	152
Figure 6.27	Measured Bar Shears : SR-1	153
Figure 6.28	Measured Bar Shears : GFR-1	153
Figure 6.29	Measured Bar Shears : NEF-1	154
Figure 6.30	Shear Transfer Assessment : Series I Slabs	154
Figure 6.31	Flexural Bond Behaviour of NEFMAC Grid	155
Figure 6.32	Compression Fans and Shear Crack : Slab NEF-1	155
Figure 6.33	Elevation View of Dissected Slab NEF-1	156
Figure 7.1	Load-deflection Response : ER1-VS	184
Figure 7.2	Load-deflection Response : Slab ER2	184
Figure 7.3	Load-deflection Response : Slab ER3	185
Figure 7.4	Load-deflection Response : ER1-CP1	185
Figure 7.5	Load-deflection Response : ER3-CP2	186
Figure 7.6	Typical Crack Pattern in Virgin Slab at a 18 kPa Applied Load	187
Figure 7.7	Crack Pattern at Failure : ER1-VS	188
Figure 7.8	Crack Pattern at Failure : ER2-CS1	189
Figure 7.9	Crack Pattern at Failure : ER3-CS2	190
Figure 7.10	Detail of CFRP Sheets After Column Push-through (ER3-CS2)	191
Figure 7.11	Tension Band Behaviour of CFRP Sheets	191
Figure 7.12	Punching Failure : ER1-CP1	192
Figure 7.13	Punching Failure : ER3-CP2	192
Figure 7.14	Plan View of Vertical Forces and Moments Acting on Slab	193
Figure 7.15	Free Body Diagrams for Moment Calculations	194
Figure 7.16	Vertical Force Statics Check : ER1-VS	195
Figure 7.17	Negative Moment Intensity Comparison : ER1-VS	195
Figure 7.18	Positive Moment Intensity Comparison : ER1-VS	196
Figure 7.19	Negative to Panel Moment Ratio : ER1-VS	196
Figure 7.20	Positive to Panel Moment Ratio : ER1-VS	197
Figure 7.21	Average Edge Slab Rotations : ER1-VS	197

Figure 7.22	ERS Rotational Stiffness : ER1-VS	198
Figure 7.23	Radial Slab Rotation : ER2 Tests	198
Figure 7.24	Top Crack Widths : ER2-VS	199
Figure 7.25	Bottom Crack Widths : ER3-VS	199
Figure 7.26	Top Crack Widths : ER2 Tests	200
Figure 7.27	Bottom Crack Widths : ER2-CS1	200
Figure 7.28	Slab Thickening (N-S) : ER3-VS	201
Figure 7.29	Top Strain Gauge Key Plans : Series II Slabs	202
Figure 7.30	Bar Forces - Gridline 1 : ER3-VS	203
Figure 7.31	Cracking Effect on Bar Forces : ER1-VS	203
Figure 7.32	Bar Force Variation - Bar D : ER1-VS	204
Figure 7.33	Bar Force Profile - Bar B : ER1-VS	204
Figure 7.34	Bar Force Profile - Bar B : ER2 Tests	205
Figure 7.35	Bar Force Profile - Bar D : ER1-VS	205
Figure 7.36	Bar Force Profile - Bar D : ER3 Tests	206
Figure 7.37	CFRP Longitudinal Strains (Ave WE) : ER2-CS1	206
Figure 7.38	CFRP Longitudinal Strains (WE-1) : ER3-CS2	207
Figure 7.39	Bar Force Gradients (2 <sup>nd</sup> Interval) : ER1-VS	207
Figure 7.40	Bar Force Gradients (2 <sup>nd</sup> Interval) : ER2 Tests	208
Figure 7.41	Bar Force Gradients (2 <sup>nd</sup> Interval) : ER3 Tests	208
Figure 7.42	CFRP Force Gradients (W-E) : ER2-CS1	209
Figure 7.43	CFRP Force Gradients (N-S) : ER3-CS2	209
Figure 7.44	Ratio of Int. Measured to Total Applied Load (ER3 Tests)	210
Figure 7.45	Bar Force Gradients (2 <sup>nd</sup> Interval) : Bar B	210
Figure 7.46	Bar Force Gradients (2 <sup>nd</sup> Interval) : Bar D	211
Figure 7.47	Bar Force Gradients (2 <sup>nd</sup> Interval) : Bar F	211
Figure 7.48	Strain Distributions in Slab Element with and without Bonded FRP	212
Figure 7.49	FBDs for Sections with and without FRP Sheets	213
Figure 7.50	Influence of Reinforcement Amount and Type on $x_{fs}$	214
Figure 7.51	Shear Crack Formation Hypothesis	214
Figure 8.1	Effect of $\rho$ and $E_r$ on Tension Stiffening	244



Figure 8.2	Crack Spacing : Sherbrooke Beams (1)	244
Figure 8.3	Crack Spacing : Sherbrooke Beams (2)	245
Figure 8.4	Idealised Moment-Curvature Response According to Proposed Model	245
Figure 8.5	Strain Distributions According to CSA S806-00	246
Figure 8.6	Assumed Strain Distributions at Failure	246
Figure 8.7	$\zeta$ Factor as a Function of $\rho$ and $E$	247
Figure 8.8	Curvature Correction due to Concrete's Tension Stiffening Effect	247
Figure 8.9	Assumed Curvature Distribution for Beam under Four Point Bending	248
Figure 8.10	Idealised Load-Deflection Response	248
Figure 8.11	Flexural Model Calibration : Slab TB BC2VA	249
Figure 8.12	Flexural Model Calibration : Slab TB BC4NA	249
Figure 8.13	Flexural Model Calibration : Slab MT C3	250
Figure 8.14	FRP Tension Chord Response (After Alvarez, 1998)	250
Figure 8.15	Crack Width – FRP Stress Relationship	251
Figure 8.16	FRP and Concrete Stress Distributions (Crack Spacing not Induced by Bond)	251
Figure 8.17	Crack Width Predictions : Beam TB BC2VA	252
Figure 8.18	Crack Width Predictions : Beam TB BC4NA	252
Figure 8.19	Crack Width Predictions : Beam MT H3	253
Figure 8.20	Crack Width Predictions : Slab GFR-1	253
Figure 8.21	Effect of $\sigma_{fr}$ , $E_f$ and $f'_c$ on Crack Width	254
Figure 8.22	Effect of $\rho_f$ on Crack Width	254
Figure 8.23	Effect of FRP Bond Strength on Crack Width	255
Figure 8.24	$E_f$ and $w_f$ Effect on FRP Strain at Crack	255
Figure 8.25	$E_f$ and $h$ Effect on FRP Strain at Crack	256
Figure 8.26	Bond Effect on FRP Strain at Crack	256
Figure 9.1	Reinforcement Strain Effect on Span-Depth Ratio	272
Figure 9.2	FRP Strain Effect on Span-Depth Ratio	272
Figure 9.3	Concrete Strain Effect on Span-Depth Ratio	273

Figure 9.4	Bond Effect on Span-Depth Ratio	273
Figure 9.5	Max. Span-Depth Ratio Based on $I_e$ Concept	274
Figure 9.6	Midspan and Column Strain Distributions for Curvature Integration-based Deflection Control	274
Figure 9.7	Effect of $k$ on Slab Deflections	275
Figure 9.8	Effect of Midspan FRP Strain and $k$ on $L/d$	275
Figure 10.1	Effect of $f'_c$ on Eq. 10.1 Predictions	296
Figure 10.2	Effect of $\rho_f$ on Eq. 10.1 Predictions	296
Figure 10.3	Size Effect on Eq. 10.1 Predictions	297
Figure 10.4	Effect of $E_f/E_s$ on Eq. 10.2 Predictions	297
Figure 10.5	Effect of $E_f/E_s$ on Eq. 10.1 Predictions	298
Figure 10.6	FRP Sheet Strengthening Scheme	298
Figure 10.7	Proposed Model : FBD of Half a Radial Strip with FRP Bands	299
Figure A.1	Schematic of Pultrusion Process	333
Figure A.2	Typical Response in Tension of FRP and Constituents	328
Figure A.3	Typical Response in Tension of Rebars	334
Figure B.1	Differential Element for Derivation of Tension Chord Model Formulation	342
Figure B.2	Crack Spacing-dependent Stress Distributions According to Tension Chord Model (After Alvarez, 1998)	343
Figure B.3	Tension Chord Forces After First Cracking	344
Figure B.4	Stress-Strain Response of Tension Chord (After Alvarez, 1998)	344
Figure C.1	Typical Test Set-up (Virgin Slab)	345
Figure C.2	Typical Test Set-up (Virgin Slab)	345
Figure C.3	Whiffle Tree Detail	346
Figure C.4	Edge Restraint System Effect	346
Figure C.5	Test ER1-VS (Before Punching)	347
Figure C.6	Test ER1-VS (After Punching)	347
Figure C.7	Test ER2-CS1 : Strengthening Layout	348
Figure C.8	Test ER2-CS1 : Slab Punching	348
Figure C.9	Test ER3-CS2 : Strengthening Layout	349

Figure C.10	Test ER3-CS2 : Slab Punching	349
Figure C.11	Slab Repair (Test ER3-CP2)	350
Figure C.12	Concrete Patch (Test ER3-CP2)	350

# LIST OF ABBREVIATIONS AND SYMBOLS

## ABBREVIATIONS

ACI	American Concrete Institute
ASCE	American Society of Civil Engineers
ASTM	American Society for Testing and Materials
CSA	Canadian Standards Association
FRP	Fibre Reinforced Polymer

## SYMBOLS

### Roman Symbols

$a$	Depth of compressive stress block at ultimate
$a_v$	Shear span
$A_f$	Area of longitudinal FRP reinforcement
$A_{f,ef}$	Effective area of longitudinal FRP reinforcement
$A_s$	Area of longitudinal steel reinforcement
$A_{s,ef}$	Effective area of longitudinal steel reinforcement
$b$	Beam or slab width
$b_f$	Width of FRP sheet
$b_i$	Normalized length of splitting failure line
$b_o$	Critical perimeter for punching shear capacity evaluation
$c$	Depth of compressive stress block
$c_c$	Clear concrete cover
$c_w$	Column width
$d$	Effective flexural slab or beam depth
$d_c$	Concrete cover measured from the centroid of the tension reinforcement to extreme tension surface
$E_c$	Elastic modulus of concrete
$E_{cf}$	Elastic modulus of carbon fibre
$E_f$	Elastic modulus of FRP rebars

$E_{fs}$	Elastic modulus of FRP sheets
$E_s$	Elastic modulus of steel
$f_c$	Average concrete compressive stress
$f_{cfm}$	Tensile concrete stress at the FRP reinforcement centroid at midspan
$f_{cfu}$	Ultimate tensile strength of carbon fibre
$f_{ck}$	Characteristic compressive strength of concrete
$f_{cm}$	Mean compressive strength of concrete
$f_{ct}$	Tensile strength of concrete
$f_{ctm}$	Mean tensile strength of concrete
$f_f$	Stress in FRP
$f_{fp}$	Stress in FRP at punching
$f_{fs}$	Stress in FRP at service load conditions
$f_{fu}$	Ultimate tensile strength of FRP
$f_r$	Concrete's modulus of rupture
$f_{su}$	Ultimate tensile strength of steel
$f_y$	Yield strength of steel reinforcement
$f'_c$	Specified cylinder strength of concrete
$f'_{spt}$	Splitting tensile strength of concrete
$g$	Distance from FRP sheet's innermost edge to column face
$h$	Slab thickness or beam full depth
$h_1$	Distance from tension reinforcement centroid to neutral axis
$h_2$	Distance from the extreme tension surface to neutral axis
$I$	Moment of inertia
$I_{cr}$	Cracked moment of inertia
$I_e$	Effective moment of inertia
$I_g$	Gross moment of inertia
$I_t$	Moment of inertia of the cross-section transformed to concrete
$I_1$	Moment of inertia in state I
$I_2$	Moment of inertia in state II
$j$	Ratio of flexural lever arm to effective flexural depth

$k$	Ratio of FRP strain at support to FRP strain at midspan at service load level
$k_{bo}$	Bond constant
$k_{ts}$	Tension stiffening factor
$k_v$	Constant for punching shear capacity equation calibration
$k_w$	Modification factor in strip model punching formulation for slabs with internal FRP
$k_\varepsilon$	FRP strain-based constant in El-Ghandour <i>et al</i> 's punching capacity equation
$K_l$	Constant depending on boundary conditions
$K_b$	Bond coefficient in CSA S806-00 crack control equation
$K_g$	Bond coefficient in Thériault and Benmokrane's crack width equation
$l$	Loaded length of slab radial strip
$l_n$	Centre-to-centre slab span in the transverse direction
$l_o$	Transfer length
$l_2$	Clear slab span in the longitudinal direction
$L$	Span length
$L_g$	Uncracked beam portion length from support
$m$	Bending moment intensity
$m_o$	Panel moment intensity
$m_r$	Bending moment resistance intensity
$m_{r,col}$	Bending moment resistance intensity of column strip
$M_a$	Applied moment
$M_{cf}^-$	Negative moment at column face
$M_{cr}$	Cracking moment
$M_m$	Midspan moment
$M_{neg}$	Negative moment
$M_o$	Statical or panel moment
$M_{pos}$	Positive moment
$M_r$	Nominal moment resistance
$M_s$	Flexural capacity of radial strip
$M_{s,neg}$	Negative flexural capacity of radial strip

$M_{s,pos}$	Positive flexural capacity of radial strip
$M_{sg}^+$	Strain gauge-based positive moment
$M_{sg,g1}^-$	Strain gauge-based negative moment at gauge gridline 1
$M_{sg,g2}^-$	Strain gauge-based negative moment at gauge gridline 2
$M_u$	Ultimate moment
$n$	Modular ratio (Steel's elastic modulus divided by concrete's elastic modulus)
$n_f$	Modular ratio (FRP sheets' elastic modulus divided by concrete's elastic modulus)
$p$	Coefficient depending on cement type
$P$	Applied point load
$P_f$	Factored load
$P_{flex}$	Flexural capacity of an isolated slab specimen in a punching shear test
$P_r$	Nominal load resistance
$P_s$	Load capacity of radial strip
$q$	Uniformly distributed load per unit area
$q_u$	Uniformly distributed load per unit area at ultimate
$q_{u,ACI}$	Uniformly distributed load per unit area at ultimate, according to ACI code
$q_{u,SM}$	Uniformly distributed load per unit area at ultimate, according to Strip Model
$R_i$	Point reaction in series II test set-up
$s$	Crack spacing
$s_f$	FRP reinforcement spacing
$s_m$	Mean crack spacing
$s_{m,c}$	Mean constrained crack spacing (not induced by bond)
$s_{max}$	Maximum crack spacing
$s_{min}$	Minimum crack spacing
$s_s$	Steel reinforcement spacing
$t$	Time
$t_f$	Thickness of FRP sheet
$v_c$	Shear strength of concrete
$V_{bar}$	Bar shear

$V_{cf}$	Shear force at column face
$V_r$	Nominal punching shear resistance
$V_u$	Observed punching shear capacity
$w$	Uniformly distributed load per unit length
$w_{DL}$	Uniformly distributed dead load per unit length
$w$	Uniformly distributed load per unit length acting on radial strip, for slabs with internal steel reinforcement
$w_f$	Crack width in a beam or slab with internal FRP reinforcement
$w_{f,e}$	Uniformly distributed load per unit length acting on radial strip, for slab with externally bonded FRP reinforcement
$w_{f,i}$	Uniformly distributed load per unit length acting on radial strip, for slabs with internal FRP reinforcement
$w_m$	Mean crack width
$w_{max}$	Maximum crack width
$w_{min}$	Minimum crack width
$w_{ms}$	Mean crack width on tension surface
$w_{m,c}$	Mean constrained crack width
$w_s$	Crack width in a beam or slab with internal steel reinforcement
$x$	Distance, neutral axis depth
$x_{cr}$	Distance from support to outermost flexural crack in shear span
$x_{fs}$	Neutral axis depth in a member with FRP reinforcement at service load level
$x_m$	Neutral axis depth at midspan
$x_s$	Neutral axis depth at a support
$x_{ss}$	Neutral axis depth in a member with steel reinforcement at service load level
$z$	Crack width control factor

### **Greek Symbols**

$\alpha$	Ratio of slab/beam thickness to effective flexural depth
$\alpha_b$	Bond coefficient for $I_e$ calculation of beams and slabs with FRP
$\alpha_l$	Ratio of average stress in rectangular compression block to the specified



	concrete compressive strength according to CSA A23.3-94
$\beta$	Combined bond and performance factor in CEB/FIP MC90
$\beta_b$	Correction factor for $I_e$ calculation of beams and slabs with FRP
$\beta_{cc}$	Time-dependent coefficient to calculate aging effect on concrete compressive strength
$\beta_1$	Concrete stress block factor in CSA A23.3-94; bond factor in CEB/FIP MC90
$\beta_2$	Performance factor in CEB/FIP MC90
$\delta$	Slip
$\Delta$	Beam or slab deflection
$\Delta_{all}$	Allowable beam or slab deflection
$\Delta_m$	Midspan beam or slab deflection
$\Delta_s$	Deflection at service load level
$\Delta_u$	Beam or slab deflection at ultimate
$\Delta\epsilon_{ts}$	Normal strain correction due to concrete's tension stiffening effect
$\Delta\epsilon_{ts,c}$	Normal strain correction due to concrete's tension stiffening effect under constrained crack spacing conditions
$\Delta\psi_{ts}$	Curvature correction due to concrete's tension stiffening effect
$\epsilon_{cm}$	Mean concrete strain
$\epsilon_{cs}$	Concrete strain at service load level
$\epsilon_{csm}$	Midspan concrete strain at extreme compression fibre at service load level
$\epsilon_{css}$	Concrete strain at extreme compression fibre at service load level at support
$\epsilon_{cu}$	Concrete strain in extreme compression fibre at ultimate
$\epsilon_f$	FRP strain
$\epsilon_{fcr}$	Midspan FRP strain immediately before first flexural cracking
$\epsilon_{fm}$	Mean strain in the FRP reinforcement
$\epsilon_{fr}$	Strain in the FRP reinforcement at a crack

$\epsilon_{fs}$	FRP strain at service load level
$\epsilon_{fsm}$	Midspan FRP strain at service load level
$\epsilon_{fss}$	FRP strain at service load level at support
$\epsilon_{fu}$	Tensile strain in FRP at ultimate (rupture strain)
$\epsilon_m$	Mean strain
$\epsilon_r$	Reinforcement strain at a crack
$\epsilon_s$	Steel strain
$\epsilon_{sm}$	Mean strain in the steel reinforcement
$\epsilon_{sr}$	Strain in the steel reinforcement at a crack
$\epsilon_{ss}$	Steel strain at service load level
$\phi$	Ratio of experimental punching failure load to flexural failure load
$\phi_b$	Bar diameter
$\phi_c$	Material reduction factor for concrete
$\phi_f$	Material reduction factor for FRP
$\phi_s$	Material reduction factor for steel
$\gamma$	Ratio of mean constrained crack spacing to maximum crack spacing
$\eta$	Moment of inertia factor in Razqpur <i>et al</i> 's deflection calculation procedure
$\lambda$	Ratio of mean to maximum crack spacing
$\lambda_f$	Ratio of mean to maximum crack spacing in a slab with FRP reinforcement
$\lambda_s$	Ratio of mean to maximum crack spacing in a slab with steel reinforcement
$\rho_f$	FRP reinforcement ratio
$\rho_{f,bal}$	Balanced FRP reinforcement ratio
$\rho_{f,ef}$	Effective FRP reinforcement ratio
$\rho_{fs}$	Radial strip's FRP reinforcement ratio
$\rho_{fs,neg}$	Radial strip's negative flexural FRP reinforcement ratio
$\rho_{fs,pos}$	Radial strip's positive flexural FRP reinforcement ratio

$\rho_s$	Steel reinforcement ratio
$\rho_{s,bal}$	Balanced steel reinforcement ratio
$\rho_{s,ef}$	Effective steel reinforcement ratio
$\sigma_{fr}$	Stress in the FRP reinforcement at a crack
$\sigma_{fro}$	Stress in the FRP reinforcement at a crack immediately after first cracking
$\sigma_{fm}$	Mean stress in the FRP reinforcement
$\sigma_{sr}$	Stress in the steel reinforcement at a crack
$\sigma_{sro}$	Stress in the steel reinforcement at a crack immediately after first cracking
$\sigma_{sm}$	Mean stress in the steel reinforcement
$\tau_b$	Bond stress
$\tau_{bo}$	Peak bond stress in rigid-perfectly plastic bond-slip formulation
$\tau_{b,max}$	Maximum bond stress
$\tau_{b,sp}$	Splitting bond strength
$\psi$	Curvature
$\psi_{ave}$	Average curvature
$\psi_{cr}$	Curvature at first cracking
$\psi_m$	Midspan curvature
$\psi_{m,ave}$	Average midspan curvature
$\psi_u$	Curvature at ultimate
$\psi_1$	Curvature in state I
$\psi_2$	Curvature in state II
$\xi$	Tension stiffening factor in CEB/FIP MC 90
$\omega_f$	FRP reinforcement index
$\zeta$	Stiffness factor

# **1 Introduction**

## **1.1 Description of the Problem**

One and two-way steel-reinforced concrete slabs constitute basic structural forms in concrete construction. Their design process is similar. The slabs are proportioned to comply with the ultimate limit states of flexure, shear and torsion, as well as serviceability requirements. One- and two-way steel-reinforced concrete slab systems have been successfully built for more than 80 years. Sozen and Siess (1963), and Fürst and Marti (1997) document their evolution process in North America and Europe, respectively.

Rising concerns regarding the adverse effects of steel corrosion in concrete structures have prompted the introduction of non-corroding materials, such as Fibre-reinforced Polymers (FRPs), as alternative to reinforce concrete. FRPs are made from thin high-strength continuous fibres impregnated in a resin. The most common fibre types are carbon (CFRP), glass (GFRP) and Aramid (AFRP). The ability to tailor FRPs into different shapes (bars, grids, strips and sheets), together with their superior corrosion resistance, magnetic neutrality, and high strength-to-weight and stiffness-to-weight ratio, makes them very appealing for slab construction. Appendix A presents a history of their development and a summary of their mechanical properties and landmark applications.

To successfully use FRP reinforcement in slab construction, it is necessary to understand the advantages and limitations of FRPs as well as which materials work and which shapes or forms suit best a given application. Under direct tension, FRPs display a brittle-elastic response that is in most cases much more flexible than that of steel. This raises some questions as to whether existing serviceability and ultimate limit state flexural and shear design procedures for steel-reinforced concrete slabs can be safely applied to FRP-reinforced concrete slabs. Due to the reduced stiffness of FRP reinforcement, FRP-reinforced concrete slabs are also prone to exhibit greater deflections and crack widths at the serviceability limit state level. From an ultimate strength perspective, the FRP elastic-

brittle nature renders conventional flexural design procedures that rely on any form of moment redistribution not applicable.

Today, after a decade of using FRPs to reinforce bridge decks, airport compass and radio pads, and hospital Magnetic Resonance Imaging (MRI) slabs, the effects of the distinctive features of FRP on the structural behaviour of concrete slabs have not received all the attention they deserve. Unlike the case of calculating deflections in flexural members from average curvatures and average strains, the effects of the reduced stiffness and bond of FRP reinforcement on the relationship between crack widths and FRP strains at cracks have not been examined in detail. Because of the superior corrosion resistance of FRP, it is often heard that cracks in FRP-reinforced members should be controlled based solely on aesthetics reasons. This is a fallacy because, as pointed out by Burgoyne (1993), the strain concentrations at cracks may lead to excessive FRP strain values for a given crack width. This is of particular relevance for GFRP-reinforced concrete slabs under sustained load because GFRP is prone to creep rupture.

As far as shear design of one- and two-way slabs with internal FRP reinforcement is concerned, existing design guidelines are mostly empirical, relying on a scarce experimental test result database. In regards to shear strengthening of two-way slabs with external FRP reinforcement, there is a need to study the feasibility of bonding FRP sheets to the slab top surface as a strengthening vehicle. Recognizing that the majority of existing punching shear models do not always explain the true cause of punching of ordinary slabs, and that no analytical model for punching of newly built or rehabilitated slabs with FRP has been devised, such examination finds ample justification.

## **1.2 Objectives, Scope and Limitations**

The main objectives of this study are i) to produce test results on two-way concrete slabs reinforced with internal or external FRP reinforcement, and ii) to examine the mechanism of load transfer in one- and two-way concrete slabs reinforced with FRP rebars, grids or sheets, with the ultimate goal of identifying the conditions under which FRP deformed

bars, FRP 2-D grids, and CFRP sheets can be effectively used to reinforce or strengthen concrete slabs. The following aspects will be examined:

- 1) The effect of the lower stiffness, bond strength and brittle-elastic nature of FRP reinforcement on the flexural and shear response of one- and two-way concrete slabs with internal FRP reinforcement.
- 2) The effect of bonding FRP sheets in cruciform patterns on the top surface of two-way concrete slabs as a slab strengthening vehicle.

The observations will lead to the development of design recommendations aimed at predicting crack widths and FRP strains at cracks in one-way FRP-reinforced slabs, controlling deflections in one-way FRP-reinforced slabs, and predicting the punching capacity of two-way slabs with internal or external FRP reinforcement.

Since the examination of the response of FRP-reinforced concrete members will be directly referred to concepts already established within the framework of steel-reinforced concrete slabs, this study is also expected to provide a better insight into the behaviour of ordinarily reinforced concrete slabs, especially on issues related to flexural cracking of one-way slabs and punching shear behaviour of two-way slabs. The study will also examine different procedures to repair ordinary concrete slabs that have punched.

This work examines two aspects of slab behaviour. Firstly, the flexural response will be examined in the context of one-way members with internal FRP reinforcement subjected to short-term monotonic loads. Temperature effects are not examined. Most of the attention will concentrate on the serviceability limit state of design. Second, the study investigates the punching shear behaviour of interior slab-column connections with either internal or external FRP reinforcement. For slabs with internal FRP reinforcement, most of the attention is concentrated on GFRP deformed bars and 2-D grids. For slabs with external FRP reinforcement, only the effects of CFRP sheets bonded to the top slab surface are assessed. Only punching due to concentric gravity-type loading conditions is examined. Slabs with shear reinforcement in the form of stirrups or studs are not

considered. The shear behaviour of one-way slabs and beams with internal FRP reinforcement or surface-bonded FRP sheets is investigated but does not receive as much attention as that in two-way slabs.

### **1.3 Organization**

Chapter 2 presents a summary of the experimental programs pertinent to this study that have been reported in the past. The attention is concentrated on those examining the flexural capacity of beams and slabs with internal FRP reinforcement and the punching capacity of two-way concrete slabs reinforced with internal FRP rebars and grids, or strengthened with bonded FRP sheets.

Chapter 3 presents the fundamental principles and theories for the serviceability flexural design of one-way steel-reinforced concrete slabs and existing analytical and experimental information for the same type of behaviour in concrete beams and one-way slabs with internal FRP reinforcement. Based on what is known for ordinary slab design, the chapter discusses the implications of using internal FRP reinforcement to reinforce concrete slabs for flexure.

Chapter 4 reports available punching shear test results and design recommendations for steel-reinforced, FRP-reinforced and FRP sheet-strengthened concrete flat plates. The chapter discusses the implications of using FRPs as internal or external slab reinforcement on the punching shear response of concrete flat plates.

Chapter 5 reports details of the experimental program carried out by the author. It consisted of two test series. The first series examines the punching shear behaviour of interior slab-column connections with internal FRP rebars and grids. The second series examines the punching shear behaviour of interior slab-column connections i) strengthened with externally bonded CFRP sheets and ii) repaired with concrete patches.

Chapter 6 presents the results, experimental observations and evaluation of results from series I tests. Chapter 7 reports the same information for series II tests. The results and

observations are used to describe the interaction between FRP reinforcement and concrete in order to explain the role of FRP and the failure cause of the slabs.

Chapter 8 examines the serviceability flexural behaviour of one-way concrete slabs and beams with internal FRP reinforcement. It examines the implications that the reduced stiffness, bond strength and non-yielding nature of FRP reinforcement have on tension stiffening, crack widths, reinforcement strains at cracks and average strains. A procedure is presented to predict the load-deflection response of one-way concrete slabs and beams reinforced with FRP, and calculate crack widths and FRP strains at cracks.

Chapter 9 examines the effect of the mechanical and material properties of FRP reinforcement on the punching capacity of concrete slabs. It evaluates the adequacy of existing design rules to evaluate the punching capacity of interior slab-column connections with FRP rebars or grids, or with bonded FRP sheets. It presents one empirical and one analytical model to predict the punching capacity of interior slab-column connections with FRP rebars and grids, and one analytical model to predict the punching capacity of interior slab-column connections with bonded FRP sheets.

Chapter 10 proposes indirect deflection control procedures in slabs with internal FRP reinforcement.

Chapter 11 presents a compendium of conclusions, proposed design recommendations and suggestions for future research.

Six appendices are reported. Appendix A presents a brief history of the development of FRP reinforcement. Appendix B presents a detailed derivation of the bond-slip differential equation and the fundamentals of the tension chord model. Appendix C presents a pictorial of relevant aspects of series II tests. Appendix D presents a summary of the geometric and material properties of test specimens loaded in four point bending reported in the literature. Appendix E presents the derivation of an indirect deflection control procedure for concrete beams and one-way slabs based on a modification of



Branson's effective moment of inertia proposed by Thériault (1998). Finally, Appendix F presents a summary of the geometric and material properties of the test specimens examined by researchers who have studied the punching shear behaviour of two-way concrete slabs with internal FRP reinforcement.

## **2 Observed Flexural and Shear Behaviour of Concrete Beams and Slabs with FRP Reinforcement**

### **2.1 General**

This chapter presents a summary of reported experimental observations from tests studying the flexural behaviour of one and two-way members with internal FRP rebars and grids, and the punching behaviour of two-way slabs with internal and external FRP reinforcement. These observations serve as a preamble for background concepts that will be thoroughly explored in chapters 3 and 4.

### **2.2 Flexural Tests on Concrete Beams and One-way Slabs Reinforced with Internal FRP Reinforcement**

Complete lists of references on the flexural behaviour of one-way members with internal FRP reinforcement are provided by ACI Committee 440 (1996) and Hall (2000). The following provide experimental evidence that will be used later in this study.

The first tests on concrete beams reinforced with glass-fibre rods were reported by **Nawy, Neuwerth and Phillips (1971)**. They tested beams with 3 mm dia. GFRP straight rods and beams with 3.2 mm dia. steel rebars with similar reinforcement ratios (0.19 to 0.41 % for GFRP and 0.22 to 0.45 % for steel). The concrete compressive strength varied from 28 to 35 MPa.

The load-deflection response of the beams with GFRP was essentially bilinear. No significant difference in the cracking load was observed due to the presence of GFRP. The flexural stiffness reduced significantly after first cracking. The slope of the load-deflection response through the elastic-cracked stage increased with the GFRP reinforcement ratio. At a given load level, the cracks in the GFRP-reinforced beams were wider than those in the beams with steel reinforcement. (Note: the above observations are representative of the flexural behaviour of beams and slabs with internal FRP reinforcement. They will not be repeated).

Nawy *et al* noted that the beams with GFRP also developed more cracks than those with steel reinforcement suggesting that the glass fibre reinforcement they used was “capable of developing good mechanical bond”. At failure, the deflection in the beams with GFRP was about three times greater than that for similar beams with steel reinforcement. Provided that long-term conditions do not affect the strength of GFRP, Nawy *et al* concluded that a very high factor of safety is available against failure for members reinforced with FRP.

The previous reference raised considerable discussion. Chandrasekhar (1972) commented that a comparison between the response of GFRP- and steel-reinforced beams should be based on the reinforcement index and not on the reinforcement ratio. Huang (1972) emphasized that the "reserve strength" of the beams with GFRP reinforcement is a drawback instead of an advantage. Huang added that "unless very high overload can be reasonably expected to occur... the large load factor cannot be justified, and the unused strength is wasted". This comment was shared by Kirstein (1972) and Almeida (1972), who inquired whether the term "reserve strength" should refer instead to an "unavailable strength". Almeida (1972) noted that the only areas where the high tensile stress of GFRP could be utilized are in prestressing operations or in the fabrication of precast prestressed concrete prisms to be used as beam reinforcement. This type of application has been recently explored by Švecová (1999).

**Nawy and Neuwerth (1977)** reported additional test results on 14 simply supported beams over-reinforced with GFRP reinforcement. The GFRP reinforcement ratio was the main variable, varying from 0.7 to 2.54 %.

In this set of beams, the beams with lower FRP amount developed fewer cracks, which contradicts previous observations of Nawy *et al* (1971). Removal of the load resulted in an almost full closing up of the cracks, as would occur in unbonded post-tensioned concrete members. At about 35 % of the ultimate load, they found the deflections to be within tolerable limits. Crack widths fell within allowable limits up to 20 % of the ultimate load. At failure, the ultimate strength of the GFRP could not be developed.

Nawy and Neuwerth concluded that using GFRP reinforcement should permit higher tolerable crack widths due to the non-corrosive nature of GFRP.

**Faza and GangaRao (1992a and 1993a)** presented test results and a summary of design aspects for members with GFRP. They note that the phenomenon of developing moment resistance in FRP-reinforced beams is identical to that of beams with steel reinforcement, provided that adequate bond between FRP and concrete develops. Due to the inability of the FRP-reinforced beams tested by Nawy and Neuwerth (1977) to develop the full strength of FRP, Faza and GangaRao recommended using high strength concrete in lightly-reinforced beams with FRP to maximize their bending resistance.

**Nakano, Matsuzaki, Fukuyama and Teshigawara (1993)** conducted flexural tests on ten beams, identical in shape, varying the type of reinforcement (AFRP, CFRP and steel), the tensile reinforcement ratio (from 0.28 to 3.23 %), and the compressive strength of concrete (either 29.4 or 76.5 MPa). They concluded that the flexural response of beams reinforced with FRP bars can be evaluated by means of conventional methods used in concrete beams with steel bars and noted that compressive flexural failures are preferred.

**Nanni (1993)** described the conceptual implications of using FRP deformed bars as non-prestressed reinforcement for flexural members. He remarked on the importance of controlling deflections in beams with FRP due to FRP's reduced stiffness. Due to FRP's brittle behaviour, Nanni noted that flexural compressive failures are preferred over flexural tension failures. Moreover, since the flexural strength of an FRP over-reinforced cross-section depends on the compressive strength of concrete, FRP reinforcement should be used in combination with high-strength concrete. He noted that the use of FRP rebars as a non-prestressed reinforcement does not result in material savings and that their use should be motivated essentially on durability aspects.

**Schmeckpeper and Goodspeed (1994)** reported tests on five beams with CFRP grids and five with hybrid carbon/glass (HFRP) grids. The response of these beams was compared to that of three control steel-reinforced specimens. The main variable was the

FRP content. The governing failure mechanism of the over-reinforced beams with FRP was either flexural due to concrete crushing or diagonal shear. They concluded that FRP grids are a potentially viable replacement for steel in concrete structures but warn that the acceptance of FRP is influenced by its non-yielding nature and its low stiffness.

Based on their test results from eight one-way concrete slabs reinforced with GFRP and CFRP bars, **Michaluk, Rizkalla, Tadros and Benmokrane (1998)** remarked that over-reinforced slabs with GFRP could fail in shear. They warn that further research is necessary prior to allowing massive use of GFRP as slab reinforcement.

**Masmoudi, Thériault and Benmokrane (1998)** examined the serviceability and ultimate flexural behaviour of beams with GFRP. They conducted tests on four sets of over-reinforced beams with GFRP deformed bars with reinforcement ratios varying from 0.56 to 2.15 %. Concrete compressive strength ranged from 45 to 52 MPa. The GFRP-reinforced beams with 0.56 % FRP reinforcement were designed to display a balanced failure.

They observed that the average crack spacing in beams with GFRP is comparable to that of steel-reinforced beams at load levels below 25 % of the ultimate load. At greater levels, the average crack spacing was 65 % of that of beams with steel. The cracks in the beams with GFRP were three to five times wider than those in the companion steel-reinforced beams. They found that the effect of the reinforcement ratio on the crack spacing is negligible. According to them, crack widths in members with FRP “should be controlled only for reason of undesirable appearance”.

**Thériault and Benmokrane (1998)** further investigated the effect of the reinforcement ratio and the concrete strength on the flexural response of beams with GFRP. The GFRP reinforcement ratio was either 1.16 or 2.77 %. Three concrete compressive strengths were examined for each reinforcement ratio: normal strength, high strength and very high strength. Each beam was duplicated.

Despite the fact that all beams were designed to fail due to concrete crushing, those with lower concrete strength failed in shear. Failure was blamed on the wide crack formation and the lower dowel action from FRP. One striking observation from this test series is that in two sets of identical beams (BC2VA-BC2VB and BC4NA-BC4NB), one of the twin beams failed in flexure due to concrete crushing and the other failed in shear.

**Matthys and Taerwe (2000b)** reported flexural test results on seven one-way slabs reinforced with carbon and hybrid carbon and glass FRP NEFMAC grids. The reinforcement ratio varied from 0.18 to 3.76 %. Six slabs were made out of normal strength concrete (around 30 MPa), whereas one slab was cast with 96.7 MPa concrete. Their research work provides a thorough coverage of serviceability and ultimate strength features of FRP grid-reinforced concrete one-way slabs.

They showed that the design of slabs with FRP is governed essentially by serviceability criteria. To ensure enough flexural stiffness, higher reinforcement ratios or depths are needed. They recognized that the full tensile strength of FRP can be rarely used up. For their over-reinforced slabs, they found that the margin between the service load and the ultimate load could be much higher than that for steel-reinforced members. They concluded that crack control in FRP-reinforced members is less restrictive than deflection control and recommended using FRP materials with good bond characteristics. For the particular case of FRP grids, they recommended using grids with closely spaced transverse ribs. Since most of their slabs displayed concrete crushing at strains in the order of  $5500 \mu\epsilon$ , they suggest that current concrete strain limits for ultimate flexural design need to be further evaluated. In summary, they concluded that FRP can not be considered as a complete substitute for steel. Other merits of the material, such as its corrosion-free nature, low conductivity and low weight should be its assets.

**Yost, Schmeckpeper and Goodspeed (2001)** evaluated the flexural performance of simply supported concrete beams with 2-D GFRP grids. The main variable was the amount of GFRP. Five beam sets of three beams each were designed to fail in flexure. Three were under-reinforced ( $\rho_f = 0.0012, 0.0021$  and  $0.0041$ ) and two were over-

reinforced ( $\rho_f = 0.127$  and  $0.135$ ). The cross-sectional beam dimensions were not constant. A single steel-reinforced concrete beam was tested as a control beam.

All beams failed in flexure except those with  $\rho_f = 0.0021$ , which failed in shear. The shear failure was attributed to a loss in aggregate interlock due to the presence of wide cracks. The tests show that the grids ensure adequate force transfer to develop the axial strength of the longitudinal ribs. They report that the flexural capacity of the beams can be predicted using the concepts accepted for steel-reinforced concrete members and note that over-reinforced conditions are preferred to compensate for the reduced stiffness and brittle-elastic nature of FRP. They note that the same conclusions, except those related to force transfer assessment, should apply to concrete beams with deformed GFRP bars.

## **2.3 Flexural Tests on Two-way Slabs with Internal FRP Reinforcement**

Nawy and Neuwerth (1977) conducted tests on 12 two-way 1067 mm square GFRP rod reinforced slab panels subjected to a uniformly distributed external pressure. The main variable was the GFRP content (0.29 to 0.77 %). The response of the slabs was also bilinear. The slope of the response curve in the cracked stage increased with the amount of FRP. Reducing the grid spacing led to an increased number of cracks. Cracks were also narrower. Crack widths increased almost linearly with a load increase. Failure was defined at the level at which the slabs became thoroughly distorted. At failure, the GFRP rods still had a significant reserve strength.

## **2.4 Punching Shear Tests on Two-way Slabs Reinforced with FRP**

### **2.4.1 Two-way Slabs with Internal FRP Reinforcement**

To the author's best knowledge, the only punching shear test results of column-supported two-way slabs with FRP 2-D grids or deformed bars available in the literature are those reported by Banthia, Al-Asaly and Ma (1995), Matthys and Taerwe (1997, 2000a and 2000c) and El-Ghandour, Pilakoutas and Waldron (1997, 2000). Ahmad, Zia, Yu and Xie (1993) reported punching tests on two-way slabs reinforced with 3-D FRP grids.

**Ahmad, Zia, Yu and Xie (1993)** reported punching shear test results on four two-way concrete slab panels reinforced with 3-D CFRP grids and two control slabs reinforced with steel reinforcement. The slabs were 690 mm by 690 mm square and 76 mm thick. The effective depth was 41 mm for the slabs with CFRP and 61 mm for the control slabs. The reinforcement ratio was 0.95 % (for all three directions) for the CFRP-reinforced slabs, and 1.18 and 1.35 % in the  $x$  and  $y$  directions, respectively, for the slabs reinforced with steel rebars. The concrete compressive strength was 30 MPa. The slabs were simply supported along their sides.

Their test results show that the pre-cracking behaviour and initial stiffness of the CFRP-reinforced slabs and conventional slabs are similar. However, the slabs with CFRP grids exhibited a significant stiffness reduction after first cracking.

**Banthia, Al-Asaly and Ma (1995)** studied the punching behaviour of two-way concrete slabs reinforced with CFRP NEFMAC grids. They tested four 600 mm square 75 mm thick concrete slabs under concentric punching. Three slab panels were reinforced with NEFMAC grids and one with steel. One of the NEFMAC-reinforced panels was built with fibre-reinforced concrete. The slabs were simply supported along the edges over a clear span of 500 mm and the load was applied on a 100 mm dia. cylindrical column stub. The main variables were the slab reinforcement type, the concrete strength and the presence or not of conventional fibres. Findings related to the effect of conventional fibres will not be considered herein. In the slabs reinforced with CFRP, the NEFMAC ribs were  $20.54 \text{ mm}^2$  in cross-section spaced at 102 mm. The effective depth was 55 mm. Ancillary test results rendered a composite tensile strength of 1200 MPa and an elastic modulus of 100 GPa. For the slab with steel, a wire mesh with a centre-to-centre bar spacing of 102 mm and a circular cross-section of  $19.62 \text{ mm}^2$  was used.

Banthia *et al* found that concrete slabs with CFRP grids absorb less energy than comparable slabs with steel reinforcement. All of their CFRP slabs failed due to reinforcement rupture. They suggest that no significant changes are needed to conventional code design provisions when extending them to FRP-reinforced slabs.



The experimental work reported by **Matthys and Taerwe (1997, 2000c)** is the most extensive test program to date on punching of two-way slabs with FRP grids. They report tests on 17 1000 mm square slabs reinforced with either deformed steel rebars (series R), CFRP NEFMAC grids (series C), CFRP sanded rebars (series CS) and hybrid carbon glass (series H). The slab thickness varied from 120 to 150 mm. Sixteen slabs were cast with 30 MPa nominal compressive strength concrete, one with high strength concrete.

Matthys and Taerwe concluded that there is a strong interaction between shear and flexural effects on the slab response. The response was also seen to depend on the bond behaviour of the reinforcement. For slabs with comparable flexural strength, the FRP-reinforced slab displayed a lower punching capacity and a less stiff response through the cracked stage than its steel-reinforced companion. They also observed that increasing either the FRP reinforcement ratio or the slab thickness leads to a FRP-reinforced slab response comparable to that of steel-reinforced slabs. They showed that existing punching shear design procedures need to be modified for the case of FRP-reinforced slabs.

**El-Ghandour, Pilakoutas and Waldron (1997, 1999)** reported test results of four two-way slabs with either GFRP or CFRP reinforcing bars. Two of the slabs had shear reinforcement (results will not be examined here). The slabs without shear reinforcement, SG1 (GFRP) and SC1 (CFRP), were 2000 mm square, 175 mm thick and had a 200 x 200 x 200 lower column stub. Slabs SG1 and SC1 had, respectively, 11 and 9 - 8.5 mm dia. GFRP bars spaced at 200 mm.

**El-Ghandour, Pilakoutas and Waldron (2000)** reported additional test results on slabs with FRP with greater reinforcement ratio. Two slabs, SG2 and SG3, were reinforced with 21 GFRP bars of this kind spaced at 100 mm. SC2 had 19 bars spaced at 100 mm. They found that bond between FRP and concrete has a tremendous effect on the response of FRP-reinforced slabs. For the case of slabs with low FRP reinforcement ratio, bond slip is viewed as the main cause of failure.

#### **2.4.2 Two-way Slabs Rehabilitated with FRP Sheets**

To the author's knowledge, the only punching shear tests available on two-way slab panels strengthened with FRP-sheets are those reported by Erki and Heffernan (1995), Chen and Li (2000), and Tan (2000). Gold and Nanni (1998) reported the use of bonded CFRP sheets in cruciform patterns in the negative moment region for the upgrading a post-tensioned concrete two-way concrete slab in Winston-Salem, North Carolina (US).

**Erki and Heffernan (1995)** investigated the effect of slab strengthening using FRP sheets. They reported test results of one and two-way slab panels with FRP sheets. The slab panels were 1000 by 1000 by 50 mm. Concrete strength was either 37 or 40 MPa. One one-way and two two-way slabs were tested as control specimens. The remaining panels were strengthened on their tension face with unidirectional GFRP or CFRP sheets. All slabs were subjected to transverse patch loads. The one-way slabs were supported on two parallel sides whereas the two-way slabs were simply supported on all four sides. The fibres were orientated at either 0 or 45 degrees, in one or two directions. The width of the CFRP sheets was 800 mm for all slabs except those with sheets orientated at 45 degrees which had 300 mm wide sheets.

The FRP strengthening led to an increase in slab stiffness and strength. However, Erki and Heffernan show that the sheet orientation affects the degree of stiffness gain. The lower stiffness increase came from the slabs strengthened with fibres at 45 degrees.

**Chen and Li (2000)** conducted tests on 18 interior two-way slab-column connection specimens strengthened with GFRP sheets. The specimens had a 1000 mm square and 100 mm thick slab with a 150 by 150 by 150 mm column stub. Specimens were divided in two series: series 1 (0.56 % steel ratio) and series 2 (1.23 % steel ratio). All slabs were simply supported along the edges and loaded from above at the column stub. Since the GFRP sheets covered the whole slab surface, slab cracks could not be observed.

Series 1 control specimens did not punch but rather failed in flexure. The other slabs punched. At failure, GFRP developed only 40% of their ultimate tensile strength. No signs of peeling between the sheets and concrete were noticed. Sheet peeling occurred after re-loading the slabs after the peak load. Chen and Li found that bonding GFRP sheets increases the punching capacity of the slabs. The effectiveness of GFRP increases for slabs with lower concrete compressive strength and steel reinforcement ratio. They also observed that the strength enhancement is not proportional to the number of GFRP layers.

**Tan (2000)** tested twelve 1000 mm square 35 mm thick slabs with either bonded CFRP plates, CFRP sheets or GFRP fabric. The slabs were reinforced internally with 6 mm diameter welded wire steel mesh spaced at 100 mm in the two directions. The effective depth of the welded mesh was 22 mm. In the slabs with CFRP plates, the plates were either 40 or 80 mm wide, spaced at either 125, 155 or 250 mm. For the slabs with CFRP sheets or GFRP fabric, the FRP covered the entire slab surface. For all three strengthening techniques, the FRP was applied in one or two directions. For the slabs with CFRP sheets and GFRP fabric, one or more layers were applied. The slabs were simply supported and loaded in the centre.

Tan found that unidirectional slab strengthening with FRP does not lead to a significant punching capacity increase. For the slabs strengthened in two directions, the punching capacity increased with the reinforcing index of the FRP.

### **3 Background on Serviceability Flexural Behaviour of One-way Concrete Slabs with Internal FRP Reinforcement**

#### **3.1 General**

This chapter reports existing design rules to control cracks and deflections in one-way FRP-reinforced concrete slabs subjected to flexure. The chapter starts by discussing the implications of the lower stiffness and brittle-elastic nature of FRP on the response of FRP-reinforced slabs. Since most available design procedures have evolved from rules applicable to steel-reinforced members, a thorough review of the latter is presented.

#### **3.2 Implications of Using FRP in the Flexural Design of One-way Concrete Slabs**

As noted by Nanni (1993) and Matthys and Taerwe (2000b), among others, the design of FRP-reinforced concrete beams and slabs is mainly governed by serviceability criteria. The reasoning behind this observation is explained with the aid of Fig. 3.1.

Figure 3.1 shows the load-deflection response of three slabs in flexure. The slabs have comparable cross-section and concrete strength but different reinforcement type and content. The curves correspond to an under-reinforced concrete slab with ordinary steel reinforcement (S), a FRP-reinforced slab (G1) with a FRP mat of lower stiffness than that of the steel-reinforced slab, and a FRP-reinforced slab (G2) with a FRP mat of similar stiffness to that in slab S. The plot shows the load level at service conditions,  $P_s$ , the factored load at ultimate,  $P_f$ , and the allowable deflection,  $\Delta_{all}$ , at service level.

The response of slab S idealizes typical under-reinforced conditions: it displays the elastic-uncracked (0-1), elastic-cracked (1-2) and post-yielding (2-3) stages. This slab fails due to concrete crushing after steel yielding.

The response of G1 and G2 represent the behaviour of slabs under-reinforced and over-reinforced with FRP. Their uncracked response is identical to that of S1 because a change in the reinforcing mat stiffness does not have significant implications on the cracking

load. However, once flexural cracking develops, the two responses diverge. Due to its lower flexural stiffness, slab G1 deforms much more than G2 for the same load level. Since G2 has the same mat stiffness as does S, the slope of the load-deflection curves for S and G2 in the cracked-elastic stage is the same. Neglecting the plastic deformation of concrete, the slope of segments 1-1' and 1-2' in G2 and G1, respectively, is constant up to failure because FRP does not yield. Slab G1 fails due to FRP rupture. G2 fails due to concrete crushing.

The objective of the slab design is to comply with the following requirements:

$$\Delta_s \leq \Delta_{all} \quad [3.1]$$

$$P_f \leq P_r \quad [3.2]$$

where  $\Delta_s$  is the deflection at service load level.

The curves in Fig. 3.1 show that all three slabs, regardless of the amount and type of reinforcement, satisfy at least the second condition. However, only slabs S and G2 satisfy the deflection requirement. G1 displays excessive deflections at service load levels. For a slab with FRP to comply with the serviceability limit state, the slab must have enough flexural stiffness. This is achieved by either over-reinforcing the slab or thickening it. Faza and GangaRao (1993b) recommended using high strength concrete to improve the performance of lightly reinforced slabs with FRP. This may increase the initial stiffness of the member but, once cracks form, the response is governed by the top mat stiffness.

### 3.3 Cracking in Steel-Reinforced Concrete Slabs

As noted by Leonhardt (1977), cracks in concrete structures are virtually unavoidable. Crack control is necessary to limit deflections, maintain appearance and prevent steel corrosion. Cracking in slabs is a relevant issue because slabs are usually lightly-reinforced. Since the cracked transformed moment of inertia of a lightly reinforced member is much smaller than its gross moment of inertia, cracking leads to a significant loss of stiffness which results in greater slab deflections (Scanlon, 1999).

The main parameters that characterize cracking in steel-reinforced slabs are the crack width and the crack spacing. As noted by Gergely and Lutz (1967), it is difficult to quantify these parameters because of the large scatter inherent to cracking and to the effects that many variables have on the problem.

### 3.3.1 Mechanics of Crack Formation

The steel-reinforced concrete prismatic member subjected to direct tension shown in Fig. 3.2 will be used to describe the mechanics of crack formation due to imposed loads. Before cracking, the strains in concrete and steel are compatible throughout the member. Concrete stresses are equal to  $f_c$  and stresses in the reinforcement are equal to  $nf_c$ , where  $n$  is the modular ratio,  $n = E_f/E_c$ .

The first crack forms randomly at a weaker spot when the concrete stress exceeds the tensile strength of concrete,  $f_{ct}$ . When concrete cracks, the tensile force carried by the concrete is transferred to the steel. As shown in Fig. 3.2a, the stress in the steel at the first crack,  $\sigma_{sr,1}$ , becomes greater than that immediately before first cracking,  $nf_{ct}$ . Once the first crack forms, the concrete tries to spring back to its original state but is restrained by the steel reinforcement through bond stresses. The transfer of tensile stresses back to concrete occurs along a distance  $l_o$  from each side of a crack. This “transfer length” defines a discontinuity region (Walraven, 2000) in which strain compatibility between concrete and steel is not maintained. The accumulation of strain differences produces relative displacements or "slips" between the reinforcement and concrete. The width of a crack at the level of the reinforcement is the sum of the two slips reaching the crack from both sides. At this level, the member is said to have entered the "single crack formation" stage (Balázs, 1993, 1999).

Bond stresses affect the distribution of stresses in both steel and concrete in the crack vicinity. The contribution of concrete tensile stresses to increase the overall axial stiffness of the member is referred to as concrete’s tension stiffening effect. This effect depends largely on the bond-slip interaction between concrete and steel, the elastic modulus of

steel and the tensile strength of concrete, as noted by Rostásy, Koch, and Leonhardt (1976), Leonhardt (1977) and ACI Committee 224 (1986).

If the load is increased, concrete stresses exceed  $f_{ct}$  at a new location, and a second crack forms at a distance  $s$  away from the first crack (see Fig. 3.2b). Concrete is now free from stress at the two cracks. The distribution of bond stresses near the second crack is qualitatively similar to that at the first crack except that the slip at the first crack is greater.

The crack formation process continues until the level of tensile stresses that can be built up in the concrete between two neighbouring cracks is less than the cracking strength of concrete. This stage is referred to as the “stabilised cracking phase” (Balázs, 1993, 1999). In this study, most of the attention will be concentrated on this behavioural stage.

### **3.3.2 Bond between Steel and Concrete**

A detailed description of the mechanics of bond between concrete and steel and information on different bond test set-ups can be found in FIB Bulletin 10 (2000) and Alvarez (1998). This section highlights what is meant by “bond” in the context of cracking resulting from tension or bending.

Working Party 8 of CEB Task Group *Bond Models* (FIB Bulletin 10, 2000) describes bond as a complex phenomenon influenced by many parameters which may lead to different failure mechanisms. Two modes of failure govern bond between deformed steel reinforcing bars and concrete: i) bar pull-out, and ii) concrete splitting. The former occurs when concrete between the bar lugs fails in a combination of shear and compression. The latter occurs when the circumferential component of the bursting forces generated by the interaction between steel and concrete exceeds the tensile strength of concrete (Tepfers, 1973).

Figure 3.3 illustrates the difference between these two failure modes. The bond-slip response linked to a pull-out failure is shown with curve A-G. Splitting-driven failure is

shown as path ABCDF'G'. The peak bond stress is lower in the latter. Any conceptual bond-slip model should identify the differences between these two failure modes.

Bond stresses are usually estimated from tests. The tests should be conducted on specimens that are representative of entire structural members in which the behaviour can be assessed on a relevant aspect of performance. Unfortunately, this is rarely satisfied. Base (1982) remarks that the concept of bond in reinforced concrete is “nebulous”. The bond stress is difficult to measure and define because the term “bond stress” means different things to researchers. For instance, most of the test results have been produced from pull-out tests. Base (1982) remarks that such a test is of little help in a study of the relationship between bond and cracks in members subjected to direct tension or bending.

### 3.3.3 Concrete's Tension Stiffening Effect in Steel-reinforced Concrete Members

Figure 3.4 shows the stress-strain response of a steel-reinforced concrete prismatic member subjected to direct tension. The solid line represents the relationship between the steel stress and the mean strain of the member. The dashed line indicates the response of the naked steel reinforcement. The strains in the latter refer to those at the crack.

The strain difference,  $\Delta\epsilon_{ts}$ , between the strain in the steel at a crack,  $\epsilon_{sr}$ , and the mean strain,  $\epsilon_{sm}$ , at a given stress level represents concrete's tension stiffening effect. This "strain correction" is greatest at first cracking and gradually reduces as the load increases because of bond deterioration (Bresler and Bertero, 1967). According to Rao (1966),

$$\Delta\epsilon_{ts} = k_{ts} \frac{f_{ct}}{\rho_s E_s} \quad [3.3]$$

where  $k_{ts}$  is a factor that depends on the steel stress at a crack, the bond stress distribution, the size of the concrete area in tension, and the distribution of concrete tensile stresses, as reported by Rostásy *et al* (1976). Consistent with Eq. 3.3, the tests of Rostásy *et al* (1976) and the analyses reported by Masicotte, Elwi and MacGregor (1990) show that concrete's tension stiffening effect becomes proportionally more significant when  $\rho_s$  reduces.



The complexity associated with the concepts of bond and concrete's tension stiffening suggests that some simplifications are required to treat these two phenomena. The following sections present different approaches to calculate crack widths and their spacing in steel-reinforced concrete members subjected to direct tension or flexure.

### **3.3.4 Crack Width and Crack Spacing Calculation Procedures**

#### **3.3.4.1 The Tension Chord Model**

This model is set up in terms of a simple yet complete formulation of the deformation process undergone by a reinforced concrete member by integrating the actual steel and concrete strains between cracks. Earlier formulations of the procedure were presented by Bachmann (1970), Bresler and Watstein (1974), Park and Paulay (1975), Rostásy, Koch and Leonhardt (1976), and Leonhardt (1977). Concepts from these procedures constitute the basis of the crack width calculation design rules for reinforced concrete members in CEB/FIP MC 90. The model has been lately the subject of considerable refinement and simplification by Sigrist and Marti (1994), Alvarez (1998), and Marti, Alvarez, Kaufmann and Sigrist (1998), who adopted the “Tension Chord Model” name. The concepts adopted in this study are those defined in the last three references.

A complete derivation of the model is presented in Appendix B. To allow future comparisons with FRP-reinforced members, the derivation has been performed assuming that the steel reinforcement remains elastic. Figure 3.5 shows the assumed stress-strain response of the cracked member in tension, as shown by Alvarez (1998). Figure 3.6 shows the dimensions of the tension chord relative to those of the entire cross-section in beams and slabs, according to CEB-FIP MC90.

One major feature of the tension chord model is the bond-slip constitutive relationship for steel. Acknowledging that the exact distribution of stresses in concrete and steel is not of primary interest as long as the resulting steel stresses and overall member strains reflect governing influences and match experimental data, Marti *et al* (1998) use a rigid-

perfectly plastic bond-slip relationship with a stepped descending branch that depends on yielding of steel.

Since the amount of slip in steel-reinforced concrete members is not significant at service load levels, CEB/FIP MC90 proposes a rigid-perfectly plastic bond-slip relationship for serviceability design of steel-reinforced concrete members:

$$\tau_{bo} = 1.8 f_{ctm} \quad [3.4]$$

where  $f_{ctm}$  is the mean tensile strength of concrete. This model, conceptually similar to that adopted by Walraven (2000), is the one adopted in Appendix B derivation.

Figure 3.7a (adapted from Alvarez, 1998) shows the distributions of stress for maximum crack spacing,  $s_{max}$ , for both steel and concrete. Due to the rigid-perfectly plastic nature of Eq. 3.4, the stresses vary linearly from the crack location to a point located midway between cracks. The dotted lines refer to mean stresses.

The stress distributions for minimum crack spacing,  $s_{min}$ , are shown in Fig. 3.7b. The model assumes that if the concrete stresses between cracks under maximum crack spacing conditions reach  $f_{ct}$  a new crack will form midway between those spaced at  $s_{max}$ . As a result, the mean crack spacing in the stabilised crack formation stage is bounded by the following limits:

$$\left( s_{min} = \frac{s_{max}}{2} \right) \leq s_m \leq s_{max} \quad [3.5]$$

or

$$0.5 \leq \left( \lambda = \frac{s_m}{s_{max}} \right) \leq 1.0 \quad [3.6]$$

where  $\lambda$  is a parameter introduced by Marti *et al* (1998). The mean crack spacing is

$$s_m = \lambda s_{max} = \frac{\lambda f_{ct} \phi_b}{2 \tau_{bo}} \left( \frac{1 - \rho_s}{\rho_s} \right), \quad 0.5 \leq \lambda \leq 1.0 \quad [3.7]$$

Due to the bond-slip simplification, the tension-stiffened response in the stabilised cracking stage (see Fig. 3.5) is parallel to that of the naked bar. Accordingly,

$$\Delta \varepsilon_{ts} = \frac{\lambda}{2} \frac{f_{ct}}{E_s} \frac{(1 - \rho_s)}{\rho_s} \quad [3.8]$$

The tension stiffening effect is maximum for  $s = s_{max}$ , and minimum for  $s = s_{min}$ .

The factor  $\lambda$  is statistical in nature. It depends on the variability of  $f_{ct}$ , the bond quality of the reinforcement and the proximity of cracks. Deák, Hamza and Visnovitz (1997) show that the distribution of crack spacing in steel-reinforced concrete members is log-normal. Walraven (2000) and CEB/FIP MC90 recommend  $\lambda = 0.75$  in steel-reinforced members. When cracking is not controlled by bond (as would be the case of cracks induced by curvature accommodation (see Base, 1982) or stress raisers such as stirrups or any other transverse reinforcement type), the  $\lambda$  concept lacks sense since  $s_m$  becomes deterministic.

Crack widths can be evaluated by solving the following differential bond-slip equation (see derivation in Appendix B).

$$\frac{d^2 \delta(x)}{dx^2} = \frac{4\tau_b(\delta(x))}{\phi_b E_s} \left( 1 + \frac{n\rho_s}{1 - \rho_s} \right) \quad [3.9]$$

However, the solution of Eq. 3.9 is not trivial for two reasons. First, since the bond stress,  $\tau_b$ , is a function of the slip,  $\delta$ , a closed form solution is difficult to obtain. Martin (1972) arrived at a solution but it is too complex for standardization. Second, the solution depends on whether the member has reached the stabilised cracking stage. If this is the case, and assuming  $s < 2l_o$ , the higher steel strains in the stabilised crack formation phase lead to a non-zero value for the change of slip,  $\delta'$ , midway between cracks. This becomes an initial condition for Eq. 3.9. As a result, a closed-form solution is difficult to obtain and numerical integration procedures have to be invoked (Balázs, 1993, 2000).

The tension chord model overcomes this problem by assuming that the mean crack width in the stabilised cracking stage can be calculated as

$$w_m = s_m (\varepsilon_{sm} - \varepsilon_{cm}) \quad [3.10]$$

where  $s_m$  is the mean crack spacing,  $\varepsilon_{sm}$  is the mean steel strain, both at the given load level, and  $\varepsilon_{cm}$  is the mean concrete strain at the end of the single crack formation phase. Based on the concrete stress distributions of Fig. 3.7,

$$\varepsilon_{cm} = \frac{\lambda}{2} \frac{f_{ct}}{E_c} \quad [3.11]$$

which leads to

$$w_m = s_m \left( \varepsilon_{sr} - \frac{\lambda}{2} \frac{f_{ct}}{E_s} \frac{(1 + \rho_s(n-1))}{\rho_s} \right) \quad [3.12]$$

Eq. 3.12 evaluates the crack width at the reinforcement level. In slabs, however, the cracks that matter are those at the tension face. These crack widths can be obtained by multiplying Eq. 3.12 by  $\left( \frac{h - xd}{d - xd} \right)$  (see Broms, 1965), where  $xd$  is the neutral axis depth.

#### 3.3.4.2 The CIRIA Model

Based on observations on flexural tests on steel-reinforced concrete beams and slabs, Base, Read, Beeby and Taylor (1965) and Beeby (1970) concluded that slip at points where the bars pass through cracks is not a major parameter controlling crack widths. The crack tapers from the reinforcement level to the surface but its width is assumed to be zero at the steel-concrete interface. This concept is the basis for the so-called “no-slip” theory for crack formation (Base, 1982).

Base (1982) divided flexural cracks into primary and secondary cracks. Primary cracks (also called “depth-” or “curvature-controlled” cracks) are necessary to accommodate deformations due to imposed loads. These bond-independent cracks propagate from the extreme tensile fibre at points where high tensile stresses and local flaws coincide. Secondary cracks are caused by bond but their spacing is not controlled by a bond

development length but rather by the cover thickness. This observation is consistent with experimental evidence gathered by Broms (1965) and Broms and Lutz (1965).

### 3.3.4.3 The Gergely-Lutz Equation

Gergely and Lutz (1967) derived the following equation to estimate maximum crack widths based on a statistical analysis of crack widths measured on the tension face of steel-reinforced concrete beams.

$$w_{\max} = 11 \times 10^{-6} \frac{h_2}{h_1} z = 11 \times 10^{-6} \frac{h_2}{h_1} \sigma_{sr} \sqrt[3]{d_c A} \quad [\text{SI}] \quad [3.13]$$

where  $h_2$  is the distance from the extreme tension surface to the neutral axis,  $h_1$  is the distance from the tension reinforcement centroid to the neutral axis,  $\sigma_{sr}$  is the steel stress at the crack,  $d_c$  is the concrete cover measured from the centroid of the tension reinforcement to the extreme tension surface, and  $A$  is the effective concrete area in tension surrounding the reinforcement having the same centroid as the reinforcement divided by the number of bars.

CSA A23.3-94 does not limit the crack width directly. Instead, it limits the magnitude of the term  $z$ . For thin one-way slabs, the maximum  $z$  values are 30000 and 25000 N/mm for interior and exterior exposure, respectively. These limits correspond to crack widths of 0.4 and 0.33 mm, respectively. The term  $\sigma_{sr}$  is calculated based on the naked steel response or assumed equal to 60 % of steel yield strength.

### 3.3.4.4 ACI 318-99

Crack control provisions in ACI 318-99 drift away from the Gergely-Lutz approach, which was adopted in previous code versions. The maximum bar spacing is now specified directly as a function of the concrete cover and the level of stress in the steel reinforcement. The new provisions are “intended to control surface cracks to a width that is generally acceptable in practice but may vary widely in a given structure”. ACI 318-99 has also abandoned the distinction between interior and exterior exposure conditions.

### **3.4 Cracking in FRP-reinforced One-way Concrete Slabs**

The formation and evolution of cracks due to imposed tension or flexure in FRP-reinforced concrete members is conceptually similar to that in steel-reinforced members. However, major differences are expected due to FRP's lower stiffness and brittle nature. These reflect in the bond behaviour of FRP and on concrete's tension stiffening effect.

#### **3.4.1 Bond Between FRP Bars or Grids and Concrete**

##### **3.4.1.1 Influential Parameters**

According to FIB Bulletin 10 (2000) and Cosenza, Realfonzo and Manfredi (1997), the most influential parameters on the bond interaction between FRP and concrete are:

- 1) Cross-sectional shape of FRP reinforcement
- 2) FRP's elastic modulus in both axial and transverse directions
- 3) Bar diameter or cross-sectional size
- 4) Surface conditions
- 5) Resin type
- 6) Concrete strength
- 7) Confinement conditions
- 8) Poisson's ratio of FRP
- 9) Position of the bar in the structural member's cross-section
- 10) Concrete cover

Achillides, Pilakoutas and Waldron (1997) report that square FRP bars develop higher bond strength than round FRP bars under full confinement conditions. However, flat FRP bars have a greater tendency to increase splitting.

The effect of FRP's elastic modulus depends on the direction being examined. As observed by Tepfers (1997), when FRP bars have a transverse elastic modulus similar or

less than that of concrete, the FRP bar deformations do not create as intense stress concentrations in concrete as do steel bars.

Achillides *et al* (1997) and Benmokrane *et al* (1996) report that bars with larger diameter develop lower average bond strength compared to smaller diameter bars.

The size, density and inclination of the surface deformations affect both the mechanical lock and the splitting forces (FIB Bulletin 10, 2000). Small dense surface deformations provide good bond transfer at low loads but may lead to splitting cracks at higher loads. For this reason, bigger ribs are preferred. Deformed bars display high bond strength under full confinement conditions but have lower bond splitting strength than sand coated bars. Rough surfaces display greater bond splitting strength than smooth surfaces.

Nanni, Al-Zaharani, Al-Dulaijan, Bakis and Boothby (1995) found that the fibre type does not appear to have a significant effect on bond of FRP rods. Instead, the resin has a greater effect. Bars with epoxy-based resins display greater bond strengths than those with vinyl ester-based systems. Since the resin shear strength is lower than that of concrete, bond failure in FRP deformed bars is often driven by the detachment of ribs, shear lugs or spirals (Daniali, 1992, Malvar, 1994, and Nanni *et al*, 1995, among others).

Chaallal and Benmokrane (1993) found that the bond strength of GFRP rods with helical indents embedded in normal-strength concrete is similar to that in high-strength concrete. According to Achillides (1998), the bond strength of Eurocrete bars (CFRP and GFRP bars with rough surface produced by a peel ply) does not depend on the concrete strength for  $f'_c$  values greater than 30 MPa. For greater concrete strengths the bond failure occurs in the surface of the FRP bar. For lower strengths, the failure occurs in the concrete.

The effect of concrete cover has significant implications on bond. Intuitively, a reduced cover may lead to concrete splitting failure. It is often heard from FRP advocates that reduced covers should be allowed in FRP-reinforced concrete members because of FRP's corrosion-free nature. This is not prudent because splitting crack development may

seriously compromise bond between FRP and concrete. In addition, sufficient cover is required for fire protection of FRP.

### 3.4.1.2 Bond Tests of FRP-reinforced Concrete Specimens

The majority of the experimental results on bond between FRP and concrete has been derived from pull-out tests. Figure 3.8 shows typical bond-slip curves from pull-out tests conducted on prisms of comparable normal strength (in the order of 20 to 30 MPa). All of the curves except that for the C-bar were drawn based on the data reported by Cosenza *et al* (1997). The C-bar's bond-slip curve was drawn based on the results reported by Karlsson (1997).

Figure 3.8 shows that both sand-blasted and smooth rods display very low bond strengths. Grain covered rods show moderate bond strengths (about 10 MPa) but display a brittle post-peak response. Ribbed and indented bars show bond strengths of about 10 MPa. Sanded deformed bars and C-bars display the highest bond strengths.

Faza and GangaRao (1992) conducted tests using the “inverted half beam” or “cantilever type beam” set-up to assess the bond strength of rough # 3 and # 8 GFRP bars. The maximum bond capacity of the # 3 bars was not recorded because the bars ruptured. The # 8 bars developed maximum average bond strengths of 2.8 and 3.2 MPa. These values are much lower than those recorded in pull-out tests.

Based also on cantilever type beam tests, Kanakubo, Yonemaru, Fukuyama, Fujisawa and Sonobe (1993) reported two design provisions evaluating the bond splitting strength of FRP. The first (influenced by the work of Fujii and Morita, 1982) deals with wedge-type splitting failure.

$$\tau_{b,sp} = 0.313(0.4b_i + 0.5)\sqrt{f'_c} \quad [3.14]$$

The second equation accounts for the geometry of bar deformations.



$$\tau_{b,sp} = 0.67 \left( \frac{h}{\phi_b} \right)^{0.22} \sqrt{f'_c} \quad [3.15]$$

where  $h/\phi_b$  is the ratio of lug height to bar diameter expressed as a percentage, and  $b_i$  is what they call a “normalised length of failure line”. Equations 3.16 and 3.17 were derived for different FRP reinforcements but did not deal specifically with C-bars.

Shield, French and Hanus (1999) used the cantilever type beam test set-up to examine the bond splitting strength of No. 5 C-bars and No. 6 Hughes Brothers bars. The main variables in the study were the concrete cover and the embedment length. The bond strength of GFRP rebars was difficult to assess because of the high variability in the mechanical properties of the products. The embedded length effect could not be observed due to the large variability in the bar strength. They identify, however, that bond in GFRP C-bars relies on mechanical interlock whereas bond in GFRP Hughes Brothers rebars relies heavily on both adhesion and friction.

#### **3.4.1.3 Bond of FRP Relative to Steel**

The bond strength of FRP is expected to be less than that of conventional steel because: i) the modulus of elasticity of FRP in both radial and longitudinal directions is lower than that of steel, ii) the resin matrix has a lower shear strength, and iii) the shear stiffness of FRP is lower than that of steel.

Based on pull-out tests of deformed GFRP rods, Brown and Bartholomew (1993) conclude that bond between FRP reinforcing bars and concrete is about two-thirds of that between steel and concrete.

Malvar (1995) examined the bond behaviour of deformed GFRP bars by means of pull-out tests under different confinement levels. For a given confinement, the bond stress developed by steel is 20 to 50 % greater than that of the equivalent GFRP bar.

Chaalal and Benmokrane (1993) reported pull-out test results of GFRP sanded deformed rods in normal and high strength concrete. The average bond strength of the GFRP rods embedded in NSC and HSC was, respectively, 72 and 40 % of that of steel.

Benmokrane, Tighiouart and Chaallal (1996) examined the bond of GFRP deformed bars through hinged beam-type and pull-out tests. The GFRP bars had helically wound deformations and sand coating. They found that the bond strength from pull-out tests is 5 to 82 % greater than that from the beam tests. The bond strength of GFRP reduces with increasing the diameter. For a 0.1 mm slip, the bond strength of GFRP bars is 36 to 89 % of that of steel. For a 0.2 mm slip, the bond strength is 50 to 99 % of that of steel.

The results reported by Achillides *et al* (1997) show that Eurocrete CFRP and GFRP bars can develop bond strengths of 80 % of that developed by steel bars.

Tepfers and Karlsson (1997) examined the effect of cover and bar diameter on the splitting bond strength of GFRP C-bars. They used a pull-out test array with eccentric bar placement similar to that presented in Tepfer's 1973 paper. When there is enough cover or confinement to prevent splitting, the C-bars are capable of displaying a similar bond-slip response as that of ordinary steel bars. The cover splitting along the bar is lower for the C-bar likely because of its softer surface. Nevertheless, when the cover is split along the bar, the bond strength could be 30 % less than that of steel.

Tepfers, Hedlund and Rosinski (1998) examined the bond of Hughes Brothers GFRP bars under similar test conditions as those previously examined. These bars have smooth surface and short spiral deformations wound around the bar. For low load levels, the bars have high stiffness due to their coarse sand coating. However, the splitting bond strength is lower than that of steel and C-bars.

#### **3.4.1.4 Bond of Grid-type FRP**

FRP grids are characterised by negligible bond along the ribs. The bond strength is provided by mechanical bearing of the grid transverse bars against concrete (Makizumi,

Sakamoto and Okada, 1993, Mochizuki and Udagawa, 1995, and Mochizuki, 1997). Experimental data on the constitutive bond-slip behaviour of FRP grids is very scarce.

### 3.4.2 Concrete's Tension Stiffening Effect in FRP-reinforced Concrete Members

Based on the analyses of 31 beams reinforced with internal FRP bars, Razaqpur *et al* (2000) concluded that the tension stiffening effect can be ignored in the post-cracking stages of members with FRP. The Canadian Standard CSA S806-00 adopted their recommendations for the serviceability design of FRP-reinforced concrete members.

According to the tension chord model fundamentals, the strain correction due to concrete's tension stiffening is highly influenced by the amount of reinforcement and the elastic modulus of the reinforcement. The effect of these variables in members with FRP could be more influential than in steel-reinforced concrete members. If the tension stiffening effect is important in the context of steel-reinforced concrete members, it does not seem sensible to neglect it for the serviceability design of FRP-reinforced concrete members.

### 3.4.3 Crack Width Calculations in Members with FRP

#### 3.4.3.1 Empirical Approaches

The majority of design provisions to calculate crack widths in members with FRP are based on modifications made to the Gergely-Lutz equation (see Faza and GangaRao, 1993a, 1993b, Thériault and Benmokrane, 1998, and ISIS M04-00).

Faza and GangaRao (1993a, 1993b) propose

$$w_{\max} = 0.076 \frac{h_2}{h_1} \frac{E_s}{E_f} \sigma_{fr} \sqrt[3]{d_c A} \quad [3.16]$$

where  $E_f$  and  $E_s$  are the elastic moduli of FRP and steel, respectively. In the derivation of Eq. 3.17, Faza and GangaRao assume that the crack width is proportional to strain rather than stress and introduce the FRP strain at the crack,  $\varepsilon_{fr} = \sigma_{fr} / E_f$ .

Thériault and Benmokrane (1998) recommend

$$w_{\max} = K_g \frac{h_2}{h_1} \sigma_{fr} \sqrt[3]{d_c A} \quad [3.17]$$

where  $\sigma_{fr}$  is the FRP strain at the crack at the specified load and  $K_g$  is an empirical factor. For C-bars, they propose  $K_g = 40.9 \times 10^{-6} \text{ mm}^2/\text{N}$ .

ISIS M04-00 (2000) suggest

$$w_{\max} = 11 \times 10^{-6} \sigma_{fr} K_b \frac{h_2}{h_1} \sqrt[3]{d_c A} \quad [3.18]$$

where  $K_b$  is a bond coefficient, taken as 1.0 for FRP bars with bond properties similar to those of steel, greater than 1.0 for FRP bars with inferior bond quality, and less than 1.0 for FRP bars with superior bond quality.

The Canadian Standard for the design of FRP-reinforced concrete structures, CSA S806-00, controls crack widths by limiting a factor,  $z$ , which is defined as

$$z = K_b \frac{E_s}{E_f} \sigma_{fr} \sqrt[3]{d_c A} \quad [3.19]$$

The maximum values for  $z$  are 45000 and 38000 N/mm, for interior and exterior exposure, respectively, and  $K_b$  is a bond coefficient equal to 1.2 for deformed FRP bars. These  $z$  values are equivalent to maximum allowable crack widths of about 1.5 times greater than those allowed for both interior and exterior exposure conditions by CSA A23.3-94 for the design of steel-reinforced concrete members. The increase in the allowable crack width limits for FRP-reinforced concrete members has been driven by the superior corrosion resistance of FRP reinforcement.

In Eqs. 3.16 to 3.19, the FRP stress, and therefore the strain, is calculated from the response of the naked FRP reinforcement. Hall (2000) proposes the following

relationship to evaluate the FRP strain from the given crack width allowed in members reinforced with FRP as

$$\frac{\varepsilon_{fs}}{\varepsilon_{ss}} = \frac{w_f}{w_s} \quad [3.20]$$

where  $\varepsilon_{fs}$  and  $\varepsilon_{ss}$  refer to the strain in FRP and steel at service load level, and  $w_f$  and  $w_s$  are the crack widths in the member with FRP and steel reinforcement, respectively.

Since the stress in the steel reinforcement at service level is usually taken as 60 percent of

its yield strength,  $\varepsilon_{ss} = \frac{0.6 f_y}{E_s} = \frac{0.6 (400)}{200000} = 0.0012$ . Assuming a  $\frac{w_f}{w_s}$  value of 1.5, for

both interior and exterior exposure conditions, Eq. 3.20 leads to  $\varepsilon_{fs} = 1.5\varepsilon_{ss} = 1.5(0.0012) = 0.0018$  as the equivalent serviceability FRP strain level in FRP-reinforced members.

#### 3.4.3.2 Crack Width Calculation Using the Finite Difference Method

Aiello and Ombres (2000) developed a non-linear procedure based on the finite difference method to predict crack widths and their spacing in FRP-reinforced concrete members. The fundamentals of the model are similar to those of the tension chord model except that a more refined bond-slip model is used (this model is described in Eligehausen, Bertero and Popov, 1982). Only the ascending branch of the bond model was used. The procedure assumes that no splitting cracks form along the bars. It renders good crack width predictions for the one-way GFRP C-bar-reinforced concrete slabs tested by Cosenza, Pecce and Manfredi (1998).

### 3.5 Serviceability Limit State of Deflections

Deflection control in FRP-reinforced concrete slabs is necessary due to FRP's moderate-to-low stiffness, brittleness, and the tendency of GFRP to creep rupture. The following sections review existing design provisions to control deflections in concrete slabs with

FRP. As a reference, design approaches for steel-reinforced concrete slabs are presented first.

### **3.5.1 Deflection Control Approaches in Steel-reinforced Concrete Slabs**

Slab deflections can be controlled directly or indirectly. Direct control refers to the direct calculation of deflections and their comparison with allowable limits. Deflection calculation methods span from classic elastic theory procedures to advanced finite element analyses. ACI Committee 435 (1974) and Branson (1977) present excellent summaries of direct deflection control procedures for steel-reinforced concrete flat plates.

“Indirect” deflection control procedures evaluate deflections by determining maximum span-thickness (or span-depth) ratios, minimum thicknesses (or depths), or minimum tension reinforcement ratios. The fundamental concept behind these approaches is to define a limiting curvature that renders a maximum target span-to-deflection value. Indirect approaches, or “rule-of-thumb” methods, are thoroughly documented by Branson (1977). Regardless of which method is used, allowable deflection, span-depth, minimum slab depth and span-to-deflection limits are largely set up based on experience. Branson (1977) recommends to use the indirect methods for initial proportioning and then to check deflections by means of a relatively simple deflection calculation method.

#### **3.5.1.1 Allowable Deflections**

Allowable deflections refer to maximum deflection limits beyond which a structure violates its serviceability limit state, ceases to be functional, or becomes aesthetically unpleasant. Typical deflection limits for structural, sensorial and aesthetic reasons, are given by ACI Committee 435 (1968). These limits are usually expressed in terms of span-deflection ratios. Table 3.1 reports allowable  $\Delta_m/L$  ratios for slabs according to CSA A23.3-94. Similar values apply in ACI 318-99. Branson (1977) reports a comprehensive survey of  $\Delta_m/L$  values recommended by different concrete codes of practice.

Deflection limits depend on how critical loading conditions are. Deflections in the order of  $L/180$  are allowed in roof slabs without underside finishing and where water ponding is not an issue. Deflection limits as stringent as  $L/750$  to  $L/1000$  may be applied in the design of slabs supporting motion-sensitive equipment. This is very relevant for FRPs since, because of their magnetic neutrality, FRPs are used in the construction of hospital MRI rooms, and radio and compass calibration pads.

### 3.5.1.2 Direct Calculation of Deflections: Branson's Method

Both ACI 318-99 and CSA A23.3-94 adopt Branson's effective moment of inertia Eq. 3.21 to calculate post-cracking deflections in steel-reinforced concrete members. The term  $I_e$  accounts for the effect of concrete tension stiffening by interpolating between the gross moment of inertia,  $I_g$ , and that of the transformed cracked section,  $I_{cr}$ .

$$I_e = \left( \frac{M_{cr}}{M_a} \right)^3 I_g + \left( 1 - \left( \frac{M_{cr}}{M_a} \right)^3 \right) I_{cr} \leq I_g \quad [3.21]$$

where  $M_{cr}$  is the cracking moment based on the gross moment of inertia and  $M_a$  is the maximum historic moment associated to  $M_{cr}$ . Figure 3.9 illustrates Branson's  $I_e$  concept.

As noted by Ghali (1993), deflection calculations based on Branson's  $I_e$  concept may be inadequate because it is impossible to find empirical equations that give constant cross-sectional properties to allow treating cracked members as prismatic. Predictions are accurate in some cases but largely in error when i) the reinforcement ratio is low, ii)  $M_{max}$  is not substantially greater than  $M_{cr}$ , and iii) the bending moment is constant over the major part of the span. These features can be considered typical of concrete slabs.

### 3.5.1.3 Deflection Calculation by Curvature Integration

This procedure is based on the assumption that deflections can be obtained by double integration of curvatures at target locations along a span. Ghali (1993) has long advocated its implementation. For an interior continuous span, assuming a parabolic curvature

distribution with curvatures measured at three slab sections, the midspan deflection,  $\Delta_m$ , is exactly

$$\Delta_m = \frac{L^2}{96} (\psi_a + 10\psi_b + \psi_c) \quad [3.22]$$

where  $L$  is the span length,  $\psi_a$  and  $\psi_c$  are the curvatures at the supports and  $\psi_b$  is the midspan curvature. For interior spans, the curvature is positive when the strain is larger at the bottom face than at the top face of the member. Therefore, in a continuous span, both  $\psi_a$  and  $\psi_c$  are negative. In general, increasing the number of sections increases the accuracy in the deflection calculation. Figure 3.10 shows typical deflection equations for uniformly loaded interior spans for three and five slab sections.

To evaluate average curvatures, the procedure given by the CEB/FIP Model Code (1990) is often adopted. This procedure is greatly influenced by the work of Rao (1966). The average curvature in ordinary steel reinforced-concrete members is defined as a weighted average of the uncracked (stage I) and fully cracked (stage II) curvatures, as shown in the moment-curvature response of Fig. 3.9.

$$\psi_{ave} = (1 - \xi) \psi_1 + \xi \psi_2 \quad [3.23]$$

where  $\psi_1$  is the curvature at uncracked section level, calculated based on the entire cross-section transformed into concrete, including the reinforcement, and  $\psi_2$  is the curvature at fully cracked level,  $\psi_2 = \frac{M}{E_c I_2}$ . The  $\xi$  factor is an empirical factor that controls

concrete's tension stiffening effect based on bond properties of steel reinforcement and the nature of loading.

$$\xi = 1 - \beta_1 \beta_2 \left( \frac{M_{cr}}{M} \right)^2 \geq 0.4 \quad [3.24]$$

where  $\beta_1$  is a bond factor, equal to 1.0 for high bond bars, and  $\beta_2$  is a performance factor, equal to 0.8 for first loading, and 0.5 for sustained loads or large number of load cycles. Eurocode 2 assumes  $\beta_1 = 1.0$ . For real-life applications in steel-reinforced concrete



members, CEB/FIP MC90 recommends  $\beta = \beta_1\beta_2 = 0.5$ . In laboratory short-term loading tests of steel-reinforced concrete members,  $\beta$  is often taken as unity.

The curvature integration approach is advantageous because its formulation depends entirely on geometrical considerations and not on material properties or load actions (Ghali, 1993). This is an asset because cracked members behave as members with variable cross-section. One of the main difficulties linked to Branson's method is the determination of the value of  $I_e$  that best describes the overall conditions of a partially cracked member for different support and load conditions.

#### **3.5.1.4 Indirect Deflection Control**

To comply with a given  $\Delta_m/L$  ratio, it is required to select an appropriate strain level in the FRP reinforcement at service load level. This is equivalent to defining a limiting curvature or a minimum reinforcement ratio. The latter concept is adopted by ACI Committee 435 (1978). Table 3.2 shows recommended minimum  $\rho_s$  values to satisfy deflection limits in steel-reinforced beams and slabs. Table 3.3 shows values of minimum thickness for non-prestressed one-way beams and slabs, according to ACI 318-99.

#### **3.5.2 Direct Deflection Control in FRP-reinforced Concrete Slabs**

There is limited guidance to control deflections in slabs with FRP reinforcement. Most of the available design recommendations refer to direct deflection calculations. The majority of such procedures have evolved from Branson's concept.

Nawy and Neuwerth (1977) report that deflection calculations using Branson's formula are unconservative for beams with low percentages of GFRP. However, the deflection estimates become more realistic as the FRP reinforcement ratio increases.

Benmokrane, Chalaal and Masmoudi (1996) modified Branson's equation as follows

$$I_e = \left( \frac{M_{cr}}{M_{max}} \right)^3 \beta_b I_g + \left[ 1 - \left( \frac{M_{cr}}{M_{max}} \right)^3 \right] I_{cr} \quad [3.25]$$

where  $\beta_b$  is a correction factor equal to 0.6 for Type 1 GFRP C-bars. Gao, Benmokrane and Masmoudi (1998) recommend

$$\beta_b = \alpha_b \left( \frac{E_f}{E_s} + 1 \right) \quad [3.26]$$

where  $\alpha_b$  is a bond-dependent coefficient equal to 0.5. Hall and Ghali (2000) recommend  $\alpha_b = 0.5$  for other types of FRP bars until more research becomes available. Other modifications to Branson's formula are proposed by Faza and GangaRao (1992b) and ACI Committee 440 (1996).

Hall and Ghali (2000) define the mean midspan curvature as

$$\psi_{m,ave} = \frac{M_{max}}{E_c I_{ave}} \quad [3.27]$$

where  $I_{ave}$  is the mean moment of inertia that one would obtain by applying the MC 90 tension stiffening formulation, defined as

$$I_{ave} = \frac{I_1 I_2}{(1 - \xi) I_2 + \xi I_1} \quad [3.28]$$

where  $I_1 = I_t$  and  $I_2 = I_{cr}$ . The term  $I_t$  is the moment of inertia of the uncracked cross section transformed to concrete. Substituting Eq. 3.28 into 3.25 and rearranging,

$$I_{ave,HG} = \frac{I_t I_{cr}}{I_t + \left( 1 + \beta_1 \beta_2 \left( \frac{M_{cr}}{M_{max}} \right)^2 \right) (I_{cr} - I_t)} \quad [3.29]$$

ISIS Canada design guidelines adopted the value proposed by Thériault (1998), which was based on a more extensive experimental database. This value is

$$I_{e,T} = \frac{I_t I_{cr}}{I_{cr} + \left(1 - 0.5 \left(\frac{M_{cr}}{M_{max}}\right)^2\right) (I_t - I_{cr})} \quad [3.30]$$

Review of Eqs. 3.29 and 3.30 reveals these two equations are identical.

The use of Branson's method to calculate deflections in members with FRP has been criticised by Hall (2000). The observations are similar to those exposed by Ghali (1993) for steel-reinforced members. Hall (2000) demonstrates that the curvature integration method mixed with the CEB/FIP MC90 approach to evaluate average curvatures leads to more accurate deflection calculations compared to Branson's approach. The latter underestimates deflections for load levels slightly greater than the cracking load. Hall (2000) assumed  $\beta$  equal to 0.5 for slabs with GFRP bars at first loading.

As far as members with FRP grids is concerned, the flexural test results on concrete beams reinforced with NEFMAC grids reported by Schmeckpeper and Goodspeed (1994) and Yost, Schmeckpeper and Goodspeed (2001) indicate that Branson's formula overestimates the stiffness, specially at loads roughly greater than the cracking load. Matthys and Taerwe (2000b) show that the tension stiffening model of CEB/FIP MC90 provides reliable deflection estimates in one-way slabs with FRP grids using  $\beta = 0.8$ .

Deflections in CSA S806-00 are based on the curvature-integration procedure developed by Razaqpur, Švecová and Cheung (2000). Deflections are calculated based on the idealised moment-curvature response of Fig. 3.11. The model assumes that the response of beams and slabs with FRP is fully defined in terms of both the uncracked,  $E_c I_g$ , and fully cracked,  $E_c I_{cr}$ , flexural stiffnesses. The model neglects concrete's tension stiffening effect.

Figure 3.12 shows closed-form deflection formulas for simply supported beams applying Razaqpur *et al*'s procedure for three different loading conditions. The term  $L_g$  refers to the

distance from the support to the point where  $M = M_{cr}$ . In cantilever beams (case not shown),  $L_g$  is the distance from the free end to the point where  $M = M_{cr}$ .

### 3.5.3 Indirect Deflection Control in FRP-reinforced Concrete Slabs

Hall (2000) proposes the following empirical equation to determine the maximum span-thickness ratio in one-way slabs reinforced with FRP:

$$\left(\frac{L}{h}\right)_f = \left(\frac{L}{h}\right)_s \sqrt{\frac{\varepsilon_{ss}}{\varepsilon_{fs}}} \quad [3.31]$$

where  $\varepsilon_{ss}$  and  $\varepsilon_{fs}$  are the strains in steel and FRP at the crack at service load levels. The equivalent span-thickness ratio for slabs with FRP intends to satisfy the deflection limits imposed to a steel-reinforced slab with span-ratio  $(L/h)_s$ . The deflection control limits of Table 3.3 needs to be modified to determine the minimum thicknesses in slabs with FRP.

**Table 3.1 Maximum Permissible Computed Deflections (CSA A23.3-94)**

Type of Member	Deflection to be considered	Deflection limitation
Flat roofs <u>not</u> supporting or attached to nonstructural elements likely to be damaged by large deflections	Immediate deflection due to specified live load	$l_n/180 *$
Floors <u>not</u> supporting or attached to nonstructural elements likely to be damaged by large deflections	Immediate deflection due to specified live load	$l_n/360$
Roof or floor construction supporting or attached to nonstructural elements likely to be damaged by large deflections	That part of the total deflection occurring after attachment of nonstructural elements (sum of the long-term deflection due to all sustained loads and the immediate deflection due to any additional live load) †	$l_n/480 ‡$
Roof or floor construction supporting or attached to nonstructural elements <u>not</u> likely to be damaged by large deflections		$l_n/240 §$

Notes: \* Limit not intended to safeguard against ponding.

† Long-time deflections shall be determined in accordance with Clause 9.8.2.5 or 9.8.4.4 of CSA A23.3-94 but may be reduced by the amount of deflection calculated to occur before the attachment of nonstructural elements.

‡ Limit may be exceeded if adequate measures are taken to prevent damage to supported or attached elements.

§ But not greater than the tolerance provided for nonstructural elements. Limit may be exceeded if camber is provided so that total deflection minus camber does not exceed the limit.

**Table 3.2**

**Recommended Tension Steel Reinforcement Ratios for Non-prestressed One-way Members to Render Acceptable Deflections (ACI Com. 435, 1978)**

Members	Cross section	Normal Weight Concrete	Lightweight concrete
Not supporting or not attached to nonstructural elements likely to be damaged by large deflections	Rectangular	$\rho_s \leq 0.35 \rho_{bal}$	$\rho_s \leq 0.30 \rho_{bal}$
	"T" or box	$\rho_s \leq 0.40 \rho_{bal}$	$\rho_s \leq 0.35 \rho_{bal}$
Not supporting or not attached to nonstructural elements likely to be damaged by large deflections	Rectangular	$\rho_s \leq 0.25 \rho_{bal}$	$\rho_s \leq 0.20 \rho_{bal}$
	"T" or box	$\rho_s \leq 0.30 \rho_{bal}$	$\rho_s \leq 0.25 \rho_{bal}$

**Table 3.3**  
**Thickness below which deflections must be computed for nonprestressed beams or one-way slabs not supporting or attached to partitions or other construction likely to be damaged by large deflections (CSA A23.3-94)**

	Minimum Thickness			
	Simply supported	One end continuous	Both ends continuous	Cantilever
Solid one-way slabs	$l_n/20$	$l_n/24$	$l_n/28$	$l_n/10$
Beams or ribbed one-way slabs	$l_n/16$	$l_n/18.5$	$l_n/21$	$l_n/8$

Note: Values given correspond to members with normal density concrete.  
 For other conditions, refer to CSA A23.3-94.

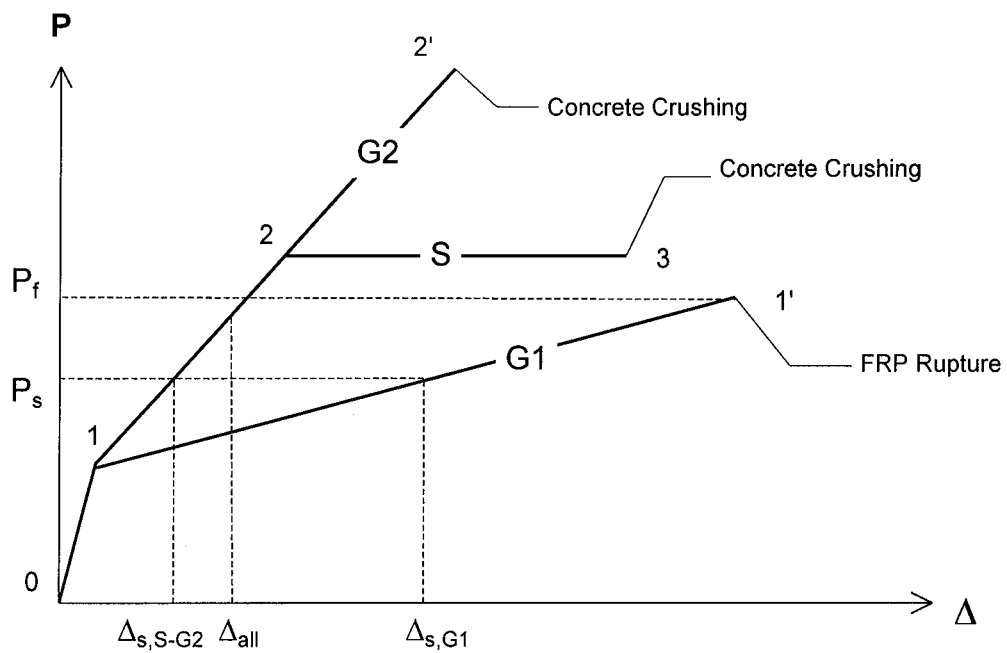


**Fig. 3.1 Flexural Response of Members with FRP**

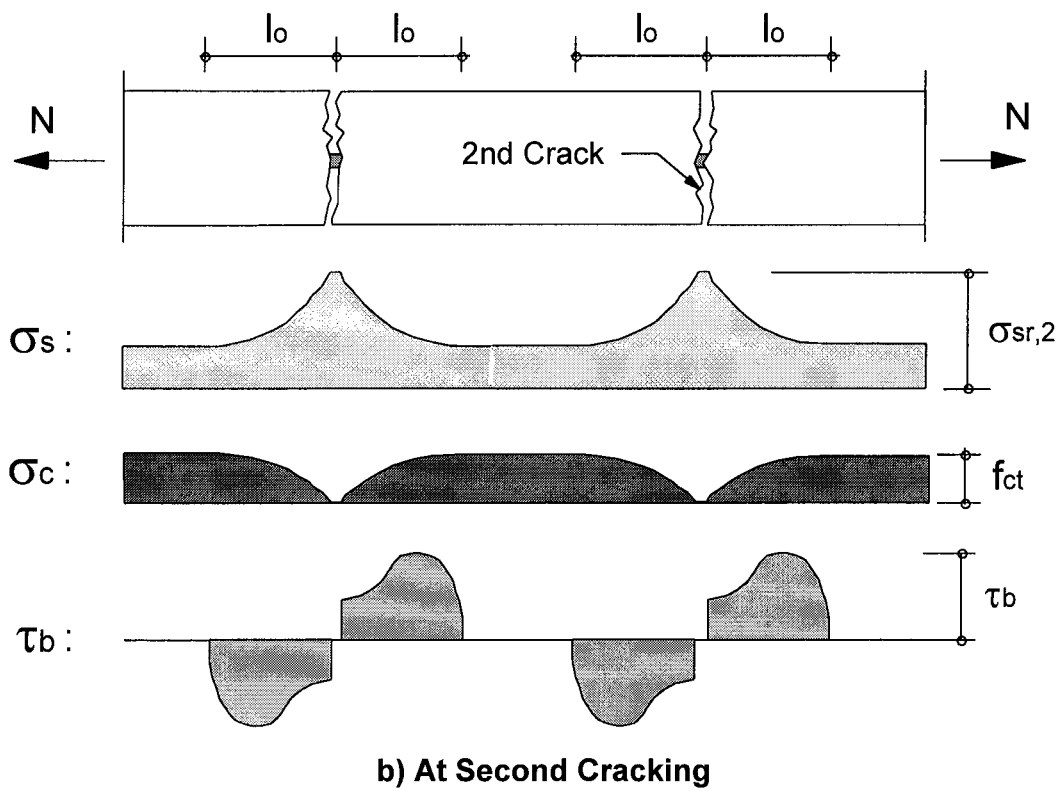
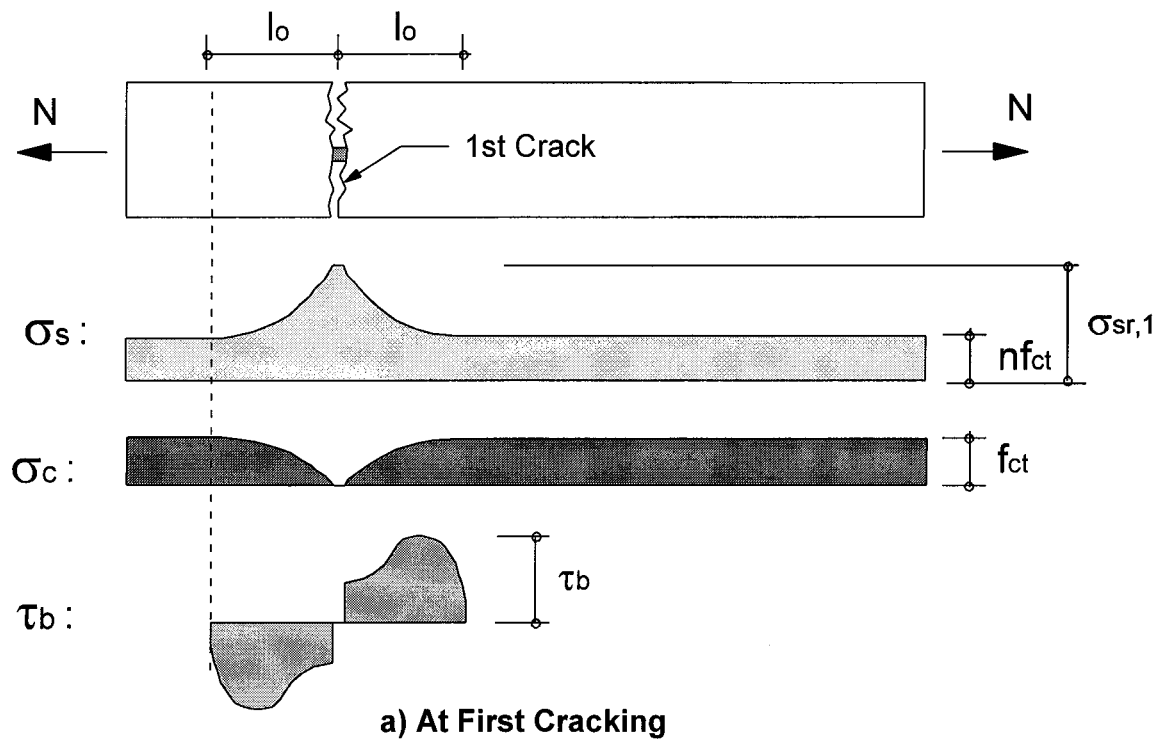


**Fig. 3.2 Stresses in Concrete Prism Subjected to Axial Tension After First and Second Crack Formation**

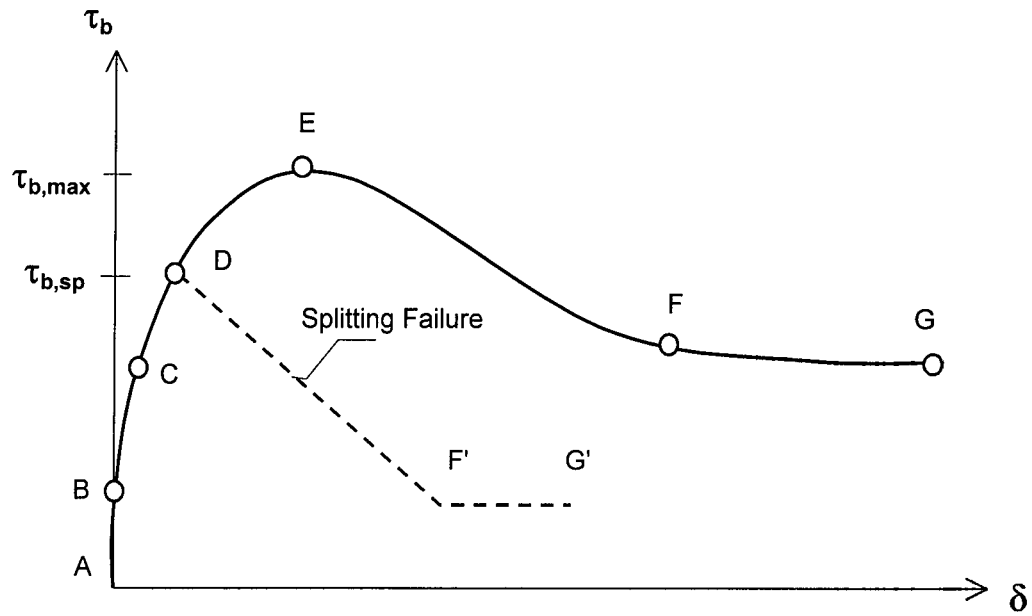


**Fig. 3.3 Splitting Effect on Bond-slip Response**

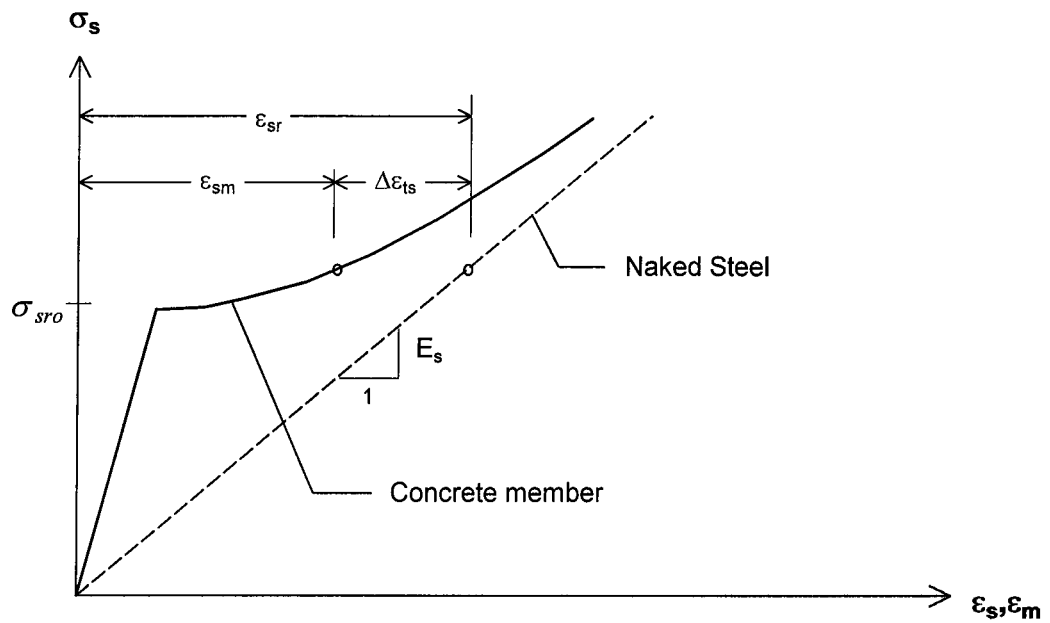


**Fig. 3.4 Concrete's Tension Stiffening Effect**



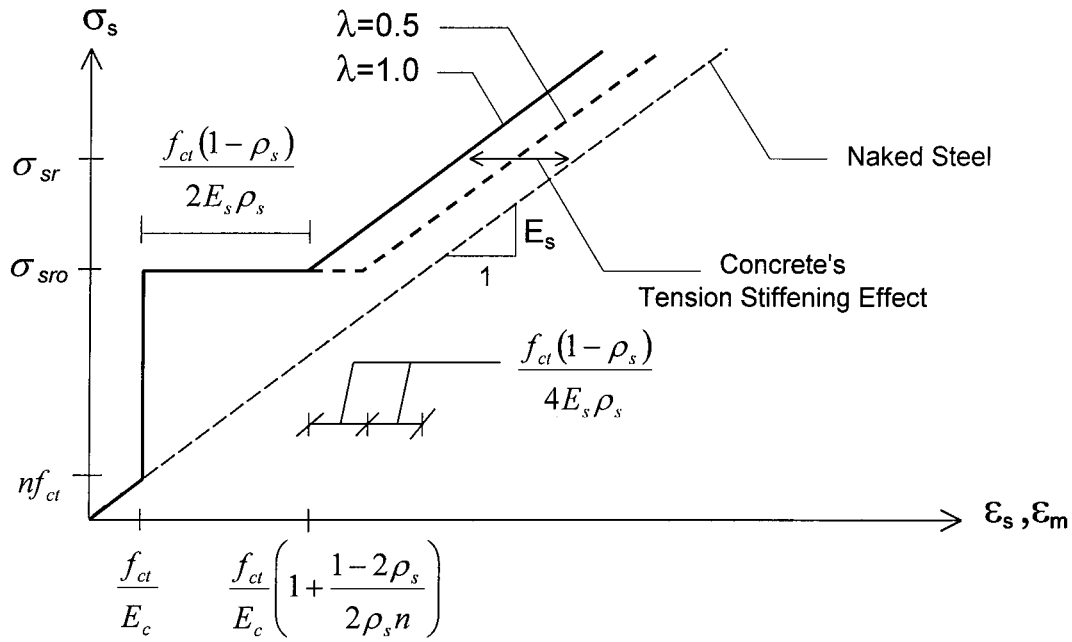


**Fig. 3.5 Stress-Strain Response of Tension Chord**

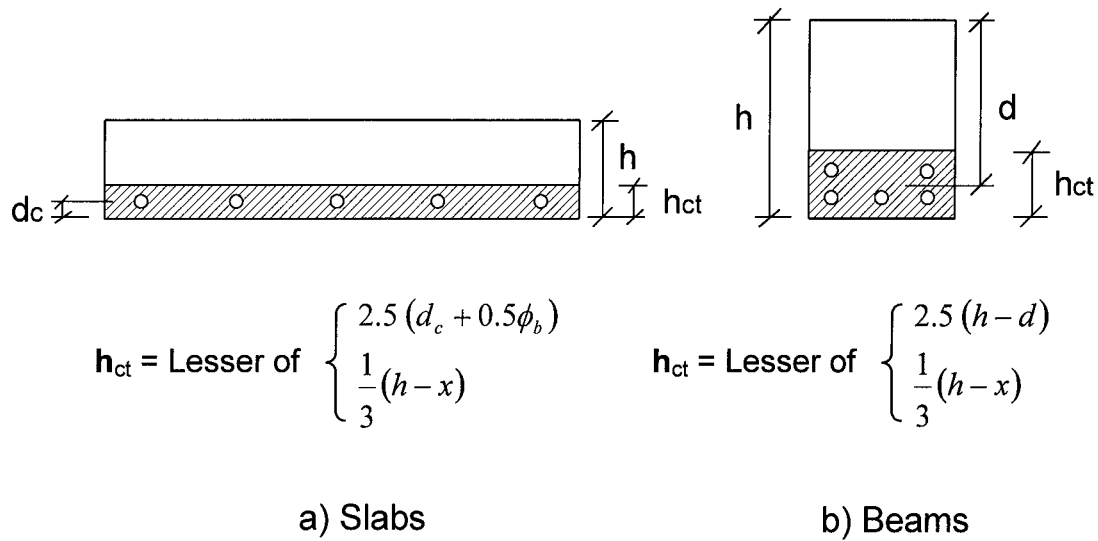
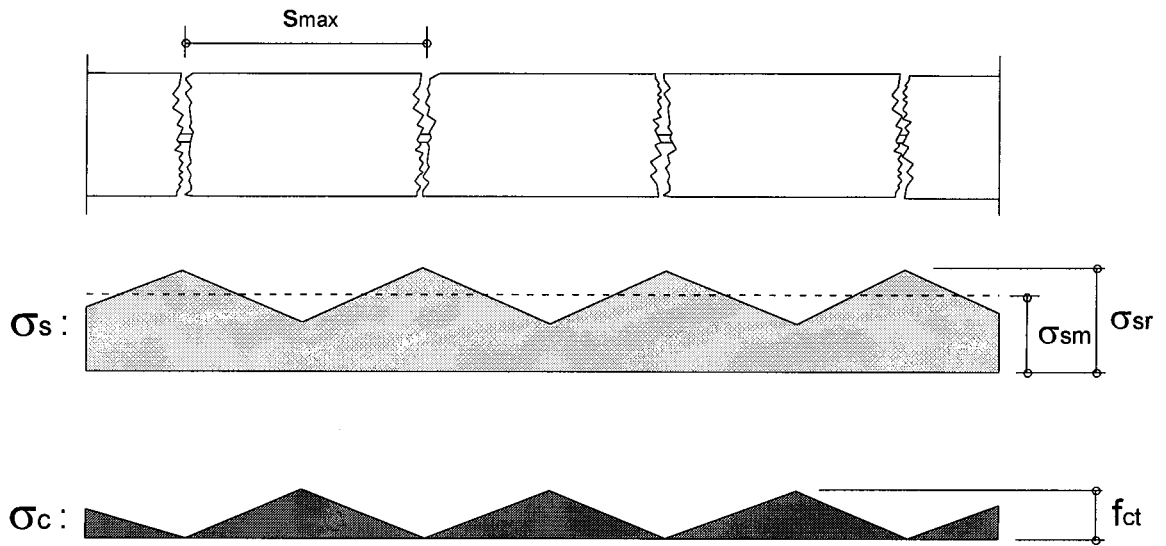
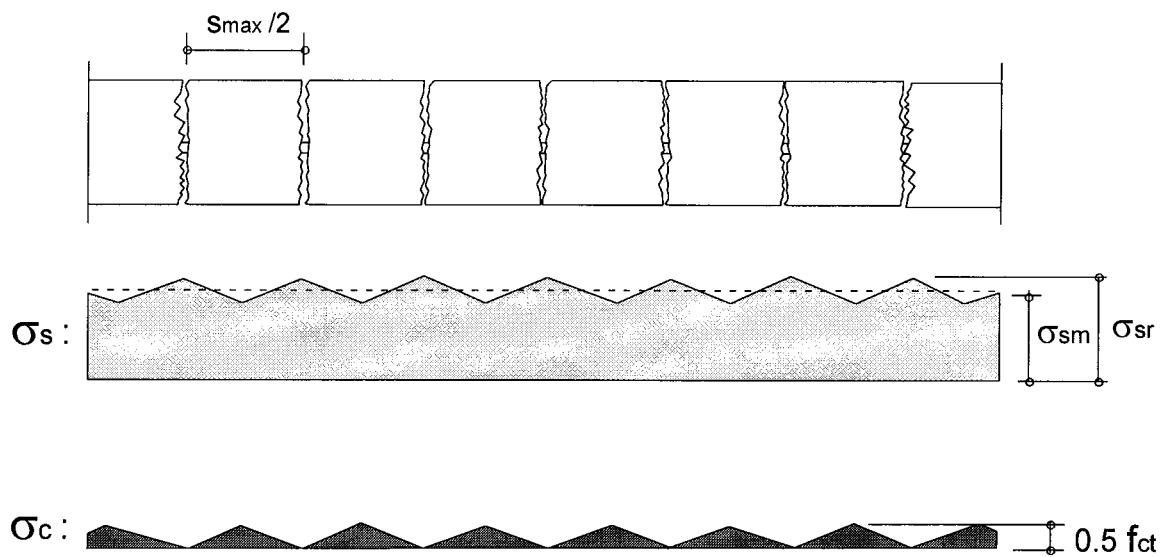


**Fig. 3.6 Effective Concrete Area in Tension (CEB/FIP MC90)**



a) Assumed Stress Distributions at Maximum Crack Spacing



b) Assumed Stress Distributions at Minimum Crack Spacing

**Fig. 3.7 Concrete and Steel Stress Distributions in terms of Crack Spacing According to Tension Chord Model (After Alvarez, 1998)**

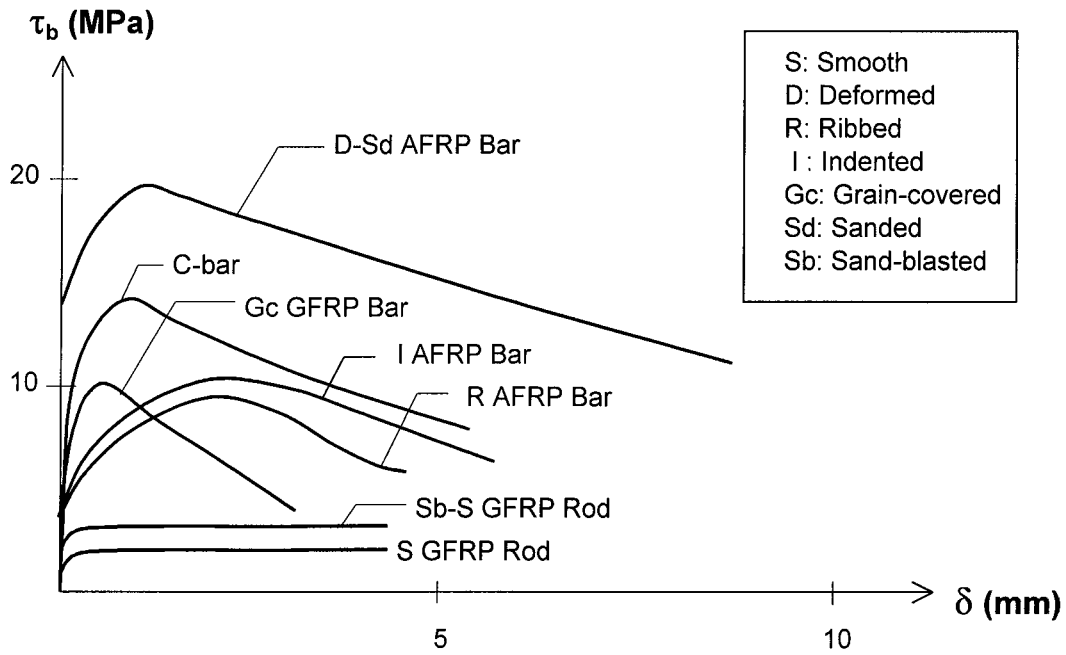


**Fig. 3.8 Typical Bond-slip Response of FRP (Pull-out Tests)**

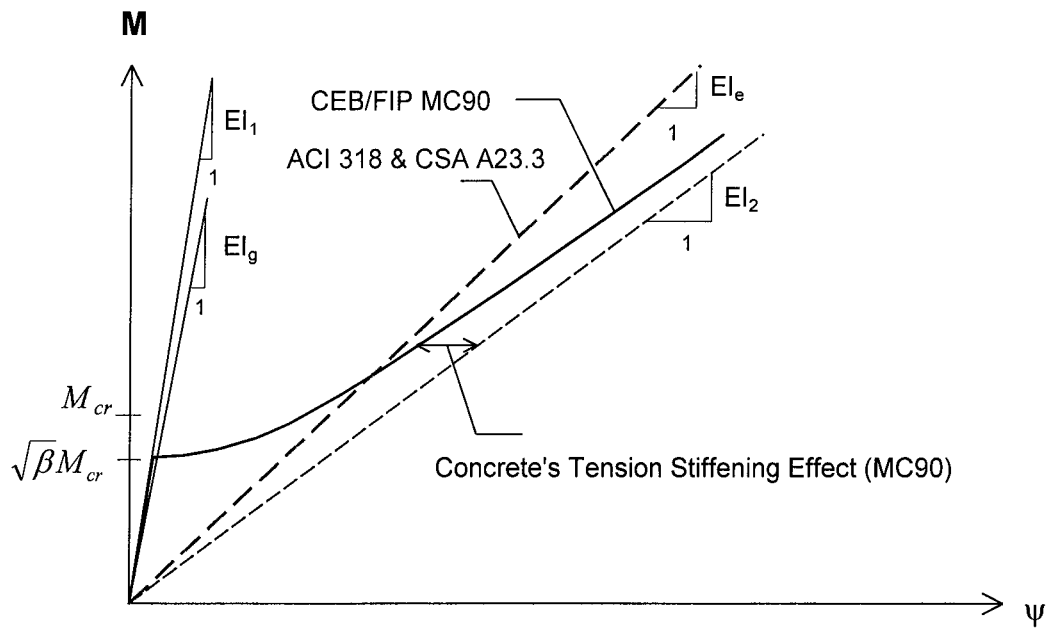


**Fig. 3.9 Tension Stiffening in ACI, CSA and CEB/FIP Codes**

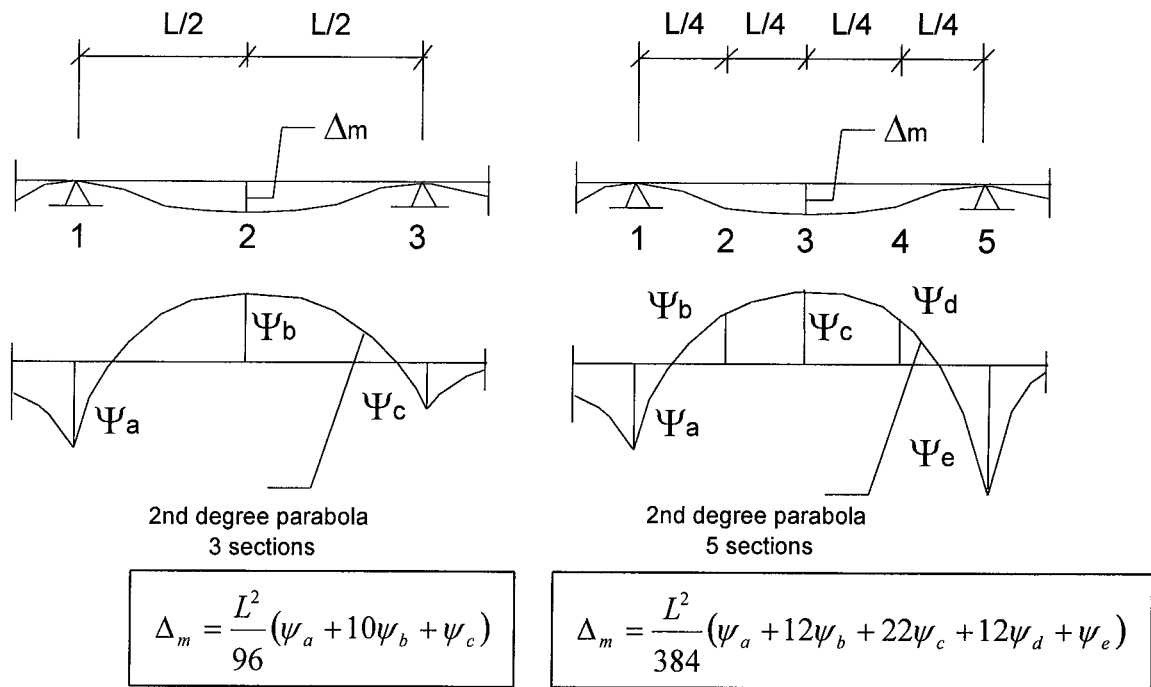


**Fig. 3.10 Deflections using Curvature Integration**

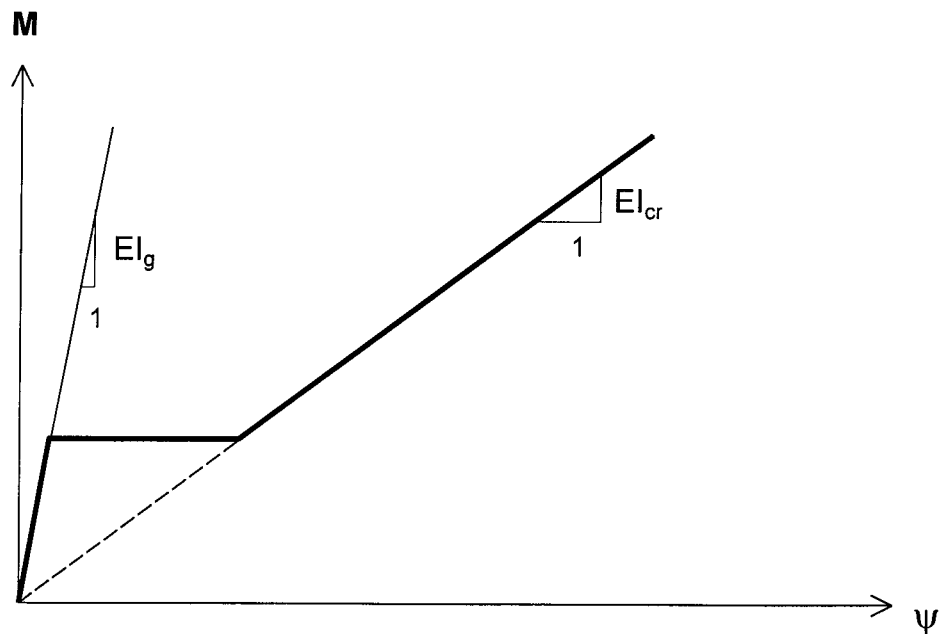
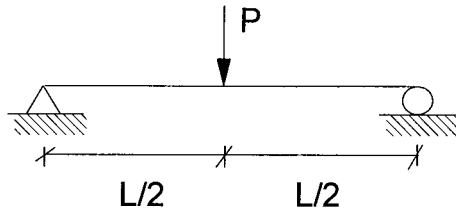
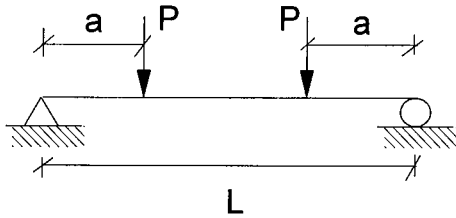


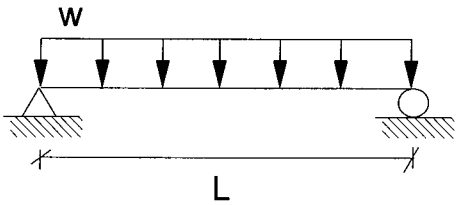
**Fig. 3.11 Idealised Moment-Curvature Response for Members with FRP (Razaqpur et al, 2000)**



$$\Delta_m = \frac{PL^3}{48E_c I_{cr}} \left( 1 - 8\eta \left( \frac{L_g}{L} \right)^3 \right)$$



$$\Delta_m = \frac{PL^3}{48E_c I_{cr}} \left[ 3 \left( \frac{a}{L} \right) - 4 \left( \frac{a}{L} \right)^3 - 8\eta \left( \frac{L_g}{L} \right)^3 \right]$$



$$\Delta_m = \frac{5wL^4}{384E_c I_{cr}} \left[ 1 - \frac{192}{5} \eta \left[ \frac{1}{3} \left( \frac{L_g}{L} \right)^3 - \frac{1}{4} \left( \frac{L_g}{L} \right)^4 \right] \right]$$

$$\eta = 1 - \frac{I_{cr}}{I_g} \quad ; \quad L_g : \text{uncracked beam portion from support.}$$

**Fig. 3.12 Deflection Calculations for Members with FRP According to CSA S806-00**

## **4 Background on Punching of FRP-reinforced Concrete Slabs**

### **4.1 General**

This chapter reports existing punching shear design provisions for interior concrete slab-column connections with internal or external FRP reinforcement. The chapter starts by defining the effect of FRP's elastic-brittle and flexible nature on slab punching capacity. Since existing punching design rules for slabs with FRP have evolved from conventional design approaches for steel-reinforced slabs, the latter are reviewed in detail.

### **4.2 Implications of Using FRP on Slab Punching Capacity**

In practice, most punching failures in interior two-way slab-column connections look the same: the column together with a slab portion push through the slab. In steel-reinforced concrete slabs, a punching failure may occur before or after a complete yield line mechanism has formed in the slab. The former defines what is herein called “brittle punching”. The latter defines what is termed “ductile punching”. Brittle punching is undesirable because it gives no failure warning.

In slabs with internal FRP reinforcement such a behavioural distinction lacks sense because conventional FRP reinforcement does not yield. As a result, a different design criterion needs to be defined. The results reported by Matthys and Taerwe (1997, 2000c) demonstrate that the amount and stiffness of the internal FRP reinforcement greatly affect the punching capacity of an interior slab-column connection. For the case of slabs with similar thickness, as the top FRP mat stiffness increases, the punching capacity increases, and the slab deformation at ultimate decreases. Since stiffer slabs are also necessary to comply with serviceability requirements, over-reinforcing the slab seems beneficial at both the serviceability and punching limit states.

To review and develop design provisions for slabs with internal FRP reinforcement accounting for the non-yielding elastic and less stiff response of FRP, the obvious frame of reference is that defined by existing design procedures for steel-reinforced concrete slabs.

### 4.3 Methods for Estimating Punching Capacities in Steel-reinforced Slabs

Former ACI Committee 426 (1974) and Regan and Braestrup (1985) present a comprehensive review of different methods for estimating the punching capacity of slabs reinforced with steel. In this study, only the following will be examined:

- a) The Control Surface Method
- b) The Yield Line Approach
- c) Kinnunen and Nylander's Approach
- d) The Strip Model

#### 4.3.1 The Control Surface Method

This method has been adopted by today's most influential codes of practice. It is extensively documented by former ACI Committee 426 (1974) and Regan and Braestrup (1985). The procedure, originally proposed by Talbot (1913), evaluates the applied shear stress at a surface located some distance from the column face and compares it with a determined concrete shear strength,  $v_c$ . Accordingly, the non-factored punching shear strength of an interior slab-column connection,  $V_r$ , is calculated as

$$V_r = v_c b_o d \quad [4.1]$$

where  $v_c$  is the nominal shear strength of concrete,  $b_o$  is the perimeter of the control surface and  $d$  is the average slab flexural depth.

Both the value of  $v_c$  and the control surface location vary from code to code. Two major schools of thought exist behind the  $v_c$  definition: both express  $v_c$  in terms of the tensile strength of concrete (typically expressed as the compressive strength of concrete raised to a given power), but one accounts for the effect of the slab reinforcement ratio and the other does not.

Figure 4.1 shows schematically the effect of the slab flexural reinforcement ratio on the load-deflection response of slab-column connections brought to punching. The figure is adapted from Criswell (1974). The term  $\phi$  represents the ratio of the measured failure load,  $P_u$ , to the theoretical flexural capacity of the slab,  $P_{flex}$ . Load levels at first yield of the slab reinforcement are indicated. The figure shows that a decrease in  $\rho_s$  leads to lower punching capacities and to more ductile behaviour. For the curves with  $\phi$  greater than 1.0, the slabs display a punching failure after reaching their flexural capacity.

The effect of  $\rho_s$  is explicitly accounted for by the British Standard BS 8110-95. In this code,  $v_c$  is calculated using a one-way shear strength with the control perimeter measured at  $1.5 d$  away from the column face.

$$v_{c,BS} = 0.79 (100\rho_s)^{1/3} \left( \frac{400}{d} \right)^{1/4} \left( \frac{f_{ck}}{25} \right)^{1/3} \quad [4.2]$$

where  $\rho_s$  is the steel reinforcement ratio,  $d$  is the average slab flexural depth, and  $f_{ck}$  is the characteristic compressive strength of concrete. In BS 8110-95, the critical perimeter is rectangular regardless of the column shape, as shown in Fig. 4.2. Equation 4.2 is considered to be a very reliable punching capacity estimator (Regan and Braestrup, 1985). The procedure was empirically derived based on an extensive test result database.

In both the American and Canadian codes, the effect of  $\rho_s$  is disregarded. In ACI 318-99,  $v_c$  is defined as

$$v_{c,ACI} = 0.33 \sqrt{f'_c} \quad [4.3]$$

where  $f'_c$  is the specified cylinder compressive strength of concrete. In CSA A23.3-94,  $v_c$  is evaluated as

$$v_{c,CSA} = 0.4 \sqrt{f'_c} \quad [4.4]$$

The effects of column rectangularity and aggregate density on  $v_c$  (which are accounted for by both codes) are not reported herein.



As noted by Afhami, Alexander and Simmonds (1998), the design provisions in CSA A23.3-94 render factored shear strength predictions that are about 85 % of those in ACI 318-99. This is because CSA A23.3-94 uses a partial material reduction factor for concrete of 0.6 whereas ACI 318 uses a performance-based reduction factor of 0.85 for punching. This leads to almost equal central factors of safety because the average load factor in CSA A23.3-94 is about 89 % of that in ACI 318-99.

Punching shear capacity predictions in ACI 318-99 and CSA A23.3-94 are considered both conservative and very scattered (Regan and Braestrup, 1985, and Braestrup, 1989). However, Alexander (1999) demonstrates that both the ACI and CSA code provisions correctly predict whether the punching capacity is greater or less than the flexural strength. This is very useful for designers because the design philosophy in ACI and CSA aims at the occurrence of slab flexural failure before does a punching failure.

Regan and Braestrup (1985) and Hallgren (1996) provide comprehensive reviews of punching shear design provisions in other codes of practice.

#### **4.3.2 Yield Line Approach for Punching**

The yield line approach for punching shear design was first proposed by Gesund and Kaushik (1970), after recognizing that for many tests reported in the literature as punching failures their ultimate load does not differ significantly from their flexural capacity. As a result, they concluded that most punching failures could be explained using yield analysis.

#### **4.3.3 Kinnunen and Nylander's Approach**

The model proposed by Kinnunen and Nylander (1960) (hereafter called the K-N model) is considered by many as the best analytical tool to predict the punching capacity of interior slab-column connections. The procedure was originally developed for slabs with ring reinforcement but was later modified by Kinnunen (1963) to account for two-way reinforcement.

The K-N model is based on the equilibrium of forces acting on a polar-symmetric slab supported by an interior column. Based on test measurements, the model assumes that the slab portion outside the shear crack rotates as a rigid body. This implies that most of the slab curvature takes place in the circumferential direction and that there is almost no curvature in the radial direction. Experimental observations by Anis (1970), Shehata (1985), Shehata and Regan (1989), and Hallgren (1996), among others, have corroborated this kinematical feature. In the original K-N model, failure is assumed to occur when the circumferential strains in the bottom of the slab nearby the face of the column reach a critical value. The model was originally conceived to render the ultimate shear capacity of a slab. However, Shehata and Regan (1989) modified the original model to predict the entire load-deflection response of a connection.

The K-N model has influenced the work on punching of isolated slabs reported by Shehata and Regan (1989), Shehata (1990), Marzouk and Hussein (1991) and Hallgren (1996), and that on laterally restrained slabs reported by Hewitt and Batchelor (1975) and Newhook and Mufti (1997). All of these punching models have kept the kinematic features of the original K-N model but have modified the failure criterion: In most cases, concrete crushing has been retained as the failure mode but using either different critical strain values or a different failure location. In some cases, additional failure criteria have been added (Shehata and Regan, 1989). Hallgren (1996) refined the K-N model by adding failure criteria based on non-linear fracture mechanics. The model assumes that punching is triggered by concrete splitting in the slab soffit close to the column face.

The concrete crushing-based punching failure criterion has been criticised by Shehata and Regan (1989). They argue that even some of Kinnunen and Nylander's slabs failed under tangential concrete strains much lower than those commonly associated with concrete crushing.

Despite of the fact that the K-N model can be programmed in a spreadsheet, perhaps its most challenging aspect refers to its highly iterative nature. Simpler codification is

however possible if some simplifications are made (see Shehata, 1990, and Nylander and Kinnunen, 1976, as reported by Hallgren, 1996).

### 4.3.4 Strip Model for Punching Shear

#### 4.3.4.1 Fundamentals

The strip model for punching developed by Alexander and Simmonds (1991, 1992) determines the punching capacity of slabs by subdividing a slab according to the dominant mechanism of shear transfer in the connection. Figure 4.3a shows the idealization of an interior slab-column connection according to this model. The connection is defined by four radial slab strips that divide the slab into four quadrants. The radial strips extend from the column to the line of zero shear on the span (for simplicity assumed as midspan) parallel to the internal slab reinforcement. The model assumes that the quadrants transfer the load to the radial strips and these in turn transfer the load to the column.

To define the governing load transfer mechanism in the strips and quadrants, the model starts from the fundamental definition of shear in one-way members being equal to bending moment gradient.

$$V = \frac{dM}{dx} = \frac{d(T jd)}{dx} = T \frac{d(jd)}{dx} + \frac{dT}{dx} jd \quad [4.5]$$

The first term in the right hand side of Eq. 4.5 refers to arching action shear. This shear transfer mechanism, typical of disturbed or “D” regions, requires a gradient in the internal flexural lever arm. The second term refers to beam action shear, typical of slender beam-type, or “Bernoulli”, or “B” regions. It requires a gradient in tensile force in the reinforcement.

The model assumes that slab quadrants transfer load to the radial strips by beam action. In transferring load to the column, and recognizing that the column is a disturbed region, the radial strips are assumed to behave as deep beams. Both of these shear transfer

mechanisms are conceptually consistent with the experimental observations made by Kinnunen and Nylander (1960) and Anis (1970).

Load transfer between the quadrants and each radial strip face is constrained by the appropriate limits of shear transfer in slender members, i.e., the availability of gradient in tensile force. Bar force gradients are limited by i) yielding of the slab reinforcement, ii) bond failure, and iii) a change in slab mechanics. The first mechanism applies only to slabs with yielding reinforcement. The other two apply to any reinforcement type. By a change in slab mechanics one refers to the transformation of one shear transfer mechanism into another depending on the behaviour of adjacent reinforcing bars.

The amount of load transferred by the radial strips depends on their flexural capacity. The ability of the slab to transfer shear to the column depends then on the interaction between the slender behavior of the slab and the deep behavior of the strips.

Unlike the control surface approach, the strip model defines a critical section that is neither fixed nor square nor circular. Instead, the critical section has a cruciform shape, as shown in Fig. 4.3b. The length “ $l$ ” is a function of the flexural capacity of the radial strip and the amount of one-way shear carried by the slab quadrants.

#### **4.3.4.2 Simplified Mathematical Formulation of the Strip Model**

The strip model describes a radial strip as a column-supported cantilever beam with negative and positive moment capacities,  $M_{neg}$  and  $M_{pos}$ , and loaded as shown in the elevation view of Fig. 4.4. The column reaction  $P_s$  represents the load transferred by the strip. The effect of torsional moments is implicitly accounted for in the applied load.

The strip model provides a lower bound estimate for the capacity of a radial strip. According to Drucker (1960), any lower bound estimate requires that (i) equilibrium must be satisfied and (ii) that the structure, i.e. the radial strip, cannot be loaded beyond its flexural capacity. For steel-reinforced concrete slabs, Alexander and Simmonds (1991) add that the strip's response must be ductile enough to allow moment redistribution.

In Fig. 4.4, the term  $w$  is a lower bound estimate of the one-way shear that can be delivered by the adjacent slab quadrant to one side of the strip at ultimate. Since each radial strip has two sides, the total uniformly distributed load on the strip is  $2w$ . Rotational equilibrium results in

$$M_s = M_{neg} + M_{pos} = \frac{2w l^2}{2} \quad [4.6]$$

where  $M_s$  is the total flexural capacity of the strip and  $l$  is the loaded length of the strip. Vertical force equilibrium leads to

$$P_s = 2w l \quad [4.7]$$

Solving Eq. 4.7 for  $l$  and substituting into Eq. 4.6 yields the capacity of a radial strip

$$P_s = 2 \sqrt{M_s w} \quad [4.8]$$

Since an interior connection consists of four radial strips, its punching shear capacity is

$$P_s = 8 \sqrt{M_s w} \quad [4.9]$$

The total flexural capacity is the sum of  $M_{pos}$  and  $M_{neg}$ . For slabs with remote ends rotationally free (like most tests in the literature), only  $M_{neg}$  needs to be calculated. The term  $w$  is taken as

$$w = 0.166 \sqrt{f'_c} d \quad [4.10]$$

Analysis of more than 200 tests on steel-reinforced concrete two-way slabs published in the literature show that the strip model is both a safe and reliable punching capacity estimator (Alexander, 1999). Its applicability for the punching shear design of FRP-reinforced or strengthened flat plates will be the subject of analysis in this study. In this context, it is necessary to evaluate the flexural capacity of the radial strip,  $M_s$ , and also to determine what is the maximum force gradient that the FRP bars or the bonded FRP sheets can transfer. This assessment will determine the best lower bound estimate for the  $w$  term.

## 4.4 Existing Punching Shear Design Recommendations for Two-way Slabs Reinforced with FRP

### 4.4.1 Punching of Two-way Slabs with Internal FRP Reinforcement

Ahmad *et al* (1993) found that their test results are underestimated by ACI code provisions and overpredicted by BS 8110-95. Matthys and Taerwe (2000c) found that current design equations in CEB/FIP MC90, EC2, and BS 8110-95 tend to overestimate the shear capacity of slabs reinforced with very flexible FRP rebars or grids. The ACI 318-99 equation, which neglects the effect of flexural reinforcement, yielded conservative estimates for slabs with CFRP and hybrid Carbon/Glass FRP (HFRP) grids but at the expense of a considerable scatter.

Matthys and Taerwe (2000c) modified the equations expressed in terms of the reinforcement ratio with the factor  $\rho_f \frac{E_f}{E_s}$ , where  $E_f$  and  $E_s$  refer to the modulus of elasticity of FRP and steel, respectively. Based on previous work reported by Gardner (1990), which is conceptually identical to that reported by Regan and Braestrup (1985), Matthys and Taerwe proposed the following equation to calculate the punching capacity of a two-way FRP-reinforced concrete slab.

$$V_{c,Ghent} = 1.36 \frac{\left( 100 \rho_f \frac{E_f}{E_s} f_{cm} \right)^{1/3}}{d^{1/4}} b_o d \quad [4.11]$$

where  $f_{cm}$  is the mean compressive strength of concrete. Ignoring the modification ratio  $\frac{E_f}{E_s}$ , Eq. 4.11 is virtually identical to the punching shear equation given by BS 8110-95 except for the resulting constant and the definition of the compressive strength of concrete. Likewise BS 8110-95, the critical perimeter  $b_o$  in Eq. 4.11 is assumed to be rectangular or square regardless of the cross-sectional shape measured at a distance of  $1.5d$  away from the column face.

Matthys and Taerwe applied Eq. 4.11 to their test results yielding mean test to predicted ratios of 1.33 and 1.15 for 8 CFRP and 5 HFRP grid-reinforced concrete slabs, respectively. Such an improved accuracy is not surprising because the BS 8110 equation is considered to be the most reliable punching capacity estimator for ordinary slabs.

In an attempt to examine different non-empirical models to predict the punching capacity of slabs with FRP, Matthys and Taerwe (2000c) also modified the models proposed by Hallgren (1996) and Men  trety (1996) for steel-reinforced concrete slabs. They found that the modified-Hallgren (MH) model rendered good predictions whereas the modified-Men  trety (MM) model was found to be overly conservative.

El-Ghandour *et al* (1997 and 2000) introduced two design procedures for the punching of two-way slabs with FRP. One is to modify the reinforcement ratio by the factor  $\rho_f \frac{E_f}{E_s} k_\epsilon$ , where  $k_\epsilon$  is a constant. Since FRP can mobilize strains in the order of 0.0045, dividing 0.0045 between 0.0025 (assumed yield strength of steel) gives 1.8, which is the value they propose for  $k_\epsilon$ .

El-Ghandour *et al* (1999) also proposed the following modification to the ACI equation.

$$v_{c, Sheffield} = 0.33 \sqrt{f'_c} \left( \frac{E_f}{E_s} \right)^{1/3} \quad [4.12]$$

#### 4.4.2 Punching of Two-way Slabs Rehabilitated with FRP Sheets

Tan (2000) found that unidirectional slab strengthening with FRP does not lead to a significant punching capacity increase. For slabs strengthened in two directions, the punching capacity increased with the reinforcing index of the FRP, defined as

$$\omega_f = \frac{A_f}{bh} \frac{f_{fp}}{f'_c} \quad [4.13]$$

where  $A_f$  is the area of FRP,  $b$  is the slab width,  $h$  is the slab thickness,  $f'_c$  is the concrete compressive cylinder strength and  $f_{fp}$  is the stress in the FRP reinforcement at punching, taken as 20 % of its ultimate tensile strength. For slabs with same FRP reinforcement index, the highest punching capacities were displayed by two-way CFRP sheets, followed by two-way GFRP fabric and by the CFRP plates.

#### **4.5 Other Strengthening and Repair Schemes for Slab-Column Connections**

When facing a repair challenge, the designer is often pushed to consider the possibility to take down the structure instead of repairing it. Under current economic constraints, demolition may be out of the question. Other than using FRP, different techniques have evolved to enhance the shear response of slab-column connections. For new construction, conventional procedures include the use of shearhead reinforcement (Corley and Hawkins, 1968), integral beams with vertical stirrups, shear stud reinforcement (Seible, Ghali and Dilger, 1980) and steel beams on the slab underside (Ramos, Lúcio and Regan, 2000).

In terms of strengthening existing slab systems, through-thickness prestressing bolts around the column (Ghali, Sargious and Huizer, 1974, and Ramos, Lúcio and Regan, 2000), insertion of through-thickness shear reinforcement and the addition of shotcreted column capitals and bonding of a steel collar below the slab (Hassanzadeh and Sundqvist, 1999) have been successfully implemented.

To repair punched slabs, Ramos, Lúcio and Regan (2000) replaced the damaged concrete by pouring new concrete around the joint. In this study, this procedure is termed as “concrete patching”. The concrete-patched slab tested by Ramos *et al* failed at a load slightly greater than the original failure load.

#### **4.6 Observations**

Based on the design approaches previously reviewed, the following observations arise:



- i ) Existing punching shear design provisions either ignore the effect of flexural reinforcement or assume implicitly that steel reinforcement is used.
- ii ) Because they do not consider the effects of the slab flexural reinforcement, the punching design provisions of both ACI 318-99 and CSA A23.3-94 predict the same strength for two slab-column connections built with the same concrete strength but with different reinforcement type.
- iii ) The British Standard BS 8110-95 accounts for the effect of slab reinforcement but does not offer any guidance as to how to deal with the reduced stiffness and brittle nature of FRP bars or grids.
- iv ) As far as Gesund and Kaushik's flexural capacity approach is concerned, it is not clear how one would define a yield-line mechanism for slabs with non-yielding reinforcement.
- v ) The current formulation of the strip model for punching is not applicable for slabs reinforced or strengthened with FRP reinforcement.

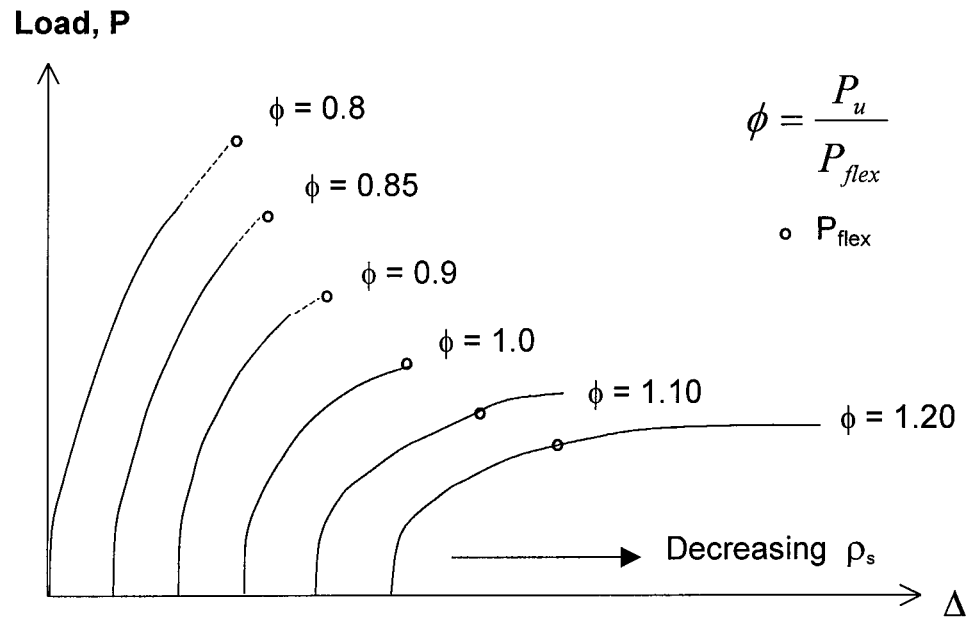


**Fig. 4.1 Effect of  $\rho_s$  on Punching Capacity  
(After Criswell, 1974)**

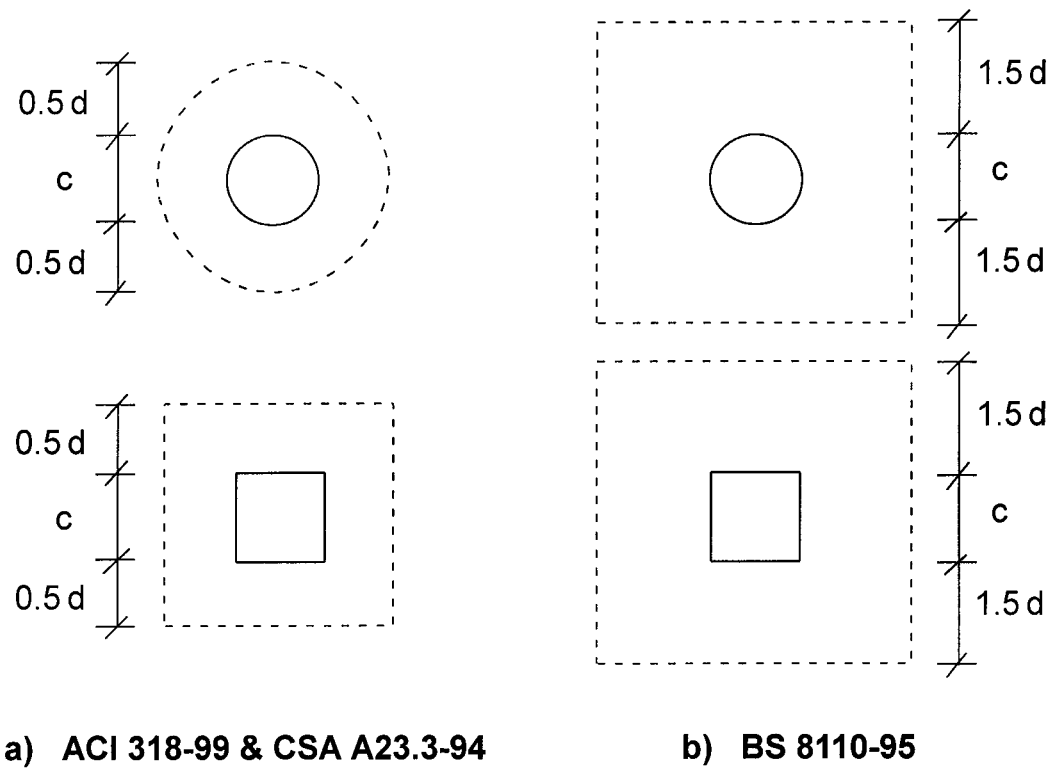
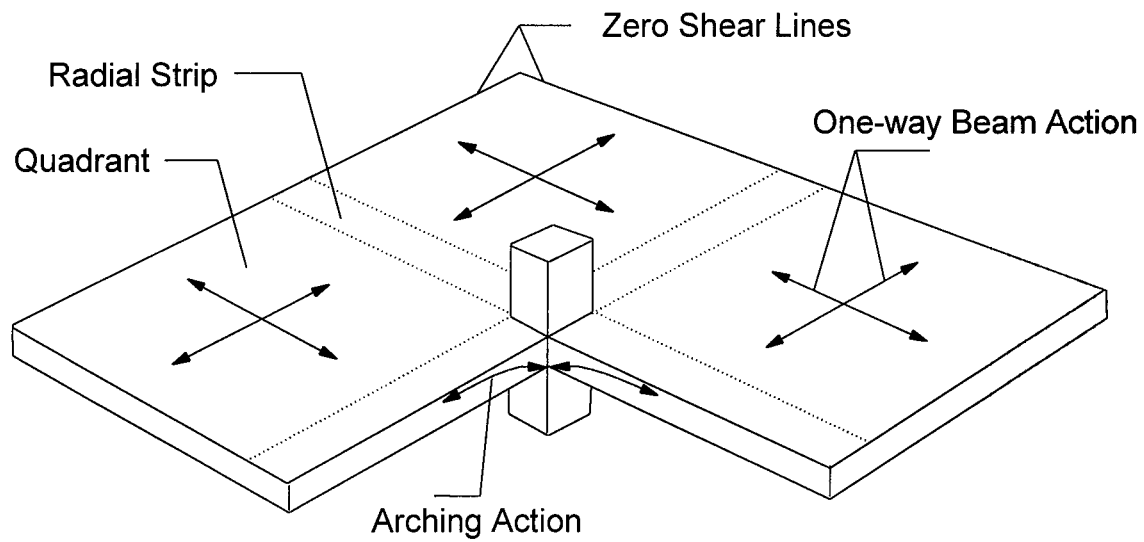
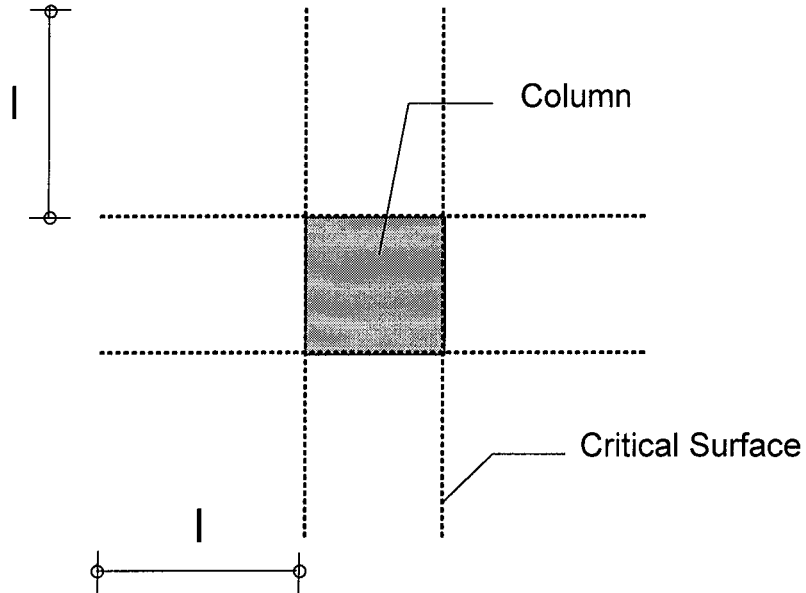


**Fig. 4.2 Control Surfaces for Punching Capacity  
Evaluation in ACI, CSA and BS Codes**



a) Assumed Force Transfer Mechanism



b) Control Surface

**Fig. 4.3 Fundamental Concepts of Strip Model for Punching  
(After Alexander and Simmonds, 1991)**

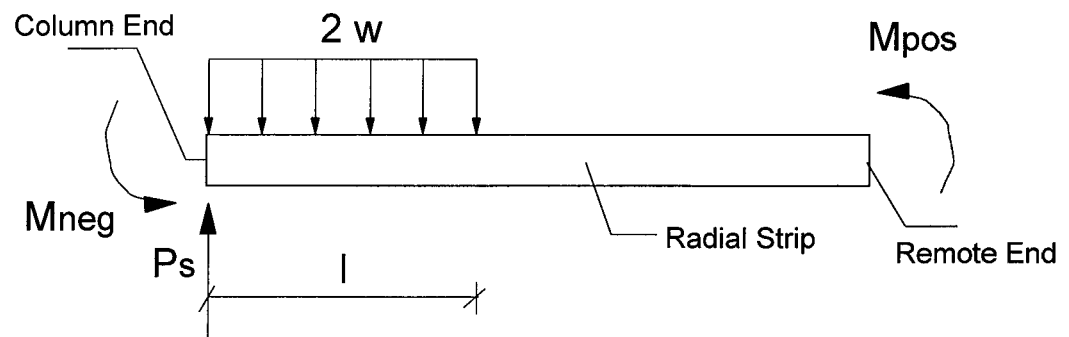


**Fig. 4.4 Free Body Diagram of Radial Strip  
According to Strip Model**



## **5 Experimental Program**

### **5.1 Objectives**

The experimental program concentrates on the punching shear behaviour of slabs with internal and external FRP reinforcement. The tests were performed with three objectives: i) evaluate the punching capacity implications of using FRP reinforcing bars or grids in new flat plate construction, ii) examine the suitability of bonded CFRP sheets on the slab top surface to reinforce interior slab-column connections in shear, and iii) examine other viable repair techniques for interior connections that have experienced punching failures.

The experimental program was divided into two series. The first series examined the effect of GFRP deformed bars and NEFMAC grids on the punching capacity of interior flat plate-column connections. The second series focused on the punching shear reinforcement and repair of two-way flat plates.

### **5.2 Series I Tests : Punching Shear Tests of Slabs with Internal FRP**

#### **5.2.1 Description of Test Specimens**

The geometrical and material properties of series I test specimens are shown in Fig. 5.1 and Table 5.1. The slab dimensions (2.1 m square) were selected to simulate the behaviour of a slab-column connection in a 4.5 m interior span prototype flat plate. The specimen dimensions match approximately the points of contraflexure along the prototype span direction.

Four isolated slab-column connection specimens were built. The main variables were the type, cross-sectional shape and amount of slab reinforcement. Two slabs were reinforced with GFRP deformed bars, commonly referred to as "C-bars", one with a GFRP NEFMAC 2-D grid, and one with ordinary steel. The latter acted as the control slab. The three reinforcement types are shown in Fig. 5.2. The NEFMAC sample observed in Fig. 5.2 was cut out of a NEFMAC grid.

Figures 5.3 to 5.7 shows elevation and plan views showing the reinforcement details in all slabs. The control slab, SR-1, had 0.87 % top steel reinforcement ratio. Slabs GFR-1 and GFR-2 had 0.73 and 1.46 % GFRP C-bars, respectively. Slab NEF-1 had 0.87 % NEFMAC reinforcement ratio. The ratios were calculated based on a nominal cross-section of 200 mm<sup>2</sup> for the steel bars and the NEFMAC ribs and 176 mm<sup>2</sup> for the GFRP C-bars. All top steel rebars in SR-1 had 180 degree hooks. No end anchors were installed in the NEFMAC grid. C-bars were provided with specially designed mechanical end anchors, as shown in Figs. 5.8, 5.11 and 5.12. The anchor consisted of a steel plate-tube assembly through which the C-bar end passed. The tube was made by welding a 13 mm diameter conventional prestressing chuck to a 38 mm o.d. 2 mm thick 80 mm long piece of aluminum electrical conduit. The gap between the tube and the C-bar was filled with a high-modulus epoxy. The epoxy was poured with the reinforcing bar in vertical position. Both the joint between the tube and the plate and that between the bar and the plate hole were siliconed before resin pouring. The goal behind the use of the prestressing chuck (notice the sloped inner walls in Fig. 5.8) was to prevent the C-bar from drawing-in upon pulling.

The bottom slab reinforcement was spaced as indicated in the elevation views of Fig. 5.3. Conventional 10M steel bars were used in SR-1. In GFR-1, GFR-2 and NEF-1, the bottom reinforcement consisted of # 4 GFRP C-bars. All slabs were provided with integrity reinforcement. In SR-1, two 15 M steel bars were used in each direction for this purpose. In GFR-1, GFR-2 and NEF-1, it consisted of two # 5 GFRP C-bars in both directions. Figure 5.9 shows the handiness of NEFMAC grids. Figs. 5.10 to 5.13 show the reinforcement mats.

### **5.2.2 Specimen Fabrication**

Specimens were fabricated in pairs. SR-1 was cast simultaneously with NEF-1, and GFR-1 with GFR-2. Fabrication involved the following steps: First, the column reinforcing cage was built by welding the longitudinal column reinforcement (2-15M C-shaped bars) to a 19 mm thick 250 mm square steel plate. The column reinforcement was used as a hook for lifting purposes. The column reinforcing cage was then inserted through a hole

left in the slab formwork. The slab reinforcement was placed later. Then, both the lower column and the slab concrete were cast with concrete mixed in the lab. Two hours later, the upper column concrete forms were set up and the top column concrete was poured. The upper column stub forms were carefully supported to avoid disturbing the fresh slab concrete. Concrete mixing and casting of the two specimens was performed by a three-men crew in about three hours. The specimens were covered with plastic sheets and cured for seven days. The slab forms were removed at the time of testing.

### **5.2.3 Test Set-up**

Figures 5.14 and 5.15 show the typical test set-up for series I slabs. The load was applied from below by pushing the lower column stub up with an 890 kN (200 kip) centre hole jack. Four 19 mm diameter steel tie rods anchored to the strong floor reacted against this load. The load in each tie rod was split into two load points by a 5" deep HSS distributing beam.

This arrangement constrained the load to be symmetric about the diagonal axes. Symmetry of deflections about diagonal axes was not enforced. An alternative arrangement using eight load rods to tie each load point directly to the lab floor was rejected. This scheme would constrain the deflections to be symmetric about the diagonal axes but would not ensure equal load in each tie rod. Afhami, Alexander and Simmonds (1998) note that an isolated slab-column connection specimen under constrained deformations will fail at a higher load than one with constrained loads.

### **5.2.4 Instrumentation**

The column load was measured with an 890 kN (200 kip) load cell. The tie rods themselves measured slab loads by converting strain readings from gauges attached to them into loads based on coupon test results.

Slab deflections were measured with LVDTs installed on the slab underside as shown in Fig. 5.16. The LVDTs were mounted on aluminum frames clamped to the bottom of the



lower column stub thereby providing a direct slab deflection measurement. Readings from the LVDTs also provided the basis to calculate rotations of the slab soffit.

Strains in the top slab mats were measured with 120-ohm electrical resistance foil-type strain gauges mounted as shown in Figs. 5.4 to 5.7. Gauges were waterproofed with a nitrile rubber coating and a silicone patch. The chosen gauge layouts allow the evaluation of average strain values at a given location from four symmetrically placed gauges. Strain gauges in SR-1, GFR-1 and GFR-2 were placed at mat crossing points. Due to the difficulty to calculate the cross-sectional area at a NEFMAC rib intersection, all of the gauges in NEF-1 except those at the column face were placed 70 mm off crossings as shown in Fig. 5.7. Makizumi, Sakamoto and Okada (1993) show that the longitudinal strain along a NEFMAC rib between two rib crossings is constant over the whole interval.

### **5.2.5 Test Procedure**

The load was applied from below in 5 to 10 kN increments by pushing the lower column stub up with the jack. Early in the tests, the loads in the tie rods were equalised by manual adjustment. The tie rod loads remained equal throughout the remainder of each test. End anchors, if any, were monitored to check for any bar slippage. Crack widths were measured at different test stages. The tests were stopped after punching failure was evident. The test of NEF-1 was suspended at a slab deflection of about 48 mm. Punching in this specimen is believed to have occurred earlier. The duration of each test ranged from 4 to 6 hours.

### **5.2.6 Ancillary Tests**

#### **5.2.6.1 Concrete**

Specimens were cast in the laboratory with 30 MPa nominal concrete batched in the lab. The maximum size of the aggregate was 19 mm. Compressive strength tests were carried out according to ASTM C42-90. As shown in Table 5.1, the concrete compressive strength at the time of testing was 36.8, 29.5, 28.9 and 37.5 MPa for slabs SR-1, GFR-1,

GFR-2 and NEF-1, respectively. The age of the slabs at testing time was 39, 19, 28 and 32 days for SR-1, GFR-1, GFR-2 and NEF-1, respectively. Tensile splitting tests were also conducted on at least three cylinders taken from each slab. The values are reported in Table 5.1. Both compressive and splitting cylinders were cured likewise their source specimens.

#### **5.2.6.2 Steel Reinforcement**

Properties of steel rebars in tension were obtained according to ASTM 370. Fig. 5.18 shows a typical stress-strain curve for a steel tension coupon. Table 5.1 shows the most relevant mechanical properties of the steel reinforcement. Yield and ultimate strengths correspond to static values.

#### **5.2.6.3 GFRP Reinforcement**

The stress-strain response of GFRP bars and GFRP NEFMAC ribs in tension was obtained from coupon tests designed following the recommendations of Castro and Carino (1998), and Rahman, Taylor and Kingsley (1993).

A typical GFRP tension coupon consisted of a sample with aluminum tubes cast at its ends as shown in Fig. 5.17. The samples were pieces of either GFRP bars or portions cut out of a NEFMAC mat. The tubes prevented the sample's ends from being crushed by the testing machine grips. The NEFMAC samples were cut from the same grid from which slab NEF-1 was reinforced.

The ancillary testing program for GFRP reinforcement was divided in two phases. The first phase (a pilot phase) was conceived to examine the effect of different end sleeve fillers. The second phase was conceived to evaluate the main mechanical properties of GFRP.

In ancillary phase 1, two fillers were examined: either a low modulus epoxy resin or mortar. The epoxy was of the type L700S manufactured by Mitsubishi Corp., which is

commonly used to bond CFRP sheets to concrete or masonry. The mortar was made by mixing anchoring cement and water in proportions of 2:1 by weight. Tensile strength tests were carried out in a MTS 1000 rock testing machine. The specimens were gripped at the ends with the heads of the testing machine with a 6.9 MPa (1000 psi) gripping pressure. The load was applied at a rate of about 150 MPa/min. The sample's free length and that of the grips were 400 and 250 mm, respectively. Strains were measured with two strain gauges located at midheight and by a 50 mm (2") gauge length extensometer.

Test results from ancillary phase 1 show that the samples with epoxy filler provided better end conditions for sample gripping. As a result, the coupon ends of ancillary phase 2 tests were cast solely with epoxy.

In ancillary phase 2, three GFRP NEFMAC rib and six GFRP C-bar samples were tested. The sample free length and the end grip length were reduced to 330 and 200 mm in an attempt to save on materials. Unfortunately, these reduced lengths were not adequate and the sleeves tried to slip relative to the epoxied end at about 50 % of the ultimate load. It is worth remarking that no slippage between the epoxy and the samples was observed which suggests that the sleeve dimensions would have worked fine had a better bond between the sleeves and the epoxy been provided. Taking advantage of FRP's linear-elastic response, the slip between the epoxied end and the tube was eliminated by increasing the gripping pressure to 10 MPa (1500 psi). This pressure level was high enough to squash the end tubes. The slippage could not be prevented in two tests despite the pressure increase. These tests had to be terminated prematurely without recording the failure load. Nevertheless, they provide useful information to evaluate the elastic stiffness of FRP. For future reference, it is recommended that the same specimen dimensions be used as in ancillary phase 1 tests.

In the successful ancillary tests, warning of failure was provided by an increasingly progressive fibre rupture. At failure, the fibres ruptured and splayed out away from the end sleeves. The average results of the GFRP ancillary phase 2 tensile tests are shown in Table 5.1. Typical stress-strain curves for GFRP and NEFMAC tension coupons before

fibre rupture initiation are shown in Fig. 5.18. Their response is compared to that obtained for one 15 M steel bar. The straight curves for the C-bar and NEFMAC rib tests show the more flexible and elastic-brittle behaviour of FRP compared to steel. Material properties were in some cases lower than those reported by the suppliers.

### **5.3 Series II Tests : Punching Shear Strengthening and Rehabilitating Tests of Interior Slab-column Connections**

Series II examines the feasibility of using CFRP sheets to strengthen interior slab-column connections and also studies the quality of other conventional techniques for the rehabilitation of flat plate-column connections that have failed in punching. Only concentric punching conditions will be examined herein. The effect of internal shear reinforcement was not considered.

Series II tests consisted of seven tests performed on three identical full-scale slab-column connection specimens. The specimens were similar in shape to those of series I but the slab segments were considerably larger and the experiments were conducted under more accurate boundary conditions. Each specimen was brought to either punching failure or to a near punching stage and later was either repaired or strengthened. The original slabs are referred to as “virgin” slabs. The next sections describe the testing plan for series II slabs, the rationale behind the virgin slab design, the design outcome and the tests performed on the slabs.

Table 5.2 describes this testing program series. Three specimens were built: ER1, ER2 and ER3. Two tests were conducted on slab ER-1. In the first test, ER1-VS, the virgin slab was brought to punching failure. The label "ER" indicates that slab 1, like all of series II slabs, was “Edge-Restrained”. This slab was the control slab.

Slab ER1 was then repaired by replacing the punched slab concrete with a through-thickness concrete patch. The concrete patch replaced only the conical portion of concrete that had punched through the slab. The slab was then re-tested and brought back to failure. This test was labeled ER1-CP1. The term “CP” indicates that the slab was

repaired with a Concrete Patch. The next digit indicates the type of patching performed. Two patching schemes were examined.

Two loading tests were conducted on slab ER2. The first was conducted on virgin slab ER2-VS. The slab was loaded up to 70 to 75 % of its estimated punching capacity and then unloaded and strengthened with FRP sheets passing by the column face. Details of FRP sheet layout, amount, etc... will be covered later. The specimen was then brought to punching failure. This test was labeled ER2-CS1. The term "CS" indicates that the slab was strengthened with CFRP Sheets. The next digit refers to the adopted sheet layout, being 1 that in which the sheets passed beside the column face.

Three tests were performed on slab ER3. The first test, ER3, was a loading test of virgin slab ER3-VS up to 70 to 75 % of its expected failure load. The load was then removed and the slab was strengthened with FRP sheets. Later, the specimen was brought to punching failure. Compared to ER2-CS1, the FRP sheets in this slab were placed farther away from the column faces. The test was labeled ER3-CS2. After failure, the slab was unloaded and the FRP sheets were removed to conduct a third test on the plate. This test was a repair test. The slab was repaired by replacing the damaged concrete from test ER3-CS2 with a high strength concrete patch. This patch was greater than that of ER1-CP1. The new concrete covering the full slab thickness was cast within a longer radius. This test was labeled ER3-CP2.

### **5.3.1 Virgin Slab Design**

Series II virgin slabs were designed to ensure that yield-line mechanisms would form almost simultaneously in the two directions before a punching shear failure occurred. The specimens were intended to model a prototype interior flat plate-column connection with at least three spans in both directions. A prototype interior span of 4.9 m with 400 mm square columns was selected. The three virgin slabs were similar in shape, concrete strength and reinforcement amount.

Unlike series I specimens, series II slabs were rotationally restrained along the edges. Due to weight constraints of the lab overhead crane, the side dimensions of each slab were limited to 4.2 m. Due to the impossibility of using an infinitely stiff edge-restraint system, the 4.2 m slab panel width models in reality a somewhat longer prototype span.

Figure 5.19 shows the geometric properties of a typical virgin slab specimen. Since the slabs were subjected only to concentric load, the column stubs protruded only 300 mm above and 330 mm below the slab. The holes on the slab indicate the location where the loading and edge restraint hardware were installed.

To avoid deflection calculations, CSA A23.3-94 recommends a minimum slab thickness for two-way flat plates equal to

$$h_{s,min} = \frac{l_n \left( 0.6 + \frac{f_y}{1000} \right)}{30} \quad [5.1]$$

where  $l_n$  is the clear span between columns and  $f_y$  is the yield strength of the slab reinforcement. For  $l_n$  equal to 4500 mm, and assuming a nominal 400 MPa yield strength for the steel reinforcement, Eq. 5.1 yields a minimum slab thickness of 150 mm. A nominal slab thickness of 152 mm (6") was selected.

The specimens satisfied CSA A23.3-94 flexural reinforcement requirements in terms of cut-off points, anchorage, development length and integrity steel.

The flexural design of the slab specimens followed a rather unorthodox procedure: Since minimum flexural requirements usually govern the positive moment design of two-way slabs, the slab was first proportioned for positive reinforcement. Then, based on the moment distribution percentages given by the direct design method, the amount of slab negative reinforcement was selected.

Since the main objective of this experimental series was to rehabilitate and repair existing slabs, minimum flexural reinforcement areas were selected according to an old Standard.

ACI 318-71 was selected for this purpose. The selected slab thickness also satisfied the limits stipulated by ACI 318-71. A minimum clear cover of 24 mm was used for both top and bottom steel.

ACI 318-71 recommends a minimum flexural reinforcement of  $0.002 A_g$ , which results in  $304 \text{ mm}^2/\text{m}$  of steel reinforcement. Using 10M bars spaced at 330 mm, yields  $A_s^+ = 303 \text{ mm}^2/\text{m}$ , which is adequate. The minimum reinforcement was placed in the direction with smallest flexural depth (W-E). As far as the top reinforcement design is concerned, the maximum and minimum theoretical effective flexural depths (for 15M bars) were, respectively, 120 and 104 mm. For bottom reinforcement calculations (for 10M bars), the maximum and minimum theoretical effective flexural depths were, respectively, 122 and 111 mm.

According to the direct design method, the total static moment in a panel,  $M_o$ , is calculated as

$$M_o = \frac{q l_2 l_n^2}{8} \quad [5.2]$$

where  $q$  is the uniformly distributed load per unit area,  $l_n$  is the clear span in the direction of the moment, and  $l_2$  is the centre-to-centre spacing between columns in the orthogonal direction.

Assuming that all bottom reinforcement yields at ultimate, and setting all material resistance factors equal to unity, the moment capacities can be calculated as

$$M_r = A_s f_y \left( d - \frac{A_s f_y}{2 \alpha_1 f'_c b} \right) \quad [5.3]$$

In CSA A23.3-94,  $\alpha_1$  is a stress block factor calculated as

$$\alpha_1 = 0.85 - 0.0015 f'_c \quad [5.4]$$

Substituting  $A_s^+ = 303 \text{ mm}^2/\text{m}$ ,  $f_y = 400 \text{ MPa}$ ,  $d = 111 \text{ mm}$  (positive flexural depth in the W-E direction),  $f'_c = 30 \text{ MPa}$  and  $\alpha_l = 0.81$  into Eq. 5.3 results in  $m_r^+ = 13.2 \text{ kN.m/m}$ . Assuming that 65 % of  $M_o$  is apportioned to the negative, and 35 % to the positive, bending sections, leads to  $0.35 m_o = 13.2 \text{ kN.m/m}$ . As a result, the static panel moment per unit width,  $m_o$ , is equal to  $37.7 \text{ kN.m/m}$ . Substituting  $m_o = 37.7 \text{ kN.m/m}$  and  $l_n = 4.5 \text{ m}$  into Eq. 5.2 results in  $q = 14.9 \text{ kPa}$ , which is the positive flexural capacity of the slab.

Likewise, the negative moment capacity is  $m_r^- = 0.65 m_o = 24.5 \text{ kN.m/m}$ . This moment is the average of that in the column and middle strips. Allotting 75 % of the panel moment to the column strip results in  $m_{r,col}^- = 0.75 \times 24.5 \times 2 = 36.8 \text{ kN.m/m}$ . Placing 15M bars spaced at 200 mm ( $A_s^- = 1000 \text{ mm}^2/\text{m}$ ) at  $d = 104 \text{ mm}$ , the unfactored negative moment capacity in the W-E direction in the column strip is  $38.3 \text{ kN.m/m}$ . Following the same rationale, the negative moment capacity of the middle strip,  $m_{r,mid}^-$ , is  $0.25 \times 24.5 \times 2 = 12.25 \text{ kN.m/m}$ .

According to Alexander and Simmonds' strip model, the punching capacity of the interior connection can be calculated as

$$P_s = 8 \sqrt{M_s w} \quad [5.5]$$

where  $w = 0.167 \sqrt{f'_c} d$ . The term  $M_s$  is the flexural capacity of the strip, evaluated as

$$M_s = c_w (m_{r,col}^- + m_{r,col}^+) \quad [5.6]$$

where  $c_w$  is the column width,  $m_{r,col}^-$  is the distributed negative moment capacity in the column strip and  $m_{r,col}^+$  is the distributed positive moment capacity in the column strip. For  $M_s = 0.4 (36.8 + 13.2) = 20 \text{ kN.m}$  and assuming  $d$  equal to the average top slab flexural depth,  $d = 112 \text{ mm}$ , leads to an unfactored punching shear capacity of  $362.1 \text{ kN}$ . Hence, the uniformly distributed load per unit area that causes punching failure according to the strip model,  $q_{u,SM}$ , is  $20.5 \text{ kPa}$ .



According to ACI 318-99, the unfactored punching shear capacity of the connection is equal to  $0.33 \sqrt{f'_c} b_o d$ . Assuming  $d = 112$  mm, and calculating the critical perimeter at  $0.5 d$  away from the column face yields a punching capacity of 414.6 kN, or  $q_{u,ACI} = 23.5$  kPa.

Figures 5.20 and 5.21 show the top and bottom reinforcement layouts for series II virgin slabs. The column longitudinal reinforcement consisted of four C-shaped bars which give a total of eight 15M steel bars. Likewise series I slabs, the longitudinal column reinforcing bars served as hooks to facilitate the slab lifting procedure. Both the upper and lower column stubs had three 10M closed-leg stirrups spaced at 100 mm. No stirrups were left within the joint region.

### 5.3.2 Slab Formwork and Additional Slab Detailing

The slab formwork was supported by a grillage of transversely braced I-shaped stranded board wooden joists resting directly on the lab strong floor. Two 19 mm thick plywood layers covered the grid. To facilitate the specimen's removal after casting, the bottom plywood layer was screwed down to the grillage and the upper layer remained loose.

To enable the installation of the loading and restraint hardware, it was necessary to block out 48 holes in the slab according to the layout shown in Fig. 5.19. This was accomplished by tying down 50 mm diameter 152 mm high aluminum conduit pieces to the formwork's upper layer. The slabs were lifted off the forms after removal of these tubes. For lifting purposes, four 15M steel hooks were placed in the slab corners during casting.

### 5.3.3 Specimen Fabrication

The specimen fabrication procedure followed three major steps. First, the lower concrete column stub was cast up to the level of the slab soffit far from the slab forms with concrete at least as strong as that used in the slab. The next day, the column stub was lifted up and inserted into the slab formwork centre hole. Later, the bottom and top slab

reinforcement mats were set up. Figure 5.22 shows the reinforcing cage of a typical virgin slab. Special care was taken to keep the slab flexural depth as originally planned.

The next day the concrete slab was cast. A local supplier delivered the concrete. A crew of three to four people cast the slab concrete in two hours. Figure 5.23 shows a typical concreting session. Special measures were taken to protect the slab reinforcement strain gauges from getting damaged during concrete vibration. The next day, the upper column forms were mounted on the slab and the upper column stub was cast with a lab-batched concrete mix. The virgin slabs were built in series.

### **5.3.4 Test Apparatus**

#### **5.3.4.1 Supports**

Each slab was tested in a location other than its casting spot. Specimens were lifted from their casting spot with a 10 Ton. capacity overhead crane and moved over their testing site. The slab was lifted from both the column stub and the slab corners. To avoid premature flexural cracking, 60 to 65 % of the dead load was taken first by the slab corners and the rest by the centre column. Figure 5.24 illustrates the lifting process. The specimens were then supported on four equidistant pedestals. Once the slab was leveled, the lifting load was removed from the column and then from the corners. Because of cracking concerns, the slab was propped up with additional supports between pedestals.

#### **5.3.4.2 Loading Assembly**

Figure 5.25 shows a view of a typical slab through the setting-up process. The test set-up is shown in Figs. 5.26 and 5.27. The test set-up was conceptually similar but far more elaborated than that adopted in series I slabs.

The lower column stub was pushed up with a 890 kN (200 kip) centre hole jack. Figure 5.28 shows the column support detail. The jack rested on a 50 mm thick 500 mm diameter steel base plate. A spherical bearing steel support was placed between the jack

piston and the base of the lower column stub. A 890 kN commercial load cell was placed in series between the jack and the lower column.

The centre column load was reacted against by four whiffle tree assemblies that were tied down to the lab strong floor. Each whiffle tree load was split into four points. As a result, the slab load was simulated by 16 point loads distributed as shown in Fig. 5.26. The horizontal tree branches were made of HSS sections. The upper vertical branches consisted of 19 mm diameter thread-ended tie rods. These rods were connected to the slab by a system of plates, 25 mm (1") dia. spherical-end Dywidag nuts, and 19 mm (3/4") dia. conventional nuts. The Dywidag nuts allowed tie-rod self-adjustment upon the slab's rotation. The rods were tied with the 19 mm dia. nuts. Figure 5.29b illustrates this detail. A 25 mm (1") dia. Dywidag bar played the role of "trunk" in each of the four loading trees. Each was tied down to the strong floor with a spherical-end Dywidag nut and a steel plates, as shown in Fig. 5.29.

#### **5.3.4.3 Edge Restraint System**

A rotational restraint system was used to properly model boundary conditions on the slabs. The selected edge restraint system consisted of eight independent frame-type assemblies (four running in each direction) mounted on top of the slab. This was done to avoid conflicts with the loading hardware and whatever instrumentation ran underneath the plate. To have the edge restraint system on the slab meant that the restraint system would work essentially in tension. This facilitated the setting up process because only a small tension tie was required to connect the uprights. A compressive-type edge restraint system, i.e., one installed underneath the plate, would have required horizontal links with much larger cross-sections. The way the loads are applied through the edge restraint system uprights to generate positive bending along the slab edges induces in-plane compressive forces in the slab. However, these forces are not significant.

Each assembly consisted of two uprights and a horizontal tie evenly distributed in the N-S and W-E directions, as shown in Fig. 5.26, 5.27 and 5.29a. Each upright was a steel square hollow column tied down to the slab with two 25 mm diameter 350 mm long

threaded rods. The tie was built by coupling two 25 mm diameter fully threaded A307 grade “Stud stock” steel rods. To monitor the tie load, a 30 kN home-made load cell was placed in series between the rods. This measurement was essential for calculation of the positive moment along the edges. To avoid conflicts with the orthogonal edge restraint system ties, the N-S uprights were somewhat taller than those in the W-E direction. Dimensions and additional details for the edge restraint system are shown in Figs. 5.26, 5.27 and 5.29a.

Installation of the edge restraint system took about two to three hours for one person to complete. Prior to removing the slab supports, the transverse ties rested on wooden posts. At the start of a test, each restraint frame was pretensioned by wrench-tightening the ties against the uprights. The load level in each transverse tie was determined based on the approximate distribution of positive moments in the prototype slab under self-weight.

Ideally, the edge restraint system should represent the midspan of the prototype slab, i.e., a zero rotation line. However, because the uprights were not infinitely stiff, the specimen ended up modeling a longer prototype span.

### **5.3.5 Instrumentation**

#### **5.3.5.1 Load Measurement**

The column load was monitored with an 890 kN (200 kip) capacity commercial load cell. The load in each whiffle tree was measured with a home-made 445 kN capacity load cell. The force in each edge restraint system tie was measured with a home-made 30 kN capacity load cell built on a 250 mm long 25 mm diameter threaded rod piece.

#### **5.3.5.2 Deflection Measurements**

Slab vertical deflections were measured on the slab underside with 10 - 250 mm (10”) range cable transducers (CTs) installed as shown in Fig. 5.30. The first eight CTs (running along N and W radial slab strips) were mounted on a metal frame clamped to the lower portion of the bottom column stub. Cable transducers 9 and 10 rested on the strong

floor. The upper movement of the lower column relative to the floor level, which is essential for calculation of slab deflections from the latter two CTs, was measured with an LVDT. Since all cable transducers were installed after moving each slab to its testing position, these devices measured only the deflections due to the applied load. Slab deflections under dead load were obtained by surveying the plate on 20 points at the time the slab supports were removed.

#### **5.3.5.3 Rotation Measurements**

Slab rotations were measured along the slab edges and nearby the column in the radial direction. Edge slab rotations were measured with 8 pairs of LVDTs. These devices were mounted horizontally on aluminum arms clamped to the slab as shown in Fig. 5.31. The LVDTs were connected to wires strung across from opposite arms. The arms were located as shown in Fig. 5.31. The LVDTs were placed at two levels. Both 25 and 50 mm range LVDTs were installed at the top level. Only 50 mm range LVDTs were placed at the bottom. The LVDT location is indicated in the footnote of the figure.

Radial slab rotations nearby the column were measured on the slab underside in the W-E and N-S direction based on the vertical deflection readings taken by CTs 1, 2, 3 and 5, 6 and 7.

#### **5.3.5.4 Crack Measurements**

Top slab cracks were measured in all four directions at 40, 160 and 500 mm (slab ER1 and ER2 tests) and at 40, 160 and 400 mm (slab ER3 tests) away from each column face as shown in Fig. 5.32. Top cracks were measured with a 2" Demec gauge and an illuminated 0.025 mm precision microscope. Top crack width measurements were taken regularly up to several load steps before failure.

Bottom crack widths were measured with the microscope on the outermost positive cracks on the column strip at mid-edge (stations H (W-E cracks) and I (N-S cracks)) and on the middle strip (station J (N-S cracks)).

The development of the internal shear cracks was also monitored. This was done by drilling six holes around the connection and injecting a dye cast at 50, 150 and 250 mm away from the column face along the S and E radial slab strips. The hole depth was smaller than the slab thickness. The procedure was not successful because the dye cast ended up diffusing inside the concrete without leaving a well-defined tracking of the internal crack growth.

#### **5.3.5.5 Strain Measurements on Steel Reinforcement**

Both top and bottom slab reinforcing bars were instrumented with 120-ohm electrical resistance foil-type strain gauges arranged as shown in Figs. 5.20 and 5.21. The gauges were mounted on the neutral plane of the rebar cross-section and then duly waterproofed. Gauge wires were taken out of the slab through holes made on the formwork sidewalls. The chosen top gauge layout allows to measure average strain values from at least two symmetrically placed gauges.

Top gauges provide information on the circumferential rebar strain distribution along radial strips and on the radial strain distribution along perimeter bars. The latter is essential to quantify force gradients developed by the slab quadrant bars. Top strain gauge readings were also used to evaluate negative moments across the slab at both the column centreline and the column face. Bottom gauges in the slab periphery provide information to calculate positive moments.

#### **5.3.5.6 Through-Slab thickness Strains**

To further monitor the formation and growth of internal shear cracks in the slab-column connection region, six through-thickness strain gauges were installed along the N and W radial strips at 50, 150 and 250 mm away from the column face. The gauges, fabricated in the lab, consisted of copper strips attached to springs. The devices were installed after drilling 5 mm diameter holes through the slab concrete.

### **5.3.5.7 Data Acquisition**

Load cell, strain gauge, cable transducer and LVDT readings were recorded electronically with one 130-channel Fluke 2400B data acquisition unit connected to a personal computer.

### **5.3.6 Rehabilitation Techniques**

#### **5.3.6.1 General**

One strengthening technique and one repair procedure were examined. The strengthening technique consisted of adhering CFRP sheets on the slab top surface. This technique was implemented before punching failure occurred. The repair technique consisted of replacing the punched slab concrete with new concrete. It was performed after punching failure occurrence.

The FRP sheet-based strengthening procedure was chosen because i) adhesion of FRP sheets on a plane surface seems a natural choice for the product, and ii) according to any shear model that accounts for the effect of the slab flexural reinforcement, bonding FRP sheets to the slab top surface should enhance both the flexural and punching capacity of the connection. Carbon fibres (CFRP) were chosen due to their higher stiffness. Two CFRP sheet strengthening arrays, shown in Figs. 5.33 and 5.34, were implemented. Figures 5.35 to 5.38 show the typical sheet lay-up process. The concrete patching repair option was selected as a relatively inexpensive post-punching repair solution. Two patching schemes were examined (see Figs. 5.39 and 5.40).

### **5.3.7 Slab-Column Connection Strengthening with CFRP Sheets**

#### **5.3.7.1 Material Description**

The CFRP sheets used were of the type MRL-T7-200, supplied by the Industrial Technology Research Institute, ITRI, Taiwan. The sheets were delivered in 500 mm wide plies wrapped onto cardboard rolls. The fibres were unidirectional, unthreaded and not pre-impregnated. The supplier's specifications of the CFRP sheets are shown in Table 5.3.

The sheets were intended to be used with a two-part primer and epoxy. The primer (to be applied on the slab surface) was obtained by mixing a primer agent (MRL-A2) with a hardener (MRL-B2) in a 100-35 proportion by volume. The epoxy (to adhere the sheets to the slab surface) was produced by mixing a resin (MRL-A3) with a hardener (MRL-B2) in a 100-35 proportion by volume.

#### **5.3.7.2 Test ER2-CS1: Rehabilitation Procedure**

The rehabilitation scheme on slab ER2 was conducted after unloading slab ER2-VS. The rehabilitation scheme is shown in Fig. 5.33. Each strip of CFRP consisted of two layers of CFRP. The CFRP installation process is shown in Figs. 5.35 to 5.38.

The FRP installation process followed the recommendations given by CSA S806-00. First, the slab surface regions where the sheets were to be applied were ground smooth and then finished with a putty. Then, a primer coat (MRL-A2 + MRL-B2) was applied on the slab (Fig. 5.35), and left to cure for one day (Fig. 5.36). Eight 250 mm wide 4600 mm long CFRP strips were cut and left ready for use.

The first sheet was laid out on a polyurethane-covered plywood sheet and impregnated with a coat of epoxy using a paint roller. Simultaneously, the slab region where the first layer was to be bonded was given a first coat of epoxy (MRL-A3 + MRL-B2). The CFRP sheet was then carefully positioned on the slab and pressed against using an epoxy-soaked paint roller with a foam roller cover. The sheet was continuously rolled up to remove trapped air bubbles.

The first bands to be installed were those along the W-E direction. The installation of upper sheets was similar to that of lower sheets except that no epoxy coating was provided on the sheets below since they were already epoxy-soaked. The N-S bands were adhered later.



All bands in slab ER2 were folded over the slab edges. To prevent fibre tearing by the sharp slab edges, the edges were ground flush, smoothened with putty and primer-coated the day before. To further prevent premature sheet peeling off, all strips were anchored with 1550 mm long 250 mm wide single layer strips placed as shown in Fig. 5.33. The installation of the four CFRP bands, i.e. eight CFRP layers, was carried out by a two-men crew in approximately 5 hours. The CFRP sheets were allowed to cured for one week.

#### **5.3.7.3 Test ER3-CS2: Rehabilitation Procedure**

Figure 5.34 shows the strengthening layout for slab ER3 for test ER3-CS2. The upgrading technique in this test was similar to that in ER2-CS1 except that the CFRP sheets were placed away from the column.

The installation process was identical to that previously reviewed. The first layers to be bonded on the slab were those in the W-E direction. However, unlike ER2-CS1, the strips in ER3-CS2 were not wrapped over the slab edges. The sheets were interrupted near the slab edge. No additional sheet anchorage was provided either.

#### **5.3.8 Slab-Column Connection Repair by Concrete Patching**

Figures 5.39 and 5.40 show the details of the two concrete patching schemes adopted. Both connection regions were patched with high strength concrete. This concrete type was selected for no other reason than its high early strength gain. Due to lab space constraints, it was required to test the repaired slabs no later than a week after concrete-patching the connection.

In test ER1-CP1, the slab was repaired by replacing the slab concrete that had punched. This test was conducted to study the feasibility of the concrete patching repair involving a minimum amount of work. The process is shown in Figs. 5.41 to 5.44. To facilitate the repair process, the middle ERS tie rods were dismantled. Then, the damaged slab concrete surrounding the joint concrete was crushed with a jack hammer (Fig. 5.41) and removed by hand. Simulating real-life conditions, where the column in a punched

connection may be still carrying significant axial load, the joint concrete was left intact. Concrete removal in the slab bottom level extended only up to 50 mm away from the column faces. As a result, the bottom face of the punching failure surface served as a mould for placing the new concrete. Figure 5.39 shows a side view of the approximate boundary between the new and old concrete.

Because the slab concrete around the column had been removed, it was necessary to install forms on the slab bottom surface. The forms were bolted together as a collar and clamped to the lower column stub. It is worth noting that due to the punching failure of slab ER1 in test ER1-VS, a 35 to 40 mm residual upward displacement of the column up remained. This is consistent with the fact that in real life, a punched slab would sink relative to the column.

The old concrete surface was soaked with water before placing the concrete (Fig. 5.42). No special bonding agent was used. The concrete was batched in the lab. The mix had coarse aggregate, sand, water and cement proportions of 1000, 870, 145 and 430 kg/m<sup>3</sup>, respectively. To improve workability, 15 kg/m<sup>3</sup> of superplasticizer were added. Two cylinders were filled at the time of casting. The average cylinder compressive strength after a week was 57.9 MPa.

Concrete placement, vibration and finishing for ER1-CP1 were difficult because the mix was very stiff. Particular care was taken to keep the original slab thickness. The slab bottom forms were removed two days later. The new concrete was allowed to cure for five days by covering it with water-soaked burlap. A view of the connection after the patch hardened and the bottom forms were removed is shown in Figs. 5.43 and 5.44.

The repair test ER3-CP2 was similar to ER1-CP1, except that the new concrete occupied a larger slab-column connection area and a better bond was ensured between the old and new concrete. Figure 5.40 illustrates the details of this repair. At the bottom, the concrete patch extended 390 mm away from the column face, which is almost eight times of that in ER1-CP1. A more vertical interface was chosen to improve the mechanical joint

between the old and the new concrete. The larger concrete patch required wider forms on the slab underside. The forms were clamped on the lower column stub and supported on the strong floor.

Likewise the previous test, the old concrete surface was cleaned and soaked with water before placing the new concrete patch. The water content of the new mix increased slightly compared to that used previously to improve workability. The average compressive strength from two cylinders filled at time of patching was 52.6 MPa. The slab bottom forms were removed two days later. Curing conditions were similar to those on repaired slab ER1.

### **5.3.9 FRP Sheet Instrumentation**

#### **5.3.9.1 FRP Sheet Strains**

Longitudinal strains in the CFRP sheets were measured with 120 mm foil-type strain gauges located as shown in Figs. 5.33 and 5.34. These gauges were not waterproofed. The gauges provided information not only on the longitudinal distribution of CFRP strains but also on the different mechanisms of moment gradient transfer that could be provided by the CFRP.

#### **5.3.10 Loading Procedure**

Both virgin and rehabilitated series II slabs were subjected to considerable damage not only to simulate fairly stringent prototype conditions but also to challenge the different strengthening/repair techniques. Prior to the start of each test, the ERS was prestressed to provide a positive moment distribution similar to that in a prototype slab under self weight.

Slab ER1-VS was brought to punching failure after imposing five load cycles. The cyclic loading was applied to simulate actual conditions in a prototype slab and cause extensive slab damage. In slabs ER2-VS and ER3-VS, the load was applied in three cycles up to first yielding of the slab reinforcement and then removed. In tests ER2-CS1 and ER3-

CS2, the strengthened slabs were loaded cyclically once more and then brought to punching. In ER1-CP1 and ER3-CP2, the repaired slab was loaded through three cycles up to punching failure.

### **5.3.11 Ancillary Tests**

#### **5.3.11.1 Concrete for Virgin Slabs**

Series II virgin slabs were cast in the laboratory with 30 MPa nominal compressive strength normal density concrete delivered by a local supplier. The maximum size of the aggregate was 19 mm. Compressive strength tests were performed on 150 by 300 mm cylinders.

Table 5.4 shows the concrete compressive strength values for the three virgin slabs and for each of the two concrete patches at the time of testing. Tests complied with ASTM C42-90. Tensile splitting tests were also conducted on a minimum of three 150 by 300 mm cylinders cast while fabricating the slabs. These results are also included in Table 5.4.

#### **5.3.11.2 Steel Reinforcement**

The properties of steel reinforcing bars under tension were obtained in accordance to ASTM 370. Table 5.4 shows mean yield, ultimate strength and Young's modulus values for the steel reinforcement used in series II slabs. Yield and ultimate strength values are static values.

#### **5.3.11.3 FRP Sheets**

The mechanical properties of the CFRP sheets in tension were obtained in accordance to ASTM D 3039-95a (1995). Tables 5.3 and 5.4 show, respectively, the mechanical properties of the CFRP sheets according to the supplier and the test results. Taking into account the variability of the strip thickness, the material properties refer to the fibre alone. The results show that mechanical properties are close to those reported by the supplier.

Figure 5.45 shows a typical stress-strain response of the CFRP coupon and the carbon fibre subjected to axial tension. For the stress evaluation of the CFRP coupon, calculations are based on a 20 mm coupon width and an average thickness of 0.5 mm. The stress in the carbon fibre was evaluated based on the manufacturer's supplied value of 0.11 mm. The response in direct tension of a 15 M steel rebar from the same batch used to reinforce slab ER3 is provided for comparison.

**Table 5.1 Series I Slabs : Properties**

Slab	Top Reinforcement Type and Spacing	$f'_c$ (MPa)	$f'_{spt}$ (MPa)	$\rho$ (%)	$E_r$ (GPa)	$f_y$ (MPa)	$f_{su}$ or $f_{fu}$ (MPa)
SR-1	15M Steel Rebars @ 200	36.8	2.37	0.87	192.0	430	682
GFR-1	# 5 GFRP C-bars @ 200	29.5	2.10	0.73	34.0	—	663
GFR-2	# 5 GFRP C-bars @ 100	28.9	2.10	1.46	34.0	—	663
NEF-1	GFRP NEFMAC Grid with ribs @ 200	37.5	2.49	0.87	28.4	—	566

**Note:**  $\rho$  values were calculated based on an average slab flexural depth of 120 mm and  $A_s = 200 \text{ mm}^2$  (steel),  $A_f = 200 \text{ mm}^2$  (NEFMAC) and  $A_f = 176 \text{ mm}^2$  (GFRP C-bars).

**Table 5.2 Series II Slabs : List of Tests**

Slab	Test	Test Description
ER1	ER1	Loading test of virgin slab ER1 up to punching failure
	ER1-CP1	Loading test of repaired slab ER1 up to punching failure
ER2	ER2	Loading test of virgin slab ER2 up to 70 % of its estimated punching capacity
	ER2-CS1	Loading test of CFRP sheet-rehabilitated slab ER2 up to punching failure
ER3	ER3	Loading test of virgin slab ER3 up to 70 % of its estimated punching capacity
	ER3-CS2	Loading test of CFRP sheet-rehabilitated slab ER3 up to punching failure
	ER3-CP2	Loading test of concrete patch-repaired slab ER3 up to punching failure

- Notes:
1. ER means series II slabs were Edge-Restrained.
  2. CS1 and CS2 refer to the two CFRP Sheet-based rehabilitation schemes used.
  3. CP1 and CP2 refer to the two Concrete Patch-based repair schemes adopted.
  4. Test ER3-CP2 was conducted after ER3-CS2 punched (the sheets were removed).
  5. Design  $d$  values are reported in Figs. 5.20 and 5.21.
  6. Measured average  $d$  values :  $d^- = 109 \text{ mm}$  and  $d^+ = 119 \text{ mm}$ .
  7. In accordance with measured  $d$  values,  $\rho^- = 0.92 \%$  in all virgin slabs.

**Table 5.3 Mechanical Properties of CFRP Sheets**

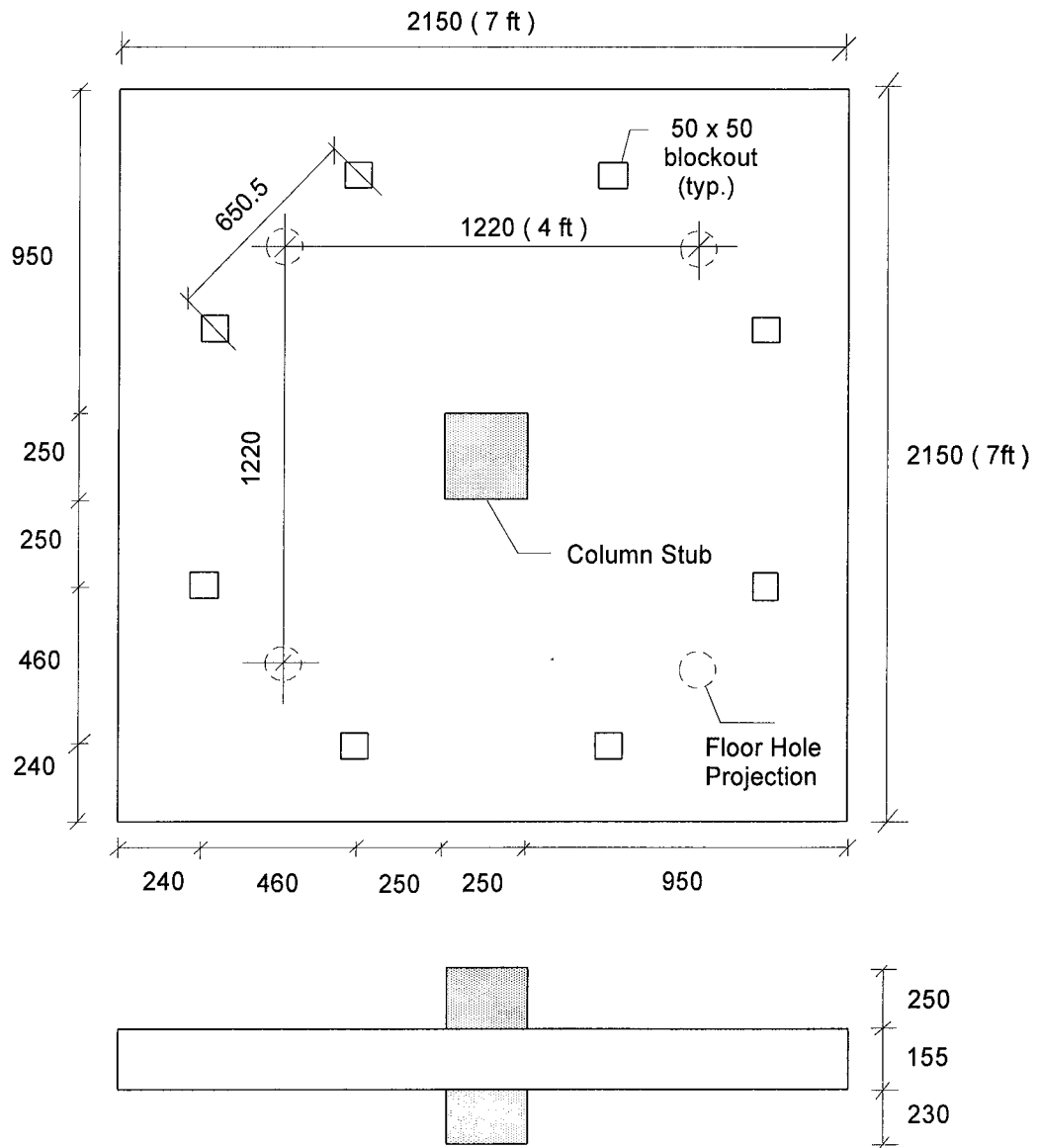
Property	Supplier	U. of A. Tests
Tensile Strength (N/cm/ply)	4511	3875
Elastic Modulus (N/cm/ply)	252995	247750
Fibre Tensile Strength (N/mm <sup>2</sup> )	4805	3523
Fibre Elastic Modulus (N/mm <sup>2</sup> )	230000	230000
Fibre Thickness (mm/ply)	0.11	0.11
Fibre Elongation (%)	2.1	1.52

- Notes: 1. CFRP Sheets were of the type MRL-T7-200, supplied by ITRI, Taiwan.  
2. Sheets were unidirectional, unthreaded and not pre-impregnated.  
3. Material properties from U. of A. tests were obtained based on 20 mm width CFRP coupons (The tests were conducted by M. Kuzik).

**Table 5.4 Series II Slabs : Ancillary Test Results**

Test	$E_s$ (GPa)	$f_{y, 15M}$ (MPa)	$f_{y, 10M}$ (MPa)	$f'_c$ (MPa)	$f'_{spt}$ (MPa)	$E_f$ (GPa)	$E_{cf}$ (GPa)	$f_{cfu}$ (MPa)
ER1-VS	200	428	441	29.8	2.87	—	—	—
ER1-CP1				57.9	4.45	—	—	—
ER2-VS	200	428	441	34.6	2.91	—	—	—
ER2-CS1						55.9	230	3523
ER3-VS	200	422	462	30.6	2.50	—	—	—
ER3-CS2						55.9	230	3523
ER3-CP2				52.6	N/A	—	—	—

- Notes: 1. N/A : Not available.  
2. The elastic modulus for both 15M and 10M steel bars was the same.  
3.  $f'_c$  values in ER1-CP1 and ER3-CP2 refer to the concrete patch.  
4.  $E_{cf}$  and  $f_{cfu}$  values refer to Carbon Fibre (calculated based on a fibre thickness of 0.11 mm).



Note: Dimensions in mm unless otherwise specified

**Fig. 5.1 Geometry of Series I Test Specimens**

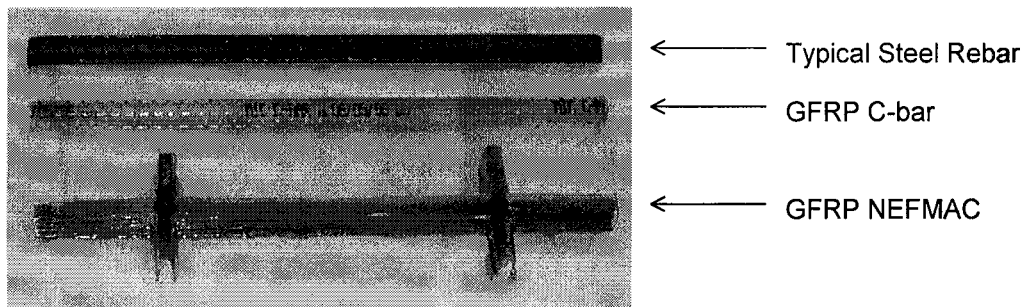
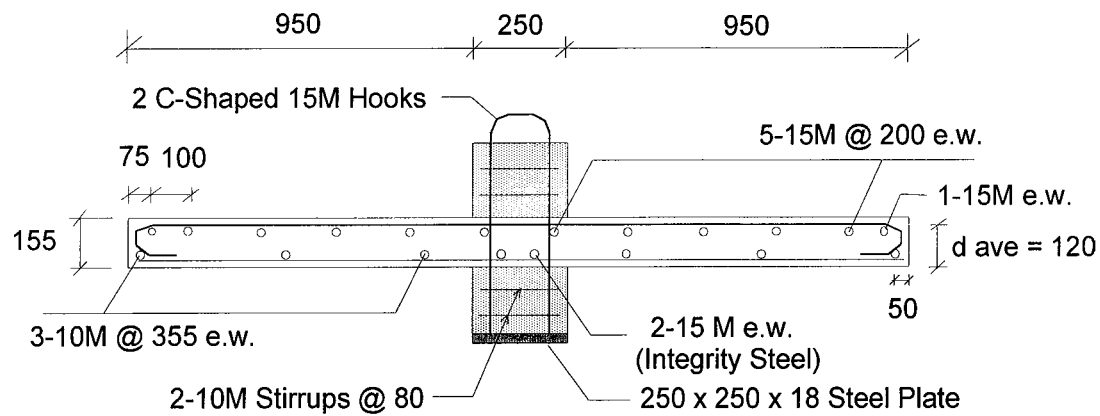
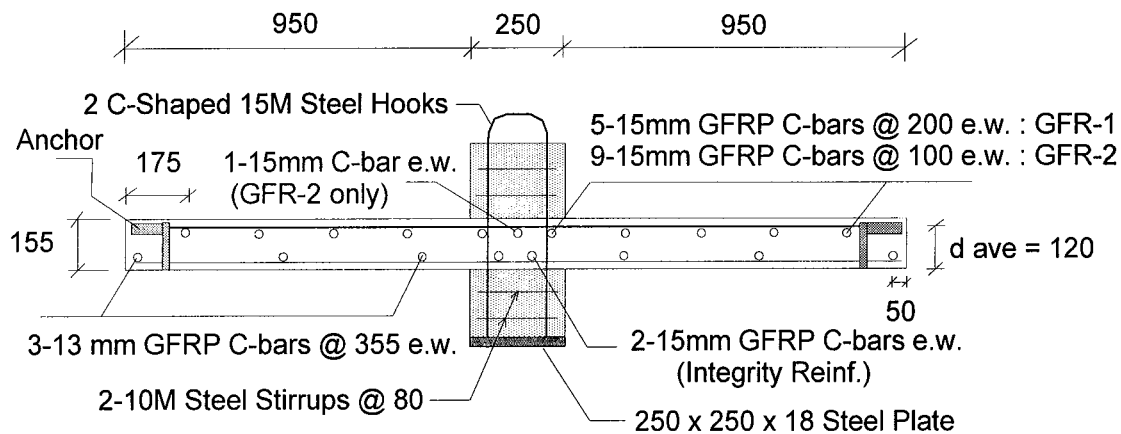


**Fig. 5.2 Types of Reinforcement : Series I Slabs**

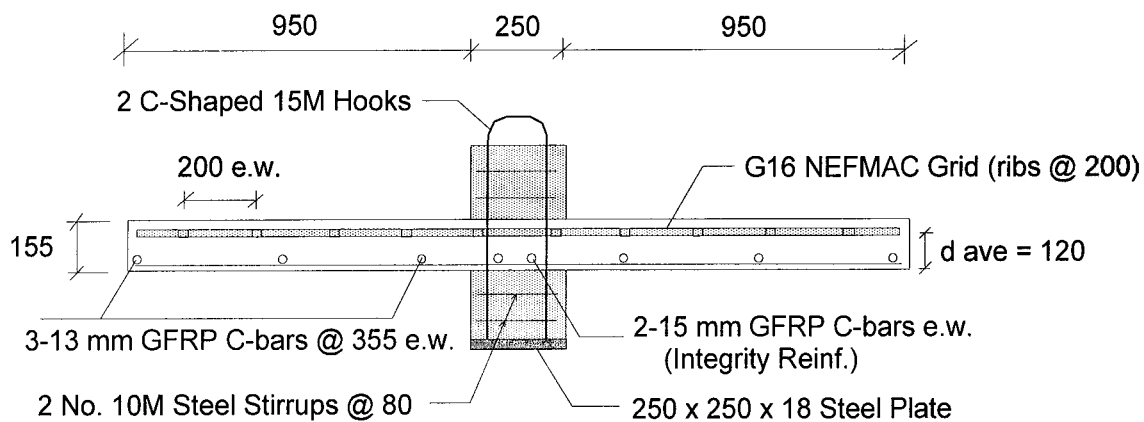




**a) Slab SR-1**



**b) Slabs GFR-1 and GFR-2**



**c) Slab NEF-1**

Note: All dimensions in mm unless specified otherwise

**Fig. 5.3 Reinforcement Details : Series I Slabs**

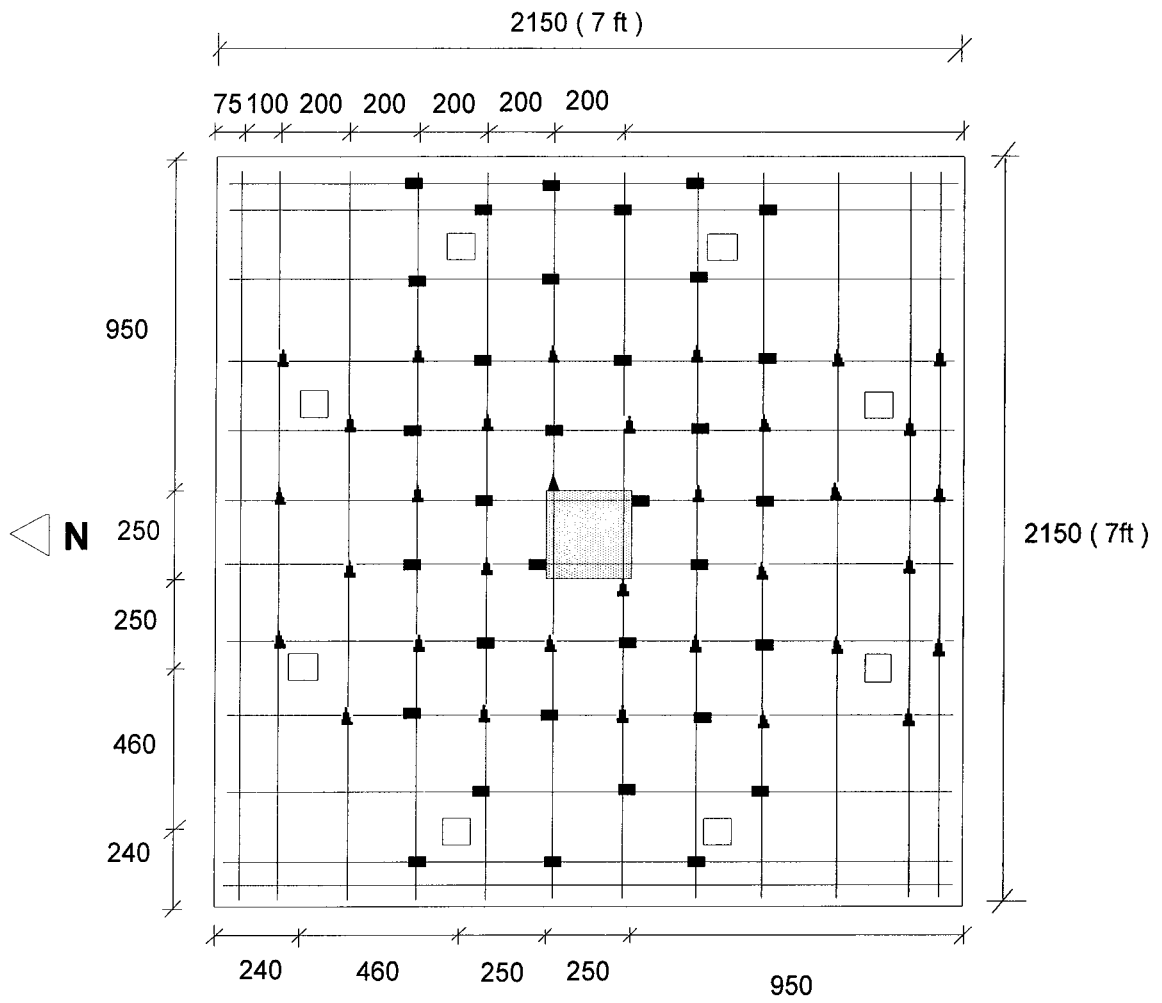
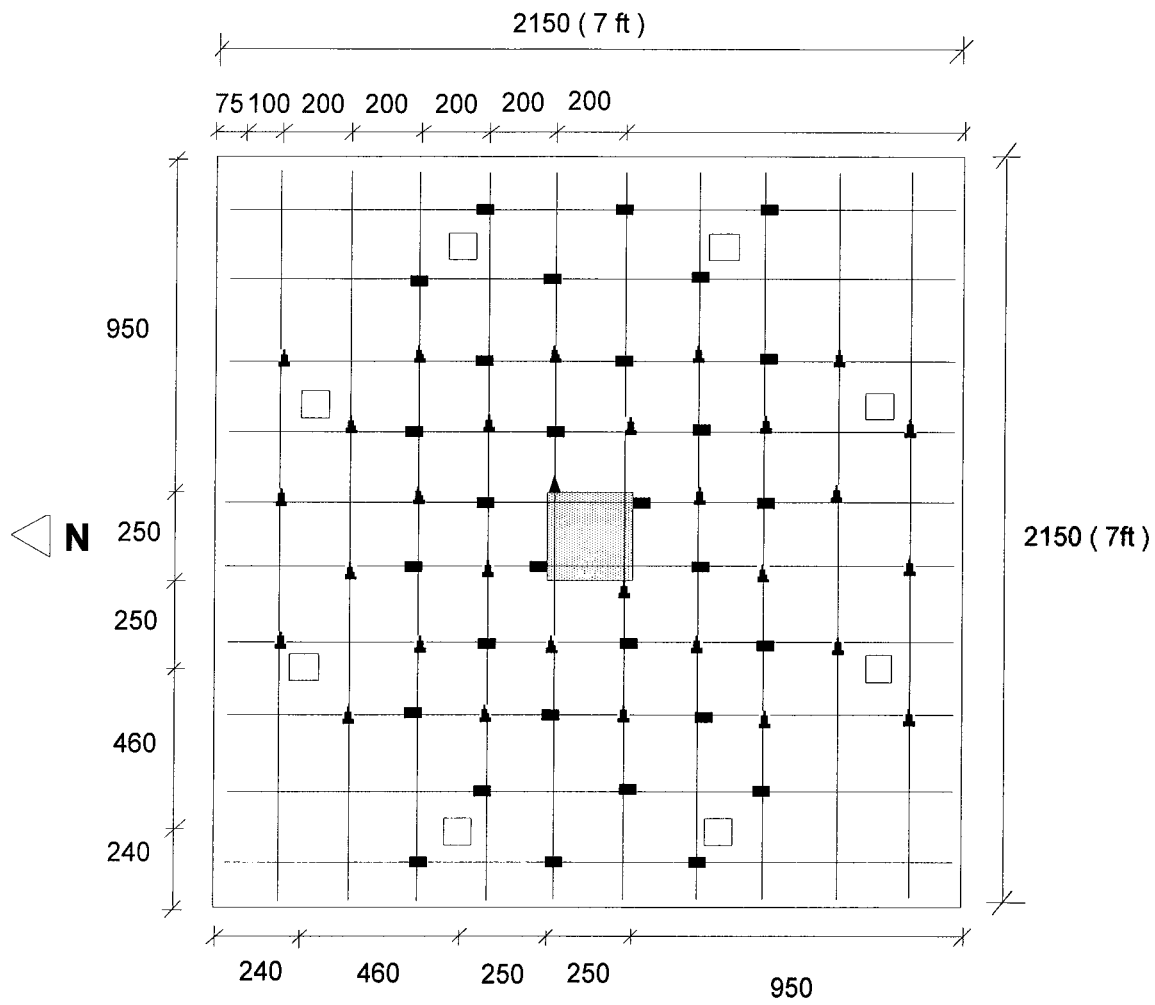
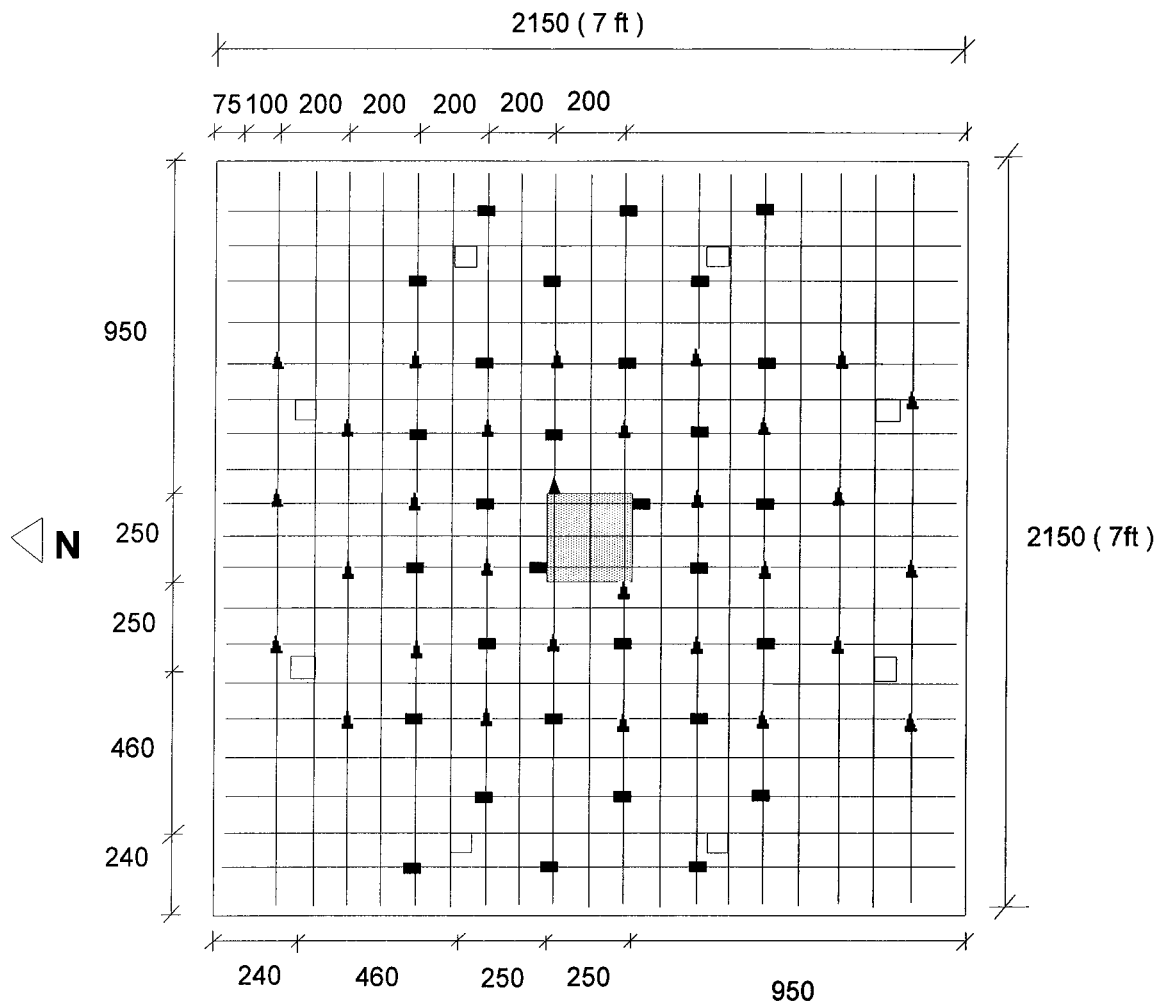


**Fig. 5.4 Top Reinforcement and Gauge Layout : Slab SR-1**



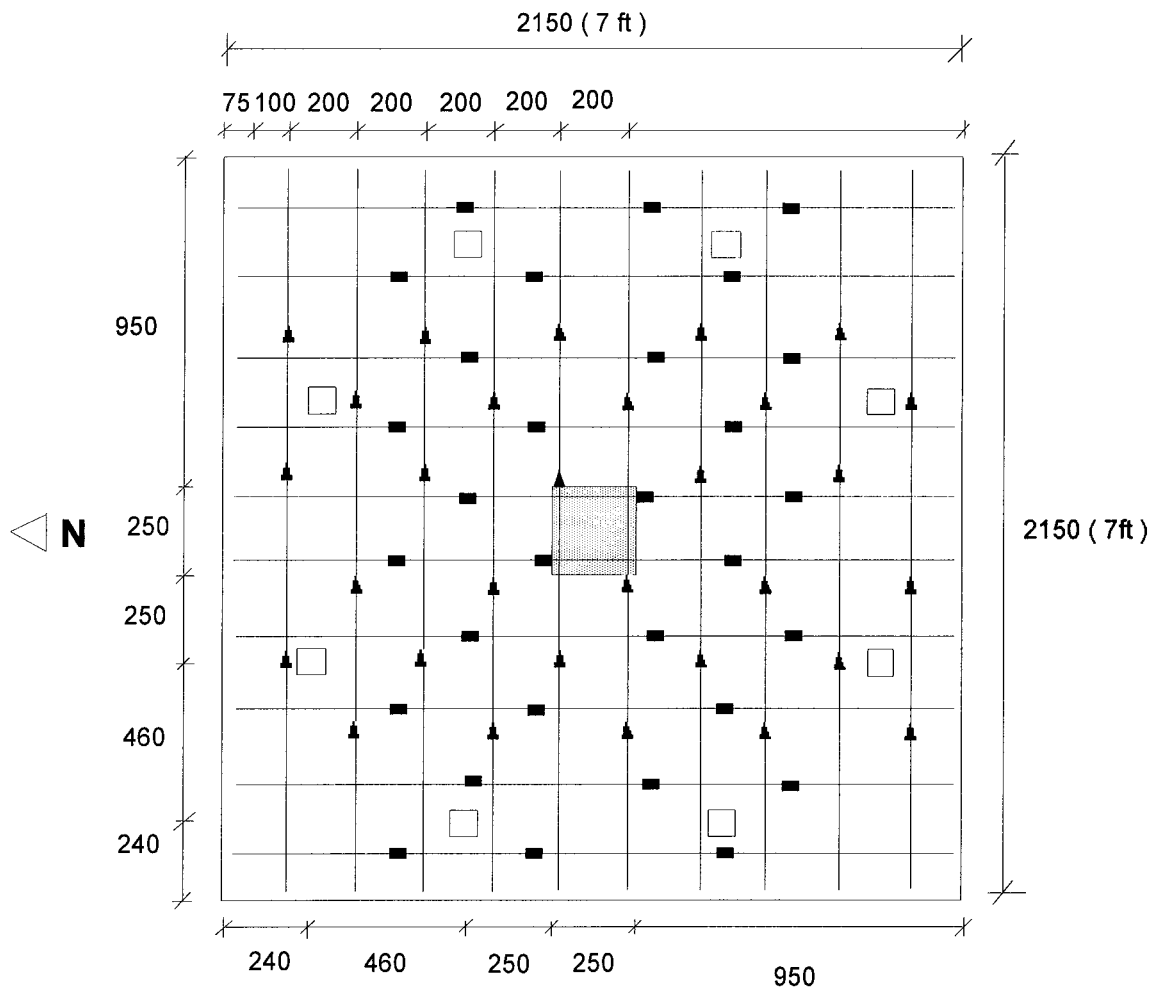
- Notes: 1. Dimensions in mm unless otherwise specified.  
2. Upper top bars ran in the N-S direction.

**Fig. 5.5 Top Reinforcement and Gauge Layout : Slab GFR-1**



- Notes: 1. Dimensions in mm unless otherwise specified.  
 2. Upper Top bars ran in the N-S direction.  
 3. GFRP C-bar Anchors not shown.

**Fig. 5.6 Top Reinforcement and Gauge Layout : Slab GFR-2**



- Notes: 1. Dimensions in mm unless otherwise specified.  
 2. All gauges except those at the column face were located 70 mm away from grid crossings as shown.

**Fig. 5.7 Top Reinforcement and Gauge Layout : Slab NEF-1**

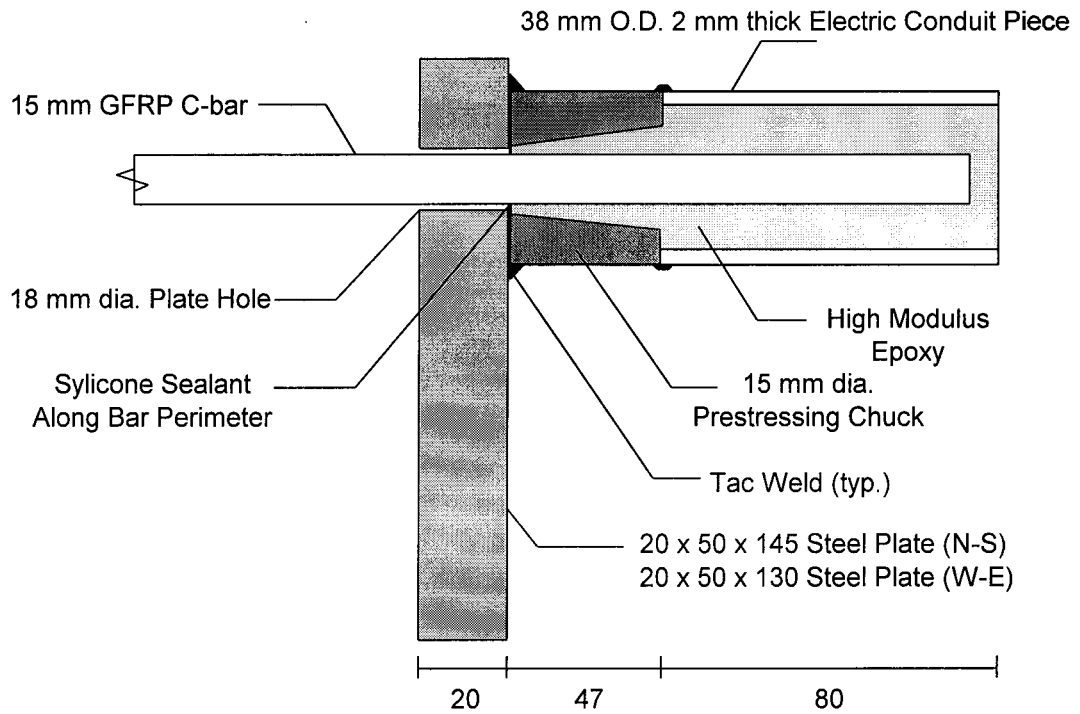


**Fig. 5.8 Anchor Detail : Slabs GFR-1 and GFR-2**



**Fig. 5.9 NEFMAC Grid Handling**

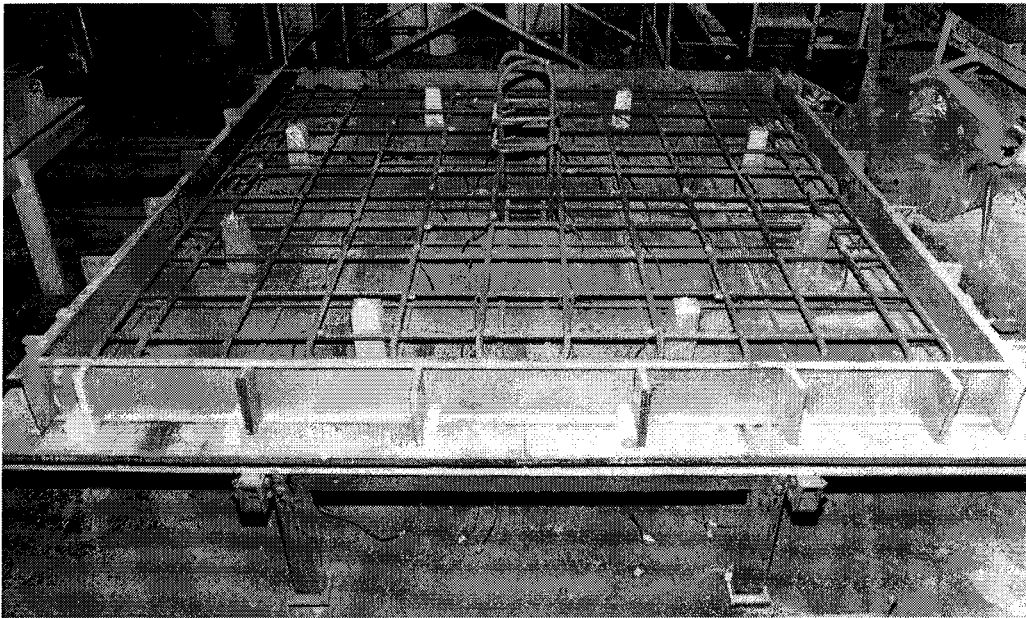


**Fig. 5.10 Reinforcing Mat : SR-1**

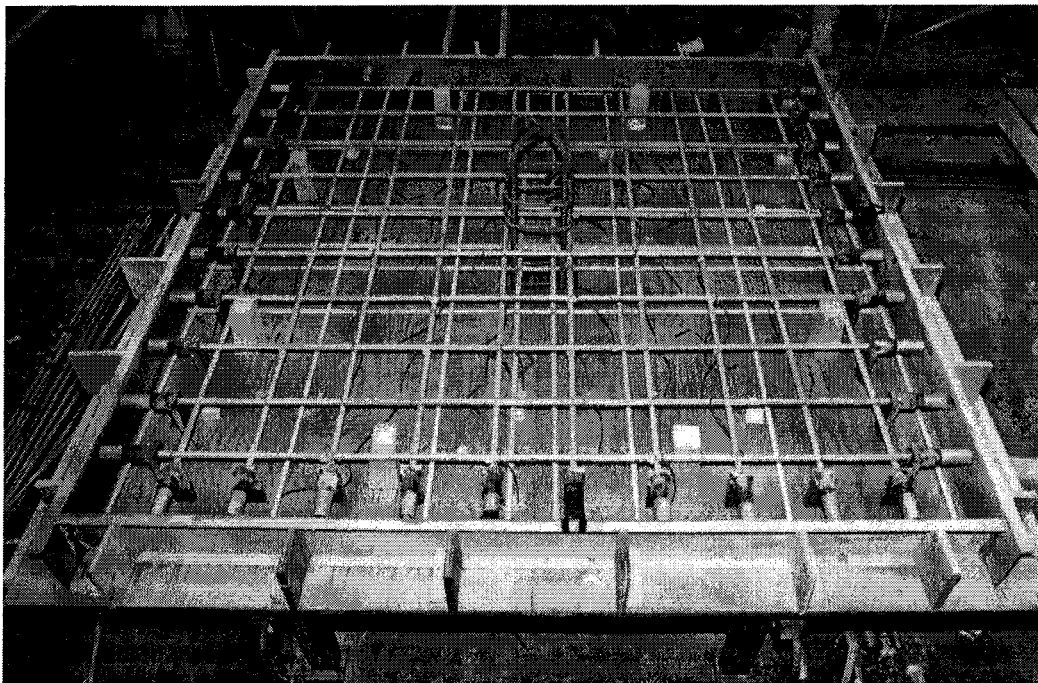


**Fig. 5.11 Reinforcing Mat : GFR-1**

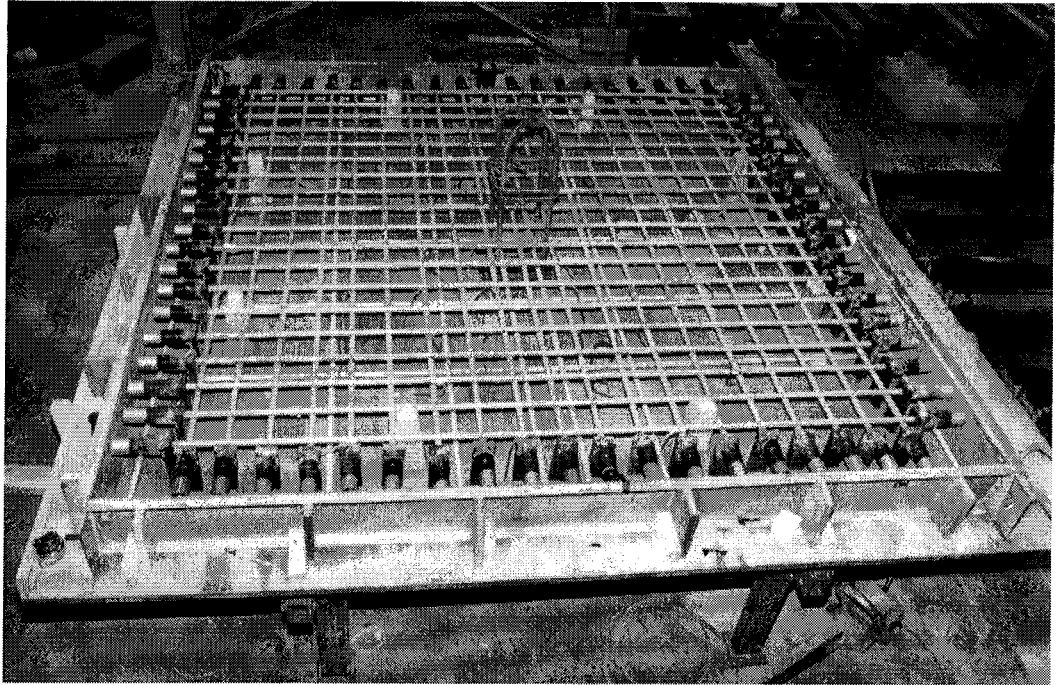


**Fig. 5.12 Reinforcing Mat : GFR-2**

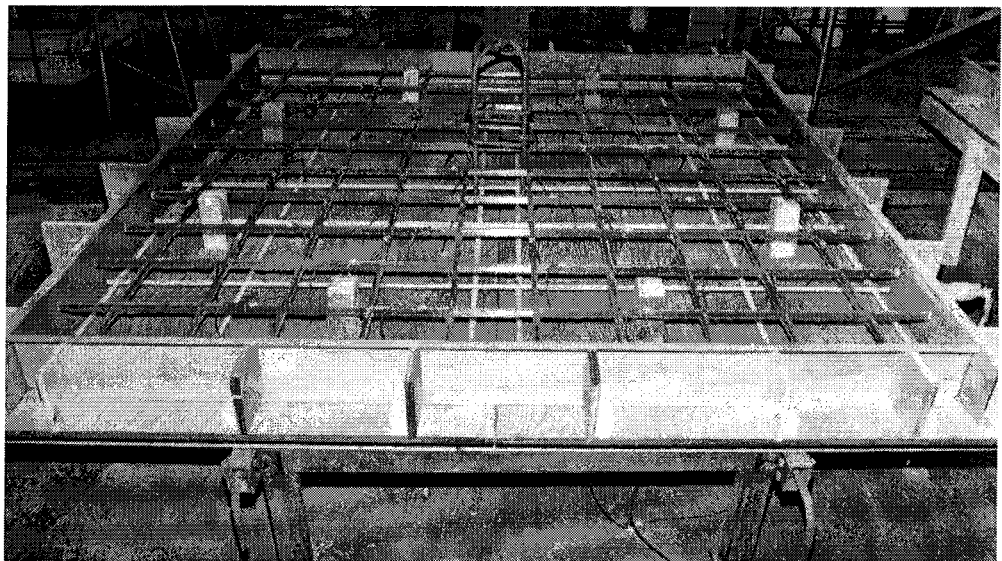


**Fig. 5.13 Reinforcing Grid : NEF-1**



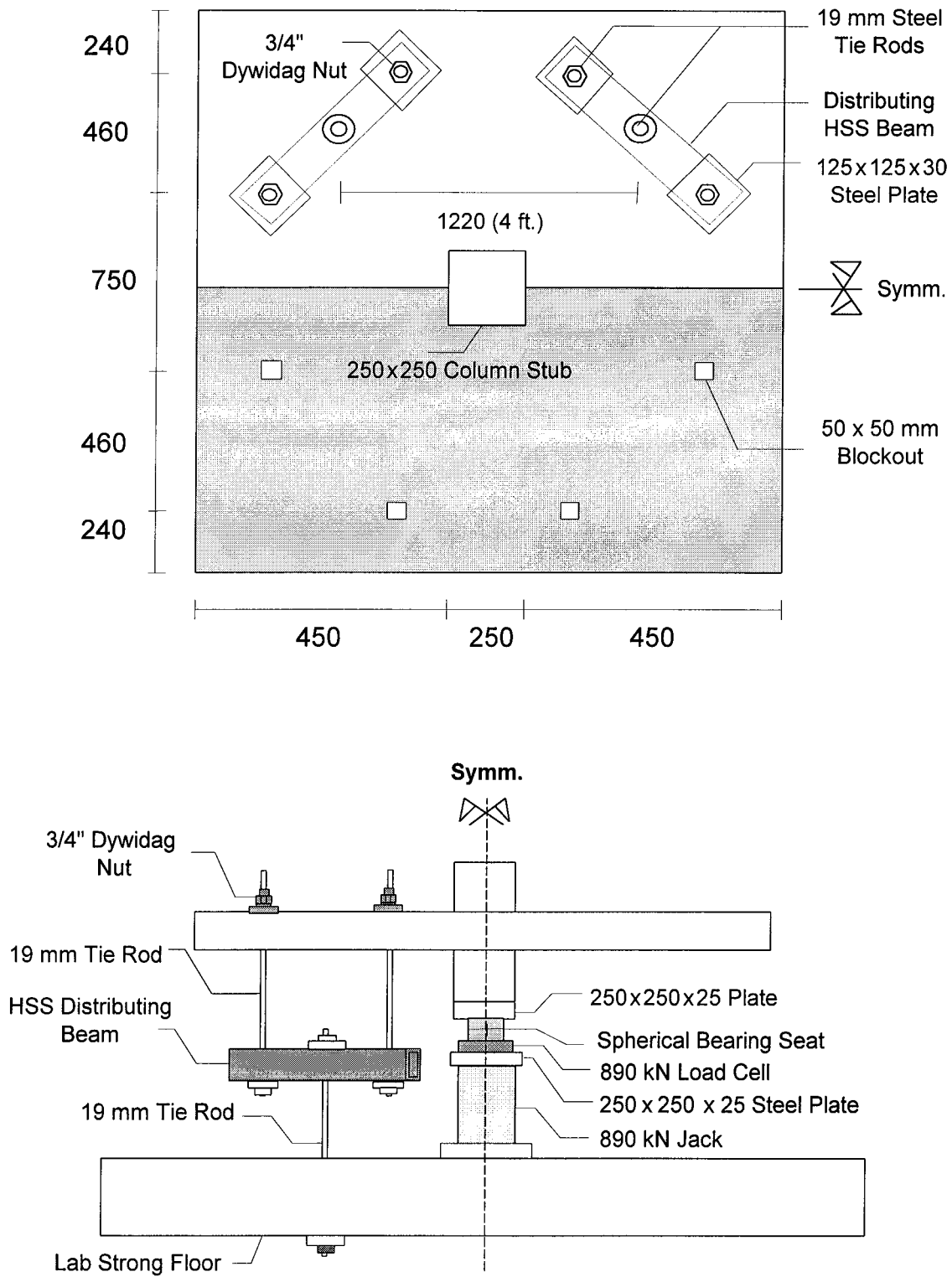


**Fig. 5. 14 Test Set-up : Series I Slabs**

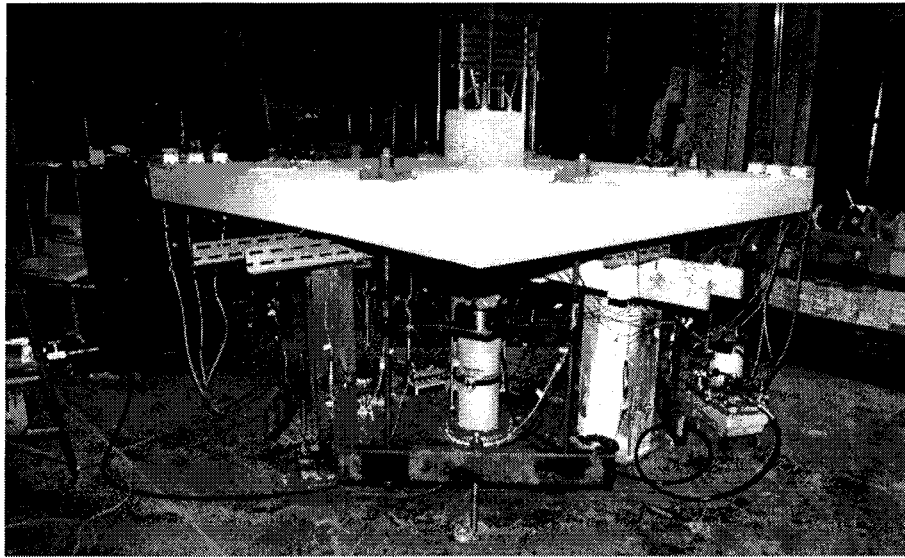


**Fig. 5.15 Test Set-up : Series I Slabs**

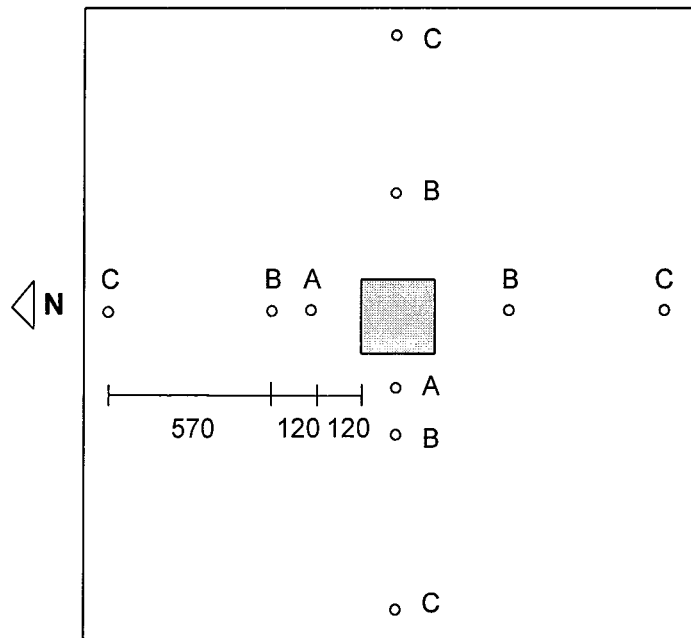


**Fig. 5.16 LVDT Location : Series I Slabs**

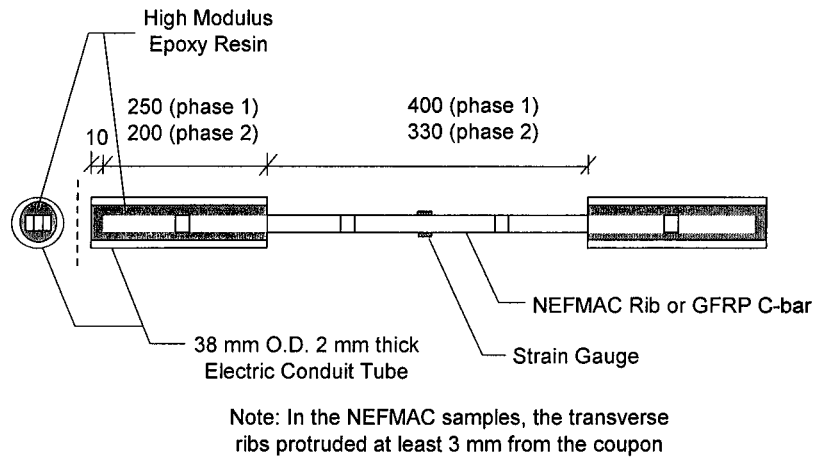


**Fig. 5.17 Detail of GFRP Tension Coupons**

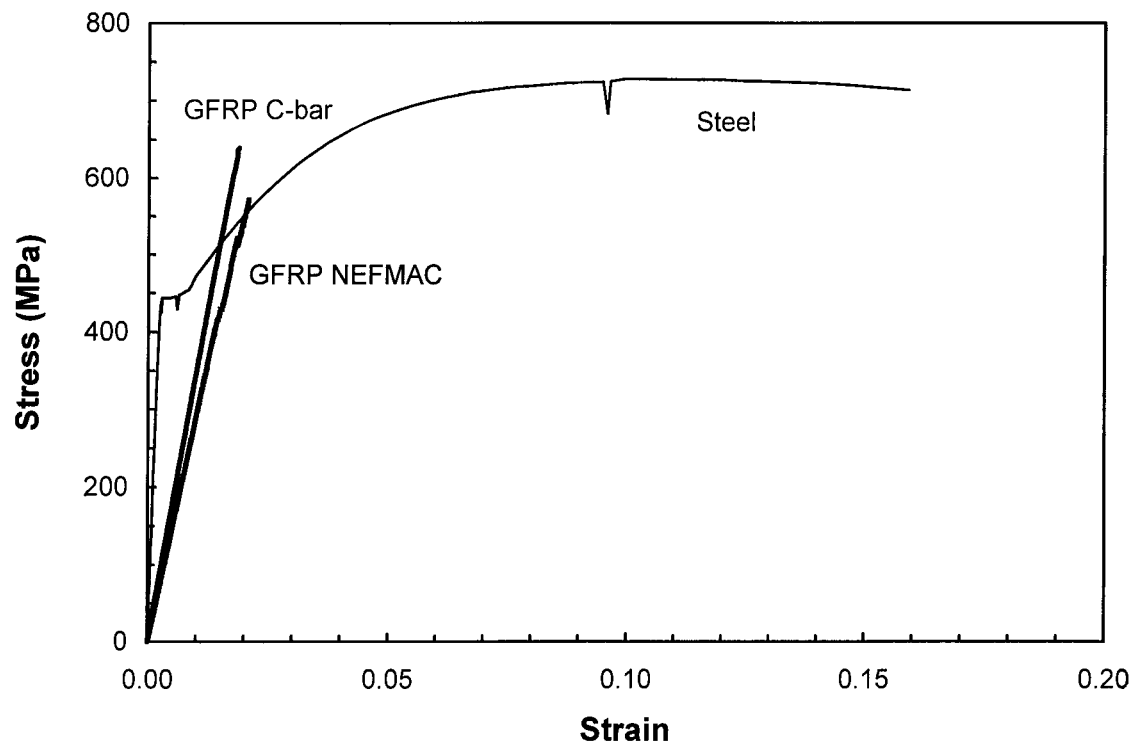


**Fig. 5.18 Stress-Strain Curves : Series I Slabs Reinforcement**

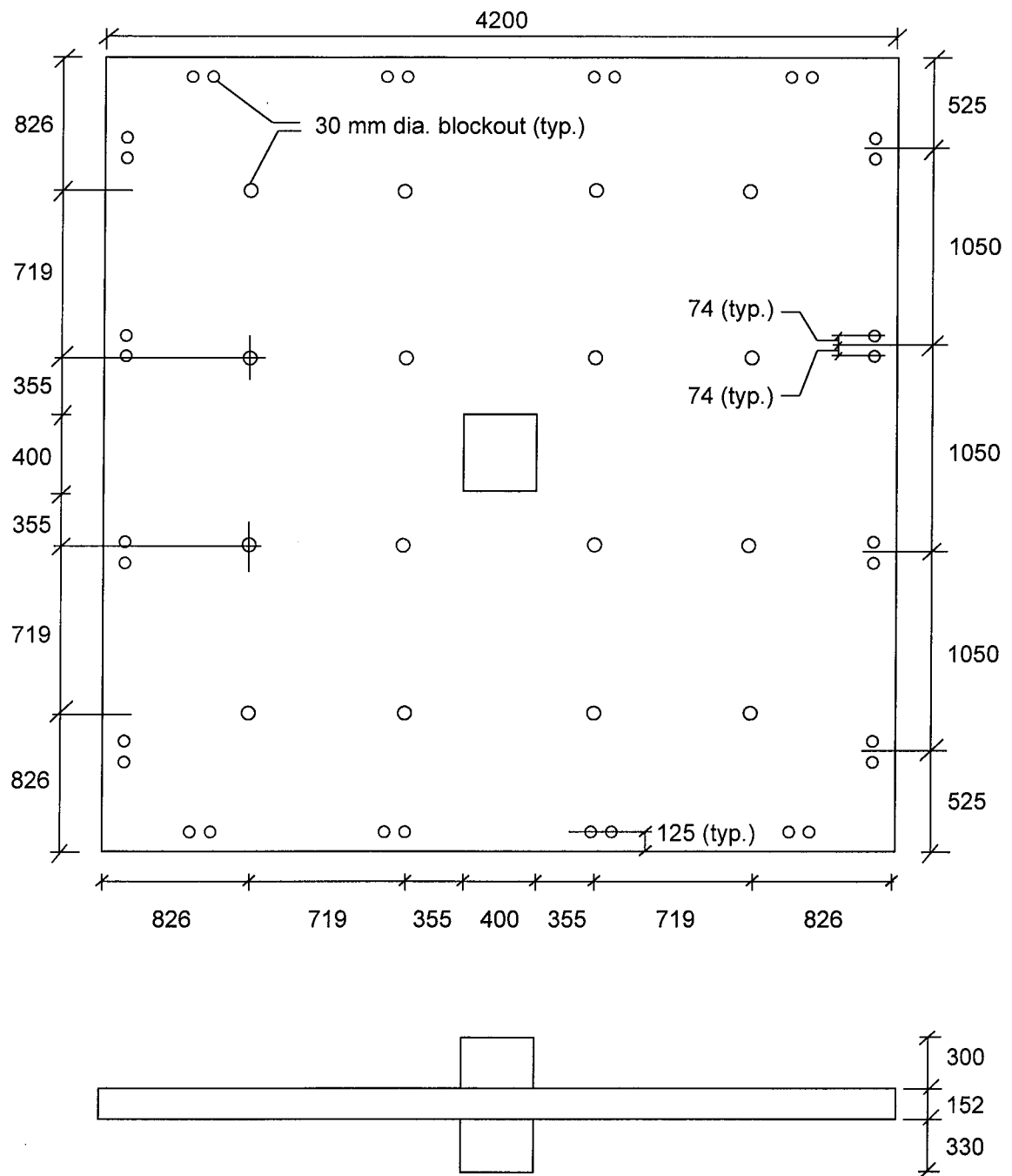
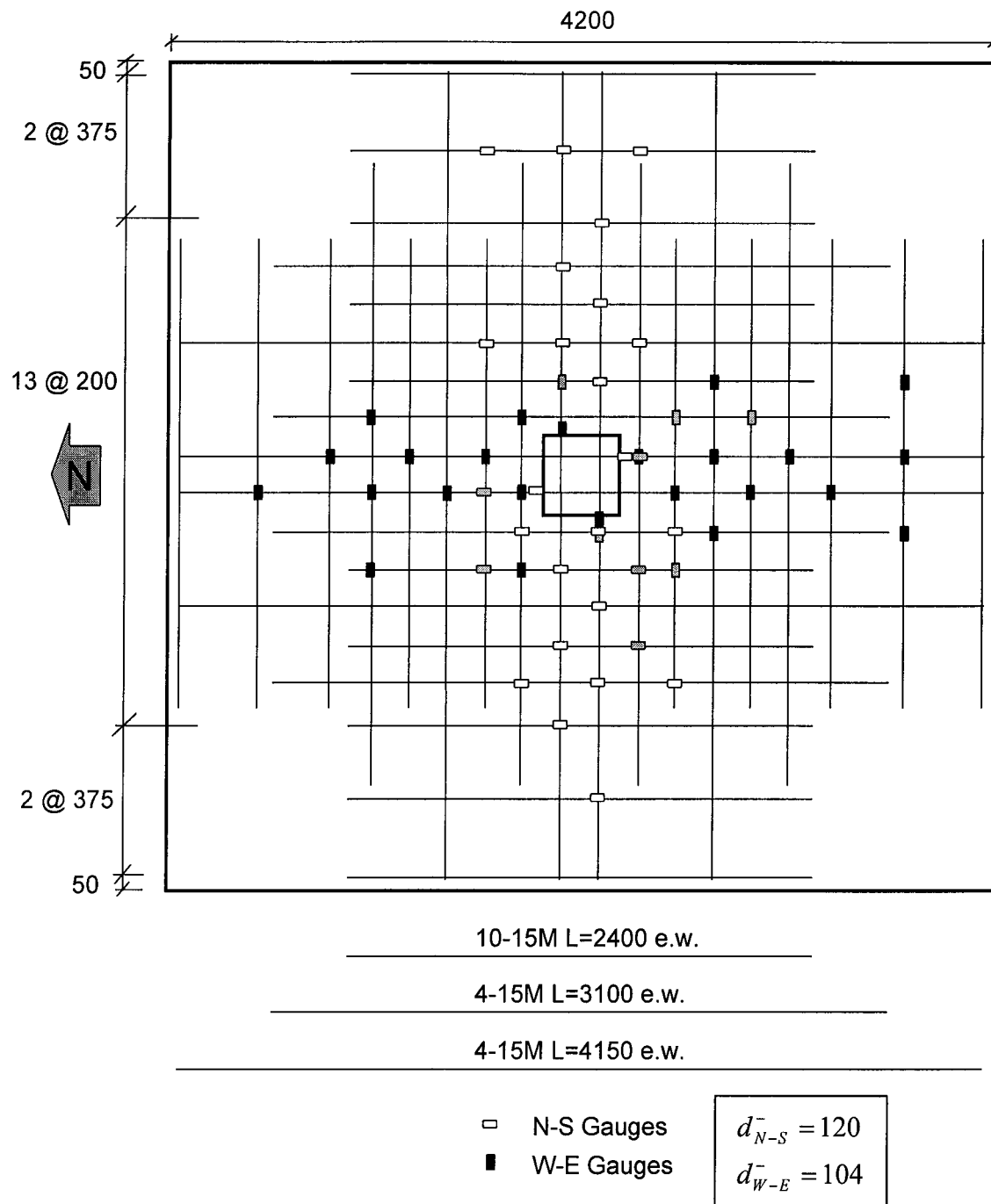
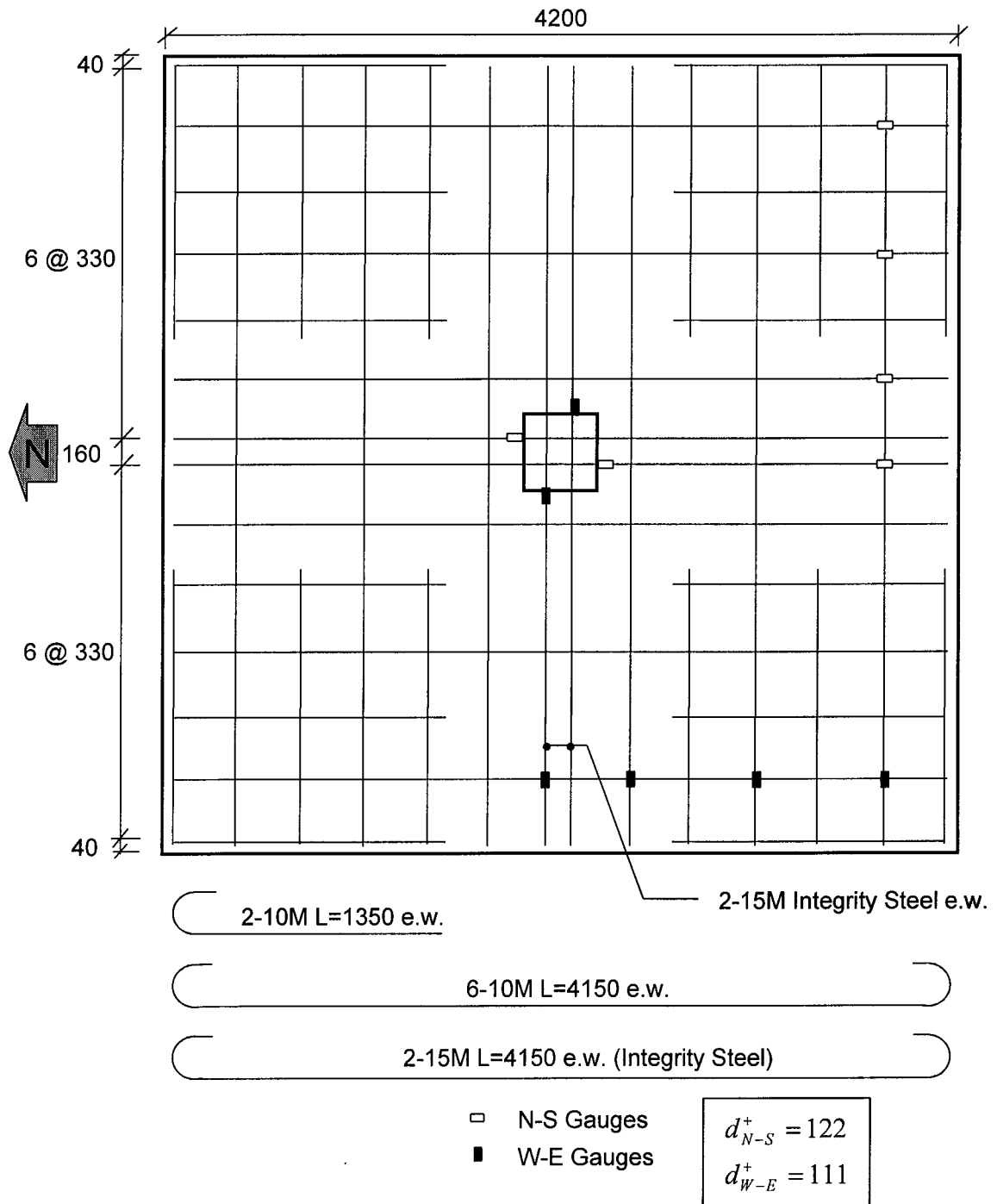


**Fig. 5.19 Slab Dimensions : Series II Slabs**



- Notes:
1. Upper top bars ran along the N-S direction.
  2. Gauges in gray were mounted only on slab ER3.
  3.  $d$  values are those used to design the slabs.

**Fig. 5.20 Top Slab Reinforcement and Gauge Layout  
(Series II Slabs)**



- Notes:
1. Bar dimensions are out-to-out dimensions.
  2. Hook dimensions are standard.
  3. Lower bottom bars ran along the N-S direction.
  4.  $d$  values are those used to design the slabs.

**Fig. 5.21 Bottom Reinforcement and Gauge Layout  
- Series II Slabs -**

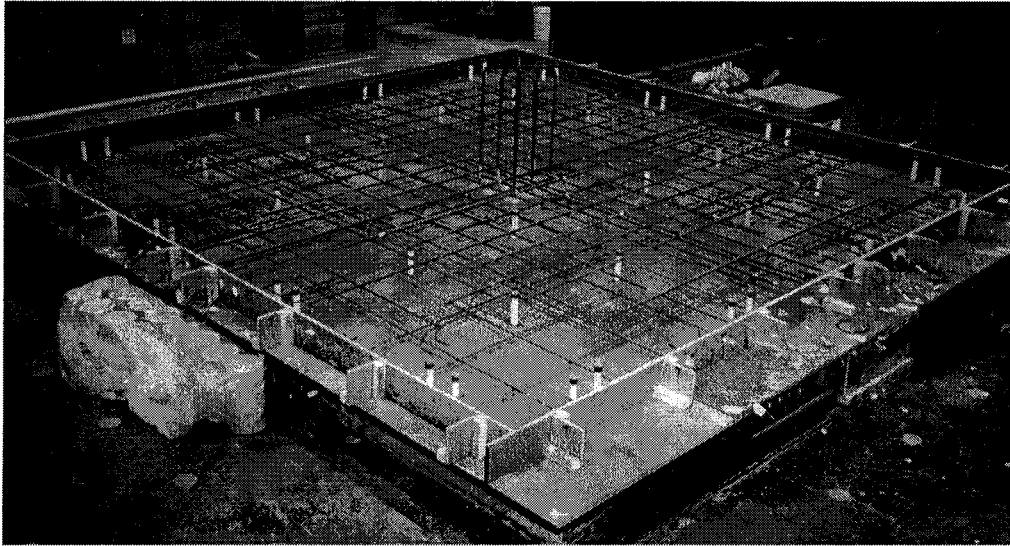


**Fig. 5.22 Typical Reinforcing Cage : Series II Slabs**

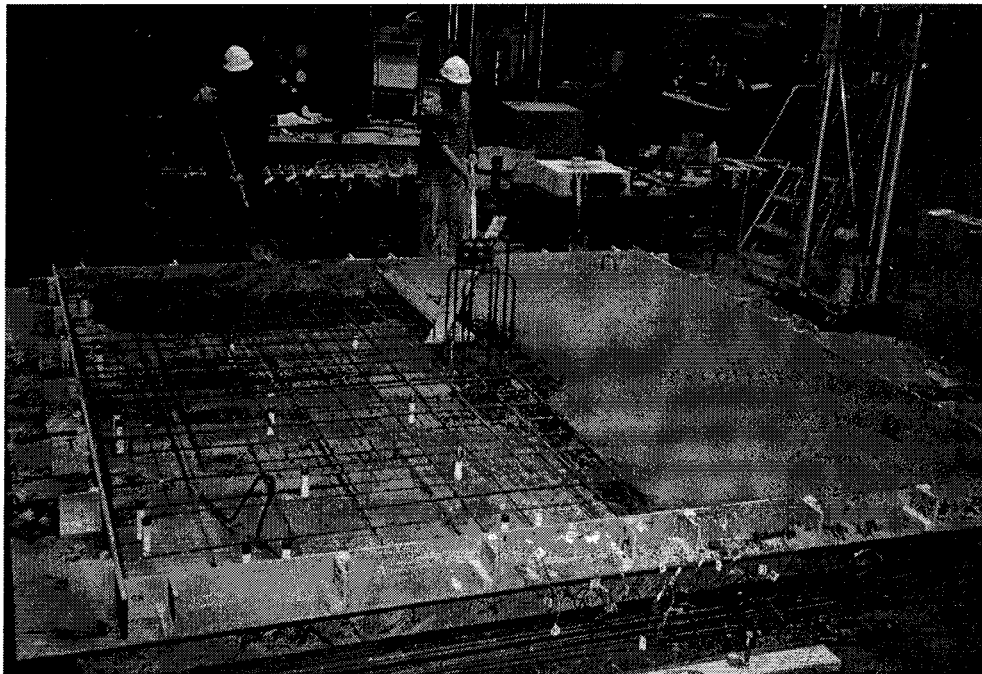


**Fig. 5.23 Slab Concreting : Series II Slabs**

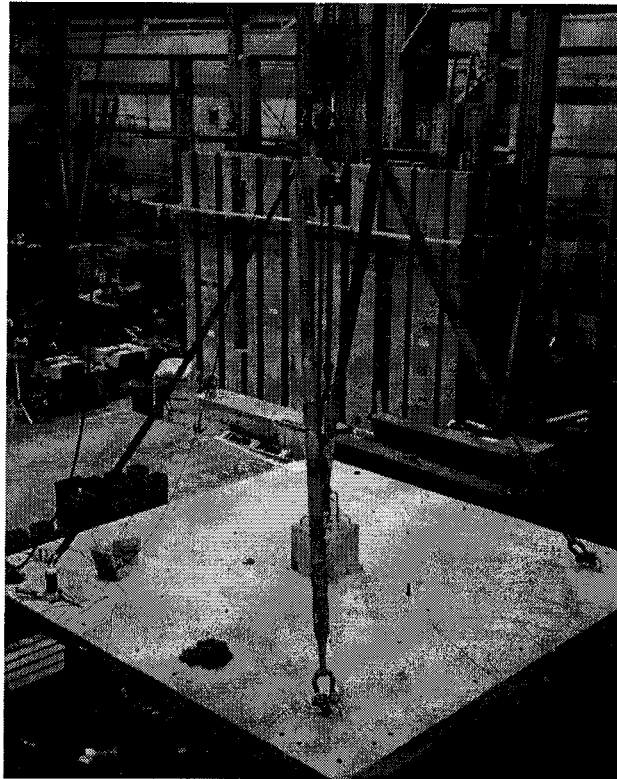


**Fig. 5.24 Slab Lifting Procedure : Series II Slabs**

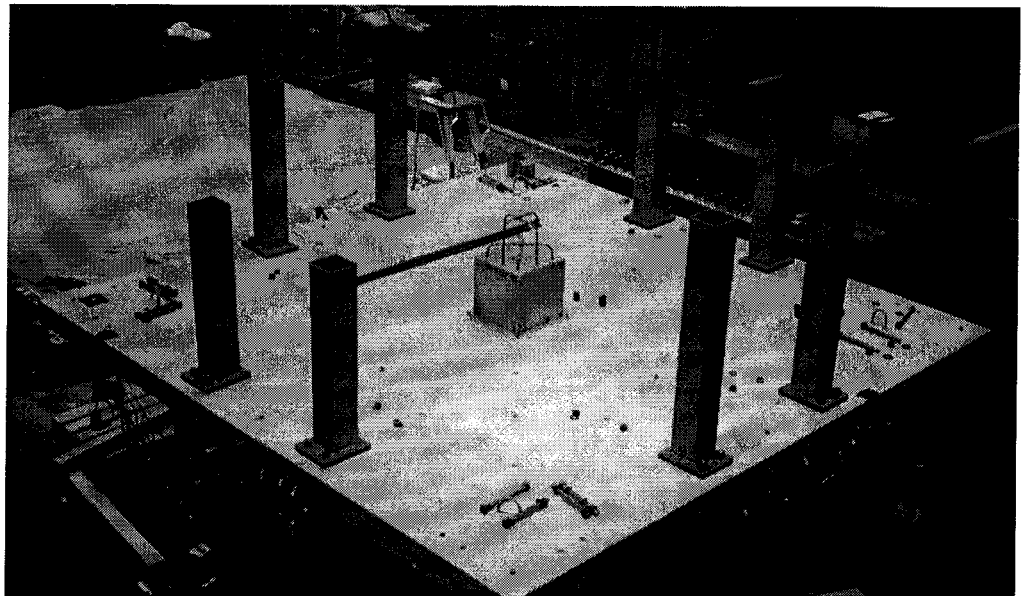


**Fig. 5.25 Test Set-up Process : Series II Slabs**



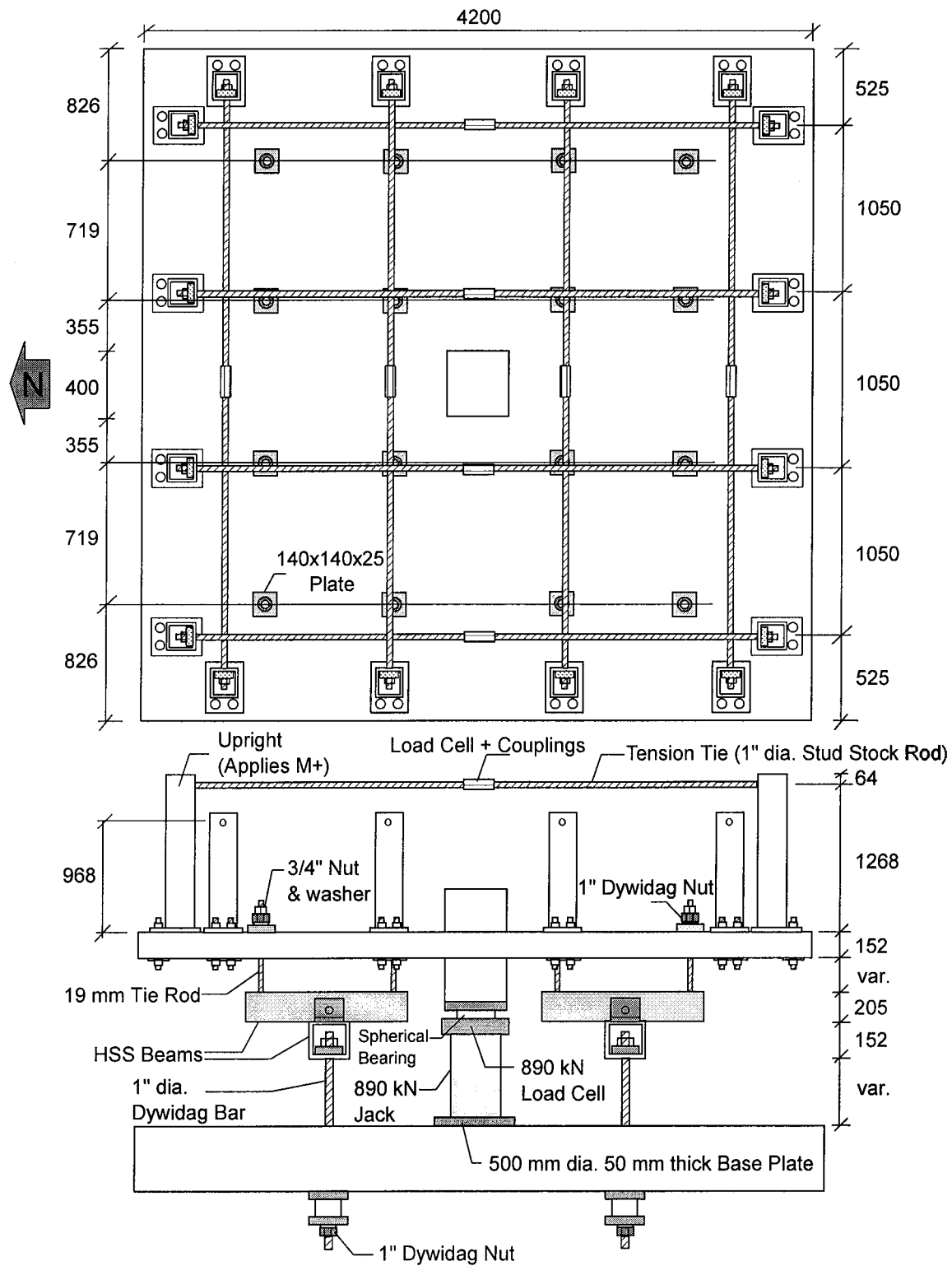


**Fig. 5.26 Typical Test Set-up : Series II Slabs**



**Fig. 5.27 Test Set-up View from SW Corner : Series II Slabs**

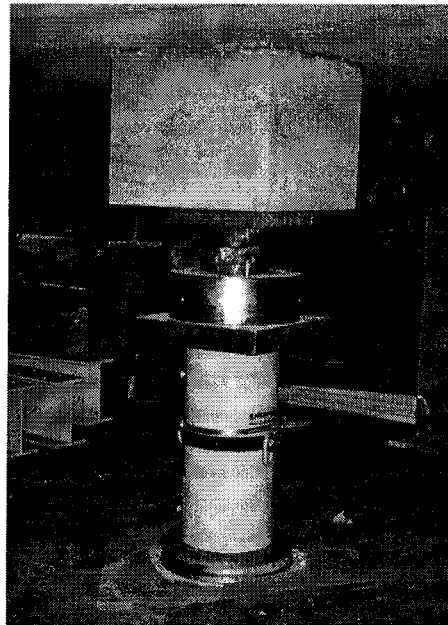
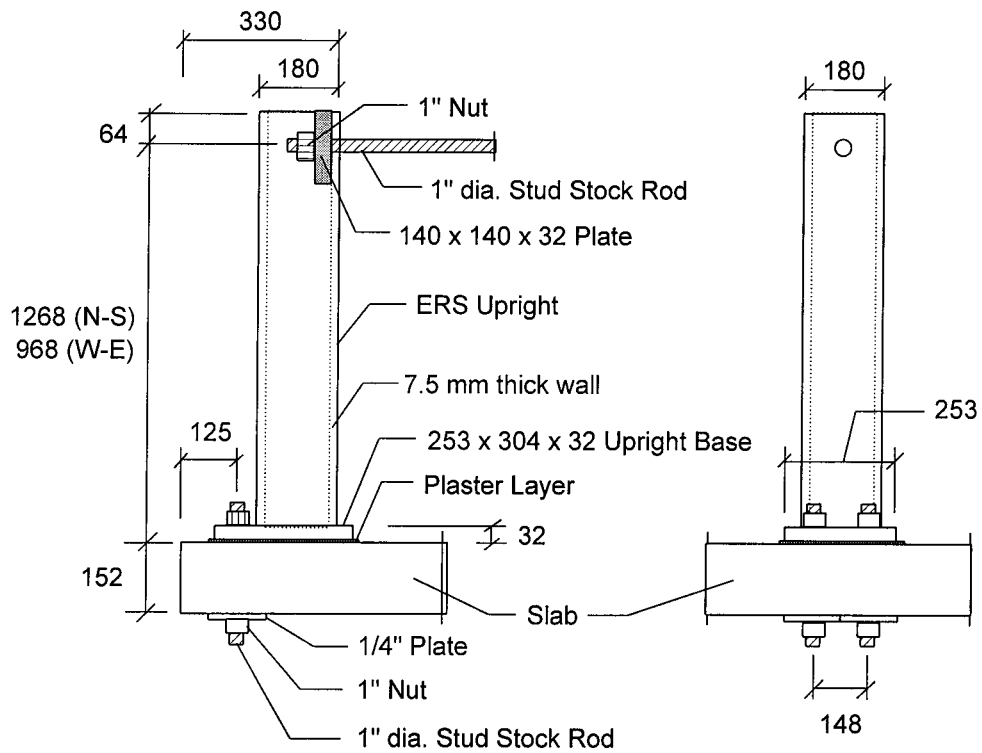
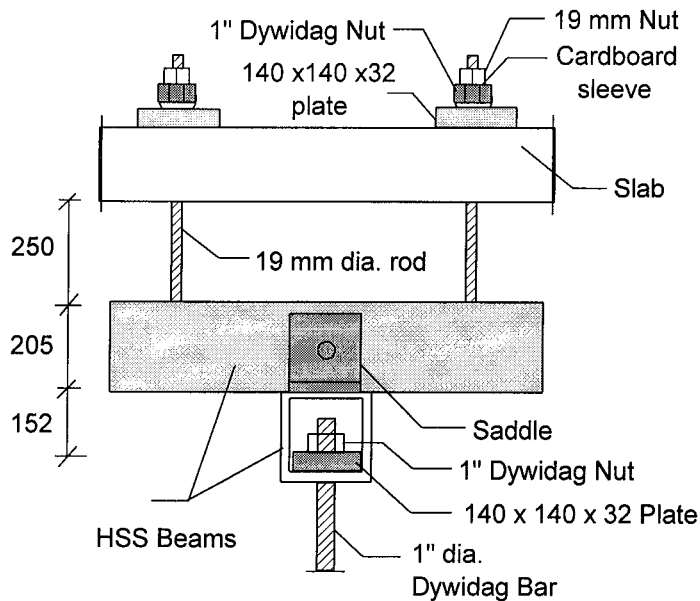


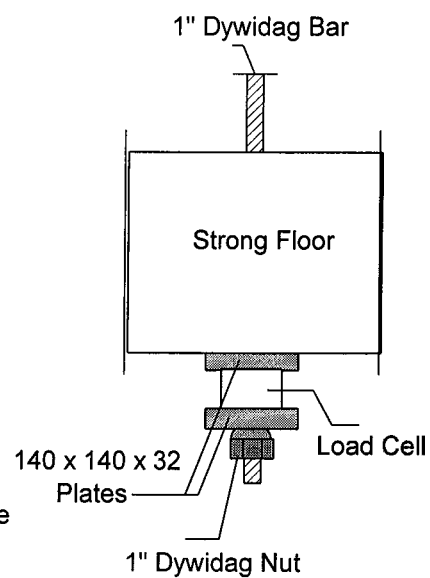
**Fig. 5.28 Lower Column Support : Series II Slabs**



a) Edge Restraint System Details



b) Upper Whiffle Tree Branching Detail



c) Whiffle Tree Load Cell Detail

**Fig. 5.29 Edge Restraint System and Loading Set-up Details  
- Series II Slabs -**

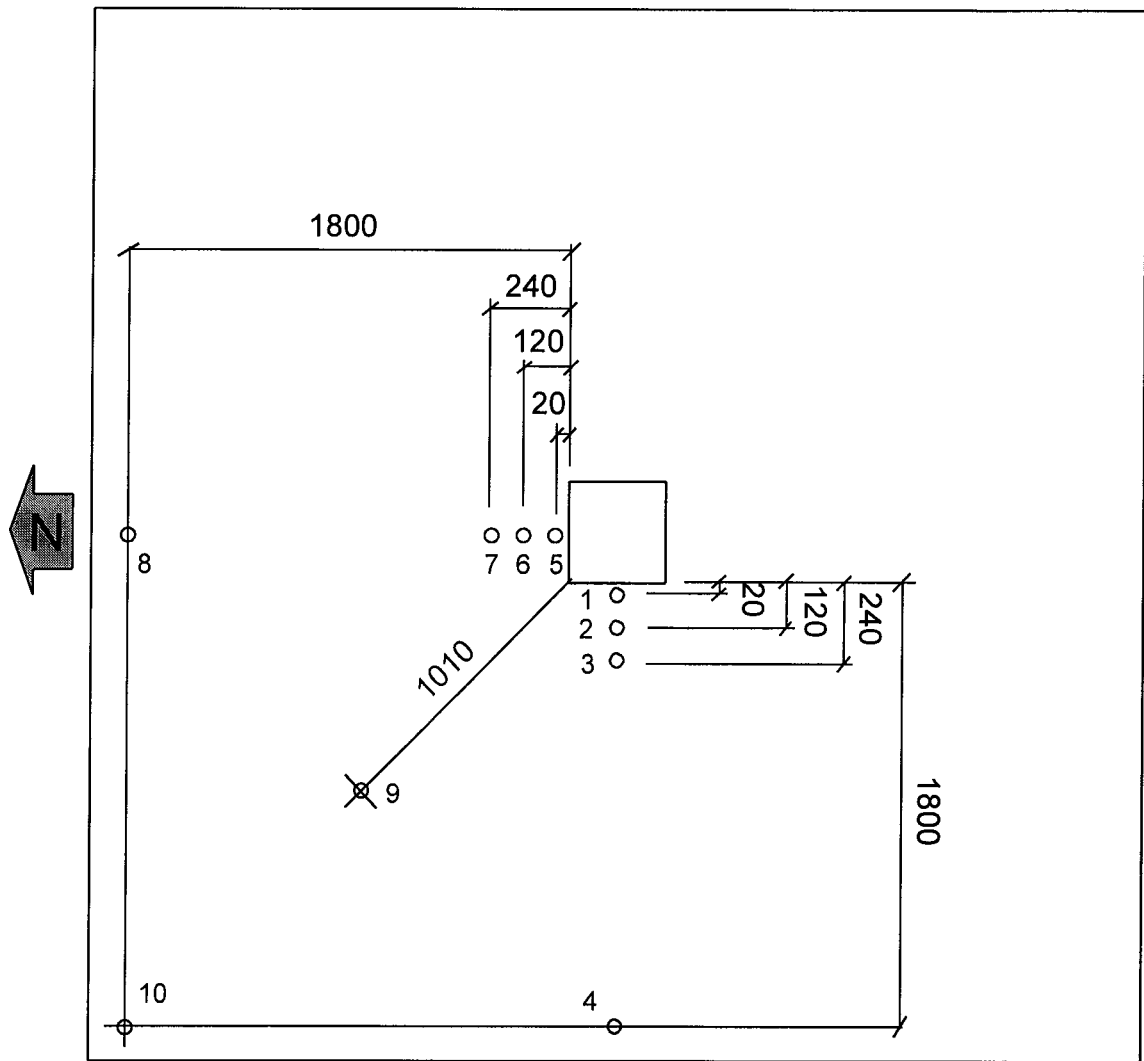
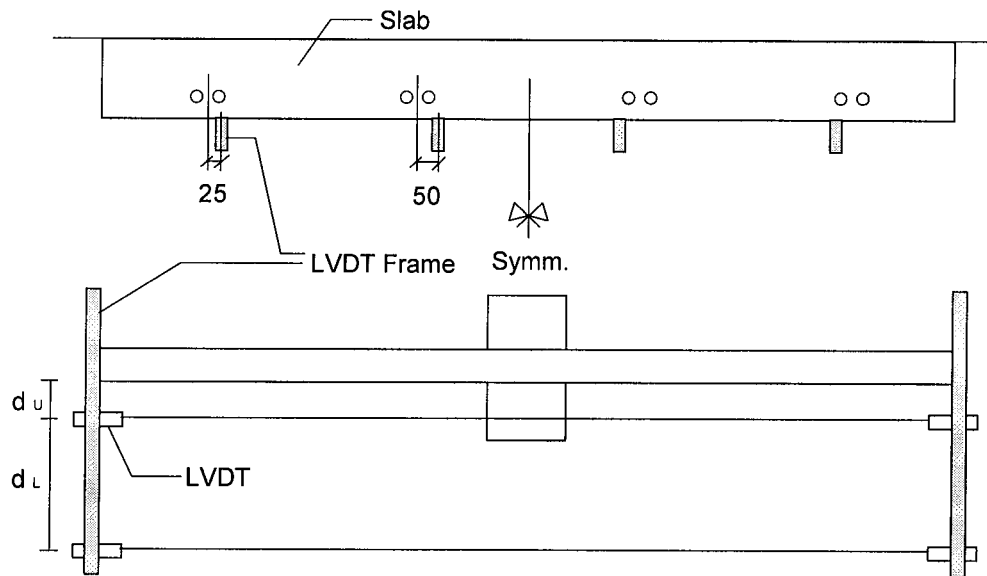


**Fig. 5.30 Cable Transducer Locations : Series II Slabs**



- Notes:
1. To avoid conflicts between the LVDT strings and the hardware below the slab, the axis of each LVDT frame did not coincide with that of the uprights.
  2.  $d_u$  and  $d_L$  were, respectively: 150 and 350 ( $\pm 5$ ) mm for the two outer LVDT frames in both directions; 150 and 350 ( $\pm 5$ ) mm for the two inner W-E LVDT frames, and 150 and 550 ( $\pm 5$ ) mm for the two inner N-S LVDT frames.

**Fig. 5.31 Horizontal LVDT Array for Slab Rotations : Series II Slabs**

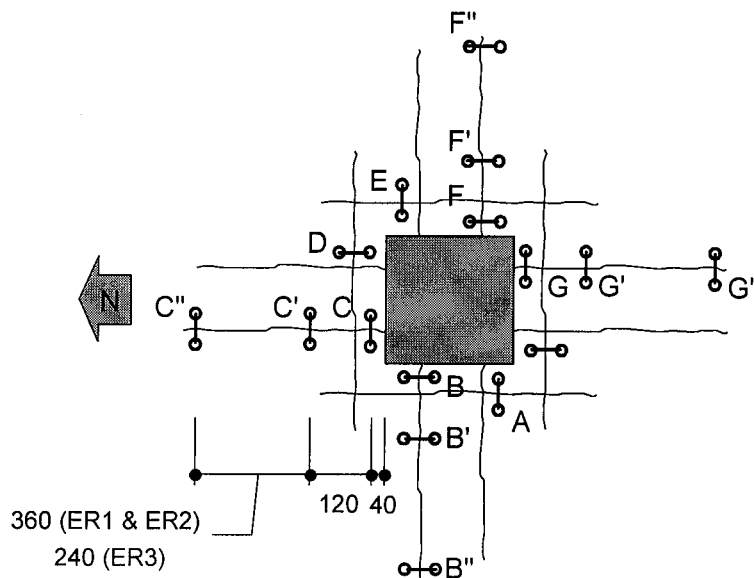
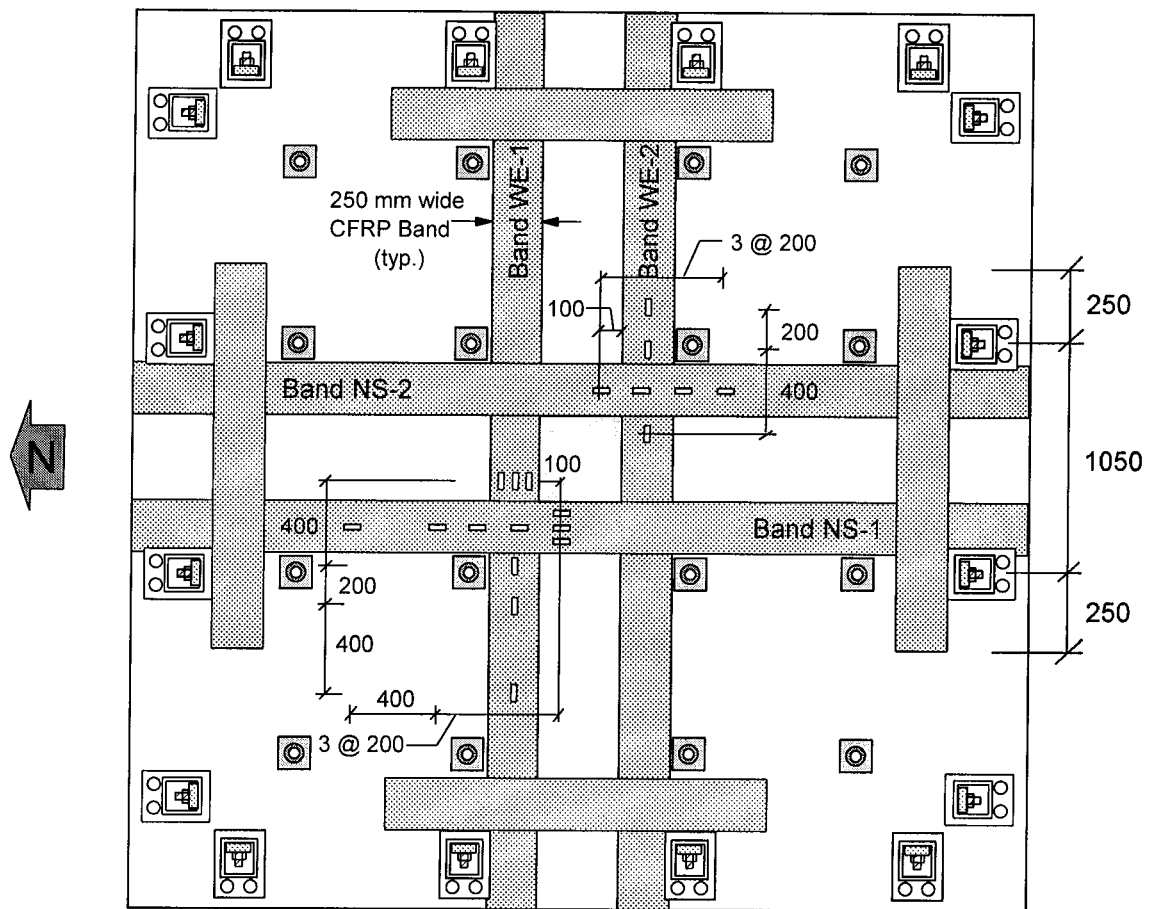
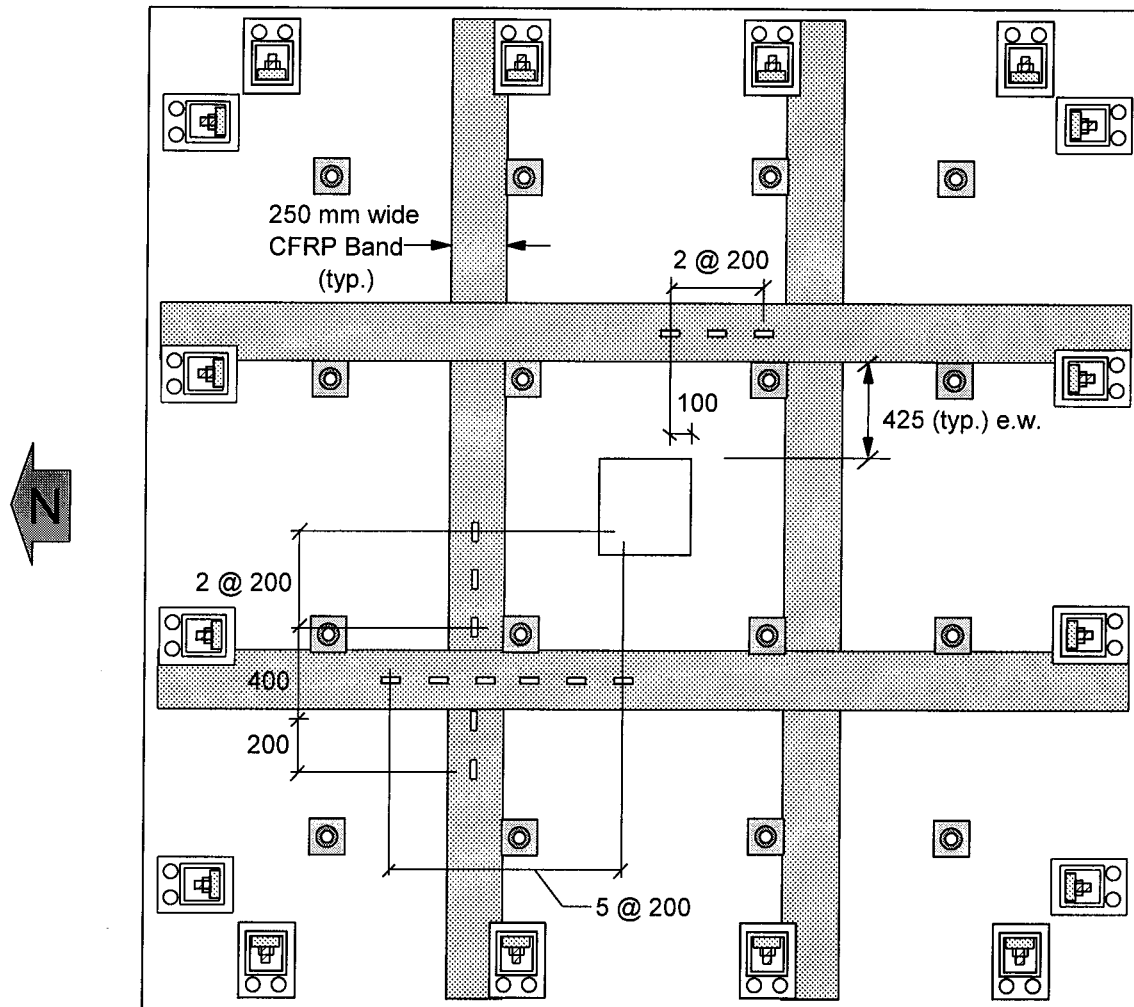


**Fig. 5.32 Top Crack Width Measurement Stations**



- Notes:
1. Each band consisted of two CFRP sheets.
  2. CFRP bands were recessed at the upright corners.
  3. Hollow rectangle symbols indicate strain gauge locations mounted on the CFRP bands.

**Fig. 5.33 Strengthening Layout on Test ER2-CS1**



- Notes:
1. Bands were recessed at the upright corners.
  2. Hollow rectangle symbols indicate strain gauges mounted on the CFRP bands.

**Fig. 5.34 Strengthening Layout on Test ER3-CS2**

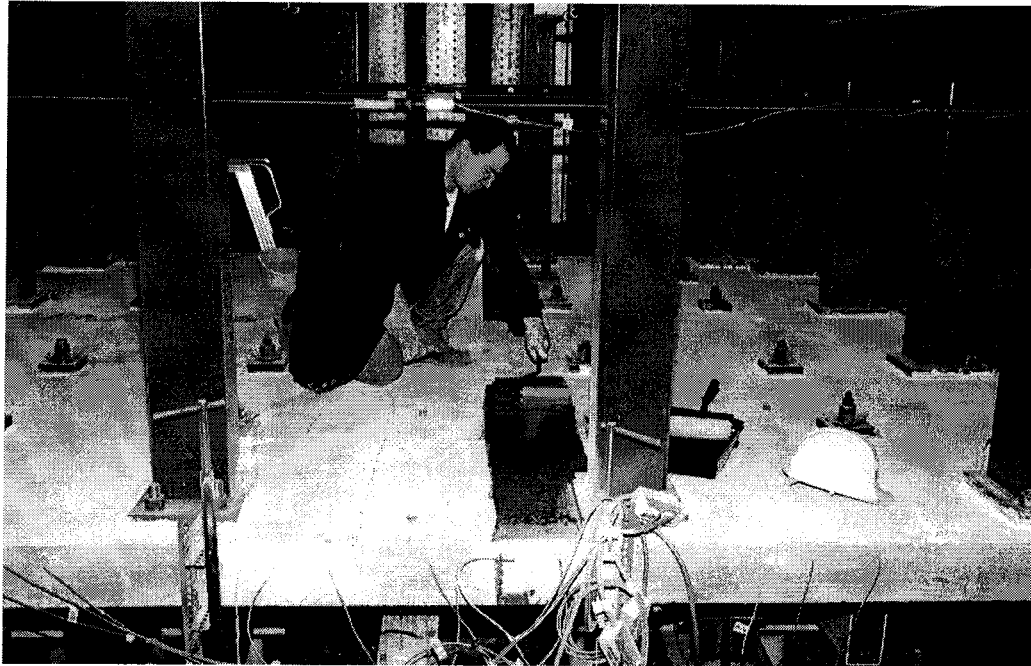


**Fig. 5.35 FRP Installation : Surface Finishing (ER2-CS1)**

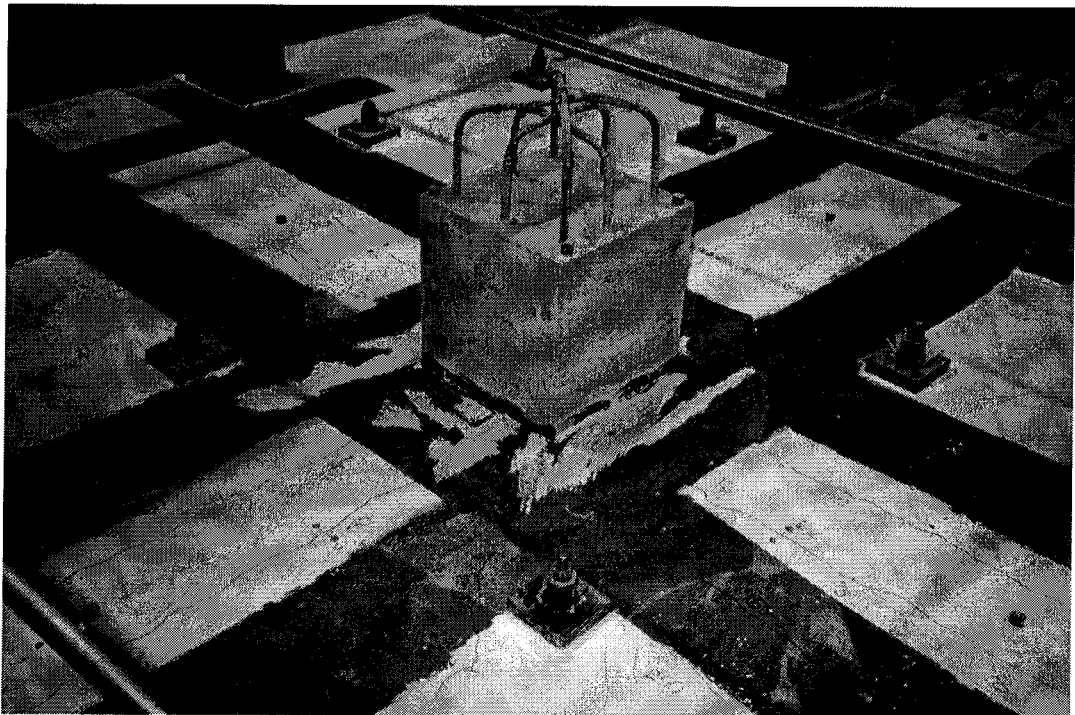


**Fig. 5.36 FRP Installation : Finished Surface (ER2-CS1)**



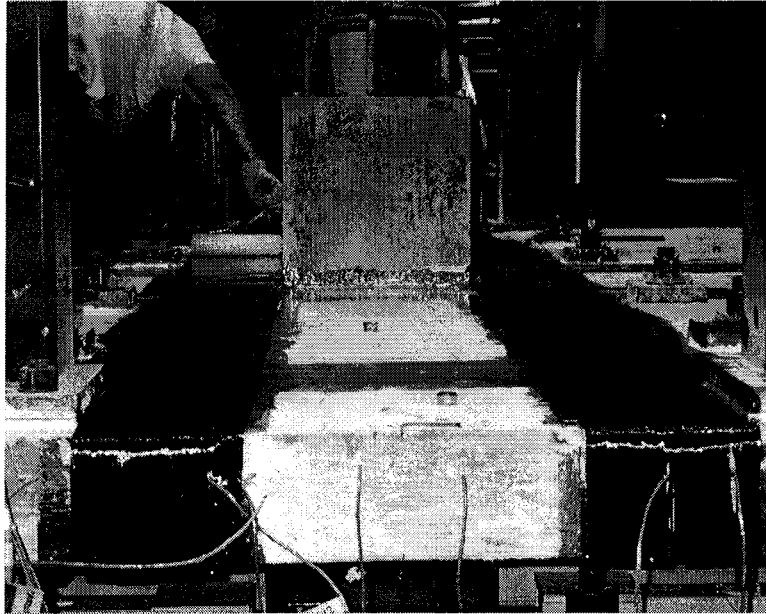


**Fig. 5.37 FRP Installation : Sheet Bonding (ER2-CS1)**

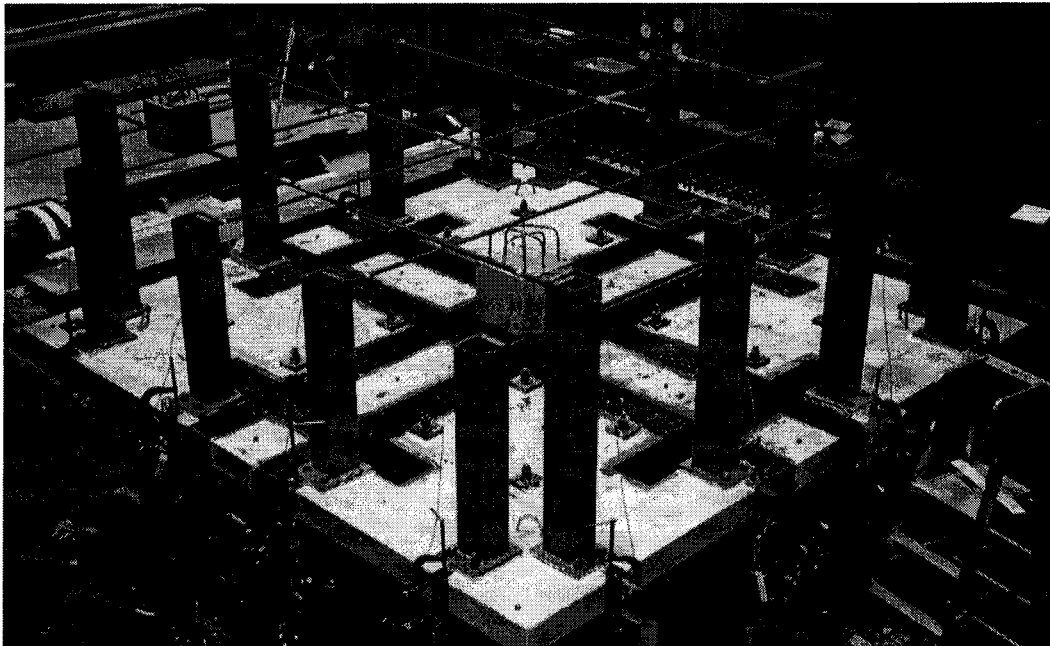


**Fig. 5.38 FRP Installation : Final Result (ER2-CS1)**

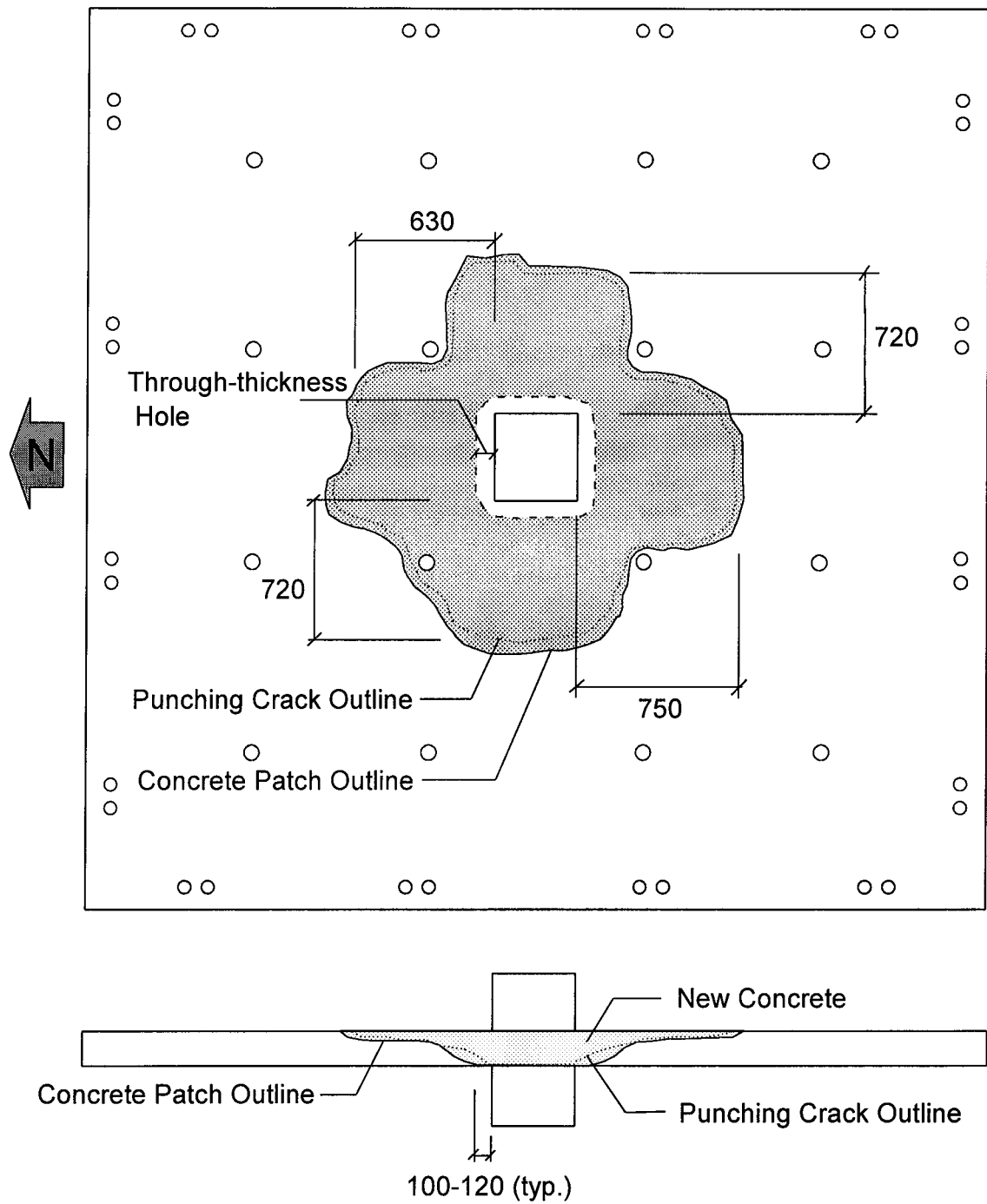


**Fig. 5.39 Concrete Patching Technique : Test ER1-CP1**

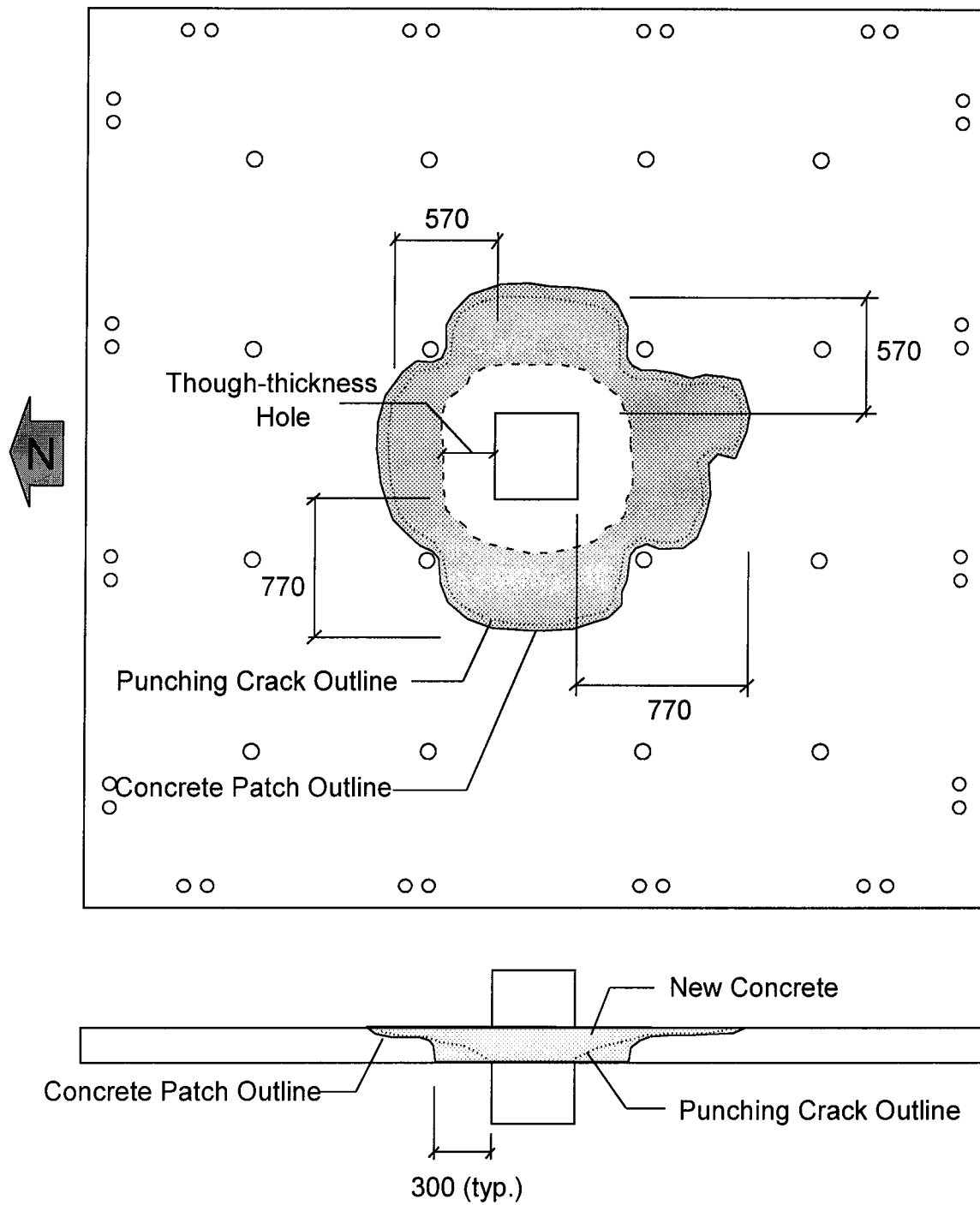


**Fig. 5.40 Concrete Patching Technique : Test ER3-CP2**

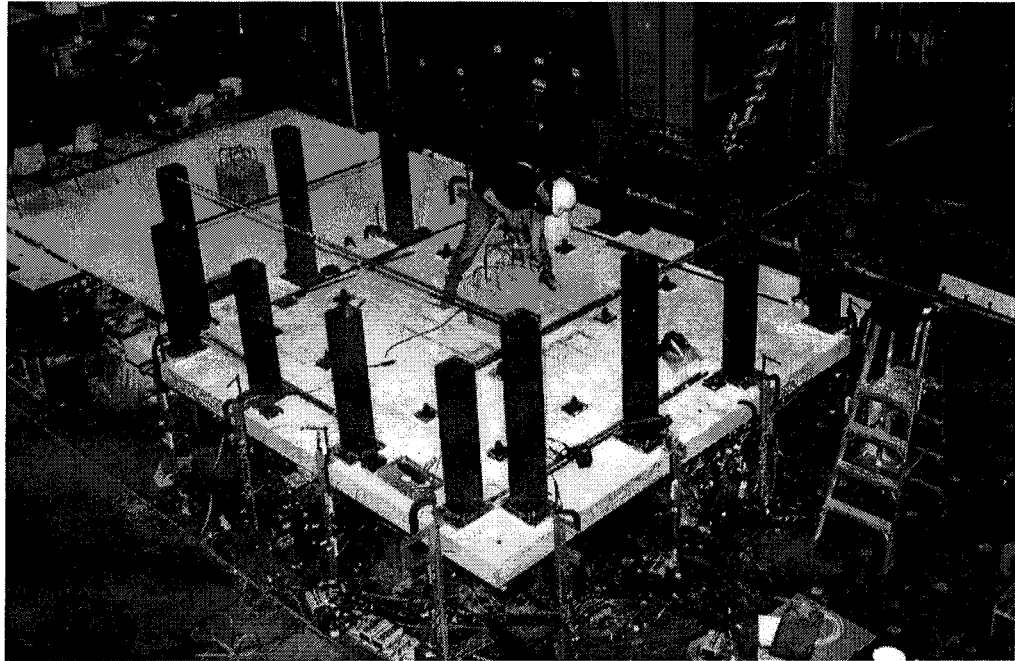


**Fig. 5.41 Concrete Patching : Jack Hammering**

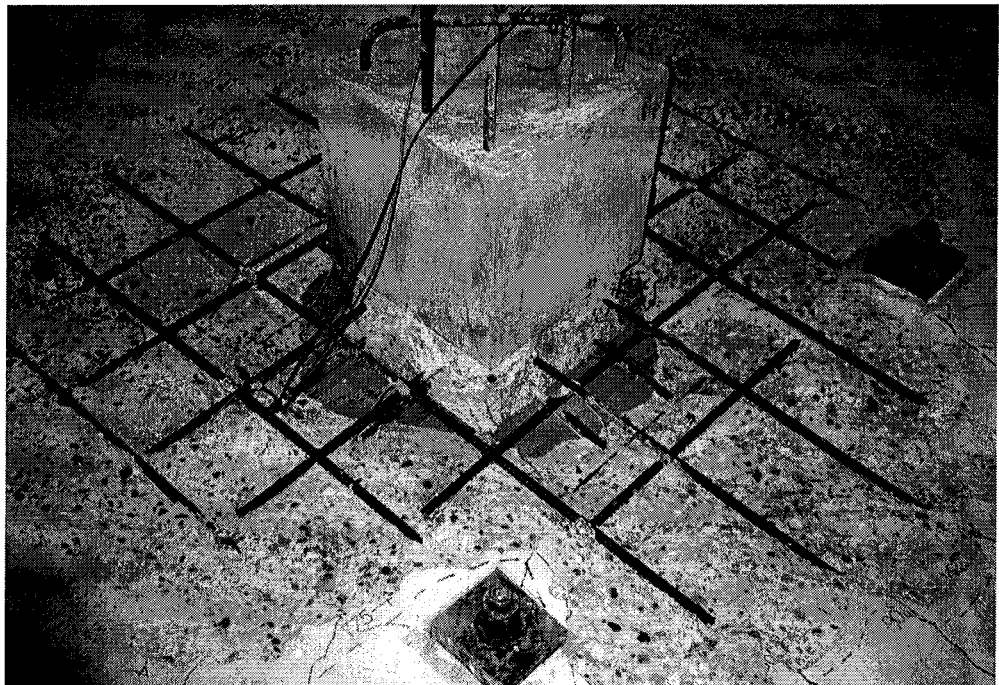


**Fig. 5.42 Concrete Patching : Formwork Detail (ER1-CP1)**

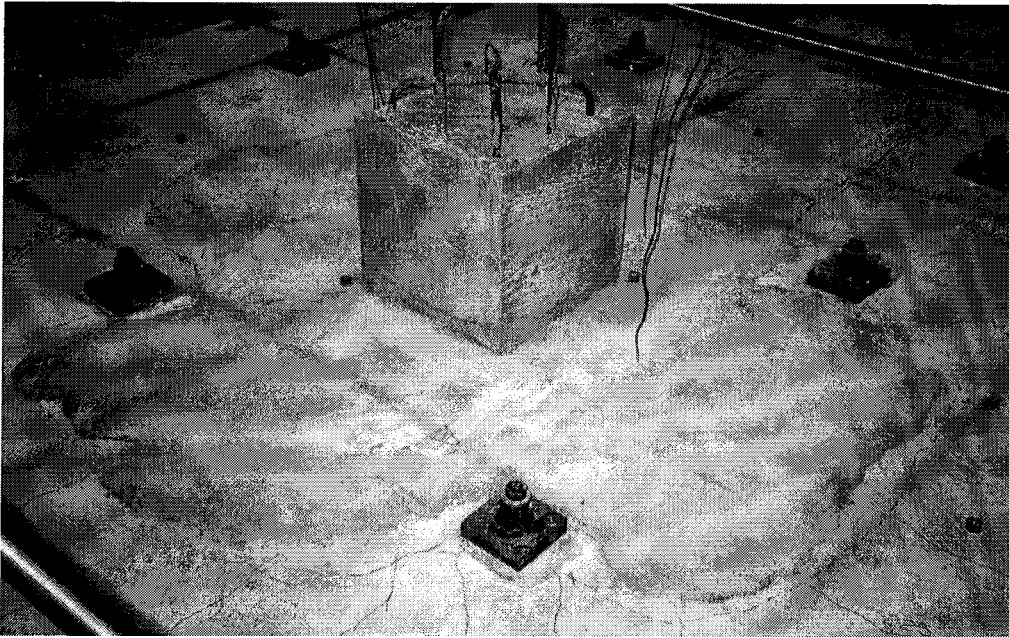


**Fig. 5.43 Concrete Patch : Top View (ER1-CP1)**

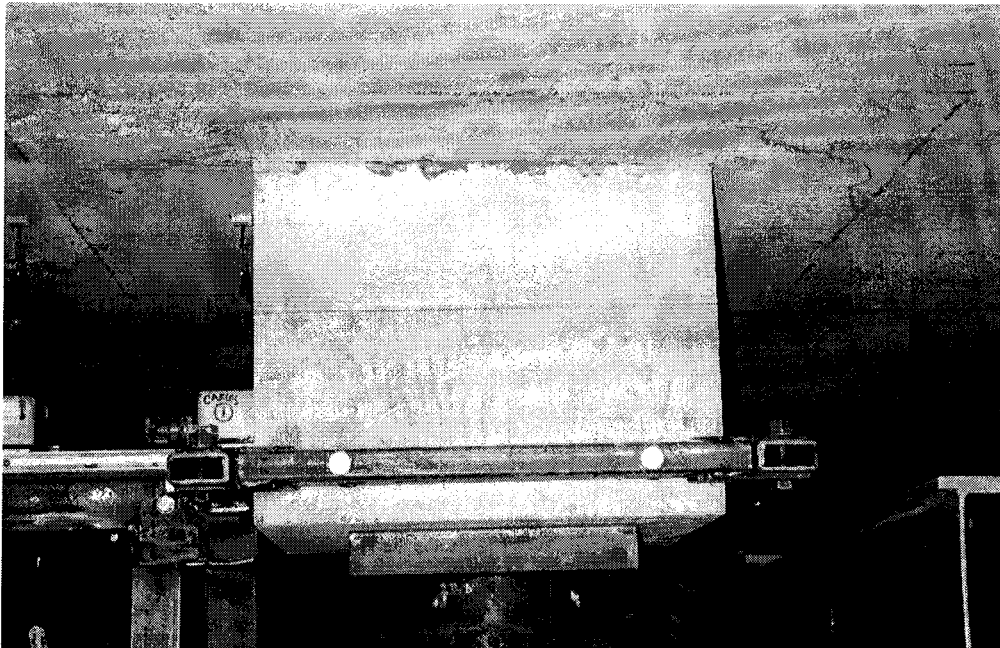


**Fig. 5.44 Concrete Patch : Bottom View (ER1-CP1)**

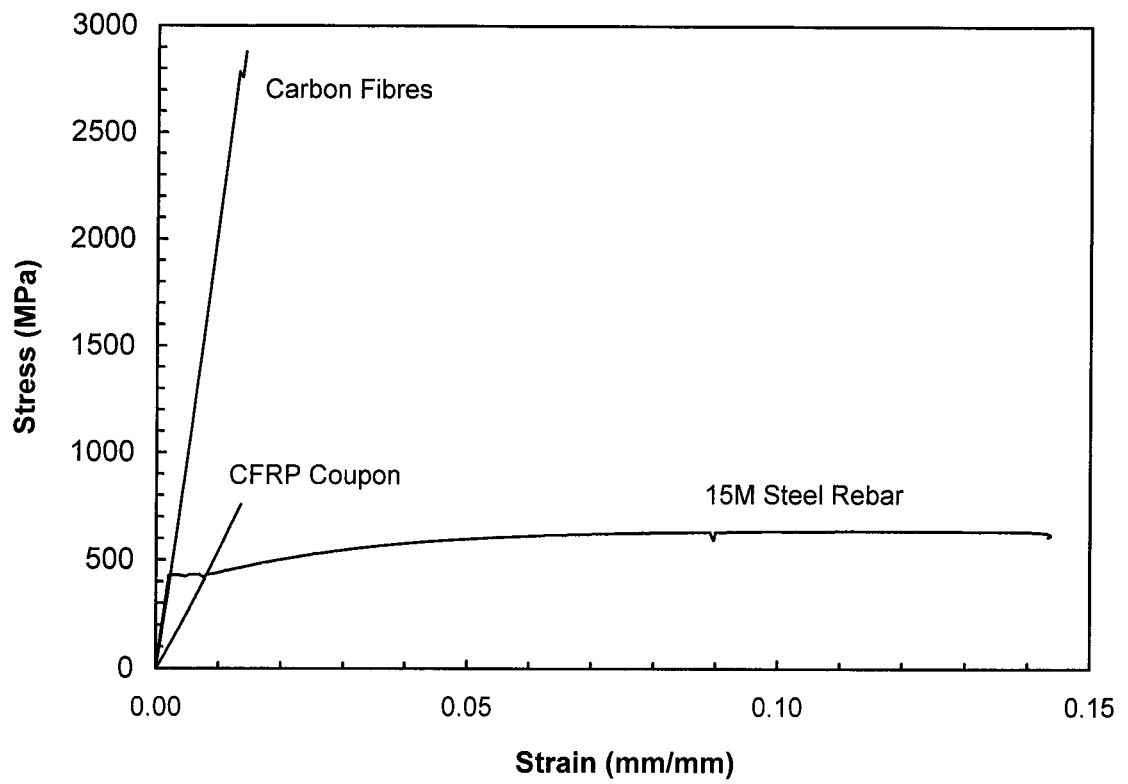


**Fig. 5.45 Response of Steel Rebar and CFRP in Tension**



## **6 Series I Tests: Results, Observations and Evaluation**

### **6.1 Load-deflection Response**

The load-deflection response of the test specimens helps to identify major changes in their behaviour and load carrying mechanisms. Significant behavioural differences are expected since the slabs were reinforced with completely different reinforcement types.

The load-deflection response of Series I slabs is shown in Fig. 6.1. The curves show the load variation as a function of the slab vertical deflection at 710 mm away from the column face. The load includes the self-weight of the slab plus that of the loading assembly (together amount to 20 kN). Deflection values are average values from deflections measured in the four radial directions and do not include the dead load deflection.

The load-deflection curves show that all slabs behaved similarly in the uncracked stage. The early kink in the load-deflection curves signals the formation of first flexural cracks. Cracking loads and the corresponding deflections for all slabs are shown in Table 6.1.

In SR-1, GFR-1 and GFR-2, first flexural cracks formed following the layout of the upper top through-joint bars (W-E direction in SR-1 and N-S direction in GFR-1 and GFR-2). Later, flexural cracks formed in the orthogonal direction, completing a cruciform crack pattern. The first flexural cracks in NEF-1 formed simultaneously in both directions because NEFMAC grids are orthotropic.

As the load increased, the cracks spread from inner to outer slab regions following the top mat reinforcement layout. First yielding of steel reinforcement in SR-1 was observed at about a 5.5 mm deflection in a bar passing through the joint at the column face. Yielding of through-joint bars spread to all column faces at a 10.6 mm deflection. The response of slabs GFR-1 and GFR-2 in the cracked stage is linear because FRP does not yield. However, the elastic-cracked response of NEF-1 was different. The load-deflection



response of this slab was jagged. The load dropped at deflections of 7.5 and 16 mm. These drops appear to be the result of grid slippage.

Slabs SR-1, GFR-1 and GFR-2 failed in classical punching fashion: the column pushed through the slab violently, leading to a significant load drop. Their ultimate loads and deflections are reported in Table 6.1. These slabs were unloaded after punching. The failure load of NEF-1 was difficult to determine because this slab did not feature either the sudden load loss or the violent column push-through at ultimate. At first sight, it appears that the load drop at a 26.7 mm deflection signals punching. This was inconclusive at the time of testing. The load drop at this level was soft and gradual.

To confirm whether NEF-1 had indeed failed or not at a 26.7 mm deflection, the slab was further loaded. Through this stage, the applied load never reached its previous peak value. The test was suspended at a 48 mm deflection to prevent the slab from squashing the instrumentation installed underneath. At that point, the slab appearance clearly suggested that NEF-1 had already punched. Whether failure occurred at the 26.7 mm deflection or at any of the load drops displayed earlier at a 7.5 or 16 mm deflection will be discussed later. Dissection of NEF-1 shows minor fibre splaying in the ribs near the column. The forensic inspection revealed that the rib longitudinal layers slipped relative to one another at crossing points located at 100 and 300 mm away from the column face. Evidence of full transverse fibre tearing or rupture was not found. Figures 6.2 to 6.5 show crack patterns for all slabs at ultimate.

Figure 6.6 shows underside slab deflections along the N-S direction in slab SR-1 immediately before punching together with those in slab NEF-1 at deflection levels of 26.7 and 32 mm. The deflected shape of SR-1 was almost straight before punching and that in NEF-1 was straight at a 26.7 mm deflection. This was also the case of GFR-1 and GFR-2 (not shown here). The straight deflection profile is consistent with a rigid body rotation of the slab in the radial direction, as observed by Kinnunen and Nylander (1960). However, the deflections in NEF-1 at a 32 mm imposed deflection at the slab edge trace a

broken profile which shows that the outer slab portion deflects less than the inner part. This observation confirms that punching of NEF-1 occurred earlier.

Figure 6.7 shows the variation of the radial slab rotation as a function of the deflection for all slabs. Rotations were calculated based on the slab underside deflection readings and the distance between them. Consistent with Kinnunen and Nylander (1960), the linear rotation-deflection curves show that the slab deformation in the radial direction is insignificant regardless of the type and amount of reinforcement. The fact that the slopes are almost equal reflects that all of the slabs had the same loading geometry. Punching is indicated at the load level beyond which the rotation starts decreasing. Figure 6.7 clearly shows that slab NEF-1 punched at a 26.7 mm deflection, as suspected initially.

## **6.2 Crack Widths**

Figure 6.8 shows the variation of load as a function of crack width for all slabs. Crack widths are average values from crack widths measured at 30 mm away from the column face on through-joint cracks in all four directions. The load-crack width relationships are qualitatively similar to the load-deflection curves of the slabs. At a given load, cracks tend to be wider as the stiffness of the top flexural mat decreases. For instance, at a load of 160 kN, which may be considered representative of service load conditions for a 4 m square interior slab panel, the crack width in SR-1 is about 0.3 mm, that in GFR-2 is two to three times greater, and that in GFR-1 and NEF-1 is about four to five times greater.

The variation of average crack widths at the column face as a function of the imposed slab deflection is shown in Fig. 6.9. Consistent with the observations made by Nawy and Neuwerth (1977), crack widths in the slabs reinforced with GFRP vary almost linearly with the slab deflection. Cracks are narrowest in SR-1. For deflections lower than 4 mm, the crack widths in the slabs with GFRP are similar. For greater deflections, NEF-1 displays the widest cracks. The increased crack widths in NEF-1 result from the reduced bond of NEFMAC ribs along the longitudinal direction in between transverse ribs.

## 6.3 Strains in Slab Reinforcement

### 6.3.1 Notation

To interpret the strain gauge output data, it is necessary to introduce some definitions with reference to Fig. 6.10. This figure shows a key plan with the strain gauge distribution in series I slabs. Each gauge represents the location of four gauges mounted as shown in chapter 5. The gauge grid is defined by the axes  $r - c$ . Labels " $r$ " and " $c$ " mean "Radial" and "Circumferential" directions, respectively. Bars passing through the joint (bar A) are referred to as *joint* bars. Those passing outside (bars B to E) are called *perimeter* bars. The gauges were lined up in three rows, 1, 2 and 3. The distance between adjacent gauges on the same bar defines an *interval*. In SR-1, GFR-1 and NEF-1, the interval width for the perimeter bars coincides with the top rebar spacing, i.e. 200 mm. In GFR-2, the gauge interval is twice the top mat spacing. In joint bar A, the uppermost gauge was located at the column face.

### 6.3.2 Validation of Strain Gauge Readings

Validation of the strain gauge readings will be performed by comparing the flexural moment estimates about the column face based on load cell reaction readings with those based on the strain gauges along gridline 1. The slight difference between the column face axis and the location of gridline 1 gauges will be ignored.

The total load cell-based flexural moment about the column face is

$$M_{cf}^- = 0.25(R_1 + R_4) + 0.71(R_2 + R_3) \quad [\text{kN.m}] \quad [6.1]$$

where  $R_1$  to  $R_4$  represent the reactions acting on one half of the slab.

The total strain gauge-based moment about gridline 1 in slab SR-1 is approximately

$$M_{sg,gl}^- = \sum A_s \varepsilon_s E_s (jd)^- = \sum A_s \varepsilon_s E_s \left( d - \frac{A_s f_y}{1.7 f_c' b} \right) \quad , \quad \varepsilon_s E_s \leq f_y \quad [6.2]$$

where  $\varepsilon_s$  is the measured steel strain and  $f_y$  is the yield strength of the reinforcement. The summation sign indicates that the total moment is evaluated from the contribution of all

reinforcing bars across the full slab width. Equation 6.2 gives reasonable moment estimates only when the slab is fully cracked. Otherwise, the equation overestimates  $jd$ .

Taking into account that FRP reinforcement does not yield, the bending moment in the slabs with FRP can be evaluated as

$$M_{sg,gl}^- = \sum A_f \varepsilon_f E_f (jd)^- \quad , \quad \varepsilon_f E_f \leq f_{fu} \quad [6.3]$$

where  $\varepsilon_f$  is the GFRP strain,  $E_f$  is the elastic modulus of FRP and  $f_{fu}$  is the ultimate tensile strength of FRP. For simplicity, calculations were made assuming  $(jd)^- = 0.90 d$ .

Figures 6.11 and 6.12 compare the strain gauge- and load cell-based negative moment predictions for slabs GFR-1 and NEF-1, respectively. The figures show that the moment estimates are consistent. The curves for the other two slabs (not shown here) show the same level of consistency. This indicates that the strain gauge output data can be trusted.

### 6.3.3 Circumferential Strains

Figures 6.13 to 6.16 show circumferential strain distribution profiles in all slabs along the radial direction at a deflection of 10.6 mm. This deflection level corresponds to full yielding of the steel around the column in control specimen SR-1. It provides a metric for comparing the different slab responses in terms of strains or bar forces.

Consistent with Kinnunen and Nylander (1960), circumferential strains for SR-1 and GFR-2 and NEF-1 along gridline 1 are inversely proportional to their radial position. However, strain profiles in GFR-1 are approximately uniform. The circumferential strains along gridline 1 in SR-1 are smaller than those in GFR-1, GFR-2 and NEF-1. This is consistent with the smaller crack widths reported for SR-1. The plots also show that the strain difference among the three profiles is smallest for SR-1 and greatest for NEF-1.

At ultimate (curves not shown), circumferential strains in SR-1 are above yielding whereas strains of about 35, 29 and 65 % of those at FRP rupture were measured in GFR-1, GFR-2 and NEF-1, respectively. The higher strains in NEF-1 at the column face are

consistent with the fact that strain gauges in the NEFMAC grid were bonded on the upper side of the grid and not on the centroid of the reinforcement as was done in the other slabs. The greater strains in NEF-1 are also consistent with the wider cracks of this slab. It is also worth noting that NEFMAC rib strains in the order of  $19000 \mu\epsilon$  were measured at a 48 mm deflection. This strain level is very close to that at NEFMAC rupture.

#### **6.3.4 Forces in Slab Reinforcement**

Figures 6.17 to 6.20 show the force variation in bar C for all slabs along gridlines 1, 2 and 3 against the slab deflection. Bar forces were obtained by converting measured strains into forces on the basis of tension coupon test results. Bar C was selected to illustrate the typical bar force variation in a region where slender beam action dominates.

As expected, the figures show that bar forces at upper gauge locations tend to increase earlier than do those at lower gauge locations. This is consistent with slab flexural cracks propagating from inner to outer slab regions and also with the fact that moments are greater at upper gauge locations. For instance, in slab GFR-1 (see Fig.6.18), the bar force at C-1 starts increasing immediately after first flexural cracks form whereas those at C-2 and C-3 are equal to zero. The bar force at C-2 starts increasing at a 4 mm deflection, which coincides with a crack passing over C-2. At this level, the bar force growth rate at C-1 starts decreasing and that at C-3 is still minimal. The bar force at C-3 starts increasing at a 7.6 mm deflection, which coincides with a crack passing over C-3. At this stage, the force growth rate at C-2 decreases. This trend applies to all slabs.

The bar force plots of Figs. 6.17 to 6.20 also show a stiffer response in SR-1 compared to that in GFR-1, GFR-2 and NEF-1. This is because of steel's greater stiffness.

#### **6.3.5 Bar Force Gradients**

Bar force gradients provide a quantitative measurement of the amount of shear transferred by beam action by the slab reinforcement. A null bar force gradient implies that shear is carried mainly by arching action.

Figures 6.21 and 6.22 show the variation of bar force gradients for joint bar A for slabs SR-1 and GFR-1. In SR-1, the bar force gradient across the first interval reached a peak of 155 N/mm at a deflection of about 3.5 mm, then remained constant up to a 5.5 mm deflection and finally dropped steadily to zero. First yielding of bar A was observed at upper gauge location A-1' at a deflection of about 5.5 mm. This indicates that the force gradient for bar A across the first interval is limited by yielding of the reinforcement. The same limitation occurred across the second interval except that a higher peak gradient of 200 N/mm was developed. The corresponding force gradient at failure was 103 N/mm.

Figure 6.22 shows that bar A's force gradients in GFR-1 were much lower than those in SR-1. The highest gradients in GFR-1 were measured across the second interval. Since FRP does not yield, the force gradient in GFR-1 is not limited by yielding of the reinforcement. Instead, it is limited by bond failure.

Figure 6.23 shows the bar force gradients for joint rib A in slab NEF-1. The force gradient across the first interval is high and grows steadily up to failure. The gradient is high because of high strains concentrated at through-joint cracks. The gradient along the second interval is much lower.

Figures 6.24 to 6.26 show the force gradients generated by perimeter bars across the second interval (2-3) for slabs SR-1, GFR-1 and NEF-1. According to Fig. 6.24, bars B and C in SR-1 developed force gradients of 132 and 150 N/mm before failure. These gradients are limited by yielding of the reinforcement at upper gauge locations. The values are lower than the peak 200 N/mm gradients reported by Alexander, Lu and Simmonds (1995) from tests on two-way slabs with steel bars of similar diameter spaced at 150 mm and than the peak 200 to 250 N/mm gradients reported by Olonisakin and Alexander (2000) from tests on one-way slabs with steel bars spaced at 150 mm..

The non-yielding nature of FRP precludes reinforcement yielding as a cause of C-bar or NEFMAC rib force gradient reduction. Instead, the major governing limitation for force

gradient development in FRP refers to bond deterioration. As to GFR-1, the bond effect can be observed in Fig. 6.25 for bar D. The force gradient reaches a peak 87 N/mm value at a deflection of 7.8 mm and then plummets to zero. Bar D was unable to develop the 117 N/mm peak gradient generated by bar B at failure.

As far as NEF-1 is concerned, Fig. 6.26 shows that the only perimeter rib to display an increasing force gradient was rib B (90 N/mm at ultimate). The other perimeter ribs displayed lower force gradients (from 30 to 72 N/mm). The early cusps at a 7 and 13 mm deflection result from low strain readings at lower gauge locations likely because the flexural crack that formed along gridline 3 did not cross the gauges.

## 6.4 Internal Shears

According to Alexander and Simmonds' strip model for punching, the punching shear capacity of an interior slab-column connection is influenced by the ability of the slab internal reinforcement to generate shear by one-way beam-action to the radial strips that frame into the column. To evaluate the shear transferred from the perimeter bars to the radial strips, two possibilities are considered (see Alexander, Lu and Simmonds, 1995).

The first assumes that the shear is carried by beam action through the first interval. In this case, the shear force associated to a single bar or simply the “bar shear”,  $V_{bar}$ , is

$$V_{bar} = \frac{T_1 - T_2}{s} jd_1 \quad [6.4]$$

If some arching action contribution across the first interval is accounted for,

$$V_{bar} = \frac{T_2 - T_3}{s} jd_1 \frac{T_1}{2T_2 - T_3} \quad [6.5]$$

In Eqs. 6.4 and 6.5,  $T_1$ ,  $T_2$  and  $T_3$  refer to the bar tensile force at gridlines 1, 2 and 3, whereas  $jd_1$  is the flexural lever arms at gridline 1. Alexander *et al* (1995) assume that the governing value of  $V_{bar}$  is the larger of the two values defined according to Eqs. 6.4 and 6.5.

Figures 6.27 to 6.29 show bar shear envelopes for the perimeter bars in slabs SR-1, GFR-1 and NEF-1, respectively. The figures show higher bar shears in SR-1 compared to those in GFR-1 and NEF-1. This is consistent with the higher punching capacity of SR-1.

According to the fundamentals of the strip model, the sum of all the bar shears delivered to the radial strips should equal the applied column load. The total shear transferred by the slab to the column based solely on strain gauge measurements can be evaluated as

$$P_{sg} = 8 \sum_{i=1}^4 V_{bar,i} \quad [6.6]$$

Figure 6.30 shows the variation of the ratio of  $P_{sg}$  to the applied column load,  $P$ , as a function of the slab deflection for slabs SR-1, GFR-1 and NEF-1. The dead load has been included in the calculations. In SR-1, the shear contribution from bar F was neglected because the strain readings at lower gauge locations were excessively low.

The three curves of Fig. 6.30 show essentially the same trend. The early cusp is the result of Eqs. 6.4 and 6.5 overestimating the  $jd$  term before the slab can be considered fully cracked. Once the slabs are fully cracked, the curves drop down to a value of about one. The fact that the three curves reach unity means that the assumed shear transfer mechanism of Alexander and Simmonds' strip model is conceptually correct. Similar results were obtained by Alexander *et al* (1995) in the punching capacity evaluation of slabs with steel and epoxy-coated reinforcement, and by Afhami *et al* (1998) in punching shear tests of a two-span slab specimen.

## 6.5 Influence of Test Variables

### 6.5.1 Top Mat Stiffness Effect

In this study, the effect of the top mat stiffness was examined by varying the slab reinforcement content and/or the FRP stiffness. Two main effects could be observed from the tests. First, an increase in the slab reinforcement ratio leads to a stiffer response in the elastic-cracked stage. Second, as the top mat stiffness increases, both the punching



strength increases and the ultimate deflection decreases. These observations are consistent with the test results reported by Matthys and Taerwe (2000c).

### **6.5.2 Reinforcement Type Effect**

In addition to their elastic stiffness, the main difference between the reinforcements was related to their bond characteristics. Both steel rebars and GFRP C-bars had a round cross-section and shear lugs. In addition to its slightly lower elastic stiffness relative to that of the C-bars, the NEFMAC ribs were rectangular in cross-section and were not provided with any bond enhancement features. Bond was provided mainly by mechanical bearing of the transverse ribs against concrete.

According to Fig. 6.1, the response of NEF-1 was significantly different than that of GFR-1 despite having a similar top mat stiffness. In the elastic-cracked stage, the load-deflection response curve of NEF-1 was jagged, accompanied by significant slippage of the NEFMAC reinforcement. The behavioural differences accentuate at ultimate; the load drop after NEF-1 punched was gradual rather than sudden, as observed not only in slab GFR-1 but also in the other two slabs reinforced with deformed rebars.

The effect of reinforcement type is also reflected in the circumferential strain profiles of Figs. 6.13 to 6.16. As shown in Fig. 6.13, the average strain at cracks in SR-1 along gridlines 1 to 3 is in the order of 1800 to 1900  $\mu\epsilon$ . This average strain is less than that in the slabs with FRP. Since the strain profiles correspond to the same imposed deformation of 10.6 mm, and since deflections are obtained by integrating strains, the strains in the FRP reinforcement between the gauges must get reduced significantly to render the same overall slab deflection. This suggests that concrete tension stiffening is proportionally more significant in slabs with GFRP than in steel-reinforced concrete slabs.

## **6.6 Flexural Bond in Slabs with Internal FRP Reinforcement**

### **6.6.1 Flexural Bond in GFRP C-bars**

The bar force gradient plots of Figs. 6.24 to 6.25 are useful to evaluate the effect of reinforcement type on the flexural bond strength of steel bars and GFRP C-bars. Let us

compare the response of the steel bars in SR-1 and that of C-bars in GFR-1. At a given deflection of 10 mm, the average force gradient in the steel bars is about 90 N/mm whereas that in the C-bars is about half. Dividing the average force gradient by the 200 mm rebar spacing results in an average flexural bond of 0.45 MPa for the steel bars and 0.22 MPa for the C-bars. This shows that, at the given 10 mm deflection, the bond strength of C-bars is about half of that developed by conventional steel bars. This also indicates that bond strength estimates from pull-out tests (typically in the order of 10 to 15 MPa for GFRP deformed bars) may be excessively liberal.

### 6.6.2 Flexural Bond in GFRP NEFMAC Grids

According to Figs. 6.25 and 6.26, the force gradients developed by the NEFMAC grid were similar to those developed by the C-bars. This indicates the bond supplied by the transverse ribs in the NEFMAC grid is equivalent to that generated continuously in the interface between the C-bar and concrete.

Figure 6.31 provides a further insight into the bond characteristics of NEFMAC grids. Figure 6.31a shows a portion of perimeter rib C bounded by the column centreline (gridline 0) and the lowermost gauge C-3. The rib is crossed by top flexural cracks #1, #2 and #3. In NEF-1, these cracks formed at deflections of about 0.3, 7.5, and 16.4 mm, respectively. The variation of rib forces as a function of the slab deflection is shown in Fig. 6.20. The typical free body diagram of a NEFMAC rib in tension is shown in Fig. 6.31b. Since bond along the ribs is negligible, the force difference  $\Delta T$  results from grid bearing against concrete. This value is taken constant along the interval.

Since the first flexural crack (crack #1) passes along gridline 1, the rib force along interval 1-2 starts increasing at a 0.3 mm deflection (see Fig. 6.20) and the rib slips at joint 1. The force along interval 0-1 was not measured. It is assumed, however, to be greater than that along interval 1-2. As shown in Fig. 6.20, the force along 1-2 (gauge C-1) increases steadily up to the formation of crack # 2 at a deflection of 7.5 mm.

The force difference between  $T_{1-2}$  and  $T_{2-3}$  up to crack # 2 formation defines path A-B in the force differential-slip ( $\Delta T$ - $\delta$ ) plot of Fig. 6.31c. The formation of crack # 2 and the slip at gridline 2 lead to an increase in rib force along interval 2-3 starting from zero and to further rib slip at 1. At this point, the force growth rate at 2 starts decreasing which leads to a reduction in the slope of the  $\Delta T$ - $\delta$  curve from B to C. The additional slip at 1 is a necessary condition for force 1-2 to be greater than that along 2-3.

Later, at a deflection of about 12 mm, the force differential between 1-2 and 2-3 becomes constant. The force in both intervals increases but no additional bond stresses develop. This results in a constant  $\Delta T$  value (Fig. 6.31c). Presumably, the bond stress shortage is the result of the gradual rib debonding at joint 1 since the crossings possess the weakest architecture in the grid. The force differential  $\Delta T$  remains constant up to the formation of crack # 3 at a deflection of 16.4 mm which signals point D in Fig. 6.31c. Beyond this level,  $\Delta T$  further drops and at a deflection of 26.7 mm, the rib slips further at 3 and bond failure occurs, as indicated by point E in Fig. 6.31c.

## **6.7 Failure Cause of Series I Slabs**

### **6.7.1 Governing Failure Mechanism**

The fact that only four slabs were tested in this series makes it difficult to report a concise explanation of the reasons behind their failure. However, it must be emphasised that the experimental variables were well established. As a result, the tests should at least indicate some basic behavioural trends on which deeper conclusions could be drawn later. The experimental observations from series I tests are particularly useful to examine conventionally accepted theories explaining punching failures in ordinary steel-reinforced concrete slabs.

As observed in Fig. 6.1, the load-deflection response of series I slabs alone does not provide a conclusive evidence to determine the governing failure mechanism in the slabs with FRP. The variations in the failure load cannot be explained by the differences in concrete strength alone, as one would expect using the punching shear capacity design

provisions in ACI 318-99 and CSA A23.3-94. The load-deflection response of GFR-1 and GFR-2 shows that there is definitely an effect associated with the amount of flexural reinforcement. This is consistent with the observations of Matthys and Taerwe (2000c).

Figure 6.1 also provides useful information on the failure triggering mechanism linked to punching of slab SR-1. From this figure, it can be conjectured that the same slope of the load-deflection curve of SR-1 through the elastic-cracked stage could be displayed by a slab with a top GFRP mat as stiff as that of SR-1. In the forthcoming discussion, this slab is referred to as the “equivalent” slab. The stiffness “equivalency” can be ensured by either spacing the GFRP C-bars tightly, using stiffer reinforcement, or combining a stiffer reinforcement with a tight spacing.

In accordance with the observations made by Criswell (1974) (see Fig. 4.1), it can be conjectured based on the response of slabs GFR-1 and GFR-2 at ultimate, that the “equivalent” slab would punch at a deflection less than that of SR-1 at ultimate. Since slab SR-1 would then deform more and would carry more load than the “equivalent” slab, it can be concluded that concrete crushing can not be the cause of failure of SR-1. The relevance of concrete crushing as a punching failure criteria in concrete flat plates has also been criticised by Shehata and Regan (1989) for slabs with steel reinforcement.

The relatively low strain values measured at ultimate in the slabs with GFRP constitutes evidence that punching is not caused by rupture of the GFRP reinforcement either. Since the slab reinforcement ratios that will be provided in prototype slabs with FRP would be higher than those supplied in slabs GFR-1 and NEF-1 (to comply with serviceability requirements), the FRP strain will further reduce.

Having discarded concrete crushing and reinforcement yielding or rupture as dominant punching failure mechanisms, the major dominant variable appears to be the quality of bond between the reinforcement and concrete. The significance of bond on the mechanics of shear transfer from slab to columns has been identified by Alexander and Simmonds (1991) in the context of steel-reinforced concrete slabs. In series I slabs GFR-1 and GFR-

2, failure is triggered by the inability of C-bars that frame into the radial strip to continue generating force gradients. As the bond limit between C-bars and concrete is reached, the slab punches.

### 6.7.2 Failure Mechanism in Slabs with GFRP NEFMAC Grids

The high rib force gradients developed by joint rib A shown in Fig. 6.23 initially suggest that NEFMAC grid ribs transfer shear by beam action in the radial strip. Moreover, the figure shows that NEFMAC ribs are able to develop much higher rib force gradients than do C-bars. This is, however, not true for the following reasons. First, the slab-column region is a highly disturbed region. Second, the high force gradients reported in Fig. 6.23 are “apparent” values in the sense that they only reflect the force *difference* between the first and second intervals at the crossing rib. The stepped tension force distribution along the rib (see Fig. 6.31a) is equilibrated by compression fans framing into the joint, as shown in Fig. 6.32. This type of shear transfer mechanism is of arching type, which is consistent with the fundamental assumptions of Alexander and Simmonds’ strip model.

For the case of NEF-1, the compression fans  $CF_1$  and  $CF_2$  shown in Fig. 6.32 form, respectively, at a slab deflection of 7.5 and 16.4 mm. These deflection values signal the slip of the NEFMAC rib at gridlines 2 and 3, respectively. At a deflection of 26.7 mm, further slippage at gridline 3 leads to more tension in the interval 2-3. As a result, the flatter compression arch  $CF_2$  is not able to equilibrate the vertical column load at the root of the slab-column joint and the column pushes through the slab.

The existence of compression fans is corroborated by the cross-sectional view of slab NEF-1 after failure shown in Fig. 6.33, which is also consistent with the punching shear crack outline shown in Fig. 6.5. As illustrated in Fig. 6.32, it can be hypothesised that the shear crack ran underneath the NEFMAC rib between gridlines 2 and 3, but surfaced at gridline 2 after significant deformation was imposed on the slab.

**Table 6.1 Series I Slabs : Test Results**

<b>Slab</b>	<b>P<sub>cr</sub></b> <b>(kN)</b>	<b>P<sub>y</sub></b> <b>(kN)</b>	<b>P<sub>u</sub></b> <b>(kN)</b>	<b>Δ<sub>cr</sub></b> <b>(mm)</b>	<b>Δ<sub>y</sub></b> <b>(mm)</b>	<b>Δ<sub>u</sub></b> <b>(mm)</b>
SR-1	64.6	319.6	365.1	0.3	10.6	13.8
GFR-1	77.6	—	199.0	0.3	—	23.3
GFR-2	72.5	—	249.0	0.2	—	16.4
NEF-1	89.4	—	203.0	0.4	—	26.7

- Notes:
1. Load values include the dead load on the slab ( $\approx 20$  kN).
  2. Deflection values do not include the dead load deflection.
  3.  $P_y$  and  $\delta_y$  values in SR-1 are those at full top slab reinforcement yielding at the column face.

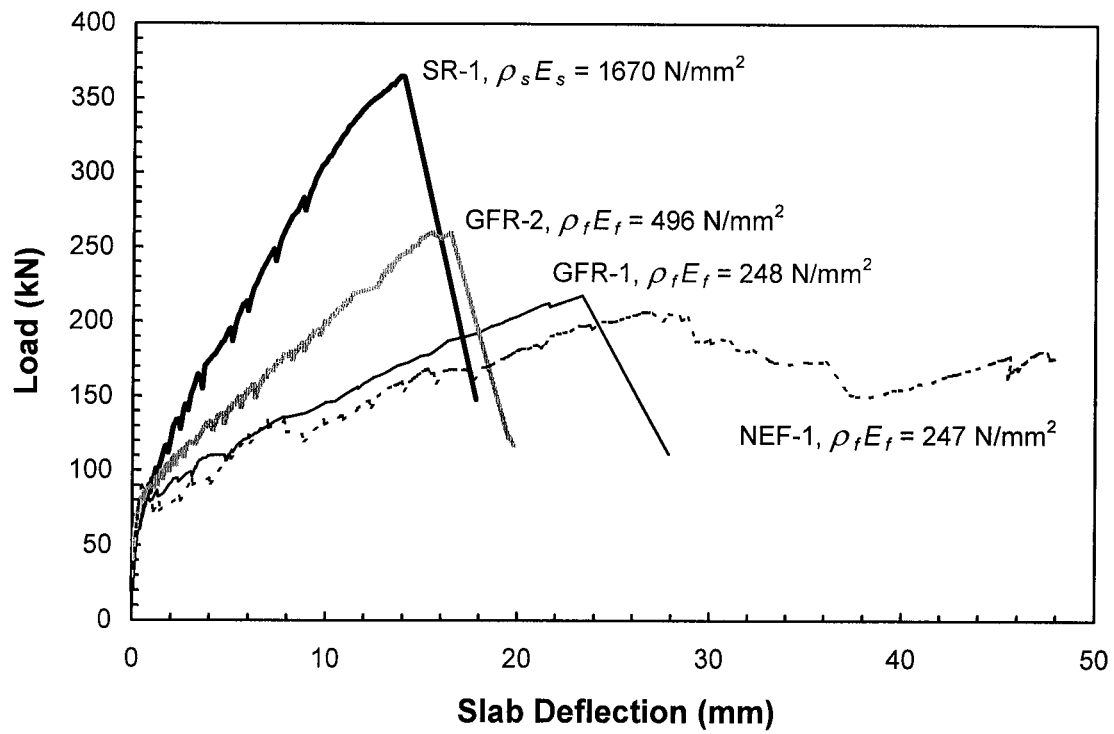


**Fig. 6.1 Response of Series I Slabs**

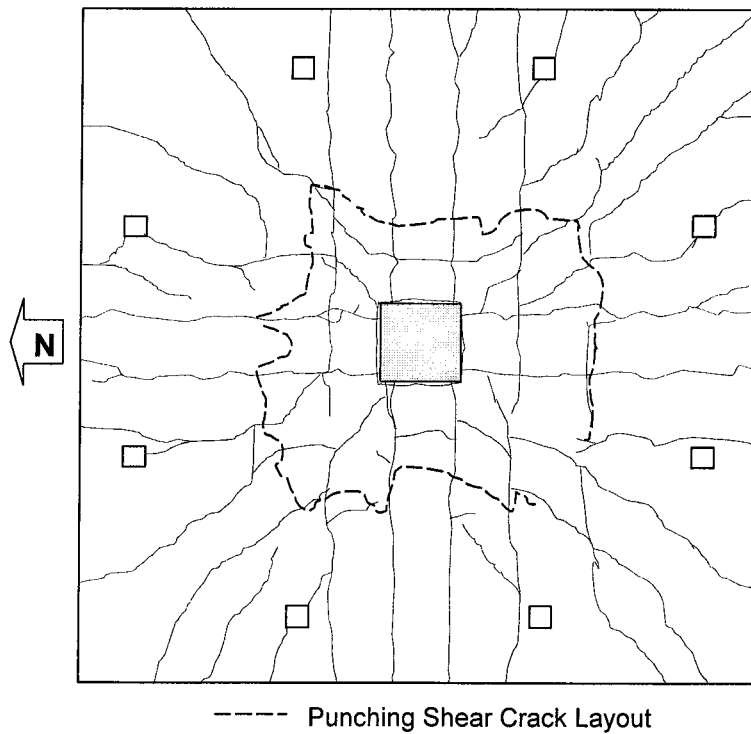
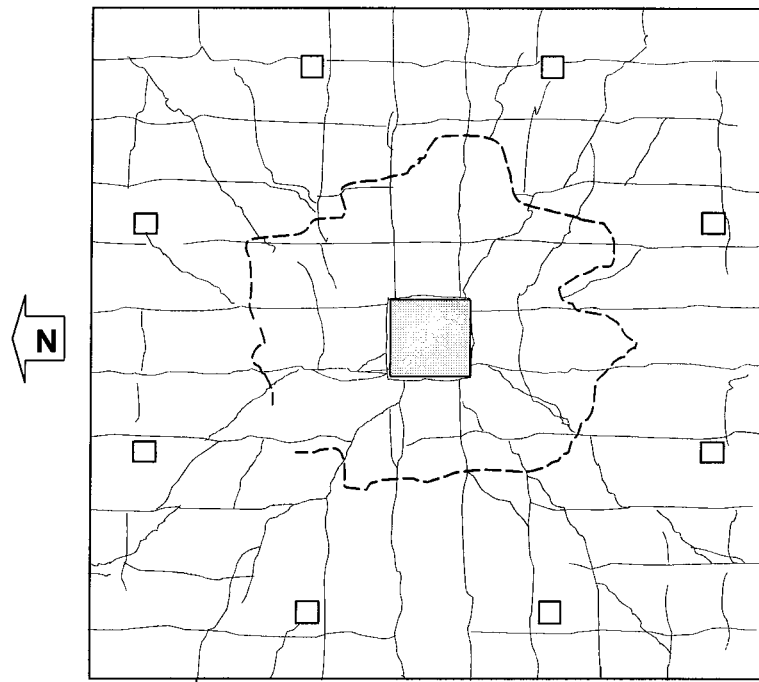
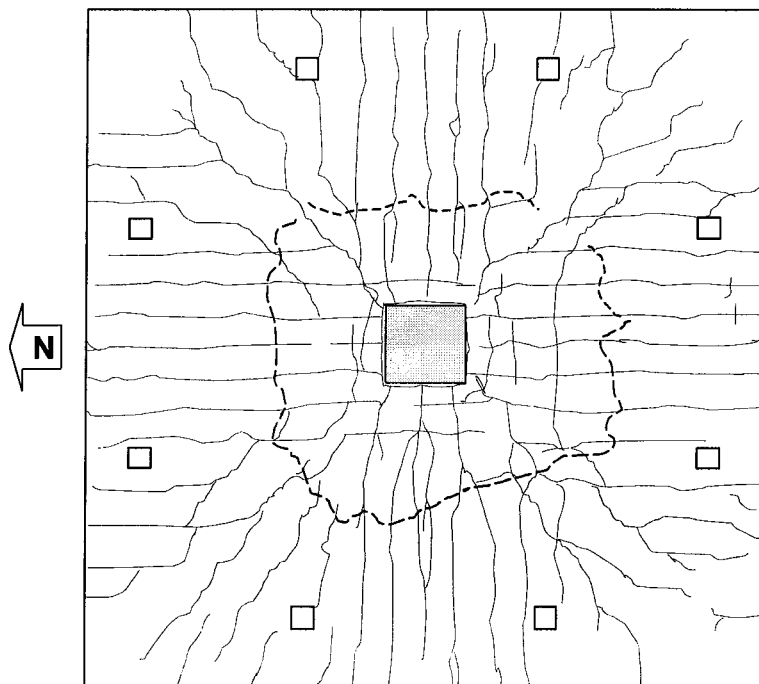


**Fig. 6.2 Crack Pattern : SR-1**



----- Punching Shear Crack Layout

**Fig. 6.3 Crack Pattern : GFR-1**



----- Punching Shear Crack Layout

**Fig. 6.4 Crack Pattern: GFR-2**



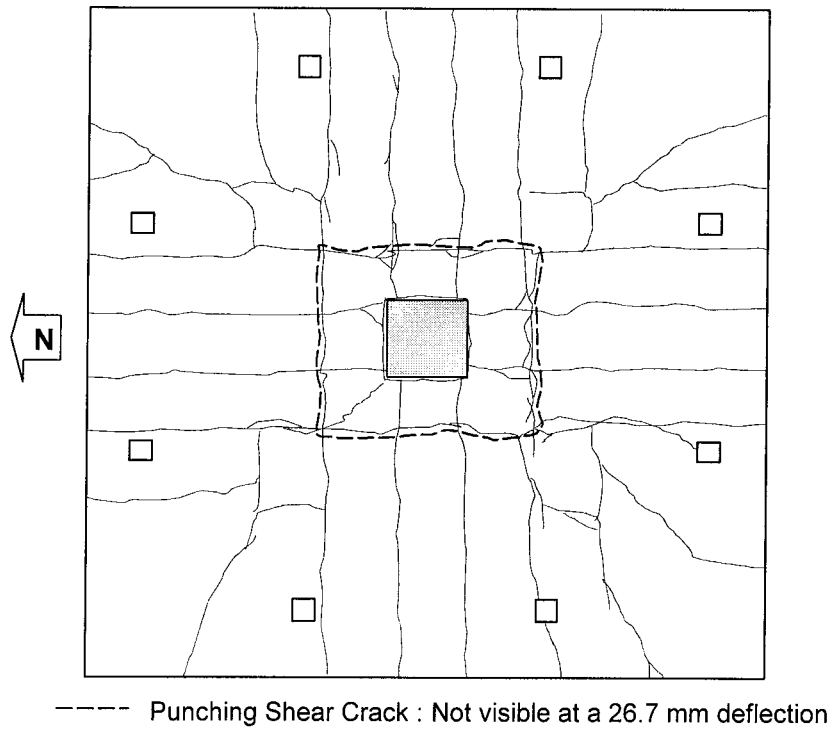


**Fig. 6.5 Crack Pattern : NEF-1**

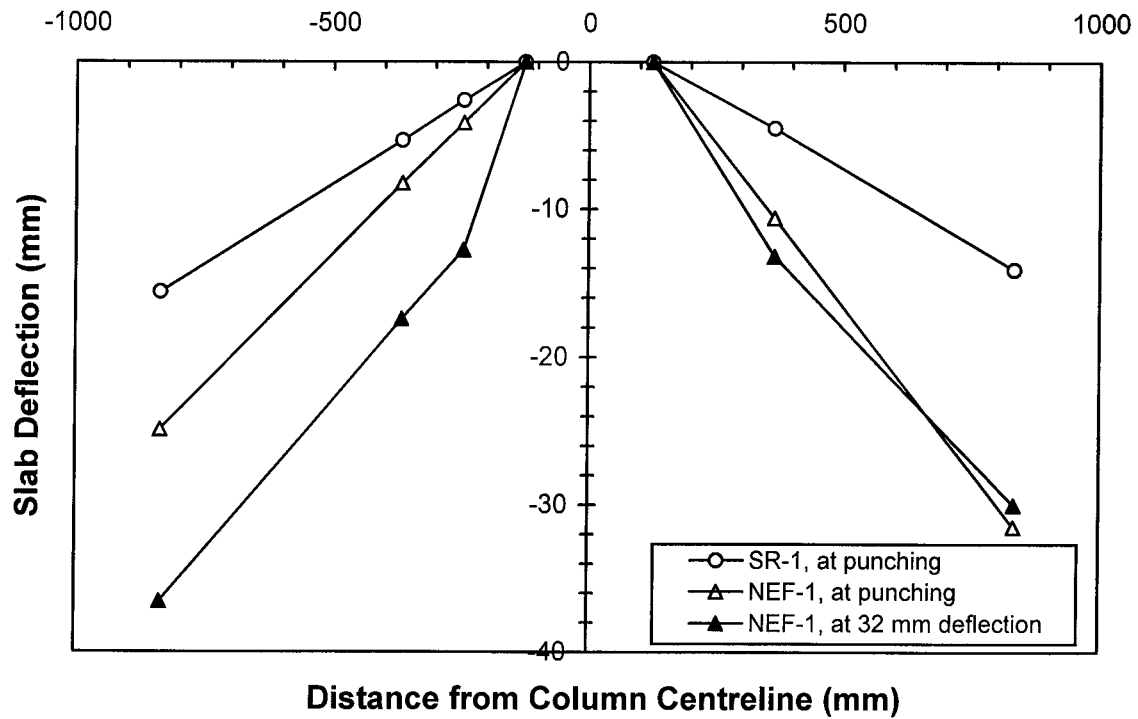


**Fig. 6.6 Underside N-S Slab Deflections : SR-1 & NEF-1**

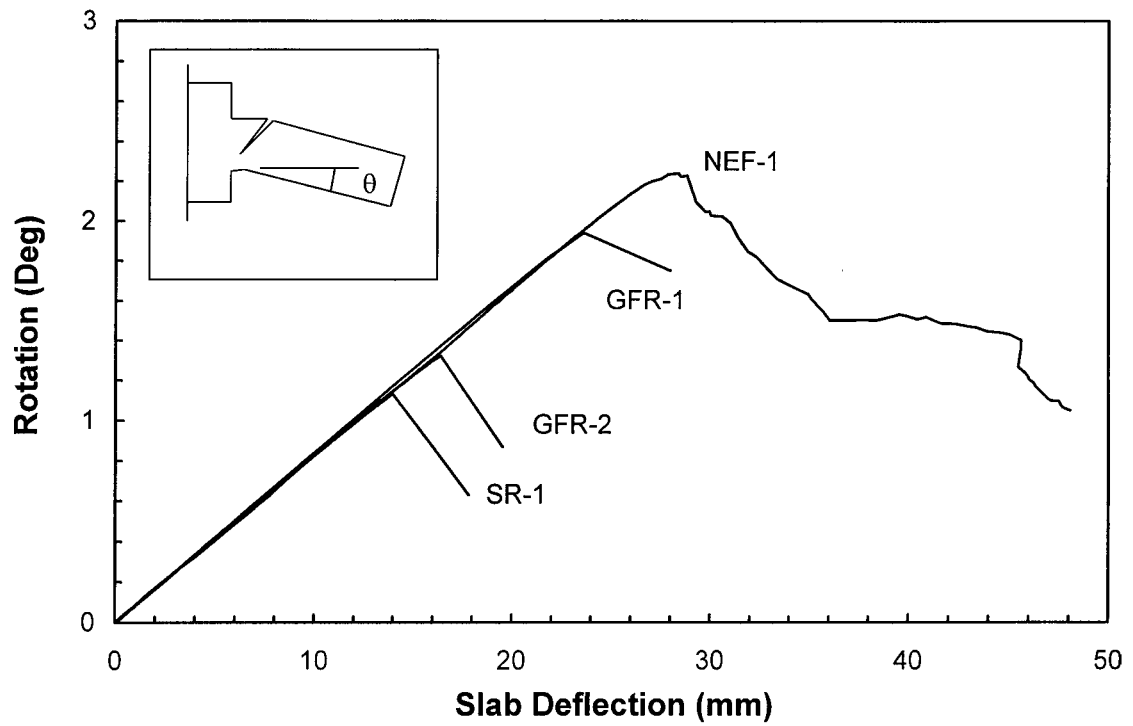


**Fig. 6.7 Underside Slab Rotations : Series I Slabs**

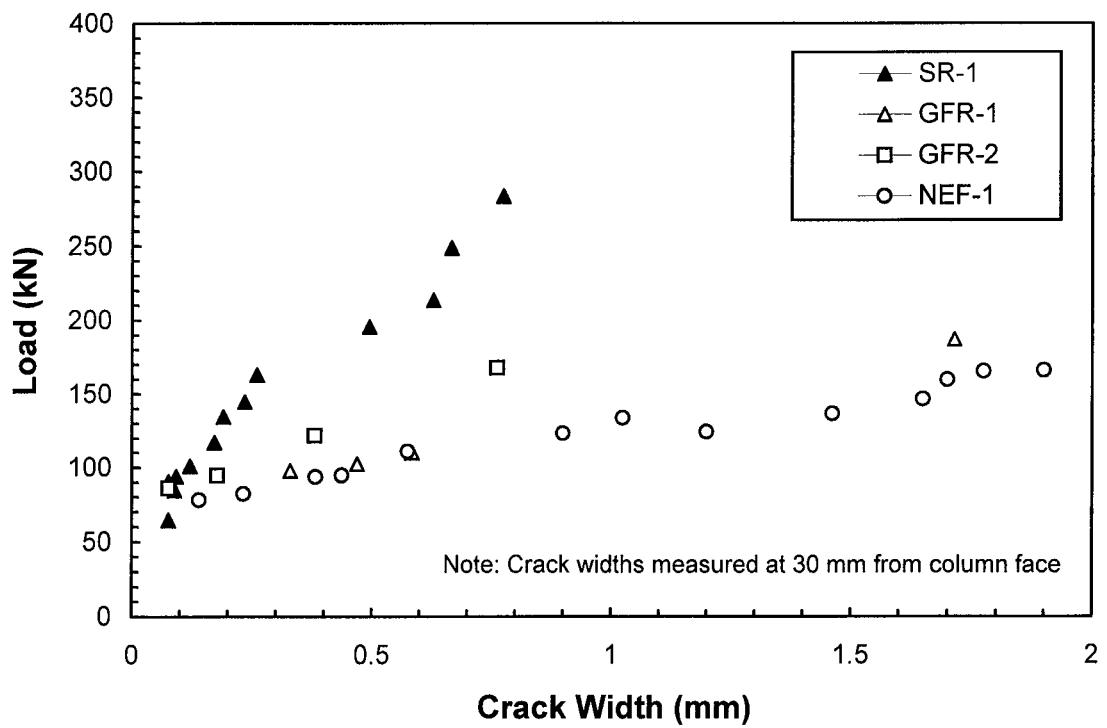


**Fig. 6.8 Ave. Crack Widths : Series I Slabs**

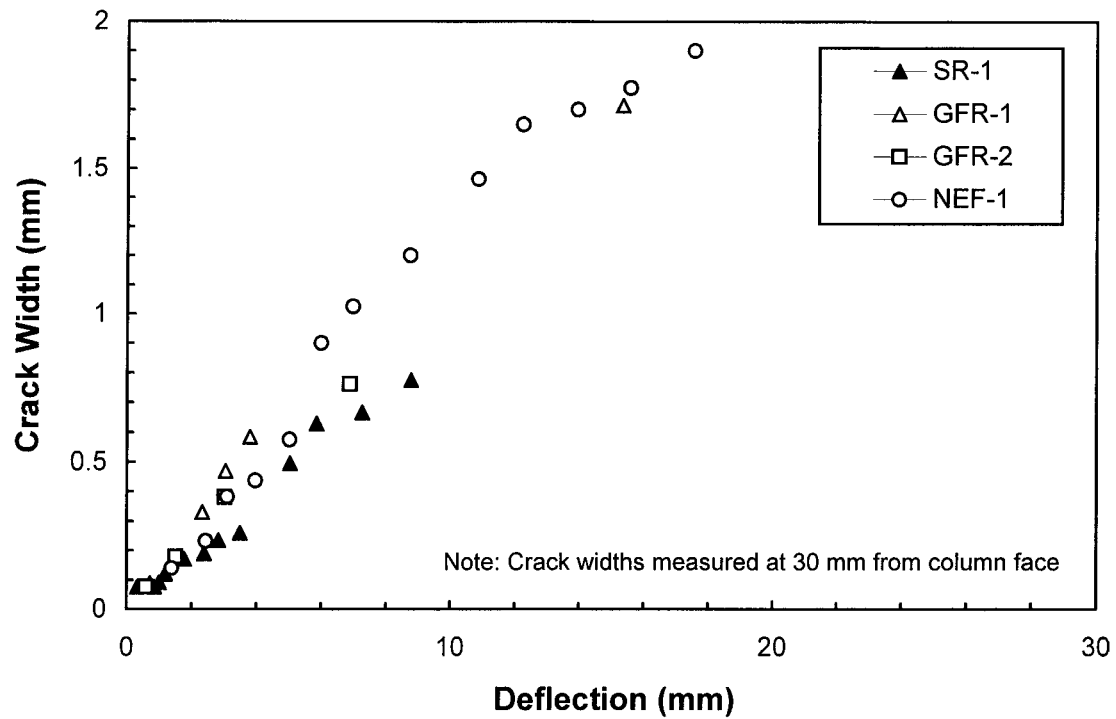


**Fig. 6.9 Ave. Crack Widths : Series I Slabs**

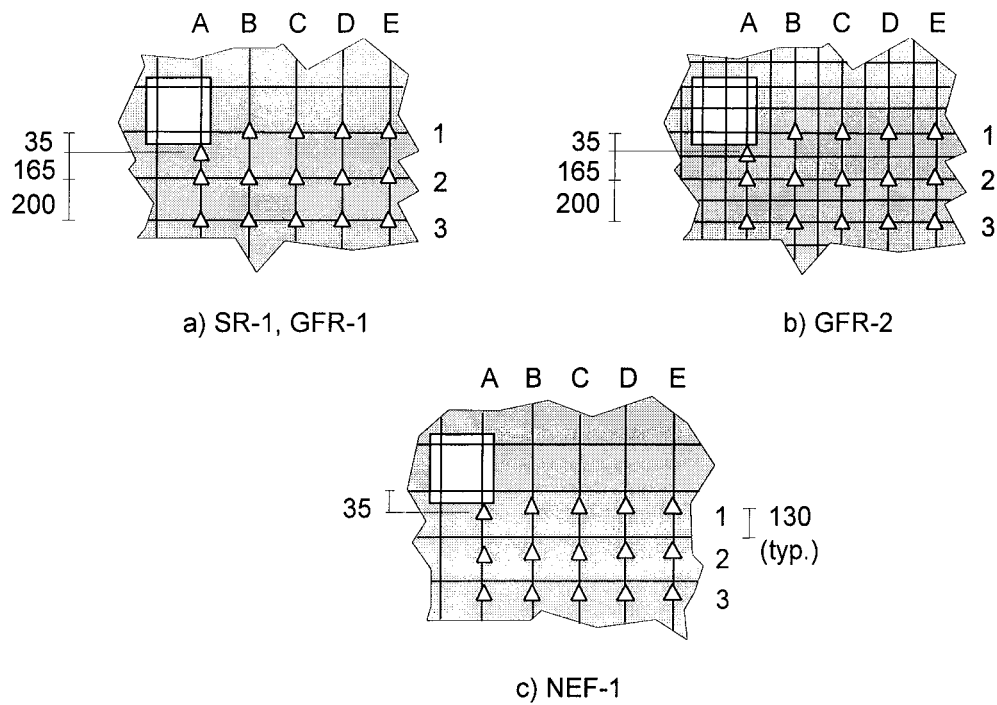


**Fig. 6.10 Strain Gauge Layout Plans : Series I Slabs**

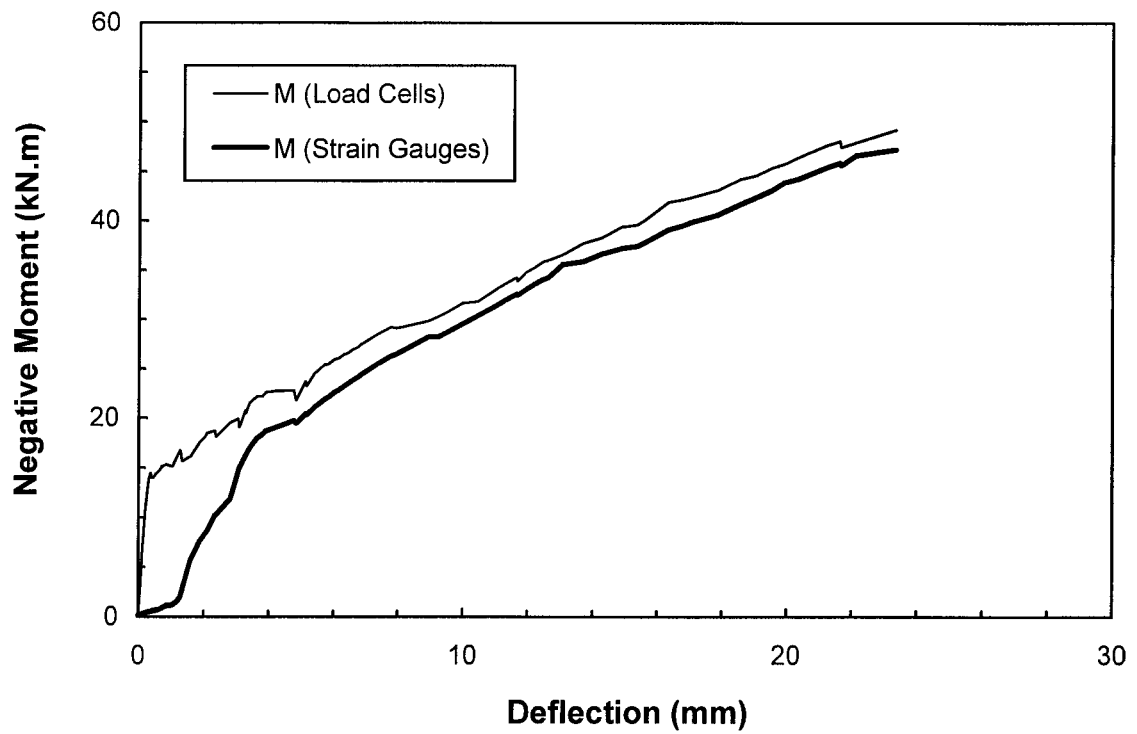


**Fig. 6.11 Moment Equilibrium Check : GFR-1**

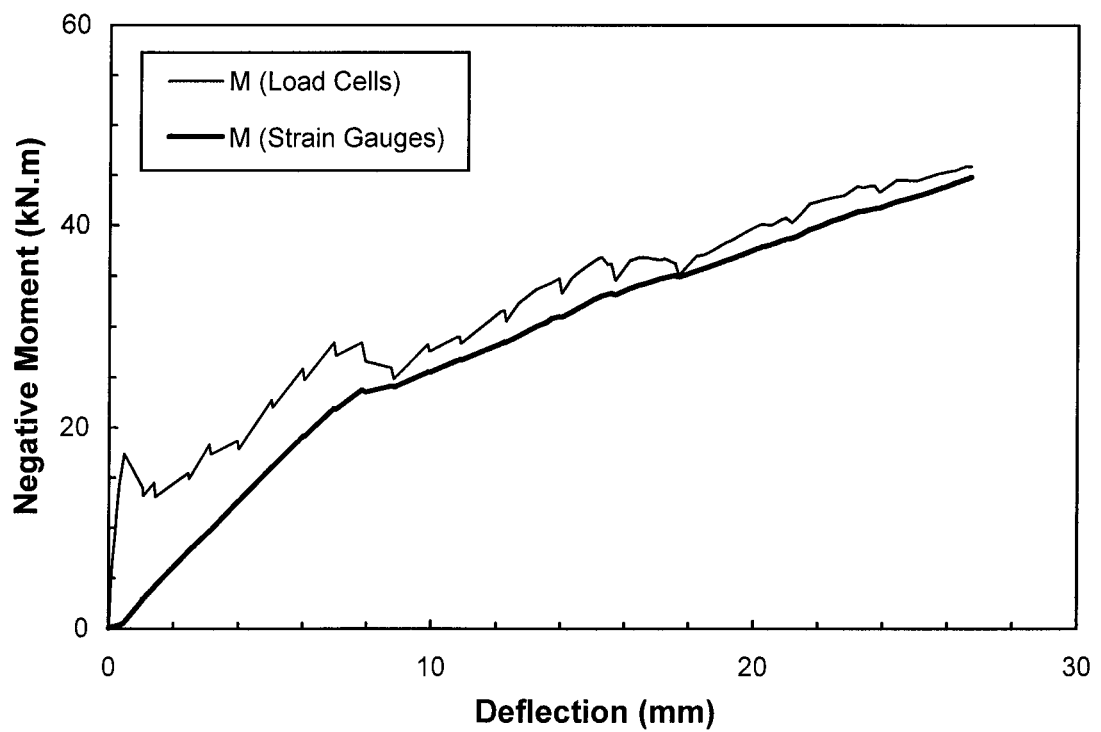


**Fig. 6.12 Moment Equilibrium Check : NEF-1**

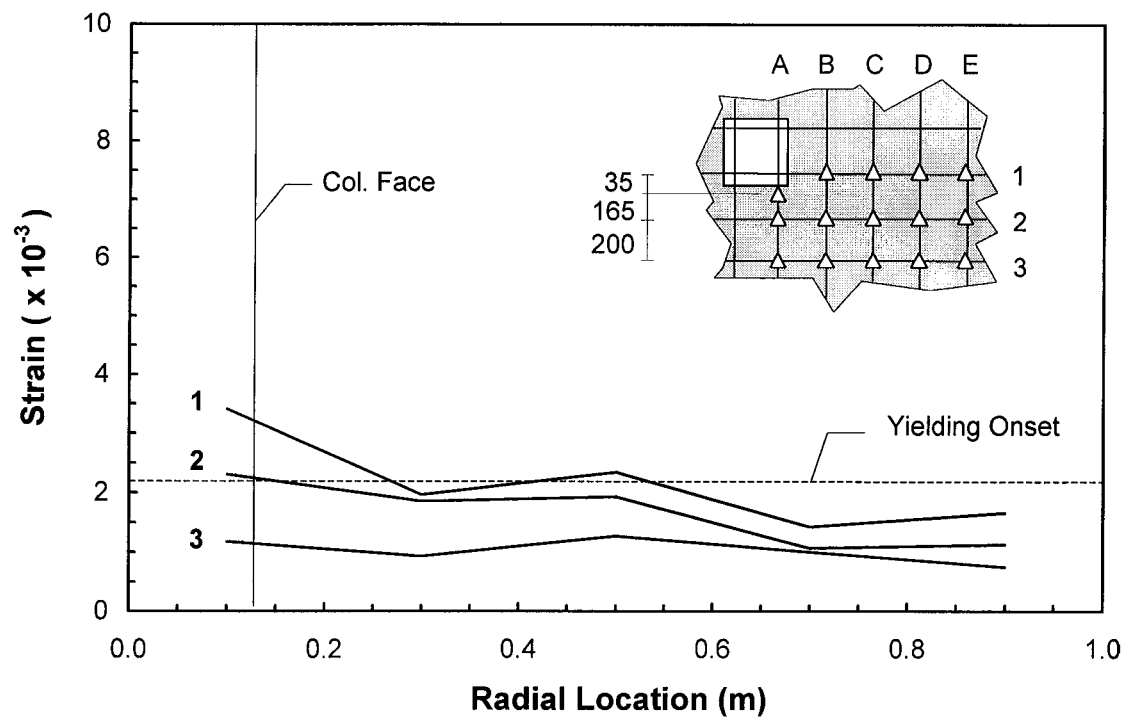


**Fig. 6.13 Ave. Circumferential Top Mat Strains : SR-1**

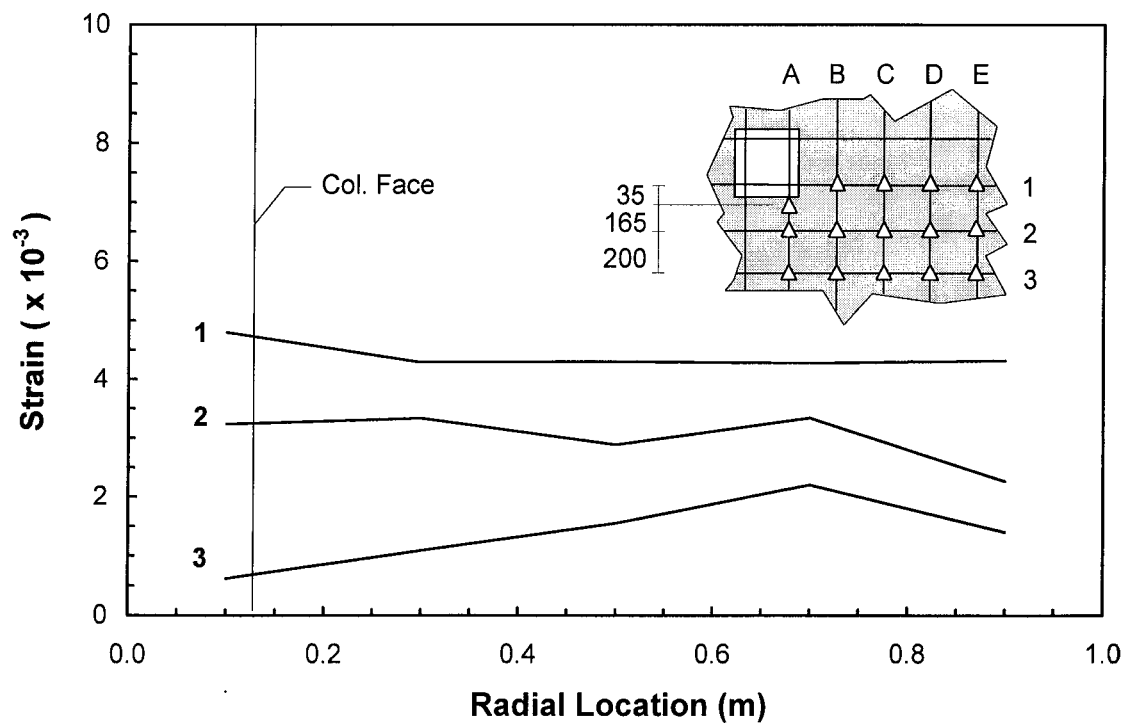


**Fig. 6.14 Ave. Circumferential Top Mat Strains : GFR-1**

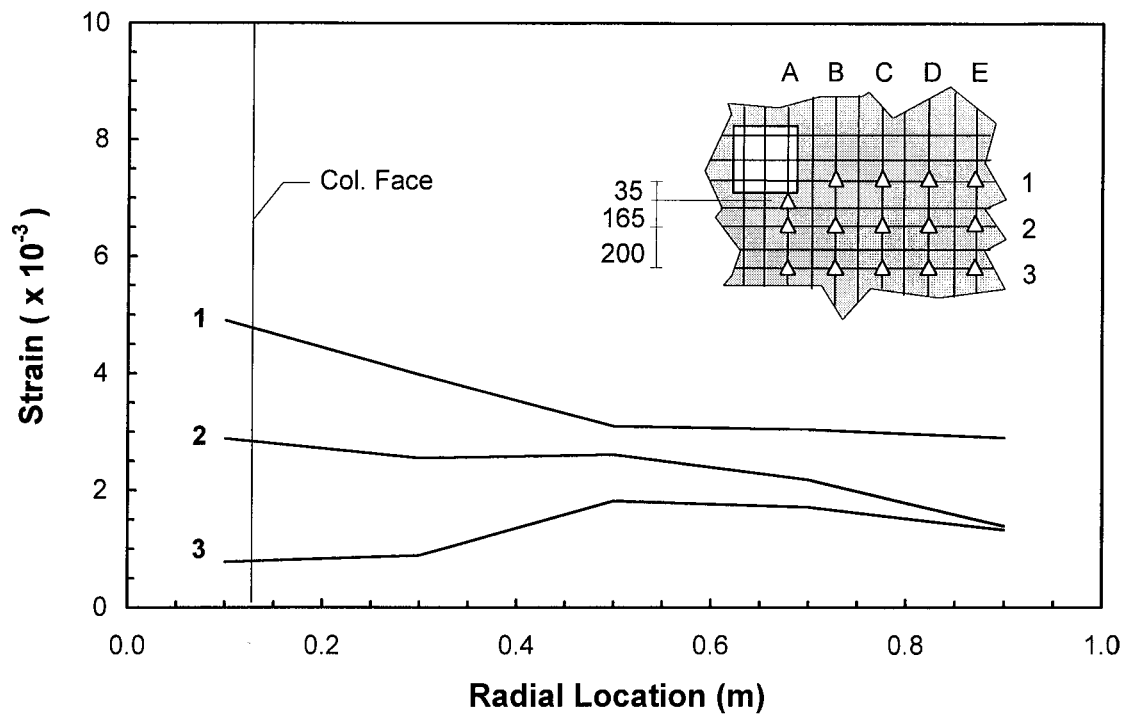


**Fig. 6.15 Ave. Circumferential Top Mat Strains : GFR-2**

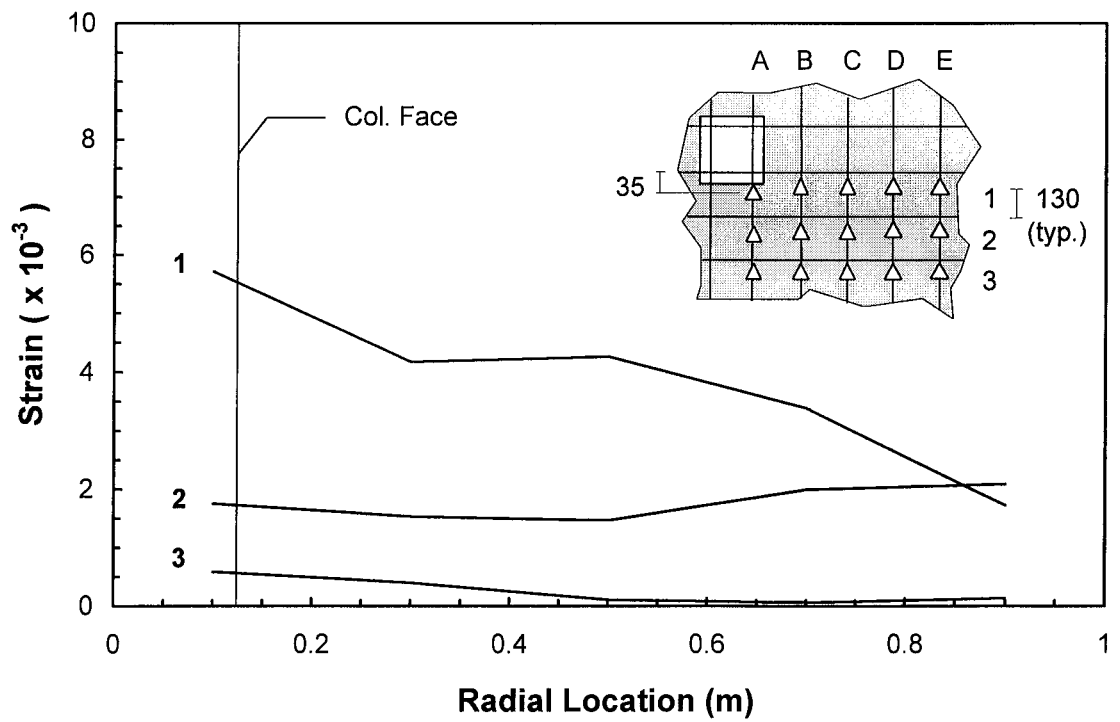


**Fig. 6.16 Ave. Circumferential Top Mat Strains : NEF-1**

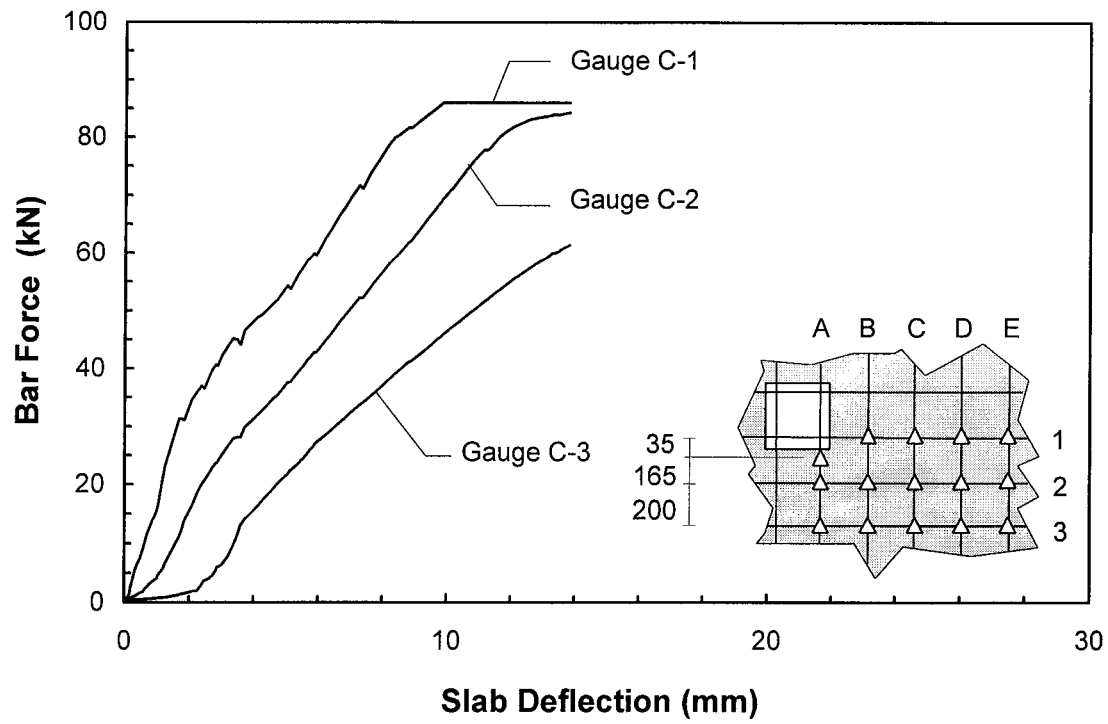


**Fig. 6.17 Force along Bar C : SR-1**

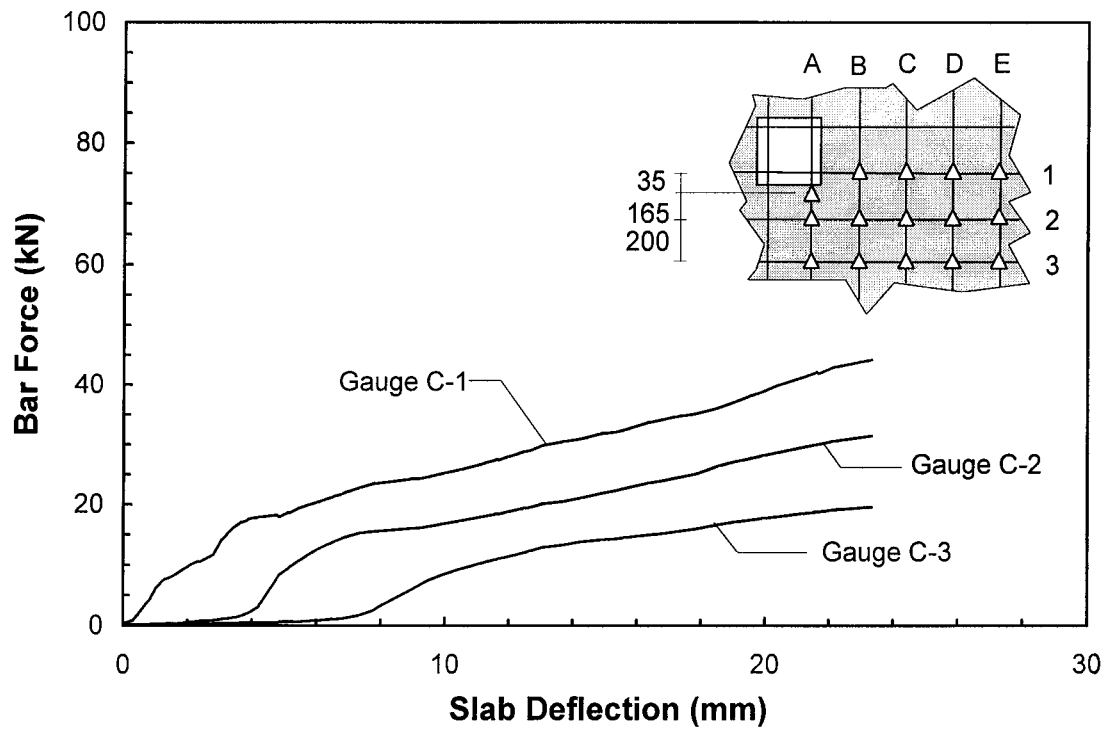


**Fig. 6.18 Force Along Bar C : Slab GFR-1**

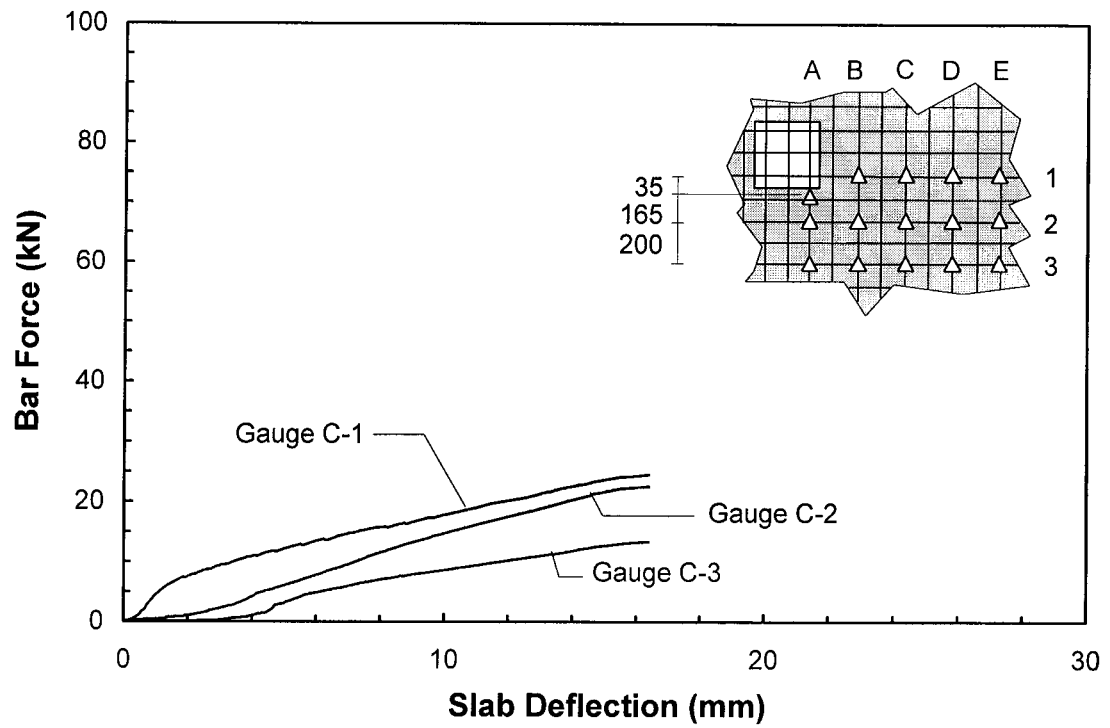


**Fig. 6.19 Force Along Bar C : GFR-2**

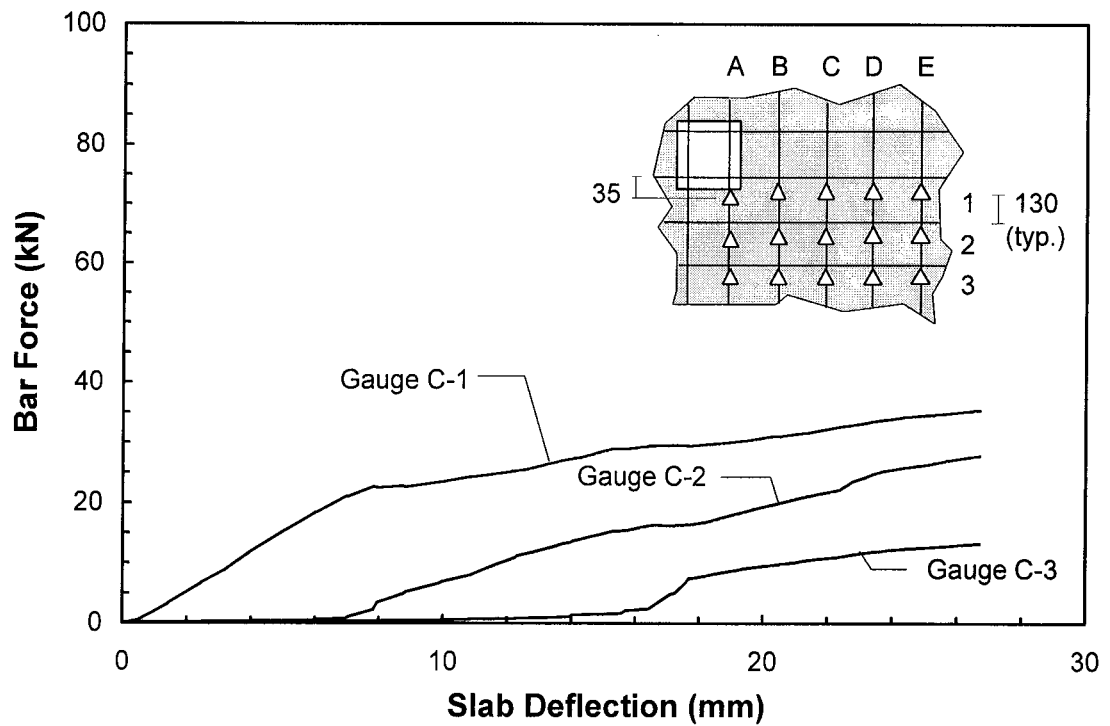


**Fig. 6.20 Force Along bar C : NEF-1**



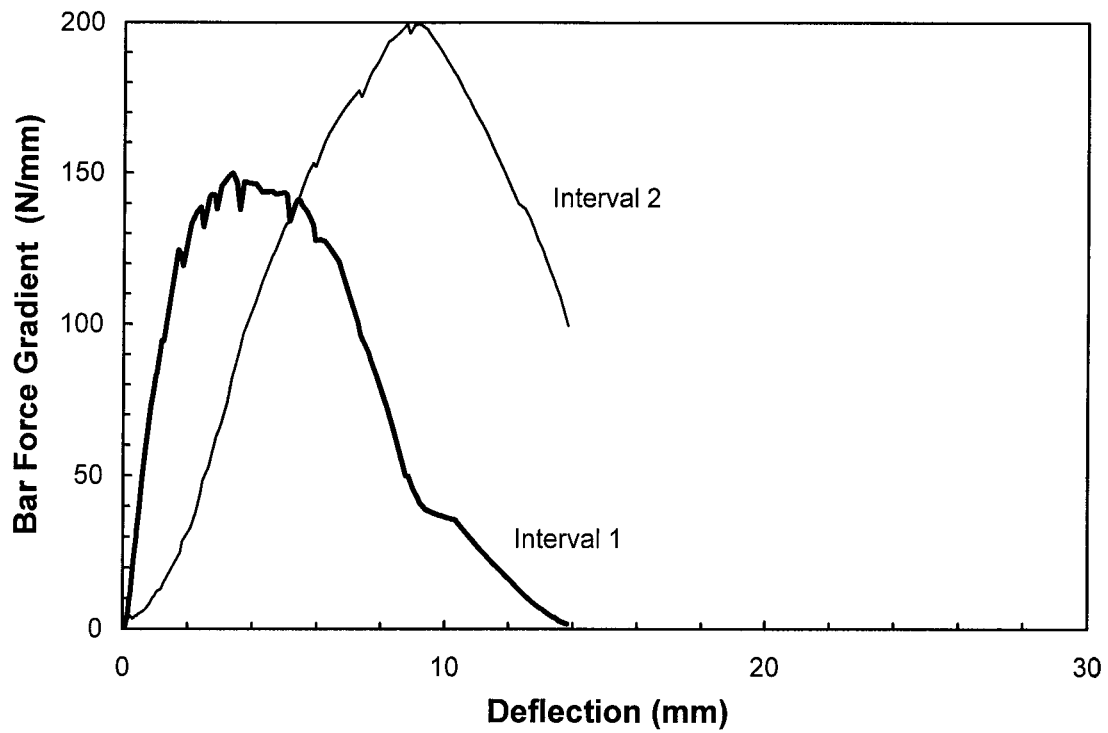


**Fig. 6.21 Bar Force Gradients - Bar A : SR-1**

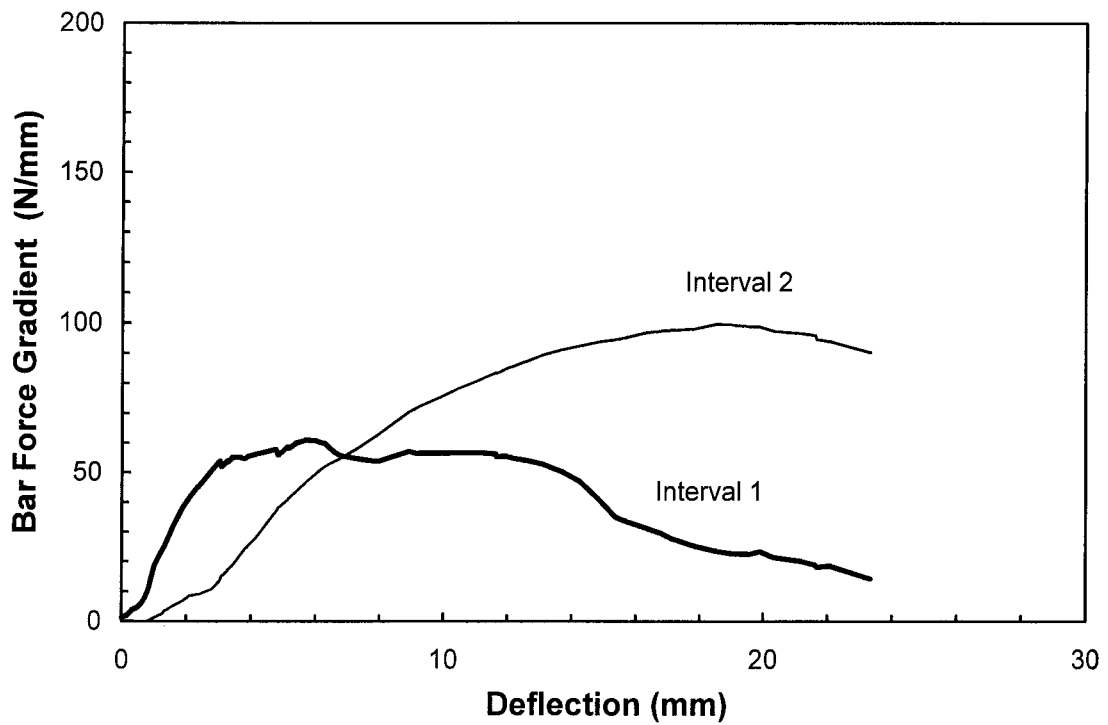


**Fig. 6.22 Bar Force Gradients - Bar A : GFR-1**

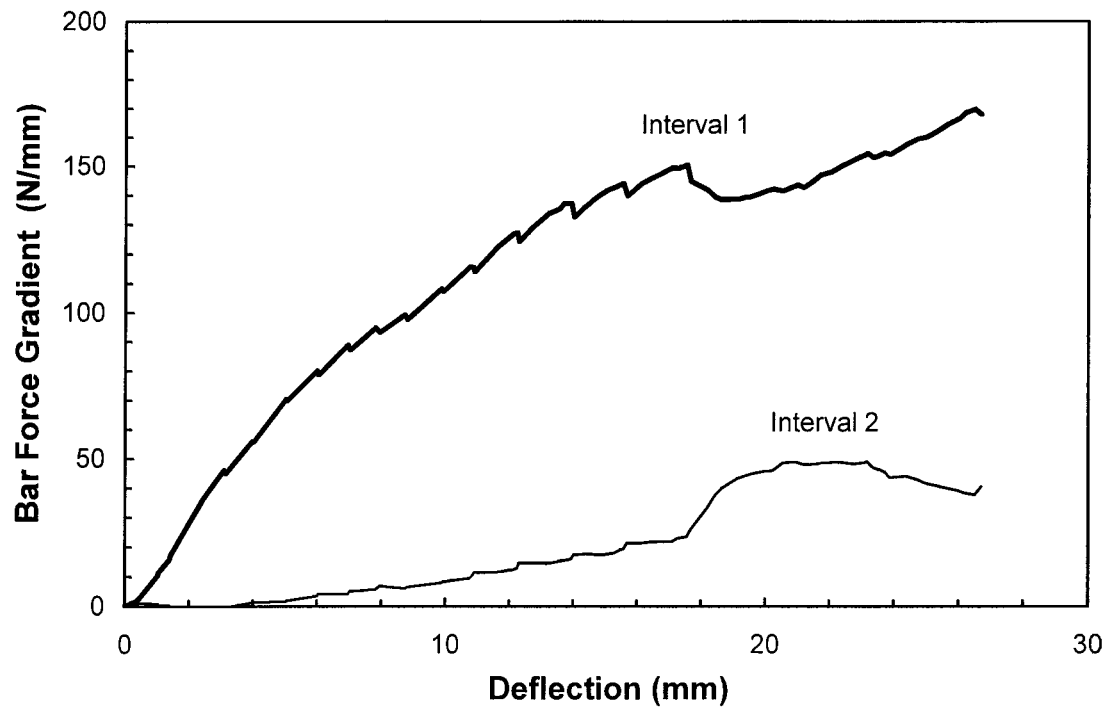


**Fig. 6.23 Bar Force Gradients - Bar A : NEF-1**

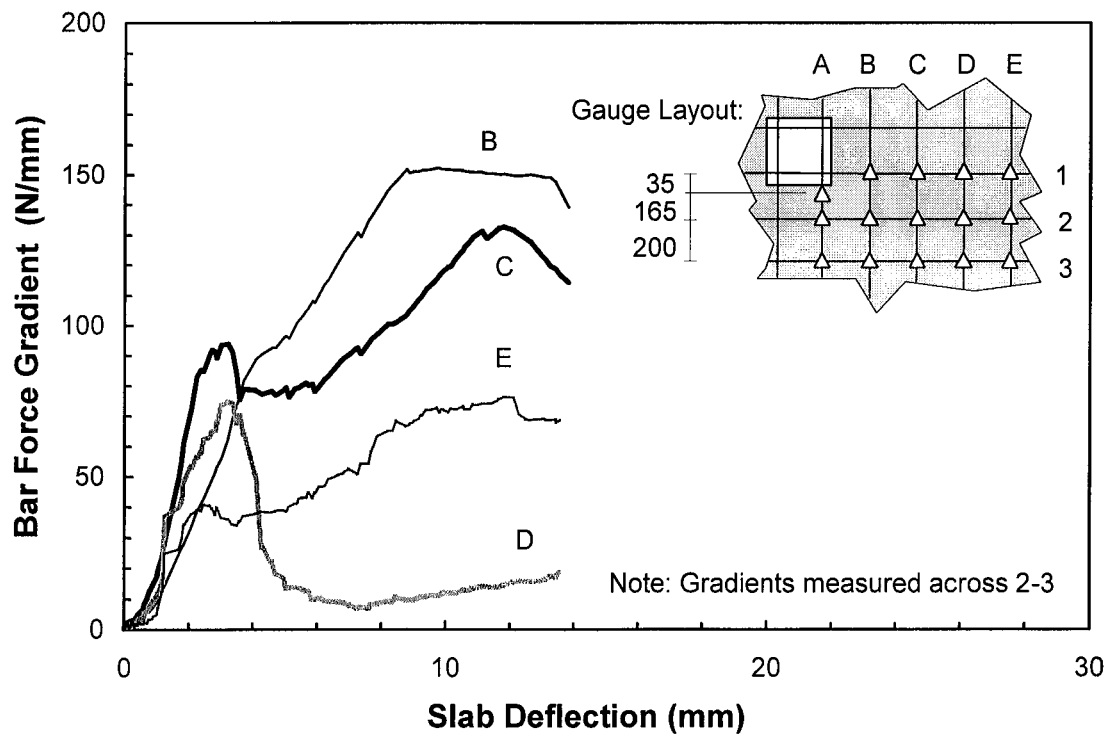


**Fig. 6.24 Bar Force Gradients - Perimeter Bars : SR-1**

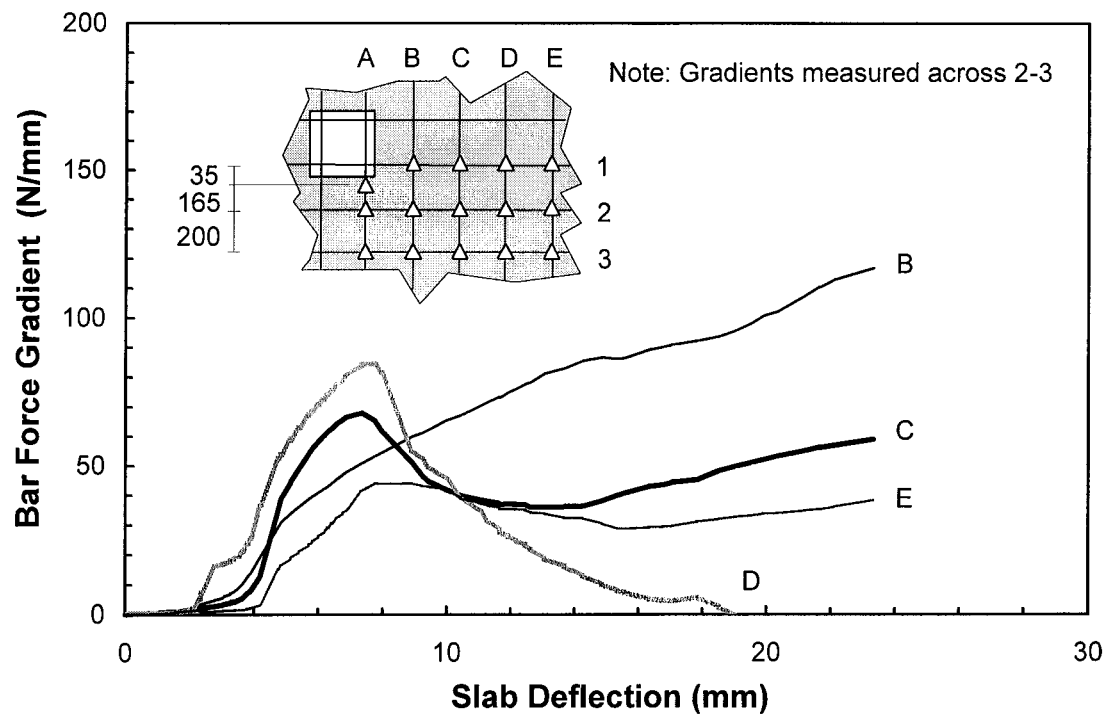


**Fig. 6.25 Bar Force Gradients - Perimeter Bars : GFR-1**

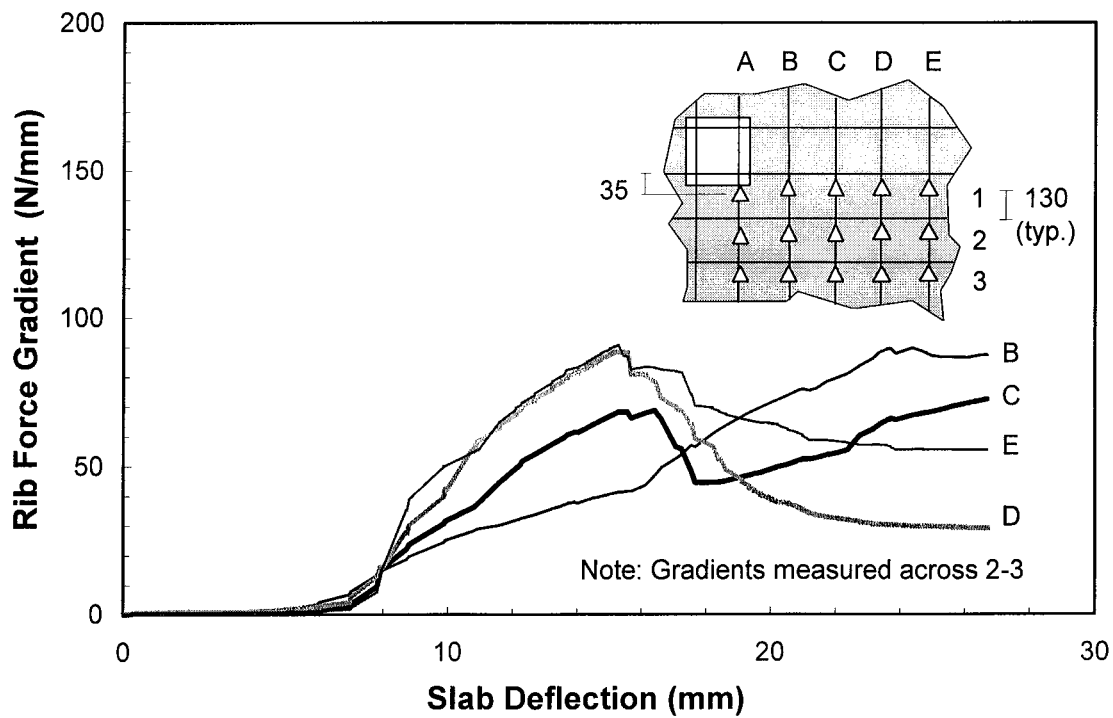


**Fig. 6.26 Rib Force Gradients - Perimeter Ribs : NEF-1**

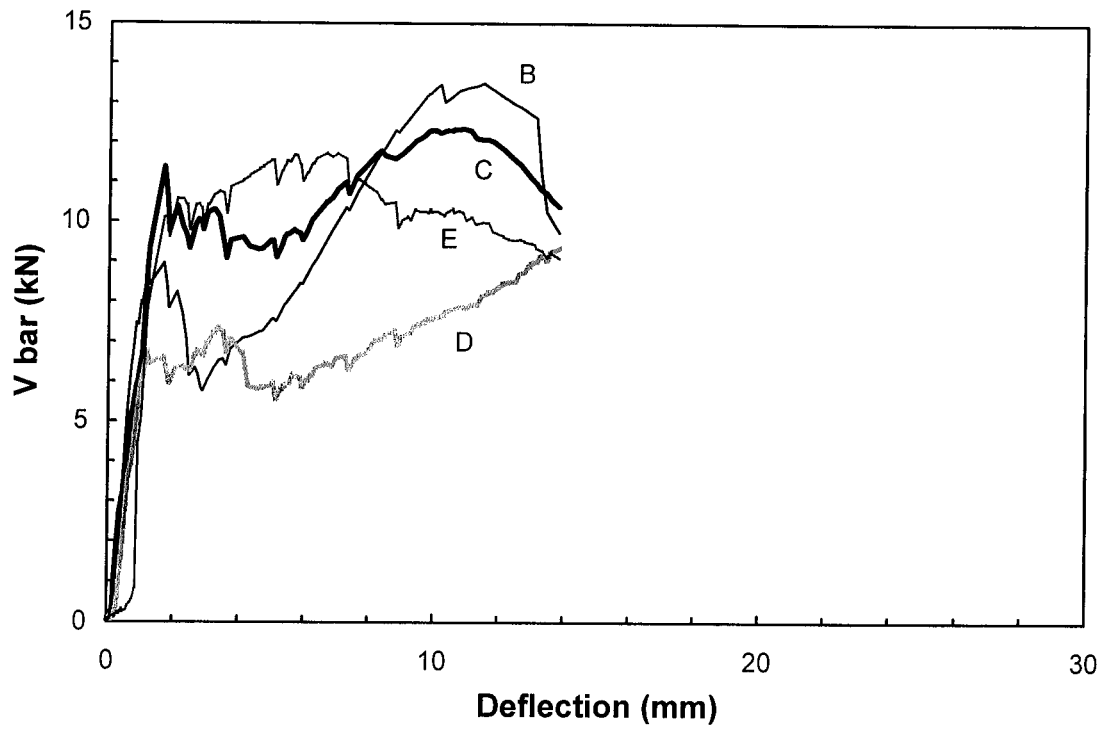


**Fig. 6.27 Measured Bar Shears : SR-1**

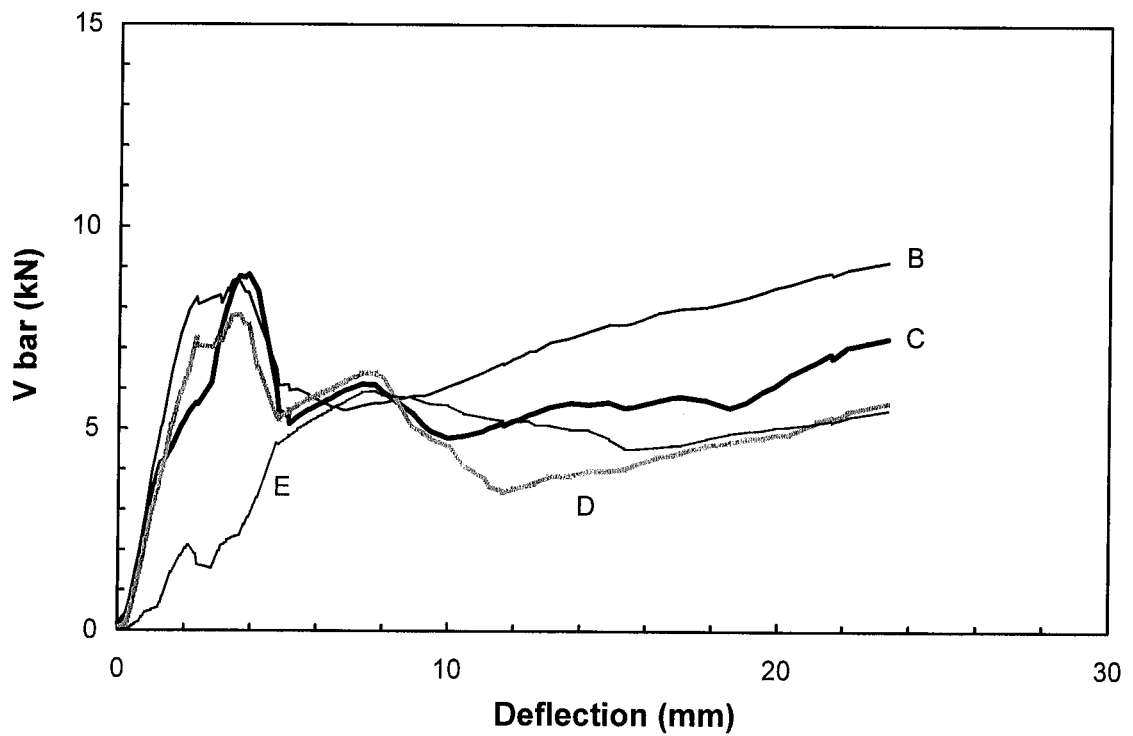


**Fig. 6.28 Measured Bar Shears : GFR-1**

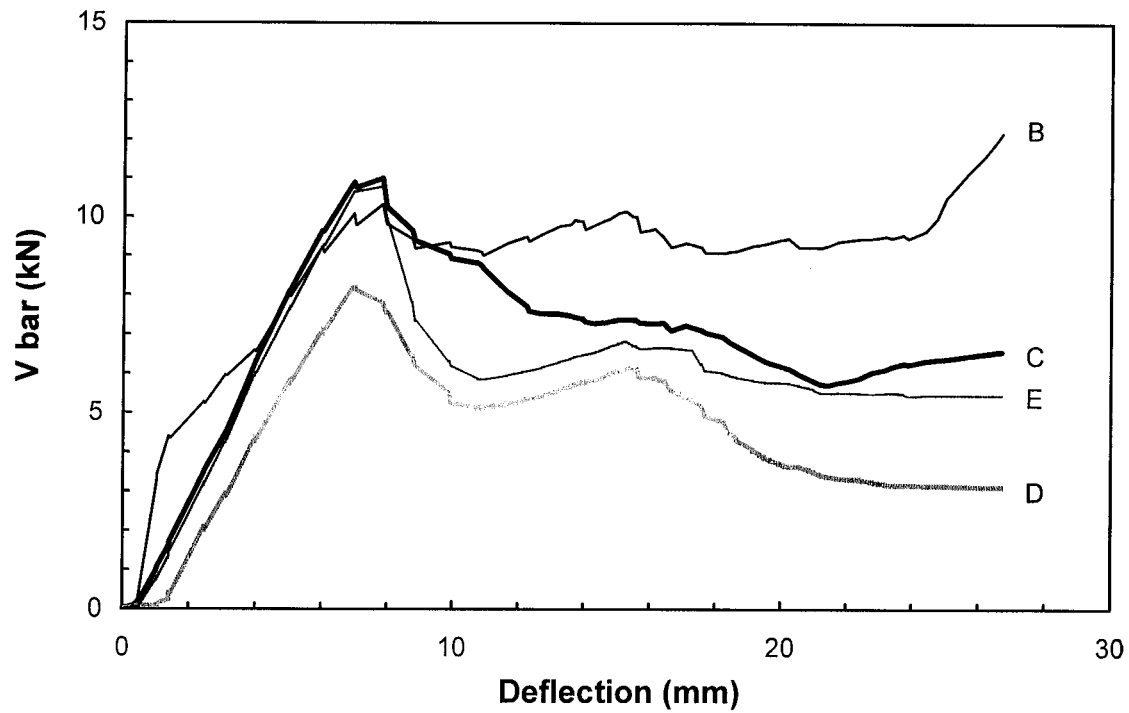


**Fig. 6.29 Measured Bar Shears : NEF-1**

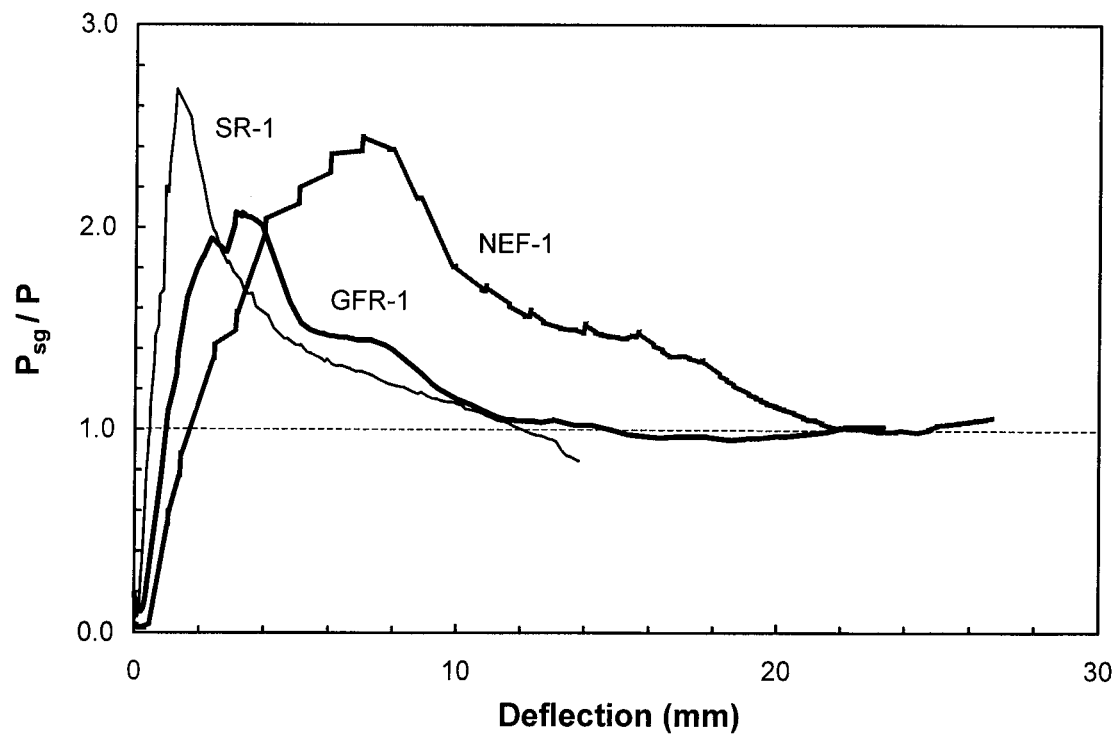
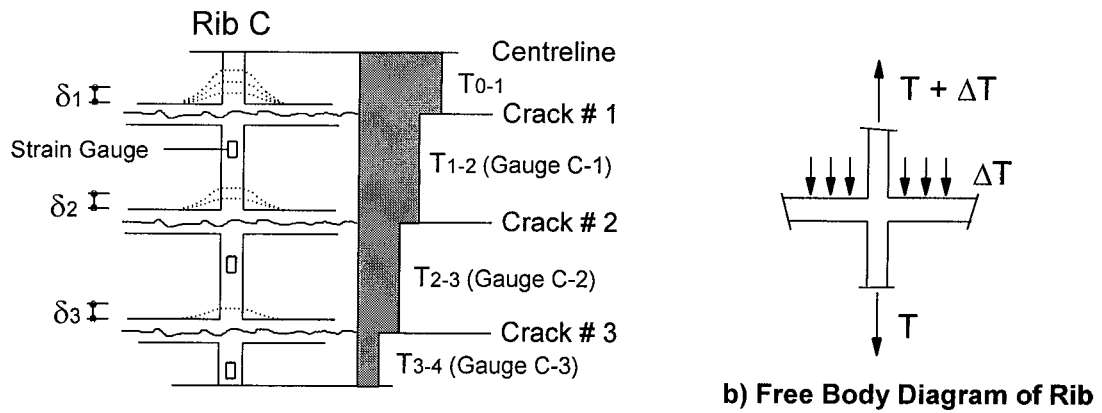


**Fig. 6.30 Shear Transfer Assessment : Series I Slabs**



a) Rib Deformation and Gauge Locations

b) Free Body Diagram of Rib

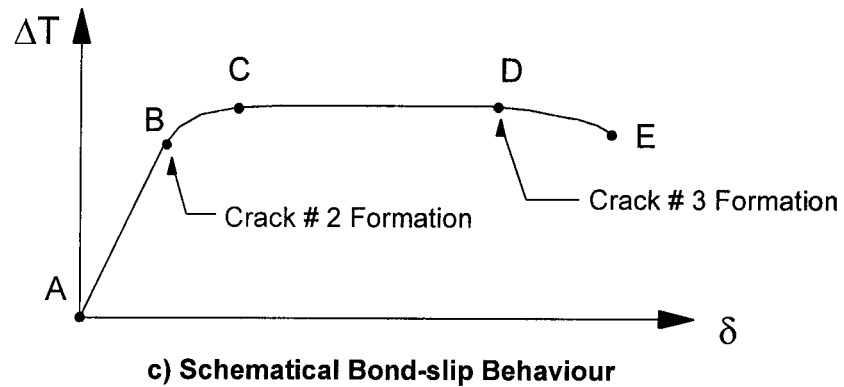


Fig. 6.31 Flexural Bond Behaviour of NEFMAC Grid

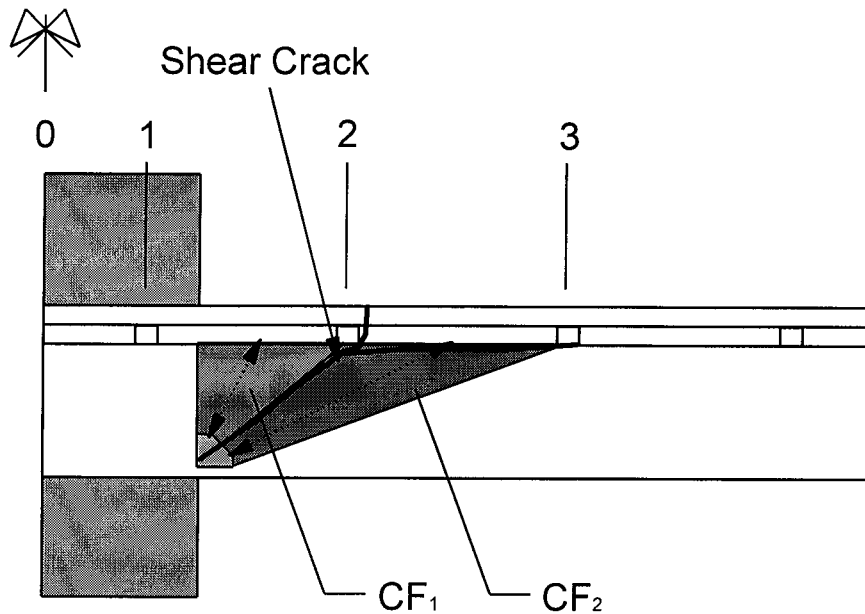
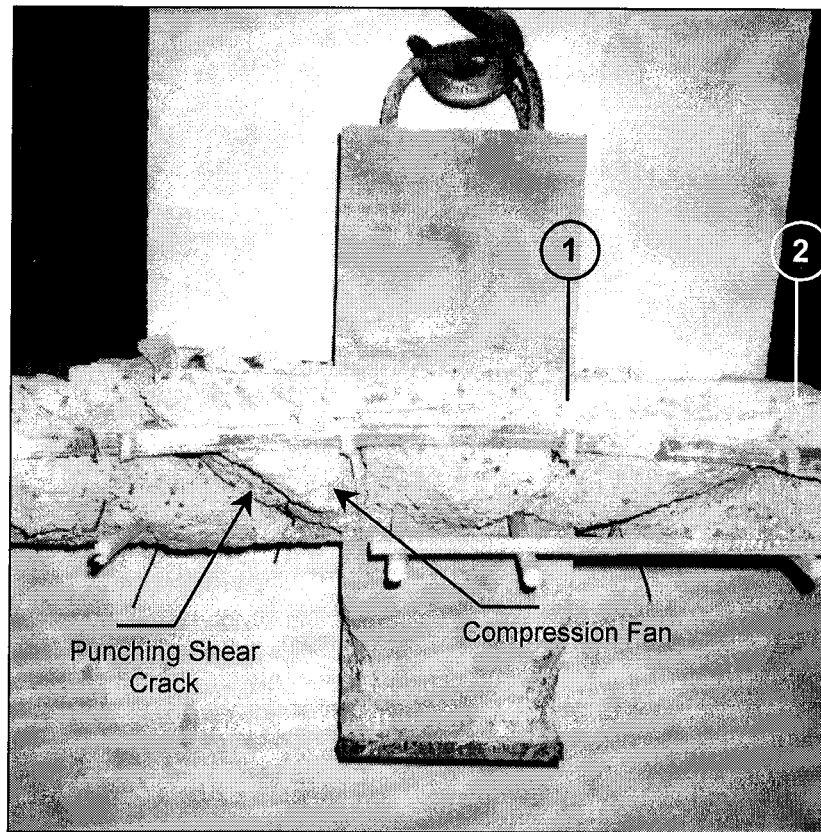


Fig. 6.32 Compression Fans and Shear Crack : Slab NEF-1



**Fig. 6.33 Elevation View of Dissected Slab NEF-1**

## **7 Series II Tests : Results, Observations and Evaluation**

### **7.1 Objectives**

This chapter reports and evaluates the experimental results from series II slab tests. The structural response of virgin, FRP-strengthened and concrete-patched slabs is described. The effects of the adopted slab strengthening and repair procedures are discussed and hypotheses for the role of the sheets and the mode of failure of the slabs are presented.

### **7.2 Overall Description of Structural Response**

Figures 7.1 to 7.5 show the load-deflection response from the seven tests conducted on the three slabs of series II. Load values correspond to the applied load on the slab divided by the slab area ( $17.64 \text{ m}^2$ ). The deflection values correspond to the average of the North and West mid-edge slab deflections (points 4 and 8 in Fig. 5.30). Neither the load nor the deflection values include the effect of dead loads.

The dead load on the slab was determined at preliminary testing stages with the column load cell after the slab was lifted off supports. The dead load on slabs ER1-VS, ER2-VS and ER3-VS was 5.05 kPa (89 kN jack load), 4.85 kPa (85.5 kN jack load) and 4.82 kPa (85 kN jack load), respectively. These values include the weight of the loading assembly. Dead load deflections were obtained by surveying the slab at 20 different locations. The deflections due to dead load were 1.5, 1.67 and 1.33 mm for ER1-VS, ER2-VS and ER3-VS, respectively. They were measured at 69, 69 and 51 days, respectively. The virgin slabs were loaded at 71, 69 and 51 days after casting.

#### **7.2.1 Response of Virgin Slabs**

Figure 7.1 shows the response of virgin slab ER1-VS. The thinner curves in Figs. 7.2 and 7.3 show the response of virgin slabs ER2 and ER3. All virgin slabs displayed the uncracked, elastic-cracked and yield phases commonly linked to prototype flat plates.

The uncracked stage is barely recognizable because first flexural cracks formed shortly after the full dead load was applied. Flexural cracking loads and corresponding



deflections are reported in Table 7.1. First flexural cracks formed on the top of the slab, following the orientation of the two through-joint bars in the N-S direction. These cracks progressed from the column towards outer slab regions followed by cracks forming in the orthogonal direction (W-E) completing a cruciform pattern.

Slab ER1-VS was unloaded at a 3.3 kPa applied load after discovering that one data-acquisition cartridge was accidentally disconnected. To further examine the proper functioning of both the loading array and the instrumentation, slab ER1-VS was reloaded and then unloaded at an imposed load of 5.1 kPa. Adding this load to the dead load on the slab (about 5 kPa) results in a total 10 kPa load which is the service load for the slabs. These first two cycles were not applied to slabs ER2-VS and ER3-VS.

As the load increased, the through-joint top cracks reached the slab edges at an applied slab load varying from 8 to 10 kPa. At this load level, the load-deflection curves of the three virgin slabs display a kink. All three slabs were unloaded at this stage.

Upon reloading, additional cracks formed on outer slab regions and along the diagonals. First bottom flexural cracks were observed in the N-S direction at about 370 to 400 mm away from the slab edges. First yielding of the slab reinforcement was observed around the column at an applied load of 15 to 17 kPa at a deflection of 15 to 16 mm, as shown in Table 7.1. First yielding of the bottom reinforcement in ER1-VS and ER3-VS occurred between 17 and 20 kPa. The formation of bottom slab cracks and the yielding of the bottom reinforcement constitute evidence that the ERS worked as planned.

After first yielding of the positive reinforcement, slabs ER2-VS and ER3-VS were unloaded in order to be strengthened with the CFRP sheets. Virgin slab ER1-VS was not unloaded because it was the control slab. The load on slabs ER2-VS and ER3-VS was not fully removed. To avoid seating problems, a 0.6 kPa load was left on. At this load level, the residual deflections in ER2-VS and ER3-VS were, respectively, 10 and 11.7 mm, as shown in Figs. 7.2 and 7.3.

Figure 7.6 shows typical top and bottom slab crack patterns at an applied load of 18 kPa, which corresponds to the load level at which ER2-VS and ER3-VS were unloaded. The pattern is very similar to that reported by Regan (1999) for prototype slabs. This confirms that the ERS fulfilled its purpose.

Slab ER1-VS was brought to failure without applying any further cycling. At about a 19 to 20 kPa load, additional top cracks formed along the diagonals close to the column and additional bottom cracks were observed at inner slab locations. Slab ER1-VS failed in typical punching fashion at an applied load of 25.6 kPa. The failure was violent and led to a significant load drop. At failure, the full positive reinforcement had not yielded. Figure 7.7 shows the top and bottom crack patterns for ER1-VS after punching failure.

### **7.2.2 Response of Slabs Strengthened with CFRP Sheets**

The load-deflection response of the CFRP sheet-strengthened slabs is shown with a thick line in Figs. 7.2 and 7.3. Reloading of the strengthened slabs (tests ER2-CS1 and ER3-CS2) started at a deflection slightly lower than that recorded at the end of the virgin slab tests because the 0.6 kPa load that was originally left on the slab dropped. As a result, the slabs seated on the supports. After strengthening the slabs, the slabs were brought back to the original 0.6 kPa applied load level but the seating effect led to smaller deflections than those previously measured.

Once the loading resumed, the strengthened slabs display a similar cracked stiffness compared to that of the virgin slabs. This was expected because, in terms of stiffness, the amount of CFRP sheets bonded on the slabs was relatively small.

To test the rehabilitation schemes, slabs ER2-CS1 and ER3-CS2 were cycled at least once before taking them to failure. They were unloaded when the applied load reached the previous peak load on the virgin slabs and then brought to failure. In the first cycle, the crack pattern was similar to that of ER1-VS at a similar load. The crack pattern remained unchanged until the 19 to 20 kPa load level, at which cracks nearby the column

in ER3-CS2 forked. Splitting cracks were also observed in the CFRP sheets' longitudinal direction in both slabs at a load of 21 kPa. These cracks are mostly resin cracks.

Both ER2-CS1 and ER3-CS2 failed in typical punching manner at applied loads of 24.2 and 22.2 kPa, respectively. Figures 7.8 and 7.9 show the crack patterns for these slabs after failure. Punching was not as violent as that of ER1-VS. No transverse fibre rupture or tearing was observed either. At failure, the CFRP sheets remained very well bonded to the slabs, as observed in Fig. 7.10 (ER3-CS2).

One interesting observation from these two tests is that, despite the virgin slabs being similar, the failures of the two sheet-strengthened slabs were markedly different. As shown in Fig. 7.8, the upper layout of the punching cone in ER2-CS1 almost coincided with the outermost edge of the sheets. In ER3-CS2, the shear cone top layout was virtually bounded by the sheets as well, except that the sheet outer edges were placed 425 mm farther away. As a result, the failure mechanism in ER3-CS2 rendered a punching shear crack much less steep than that in ER2-CS1. According to ACI 318-99 or CSA A23.3-94, these two slabs should have displayed similar shear failure surfaces and capacities.

Forensic slab inspection around the column revealed the existence of diagonal top slab cracks underneath the sheets for slab ER2-CS1 as shown in Fig. 7.8. These cracks formed at 45 degrees with respect to the orthogonal slab axes. These cracks were not present in ER1-VS nor in ER2-CS1. These cracks result from in-plane shear stresses due to the biaxial tension exerted on the column corners by the CFRP sheets. The sheets behave as “tension bands”, as conceptually illustrated in Fig. 7.11. The tension forces generated in the strips are equilibrated by compression struts that frame into the lower joint portion.

### **7.2.3 Response of Slabs Repaired with Concrete Patches**

The load-deflection response of the slabs repaired with concrete patches (ER1-CP1 and ER3-CP2) is shown in Figs. 7.4 and 7.5. Test ER1-CP1 was conducted after virgin slab ER1-VS punched. Test ER3-CP2 was conducted after the strengthened slab ER3-CS2

punched and the CFRP sheets were removed. For neatness, the response of these repaired slabs is shown independently of their predecessor tests.

Punching of predecessor slabs ER1-VS and ER3-CS2 led to a minor slab sinking relatively to the column as would occur in a real-life structure. At the end of these tests, the permanent depression of the slab top level relative to its original level after full slab unloading was about 30 to 35 mm nearby the column for both slabs. In Figs. 7.4 and 7.5, the point of zero deflection refers to this new slab level after the dead load was on.

Consistent with its higher strength, first flexural cracks on the HSC concrete patch in both slabs formed at applied loads slightly greater than those on the virgin slabs. In both tests, the slabs were cycled twice with peaks at loads of about 10, 15 kPa and then brought to failure. The response of ER1-CP1 was essentially linear up to punching failure whereas that in ER3-CP2 displayed a non-linear response beyond a 18 kPa load.

Slab ER1-CP1 punched suddenly at an applied slab load of 18.2 kPa at a deflection of 13 mm. Punching was violent and led to a significant load reduction. The punching crack formed right across the interface between the old concrete and the patch (see Fig. 7.12).

Slab ER3-CP2 punched at an applied load of 27.2 kPa and a corresponding deflection of 29 mm. Punching was violent and led to a significant load drop. The punching crack formed outside the boundary between the old and new concrete (see Fig. 7.13). The slab was subjected to further loading immediately after failure. The post-failure response (not shown) indicates no significant load increase for an additional 9 mm imposed deflection.

## **7.3 Measurements**

### **7.3.1 Force and Moment Resultants**

The main objectives of this section are: i) to perform a statical check to corroborate whether externally applied forces and moments on series II slabs compare well with internally measured forces and moments and ii) examine the behaviour of the ERS.

The relationships between forces and moments acting on the slab are based on the free body diagrams (FBDs) of Figs. 7.14 and 7.15. Figure 7.14 shows a plan view of the slab with acting bending moments and vertical forces. Upper case moments refer to total moments. Lower case moments refer to average moment intensities or average distributed moments. Figure 7.15 shows free body diagrams (FBD) for different slab elevations at arbitrary cross-sectional cuts. These FBDs apply for both the  $x$  and  $y$  directions. Both Figs. 7.14 and 7.15 are interrelated. Since each slab is 4.2 m wide, each force  $R$  in the FBD of Fig. 7.15a represents the sum of the four upper whiffle tree reactions lined up at 355 and 719 mm away from the column face, as shown in Fig. 7.14.

Figure 7.16 shows the ratio of applied load to measured reactions for slab ER1-VS. The applied load is that imposed by the lower column jack. The reactions is the sum of the four point reactions on the NE, SE, SW and NW slab quadrants measured with load cells. The effect of the dead loads is not included in either of them. The figure shows good agreement between the applied vertical force and the sum of all vertical reactions throughout the test. The same agreement was observed in all the other tests.

According to the FBDs of Figs. 7.15a and that on the right hand side of Fig. 7.15b, the total negative moment at the column face,  $M_{cf}^-$ , about the  $x$  or  $y$  direction is

$$M_{cf}^- = -M^+ + 1.429R + w_{DL} \frac{(1.9)^2}{2} \quad [7.1]$$

where  $M^+$  is the positive moment applied on the slab edge and  $w_{DL}$  is the uniformly distributed dead load per unit length on the slab segment. In this evaluation, the latter includes the weight of the loading assembly.

The positive moment applied on the slab edge,  $M^+$ , can be calculated based on either the tie rod force measurements or the readings from the strain gauges attached to the positive slab reinforcement along the slab periphery. The total positive moment in each direction is equal to the sum of the four moments applied by each of the four restraining frames

mounted in each direction. Each of these moments is calculated as the product of the load cell-measured tension tie force by the distance between the tension tie and the slab centroid. For the N-S and W-E directions, this distance is 1.344 and 1.044 m, respectively. Accordingly,

$$M_x^+ = \sum_{i=1}^4 M_{xi}^+ = 1.344 \sum_{i=1}^4 T_{NSi} \quad [7.2]$$

$$M_y^+ = \sum_{i=1}^4 M_{yi}^+ = 1.044 \sum_{i=1}^4 T_{WEi} \quad [7.3]$$

In Eqs. 7.2 and 7.3, the terms  $T_{NSi}$  and  $T_{WEi}$  refer, respectively, to the load-cell based tension tie force in the N-S and W-E directions.

Based on the strain gauges mounted on the bottom reinforcing bars on the slab periphery and setting both load and resistance factors equal to unity, the total positive moment at a given load level, according to ACI 318-99, can be approximately calculated as

$$M_{sg}^+ = A_s^+ f_s (jd)^+ = A_s^+ f_s \left( d^+ - \frac{A_s^+ f_y}{1.7 f_c' b} \right), \quad f_s \leq f_y \quad [7.4]$$

where  $A_s^+$  is the total reinforcement area across the slab width,  $f_s$  is the steel stress at the given load level, averaged out from the readings of at least two bottom bar strain gauges, and  $d^+$  is the flexural depth of the positive reinforcement along either the N-S or the W-E direction. The *measured* positive flexural depths after the slabs were cut open were 125 mm (N-S) and 113 mm (W-E). In the  $jd$  calculations, it was assumed that the steel yields. This leads to lever arm depth overestimates before fully cracked conditions apply. In Eq. 7.4, the contribution from the integrity steel bars (15M bars) was accounted for.

To calculate the total negative moment at the column face based on the readings from gridline 2 strain gauges, it is necessary to solve first for the shear force  $V_{cf}$  based on the left hand side free body diagram of Fig. 7.15b. From vertical force equilibrium,

$$V_{cf} = \frac{P}{2} - \frac{w_{DL} c_w}{2} \quad [7.5]$$

where  $c_w$  is the column width. Taking moments about a point at a distance  $e$  away from the column face, and substituting Eq. 7.5 into the resulting moment equilibrium equation leads to

$$M_{cf}^- = M_{sg,g2}^- - \frac{Pe}{2} + \frac{w_{DL}}{2}(c_w e + e^2) \quad [7.6]$$

where  $M_{sg,g2}^-$  is the strain-gauge based negative moment calculated from gridline 2 strain gauges,  $P$  is the applied jacking load measured by the column load cell and  $e$  is the distance between the gauges and the column face. The moment  $M_{sg,g2}^-$  can be approximately calculated as

$$M_{sg,g2}^- = A_s^- f_s (jd)^- = A_s^- f_s \left( d^- - \frac{A_s^- f_y}{1.7 f_c' b} \right), \quad f_s \leq f_y \quad [7.7]$$

*Measured* average values for  $d^-$  after dissecting the slabs were 117 mm (N-S) and 101 mm (W-E). These values are slightly less than those used in the virgin slab design because the top mat level lowered during construction.

Figure 7.17 shows the ratio of strain gauge-based versus ERS load cell-based negative moment intensities at the column face in both the N-S and W-E directions for ER1-VS. Moment intensities were calculated by dividing the total negative moments from Eqs. 7.1 and 7.6 by the full slab width. In Eq. 7.1, the positive moment was calculated according to Eqs. 7.2 and 7.3. In Eq. 7.6, the values of  $M_{sg,g2}^-$  were calculated by averaging the readings of two strain gauges.

Figure 7.17 shows that the strain gauge-based calculations significantly underestimate the negative moment at early test stages. This is expected because the strain gauges in regions where concrete remains uncracked do not show significant tension. When cracks further spread out, reasonable agreement between the values is observed. The agreement is slightly better in the N-S direction. The spikes in the curves at a 5.5 and 10 mm deflection indicate the unloading and reloading of ER1-VS.

The comparison between average positive moment intensities based on the ERS load cells and the strain gauges is shown in Fig. 7.18. The figure shows poor agreement between the ERS-based and the strain gauge-based positive moment intensities at early test stages and good agreement for fully cracked slab conditions. The significant difference between moment values at early test stages confirms how sensitive the gauge-based calculations are to the extent of concrete cracking.

Figures 7.19 and 7.20 show, respectively, the variation of the negative to panel and the positive to panel moment ratios versus slab deflection for slab ER1-VS in the N-S and W-E directions. In Fig. 7.19, the negative moments were calculated based on Eq. 7.1 (using load cell measurements). In Fig. 7.20, the positive moments were calculated according to Eqs. 7.2 and 7.3. The N-S and W-E labels refer to the orientation of the load cells used to evaluate the positive moments. The panel moment was calculated assuming a prototype clear span of 4.2 m. This clear span value is “artificial” in the sense that it is only used to evaluate whether the relative ratios between negative and positive moments with respect to the panel moment are close to code-stipulated values. Its exact value cannot be obtained unless the prototype span is accurately estimated.

The spikes in the curves indicate the intermediate unloading and reloading stages. The initial positive to panel moment ratio of 0.35 was calculated based on an imposed average positive moment of 3.6 kN.m/m at the beginning of the test.

According to Fig. 7.19, the negative to panel moment ratio in ER1-VS drops from an initial value of about 0.7 down to about 0.55 measured between the beginning of the test and a 9 mm deflection. The continuous moment ratio drop results from the moment redistribution associated with the growth of slab cracking. The reduction in the negative moment is consistent with an increase from 0.35 to 0.42 in the positive to panel moment ratio shown in Fig. 7.20 for a similar deflection range.



At a deflection of 10 mm, slab ER1-VS can be considered to be fully cracked. Beyond this point, the ratio of negative moment to panel moment increases slightly and stabilizes at about a 0.6 to 0.62 value up to punching failure. For the same deflection range, Fig. 7.20 shows a reduction in the positive to panel moment ratio down to about 0.33.

Both the 0.6 and 0.33 ratios are relatively consistent with the 0.65-0.35 rule recommended by direct design method procedures for negative and positive moment evaluation in interior panels. The two ratios do not add up to 1 because the edge slab rotation was not zero for reasons already explained. This result shows that the boundary conditions imposed by the edge restraint system reasonably simulate those in a prototype slab.

### **7.3.2 Slab Rotations**

#### **7.3.2.1 Edge Slab Rotations**

Measurement of edge slab rotations allows determination of the rotational restraint imposed by the edge restraint system. Figure 7.21 shows average slab rotations for ER1-VS along the N-S and W-E directions. Each curve is the average of the rotations measured by each restraining frame. Consistent with their higher degree of prestressing, the rotations at the two interior frames (not shown) are greater than those measured in the extremes. This accounts for the fact that most of the bending deformation concentrates around the column.

Figure 7.21 shows that the rotation increased linearly with deflection up to a 6 mm deflection. This deflection level corresponds to the point at which top slab cracks reached the slab edges. Beyond this level, the rotations become almost independent of the slab deflection. In general, the average W-E rotations are slightly lower than those in the N-S direction.

Figure 7.22 shows the variation of the positive moments calculated from the restraining tie rods as a function of the average edge rotation for slab ER1-VS. The initial moment value indicates the initial positive moment imposed by the edge restraint system at the

beginning of the test. The rotation values do not show the effect of the dead loads. Figure 7.22 shows that the rotational stiffness in both directions remained virtually constant through the test up to late test stages.

#### **7.3.2.2 Inner Slab Rotations**

Measurement of slab underside rotations at inner slab locations in the radial direction provide useful information on the slab deformation regime. Figure 7.23 shows inner slab rotation values as a function of the slab deflection for tests ER2-VS and ER2-CS1. The radial slab rotations were calculated by dividing the relative vertical slab soffit deflection readings between cable transducers by the horizontal distance between them. The cable transducers are located as shown in Fig. 5.30.

The rotation-deflection curves are essentially linear and have the same slope for both virgin and strengthened slab tests. The second segment slightly offsets that of the virgin slabs probably because of a slight change in the initial edge restraint prestressing force in the rehabilitated slab. The abrupt change in the rotation-deflection curves at late test stages signals punching failure.

The linearity between rotations and deflections at the slab underside implies that a rotationally restrained two-way slab displays a rigid body rotation in the radial direction near the column. This observation is consistent with previously available experimental observations reported by Kinnunen and Nylander (1960) for isolated edge-free slabs. The observation is also consistent with the experimental evidence gathered from series I test results. The existence of a rigid body rotation in the radial direction implies that most of the slab deformation occurs along the circumferential direction.

### **7.3.3 Crack Widths**

#### **7.3.3.1 Slab Surface Crack Widths**

Figure 7.24 shows crack widths within the connection region at stations F, F' and F'' (W-E crack) and G, G', G'' (N-S crack) for virgin slab ER2-VS. These crack widths are

representative of those measured at similar locations in the other two virgin slabs. According to Fig. 7.24, the relationship between the applied load and the crack widths is essentially linear. The cracks also tend to narrow the farther they are from the column face. The cracks in the W-E direction (at F, F' and F'') are slightly wider than those in the N-S direction at comparable load levels.

Figure 7.24 also shows the residual crack widths at the end of virgin slab test ER2-VS after the live load was removed. At the column face, the top crack widths span from 0.36 to 0.44 mm in the N-S and W-E directions, respectively. These values are close to the maximum 0.4 mm stipulated by CSA A23.3-94 for interior exposure conditions. It is worth noting that before unloading, the slabs were subjected to a load level of about four times that experienced at service load conditions.

Figure 7.25 shows typical crack width measurements on one of the outermost bottom cracks running N-S in slab ER3-VS in the middle strip region. The relationship between the applied load and the bottom crack width is also linear. The figure shows that bottom cracks could be as wide as those at the top.

Figure 7.26 shows top crack width measurements taken at stations F'' and G'' before and after rehabilitating slab ER2. Taking into account that these stations are the closest ones to the edge of the CFRP sheets, the corresponding crack widths allow examination of the efficacy of the strengthening schemes in terms of crack width control. Solid and empty symbols refer, respectively, to crack widths on the strengthened and virgin slab. Crack width measurements during unloading stages are not shown for neatness.

The four sets of crack widths define straight lines that intersect at about a 14 kPa load. For greater loads, the cracks in the strengthened slab are slightly narrower than those in the virgin slab. This suggests that the adopted sheet strengthening layout provides some benefits as far as crack control is concerned. However, it is worth noting that an imposed slab load of 15 kPa or greater represents an amount of load that a slab would rarely

experience at service load conditions. Under load levels of this magnitude, the slab is approaching its ultimate limit state.

Figure 7.27 shows bottom crack widths at stations H, I and J for the rehabilitated slab ER2-CS1. These crack widths are comparable with those shown in Fig. 7.25 before slab ER3 was strengthened. No significant benefit from the adopted rehabilitation scheme in ER2-CS1 as far as bottom crack width reduction is concerned. This is sensible because the sheets in ER2-CS1 were not installed on the slab underside.

#### **7.3.3.2 Through-thickness Crack Measurements**

Figure 7.28 shows the slab thickening based on the through-thickness strain readings from gauges installed in the N and W radial strips at 50 mm (gauge # 4), 150 mm (gauge # 5) and 250 mm (gauge # 6) from the column face in ER3-VS. The deformations have been calculated over a gauge length equal to the slab thickness.

Figure 7.28 shows very low deformations. Gauge # 4 readings (at 50 mm from the column face) are greater than those at the outer locations, suggesting that an internal crack formed through the line of measure of the innermost gauge, probably at a 6 kPa load and then continued to grow. The higher deformations at inner gauge stations suggest that the internal crack runs from the column to outer slab regions. However, this is inconclusive because several cracks could have formed across the slab depth. The curves also show that slab unloading closes the cracks. Slab thickening readings from gauges installed in the W-E direction show lower values.

#### **7.3.4 Strains in Internal Slab Reinforcing Bars**

Strain readings from top reinforcing bar gauges allow plotting of bar force profiles. These diagrams are useful to monitor the extent of yielding in the slab reinforcement, measure average bond stresses and most importantly, evaluate the variation of bar force between two points which is defined as a bar force gradient.

Figure 7.29 shows gauge key plans for the three slabs against which the strain readings will be referenced. Figures 7.29b and 7.29c show the location of the CFRP bands in tests ER2-CS1 and ER3-CS2 relative to the gauge grid. The gauges mounted on the CFRP sheets are not shown.

#### **7.3.4.1 Circumferential Bar Force Profiles**

Figure 7.30 shows the circumferential bar force profile (CBFP) along the radial direction in slab ER3-VS along gridline 1. Bar forces correspond to the last loading cycle at imposed load levels of 5, 10 and 15 kPa. The force required to yield a bar is also shown. Consistent with Kinnunen and Nylander (1960), the force profiles show that circumferential strains are inversely proportional to their radial position at regions inside the slab inflexion point. The circumferential bar force decay with radial location in slabs ER1-VS and ER2-VS along gridline 1 was not as pronounced as in ER3-VS. Bar force profiles were more uniform and almost all top bars yielded.

Figure 7.31 shows the load cycling effect on the circumferential bar force profiles for gridline 1 gauges in ER1-VS at a 5 kPa applied slab load during the second, third and fourth cycles. The figure shows a bar force increase as the number of load cycles increases. The difference is not significant between the second and third loading cycle, but is considerable between the third and fourth. This suggests that the bar force profiles of Fig. 7.30 may display lower values when referenced to earlier load cycles.

#### **7.3.4.2 Force Variation Along Perimeter Bars**

Figure 7.32 shows the typical force variation in a perimeter bar in slab ER1-VS. The bar forces were calculated from gauges located at D-1, D-2 and D-3. The development of bar forces is consistent with that examined for series I slabs.

Figures 7.33 to 7.36 show the bar force variation along perimeter bars B and D in the two tests conducted on slabs ER1-VS and ER2-CS1, and tests ER3-VS and ER3-CS2. Bar forces are shown at 100, 300 and 500 mm away from the column centreline. Bars B and

D were selected because these bars were located immediately below the sheets in tests ER2-CS1 and ER3-CS2, respectively. Strain readings at these locations provide information on the effect that the strengthening schemes had on the behaviour of these bars. Bar B is located in a disturbed region whereas bar D is located in a region where slender beam action is assumed to dominate. The solid lines in Figs. 7.33 to 7.36 represent force profiles measured in the last load cycle at applied load levels of 5, 10 and 15 kPa and at ultimate. The dotted lines represent force profiles at comparable load levels but at an earlier cycle (4th cycle in ER1-VS and 2nd cycle in both ER2-VS and ER3-VS).

Figures 7.33 to 7.36 show that the loading history has a significant effect on the top reinforcing bar forces. Bar forces increase as the amount of cycling increases. The force increase is significant, as can be observed by comparing the force variation from the 2<sup>nd</sup> to 5<sup>th</sup> cycle at a 10 kPa load. The force gain rate reduces as the load increases.

In a bar force profile, a sloping line indicates that shear is mostly transferred by beam action. Conversely, a flat line indicates that shear is transferred by arching action. According to the strip model, the shear transferred from the slab quadrants to the radial strip is delivered at the face of the radial strip. Since the first gauge is located 100 mm past the radial strip face, and since bar forces were not measured at the radial strip face, it is more appropriate to evaluate the shear transfer across the second interval.

The bar force profiles for bar B in the control slab (Fig. 7.33) and on ER2-CS1 (Fig. 7.34) show a slight contribution from beam action across the second interval at ultimate. Conversely, bar B transfers shear by arching action across the first interval. This is consistent with the fact that this bar is located in a highly disturbed region. This suggests that readings from gridline 1 may still be useful to assess the source of shear transfer.

Figures 7.35 and 7.36 show the bar force profiles for bar D in virgin slab ER1-VS and ER3-CS2, respectively. Figure 7.35 shows sloping force profiles across both intervals which is consistent with beam action-type shear transfer. In contrast, the bar force profiles in ER3-CS2 are flat across both intervals at ultimate.

### 7.3.5 Strains in CFRP Bands

Figures 7.37 and 7.38 show longitudinal strain profiles along the CFRP bands at imposed loads of 10 kPa, 15 kPa and at ultimate in tests ER2-CS1 and ER3-CS2. In Fig. 7.37, the strains are the average of the strain readings in the W-E bands. In Fig. 7.38, the profiles correspond to one of the W-E bands.

The profiles are essentially linear except in ER3-CS2 nearby the column where the strain drops slightly. The strain profiles in ER2-CS1 are steeper than those in ER3-CS2 because of the higher slab curvatures around the column. The sheet strains in both slabs became negligible at about 1000 mm away from the column, which confirms that the slab inflexion point lies close to this position. This suggests that no special sheet end anchoring is necessary in this type of application because the sheets can be laid on the slab for as long as it is required. In their investigation of bond of CFRP sheets to concrete, Miller and Nanni (1999) measured strain gradients in the order of  $88 \mu\epsilon/\text{mm}$  required to cause peeling of sheets used as positive reinforcement in simply supported concrete beams. According to Figs. 7.37 and 7.38, the peak CFRP strain gradients are about 4 to 5  $\mu\epsilon/\text{mm}$ , which are much less than those required to cause sheet peeling.

The relatively low ultimate CFRP strain values indicate that rupture of the sheets is not a concern in this particular type of application. The strains at ultimate at 100 mm past the column face were 3500  $\mu\epsilon$  in ER2-C1 and 2700  $\mu\epsilon$  in ER3-CS2. These values are about 12 to 17 % of those at sheet rupture. The latter is close to the 20 % value reported by Tan (2000) from tests on small slab panels strengthened with CFRP and GFRP, but far from the 40 % ratio reported by Chen and Li (2000) for punching shear tests on small slab panels strengthened with GFRP.

### 7.3.6 Force Gradients in Internal Slab Reinforcement

Figures 7.39 to 7.41 show the force gradient variation across the second interval versus slab deflection in bars B, D, and F for slabs ER1-VS, the two tests on slab ER2 and the

first two tests on slab ER3, respectively. The end of the curves signals punching failure. The gradient for bar H was not included because the lower gauges in this bar were located at uncracked concrete regions resulting in unrealistically high bar force gradients.

According to Fig. 7.39, the force gradients in ER1-VS increase steadily up to a peak value and then remain relatively constant (D and F) or drop (B). The peak force gradient in bars B, D and F are, respectively, 160, 90 and 150 N/mm. The first value is consistent with the peak gradients measured in series I slab SR-1. According to CSA A23.3-94, the development length of a 15M bar assuming  $f_y = 430$  MPa and  $f'_c = 30$  MPa is about 450 mm. This length is consistent with a bar force gradient of approximately 190 N/mm. The steady force gradient drop in bar B at a deflection of 23 mm is the result of yielding at the upper gauge location (B-2). This is consistent with the fact that bars nearby the column transfer shear mostly by arching action. Unlike bar B, the force gradient in bars D and F is not limited by yielding of the reinforcement but rather by bond deterioration.

Figure 7.40 shows bar force gradients in slab ER2 before and after bonding the sheets. It is worth recalling that in ER2-CS1 the CFRP strips passed above bar B. At virgin stages, the gradients in all bars are similar to those measured in slab ER1-VS. Following the slab strengthening, reloading of ER2 up to the previous peak load led to force gradients as high as those measured in bars D and F before unloading. However, the CFRP strips attenuated the force gradient development in bar B in about 30 %. Later at a deflection of 22.5 mm, the force gradient in bar B further dropped due to yielding at upper gauge B-2.

Figure 7.41 shows the bar force gradients for bars B, F and D in tests ER3-VS and ER3-CS2. At virgin stages, bars B, D and F reached, respectively, peak gradients of 150, 60 and 125 N/mm which are also consistent with those in ER1-VS. The gradient drop in bar B at a 17 mm deflection is the result of yielding at upper gauge B-2. The addition of the sheets led to a force gradient reduction in all bars. The gradient in bar B, which had started decreasing due to yielding before strengthening the slab, dropped further more, that in bar D was virtually zeroed and that in bar F reached a peak of only 50 N/mm.



Bar force gradients in concrete-patched slab ER1-CP1 are not reported since most of the gauges close to the column did not survive test ER1-VS. Strains in ER3-CP2 were not measured.

### **7.3.7 Force Gradients in CFRP Bands**

Figures 7.42 and 7.43 show the variation of the CFRP band force gradients as a function of the slab deflection up to failure for tests ER2-CS1 and ER3-CS2 at the first two intervals. As a reference, the figures show the deflection value signaling the start of the tests. The gradients are average values of those measured in the W-E and N-S for ER2-CS1 and ER3-CS2, respectively. Due to the high non-uniformity of the CFRP strip thickness, sheet force gradients were calculated based on the fibre properties and not on the CFRP properties. Gradients were calculated based on a 0.11 mm sheet thickness and a width of 250 mm. The calculations accounted for the fact that two sheets were adhered per strip. For completeness, the measured thickness for the two plies including the resin varied from 1.1 to 1.5 mm.

The figures show similar sheet force gradients at ultimate for both slabs across the first two intervals. The peak gradients occur at the end of the tests. The peak values are in the order of 65 N/mm in the first interval and 20 to 30 N/mm in the second interval. These values are much lower than those developed by the internal steel reinforcement. At ultimate, the sheet gradients are similar to those developed by the steel bars in ER3-CS2 and less than those in ER2-CS1.

### **7.3.8 Internal Shears**

Figure 7.44 shows the variation of the ratio of the total load calculated as the sum of bar shears to the total load applied by the column, for tests ER3-VS and ER3-CS2. The dead load effect and the CFRP sheet contribution are accounted for. Near failure, there is reasonable agreement between the internally and externally measured load values. This is an indication that the fundamentals of the strip model for punching in slabs with CFRP sheets are also correct.

### 7.3.9 Influence of CFRP Sheets

The most dominant effect of the CFRP sheets is to reduce the force gradient developed in the internal slab reinforcement. The sheets transform the intrinsic beam action behavioural type associated with the internal perimeter reinforcing bars into arching action.

Figures 7.45 to 7.47 compare the effect of the CFRP sheets on the development of force gradients in perimeter bars B, D and F along the second interval for slabs ER1-VS, the two tests on slab ER2 and the two tests on slab ER3. The circles signal the load level at which virgin slabs were unloaded prior to strengthening the slabs.

As shown in Fig. 7.45, bar B's ability to generate force gradients is negatively affected by the presence of the CFRP sheets in both ER2-CS1 and ER3-CS2. In both slabs, the virgin gradients in bar B are lower than those measured after bonding the sheets.

Figure 7.46 shows the variation of force gradient in bar D. The effect of the sheets in ER2-CS1 is not noticeable because bar D is located outside the region bounded by the sheets. Contrary to tests ER1-VS and ER2-CS1, the force gradient in bar D for slab ER3-CS2 is completely shut down by the sheets.

Figure 7.47 shows the force gradients in bar F. The figure shows no negative effect from the sheets in ER2-CS1, but shows some harmful effect on test ER3-CS2 despite the fact that the force gradient had already started decreasing due to yielding before bonding the sheets.

Taking into account that bars D and F could transfer more shear by beam action in ER2-CS1 than in ER3-CS2, it can be concluded that the strengthening layout used in test ER3-CS2 is more adverse than that on ER2-CS1. This is also confirmed by similar force gradient reductions measured for bars C and E in test ER3-CS2.

## **7.4 Behavioural Assessment of CFRP-Strengthened Slabs**

### **7.4.1 Observations**

The upgrading of concrete slabs by means of adding externally bonded FRP reinforcement aims at either a stiffer slab response or a higher capacity, or both. If the goal is to enhance the stiffness, it is essential to identify the best place and orientation to install the CFRP sheets, as recognised by Erki and Heffernan (1995). If the objective is rather to ensure a higher capacity, virtually all existing punching shear models that account for the effect of the slab reinforcement assume that an increase in that reinforcement leads to a punching capacity enhancement. For the case of slabs with bonded FRP sheets, the models proposed by Chen and Li (2000) and Tan (2000), together with the experimental observations of Erki and Heffernan (1995), support this trend.

In the tests conducted in this study, a significant gain in stiffness was not expected in the strengthened slabs because the amount of CFRP provided was low. Since the virgin slabs were designed so that the flexural reinforcement yielded shortly before punching, a significant load capacity increase was not expected either.

Surprisingly, the load-deflection response of the two upgraded slabs, as observed in Figs. 7.2 and 7.3, show that the addition of CFRP sheets on the slab top surface in cruciform patterns led to lower punching capacity and less ductility than that exhibited by control virgin slab ER1-VS. According to Table 7.1, the punching capacity of slabs ER2-CS1 and ER3-CS2 was, respectively, 95 and 87 % of that displayed by ER1-VS.

The following section attempts to explain why the addition of the CFRP sheets in cruciform patterns on the top slab surface did not lead to a punching capacity enhancement in the experiments conducted herein. The section describes the role of the sheets and their interaction with the internal slab reinforcement and provides an hypothesis to explain the mode of failure of the strengthened slabs. A design procedure for the punching capacity assessment of slabs strengthened with bonded FRP sheets will be presented in chapter 10.

#### **7.4.2 The Role of the CFRP Sheets on the Failure of Rehabilitated Slabs**

The experimental evidence reported in this chapter shows that the CFRP sheets affected the behaviour of the internal slab reinforcement in three major respects:

- 1) The sheets reduce the force gradients in the internal slab reinforcing bars.
- 2) The sheets' presence affects the behaviour of all bars located inside the banded slab region. The effect is less noticeable the closer the sheets are placed relative to the column.
- 3) For the case of reinforcing bars passing nearby the column face, the sheets' effect on the internal reinforcement is irrelevant because these bars are located in a highly disturbed region in which arching action tends to prevail and the force gradient generation mechanism is already compromised.

The interaction between the bar force gradients developed by the internal and external slab reinforcement will be studied with reference to Figs. 7.48 and 7.49. Figures 7.48a and 7.48b show the cross-section and side view of a one-way concrete slab element of length  $dx$ , internally reinforced with ordinary steel and externally reinforced with a bonded FRP sheet. The element is assumed to be situated in the negative moment region of a flat plate in a region where slender beam action dominates, e.g. along the circumferential direction. Figures 7.48c and 7.48d show, respectively, the strain distributions in the cracked stage for a slab element without FRP sheets and with FRP sheets. For simplicity, it has been assumed that the depth of the neutral axis remains constant through the cracked stage in both cases.

The free body diagrams of Fig. 7.49a and 7.49b show forces and moments acting on the section before and after bonding the FRP sheets, respectively. The shear has been assumed constant on both sections. From equilibrium of forces, the force gradient in the steel reinforcement for the element without FRP sheets is

$$\left(\frac{dT_s}{dx}\right)_s = \frac{1}{\left(d - \frac{xd}{3}\right)} \frac{dM}{dx} \quad [7.8]$$

where  $x$  is the ratio of the depth of the neutral axis and the flexural depth of the slab for the case of steel reinforcement only, defined as

$$x = \sqrt{\rho_s^2 n^2 + 2\rho_s n} - \rho_s n \quad [7.9]$$

For the slab element with bonded FRP sheets, the sheet tension also contributes to the bending moment. Assuming that the sheet thickness is small relative to the depth of the member, the change in bending moment in the element with bonded FRP sheets is

$$dM = dT_s \left(d - \frac{x_{fs} d}{3}\right) + dT_f \left(h - \frac{x_{fs} d}{3}\right) \quad [7.10]$$

where  $x_{fs}$  is the ratio of the neutral axis' depth and the flexural depth of the beam with FRP. Applying force equilibrium and strain compatibility leads to

$$x_{fs} = \sqrt{(\rho_s n + \rho_{fs} \alpha)^2 + 2(\rho_s n + \rho_{fs} \alpha^2 n_{fs})} - (\rho_s n + \rho_{fs} \alpha) \quad [7.11]$$

where  $\rho_{fs} = \frac{A_f}{bh}$ ,  $\alpha = \frac{h}{d}$  and  $n_{fs} = \frac{E_{fs}}{E_c}$ .

Figure 7.50 shows the variation of the ratio  $x_{fs}$  to  $x$  for a change in the external FRP reinforcement ratio,  $\rho_{fs}$ , for a concrete slab with internal steel reinforcement ratio,  $\rho_s$ , equal to 1 %. The figure shows that  $x$  is not necessarily equal to  $x_{fs}$ . In this case, the depth of the neutral axis increases when the amount of external bonded reinforcement increases and when stiffer sheets are installed.

Dividing both sides of Eq. 7.10 by  $dx$ , and rearranging terms, the gradient in the internal steel reinforcement in the element with the bonded FRP sheets is

$$\left(\frac{dT_s}{dx}\right)_{fs} = \frac{1}{\left(d - \frac{x_{fs}d}{3}\right)} \frac{dM}{dx} - \frac{dT_f}{dx} \left(\frac{h - \frac{x_{sf}}{3}}{d - \frac{x_{fs}}{3}}\right) \quad [7.12]$$

Equation 7.12 shows that the force gradient developed by the sheets,  $\frac{dT_f}{dx}$ , reduces the amount of force gradient developed by the internal reinforcement in the slab with FRP sheets. However, despite the fact that  $x_{fs}$  is not necessarily equal to  $x$ , the term  $\left(d - \frac{x_{fs}d}{3}\right)$  is approximately equal to  $\left(d - \frac{xd}{3}\right)$ . This leads to the following approximation

$$\left(\frac{dT_s}{dx}\right)_{fs} \approx \left(\frac{dT_s}{dx}\right)_s - \frac{dT_f}{dx} \left(\frac{h - \frac{k_{sf}}{3}}{d - \frac{k_{fs}}{3}}\right) \quad [7.13]$$

which shows that the force gradient in the internal slab reinforcement in Bernoulli-type regions of a slab with bonded FRP sheets,  $\left(\frac{dT_s}{dx}\right)_{fs}$ , is less than that which would normally develop in a slab with the *same* amount of internal reinforcement without the FRP sheets,  $\left(\frac{dT_s}{dx}\right)_s$ . This observation corroborates the experimental findings from tests ER2-CS1 and ER3-CS2. In these tests, the peak force gradient in the FRP sheets across the second interval varied approximately from 25 to 30 N/mm. The observed force gradient drop in the internal slab reinforcement in ER2-CS1 and ER3-CS2 is slightly greater than this range of values.

Further examination of the effect of  $x_{fs}$  on Eq. 7.13 shows that an increase in  $x_{fs}$  leads to a reduction in the force gradient developed by the internal slab reinforcement. This shows that the addition of more FRP sheets or the placement of stiffer sheets is not beneficial either.

At this stage, it is necessary to emphasize that Eq. 7.13 provides a rational explanation for the force gradient drop in the perimeter bars running underneath the FRP sheets but does not explain why the slabs punched at a lower load and at a lower deflection compared to the virgin slab. Since the shear transferred by the two elements of Fig. 7.49 is the same, the amount of beam action-type shear transferred by the FRP sheet should, in theory, compensate for the force gradient loss in the internal reinforcement so that the total transferred beam action-type shear matches that in the slab without FRP. This was not the case; even though the sheets somewhat relieved the internal slab reinforcement from generating force gradients, the additional load path brought about by the sheet bonding scheme lumped higher shear stresses on the internal reinforcement-cover interface, as indicated in the FBD of Fig. 7.49b. This shear stress increase together with the degradation of the concrete cover by the sheets' tensile action, compromises the ability of the internal slab reinforcement to generate force gradients, leading to a premature failure.

The additional load path imposed after bonding the sheets relies heavily on the bond stresses that develop between the sheets and the concrete. This bond mechanism is stiffer and more brittle than that developing between concrete and conventional steel reinforcement. As a result, the addition of the sheets leads to a slightly stiffer and brittle response, as observed in the load-deflection plots of Figs. 7.2 and 7.3, but does not necessarily result in a punching capacity enhancement, as evidenced in the same figures.

It is also worth noting that the FRP sheets affected not only the behaviour of the internal bars running directly below but also that of the bars enclosed within the banded region. The FRP sheets compensate for the internal bar force gradient loss only in slab portions tributary to the internal bars below the sheets. The sheets cannot supply the extra gradient required at other locations because there are no FRP sheets bonded at those locations, as occurred in ER3-CS2. This explains why the small slab panels fully covered with FRP sheets tested by Erki and Heffernan (1995) and Tan (2000) outperformed those without FRP sheets, and suggests that the FRP bands in the two tests reported herein were probably too narrow.

The strong influence of bond between both the FRP sheets and the internal reinforcement and concrete on slab failure is supported by perhaps the most striking feature of tests ER2-CS1 and ER3-CS2: their punching shear crack outline was completely different despite the fact that they reached similar failure loads. In both slabs, the shape of the punching generatrix was constrained by the location of the sheets. The angle of the punching crack in ER2-CS1 (about  $31^\circ$ ) was similar to that in control slab ER1-VS. This, in turn, was steeper than that in slab ER3-CS2 (about  $13^\circ$ ). Since all virgin slabs were comparable, the location and inclination of the initial diagonal tension crack is expected to be similar for them, as shown in the sketch of Fig. 7.51a. Once the slabs were strengthened, the internal crack growth regime was altered by the sheets' presence. In ER2-CS1, the additional shear stress demand on the internal reinforcement-cover boundary imposed by the CFRP sheets led to the formation of a steep punching shear crack, as shown in Fig. 7.51a. In ER3-CS2, since the sheets were located farther away from the column, the critical shear conditions in the cover-rebar interface forced the punching shear crack to zip through at a flatter angle. Readings from the through thickness gauges installed on ER3-CS2 support the hypothesis that the upper tip of the initial shear crack(s) runs from inner to outer slab zones.

#### **7.4.3 Behavioural Assessment of Slabs Repaired with Concrete Patches**

Due to the fact that most of the internal strain gauges in the slabs with concrete patches became non-functional after tests ER1-VS and ER3-CS2, the evaluation of the two rehabilitation techniques examined in tests ER1-CP1 and ER3-CP2 will be performed based on their load-deflection response.

Among all the rehabilitation tests conducted in this series, the repair scheme implemented in test ER3-CP2 (after punching of ER3-CS2) was the most efficient. According to Table 7.1, the punching capacity of ER3-CP2 was 6 % greater than that of the control slab. The ultimate deflection was approximately 84 % of that in ER1-VS. It is worth noting that test ER3-CP2 started with a residual slab depression of about 30 mm at the vicinity of the column due to previous punching. The forensic investigation shows evidence that failure



was not of frictional type between the old and new concrete. Instead, the punching crack formed below this boundary.

The least invasive concrete patching solution (ER1-CP1) was the least beneficial repair procedure of all, failing at a 18.2 kPa applied load. This is 71 % of the failure load in ER1-VS. This value is however, almost four times that which would be applied at service load level in a prototype plate of similar dimensions. Failure in ER1-CP1 was of frictional type between the old and new concrete. Both the punching failure cone and the top crack layout matched that of slab ER1-VS.

Despite the loss of most slab gauges around the column, it was possible to evaluate the development of bar force gradients in ER1-CP1. The placement of concrete in the joint did not hamper the slab internal bars to continue transferring shear by beam action. However, this process was interrupted due to the premature frictional failure.

**Table 7.1 Series II Slabs : Test Results**

Test	$q_{cr}$ (kPa)	$\Delta_{cr}$ (mm)	$q_{top-y}$ (kPa)	$\Delta_{top-y}$ (mm)	$q_{bot-y}$ (kPa)	$\Delta_{bot-y}$ (mm)	$q_u$ (kPa)	$\Delta_u$ (mm)	Efficiency *
ER1-VS	0.4 (5.43)	0.03	16.8 (21.9)	15.9	20.3 (25.4)	20.3	25.6 (30.7)	34.5	1.00
ER1-CP1	-	-	-	-	-	-	18.2	13.3	0.71
ER2-VS	0.78 (5.63)	0.19	16.0 (20.9)	15.6	16.0 (20.9)	15.6	-	-	-
ER2-CS1	-	-	-	-	-	-	24.2 (29.1)	25.2	0.95
ER3-VS	0.84 (5.88)	0.16	14.6 (19.4)	15.0	16.7 (21.5)	17.2	-	-	-
ER3-CS2	-	-	-	-	-	-	22.2 (27.0)	27.2	0.87
ER3-CP2	-	-	-	-	-	-	27.2 (32.0)	29.0	1.06

**Notes:** 1. Values in parentheses indicate total dead load on slab.

2. *top-y* and *bot-y* subscripts refer to first yielding of top and bottom steel.

\* Defined as the ratio of the failure load to that of control test ER1-VS.

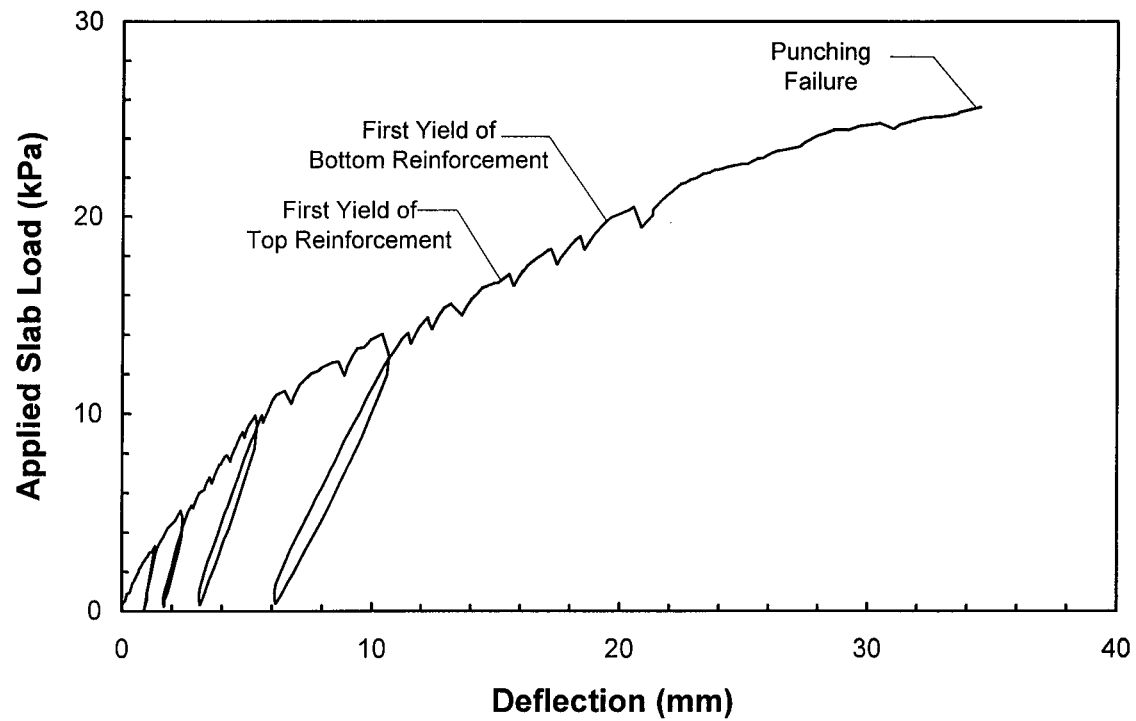


**Fig. 7.1 Load-deflection Response : ER1-VS**

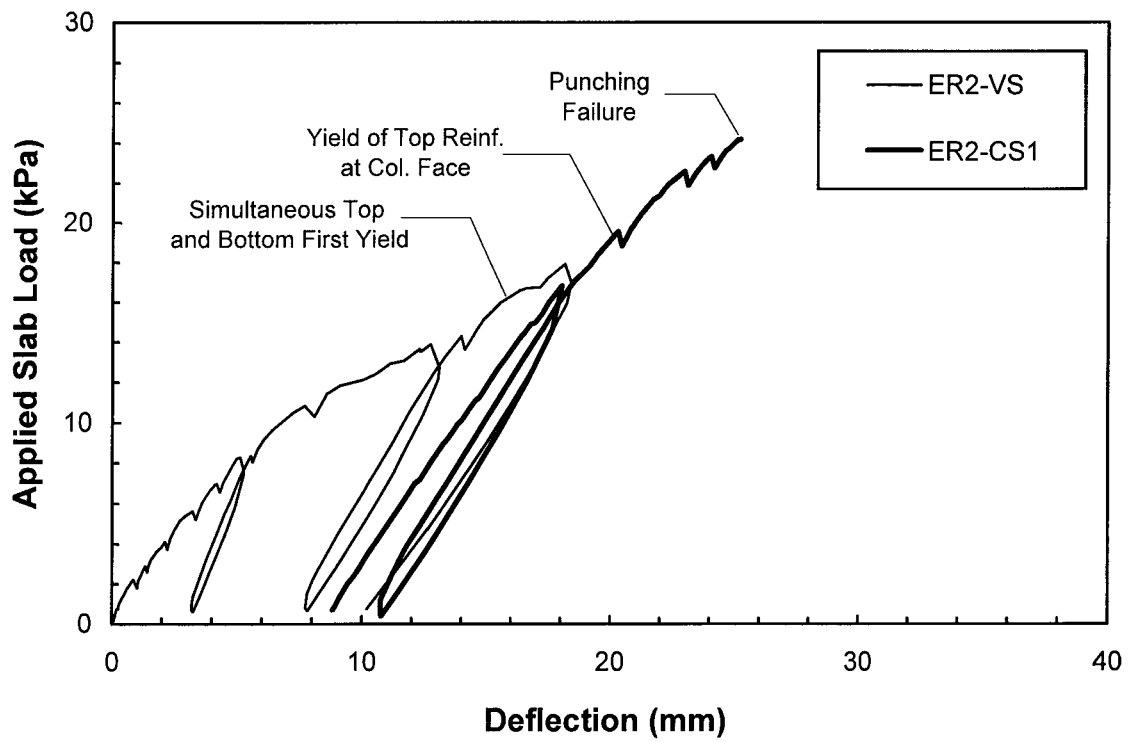


**Fig. 7.2 Load-deflection Response : Slab ER2**

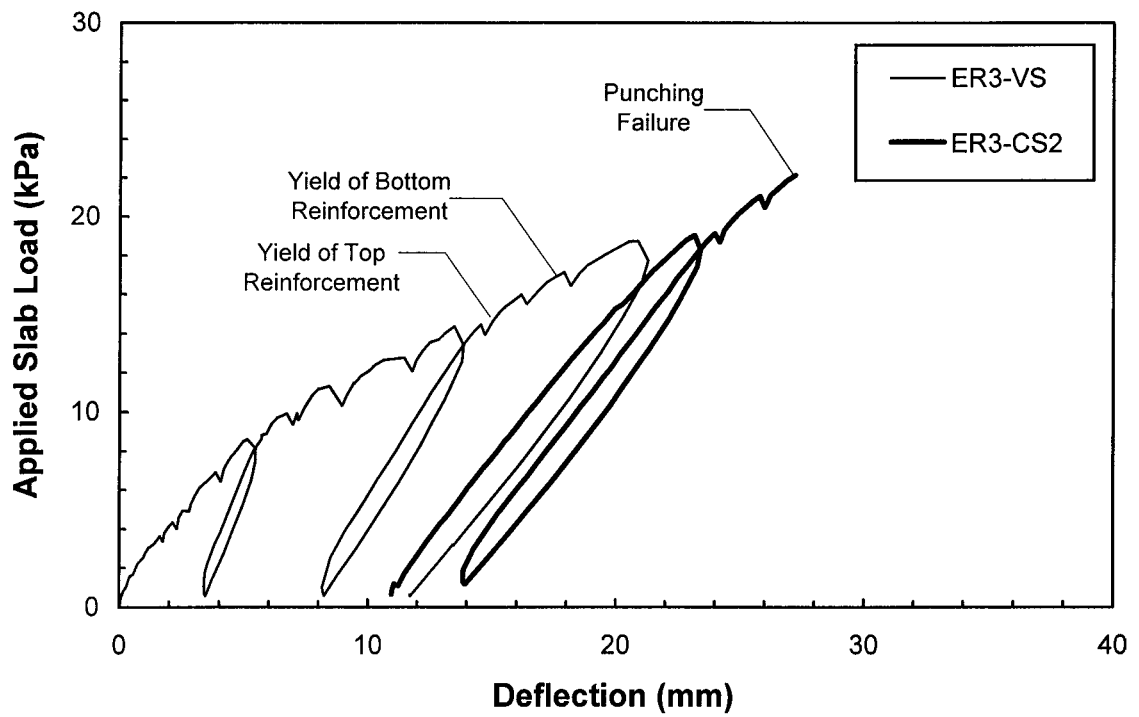


**Fig. 7.3 Load-deflection Response : Slab ER3**

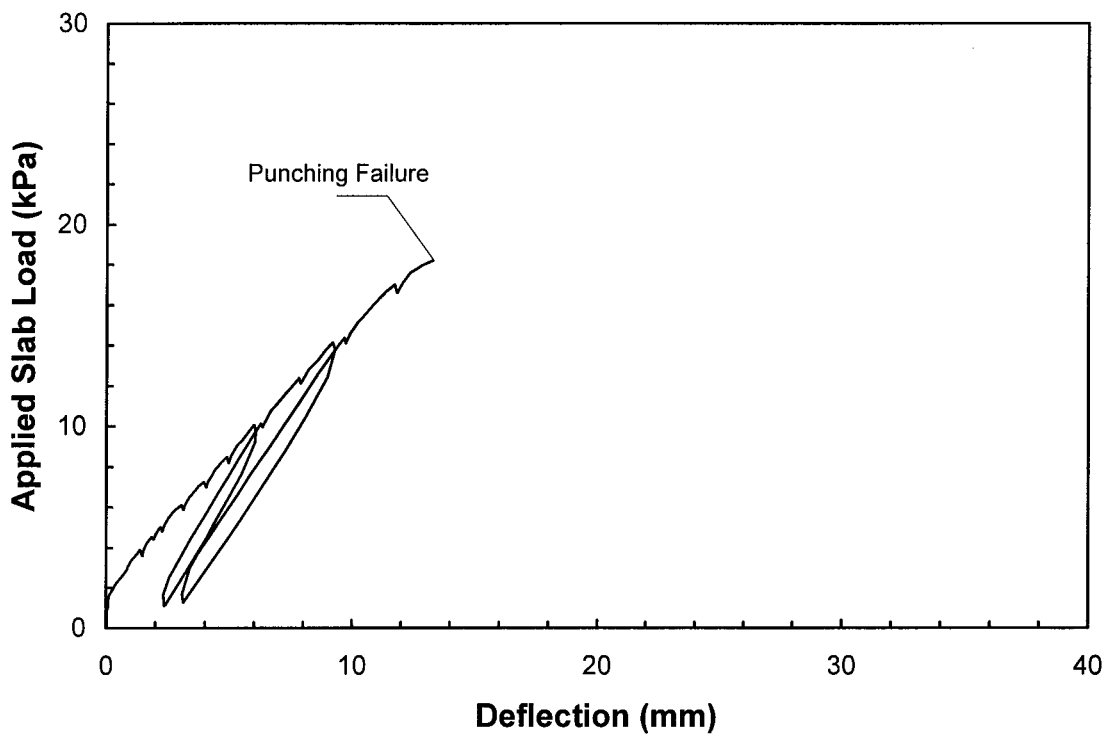


**Fig. 7.4 Load-deflection Response : ER1-CP1**

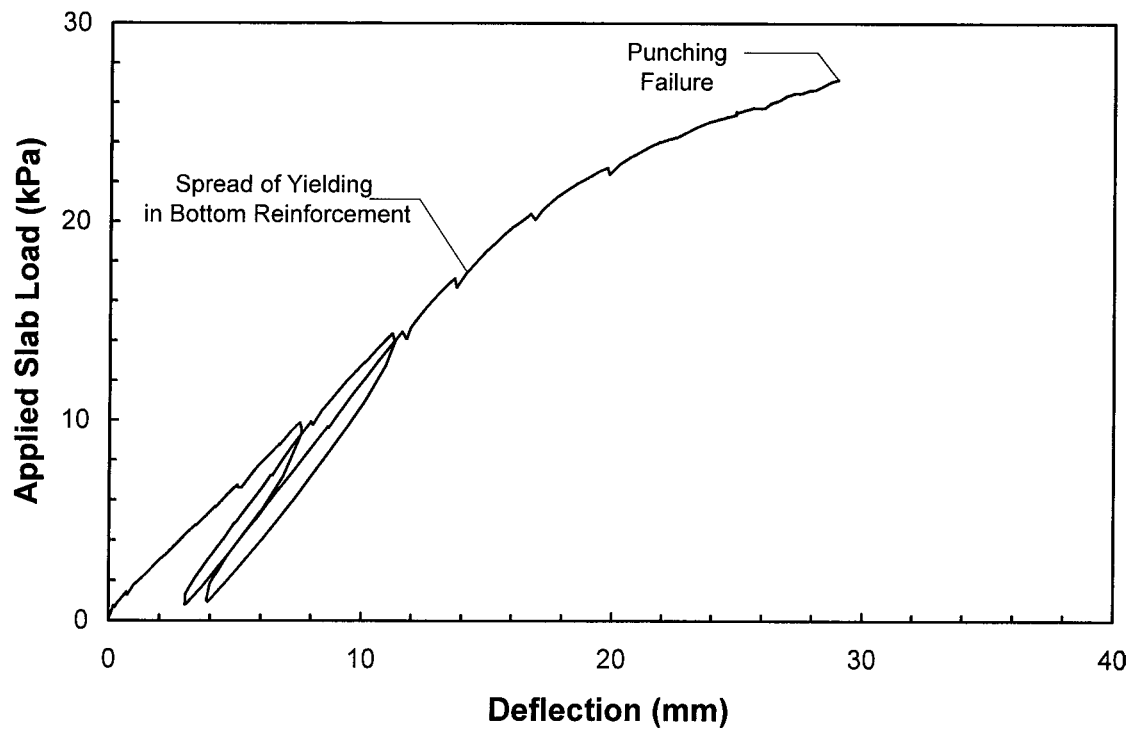


**Fig. 7.5 Load-deflection Response : ER3-CP2**

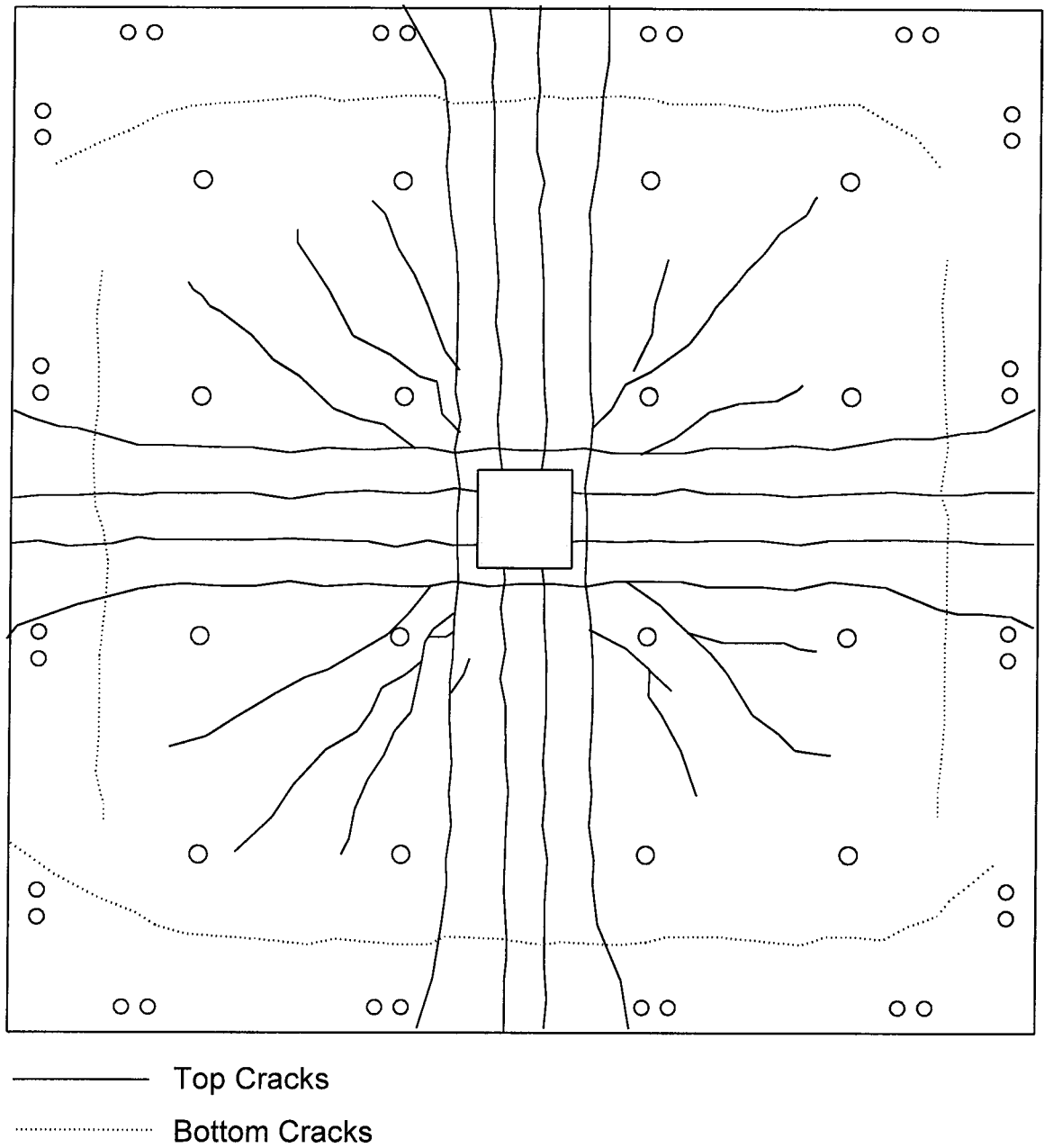
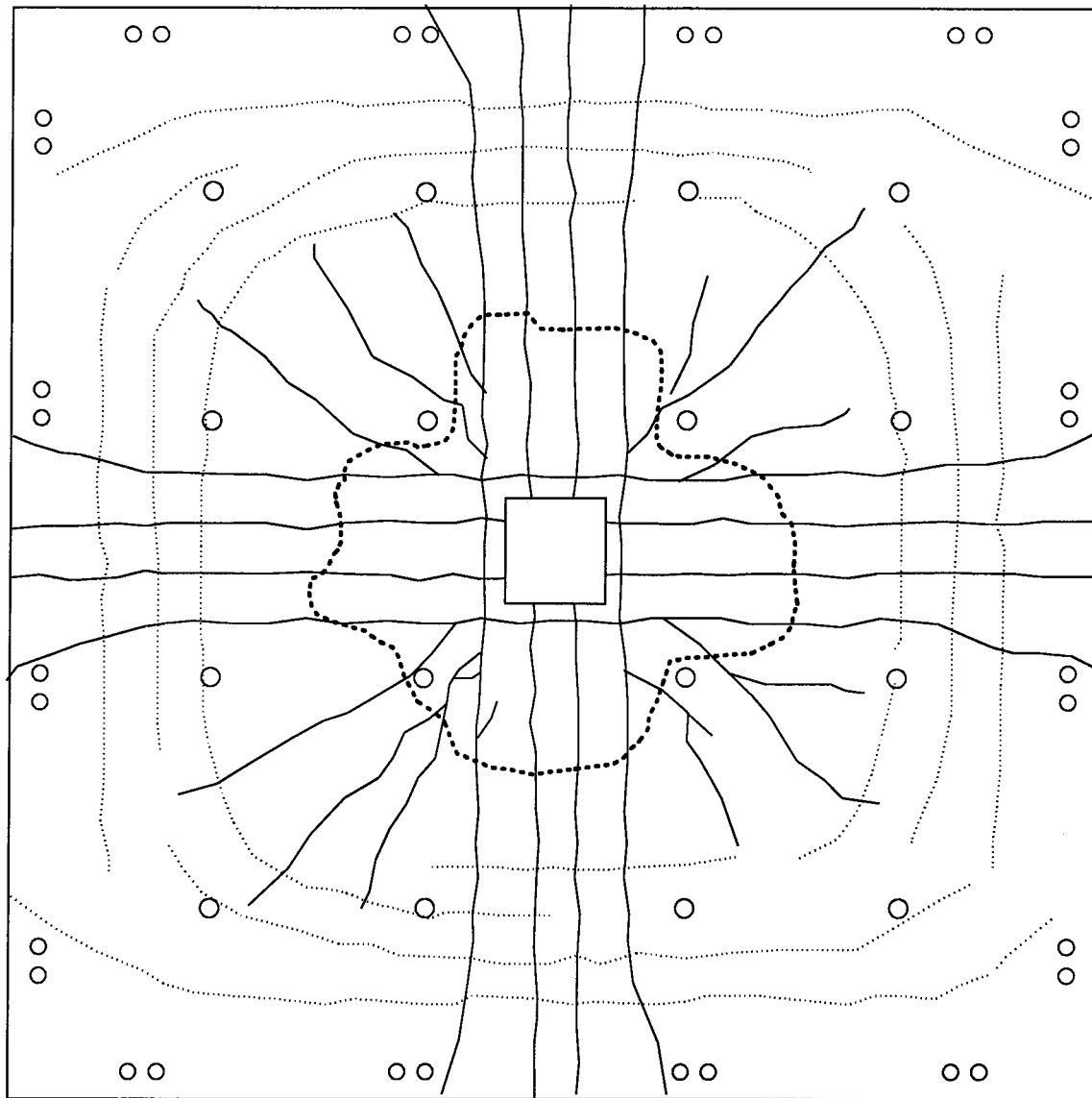
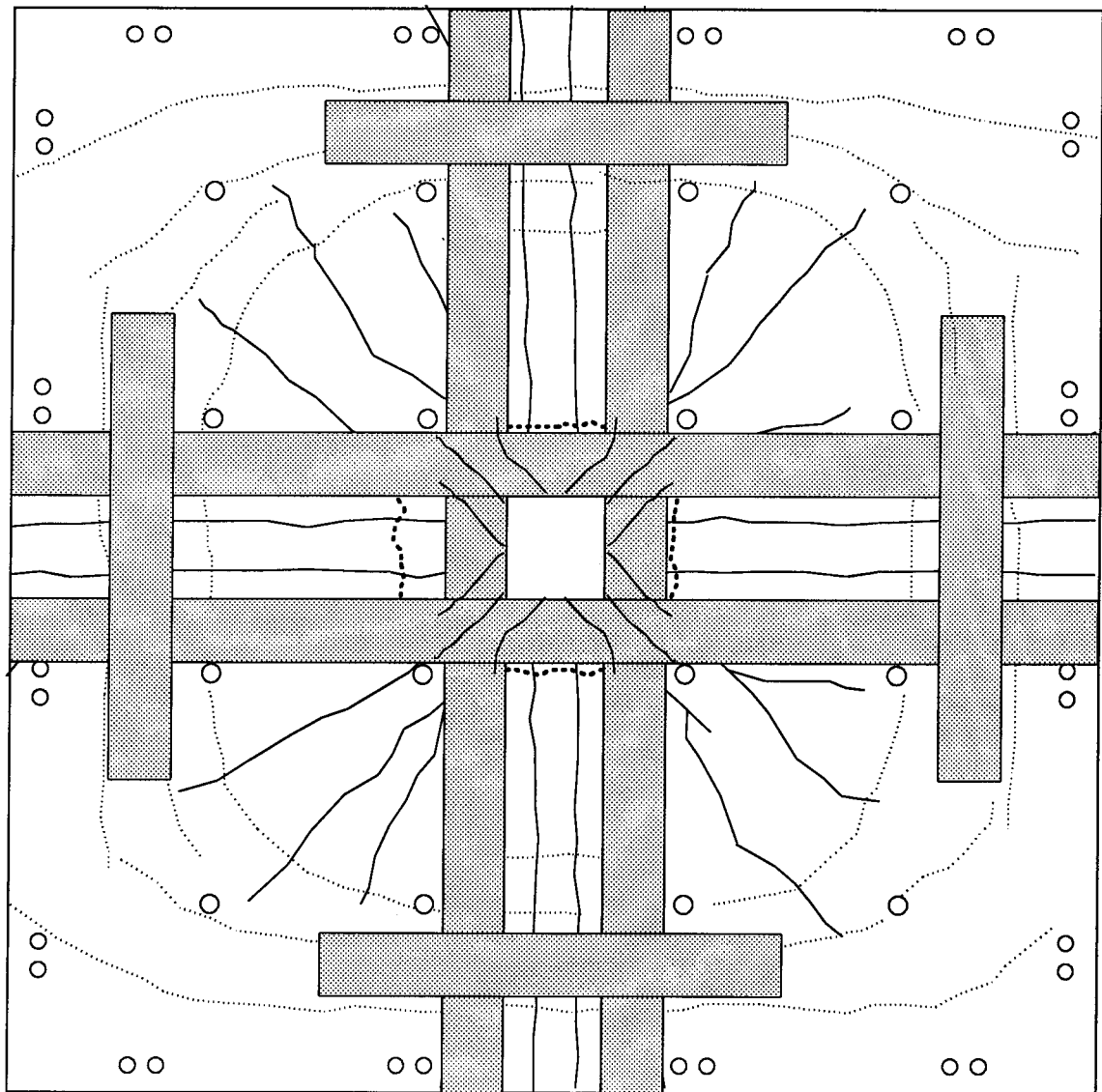


**Fig. 7.6 Typical Crack Pattern in Virgin Slab  
at a 18 kPa Applied Load**



- Top Cracks
- ..... Bottom Cracks
- ..... Punching Crack Outline

**Fig. 7.7 Crack Pattern at failure : ER1-VS**



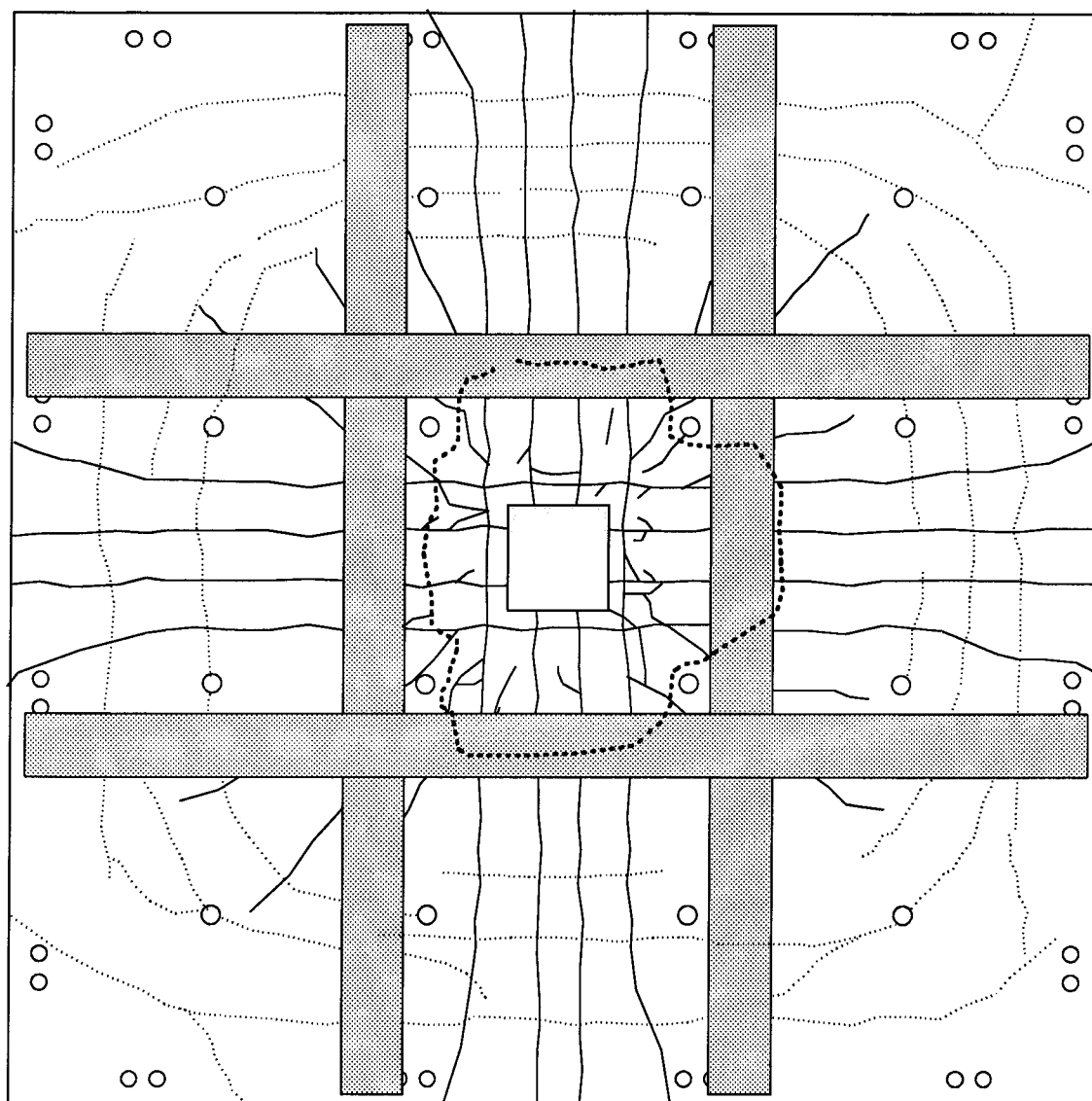
- Top Cracks
- ..... Bottom Cracks
- ..... Punching Crack Outline

**Note:**

The set of top cracks oriented at 45° around the column formed below the sheets. These cracks became visible only after the sheets were removed.

**Fig. 7.8 Crack Pattern at failure : ER2-CS1**





- Top Cracks
- ..... Bottom Cracks
- ..... Punching Crack Outline

**Fig. 7.9 Crack Pattern at failure : ER3-CS2**



**Fig. 7.10 Detail of CFRP Sheets After Column Push-through (ER3-CS2)**

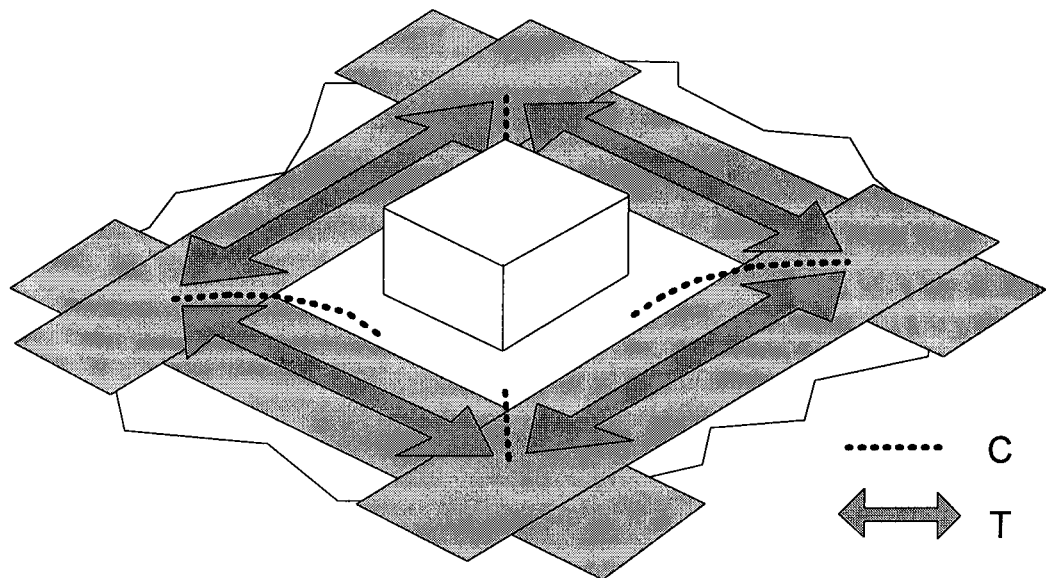


**Fig. 7.11 Tension Band Behaviour of CFRP Sheets**

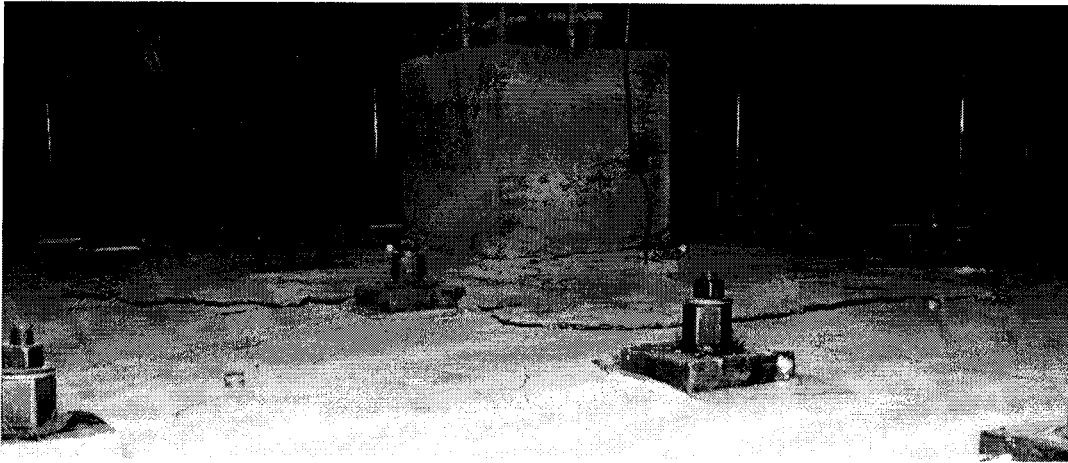


**Fig. 7.12 Punching Failure : ER1-CP1**

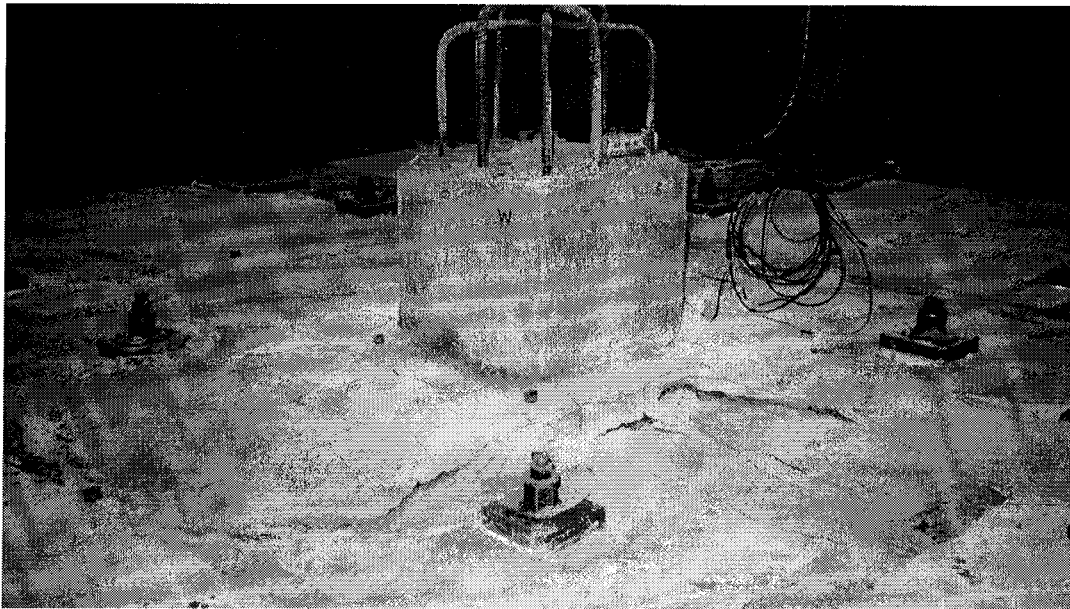


**Fig. 7.13 Punching Failure : ER3-CP2**

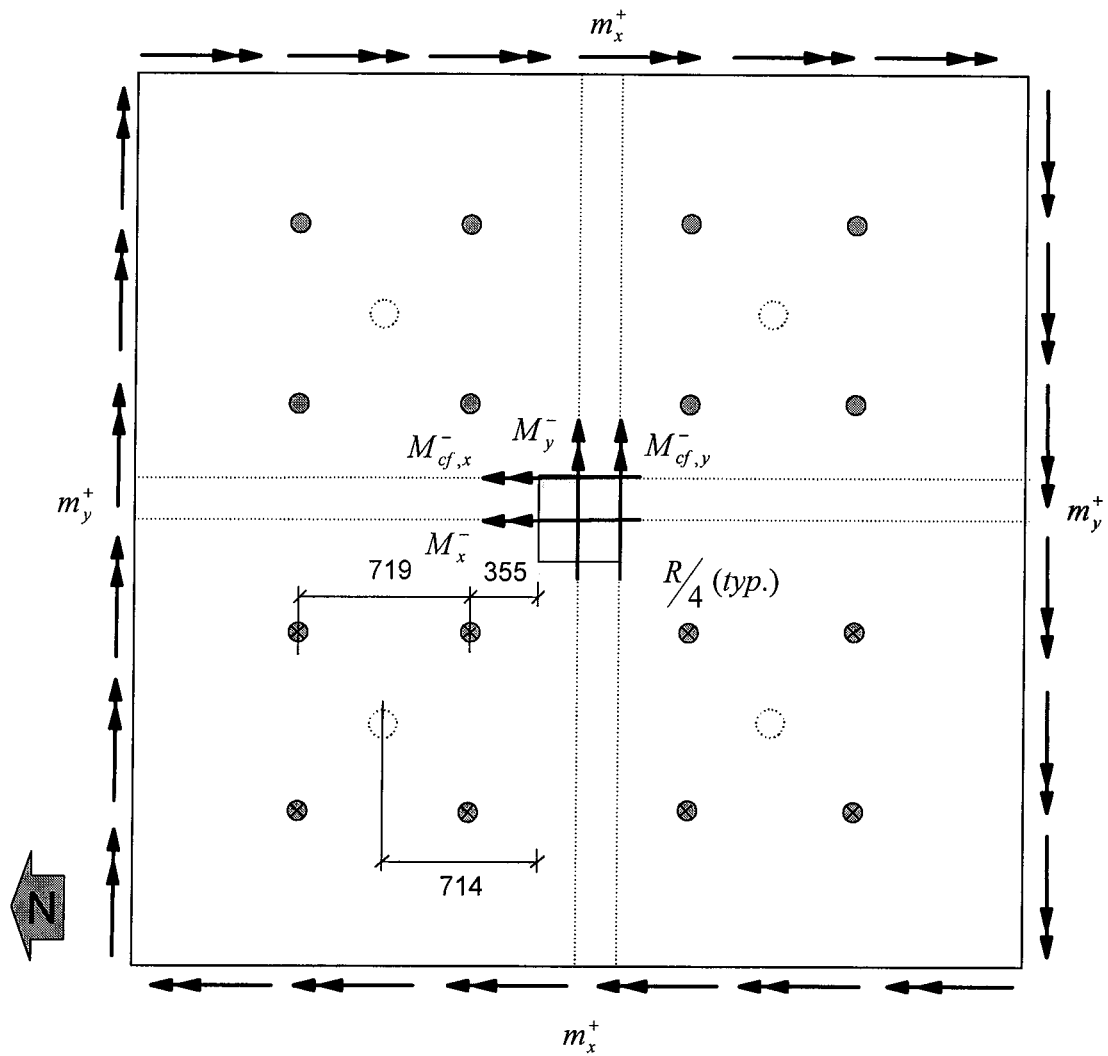


**Fig. 7.14 Plan View of Vertical Forces and Moments Acting on Slab**

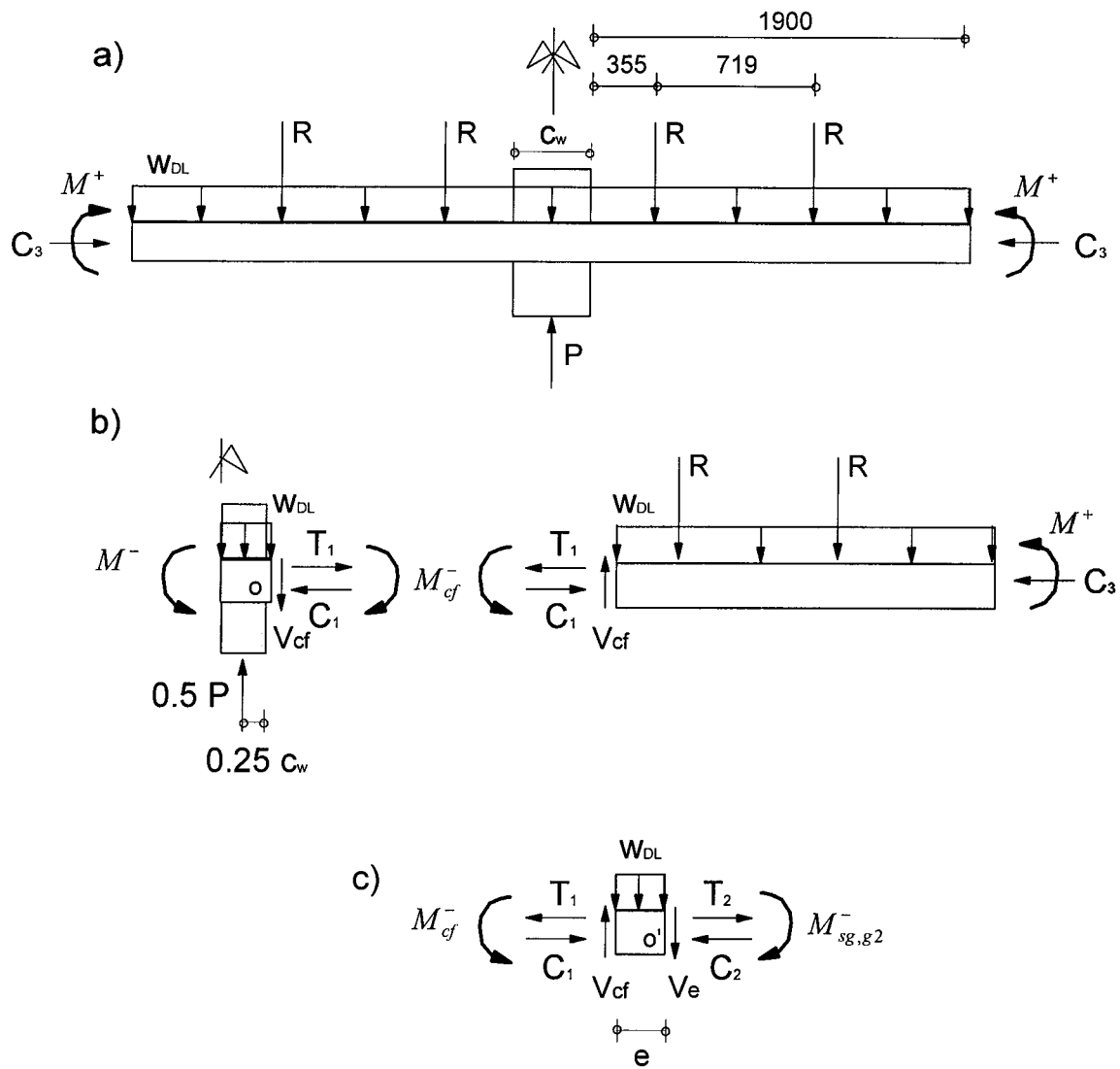


**Fig. 7.15 Free Body Diagrams for Moment Calculations**

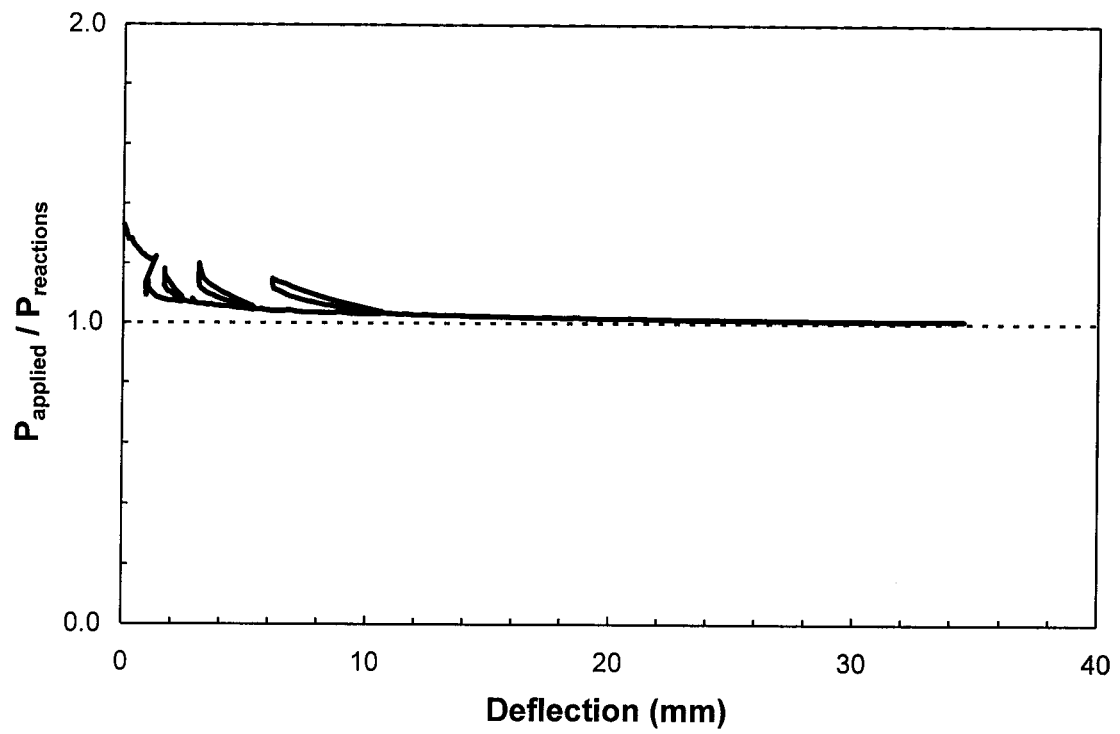


**Fig. 7.16 Vertical Force Statics Check : ER1-VS**

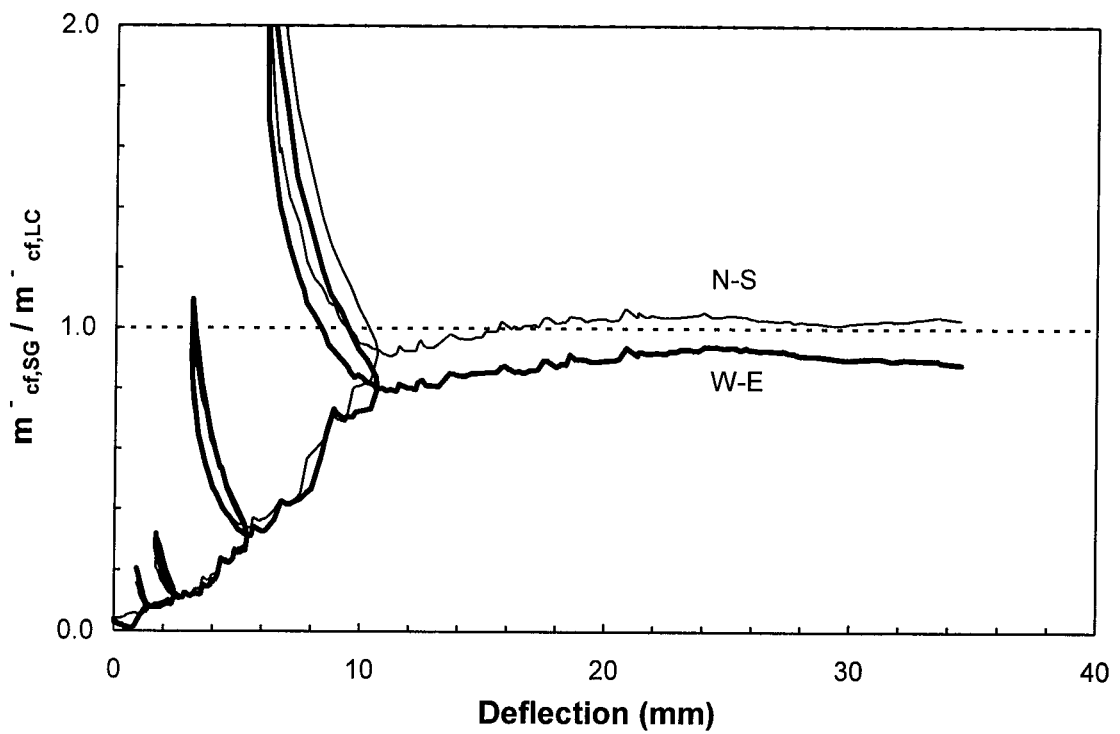


**Fig. 7.17 Negative Moment Intensity Comparison: ER1-VS**

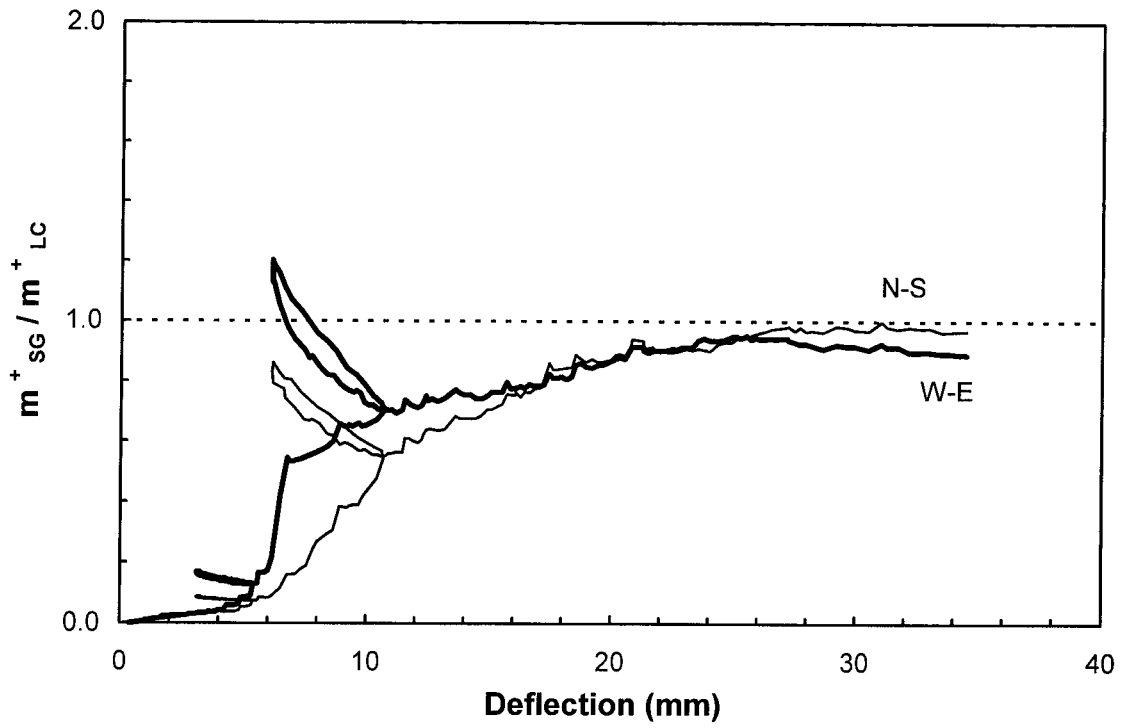


**Fig. 7.18 Positive Moment Intensity Comparison: ER1-VS**

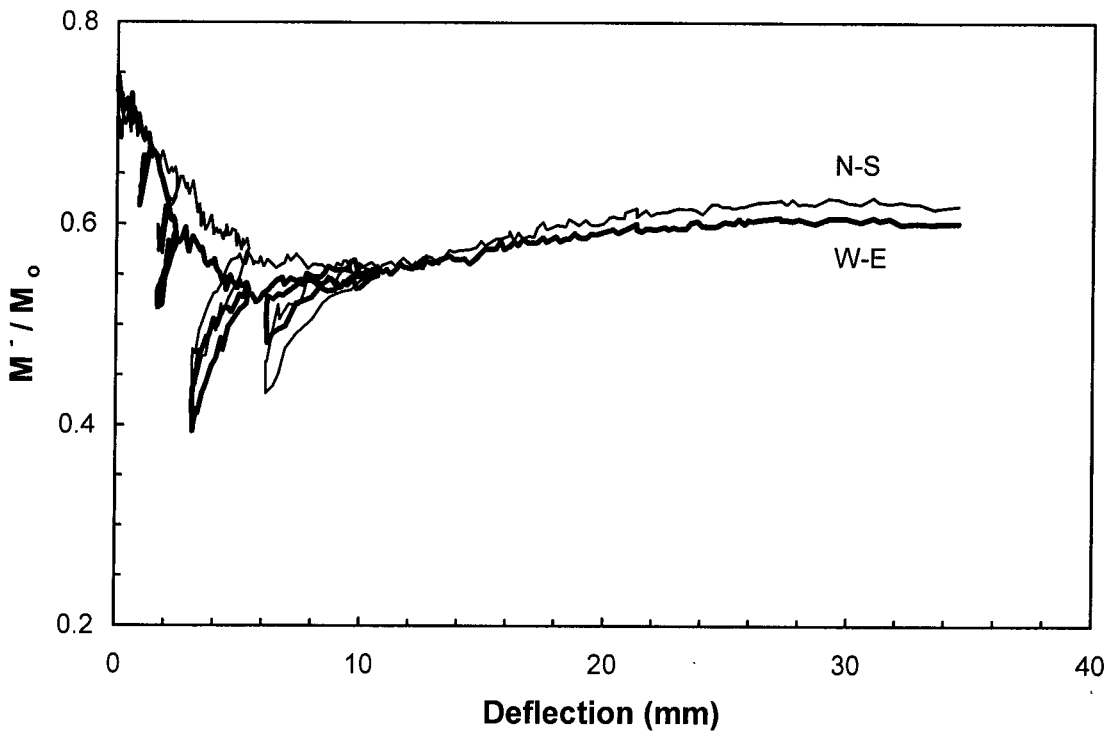


**Fig. 7.19 Negative to Panel Moment Ratio : ER1-VS**

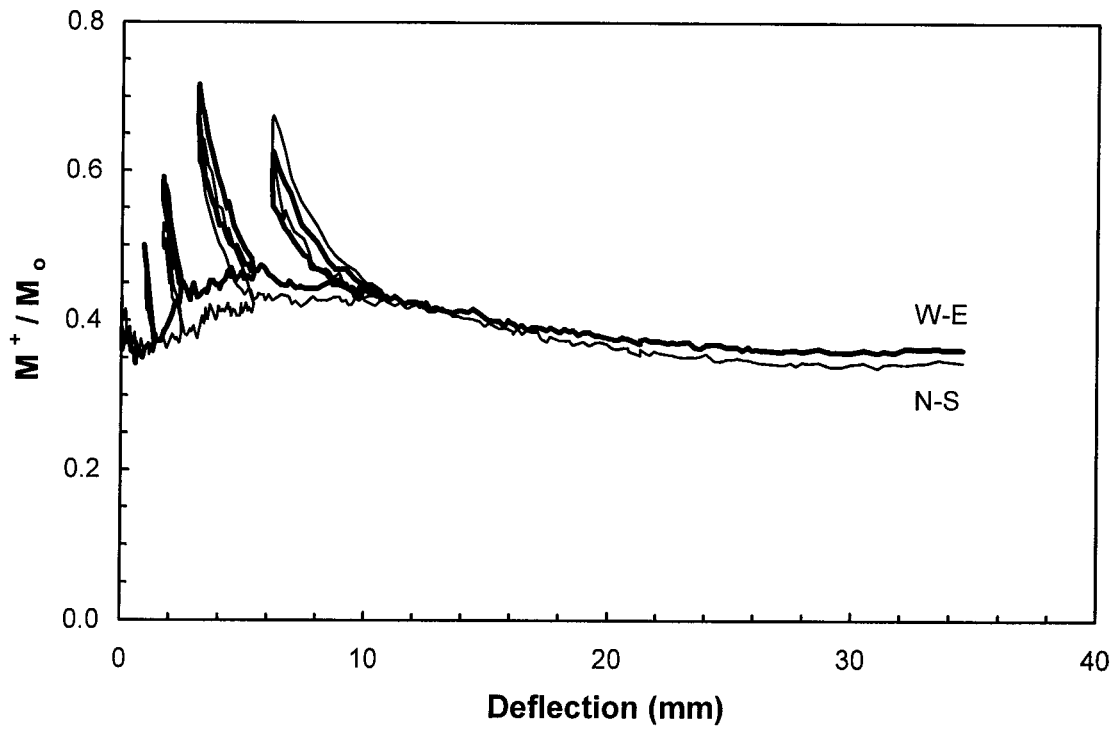


**Fig. 7.20 Positive to Panel Moment Ratio : ER1-VS**

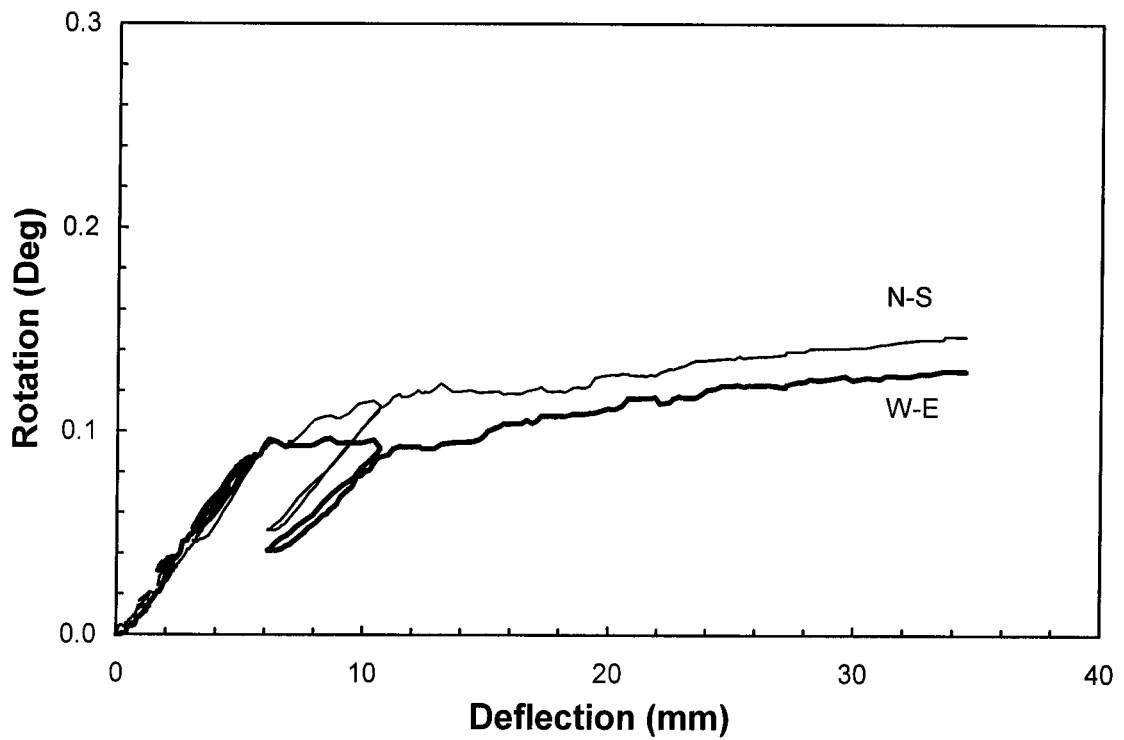


**Fig. 7.21 Average Edge Slab Rotations : ER1-VS**



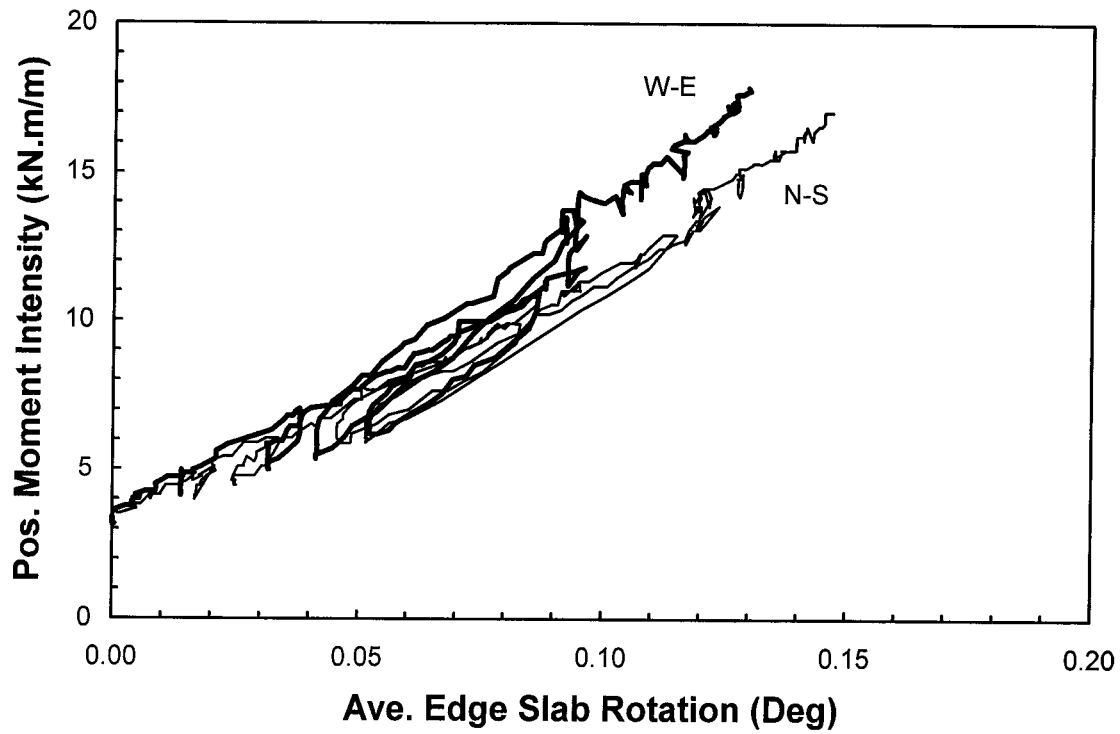


Fig. 7.22 ERS Rotational Stiffness : ER1-VS

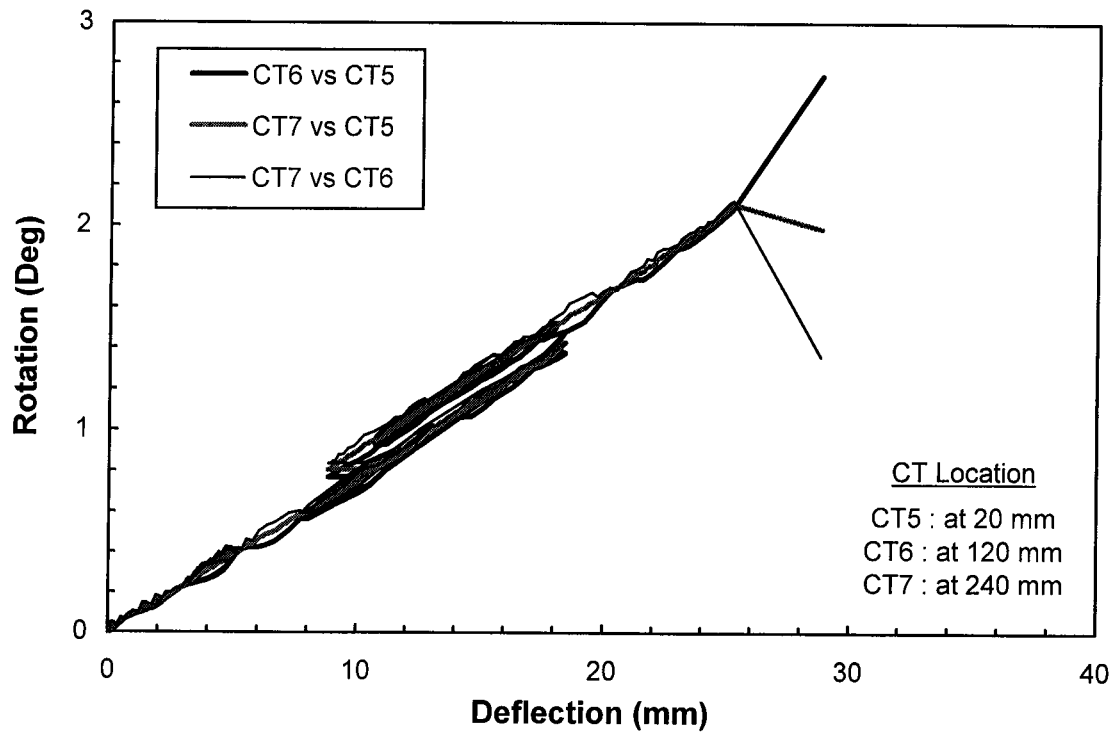


Fig. 7.23 Radial Slab Rotation : ER2 Tests

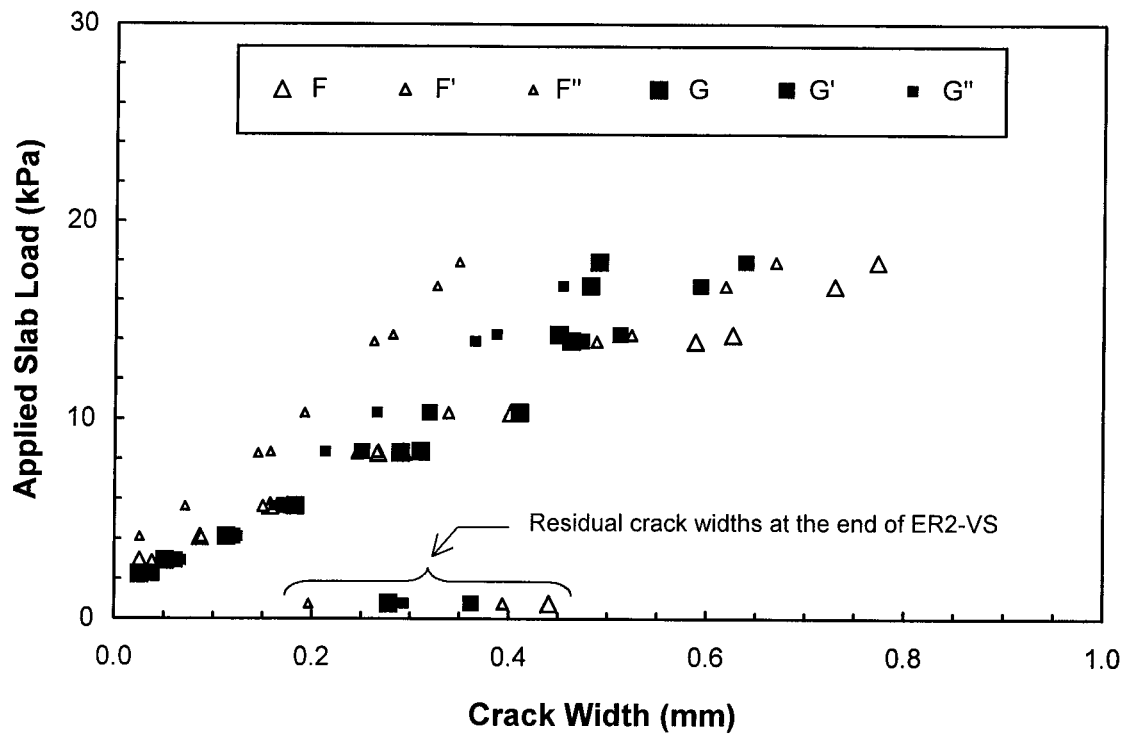


Fig. 7.24 Top Crack Widths : ER2-VS

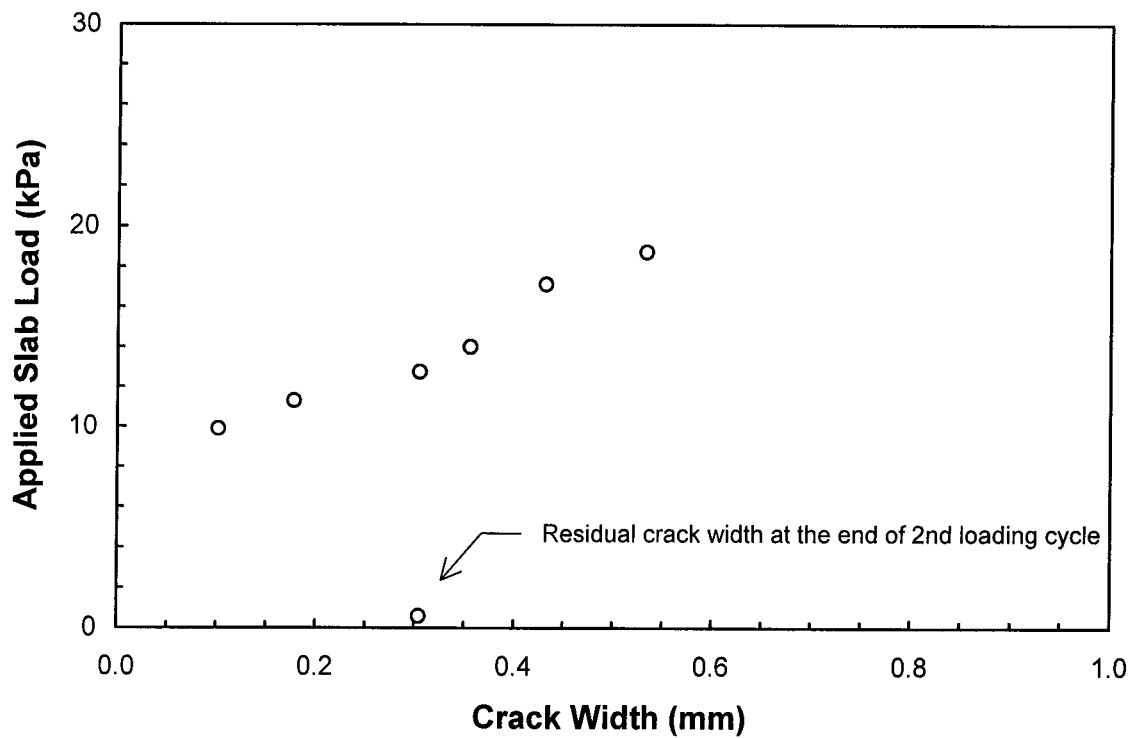


Fig. 7.25 Bottom Crack Widths : ER3-VS

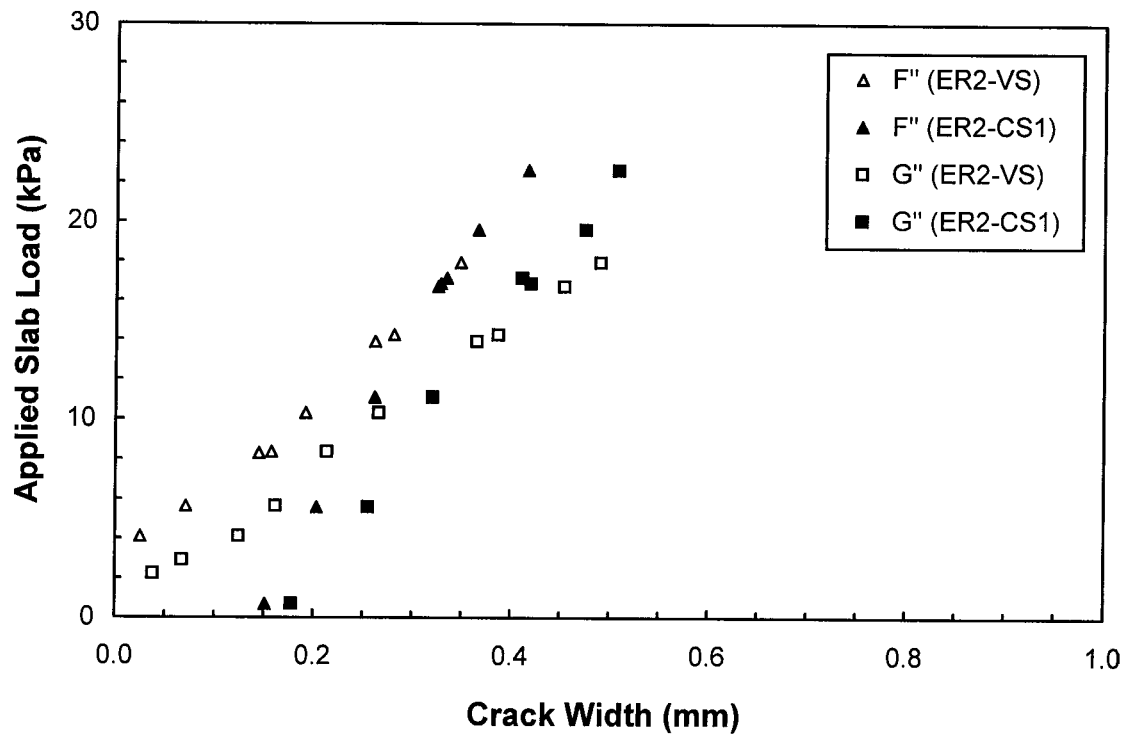


Fig. 7.26 Top Crack Widths : ER2 Tests

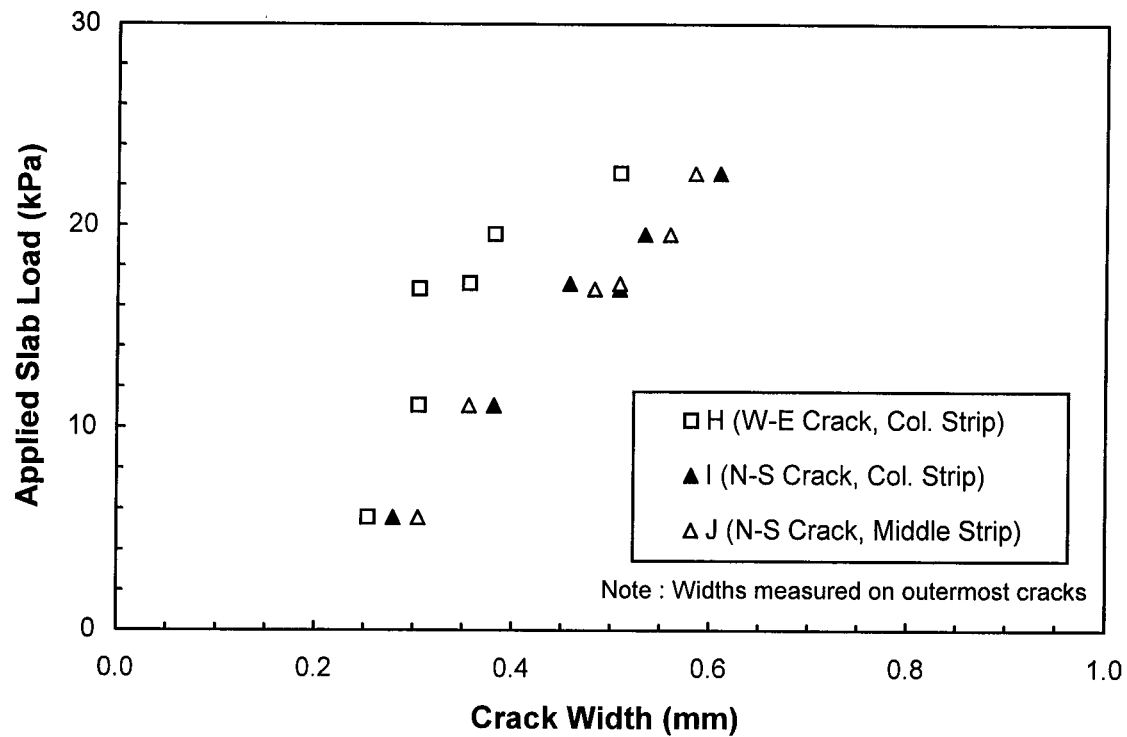


Fig. 7.27 Bottom Crack Widths : ER2-CS1

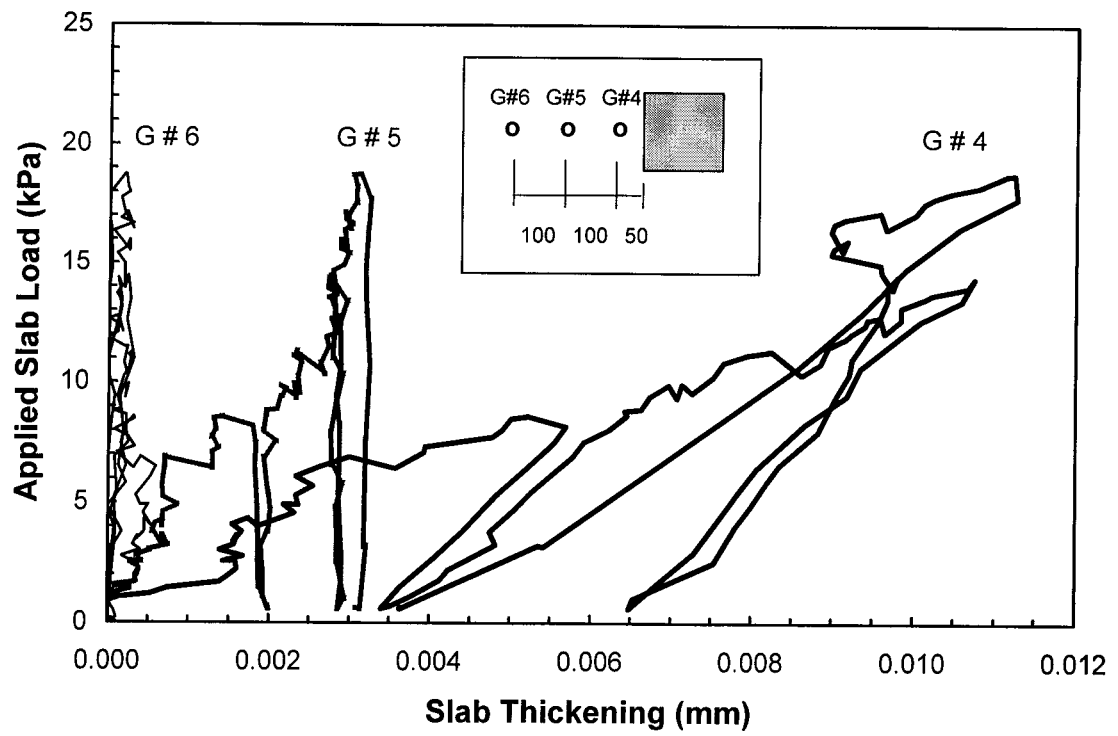
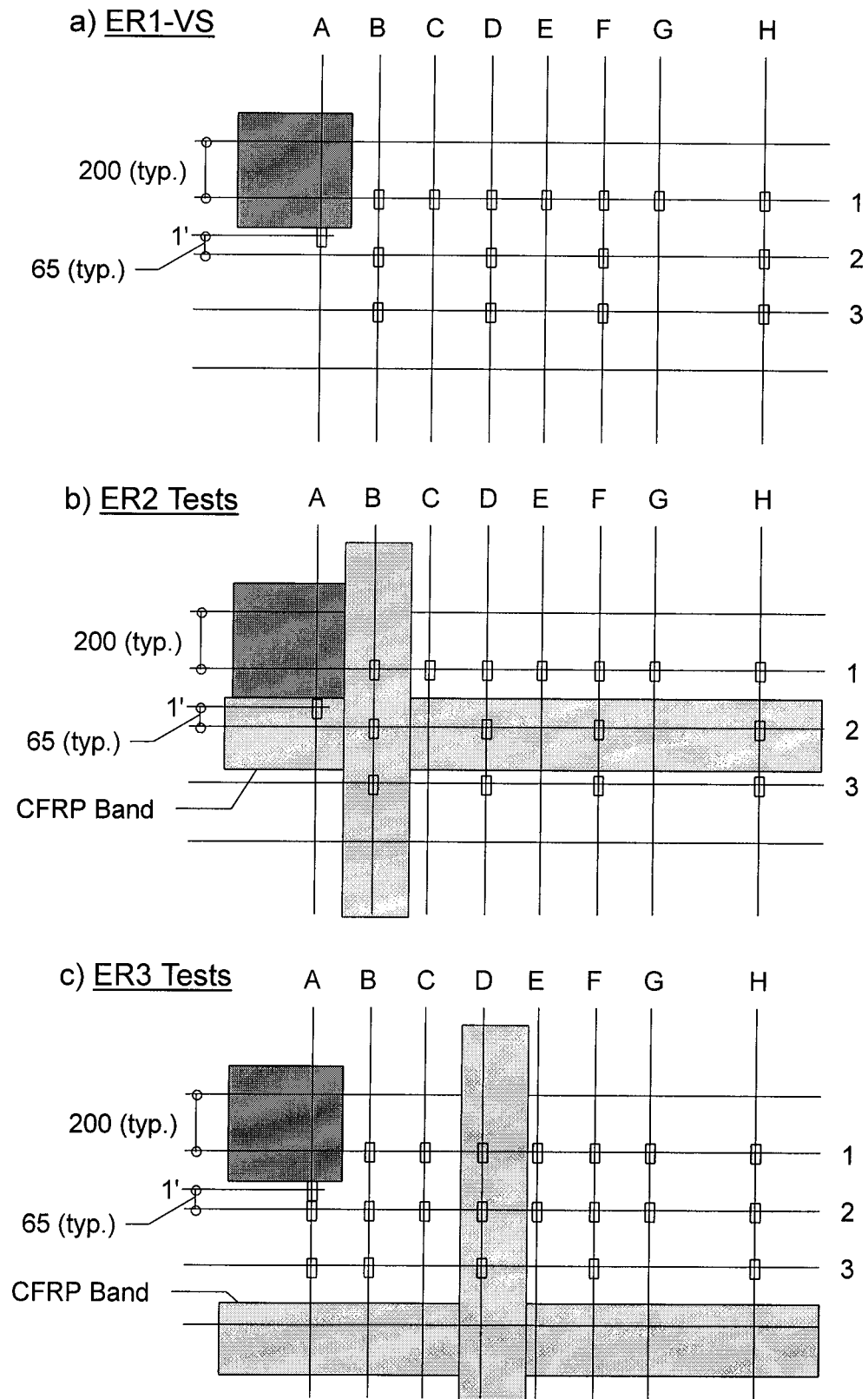


Fig. 7.28 Slab Thickening (N-S) : ER3-VS



**Fig. 7.29 Top Strain Gauge Key Plans : Series II Slabs**

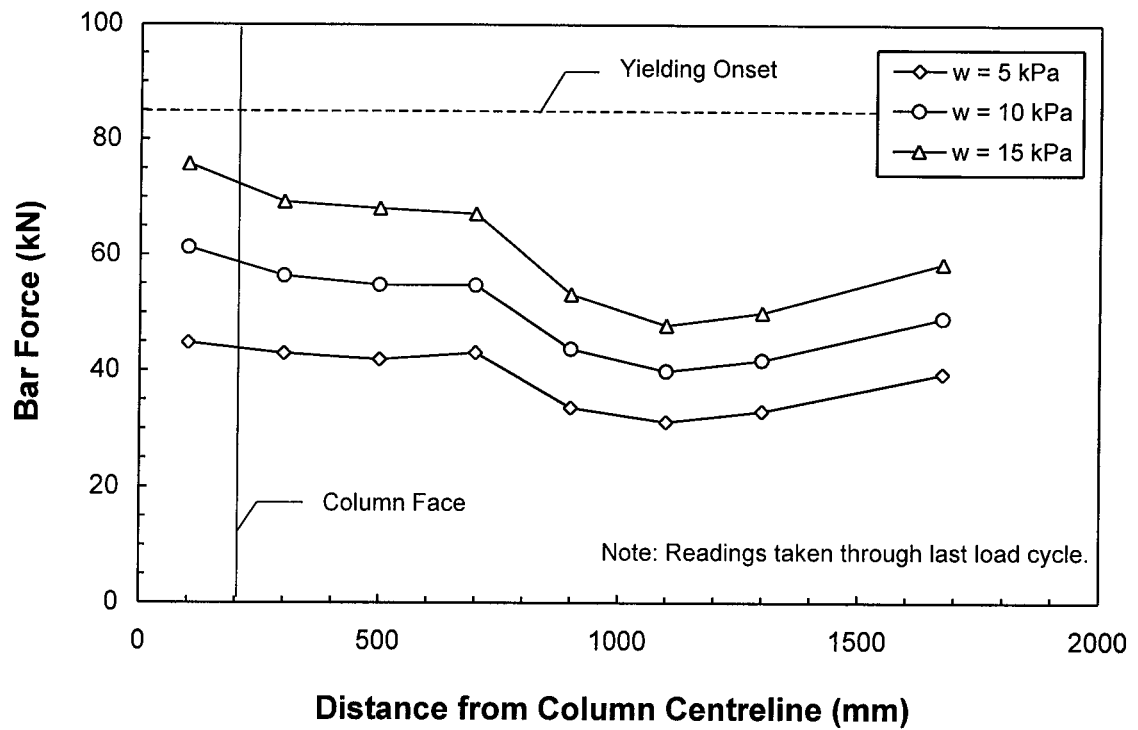


Fig. 7.30 Bar Forces - Gridline 1 : ER3-VS

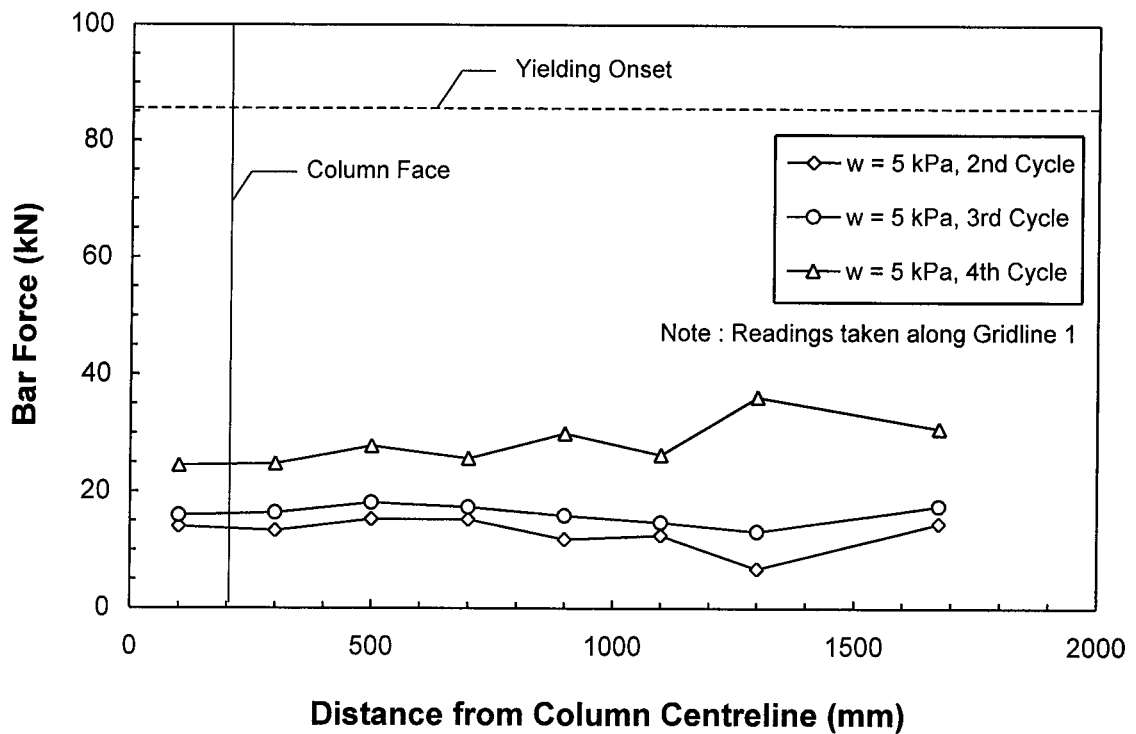
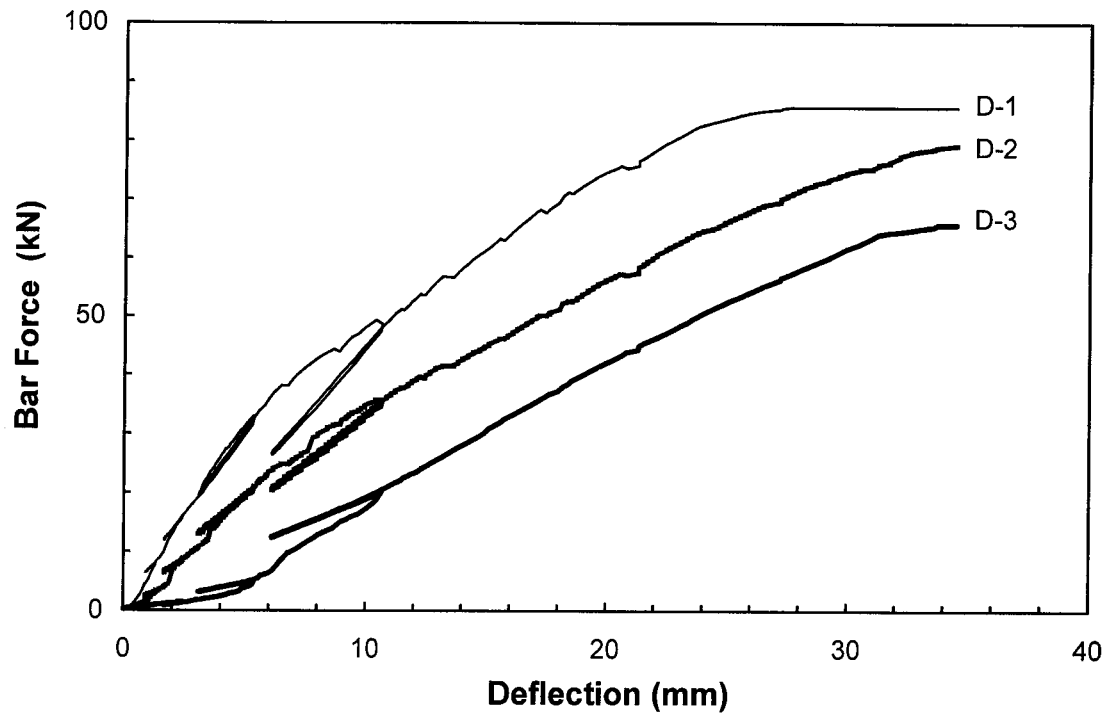
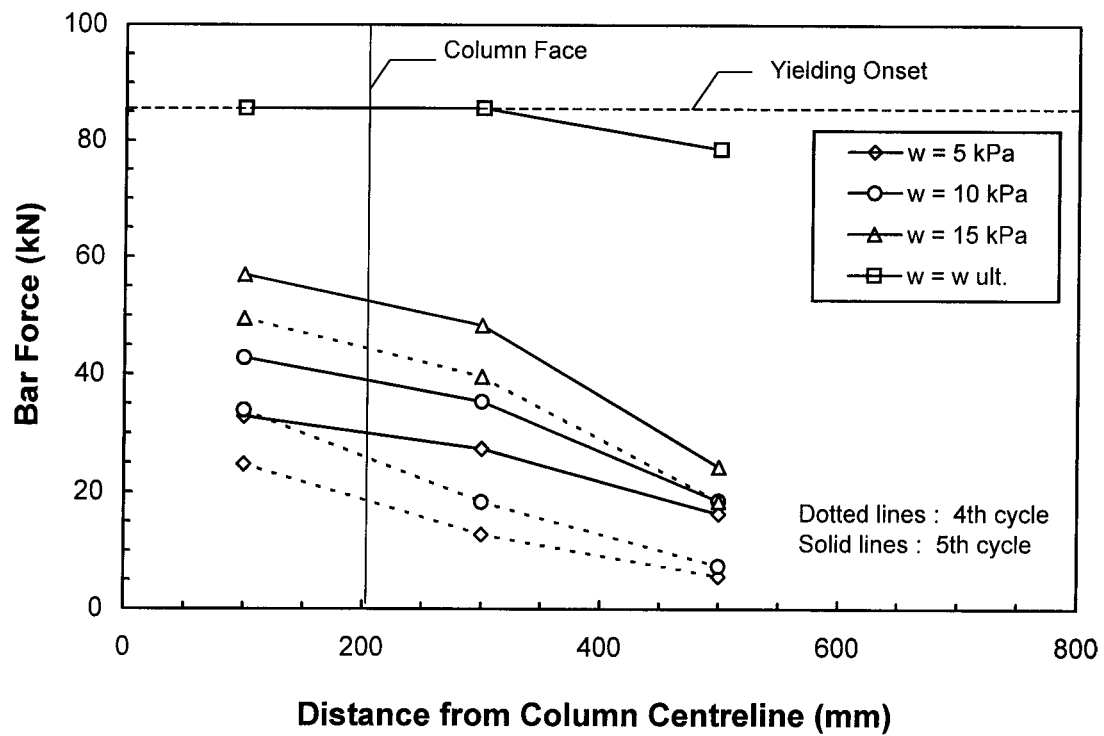


Fig. 7.31 Cracking Effect on Bar Forces : ER1-VS



**Fig. 7.32 Bar Force Variation - Bar D : ER1-VS**



**Fig. 7.33 Bar Force Profile - Bar B : ER1-VS**

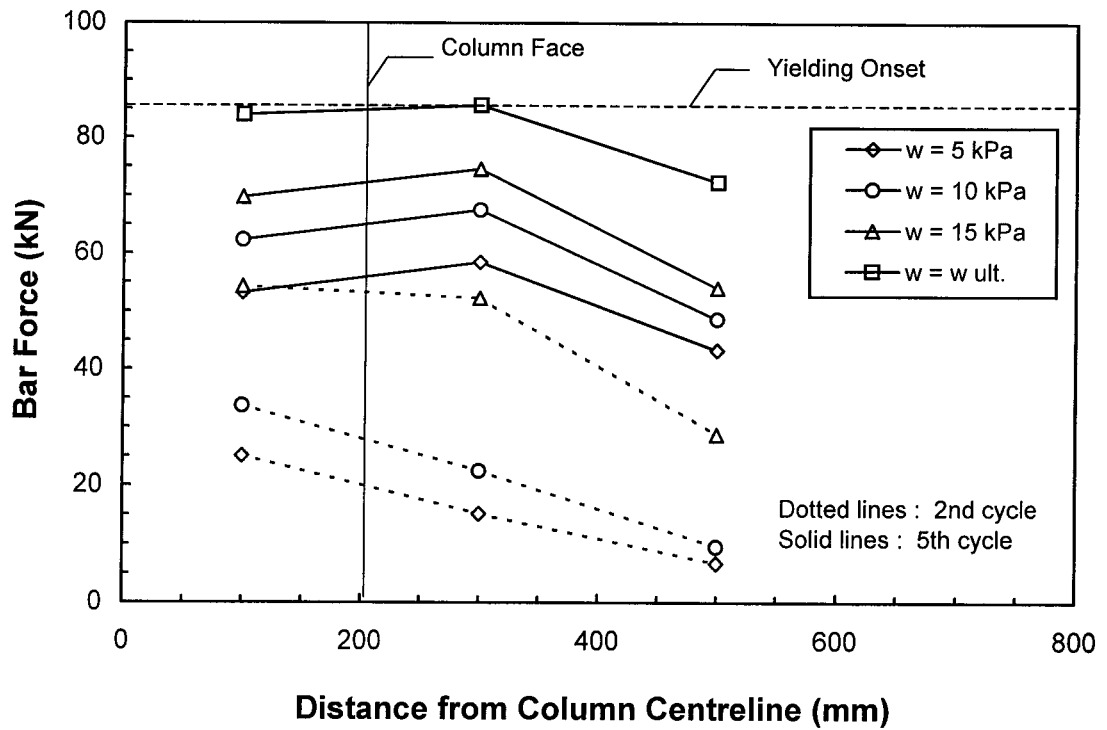


Fig. 7.34 Bar Force Profile - Bar B : ER2 Tests

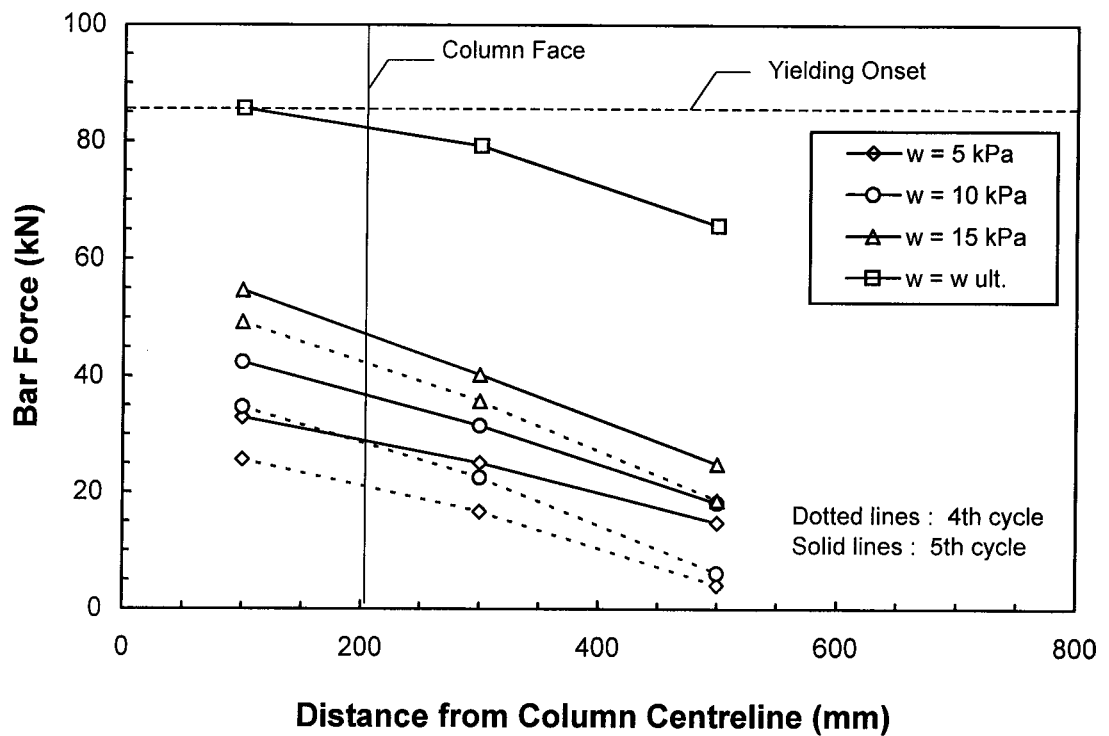


Fig. 7.35 Bar Force Profile - Bar D : ER1-VS



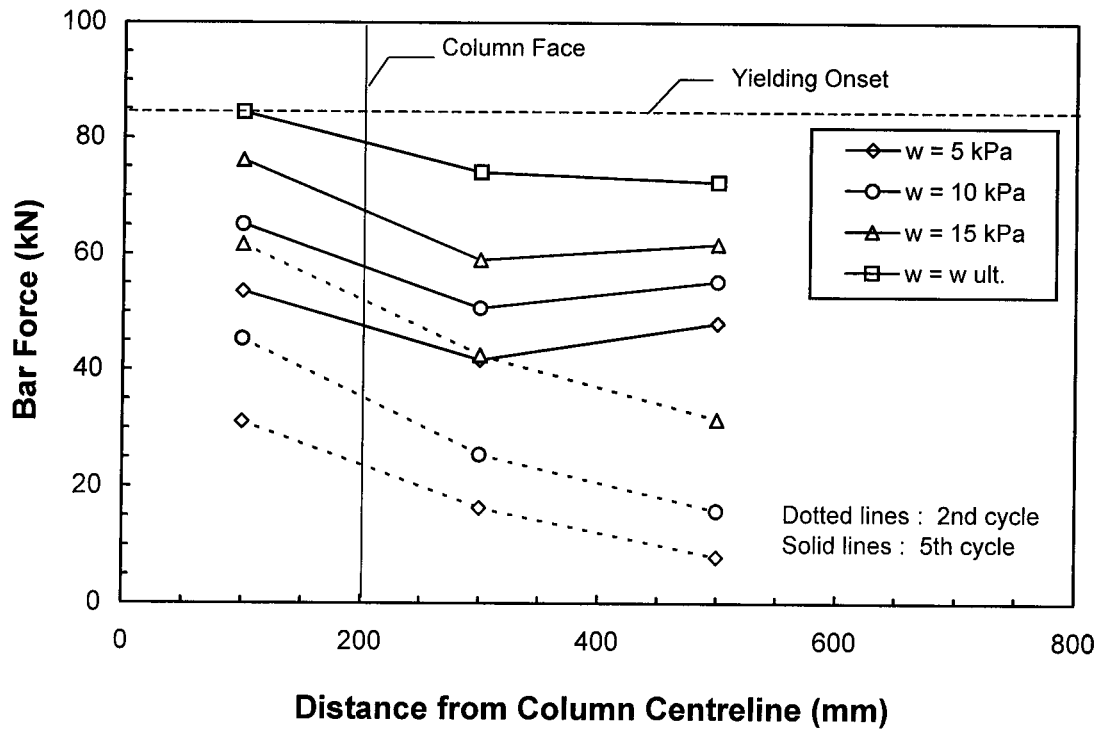


Fig. 7.36 Bar Force Profile - Bar D : ER3 Tests

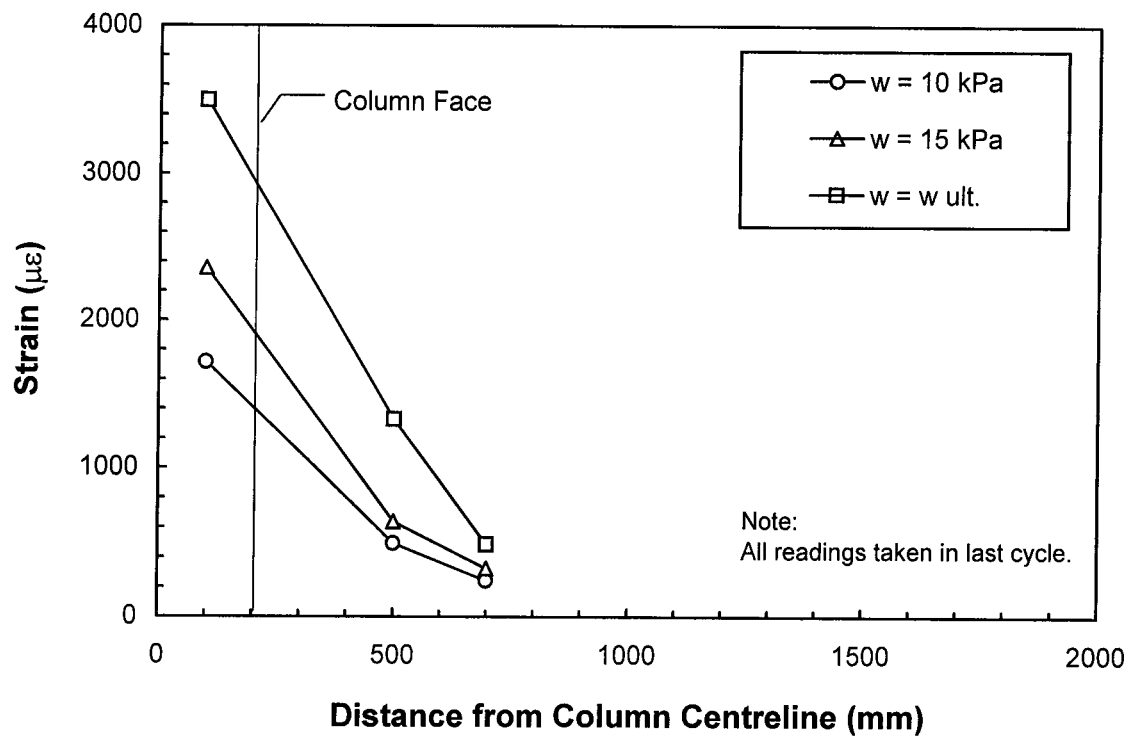


Fig. 7.37 CFRP Longitudinal Strains (Ave WE) : ER2-CS1

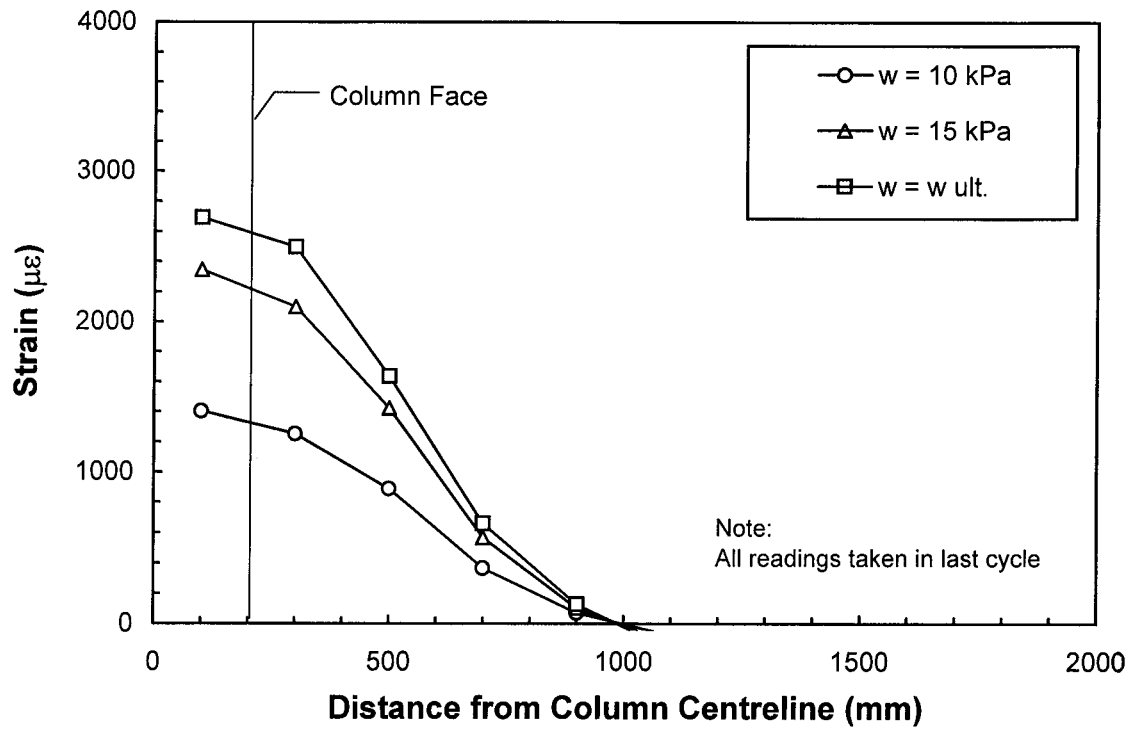


Fig. 7.38 CFRP Longitudinal Strains (WE-1) : ER3-CS2

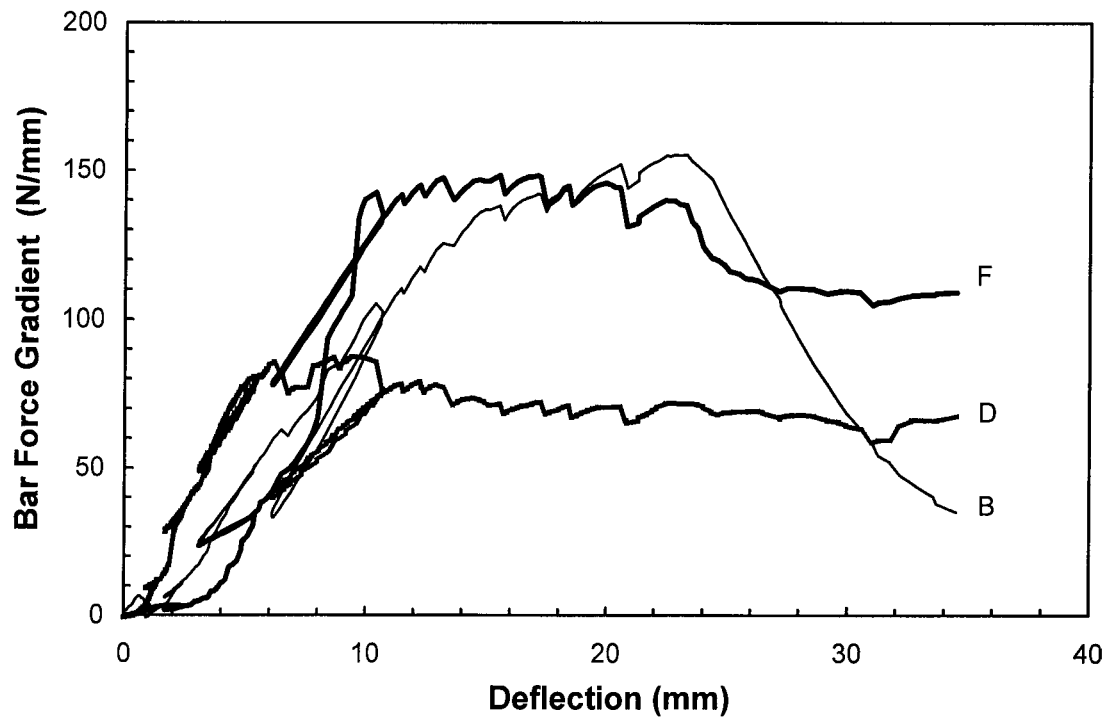
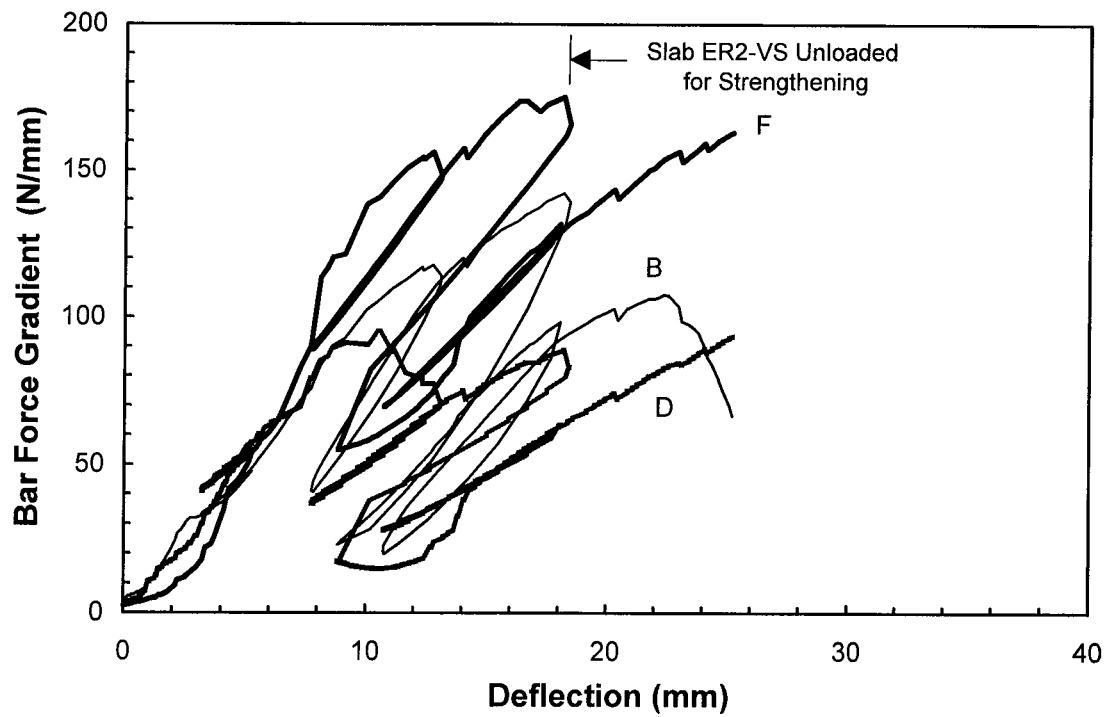
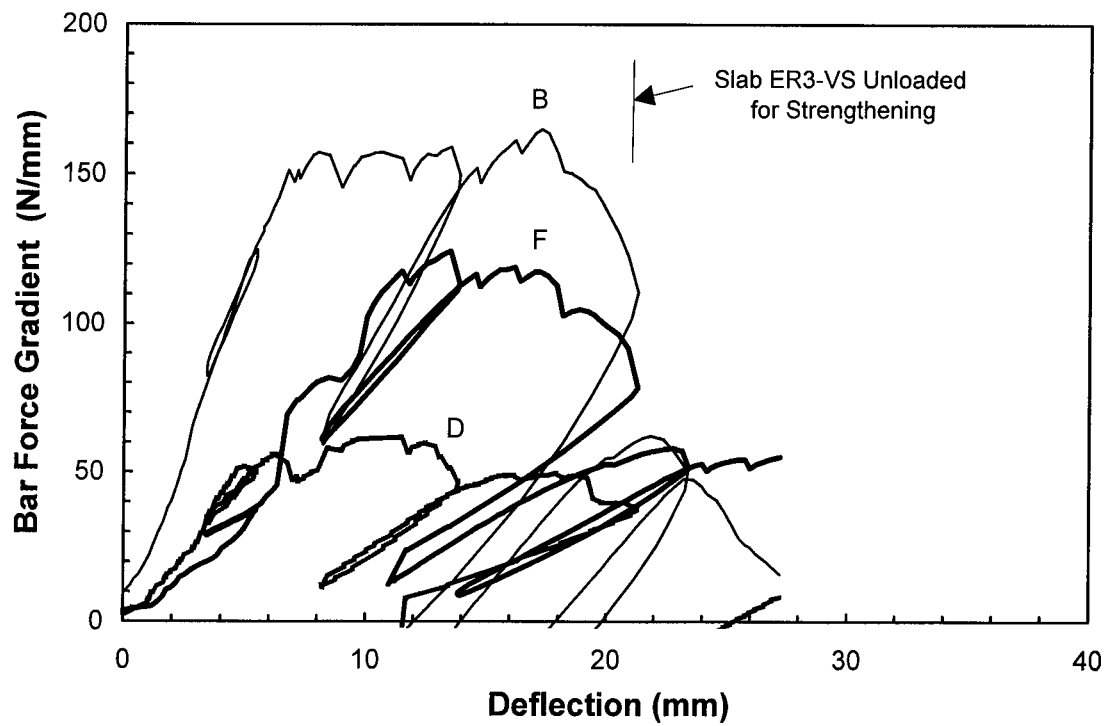


Fig. 7.39 Bar Force Gradients (2nd Interval) : ER1-VS



**Fig. 7.40 Bar Force Gradients (2nd Interval) : ER2 Tests**



**Fig. 7.41 Bar Force Gradients (2nd Interval) : ER3 Tests**

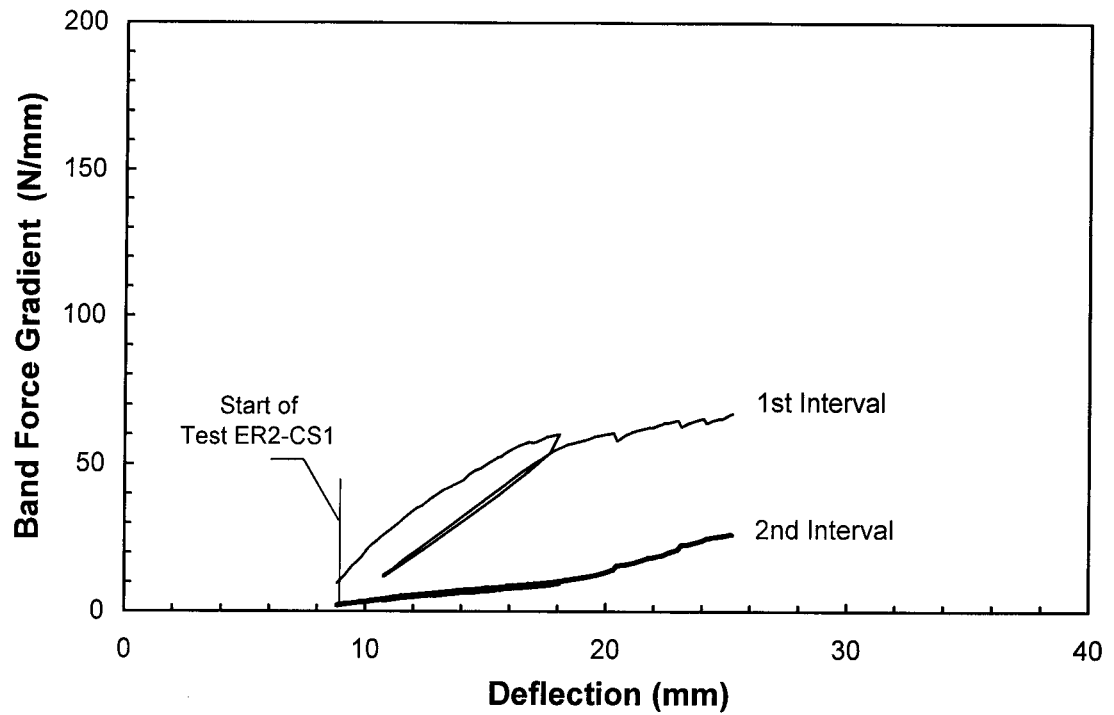


**Fig. 7.42 CFRP Force Gradients (W-E) : ER2-CS1**

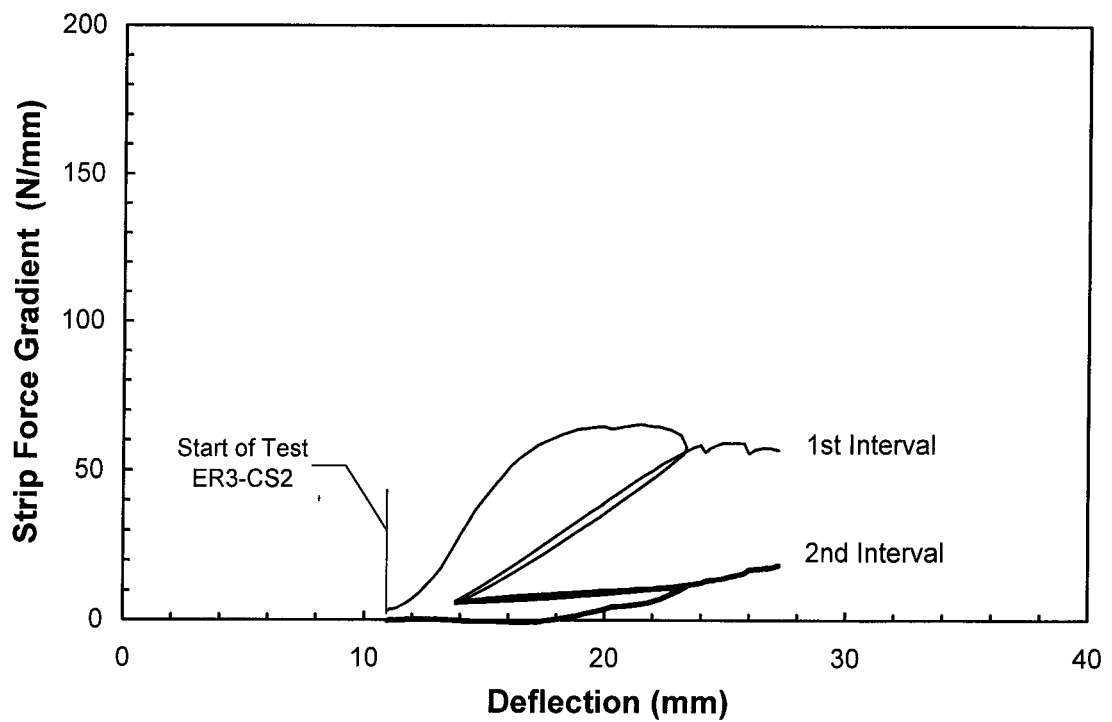


**Fig. 7.43 CFRP Force Gradients (N-S) : ER3-CS2**

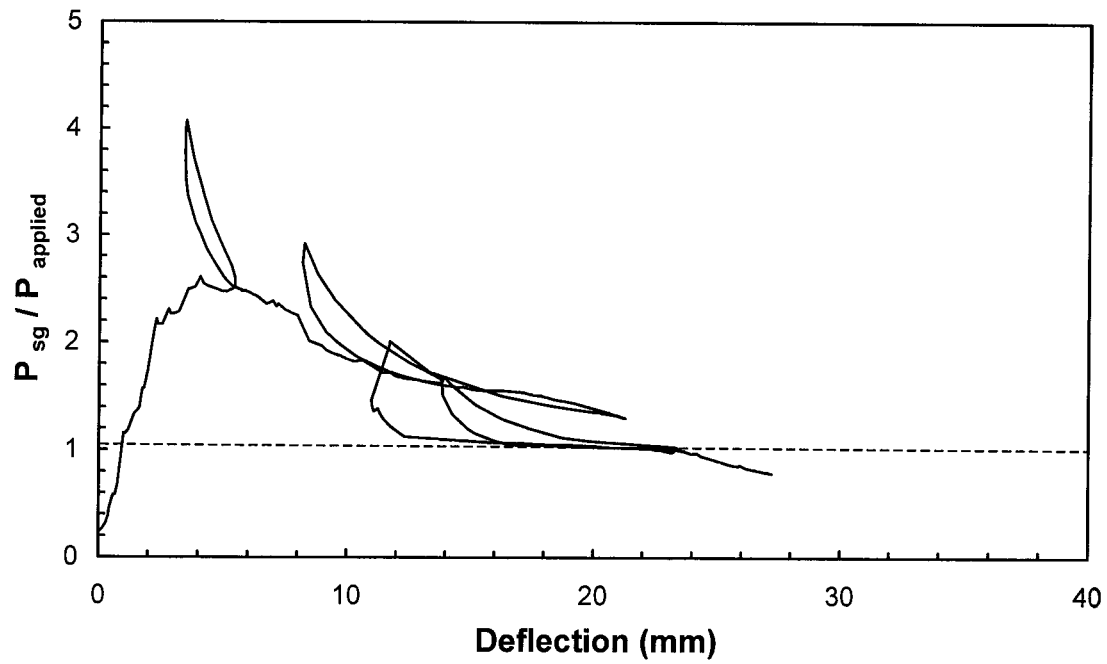


**Fig. 7.44 Ratio of Int. Measured to Total Applied Load (ER3 Tests)**

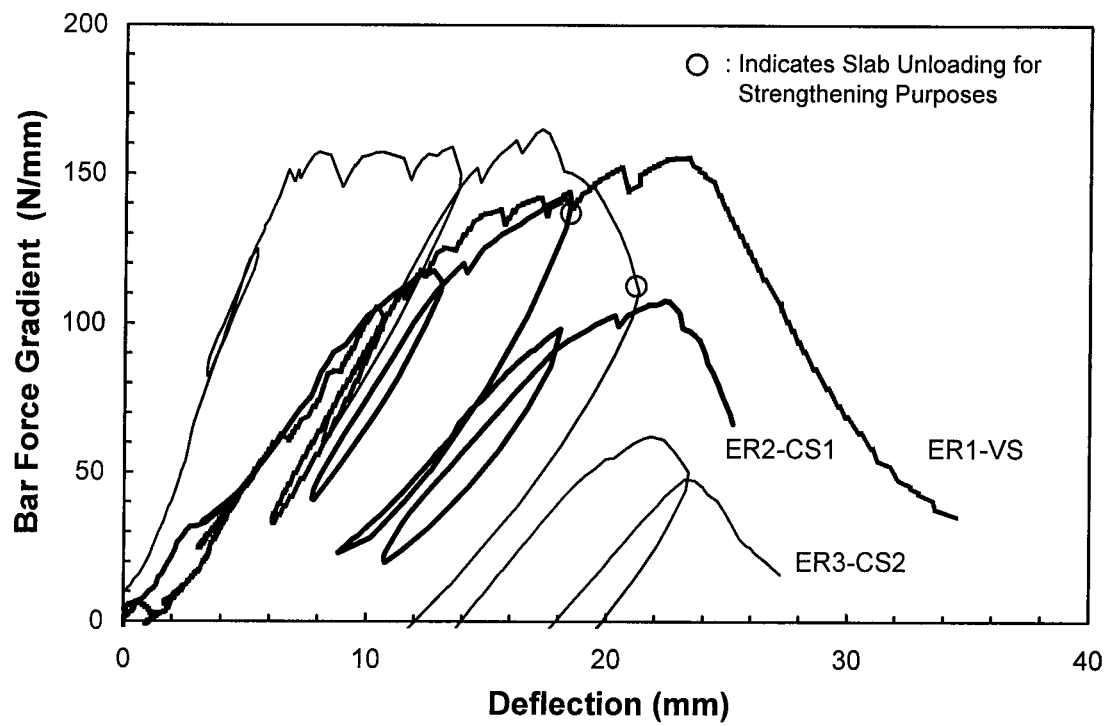


**Fig. 7.45 Bar Force Gradients (2nd Interval) - Bar B**

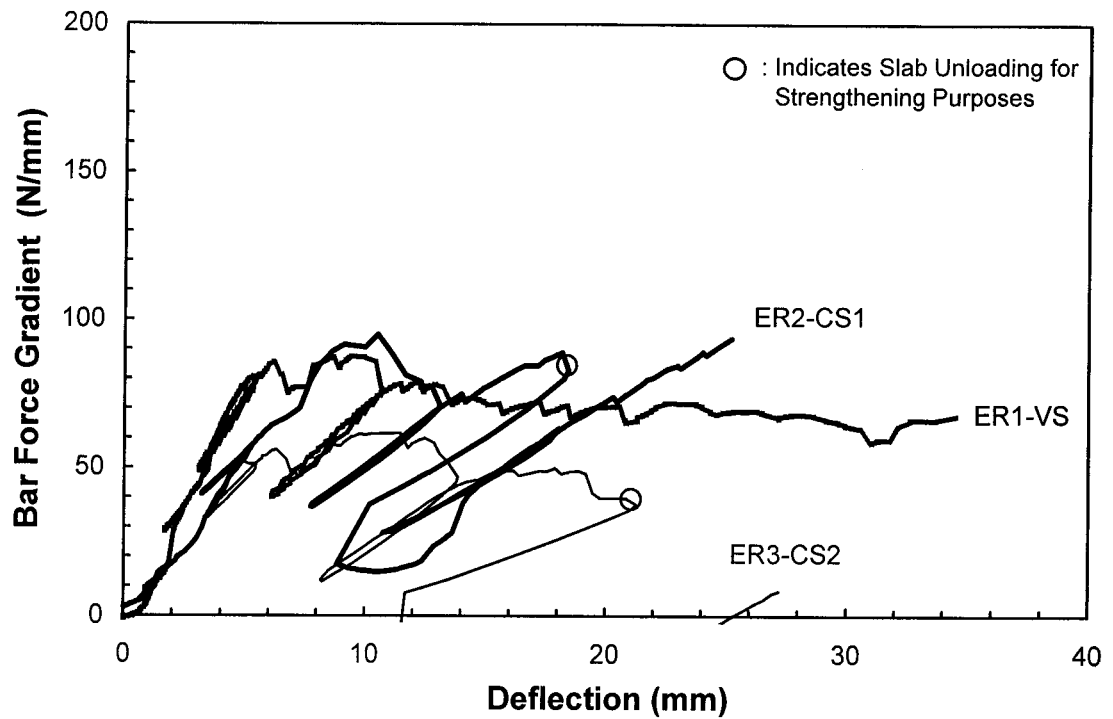


**Fig. 7.46 Bar Force Gradients (2nd Interval) : Bar D**

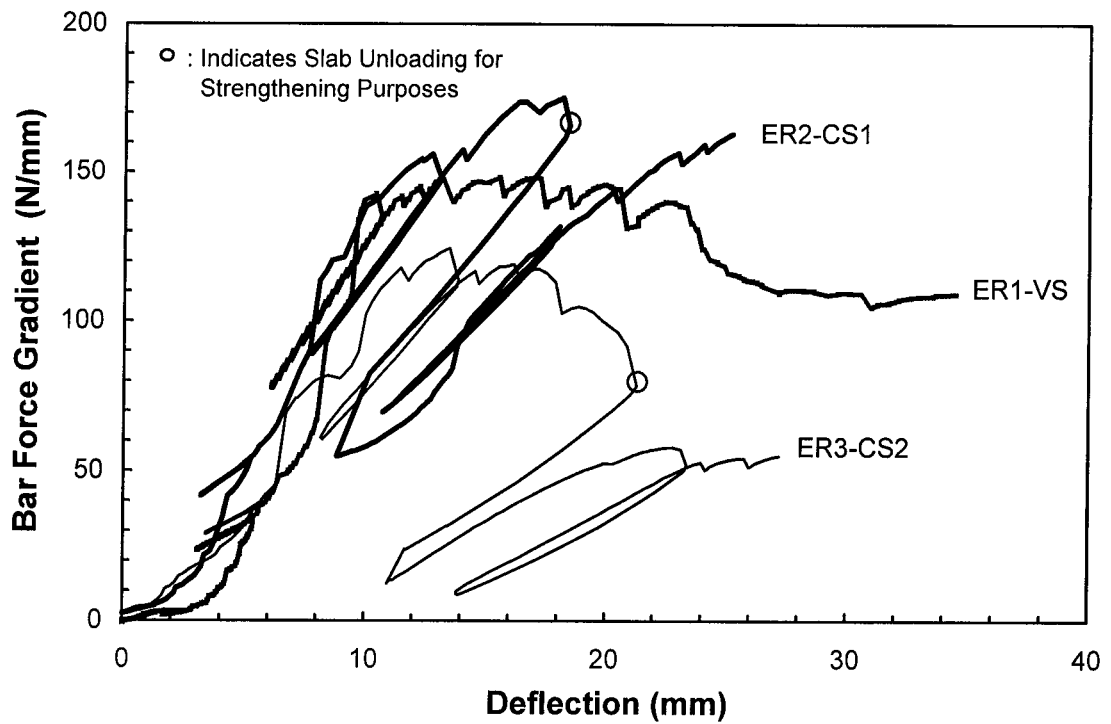


**Fig. 7.47 Bar Force Gradients (2nd Interval) : Bar F**

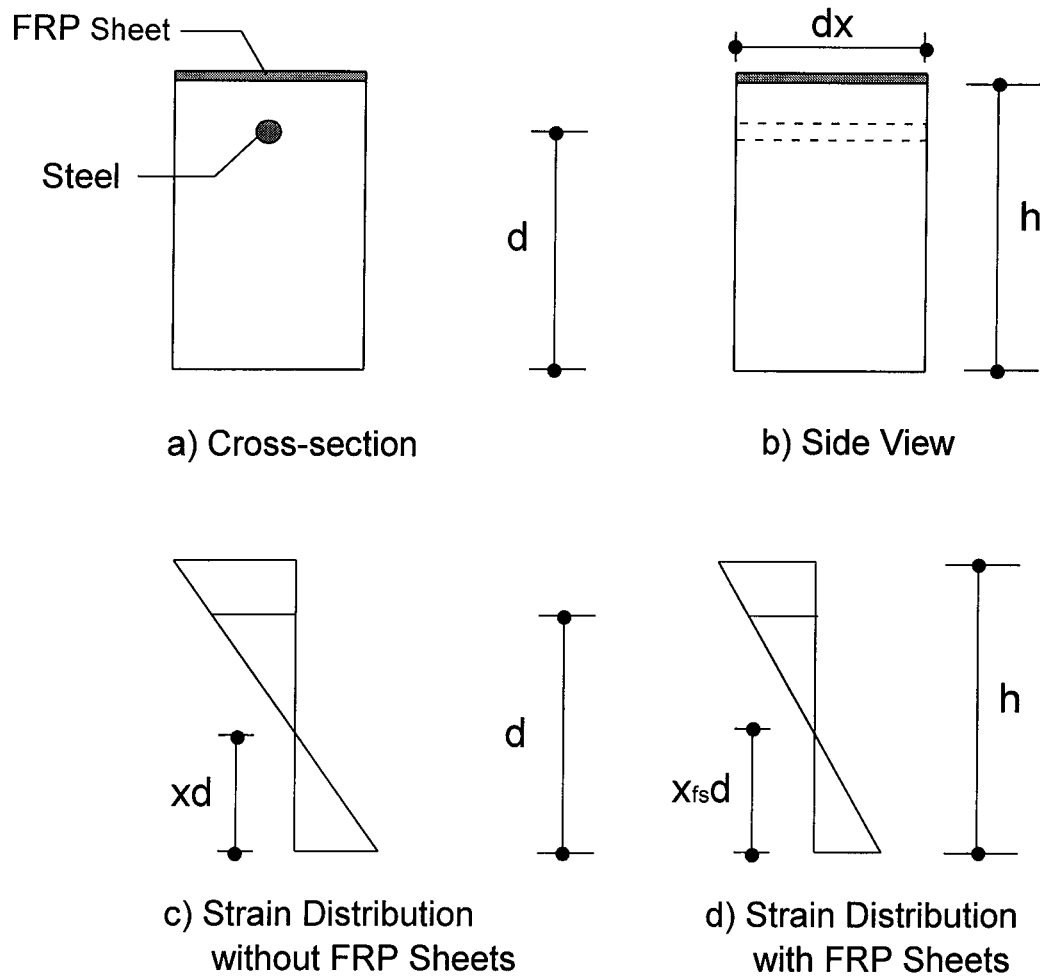
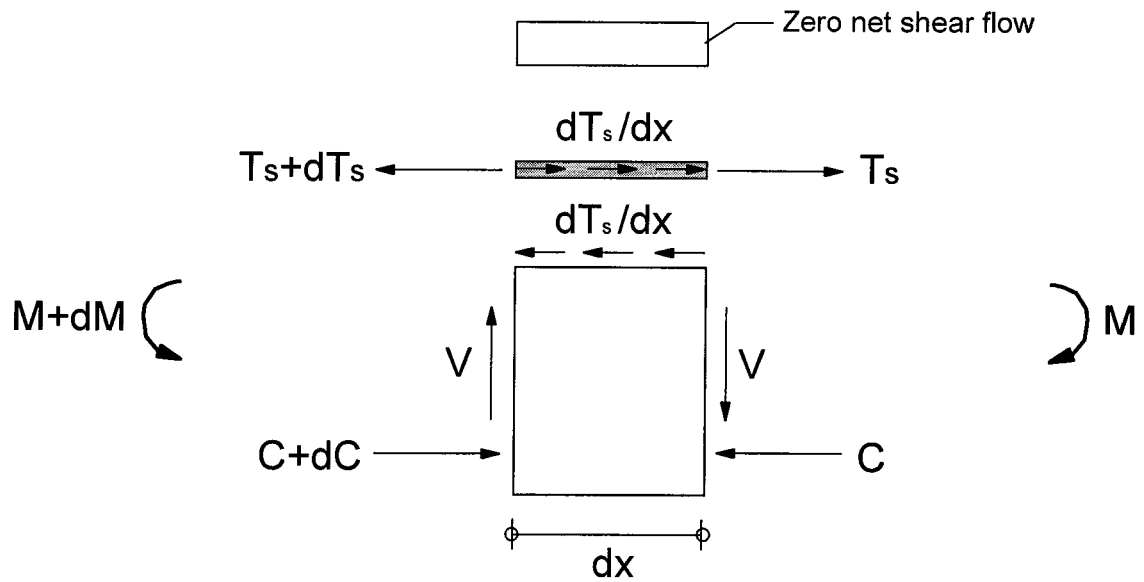
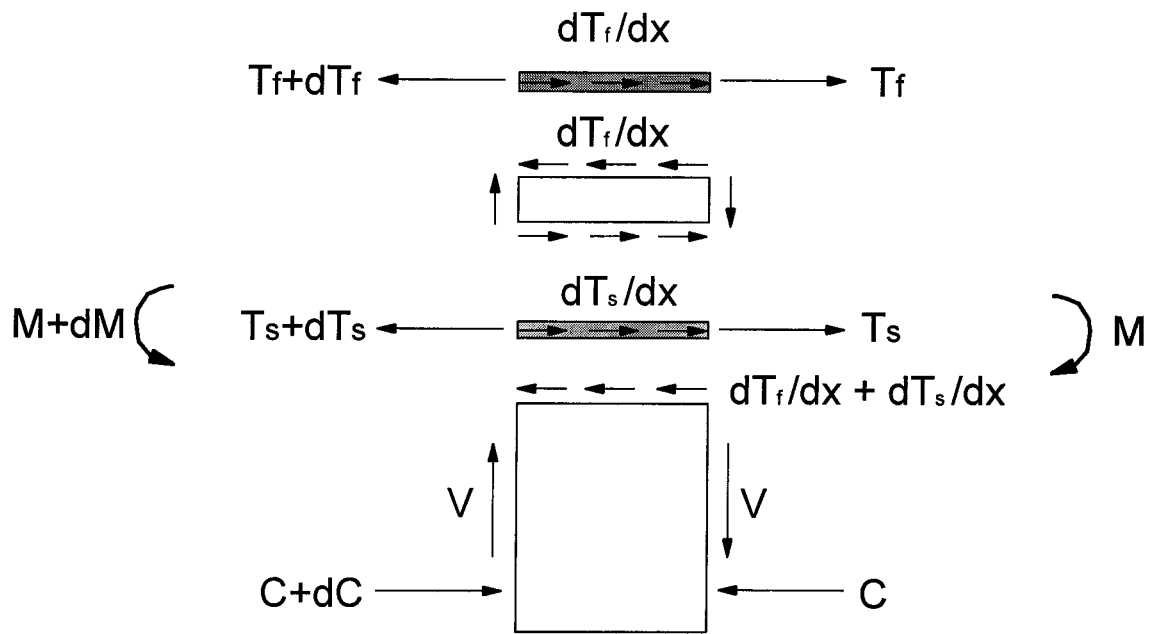


**Fig. 7.48 Strain Distributions in Slab Element with and without Bonded FRP**



a) Free Body Diagram : Section Without Bonded FRP



b) Free Body Diagram : Section with Bonded FRP

**Fig. 7.49 FBDs for Sections with and without FRP Sheets**



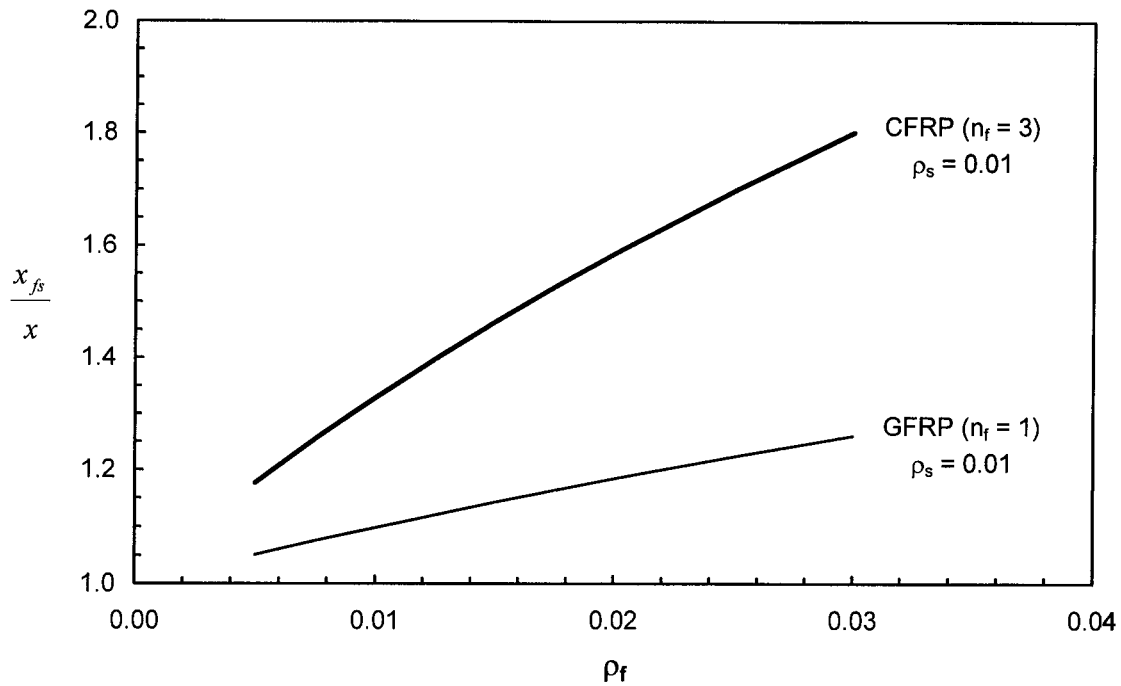
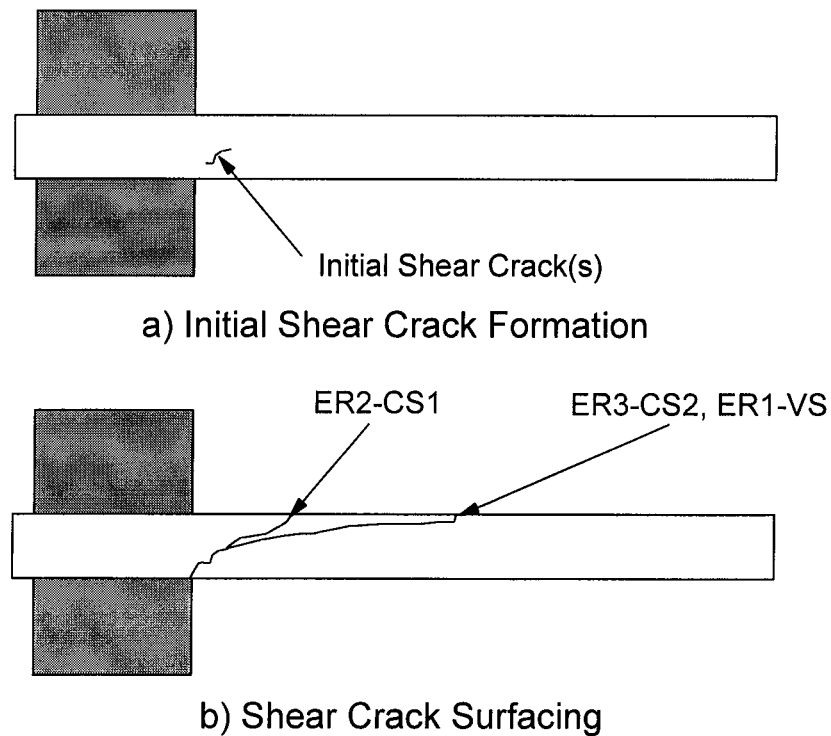


**Fig. 7.50 Influence of Reinf. Amount and Type on  $x_{fs}$  Effect**



Note: Additional Slab cracks have been omitted.

**Fig. 7.51 Shear Crack Development Hypothesis**

## 8 Evaluation of the Serviceability Flexural Behaviour of Concrete Slabs with Internal FRP Reinforcement

### 8.1 Objectives

The implications on the serviceability behaviour of slabs with FRP brought about by the lower stiffness, brittle-elastic nature and specific bond features of FRP reinforcement are felt both globally and locally. Globally, they affect the overall load-deflection response of the member. Locally, they influence concrete's ability to shed tension, thereby modifying the relationships among crack widths, FRP strains at cracks and average FRP strains.

The literature survey of chapter 3 showed that research on “global” effects has received much more attention than that on “local” effects. As a result, very comprehensive research studies evaluating “mean” strains and “mean” curvatures to calculate deflections have been produced (see for instance Hall, 2000). Conversely, studies evaluating the effect of FRP's distinctive properties on the relationship between crack widths and strains at cracks are scarce. This is important because, due to the tendency of commercial GFRP reinforcement to creep rupture, it is essential to keep FRP strains within safe limits. The major objective of this chapter is to examine these effects by using a mechanical model that treats the tension stiffening effect of concrete by explicitly accounting for FRP's relevant properties.

In the tension stiffening model of CEB/FIP MC90, which is considered one of the best tools to evaluate average strains to calculate deflections, the factor  $\beta = \beta_1\beta_2$  represents a whole set of influencing variables under a single number. The concept is practical and works effectively for deflection calculations but does not explicitly handle the effect of FRP amount and elastic modulus. One simple tool that accounts comprehensively for these effects is the tension chord model formulation developed by Marti *et al* (1998).

The development of a design procedure to calculate deflections in FRP-reinforced concrete members is not a major objective of this chapter. However, a simple design

model will be presented to corroborate the importance of accounting for concrete's tension stiffening effect in deflection calculations.

The study will be restricted to FRP-reinforced concrete slabs subjected to imposed monotonic short-term loads. Most of the attention will concentrate on slabs reinforced with GFRP C-bars and NEFMAC grids along the stabilised cracking stage. Influential aspects such as flexural bond between FRP and concrete, and the tension stiffening effect of concrete in members with internal FRP reinforcement will be examined before applying the tension chord model and the deflection calculation procedure.

## **8.2 Flexural Bond in FRP-reinforced Concrete Members**

The term “flexural bond” refers to those stresses that develop along the interface between the reinforcement and concrete for a force gradient to be generated by the reinforcement. The literature survey of chapter 3 revealed that despite the availability of numerous studies on bond of FRP to concrete, there is limited information on flexural bond of FRP to concrete.

The most reliable procedure to obtain realistic flexural bond stress estimates is the flexural or shear test of a one-way slender member. Since the amount of one-way shear generated by beam action is proportional to the flexural bond, the latter can be evaluated by measuring the tensile force variation in the reinforcement along the shear spans.

The experimental results from series I slabs provide valuable information on the ability of GFRP reinforcement to generate bar force gradients. The peak bar force gradients generated by the GFRP C-bars (slab GFR-1) and NEFMAC ribs (slab NEF-1) for fully cracked slab conditions is in the order of 100 to 115 N/mm. Since the reinforcement spacing in these slabs was 200 mm, a peak gradient of 115 N/mm results in an average horizontal shear stress of  $115/200 = 0.58$  MPa.

In the steel-reinforced slab (SR-1), the peak force gradient was about 150 N/mm for the perimeter bars. This value is less than the 200 N/mm peak force gradient reported by

Alexander *et al* (1995) from tests on two-way slabs with steel bars of similar diameter spaced at 150 mm, and the 200 to 250 N/mm peak gradients reported by Olonisakin and Alexander (1998) from tests on one-way slabs with steel bars spaced at 150 mm. A force gradient varying from 150 to 250 N/mm for steel bars spaced at 200 mm is equivalent to an average horizontal shear stress ranging from 0.75 to 1.25 MPa, respectively. For a 150 mm spacing, the 200 N/mm gradient is equivalent to an average shear stress of 1.33 MPa. These values are about twice those measured in slabs GFR-1 and NEF-1.

As a result, one can infer that flexural bond of GFRP is about half of that of steel reinforcing bars. The 50 % reduction is qualitatively consistent with Hall's assumption that using  $\beta = 0.5$  in the CEB/FIP MC90 tension stiffening model leads to accurate deflection predictions for slabs with FRP. The reduction is also similar to that observed in the hinged beam bond tests conducted by Benmokrane *et al* (1996).

In the context of steel-reinforced concrete members, Marti *et al* (1998) note that the exact bond-slip response of the reinforcement is not necessary as long as resulting stresses and member strains reflect governing influences and agree with experimental evidence. For simplicity, it will be assumed a rigid-perfectly plastic bond-slip relationship of the form

$$\tau_{bo} = k_{bo} f_{ctm} \quad [8.1]$$

where  $f_{ctm}$  is the mean tensile strength of concrete, which Rüsç (1975) defined as

$$f_{ctm} = 0.3(f_{cm})^{\frac{2}{3}} \quad [8.2]$$

Since CEB/FIP MC 90 uses  $k_{bo} = 1.8$  for short term loading of steel-reinforced concrete slabs,  $k_{bo} = 0.9$  is a conservative estimate for flexural bond in FRP-reinforced concrete members for first loading. When there is evidence that bond between FRP and concrete is superior than that between steel and concrete,  $k_{bo}$  may even exceed 1.8. This would be the case of some sanded deformed FRP bars.

As far as NEFMAC grids is concerned, chapter 6 test results show that the discrete bond behaviour of NEFMAC grids can be treated as equivalent as that in C-bars. For this reason, the factor  $k_{bo}$  for slabs with NEFMAC grids will be assumed to be 0.9 as well.

At this stage, there is no experimental evidence to allow a more precise definition of  $k_{bo}$  for members with GFRP C-bars or grids.

### 8.3 Concrete's Tension Stiffening Effect in Members with FRP

According to the tension chord model, the normal strain correction due to concrete's tension stiffening effect,  $\Delta\epsilon_{ts}$ , in a member with FRP subjected to direct tension is

$$\Delta\epsilon_{ts} = \frac{\lambda_f}{2} \frac{f_{ct}}{E_f} \left( \frac{1 - \rho_f}{\rho_f} \right) \quad [8.3]$$

where  $\lambda_f$  is the ratio of mean to maximum crack spacing in the member with FRP. The equation applies only to bond-induced cracks. Assuming that cracks in FRP-reinforced members distribute similarly to those in steel-reinforced members, i.e.  $\lambda_f = \lambda_s = \lambda$ , the tension stiffening effect is mostly governed by  $E_f$  and/or  $\rho_f$ . The effect of  $f_{ct}$  is not key because similar concrete strengths are used regardless of the reinforcement type.

Leaving  $\rho_f$  aside, Eq. 8.3 shows that the tension stiffening strain correction increases as  $E_f$  decreases. Due to FRP's reduced stiffness, most of the bond-induced deformations are concentrated on the FRP and not on the concrete between cracks, as observed by Nanni *et al* (1995) and in series I slabs. On the contrary, leaving  $E_f$  aside, a reduction in  $\rho_f$  leads to a proportionally greater tensile contribution from concrete. This effect is consistent with the findings of Bresler and Bertero (1968) and Masicotte *et al* (1990).

However, Eq. 8.3 shows that the combined effect of  $E_f$  and  $\rho_f$  is counteractive. A reduction in  $E_f$  (as would be the case of using FRP compared to steel) counteracts the increase in  $\rho_f$  required for FRP-reinforced slabs to satisfy the same serviceability requirements as steel-reinforced members with comparable depth.

The combined effect of these two variables is examined in Fig. 8.1. The figure shows the variation of  $\Delta\varepsilon_{ts}$  versus  $\rho$  for three slabs reinforced with steel ( $E_s = 200$  GPa), CFRP ( $E_f = 100$  GPa) and GFRP ( $E_f = 40$  GPa), assuming  $f'_c = 30$  MPa and  $\lambda = 0.67$ . The figure shows that for a given reinforcement ratio, the tension stiffening effect increases as the elastic modulus of the reinforcement reduces. However, this comparison is not adequate in the sense that, for a given slab depth, one would expect a GFRP mat to be denser than a CFRP mat and this one, in turn, to be denser than a steel mat. Consider for instance three slabs with identical cross-section and the same mat stiffness, say  $\rho E = 4000$  N/mm<sup>2</sup>. The tension stiffening evaluation needs to be made for reinforcement ratios of 0.02, 0.04 and 0.10 for the steel, CFRP and GFRP-reinforced slabs, respectively. The corresponding  $\Delta\varepsilon_{ts}$  values are about the same regardless of the reinforcement type.

However, as far as typical flat plate systems ( $h = 150$  to  $200$  mm) is concerned, it is very difficult to supply GFRP mats that are as stiff as those made of steel unless the slab depth is increased. Moreover, the GFRP spacing could be so tight that proper concrete placement is harmed. At best, GFRP-reinforced slabs will be usually provided with slightly less stiff mats. If this occurs,  $\Delta\varepsilon_{ts}$  increases relative to that for the CFRP and steel-reinforced cases. Since the tension stiffening effect of concrete is seldom neglected for a detailed calculation of deflections in steel-reinforced concrete members, it does not seem appropriate to ignore it for the case of FRP-reinforced members, in which its relevance could be significant, as shown previously.

One relevant observation on the variation of  $\Delta\varepsilon_{ts}$  is its dependency on  $\lambda$ . If the crack spacing is bond-induced, the tension chord model defines  $0.5 \leq \lambda \leq 1.0$ . This leads to a 25 % reduction or a 49 % increase in the  $\Delta\varepsilon_{ts}$  values shown in Fig. 8.1. The  $\lambda$  factor is statistical in nature and strongly depends on the variability of the material properties of the FRP reinforcement. At present, there are no existing recommendations on how to treat  $\lambda$  in the context of members with FRP reinforcement.

Without conducting a rigorous statistical analysis to assess  $\lambda$  (which would fall outside the scope of the study),  $\lambda$  can be evaluated by comparing the predicted response of FRP-reinforced concrete members with the observed overall behaviour.

Figures 8.2 and 8.3 show experimental and predicted values of crack spacing at 0.25 and 0.5  $M_u$  on selected beams with FRP tested at Université de Sherbrooke (Canada) by Masmoudi, Benmokrane and Chaallal (1996) (IS and KD Series), Thériault and Benmokrane (1998) (BC Series) and Masmoudi, Thériault and Benmokrane (1998) (CB Series). The properties of these specimens are reported in Table 8.1. The first digit in the beam labels reflects the number of bars, e.g. IS3B1 has 3 GFRP bars. Since the cross-section has been kept constant for each beam series, an increase in this number expresses a reinforcement ratio increase. Predicted maximum crack spacing values were calculated according to

$$s_{\max} = \frac{\phi_b}{2k_{bo}} \left( \frac{1 - \rho_{f,ef}}{\rho_{f,ef}} \right) \quad [8.4]$$

The  $\rho_{f,ef}$  value refers to the effective reinforcement ratio in the tension zone of the flexural member whose geometry is defined in Fig. 3.6. In the calculations,  $k_{bo}$  was taken equal to 0.9. The minimum crack spacing,  $s_{\min}$ , is half that estimated with Eq. 8.4. The flexural depth of the members and the stirrup spacing in the beams are also reported as these variables may influence the crack spacing (Base, 1982).

The most striking feature of Figs. 8.2 and 8.3 is that the observed  $s_m$  values are relatively constant compared to the significant variation in the predicted  $s_{\max}$  and  $s_{\min}$  values according to the model. In the KD and IS beam series, the  $s_m$  values are very close to the flexural depth of the beams whereas those in the BC and CB beams are very close to the stirrup spacing. The former sort of behaviour is what Base (1982) refers to as "deformation-controlled" cracking. These cracks result from the beams accommodating the imposed deformations. Their spacing is not controlled by the bond interaction between FRP and concrete. In the second case, the cracks are initiated by a combination of the "disturbing" stirrups's presence and a low concrete cover. For instance, in beam

CB2B-1, the observed  $s_m$  is about half the value that the tension chord formulation would predict for  $s_{min}$ . This crack could not have been caused by any accumulation whatsoever of tensile stresses in between preexisting bounding cracks.

The observation that the crack spacing is not always driven by bond has important implications on the evaluation of stresses and strains in a cracked member using the tension chord model. Under these conditions, the  $\lambda$  concept lacks meaning because the crack spacing is now a constrained value,  $s_{m,c}$ , of deterministic nature.

In this case, dividing Eq. B.23 by the elastic modulus of FRP, leads to

$$\varepsilon_{rr} = \varepsilon_{rm} + \Delta\varepsilon_{ts,c} = \varepsilon_{rm} + \frac{\tau_{bo} s_{m,c}}{\phi_b E_f} \quad [8.5]$$

where  $\Delta\varepsilon_{ts,c}$  is the normal strain correction due to concrete's tension stiffening effect for crack spacing constrained by issues other than bond.

## 8.4 Prediction of the Overall Flexural Response of Slabs with FRP

This section presents a simple model to predict the moment-curvature response of flexural members reinforced with FRP rebars or grids, accounting for concrete's tension stiffening effect in the post-cracking stage. The model makes use of the second moment-area theorem to predict the load-deflection response of beams and slabs subjected to four point bending. The approach is conceptually similar to that envisaged by Razaqpur *et al* (2000) and Yost *et al* (2001) except that the tension stiffening effect of concrete is explicitly accounted for in the post-cracking stage.

The model was conceived to be applied without the use of a spreadsheet or a computer. It has the following limitations: i) it is not able to describe concrete's plastic behaviour, ii) it does not model the slippage of the reinforcement relative to concrete, and iii) it does not realistically model the tension stiffening effect at load levels much greater than those at typical service conditions. These drawbacks are minimal because the model is conceived to predict deflections at service load levels. At this level, concrete usually



behaves elastically, rebar slippage is minimal and concrete's tension stiffening effect is highest.

The predicted response is idealised by determining key points in the moment-curvature response. Path 0-1-2-3 in Fig. 8.4 shows the idealised moment-curvature ( $M-\psi$ ) response of a flexural member in the uncracked (State I: 0-1), crack formation (1-2), and stabilised cracking (State II: 2-3) stages. Path 0-3' represents the response of the naked FRP reinforcement.

The prediction of the  $M-\psi$  curve depends mostly on the location of points 1 and 3. Point 3 is located from 3' after quantifying  $\Delta\epsilon_{ts}$  depending on whether the crack spacing is bond-induced or not. Point 2 is located by drawing a line parallel to 0-3' until intersecting a horizontal line passing through 1. The slope of line 2-3 is assumed constant for two reasons: i) at low load levels the neutral axis in beams with internal FRP reinforcement remains relatively constant, as noted by Nanni (1993), Benmokrane *et al* (1996) and Thériault and Benmokrane (1998), and ii) to be consistent with the assumption of using a rigid-perfectly plastic bond-slip constitutive relationship for FRP.

Point 1 is located by defining the cracking moment,  $M_{cr}$ , and the curvature at first flexural cracking,  $\psi_{cr}$ . From the strain diagram of Fig. 8.5a,

$$\psi_{cr} = \frac{2f_r}{hE_c} \quad [8.6]$$

where  $f_r$  and  $E_c$  are concrete's modulus of rupture and elastic modulus, respectively. Based on the findings of Masmoudi *et al* (1998),  $M_{cr}$  in members with FRP can also be calculated as

$$M_{cr} = \frac{f_r b h^2}{6} \quad [8.7]$$

The slope of the  $M-\psi$  curve along phase 0-1 (state I) is  $E_c I_g$ , where  $I_g$  is the gross moment of inertia, calculated according to CSA A23.3-94 or ACI 318-99. In state I,

CEB/FIP MC90 evaluates a moment of inertia,  $I_t$ , accounting for the steel contribution. Since the stiffness of most FRP slab reinforcements is similar to that of concrete, it is reasonable to assume  $I_g = I_t$ .

Point 3' is located based on the governing failure mode. Unlike conventional steel-reinforced concrete members, compression failures are preferred in members with FRP to satisfy serviceability requirements, particularly for rectangular cross-sections. Over-reinforced T-beams are impractical in the positive moment regions.

Theoretical strain distributions at ultimate for flexural failure due to concrete crushing and FRP rupture according to CSA S806-00 are shown in Figs. 8.5b and 8.5c, respectively. These distributions are slightly different from those adopted by the proposed model, shown in Fig. 8.6. In the latter, the neutral axis depth has been assumed constant through the cracked-elastic stage.

According to CSA S806-00, the ultimate curvature in over-reinforced flexural concrete members is calculated as

$$\psi_u = \frac{\varepsilon_{cu}}{c} = \frac{\varepsilon_f}{d - c} \quad [8.8]$$

where  $\varepsilon_{cu}$  is the concrete compressive strain, equal to 0.0035,  $\varepsilon_f$  is the FRP strain at ultimate,  $c$  is the neutral axis depth at ultimate,  $c = a/\beta_1$ , where  $a$  is the depth of the compressive stress block, and  $\beta_1$  is a stress block factor, defined as in CSA A23.3-94.

The factored moment resistance,  $M_f$ , is

$$M_f = C_f \left( d - \frac{a}{2} \right) = T_f \left( d - \frac{a}{2} \right) = A_f \phi_f f_f \left( d - \frac{a}{2} \right) \quad [8.9]$$

The depth of the compressive stress block,  $a$ , can be solved from the quadratic

$$\left( \frac{\alpha_1 \phi_c f'_c}{\rho_f \phi_f E_f \varepsilon_{cu}} \right) a^2 + da - \beta_1 d^2 = 0 \quad [8.10]$$

which results in

$$a = \frac{\phi_f \rho_f E_f \varepsilon_{cu} d}{2 \phi_c \alpha_1 f'_c} \left( \sqrt{1 + \frac{4 \alpha_1 \beta_1 \phi_c f'_c}{\phi_f \rho_f E_f \varepsilon_{cu}}} - 1 \right) \quad [8.11]$$

From equilibrium of forces,

$$a = \frac{\rho_f d \phi_f f_f}{\alpha_1 \phi_c f'_c} \quad [8.12]$$

Equating Eqs. 8.11 and 8.12, the stress in the FRP reinforcement at failure,  $f_f$ , is

$$f_f = \left[ \frac{E_f \varepsilon_{cu}}{2} \sqrt{1 + \frac{4 \alpha_1 \beta_1 \phi_c f'_c}{\rho_f \phi_f E_f \varepsilon_{cu}}} - 1 \right] \quad [8.13]$$

In the proposed model, the curvature at ultimate for over-reinforced slabs with FRP is

$$\psi_u = \frac{\varepsilon_{cu}}{xd} \quad [8.14]$$

where  $\varepsilon_{cu}$  is the concrete compressive strain at ultimate and  $xd$  is the depth of the neutral axis assuming elastic-cracked conditions. The ratio  $x$  is given as

$$x = \sqrt{(n \rho_f)^2 + 2 n \rho_f} - n \rho_f \quad [8.15]$$

The ultimate moment,  $M_u$ , i.e., that at point 3', is

$$M_u = C \left( d - \frac{xd}{3} \right) = T \left( d - \frac{xd}{3} \right) = A_f f_f \left( d - \frac{xd}{3} \right) \quad [8.16]$$

From strain compatibility and invoking Hooke's law, the FRP stress at ultimate in a compression-type flexural failure is

$$f_f = E_f \varepsilon_f = E_f \varepsilon_{cu} \left( \frac{1-x}{x} \right) \quad [8.17]$$

For under-reinforced sections, the curvature at ultimate according to CSA S806-00 is

$$\psi_u = \frac{\varepsilon_{fu}}{d - c} \quad [8.18]$$

where  $\varepsilon_{fu}$  is the rupture FRP strain. In limit state design format, the factored moment resistance,  $M_f$ , for under-reinforced conditions is

$$M_f = T_f \left( d - \frac{a}{2} \right) = A_f \phi_f f_{fu} \left( d - \frac{a}{2} \right) \quad [8.19]$$

$$\text{with } a = \frac{\rho_f d \phi_f f_{fu}}{\alpha_1 \phi_c f'_c} \quad [8.20]$$

In the proposed model, the ultimate moment,  $M_u$ , is

$$M_u = T \left( d - \frac{xd}{3} \right) = A_f f_{fu} d \left( 1 - \frac{x}{3} \right) \quad [8.21]$$

The slope of line 0-3' defines the cracked flexural stiffness,  $EI_{cr}$ ,

$$E_c I_{cr} = \rho_f b d^3 E_f \left( 1 - \frac{x}{3} \right) (1 - x) \quad [8.22]$$

Accordingly, the curvature at ultimate can be obtained as

$$\psi_u = \frac{M_u}{\zeta \rho_f b d^3} \quad [8.23]$$

$$\text{where } \zeta = \frac{E_c I_{cr}}{\rho_f b d^3} \quad [8.24]$$

Figure 8.7 shows values of  $\zeta$  as a function of  $\rho_f$  and  $E_f$ .

To locate point 3 it is necessary to evaluate the curvature correction due to concrete's tension stiffening effect,  $\Delta\psi_{ts}$ . Figure 8.8 shows the strain distribution of a cross-section under bending action. Dotted and solid lines correspond to the strain distributions of the naked FRP and the FRP-reinforced member, respectively. The strain and curvature

difference between the naked FRP and the overall member shows the effect of concrete tension stiffening. Since the strain in the compression zone is hardly influenced by the tension stiffening effect (Walraven, 2000), for small deformations the curvature correction due to tension stiffening under flexural conditions is

$$\Delta\psi_{ts} = \frac{\Delta\epsilon_{ts}}{d} \quad [8.25]$$

For crack spacing induced by bond,

$$\Delta\psi_{ts} = \frac{\lambda}{2} \frac{f_{ct}}{E_f d} \left( \frac{1 - \rho_{f,ef}}{\rho_{f,ef}} \right) \quad [8.26]$$

where  $\rho_{f,ef}$  is the effective FRP reinforcement ratio, calculated with respect to the effective concrete area in tension.

For crack spacing not induced by bond,

$$\Delta\psi_{ts} = \frac{\tau_{bo} s_m}{\phi_b E_f d} \quad [8.27]$$

The load-deflection response can be predicted by applying the second moment-area theorem. The effect of shear deformations will be disregarded. Figure 8.9 shows the assumed curvature distribution in a beam or slab loaded in four point bending. As in Razaqpur *et al* (2000) and Yost *et al* (2001), the model assumes that the shear span is cracked. The dashed line represents the response of the naked FRP. The solid line represents the proposed curvature distribution. The distance  $x_{cr}$  is calculated as

$$x_{cr} = \frac{2M_{cr}}{P} = \frac{M_{cr} a_v}{M} \quad [8.28]$$

where  $P$  is the total applied load on the beam,  $a_v$  is the shear span, and  $M$  is the bending moment at midspan at a given load level. The curvature at first flexural cracking is

$$\psi_{cr} = \frac{M_{cr}}{E_c I_g} \quad [8.29]$$

and

$$\psi_2 = \frac{M_{cr}}{EI_{cr}} - \Delta\psi_{ts} \quad [8.30]$$

with  $\Delta\psi_{ts}$  evaluated using either Eq. 8.26 or 8.27. The curvature at ultimate,  $\psi_u$ , is calculated using Eqs. 8.23 and 8.24.

The resulting load-deflection response is shown in Fig. 8.10. The total load at first flexural cracking,  $P_{cr}$ , and the deflections  $\Delta_{cr}$  and  $\Delta_2$  are, respectively,

$$P_{cr} = \frac{2M_{cr}}{a_v} \quad [8.31]$$

$$\Delta_{cr} = \frac{\psi_{cr}}{24} (3L^2 - 4a_v) \quad [8.32]$$

$$\Delta_2 = \frac{\psi_{cr}a_v^2}{3} + \frac{1}{2} \left( \frac{M_{cr}}{E_c I_{cr}} - \Delta\psi_{ts} \right) \left( \frac{L}{2} - a_v \right)^2 \quad [8.33]$$

At ultimate,

$$P_u = \frac{2M_u}{a_v} \quad [8.34]$$

$$\begin{aligned} \Delta_u = & \frac{1}{3} \frac{M_{cr}}{E_c I_g} x_{cr}^2 + \frac{M_{cr}}{6E_c I_{cr}} (a_v^2 + a_v x_{cr} - 2x_{cr}^2) + \frac{\Delta\psi_{ts}}{2} \left( x_{cr}^2 - \frac{L^2}{4} \right) \\ & + \frac{\psi_u}{6} \left( \frac{3}{4} L^2 - a_v^2 - a_v x_{cr} - x_{cr}^2 \right) \end{aligned} \quad [8.35]$$

#### 8.4.1 Application of the Overall Response Flexural Model

Figures 8.11 to 8.13 compare the predicted and observed response of beams TB BC2VA and TB BC4NA tested by Thériault and Benmokrane (1998), and one-way slab MT C3 tested by Matthys and Taerwe (2000). The former were reinforced with GFRP C-bars whereas the latter was reinforced with a CFRP NEFMAC grid. The specimens, designed

to exhibit a compressive flexural failure, failed as expected. Ultimate load predictions were made assuming  $\epsilon_{cu} = 0.0035$  mm/mm. Since the deflection procedure is very sensitive to  $M_{cr}$ , the predictions were made based on the experimental  $M_{cr}$  values. For the case of BC2VA and BC4NA, it was assumed that the crack spacing was not induced by bond. The curvature correction for these two slabs was calculated assuming a “constrained” crack spacing,  $s_{m,cs}$  of 80 and 90 mm, respectively, with  $k_{bo} = 0.9$ . Matthys and Taerwe (2000) reported that the crack spacing in slab C-3 (as the rest of their slabs) was constrained by the transverse spacing of the CFRP grids (In C-3, the grid spacing was 100 mm). In the tension stiffening correction calculations for C-3 it was assumed  $s_{m,c} = 100$  mm. For comparison, the figures show the response of the naked reinforcement.

Figures 8.11 and 8.12 show that concrete’s tension stiffening effect is important for proper calculation of deflections in slabs with GFRP C-bars, specially at load levels roughly greater than the cracking load. The observed responses show that the tension stiffening effect reduces as the load increases. The model could not capture this behaviour for reasons already mentioned. The figures also show that the assumption of a constant slope through the cracked stage for low to medium load levels is reasonable.

Figure 8.13 shows that the tension stiffening effect in slabs with FRP grids is negligible. Similar responses were observed for the other slabs with NEFMAC grids tested by Matthys and Taerwe (not reported). This observation is consistent with previous findings reported by Yost *et al* (2001). The reduced tension stiffening effect is sensible because bond between FRP grids and concrete is not provided along the ribs longitudinal direction but rather mechanically due to transverse rib bearing against concrete.

To further examine the need to account for concrete’s tension stiffening effect in deflection calculations in the post-cracked state, the experimental deflection measurements from 25 tests on simply supported beams with FRP rebars under four point loading were compared with those from the proposed model, the procedure given in CSA S806-00 and Hall’s procedure (Hall, 2000). The latter uses the empirical tension stiffening formulation adopted by CEB/FIP MC 90. The properties of the test specimens

are shown in Appendix D. The deflections were calculated at a load level of twice the flexural cracking load. Since the predictions strongly depend on the evaluation of  $M_{cr}$ , both the proposed model, CSA S806-00 and Hall's approach predictions were based on the observed  $M_{cr}$  values. In the proposed model's predictions, the assumption that crack spacing was not induced by bond was only applied to the BC, CB, IS and KD beam series. The other references do not provide enough information to infer that crack spacing was not bond-induced.

The author is aware of the existence of additional test results. However, many of these are not thoroughly documented, e.g. reinforcement size, bar diameter or reinforcement content values are not reported. Experiments showing excessive FRP slippage were also discarded. Specimens with very low FRP reinforcement content were also ignored.

Table 8.1 compares the quality of deflection predictions using CSA S806-00, Hall's and the proposed procedure. Deflection predictions using the proposed model demonstrate the need to account for concrete's tension stiffening effect at load levels roughly greater than the cracking load. The CSA S806-00 approach, which disregards the aforementioned effect in the post-cracking range, gives the most conservative deflection estimates at this load level (see BC beams). Hall's model gives the most accurate predictions.

## **8.5 Cracking Model for Concrete Slabs Reinforced with FRP**

This section makes use of tension chord model concepts to predict crack widths in the stabilised cracking stage for FRP-reinforced concrete one-way slabs subjected to flexure or direct tension, for crack spacing i) induced by bond, and ii) not induced by bond.

### **8.5.1 Bond-induced Crack Spacing**

Under these conditions, the exact mean crack width and spacing is difficult to estimate. At best, only the most likely values can be estimated. For this reason, it is more useful for the designer to define a range of crack widths or crack spacings within which the cracks are expected to fall.



To evaluate crack widths in the stabilised crack formation, the axial stress-strain response of the FRP-reinforced tension chord shown in Fig. 8.14 will be used. The figure is that presented by Alvarez (1998) except that the terminology now refers to FRP reinforcement. The dotted line represents the response of the naked FRP reinforcement. The solid and dotted lines represent the stress-average strain response of the chord according to the maximum and minimum crack spacing.

Adopting the rationale of CEB/FIP MC90, the mean crack width in the stabilised cracking stage can be defined as

$$w_m = s_m (\varepsilon_{fm} - \varepsilon_{cm}) \quad [8.36]$$

where  $s_m$  is the mean crack spacing,  $\varepsilon_{fm}$  is the mean FRP strain and  $\varepsilon_{cm}$  is the mean concrete strain at  $\sigma_{fr} = \sigma_{fro}$ . This leads to

$$w_m = \frac{\lambda s_{\max}}{E_f} \left( \sigma_{fr} - \frac{\lambda}{2} \sigma_{fro} \right) \quad [8.37]$$

where

$$s_{\max} = \frac{f_{ct} \phi_b (1 - \rho_{f,ef})}{2 \tau_{bo} \rho_{f,ef}} \quad [8.38]$$

Since  $(s_{\min} = 0.5 s_{\max}) \leq s_m \leq s_{\max}$ , the following equation defines the extreme values for bond-induced cracks in the stabilised cracking phase.

$$\frac{s_{\min}}{2E_f} \left( \sigma_{fr} - \frac{\sigma_{fro}}{4} \right) \leq w_m \leq \frac{s_{\max}}{E_f} \left( \sigma_{fr} - \frac{\sigma_{fro}}{2} \right) \quad [8.39]$$

Equation 8.39 estimates crack widths at the reinforcement level. To calculate crack widths on the surface, a reasonable assumption is to multiply both sides of Eq. 8.39 by the gradient  $\left( \frac{h - xd}{d - xd} \right)$ , as proposed by Broms (1965), where  $xd$  is the depth of the neutral

axis at service load conditions. This gradient is equivalent to the  $h_2/h_1$  ratio used by Gergely and Lutz (1967).

Recalling that  $\tau_{bo} = k_{bo} f_{ct}$ , the minimum and maximum crack widths are given as

$$\begin{aligned} & \frac{\phi_b}{4k_{bo}E_f} \frac{(1-\rho_{f,ef})}{\rho_{f,ef}} \left( \sigma_{fr} - \frac{f_{ct}}{4} \left( \frac{1+\rho_{f,ef}(n-1)}{\rho_{f,ef}} \right) \right) \left( \frac{h-xd}{d-xd} \right) \\ & \leq w_m \leq \frac{\phi_b}{2k_{bo}E_f} \frac{(1-\rho_{f,ef})}{\rho_{f,ef}} \left( \sigma_{fr} - \frac{f_{ct}}{2} \left( \frac{1+\rho_{f,ef}(n-1)}{\rho_{f,ef}} \right) \right) \left( \frac{h-xd}{d-xd} \right) \end{aligned} \quad [8.40]$$

Figure 8.15 qualitatively illustrates the relationship between the mean crack width and the FRP stress at a crack for monotonic loading conditions in a member with bond-induced crack spacing. The solid lines represent the mean crack width accounting for the tension stiffening effect of concrete. The dashed lines indicate the crack width variation ignoring this effect. The dashed lines meet exactly at  $\sigma_f = \sigma_{fcr}$ , which is the FRP stress immediately before first cracking. Consistent with the assumed bond-slip constitutive relationship, solid and dashed lines are parallel. The vertical difference between dotted and solid lines depends on the amount of tension stiffening. Ignoring this effect leads to a crack width overestimation. There is scarce information reported in the literature as to the shape of the  $w$ - $\sigma$  curve between the first cracking instant and the end of the single crack formation stage. For this reason, the path has been interrupted in this region. The study of this aspect falls well beyond the scope of this work.

### 8.5.2 Crack Spacing not Induced by Bond

The following formulation is useful for estimation of FRP strains at cracks when the crack spacing is given. It applies only for the case where crack spacing is not driven by bond.

Figure 8.16 shows the assumed distribution of stresses in FRP and concrete for “constrained” crack spacing conditions, for the specific case  $s_{m,c} < s_{min}$ . It has been assumed that the slope of the stress distribution in FRP and concrete is equal to that for

the bond-induced crack spacing case (see Fig. B.2). The mean tensile stress in concrete is defined as

$$\sigma_{cm} = \frac{\gamma}{2} f_{ct} \quad [8.41]$$

where

$$\gamma = \frac{s_{m,c}}{s_{max}} \quad [8.42]$$

Solving for  $\varepsilon_{fr}$  from Eq. 8.5 and substituting 8.42 and 8.41 into the resulting equation, the mean constrained crack width,  $w_{m,c}$ , associated to cracks formed due to deformation accommodation or to strain raisers is

$$w_{m,c} = s_{m,c} \varepsilon_{fr} - \frac{\tau_{bo} s_{m,c}^2}{\phi_b E_f} - \frac{\gamma}{2} \frac{f_{ct}}{E_c} s_{m,c} \quad [8.43]$$

where  $\varepsilon_{fr}$  is the FRP strain at the crack. The mean constrained crack width on the surface is

$$w_{m,c} = \left( s_{m,c} \varepsilon_{fr} - \frac{\tau_{bo} s_{m,c}^2}{\phi_b E_f} - \frac{\gamma}{2} \frac{f_{ct}}{E_c} s_{m,c} \right) \left( \frac{h - xd}{d - xd} \right) \quad [8.44]$$

### 8.5.3 Application of Cracking Model for FRP-reinforced Concrete Members in Flexure

This section compares the quality of crack width predictions for beams, one-way and two-way slabs reinforced with FRP with observed values. Predictions were carried out based on the tension chord model, the modified Gergely-Lutz equation proposed by Thériault and Benmokrane (1998) and the design equation given by ISIS M04-00. The latter two are essentially empirical.

The modified Gergely-Lutz equation proposed by Thériault and Benmokrane (1998) is

$$w_{max} = K_g f_f \frac{h_2}{h_1} \sqrt[3]{d_c A} \quad [8.45]$$

with  $K_g = 0.0000409 \text{ mm}^2/\text{N}$  for GFRP C-bars.

Maximum crack widths according to ISIS M04-00 are given by

$$w_{\max} = 11 \times 10^{-6} \frac{E_s}{E_f} \sigma_{fr} K_b \frac{h_2}{h_1} \sqrt[3]{d_c A} \quad [8.46]$$

where  $K_b = 1.2$ . Equation 8.46 is conceptually similar to the crack control design provisions of CSA S806-00.

### 8.5.3.1 Beams Reinforced with GFRP C-bars

Figures 8.17 and 8.18 show observed maximum crack width values for beams TB BC2VA and TB BC4NA tested at Université de Sherbrooke. Since the crack spacing in these beams was driven by the stirrups' spacing, the crack width estimate refers to a mean constrained crack width. Maximum crack width predictions according to Eq. 8.45 and 8.46 are also shown.

Figure 8.17 shows that the predicted mean crack widths according to the tension chord model are lower than the maximum observed values. The crack width estimates of the modified Gergely-Lutz equation are slightly more liberal whereas those using the ISIS M04-00 equation lead to good crack predictions at low load levels but wider crack values at higher loads.

Figure 8.18 shows that mean crack width predictions for beam TB BC4NA using the proposed model are conservative. The slope of the predicted curve is similar to that of the observed curve at bending moment values below 12 kN.m. Beyond this level, however, the cracks start closing due to the shifting down of the neutral axis. This cannot be captured by the proposed model. The modified Gergely-Lutz equation leads to slightly more accurate predictions but the slope of the moment-crack width line is not consistent with that of the measured values. The crack width predictions according to ISIS M04-00 are overly conservative which suggests that the recommended  $k_b$  value of 1.2 seems excessive.

### 8.5.3.2 One-way Members Reinforced with FRP Grids

Figure 8.19 compares the quality of crack width predictions with observed mean values for one-way slab H3 tested by Matthys and Taerwe (2000b). This slab was reinforced with a hybrid CGFRP NEFMAC grid. Properties of this slab are as follows:  $b = 1000$  mm,  $h = 150$  mm,  $d = 122$  mm,  $f'_c = 26.3$  MPa,  $\rho_f = 1.28$  %,  $E_f = 44.8$  GPa,  $f_{fu} = 640$  MPa). Due to lack of experimental evidence, the  $K_g$  and  $k_b$  coefficients for NEFMAC in the modified Gergely-Lutz and ISIS crack width predictions were taken equal to those of GFRP C-bars. Matthys and Taerwe (2000b) report that the crack spacing in C3 was constrained by the spacing of the transverse grid ribs (150 mm). As a result, the crack width predictions based on the tension chord model were calculated according to Eq. 8.44.

The figure shows that the tension chord model crack width predictions are very close to the observed mean crack width values. The slopes of the lines are virtually identical. The modified Gergely-Lutz, which provides maximum crack width estimates gives reasonable predictions at low load levels. The ISIS procedure gives conservative estimates.

### 8.5.3.3 Two-way Slabs Reinforced with GFRP C-bars

Figure 8.20 shows the mean crack width values measured on series I slab GFR-1. The experimental crack widths are average values from measurements taken on the slab surface at 30 mm from the column face in two directions. The crack width predictions according to the tension chord model were made based on  $\rho_{f,ef} = 2.5$  %. This value was determined based on an effective concrete area in tension defined as per Fig. 3.6, assuming  $\rho_f = 0.733$  %,  $\phi_b = 14.9$  mm,  $c_c = 20$  mm and  $xd = 16$  mm. It was assumed  $k_{bo} = 0.9$ . In this slab, as would be the case of a prototype two-way plate, the crack spacing is constrained by the spacing of the top reinforcing mat (200 mm).

Figure 8.20 shows that the proposed procedure leads to mean crack width predictions that approach the experimental values in a reasonable fashion in the stabilised cracking stage.

## 8.6 Parametric Study

### 8.6.1 Members in Direct Tension

The equations developed for flexural members with FRP can be applied to members subjected to direct tension by replacing  $\rho_{f,ef}$  by  $\rho_f$  and disregarding the correction proposed by Broms. In this part of the analysis, it will be assumed that crack spacing is governed by bond.

Figure 8.21 shows mean crack width predictions in the stabilised cracking phase in terms of the FRP stress at a crack,  $\sigma_{fr}$ , for different  $E_f$  values,  $\rho_f = 0.025$ ,  $f'_c = 30$  MPa,  $k_{bo} = 0.9$  and  $\lambda = 0.67$ . Also plotted is the crack width variation as a function of the reinforcement stress at the crack for a steel-reinforced member of same concrete strength with  $\rho_s = 0.025$ ,  $k_{bo} = 1.8$  and  $\lambda = 0.67$ . The minimum FRP stress for the different curves shown in the plot signals  $\sigma_{fro}$  (FRP case) and  $\sigma_{fro}$  (steel case).

According to Fig. 8.21, the crack widths increase with the FRP stress at the crack. This has been observed by Nawy *et al* (1971), Nawy and Neuwarth (1977), Michaluk *et al* (1997), Matthys and Taerwe (2000a) and Alkhrdaji *et al* (2000). The cracks grow at a faster rate as the reinforcement becomes more flexible. Similar calculations as those in Fig. 8.22 were made assuming  $f'_c = 50$  MPa (the curves are not shown). The increase in concrete strength does not lead to a significant change in the crack width estimates.

The mean crack width variation in the stabilised cracking phase as a function of the FRP stress at a crack for three different FRP reinforcement ratios is shown in Fig. 8.22. It has been assumed  $E_f = 40$  GPa (GFRP). The crack widening rate decreases as the FRP content increases. The initial crack width also decreases as the FRP content increases.

Figure 8.23 shows the effect of FRP's bond strength on crack widths in the stabilised cracking phase for a member with 30 MPa concrete,  $\rho_f = 0.025$  and  $\lambda = 0.67$ . Mean crack width estimates correspond to bond strengths varying within a  $\pm 20$  % margin of the

assumed bond strength of GFRP, calculated assuming  $k_{bo} = 0.9$ . At a given FRP stress at a crack, a bond strength increase leads to narrower cracks.

### 8.6.2 Slabs in Flexure

The objective of this section is to establish design guidelines to evaluate FRP strains at cracks as a function of the slab thickness, reinforcement spacing, and material properties, for specified maximum crack width limits. The study will be confined to bond-induced crack spacing conditions.

Consider a slab of uniform thickness  $h$ , with flexural depth  $d$  and concrete cover  $c_c$ , with FRP reinforcement uniformly spaced at  $s_f$ . Substituting Eqs. 8.43 and 8.42 results in

$$w_m = \lambda \frac{\phi_b}{2} \frac{(1 - \rho_{f,ef})}{\rho_{f,ef}} \left( \frac{\sigma_{fr}}{E_f} - \frac{\lambda}{2} \frac{f_{ct}}{E_f} \left( \frac{1 + \rho_{f,ef}(n-1)}{\rho_{f,ef}} \right) \right) \quad [8.47]$$

which can be re-arranged as

$$\sigma_{fr} = \frac{2}{\lambda} \frac{k_{bo} E_f w_m}{\phi_b} \frac{\rho_{f,ef}}{(1 - \rho_{f,ef})} + \frac{\lambda}{2} f_{ct} \left( \frac{1 + \rho_{f,ef}(n-1)}{\rho_{f,ef}} \right) \quad [8.48]$$

$$\text{with } \rho_{f,ef} = \frac{A_f}{s_f h_{ct}} = \frac{\pi \phi_b^2}{4 s_f h_{ct}} \quad [8.49]$$

where  $h_{ct}$  is the height of the effective concrete area in tension, defined in Fig. 3.6. Since the crack width to control is that on the slab surface, the term  $w_m$  in Eq. 8.47 needs to be modified by Brom's gradient. Accordingly, the FRP strain at the crack is

$$\varepsilon_{fr} = \frac{2}{\lambda} \frac{k_{bo} w_{ms}}{\phi_b} \frac{(d - xd)}{(h - xd)} \frac{\rho_{f,ef}}{(1 - \rho_{f,ef})} + \frac{\lambda}{2} \frac{f_{ct}}{E_f} \left( \frac{1 + \rho_{f,ef}(n-1)}{\rho_{f,ef}} \right) \quad [8.50]$$

where  $w_{ms}$  is the crack width on the slab surface.

Figure 8.24 shows the variation of the strain at a crack as a function of the reinforcement spacing for three slabs with  $h = 180$  mm. The slabs are reinforced with steel ( $E_f = 200$

GPa), CFRP ( $E_f = 120$  GPa) and GFRP ( $E_f = 40$  GPa). In the calculations, it has been assumed  $f'_c = 30$  MPa,  $k_{bo} = 1.8$  (slab with steel),  $k_{bo} = 0.9$  (slabs with CFRP and GFRP),  $\lambda = 0.67$  (for both steel and FRP),  $\phi_b = 15$  mm, and a clear cover,  $c_c$ , of 25 mm. The strain values are plotted for maximum allowable crack widths of 0.3 and 0.5 mm. The former is typical of exterior exposure conditions for steel-reinforced concrete members. The latter is the maximum value for exterior exposure conditions recommended by ISIS M04-00 for members reinforced with FRP. The assumed rupture strain values for CFRP and GFRP are 0.012 and 0.016, respectively.

Figure 8.24 shows that, for the three reinforcement types considered, the strains at the crack tend to increase at a higher rate as the spacing reduces. This so-called “strain localization” is not a concern in high ductility steels; becomes problematic in slabs with CFRP; and is a critical issue in slabs with brittle-elastic reinforcement prone to creep rupture, such as GFRP. The figure also shows that as the allowable crack width increases, the strain localization effect increases.

To compare the quality of strain predictions, let us assume that the spacing in the steel-reinforced slab is 250 mm and that, since a tighter spacing is required in an FRP-reinforced slab to compensate for FRP’s lower stiffness, the CFRP and GFRP reinforcement in the other two slabs is spaced, respectively, at 150 mm and 50 mm. For simplicity, it will be assumed that the latter permits proper concrete placement. The arrows in Fig. 8.24 show the reinforcement spacing for each slab.

According to Fig. 8.24, the strain at the crack associated with a 0.3 mm crack width for steel rebars is 0.0016 whereas those for the slabs with CFRP and GFRP rebars associated with a 0.5 mm crack width are, respectively, 0.0021 and 0.0058. The ratio between the CFRP and the steel strains is 3.625, which is more than twice the  $0.5/0.3 = 1.67$  value that Hall’s Eq. 3.20 would predict. The ratio between the GFRP and steel strains is 1.31, which is lower than what Hall’s would predict.



Considering each slab independently, the strain increase associated with a crack width of 0.3 to 0.5 mm for the slab with steel reinforcement is in the order of 50 % which is less than  $0.5/0.3 \times 100 = 67$  %, which would be the ratio that Hall's equation would predict. For the slabs with CFRP and GFRP, the strain increase is, respectively, 50 and 60 %.

These observations lead to the conclusion that Hall's Eq. 3.20 is not conceptually correct. Hall's equation is simple but does not account for the effects that the reduced stiffness and bond strength of FRP reinforcement have on the relationship between crack widths and strains at cracks. Moreover, for the slab with GFRP reinforcement, the 0.0058 strain at the crack is greater than the maximum strain limit allowed by CSA S806-00 (30 % of  $f_{fu}$ , i.e.  $0.30 \times 0.016 = 0.0048$ ). CSA S806-00 allows crack widths in the order of 0.6 mm for interior exposure. Such an increased crack width limit would lead to strains at cracks that would further violate the maximum FRP strain limit.

Figure 8.25 examines the variation in strains at cracks for a crack width of 0.5 mm for slab thicknesses of 150, 200 and 250 mm. The figure shows that the strain localization reduces as the slab thickness increases. For  $h = 200$  mm and a GFRP mat spaced at 75 mm, the strain at the crack is about 0.00375, which is about 26 % of the rupture strain. This value is slightly less than the maximum 30 % limit stipulated by CSA S806-00 and very close to the maximum 25 % limit allowed by C-bar manufacturers. The strains for a tightly spaced CFRP grid are of similar magnitude except that CFRP rebars do not creep. For instance, for the case of CFRP rebars spaced at 100 mm (which would lead to a stiffer mat and allow proper concrete placement), the strain at the crack for a 200 mm thick plate is about 0.0028 which is only 23 % of CFRP's assumed rupture strain. As shown in Fig. 8.25, the beneficial slab thickening effect disappears as the rebar spacing increases.

The effect of a variation in the bond strength of the bars on the evaluation of strains at cracks is shown in Fig. 8.26 for a 200 mm thick plate with either GFRP or CFRP, assuming a maximum allowable crack width of 0.5 mm. The figure shows that as bond increases the strain localization effect becomes more acute. The detrimental effect of

bond between FRP and concrete on FRP strains at cracks was identified by Burgoyne (1993). This suggests that any improvement of the bond features of FRP reinforcement is not beneficial. In theory, this suggests that use of FRP grids (whose bond is provided by transverse rib bearing instead of friction or mechanical interlock between lugs and concrete) is more helpful for crack control. Unfortunately, there is scarce experimental evidence studying this effect. Figure 8.26 also shows no significant effect of the FRP type on the bond effect for very tight mats, which is usually the case.

## **8.7 Concluding Statements**

### **8.7.1 Deflection Calculations**

A comparison between deflection predictions and observed deflection values at load levels of twice the cracking load for 25 simply supported beams subjected to four point bending reported in the literature demonstrated the need to account for concrete's tension stiffening effect in deflection calculations for slabs with FRP rebars at relatively low service load levels.

Consistent with the results reported by Matthys and Taerwe (2000b) and Yost *et al* (2001), the results from this chapter indicate that the tension stiffening effect of concrete does not play a major role in the deflection predictions of slabs with FRP grids.

Since current deflection calculation provisions in CSA S806-00 ignore the tension stiffening effect of concrete in the post-cracking stage, these design provisions tend to be very conservative for slabs with FRP rebars at load levels roughly greater than the cracking load. The provisions can be safely used to calculate deflections in slabs with FRP grids.

Current design provisions in S806-00 are appealing for treatment of boundary conditions typically found in laboratory conditions but fail to account for realistic prototype loading cases and boundary conditions.

The deflection results examined in this study suggest that the deflection procedure envisaged by Hall (2000), based on the curvature integration method using CEB-FIP MC 90's tension stiffening approach, gives very accurate deflection predictions at service load levels.

### **8.7.2 Crack Control in Slabs with FRP**

#### **8.7.2.1 Conclusions Based on Crack Width Estimates**

The consistencies among observed overall response, crack spacing and width predictions with predicted values applying tension chord model principles indicate that the flexural cracking phenomenon in FRP-reinforced slabs can be handled rationally.

The experimental evidence presented in this chapter shows, as suggested by Base (1982), that the spacing of flexural cracks is not always governed by bond between the reinforcement and concrete. Test results from a dozen beams and one-way slabs with FRP tested in Canada and Belgium show that “deformation-controlled” cracking or cracking due to strain raisers, such as stirrups or reinforcement running transversely, is often more dominant.

A procedure to evaluate the tension stiffening effect of concrete and the width of cracks under conditions not induced by bond is proposed. The procedure intends to predict crack widths in one-way concrete slabs with internal FRP reinforcement. The predictions compare well with observed crack width values from experiments. The model is able to capture the variation of crack width in terms of load or reinforcement strain at the crack at service load levels.

The modification of the Gergely-Lutz equation proposed by Thériault and Benmokrane (1998) and the design provisions in ISIS M04-00 for crack width calculations were also examined. Thériault and Benmokrane's empirical procedure gave reasonable predictions. ISIS M04-00 guidelines were found to be very conservative. The limited crack width evaluation reported herein suggest that  $K_b = 1.2$ , as used in the current ISIS equation, tends to overestimate maximum crack width predictions.

Additional load tests on FRP-reinforced concrete slabs with slender flexural spans with thorough documentation of mean and maximum crack widths and spacings are required.

#### **8.7.2.2 Conclusions Based on Estimates of FRP Strains at Cracks**

The parametric studies revealed that slabs with FRP tend to exhibit strain localization at cracks for the case of tight reinforcing mats. The effect worsens as the slab thickness decreases. This problem is critical in slabs with GFRP and less severe in slabs with AFRP or CFRP since GFRPs are prone to creep rupture.

Hall's assumption that the relationship between crack widths and strains at cracks is independent of the reinforcement type is not conceptually correct. The strain growth due to an increase in crack width is affected by the type, amount and bond strength of FRP. Hall's assumption that the increase in FRP strain is a linear function of the crack width increase is also debated by the results shown in this chapter. Her predictions may lead to unsafe strains at cracks at service load levels for slabs with GFRP.

The fact that FRP reinforcement performs satisfactorily in corrosive environments does not imply that wider cracks should be allowed in FRP-reinforced members at service load levels. The appropriateness of a given crack width limit strongly depends on the slab depth, and the type and amount of FRP reinforcement. To allow wider cracks may lead to excessive strains at cracks. In this way, what is thought to be gained in terms of flexural stiffness when providing dense GFRP mats may turn out to be harmful in situations where sustained load prevails.

An increase in the bond strength of the reinforcement enhances the strain localization effect. This means that future generations of GFRP reinforcements should not aim at improving bond features of bars and grids.

In regards to the role of bond between FRP and concrete in the behaviour of concrete slabs, Burgoyne's 1993 key question "should FRP be bonded to concrete?" can be

answered by stating that bonded FRP reinforcement should be allowed in slab construction so long as the crack control design philosophy drifts away from the current belief that wider cracks should be allowed simply because FRPs have superior corrosion resistance.

The results from this chapter suggest that dense GFRP mats made from C-bars or NEFMAC grids can be safely used in slabs under sustained load if a minimum slab thickness of 200 mm is complied with. To facilitate concrete placement, the minimum FRP transverse spacing shall not be less than 100 mm. The slab thickness and amount of GFRP and CFRP reinforcement required to satisfy deflection control limits shall be determined based on the recommendations of chapter 9.

**Table 8.1 Comparison of Deflection Calculations for  $M = 2 M_{cr, exp}$**

Ref.	Specimen	$\Delta_{obs}$ (mm)	$\Delta_{S806}$ (mm)	$\Delta_{Hall}$ (mm)	$\Delta_{Prop}$ (mm)	T/P S806	T/P Hall	T/P Prop
MBC	IS2B1	16.7	23.5	16.9	16.9	0.71	0.99	0.99
	K2B1	22.1	28.8	19.7	22.7	0.77	1.12	0.97
	IS3B1	13.2	18.3	13.4	14.0	0.72	0.99	0.94
	KD3B1	11.5	16.0	10.9	12.1	0.72	1.06	0.95
	IS4B1	11.1	17.8	10.6	14.0	0.62	1.05	0.79
	KD4B1	13.1	15.7	12.6	12.4	0.84	1.04	1.06
TB	BC2NA	6.9	9.2	8.9	8.5	0.75	0.78	0.81
	BC2HA	9.3	9.4	9.7	8.3	0.99	0.96	1.13
	BC2VA	10.7	9.5	9.5	7.9	1.13	1.13	1.35
	BC4NA	5.9	6.8	7.0	5.7	0.86	0.84	1.03
	BC4VA	8.7	7.6	9.7	5.9	1.14	0.90	1.48
MTB	CB2B-1	11.8	19.0	13.1	17.2	0.62	0.90	0.68
	CB3B-1	13.2	18.4	9.8	16.7	0.72	1.35	0.79
	CB4B-1	9.0	12.5	11.8	10.8	0.72	0.76	0.84
	CB6B-1	5.0	8.8	7.9	7.1	0.57	0.63	0.70
NMFT	RC-A3	9.4	11.5	9.6	10.0	0.82	0.98	0.94
	RC-A4	5.3	6.8	5.7	6.0	0.78	0.93	0.89
	RC-A5	2.9	3.8	3.2	3.5	0.77	0.91	0.84
	RC-C1	6.4	8.0	6.7	7.2	0.80	0.96	0.89
MRTB	I-200-C	27.2	41.2	22.6	28.4	0.66	1.20	0.96
	LL-200-C	26.1	32.8	26.9	24.1	0.80	0.97	1.08
NN	BF6	3.8	6.6	3.1	4.4	0.58	1.23	0.86
	BF7	4.3	6.8	3.7	4.4	0.64	1.17	0.97
	BF9	3.7	5.5	3.0	3.7	0.67	1.25	0.99
	BF11	4.9	6.1	4.3	4.3	0.81	1.13	1.15
Mean:						0.77	1.01	0.96
Std. Dev:						0.15	0.17	0.18
COV (%):						19.0	16.5	18.8

**Notes:** MBC (Masmoudi, Benmokrane & Chaalal, 1995)  
TB (Thériault & Benmokrane, 1998)  
MTB (Masmoudi, Thériault & Benmokrane, 1998)  
NMFT (Nakano, Matsuzaki, Fukuyama & Teshigawara, 1993)  
MRTB (Michaluk, Rizkalla, Tadros & Benmokrane, 1997)  
NN (Nawy & Neuwarth, 1977).

1. Deflection calculations were performed based on observed cracking moment values.
2. Deflection calculations using Hall's procedure were performed by integrating curvatures in three sections (at supports and at midspan). For simple spans, i.e. all beams listed above, the curvature at the supports is zero.

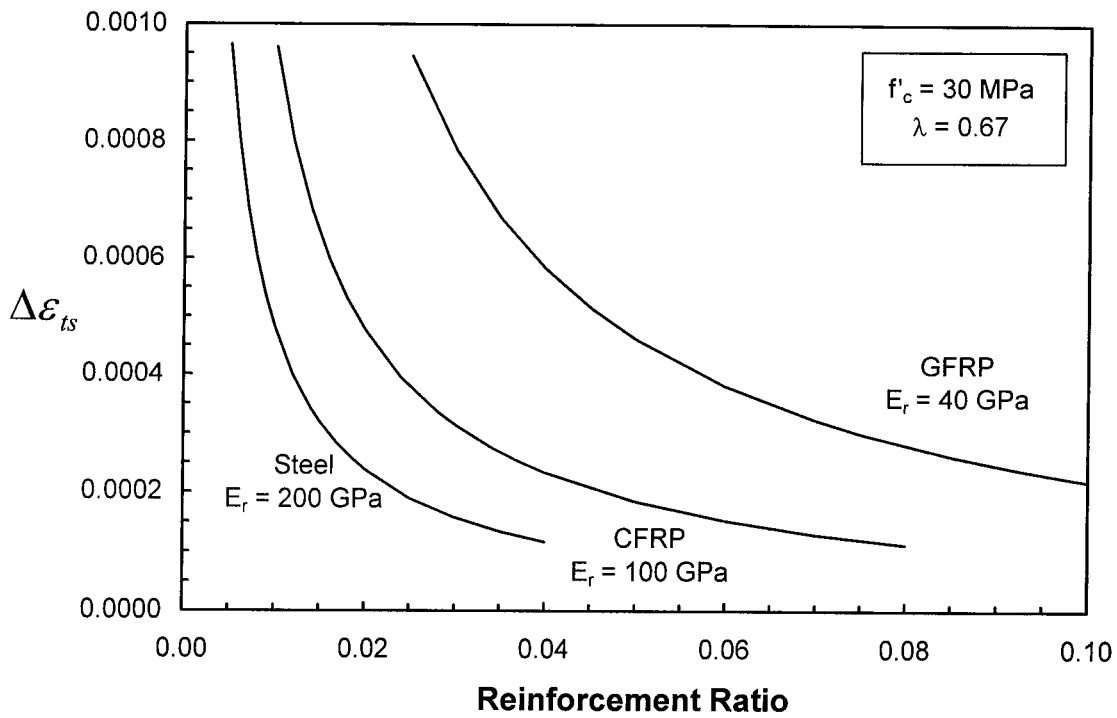


Fig. 8.1 Effect of  $\rho$  and  $E_r$  on Tension Stiffening

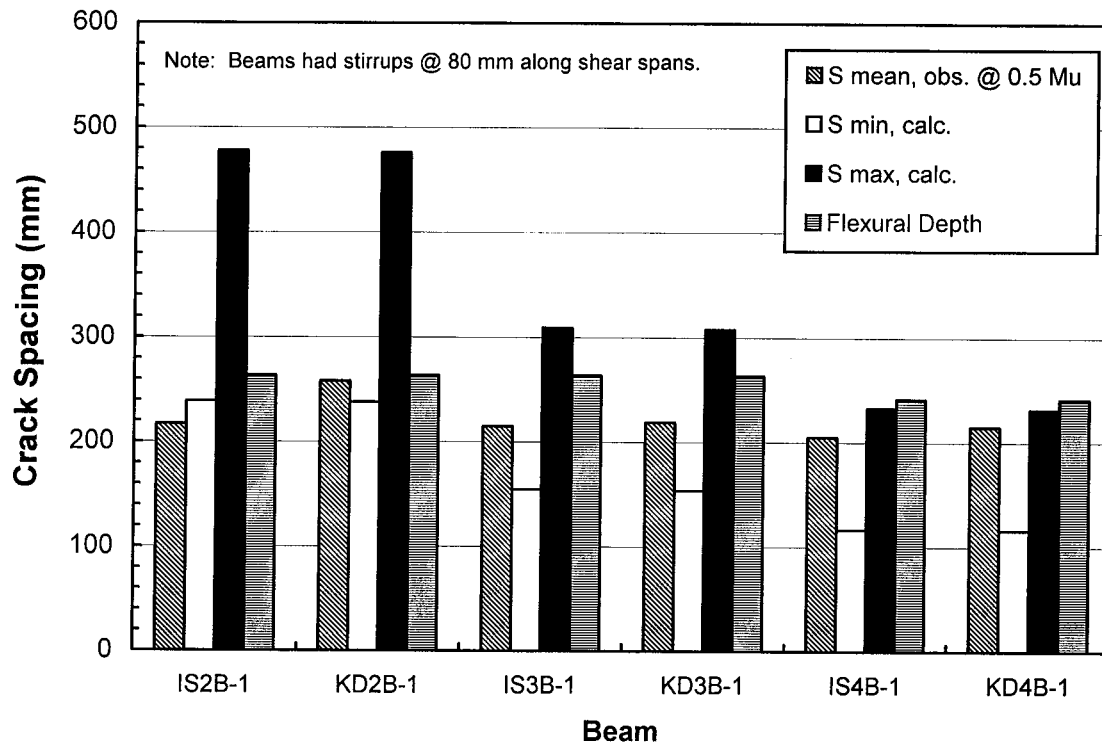
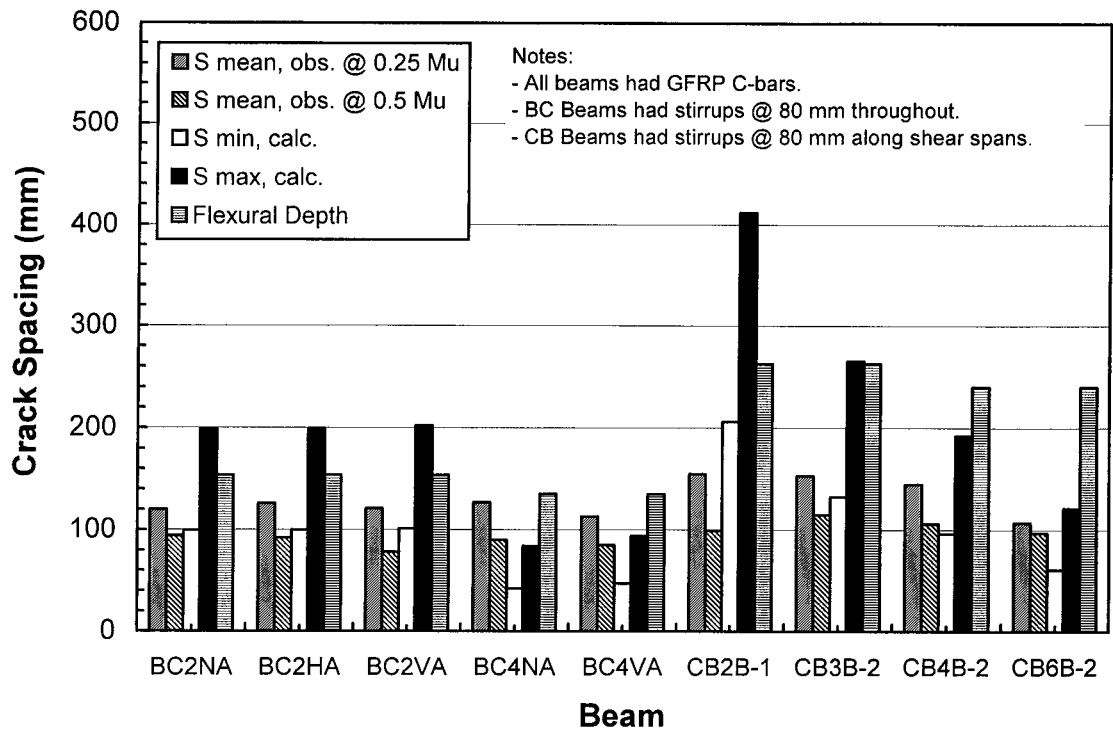
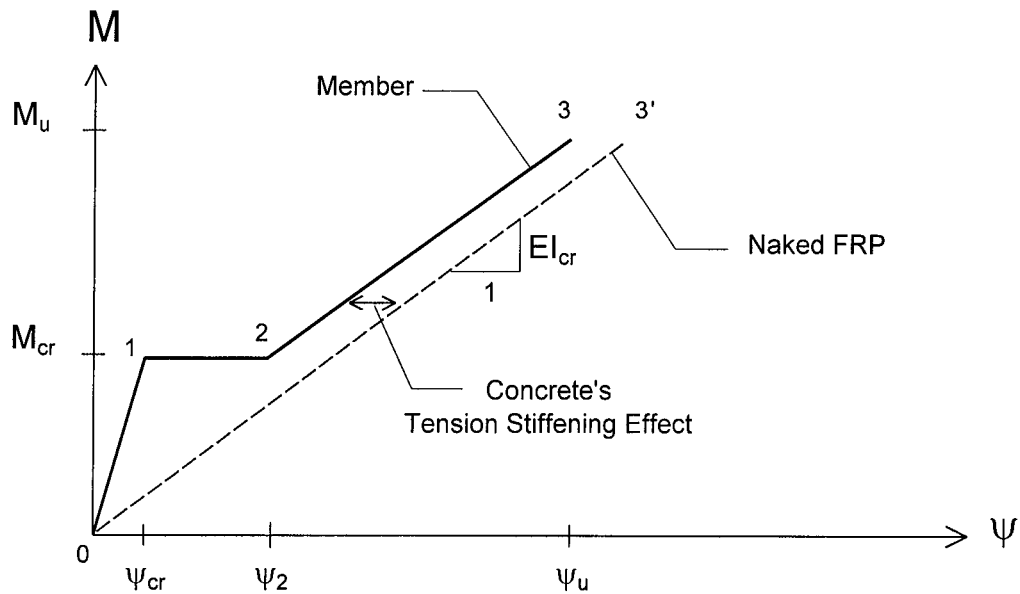


Fig. 8.2 Crack Spacing : Sherbrooke Beams (1)



**Fig. 8.3 Crack Spacing : Sherbrooke Beams (2)**



**Fig. 8.4 Idealised Moment-Curvature Response According to Proposed Model**



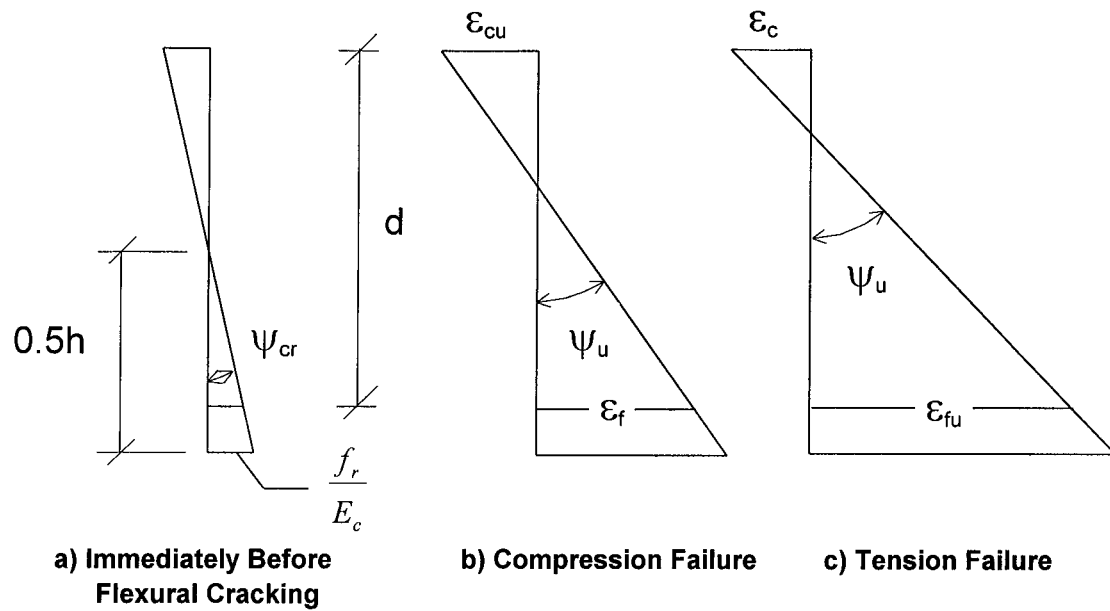


**Fig. 8.5 Strain Distributions According to CSA S806-00**

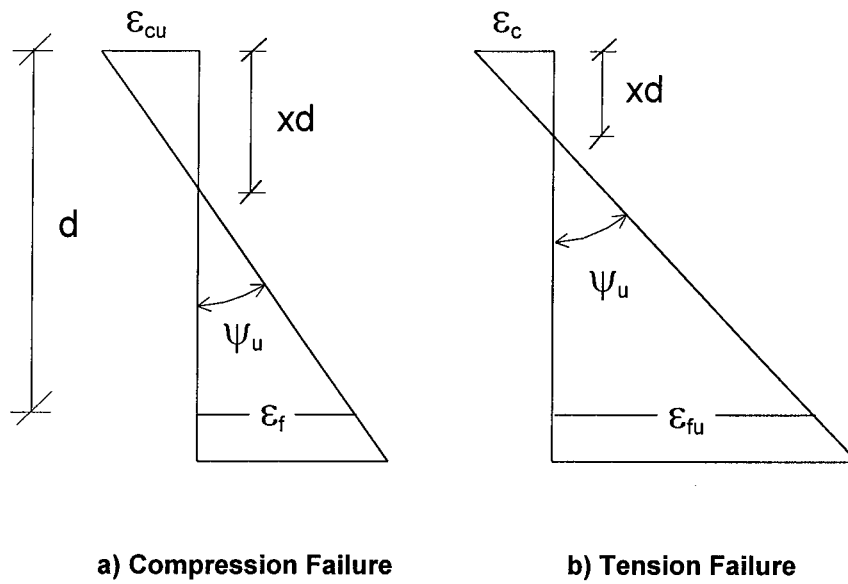


**Fig. 8.6 Assumed Strain Distributions at Failure**

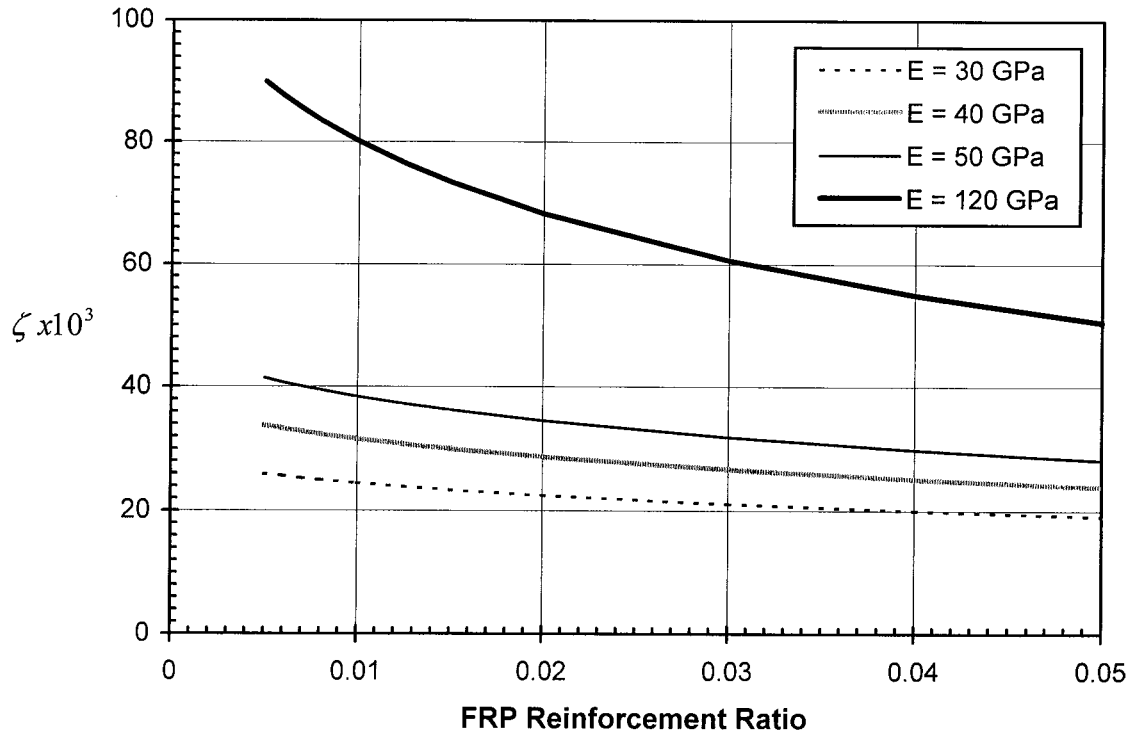


Fig. 8.7  $\zeta$  Factor as a Function of  $\rho$  and  $E$

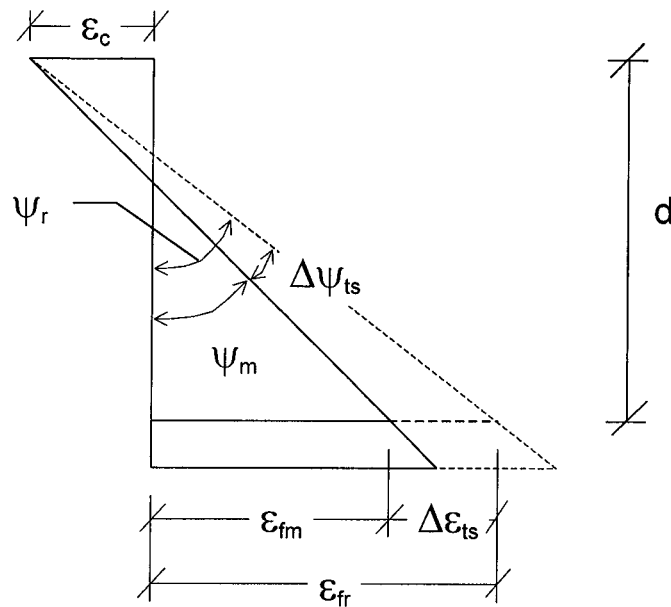
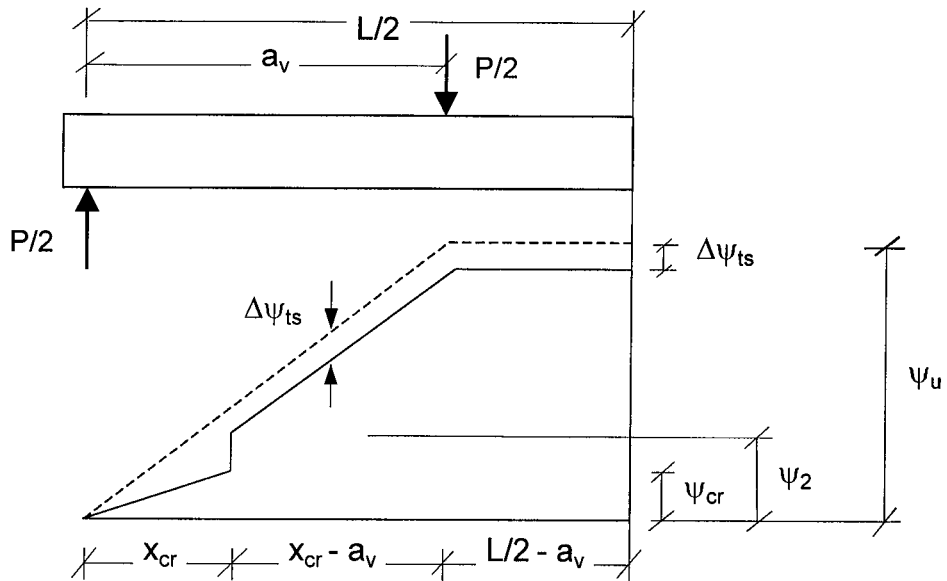
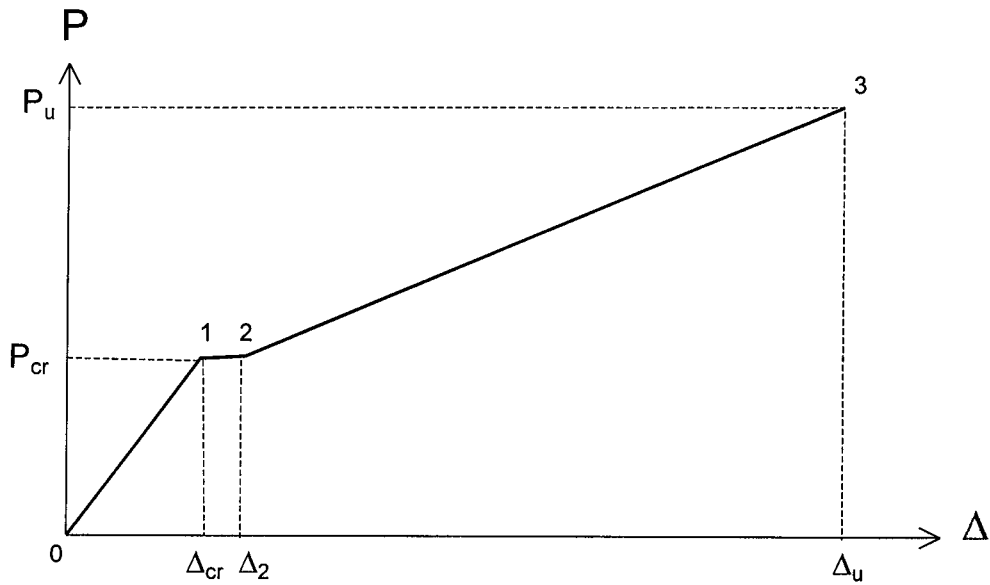


Fig. 8.8 Curvature Correction due to Concrete's Tension Stiffening Effect



**Fig. 8.9 Assumed Curvature Distribution for Beam under Four Point Bending**



**Fig. 8.10 Idealised Load-Deflection Response**

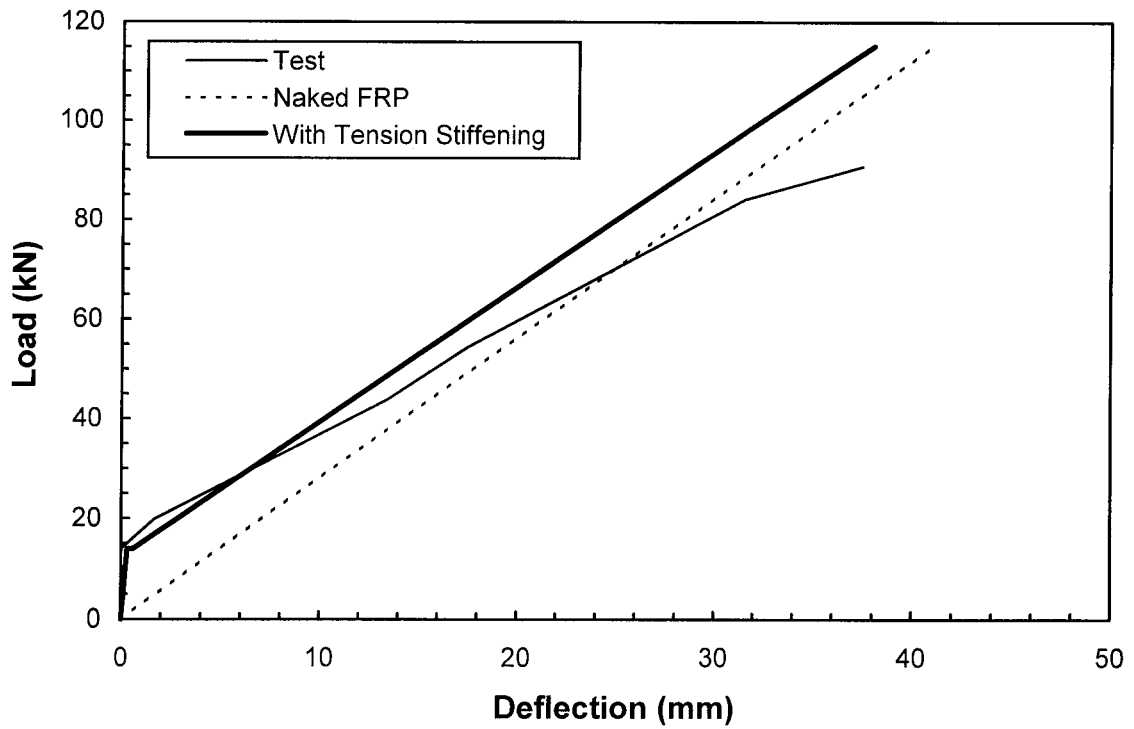


**Fig. 8.11 Flexural Model Calibration : Slab TB BC2VA**

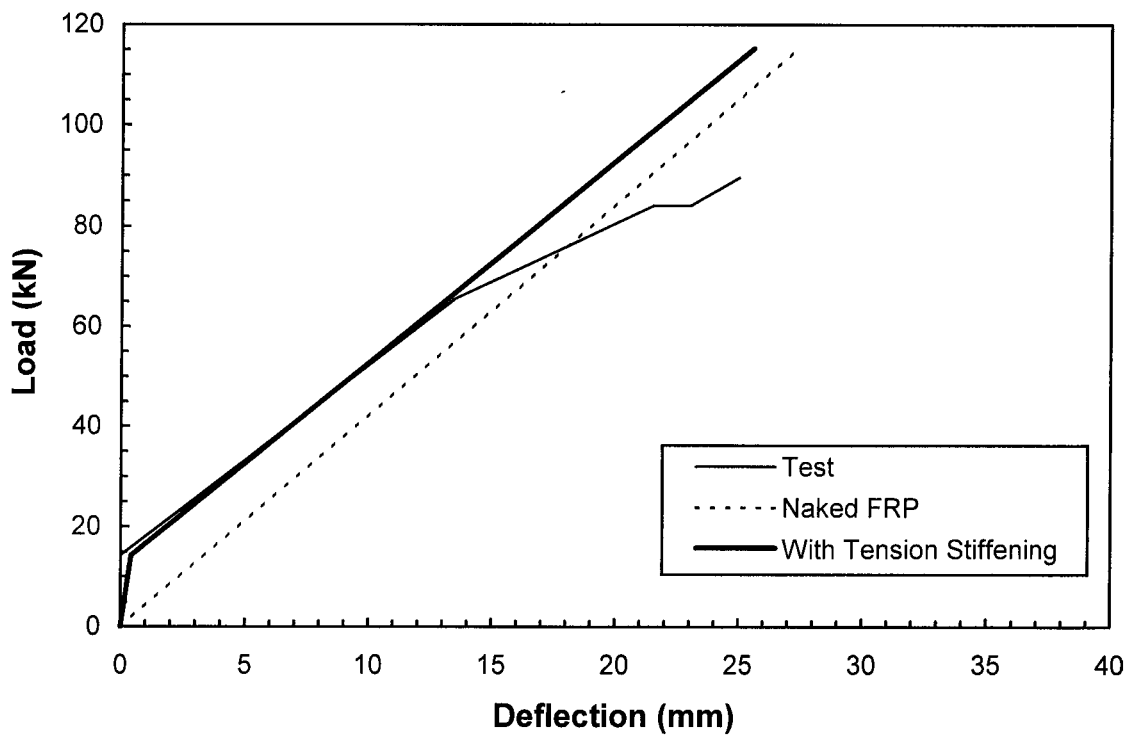


**Fig. 8.12 Flexural Model Calibration : Slab TB BC4NA**

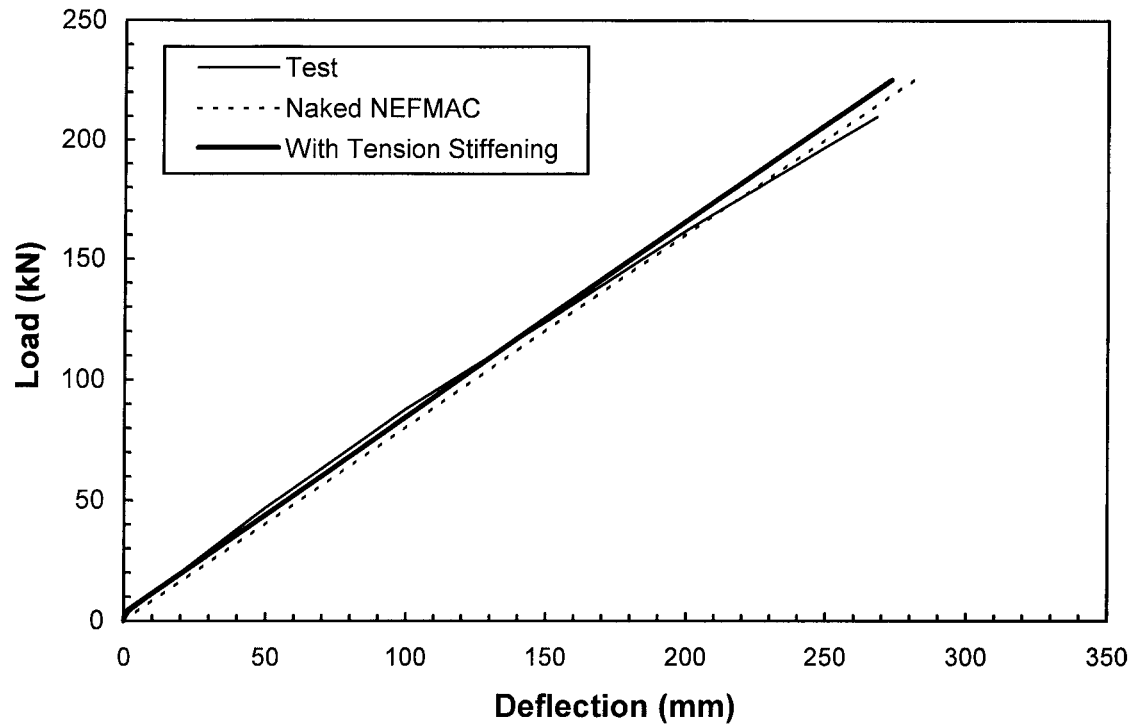


**Fig. 8.13 Flexural Model Calibration : Slab MT C3**

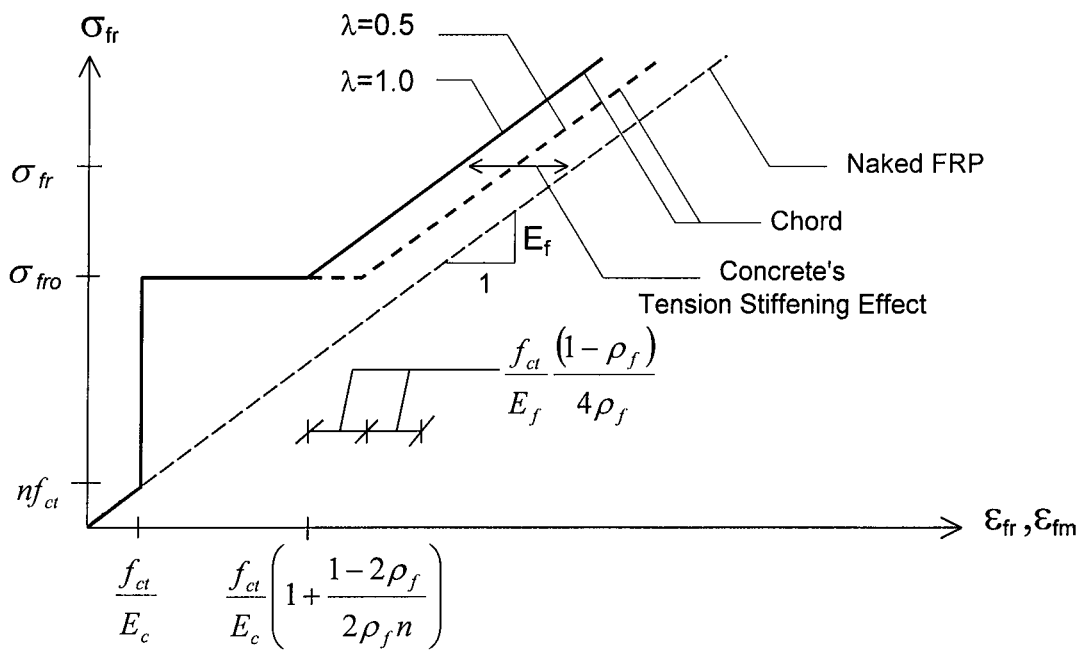


**Fig. 8.14 FRP Tension Chord Response (After Alvarez, 1998)**

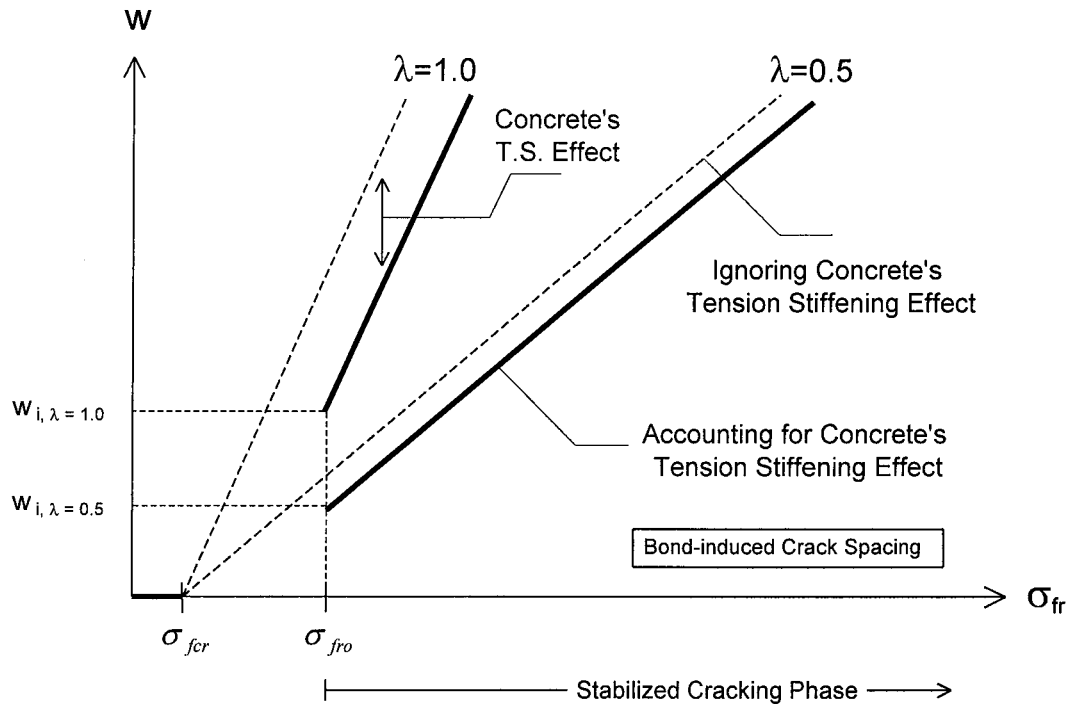


**Fig. 8.15 Crack width - FRP Stress Relationship**

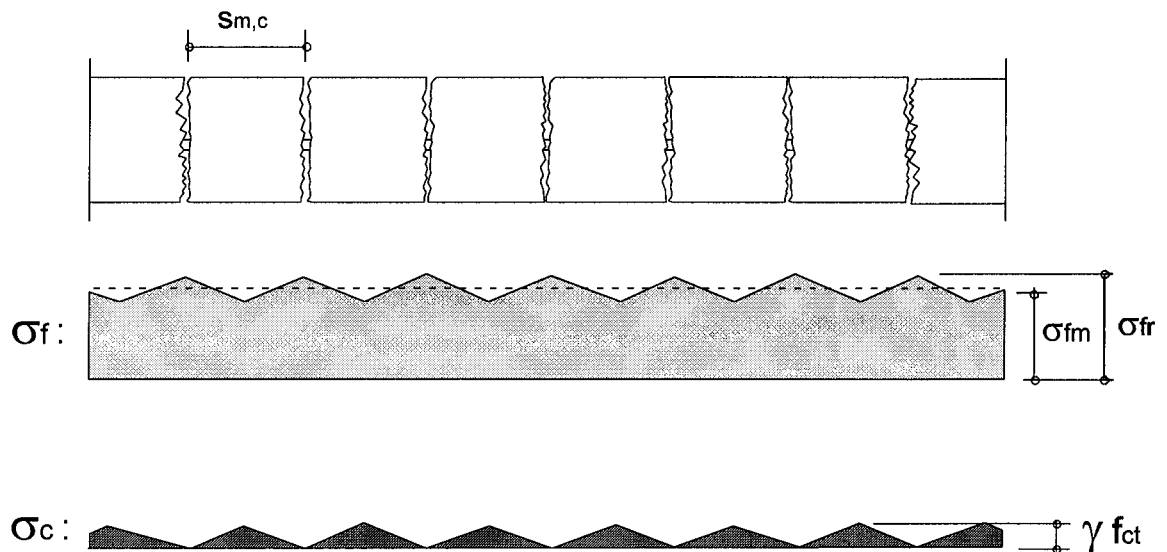


**Fig. 8.16 FRP and Concrete Stress Distributions  
(Crack Spacing not Induced by Bond)**

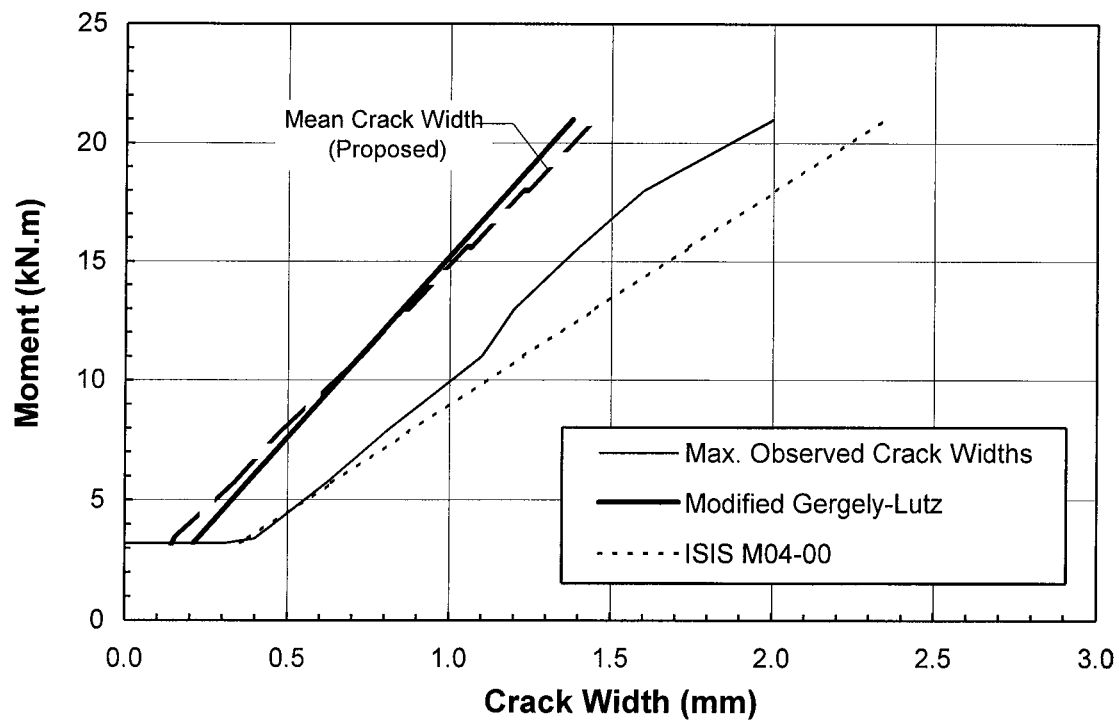


**Fig. 8.17 Crack Width Predictions : Beam TB BC2VA**

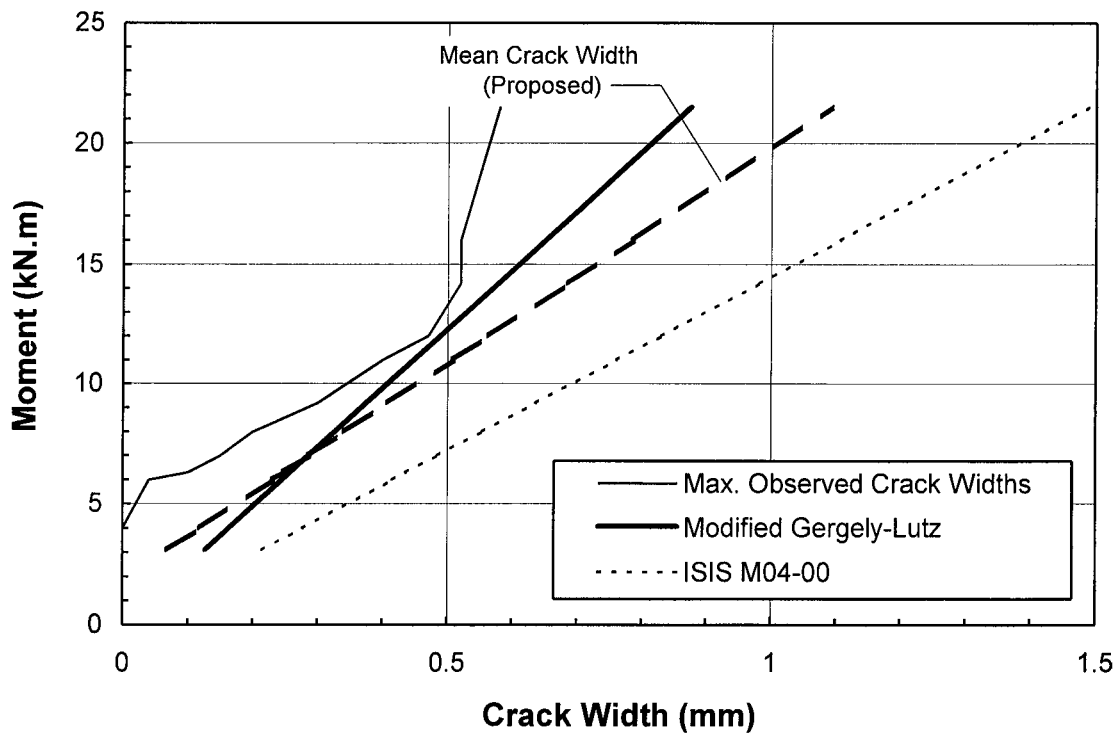


**Fig. 8.18 Crack Width Predictions : Beam TB BC4NA**

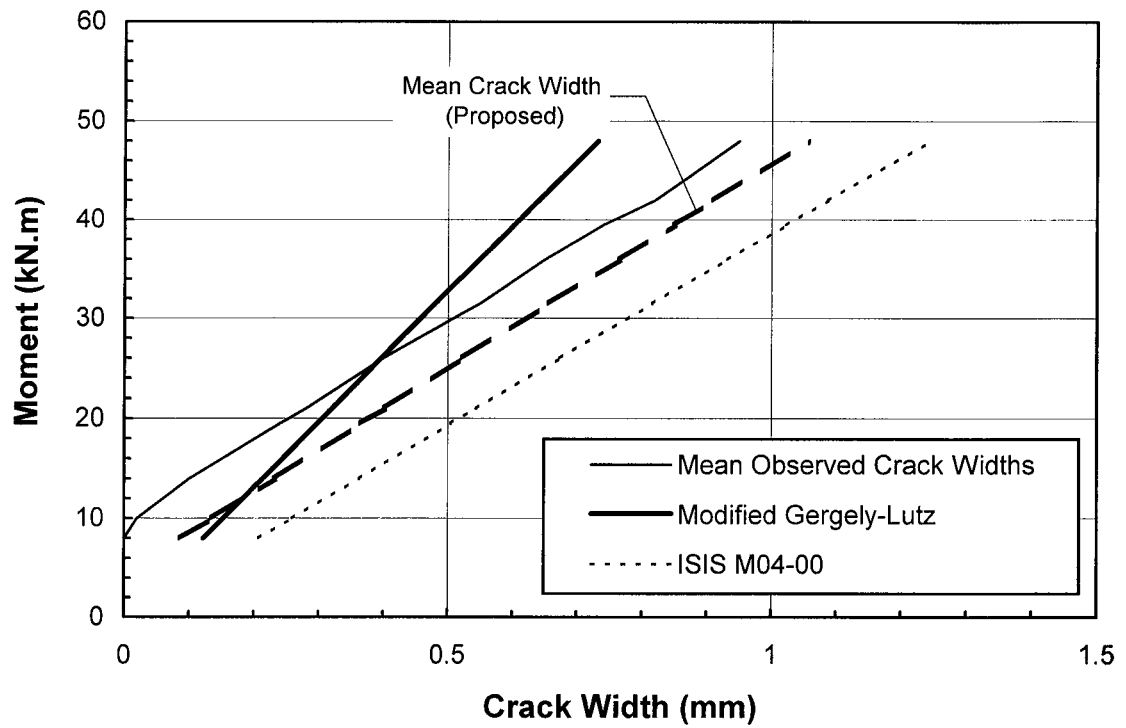


**Fig. 8.19 Crack Width Predictions : Beam MT H3**

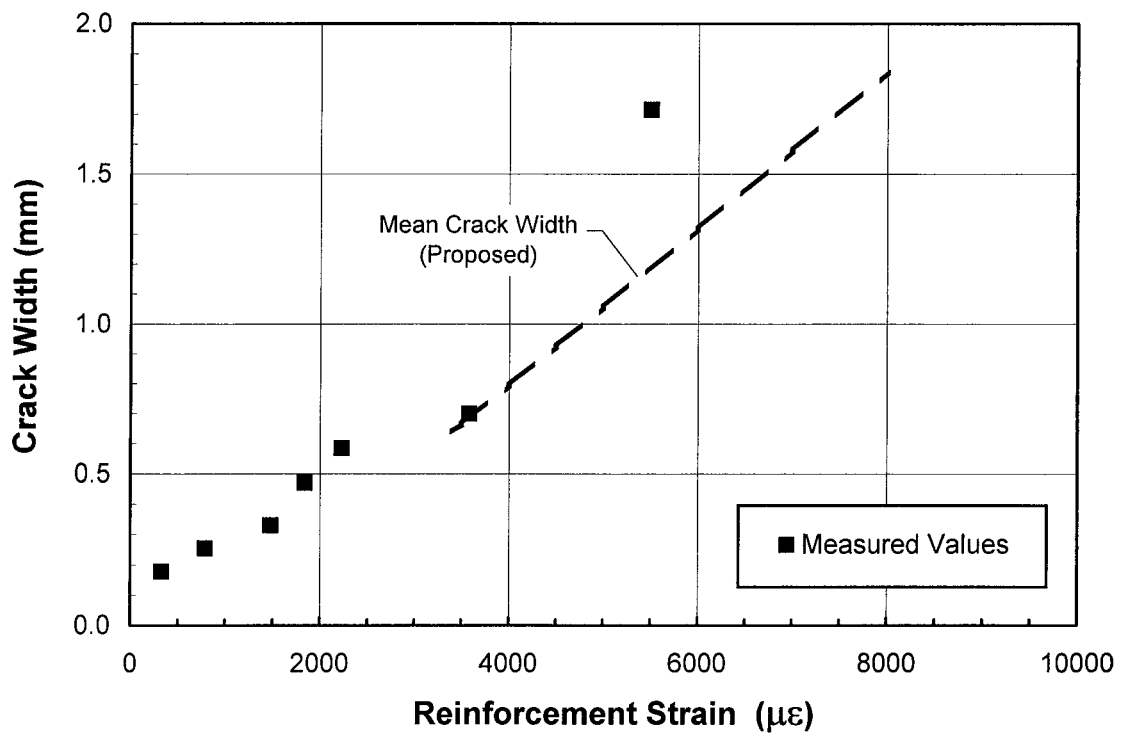


**Fig. 8.20 Crack Width Predictions : Slab GFR-1**



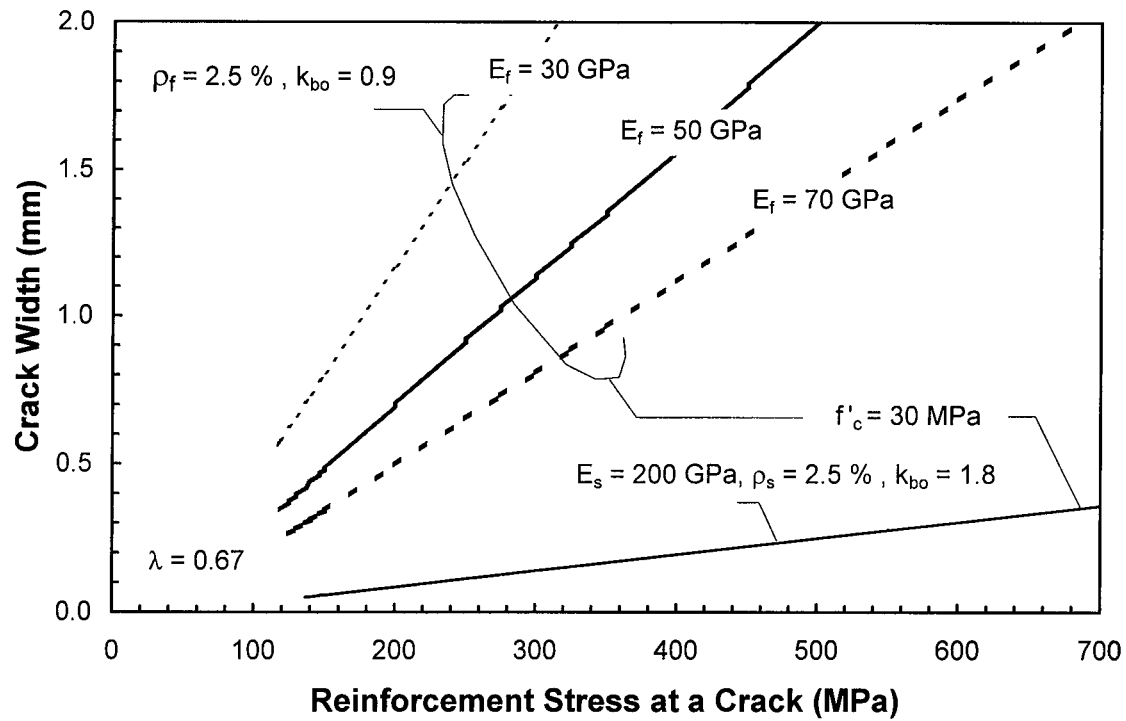


Fig. 8.21 Effect of  $\sigma_{fr}$ ,  $E_f$  and  $f'_c$  on Crack Width

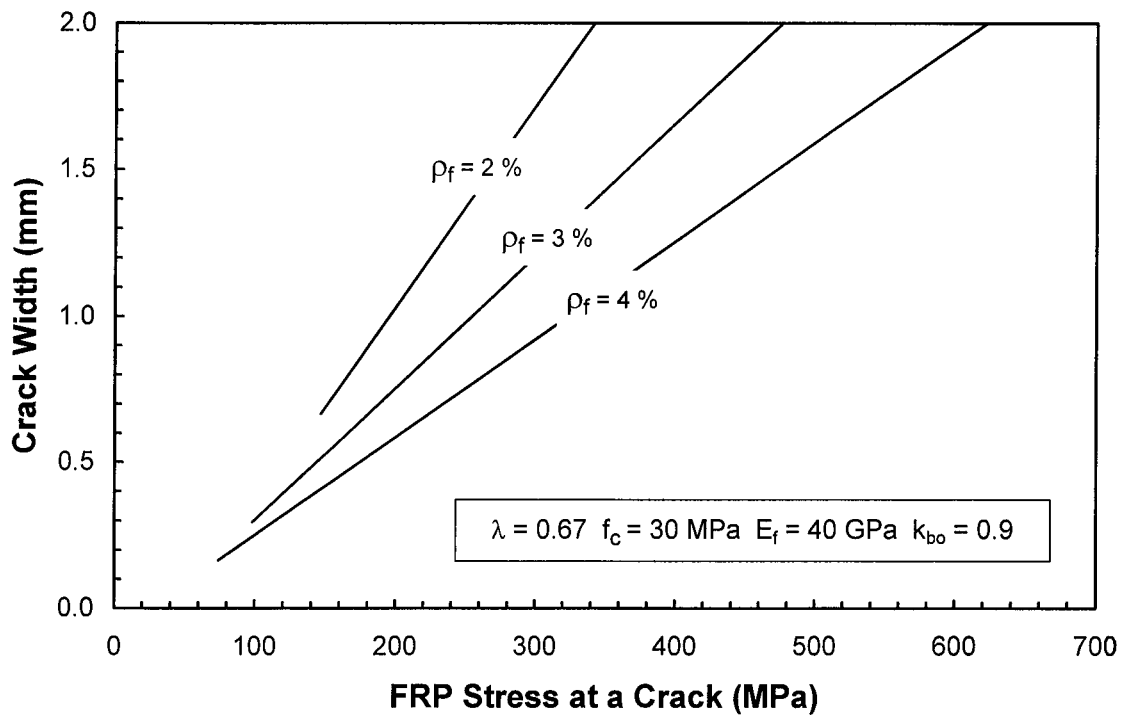


Fig. 8.22 Effect of  $\rho_f$  on Crack Width

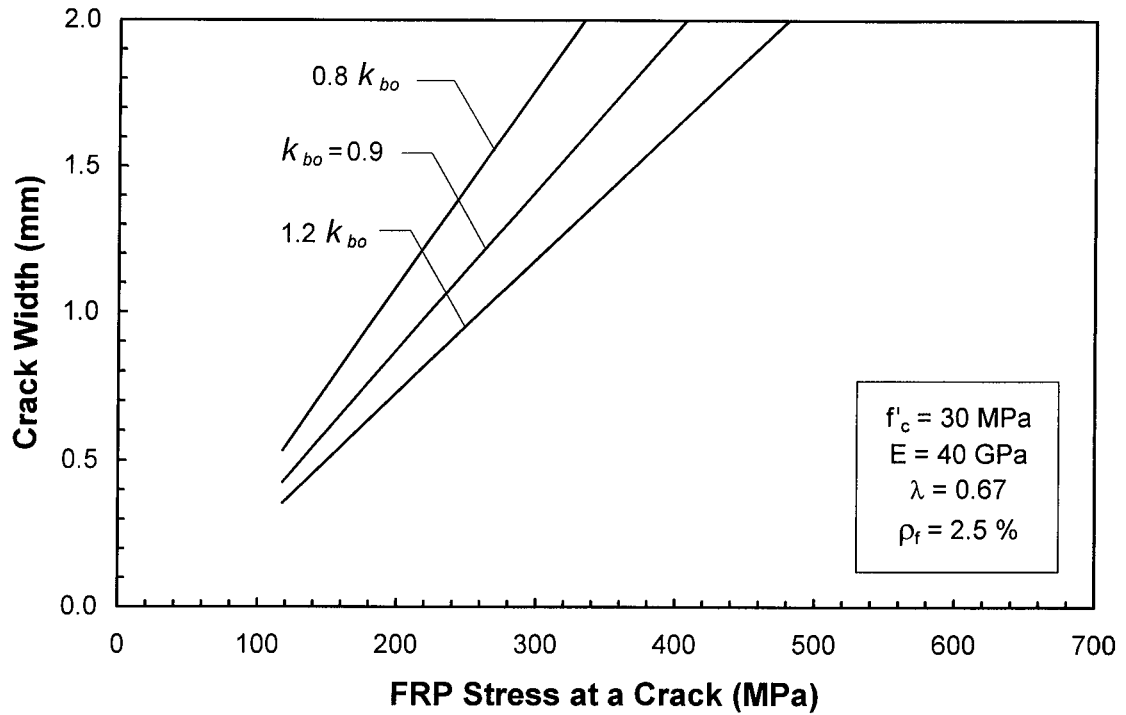


Fig. 8.23 Effect of FRP Bond Strength on Crack Width

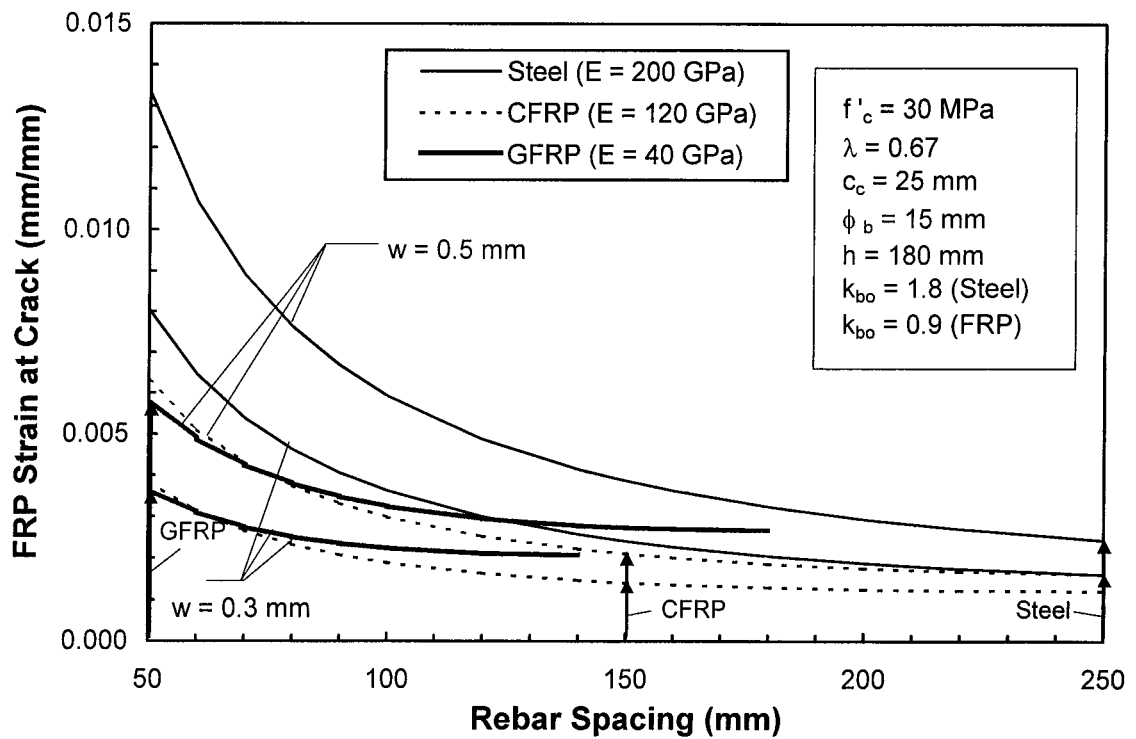


Fig. 8.24  $E_f$  and  $w$  Effect on Reinf. Strain at Crack

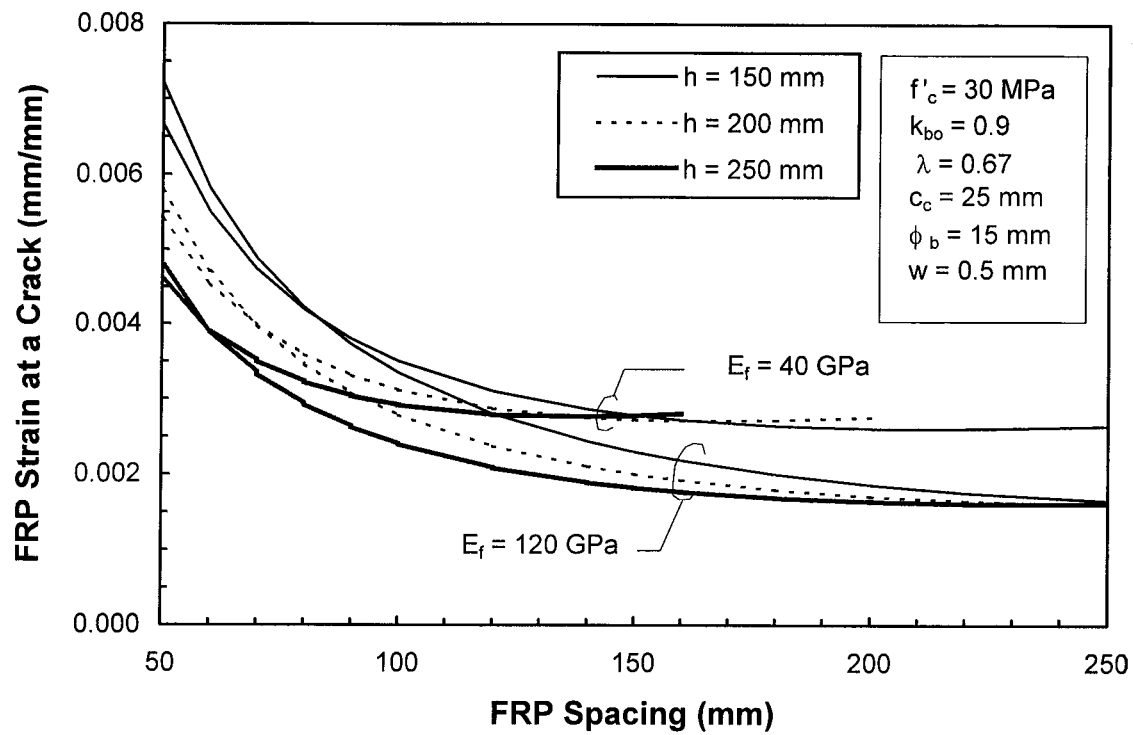


Fig. 8.25  $E_f$  and  $h$  Effect on FRP Strain at Crack

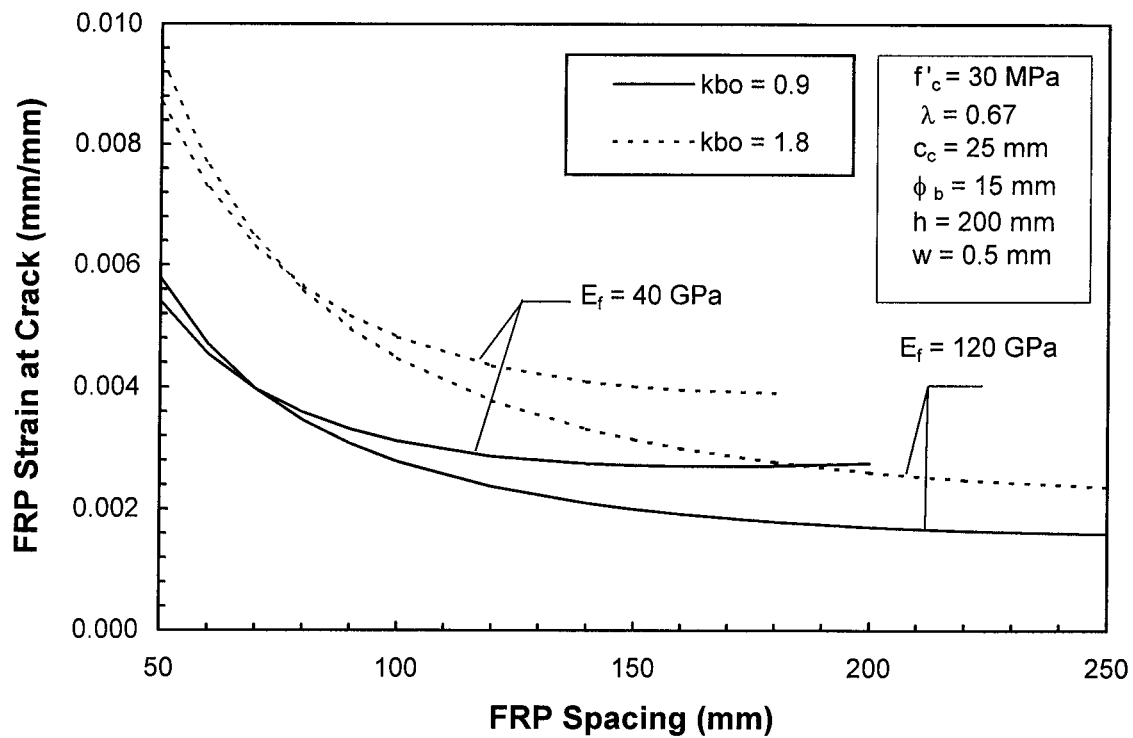


Fig. 8.26 Bond Effect on FRP Strain at Crack

## 9 Deflection Control in One-way Concrete Slabs with Internal FRP Reinforcement

### 9.1 Objective

The objective of this chapter is to present different alternatives to control short-term deflections in one-way slabs with internal FRP reinforcement in an indirect fashion by specifying maximum span-depth ratios.

Procedures are based on the concepts of limiting curvatures, integrating curvatures, and Branson's effective moment of inertia,  $I_e$ . When accounted for, the tension stiffening effect of concrete has been added to the formulations by adopting either the CEB/FIP MC90 format or defining an average effective moment of inertia that renders the same tension stiffening effect as that of MC 90 (see Hall and Ghali, 2000).

### 9.2 Indirect Deflection Control Procedures

#### 9.2.1 Simplified Procedure Disregarding Concrete's Tension Stiffening Effect

This indirect deflection control procedure is based on the concept of limiting curvatures. The procedure is set up independent of the traditional effective moment of inertia concept and neglects concrete's tension stiffening effect.

The midspan deflection,  $\Delta_m$ , of a one-way slab under a uniformly distributed load, continuous at one or both ends, is given as

$$\Delta_m = K_1 \left( \frac{5}{48} \right) \left( \frac{M_m L^2}{E_c I_e} \right) \quad [9.1]$$

where  $M_m$  is the midspan moment,  $L$  is the span length,  $E_c$  is concrete's Young modulus and  $I_e$  is the effective moment of inertia.  $K_1$  is a constant that depends only on boundary conditions,

$$K_1 = 1.2 - 0.2 \frac{M_o}{M_m} \quad [9.2]$$

where  $M_o$  is the statical moment ( $M_o = \frac{wL^2}{8}$ ),  $K_I=1$  for simply supported spans,  $K_I = 0.8$  for fixed-hinged beams and  $K_I = 0.6$  for fixed-fixed beams. The moments  $M_o$  and  $M_m$  result from the same loading. Since the objective is to set up a deflection control procedure that is independent of  $I_e$ , Eq. 9.2 can be rewritten as

$$\Delta_m = K_I \left( \frac{5}{48} \right) \psi_m L^2 \quad [9.3]$$

where  $\psi_m$  is the curvature at midspan. Dividing both sides by  $L$  results in

$$\frac{\Delta_m}{L} = K_I \left( \frac{5}{48} \right) \psi_m L \quad [9.4]$$

Assuming fully cracked behaviour, the curvature at midspan,  $\psi_m$ , is

$$\psi_m = \frac{\varepsilon_{fsm}}{d(1-x_m)} \quad [9.5]$$

where  $\varepsilon_{fsm}$  is the midspan FRP strain at service load level,  $d$  is the effective flexural depth of the slab, and  $x_m$  is the ratio of the neutral axis depth at service to the flexural slab depth at midspan. Substituting Eq. 9.5 into 9.4,

$$\frac{\Delta_m}{L} = K_I \left( \frac{5}{48} \left( \frac{\varepsilon_{fsm}}{d(1-x_m)} \right) \right) L \quad [9.6]$$

From compatibility of normal strains,

$$x_m = \frac{\varepsilon_{csm}}{\varepsilon_{csm} + \varepsilon_{fsm}} \quad [9.7]$$

where  $\varepsilon_{csm}$  is the midspan concrete strain at the extreme fibre at service load level, often taken between  $0.3 \frac{f'_c}{E_c}$  to  $0.5 \frac{f'_c}{E_c}$ . Substituting Eq. 9.7 into 9.6 and rearranging terms,

$$\frac{L}{d} \leq \frac{48}{5 K_I} \left( \frac{1}{\varepsilon_{fsm} + \varepsilon_{csm}} \right) \frac{\Delta_m}{L} \quad [9.8]$$

which is independent of the member's flexural stiffness and the applied load. In Eq. 9.8, the concrete and FRP strain define a limiting curvature. The maximum span-depth ratio is defined based on this limiting curvature assuming a maximum value of  $\Delta_m/L$ . This approach is conceptually similar to that adopted by ACI Committee 435 (1978) in which minimum reinforcement ratios for deflection control of steel-reinforced concrete slabs are defined. These ratios are shown in Table 3.2. Typical  $\Delta_m/L$  values are shown in Table 3.1.

To control deflections in terms of span-thickness ratios, Eq. 9.8 can be re-arranged as

$$\frac{L}{h} \leq \frac{48}{5 \alpha K_1} \left( \frac{1}{\varepsilon_{fsm} + \varepsilon_{csm}} \right) \frac{\Delta_m}{L} \quad [9.9]$$

where  $\alpha = h/d$ . In residential and office building slabs,  $\alpha$  varies from 0.85 to 0.95.

Figure 9.1 shows the effect of an FRP strain variation at midspan at service load level from 0.001 to 0.003 on the maximum span-depth ratio of a continuous span for different support fixity conditions. According to CSA S806-00, the maximum allowable FRP strain level at service load conditions is 30 % of the FRP rupture strain. Assuming  $\varepsilon_{fu} = 0.016$  leads to  $\varepsilon_{fsm,max} = 0.048$ . In Fig. 9.1, the effect of support conditions is represented by the  $M_o / M_m$  ratio. For instance, a  $M_o / M_m$  value of about 2.0 simulates an edge span supported by a masonry wall at the edge with the first interior support continuous. In a typical prototype interior span,  $M_o / M_m$  is about 2.8 to 3.0. Calculations are made for a maximum deflection/span ratio of 1/360, assuming that the ratio of the neutral axis depth to the flexural depth of the slab is 0.25. For comparison, the  $L/d$  variation for a strain of 0.0012 is also shown. This is a typical strain reference associated to service load conditions in steel-reinforced concrete members ( $\varepsilon_{ssm} = 0.0012$  is about 60 % of the yield strain of steel).

Figure 9.1 shows that as  $\varepsilon_{fsm}$  increases,  $L/d$  decreases. The effect of a change in boundary conditions becomes more noticeable at lower FRP strain levels. For interior span conditions in a one-way solid slab, Table 3.3 requires a minimum thickness of  $L/28$ .

Assuming  $\alpha = h/d = 1.1$ , the minimum slab flexural depth becomes  $L/31$ . According to Fig. 9.1, for interior span conditions ( $M_o/M_m$  of about 2.8) the  $L/31$  limit is reached when  $\varepsilon_{fsm}$  is about 0.001. If greater strains are sought at service load levels, the slab thickness for a given span length needs to be increased. For instance, allowing an FRP strain of 0.003 leads to  $L/d$  of about 10.5. This means that the slab with FRP needs to be about three times thicker than a steel-reinforced concrete slab with comparable span.

The need for thicker FRP-reinforced concrete slabs to satisfy deflection limits has significant economic consequences. The most immediate is that greater amounts of concrete are needed per unit area. The slab thickening choice is also critical in situations where there are limits on building height because of the potential reduction in the number of commercially available floors. It is worth noting that greater span-depth ratios can be also achieved by shortening the spans. However, this concept is not sensible. Conceptually, it fosters the belief that a structural system has to be adapted to the particular characteristics of a reinforcing material. Furthermore, such an approach may lead to impractical span ranges for certain conditions. For instance, based on Fig. 9.1 data, if only the span is modified for the same deflection limit to apply, its length needs to be three times shorter.

### 9.2.2 Simplified Procedure Accounting for Concrete's Tension Stiffening Effect

This procedure is similar to that previously examined except that concrete's tension stiffening effect is explicitly accounted for in the indirect deflection control procedure. The starting point is to rewrite Eq. 9.3 in terms of the average midspan curvature.

$$\frac{\Delta_m}{L} = K_1 \left( \frac{5}{48} \right) \psi_{m,ave} L \quad [9.10]$$

Adopting concrete's tension stiffening model of CEB/FIP MC90,

$$\psi_{m,ave} = (1 - \xi) \psi_1 + \xi \psi_2 \quad [9.11]$$

where  $\psi_1$  is the curvature at the uncracked section level,  $\psi_2$  is the curvature at fully cracked level, and  $\xi$  is a factor defined as

$$\xi = 1 - \beta_1 \beta_2 \left( \frac{M_{cr}}{M_m} \right)^2 \geq 0.4 \quad [9.12]$$

For FRP-reinforced concrete members, Hall (2000) recommends  $\beta = \beta_1 \beta_2 = 0.5$  for short-term first loading. At this point in time, there is no experimental evidence to define a  $\beta$  value for repetitive or cyclic loading of members with FRP. The adequacy of the 0.4 lower bound in Eq. 9.12 has not been examined in the context of members with FRP either. Study of these two aspects falls beyond the scope of this study.

Substituting Eq. 9.11 into Eq. 9.10 leads to

$$\frac{\Delta_m}{L} = \frac{5}{48} K_1 L [(1 - \xi) \psi_1 + \xi \psi_2] \quad [9.13]$$

The midspan curvatures  $\psi_1$  and  $\psi_2$  are defined as

$$\psi_1 = \frac{\varepsilon_{fcr}}{d - \frac{h}{2}} \quad [9.14]$$

$$\psi_2 = \frac{\varepsilon_{fsm}}{d(1 - x_m)} \quad [9.15]$$

where  $\varepsilon_{fcr}$  is the midspan FRP strain immediately before first flexural cracking. Substituting Eqs. 9.14 and 9.15 into 9.13,

$$\frac{\Delta_m}{L} = \frac{5}{48} K_1 L \left[ (1 - \xi) \frac{\varepsilon_{fcr}}{d - \frac{h}{2}} + \xi \frac{\varepsilon_{fsm}}{d(1 - x)} \right] \quad [9.16]$$

$$\text{where } \varepsilon_{fcr} = \frac{n f_{cfm}}{E_f} \quad [9.17]$$



In Eq. 9.17,  $f_{cfm}$  is the concrete stress at the centroid of the FRP reinforcement at midspan immediately before first cracking. From strain compatibility,

$$f_{cfm} = \frac{2f_r \left( d - \frac{h}{2} \right)}{h} \quad [9.18]$$

Substituting Eq. 9.18 into Eq. 9.17, and setting  $n = E_f / E_c$ ,

$$\varepsilon_{ferm} = \frac{2f_r \left( d - \frac{h}{2} \right)}{hE_c} \quad [9.19]$$

Substituting Eq. 9.19 into Eq. 9.16,

$$\frac{\Delta_m}{L} = \frac{5}{48} K_1 L \left[ (1 - \xi) \frac{2f_r}{hE_c} + \xi \frac{\varepsilon_{fsm}}{d(1 - x_m)} \right] \quad [9.20]$$

For  $f_r = 0.6\sqrt{f'_c}$ ,  $E_c = 4500\sqrt{f'_c}$ ,  $\alpha = h/d$ ,  $x_m = \frac{\varepsilon_{csm}}{\varepsilon_{csm} + \varepsilon_{fsm}}$ , and rearranging terms,

$$\frac{L}{d} \leq \frac{48}{5K_1} \left[ \frac{(1 - \xi)}{3750\alpha} + \xi (\varepsilon_{fsm} + \varepsilon_{csm}) \right] \frac{\Delta_m}{L} \quad [9.21]$$

Figure 9.2 shows the effect of concrete's tension stiffening on maximum span-depth ratio predictions for different  $M_m / M_{cr}$  ratios. Calculations are based on  $\Delta_m / L = 1/360$ ,  $\varepsilon_{csm} = 0.5 \frac{f'_c}{E_c}$ ,  $f'_c = 30$  MPa,  $\alpha = 1.1$ ,  $M_o / M_m = 2.8$  (interior span conditions) and  $\beta = 0.5$ , for midspan FRP strains of 0.001 and 0.002.

According to Fig. 9.2, applying Eq. 9.21 leads to curves that approach asymptotically the values defined by ignoring concrete's tension stiffening effect. This reflects the bond stresses deterioration under continuous loading as noted by Bresler and Bertero (1967). Figure 9.2 also shows that the slab thickening penalty one would expect by ignoring concrete's tension stiffening effect in the deflection control formulation is softened for cases where the midspan moment is up to twice the cracking moment, which is a typical

upper load limit in prototype residential building slabs. The benefits are proportionally more notorious as the FRP strain level at service load reduces.

Figure 9.3 examines the effect of a 20 % variation in the assumed concrete strain at the extreme top fibre at service load conditions for a interior span conditions, assuming  $\epsilon_{fsm} = 0.002$ . The dotted lines reflect the response including concrete's tension stiffening effect. The figure shows that an increase in the extreme compressive strain leads to more stringent maximum span-depth requirements. However, the effect is minimal.

Figure 9.4 shows the effect of the reinforcement's bond quality on the span-depth ratio predictions under short-term loading. The bond quality has been modeled in terms of the term  $\beta = \beta_1\beta_2$ . The value  $\beta = 0.5$  (Hall, 2000) represents the response of a slab with FRP with bond performance inferior to that of steel. The value  $\beta = 1.0$  represents the response of a slab with FRP having a bond performance similar to that of steel. The capping off in the latter curve is the result of the lower limit for Eq. 9.12. Figure 9.4 shows that the maximum allowed  $L/d$  value increases as bond between FRP and concrete improves.

### 9.2.3 Procedure Based on $I_e$ Concept

Two indirect deflection control approaches are proposed in this section. Both are based on the procedure developed by Branson (1968) and refined by Wang and Salmon (1973) for beams and slabs with ordinary steel reinforcement. The tension stiffening effect of concrete is adopted in two manners: i) through a modified  $I_e$  value proposed by Thériault and Benmokrane (1997) for members with FRP, and ii) through a mean  $I_e$  value that renders the same tension stiffening effect that one would obtain by applying the CEB/FIP MC90 tension stiffening model, as proposed by Hall and Ghali (2000) (see chapter 3).

The procedure starts by defining the midspan deflection of a continuous member as per

Eq. 9.1. Multiplying and dividing Eq. 9.1 by  $M_{cr} = \frac{f_r I_g}{y} = \frac{2f_r I_g}{h}$ , results in

$$\Delta_m = K_1 \frac{5}{24} \left( \frac{M_m L^2}{E_c I_e} \right) \frac{f_r I_g}{h M_{cr}} \quad [9.22]$$

Rearranging Eq. 9.23 and setting  $\alpha = h/d$ ,

$$\frac{L}{d} \leq \frac{24\alpha}{5} \frac{\Delta_m}{L} \left( \frac{E_c}{f_r K_1} \right) \left( \frac{M_{cr}}{M_m} \right) \left( \frac{I_e}{I_g} \right) \quad [9.23]$$

Making use of Branson's  $I_e$  concept, Thériault and Benmokrane (1997) recommend the following  $I_e$  definition for members reinforced with FRP.

$$I_e = \left( \frac{M_{cr}}{M_a} \right)^3 \beta_b I_g + \left[ 1 - \left( \frac{M_{cr}}{M_a} \right)^3 \right] I_{cr} \quad [9.24]$$

where  $\beta_b$  is a reduction coefficient, equal to 0.6 for type 1 C-bars (Thériault *et al* , 1997). Gao *et al* (1998) recommend

$$\beta_b = \alpha_b \left( \frac{E_f}{E_s} + 1 \right) \quad [9.25]$$

where  $\alpha_b$  is a bond-dependent coefficient, equal to 0.5.

In Branson's original procedure, for the case of simple spans,  $I_e$  is usually calculated at midspan. For continuous spans,  $I_e$  is calculated as a weighted average of the  $I_e$  values at midspan and at supports. In the context of continuous slabs with FRP, there is no guidance available on how to define  $I_e$ . The term  $M_a$  refers to the historic peak moment associated with that determining cracking according to the load combination being examined. For simple spans,  $M_a = M_m$ . For instance, if the allowable  $\Delta_m / L$  value is incremental and refers to live loads only, the maximum moment refers to the live load loading case only. MacGregor and Bartlett (2000) warn that  $M_a$  should not be taken from the envelope moment diagram to avoid overly conservative deflection control measures.

Dividing both sides of Eq. 9.24 by the gross moment of inertia,  $I_g$ , yields

$$\frac{I_e}{I_g} = \left( \frac{M_{cr}}{M_a} \right)^3 \beta_b + \left[ 1 - \left( \frac{M_{cr}}{M_a} \right)^3 \right] \frac{I_{cr}}{I_g} \quad [9.26]$$

$$\text{where } I_{cr} = \frac{b(xd)^3}{3} + n\rho_f bd^3 (1-x)^2 \quad [9.27]$$

Dividing Eq. 9.27 by  $I_g$  results in

$$\frac{I_{cr}}{I_g} = \frac{4}{\alpha^3} \left[ \frac{x^3}{3} + 3n\rho_f (1-x)^2 \right] \quad [9.28]$$

$$\text{where } x = \sqrt{(\rho_f n)^2 + 2\rho_f n} - \rho_f n \quad [9.29]$$

Assuming elastic-cracked conditions for concrete at service load levels,

$$M_a = T_f \left( d - \frac{x}{3} \right) = \rho bd^2 \varepsilon_{fs} E_f \left( 1 - \frac{x}{3} \right) \quad [9.30]$$

where  $\varepsilon_{fs}$  is the FRP strain at service load level. Dividing both sides of Eq. 9.30 by

$$M_{cr} = \frac{\alpha^2 f_r bd^2}{6}, \text{ leads to}$$

$$\frac{M_a}{M_{cr}} = \frac{6\rho_f \varepsilon_{fs} E_f}{\alpha^2 f_r} \left( 1 - \frac{x}{3} \right) \quad [9.31]$$

The FRP strain at service load level is estimated either as

$$\varepsilon_{fs} = \frac{M_a}{\rho_f bd^2 E_f \left( 1 - \frac{x}{3} \right)} \quad [9.32]$$

or, as a function of the  $\frac{M_a}{M_{cr}}$  ratio, as

$$\varepsilon_{fs} = \frac{M_a}{M_{cr}} \frac{\alpha^2 f_r}{6\rho_f E_f} \frac{1}{\left( 1 - \frac{x}{3} \right)} \quad [9.33]$$

Due to lack of information on how to determine  $I_e$  for continuous spans with FRP, the indirect deflection control procedure presented in this section will be applied to simple spans only. As a result,  $M_a = M_m$ ,  $x = x_m$ , and  $\varepsilon_{fs} = \varepsilon_{fsm}$ . The procedure is as follows:

- 1) Proportion the member for ultimate strength, i.e. select  $d$ ,  $n$ , and  $\rho_f$ .
- 2) Calculate  $x$  (Eq. 9.29).
- 3) Determine  $I_{cr}$  (Eq. 9.27).
- 4) Calculate  $\varepsilon_{fs}$  (using either Eq. 9.32 or 9.33).
- 5) Evaluate  $\frac{M_a}{M_{cr}}$  (Eq. 9.31).
- 6) Solve for  $\frac{I_e}{I_g}$  (Eq. 9.26). This value cannot exceed 1.0.
- 7) Calculate the associated span-depth ratio (Eq. 9.23).
- 8) If the resulting span-depth value is less than the minimum stipulated value, different values for  $d$ ,  $\rho$  or  $n$  need to be selected. The iterative nature of the procedure results from the fact that a closed form solution for Eq. 9.26 is difficult to obtain.

As far as slabs with FRP is concerned, Nawy *et al* (1971), Hall (2000) and Hall and Ghali (2000) found that Branson's approach tends to underestimate short-term deflections, specially at load levels roughly greater than the cracking load. Hall (2000) and Hall and Ghali (2000) recommend using the tension stiffening model of CEB/FIP MC90 for deflection control of slabs with FRP. Hall and Ghali (2000) derived an expression for the mean moment of inertia that one would obtain by applying the CEB/FIP MC 90 tension stiffening formulation. The equation (see derivation in chapter 3) is

$$I_{mean} = \frac{I_t I_{cr}}{I_t + \left( 1 + \beta_1 \beta_2 \left( \frac{M_{cr}}{M_{max}} \right)^2 \right) (I_{cr} - I_t)} \quad [9.34]$$

ISIS M04-00 also provides similar cautionary notes on the applicability of Eq. 9.24 for deflection calculations because the correction factor  $\beta_b$  in Eq. 9.25 was derived based on

a limited test database on simple span tests. ISIS M04-00 adopted the  $I_e$  value developed by Thériault (1998), which is

$$I_e = \frac{I_t I_{cr}}{I_{cr} + \left(1 - 0.5 \left(\frac{M_{cr}}{M_{\max}}\right)^2\right) (I_t - I_{cr})} \quad [9.35]$$

which is identical to Eq. 9.34. Applying the concepts presented at the beginning of this section to Thériault's Eq. 9.35 leads to (see derivation in Appendix E),

$$\frac{L}{d} \leq \frac{\alpha}{2} \frac{\Delta_m}{L} \left(\frac{E_c}{f_r K_1}\right) \left(\frac{M_{cr}}{M_a}\right) \frac{\frac{I_{cr}}{I_g}}{\frac{I_{cr}}{I_g} + \left(1 - 0.5 \left(\frac{M_{cr}}{M_a}\right)^2 \left(1 - \frac{I_{cr}}{I_g}\right)\right)} \quad [9.36]$$

with  $\frac{I_{cr}}{I_g}$  calculated according to Eq. 9.28.

Figure 9.5 shows the effect of a variation in the FRP strain at service load at midspan and the amount and type of reinforcement required for ultimate strength on the maximum span-depth ratio of a simply supported slab with FRP. The deflection control curves were plotted using  $I_e$  defined according to Eqs. 9.24 (Thériault *et al*, 1997) and 9.35 (Thériault, 1998) for a maximum allowable  $\Delta_m/L$  limit of 1/360. For comparison, the control curve for a strain of 0.0012 which represents typical strain conditions at service load levels in steel-reinforced concrete slabs is also shown. To plot the latter curve, the  $I_e$  definition given by CSA A23.3-94 has been invoked.

Consistent with previous findings, Fig. 9.5 shows that the use of higher FRP strains at service load conditions is also possible if the maximum span-depth ratio decreases, i.e. if the slab depth is increased. The difference between the span-depth predictions using Eq. 9.29 and 9.38 is significant for low  $n\rho$  values and becomes irrelevant for large  $n\rho$  values. For a given span length,  $L$ , assuming that  $n\rho$  required for strength is 0.025, and assuming  $\varepsilon_{fsm} = 0.002$ , the deflection control procedure based on Thériault's  $I_e$  value leads to a slab

that is 38 % deeper than that defined using Eq. 9.24. Assuming  $L = 4000$  mm, the required depth using Eq. 9.38 is 350 mm.

The main advantage of this deflection control procedure is that it allows to identify the implications of having excess reinforcement at service load levels. The procedure gives benefit to excess reinforcement since a strain reduction (which would be obtained as  $\rho_n$  required for strength increases) leads to a higher  $L/d$  values.

#### 9.2.4 Simplified Procedure based on Curvature Integration

This procedure is based on the concept that deflections can be evaluated by integrating curvatures. The procedure reported in this section does not account for concrete's tension stiffening effect.

Assuming a parabolic curvature distribution along a continuous span, the midspan deflection,  $\Delta_m$ , evaluated from curvature estimates at three sections is exactly

$$\Delta_m = \frac{L^2}{96} (\psi_a + 10\psi_b + \psi_c) \quad [9.37]$$

where  $L$  is the span,  $\psi_a$  and  $\psi_b$  are the curvatures at the supports and  $\psi_c$  is that at midspan. In Eq. 9.37, the curvature is considered positive when the strain is larger at the bottom face than at the top face of the member.

Figure 9.6 shows assumed strain distributions at midspan and at a typical interior support in a continuous span. At midspan, the curvature is calculated as

$$\psi_m = \frac{\epsilon_{fsm}}{d(1-x_m)} = \frac{\epsilon_{fsm}}{d \left( 1 - \frac{\epsilon_{csm}}{\epsilon_{csm} + \epsilon_{fsm}} \right)} = \frac{\epsilon_{csm} + \epsilon_{fsm}}{d} \quad [9.38]$$

where  $x_m$  is the ratio of the neutral axis depth to the flexural depth at midspan,  $\epsilon_{csm}$  is the midspan concrete strain and  $\epsilon_{fsm}$  is the midspan FRP strain, all measured at service load

levels. As an approximation, it will be assumed that the FRP strain at the support can be expressed as a multiple of the FRP strain at midspan. The curvature at the support is

$$\psi_s = \frac{\varepsilon_{fss}}{d(1-x_s)} = \frac{k\varepsilon_{fsm}}{d(1-x_s)} = \frac{\varepsilon_{fsm}}{d\left(1 - \frac{\varepsilon_{css}}{\varepsilon_{css} + k\varepsilon_{fsm}}\right)} = \frac{\varepsilon_{csm} + k\varepsilon_{fsm}}{d} \quad [9.39]$$

where  $x_s$  is the ratio of the neutral axis depth to the flexural depth at the support,  $\varepsilon_{css}$  is the concrete strain in the extreme fibre at the support,  $\varepsilon_{fss}$  is the FRP strain at the support, both at service load levels, and  $k$  is a factor defined as the ratio of  $\varepsilon_{fss}$  to  $\varepsilon_{fsm}$ . Substituting Eqs. 9.38 and 9.39 into Eq. 9.37, and assuming  $\psi_a = \psi_c$ , i.e. interior conditions,

$$\Delta_m = \frac{L^2}{96d} \left[ -2(\varepsilon_{css} + k\varepsilon_{fsm}) + 10(\varepsilon_{csm} + \varepsilon_{fsm}) \right] \quad [9.40]$$

Since a variation in the concrete strain does not lead to a significant curvature variation, let us further assume that  $\varepsilon_{css} = \varepsilon_{csm}$ . This results in

$$\Delta_m = \frac{L^2}{96d} \left[ 8\varepsilon_{css} + \varepsilon_{fsm}(10 - 2k) \right] \quad [9.41]$$

Figure 9.7 shows deflection calculations based on Eq. 9.41 for a continuous interior span. Deflections are expressed as a factor of  $96d/L^2$ . Consistent with previous findings, for members with comparable  $L$  and  $d$  values, the midspan deflections increase with the midspan strain. The figure also shows that as the FRP strain at the support increases relative to that at midspan, the rate of midspan deflection growth reduces. The reduction is relatively independent of the midspan FRP strain level. For instance, for  $\varepsilon_{fsm} = 0.002$ , the midspan deflection reduction by increasing  $k$  from 1.0 to 2.0 is 20 %. The reduction for the same change in  $k$  for  $\varepsilon_{fsm} = 0.003$  is only 22 %.

According to Eq. 9.41, midspan deflections could be slightly reduced by allowing  $k$  values in the order of 1.5 to 2.0. However, this is impractical for two reasons: i) the case  $k = 2.0$  represents full fixity conditions which are rarely achieved in prototype elements, ii) allowing high strains at supports may not be adequate when using non-yielding



reinforcement that is susceptible to creep rupture, and iii) allowing high strains at supports may have negative implications on the deformation of adjacent spans.

In search of a simple indirect deflection control procedure, Eq. 9.41 can be re-arranged as

$$\frac{L}{d} \leq 96 \frac{\Delta_m}{L} \frac{1}{(8\varepsilon_{csm} + \varepsilon_{fsm}(10 - 2k))} \quad [9.42]$$

Figure 9.8 shows the effect of FRP strain at midspan on maximum  $L/d$  ratios for  $k$  values of 1.0, 1.5 and 2.0. The curves have been plotted for an allowable midspan deflection of  $L/360$ . Consistent with previous procedures, an increase in the FRP strain at midspan is only possible at the expense of deepening the slab for a given span length. The effect of  $k$  is not significant. This suggests that shaping the distribution and the amount of slab reinforcement is not as effective as the slab thickening option. However, as  $k$  increases, the deepening penalty on FRP-reinforced slabs slightly reduces.

### 9.3 Concluding Statements

This chapter shows that indirect deflection control procedures originally envisaged for slabs with steel reinforcement can be adopted to control deflections in slabs reinforced with FRP rebars or grids.

The definition of a maximum span-depth ratio in a slab with FRP reinforcement is affected by the level of FRP strain at a crack at service load level. The proposed deflection control procedures show that, for the case of comparable spans, slabs with FRP need be thickened to satisfy the same maximum deflection-span limit for slabs with steel.

If the tension stiffening effect of concrete is accounted for in the deflection control procedure, the slab thickening penalty is somewhat softened, specially at load levels roughly greater than that at first cracking. Load conditions in this range are typical in residential and office building slabs. In terms of deflection control, the slab thickening penalty also reduces as the bond strength of the FRP reinforcement increases.

Experimental evidence studying deflections in FRP-reinforced concrete members under uniformly distributed loads is needed to examine the quality of the proposed procedures. Tests on both simple and continuous spans are desired.

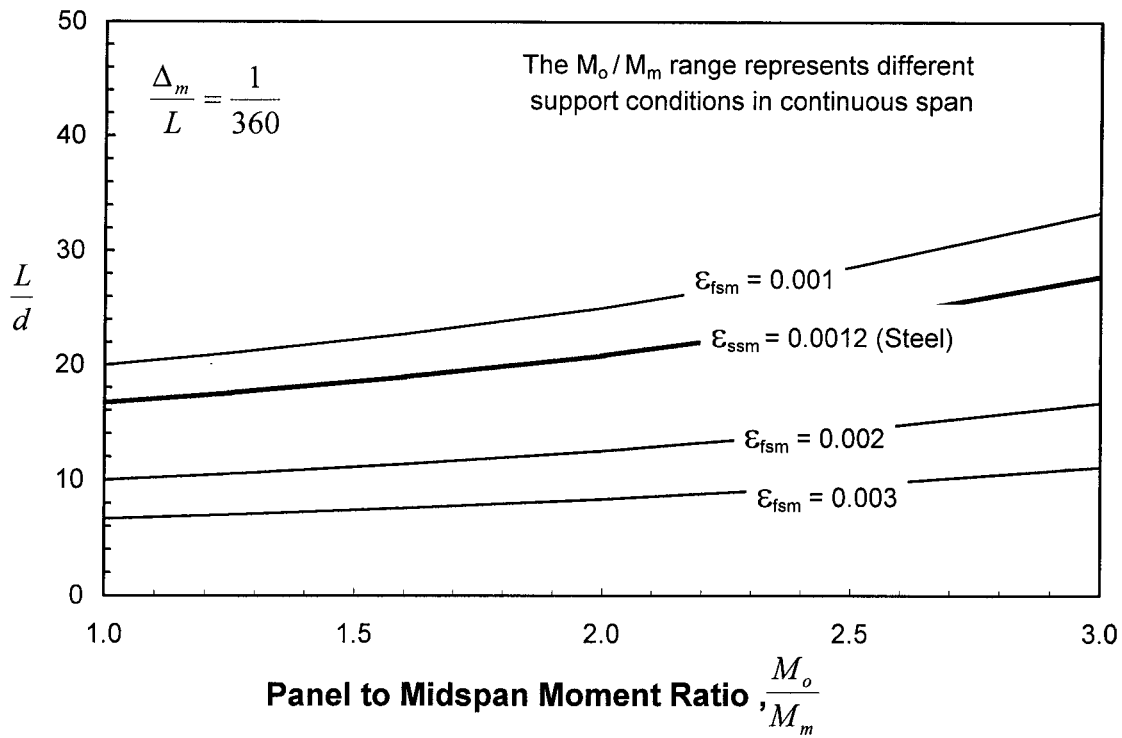


**Fig. 9.1 Reinforcement Strain Effect on Span-Depth Ratio**

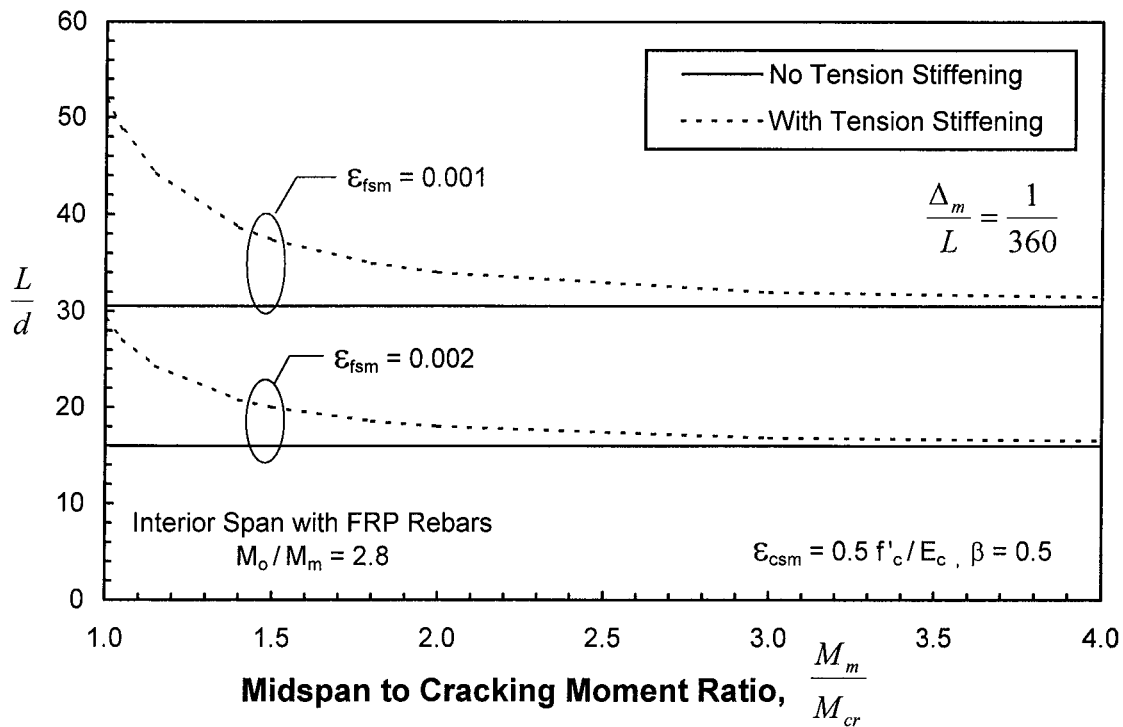


**Fig. 9.2 FRP Strain Effect on Span-Depth Ratio**

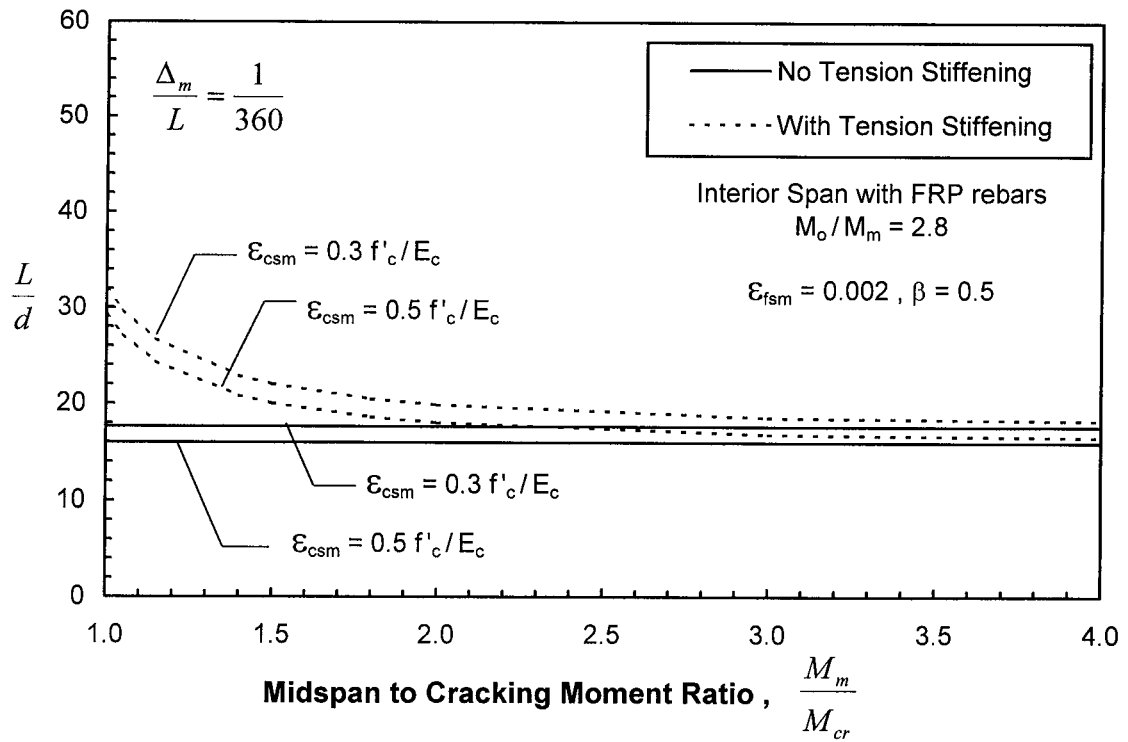


**Fig. 9.3 Concrete Strain Effect on Span-Depth Ratio**

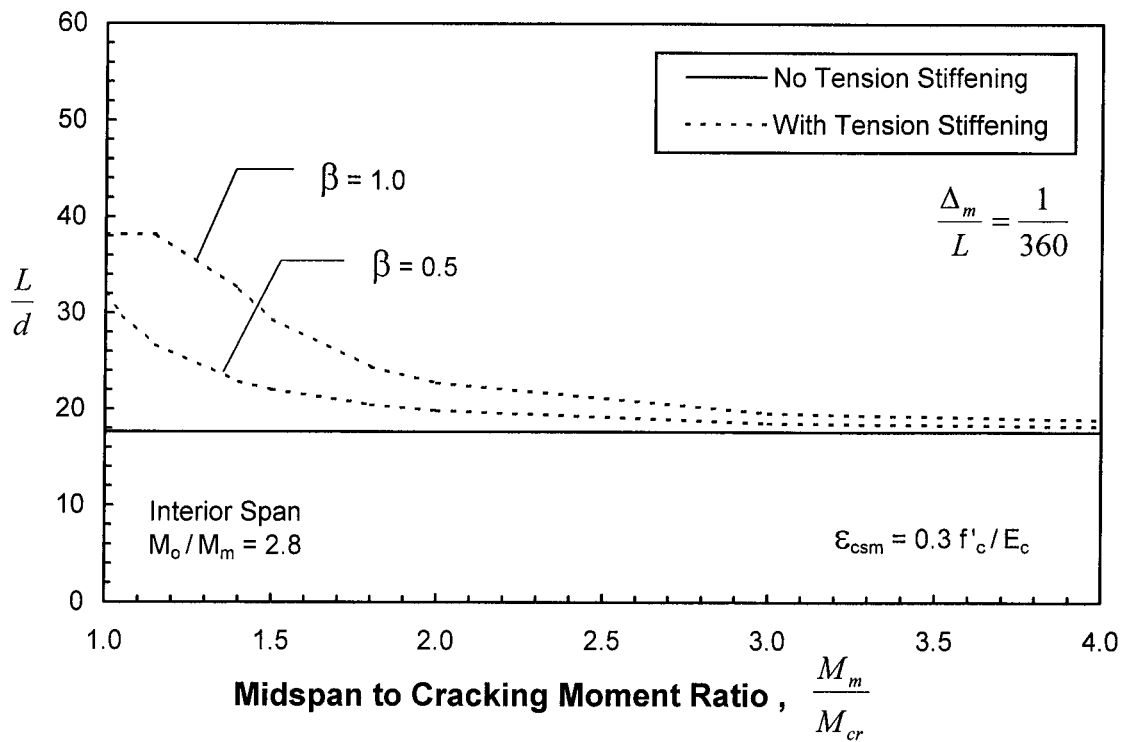


**Fig. 9.4 Bond Effect on Span-Depth Ratio**

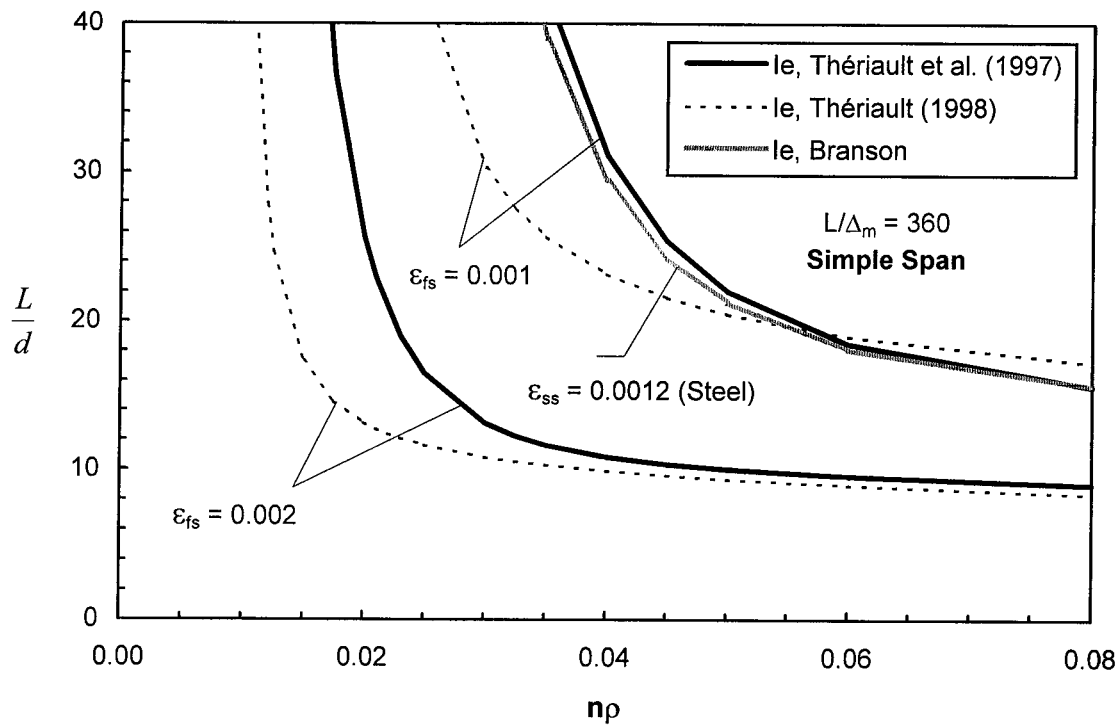


**Fig. 9.5 Max. Span-depth Ratio Based on  $I_e$  Concept**

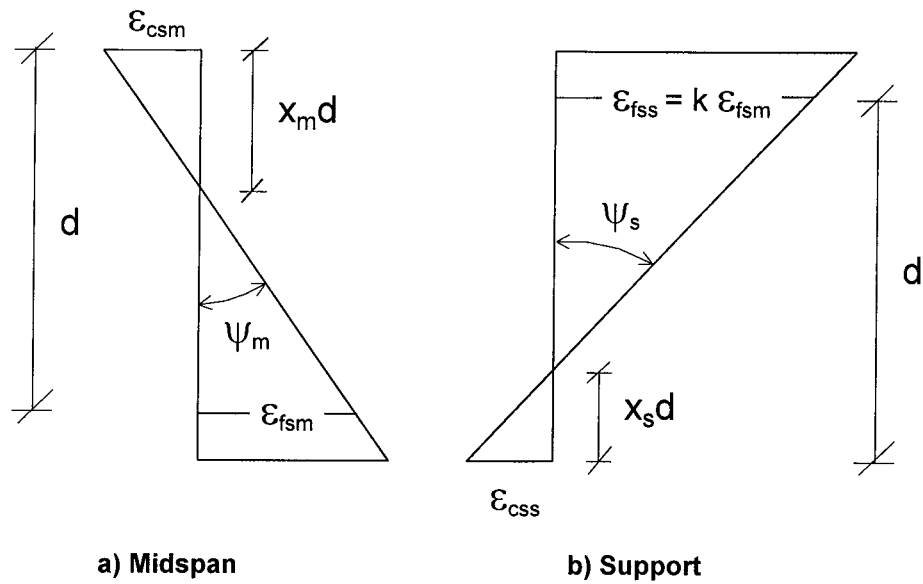


**Fig. 9.6 Midspan and Column Strain Distributions for Curvature Integration-based Deflection Control**

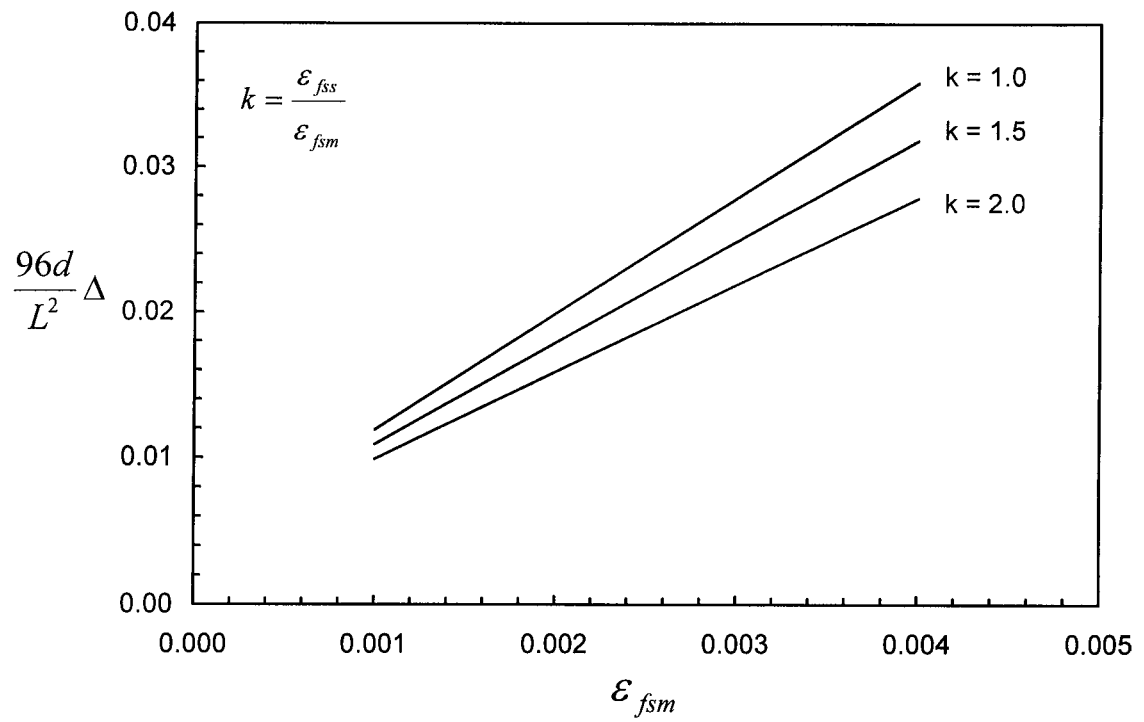


Fig. 9.7 Effect of  $k$  on Slab Deflections

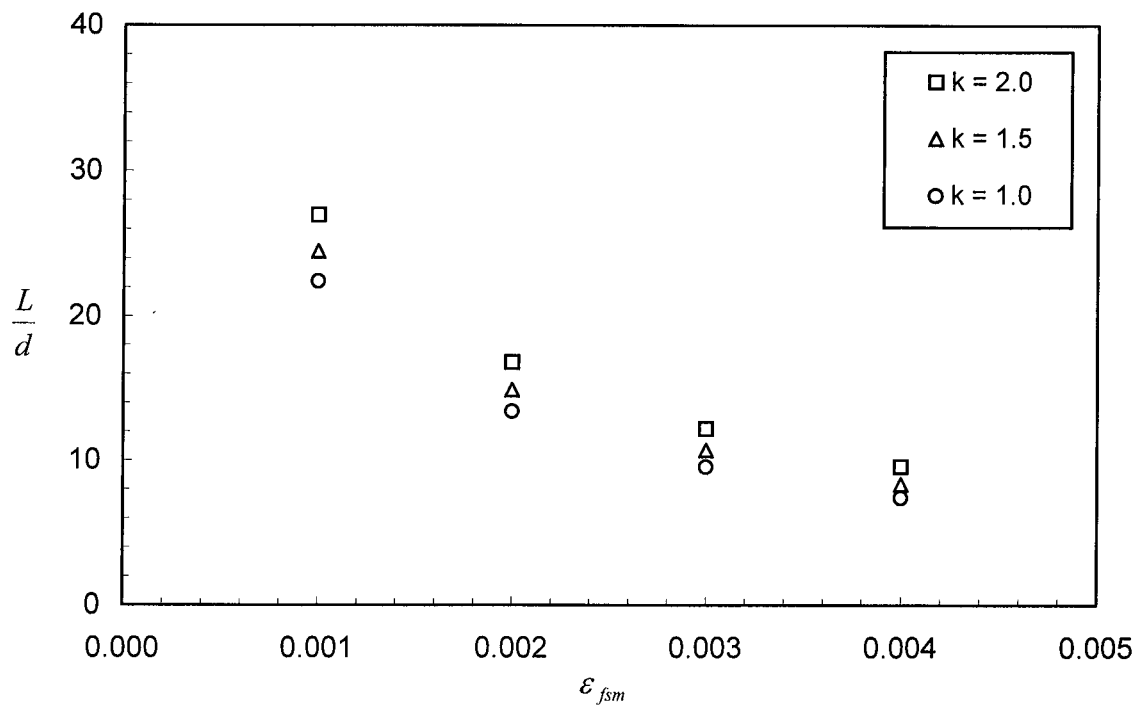


Fig. 9.8 Effect of Midspan FRP Strain and  $k$  on  $L/d$



## 10 Punching of Column-Supported Two-way Concrete Slabs Reinforced or Strengthened with FRP

### 10.1 Objectives

The main objectives of this chapter are: i) to evaluate existing design procedures for determining the concentric punching capacity of concrete slabs with internal FRP reinforcement, ii) to propose an empirical model for predicting the punching capacity of slabs with internal FRP reinforcement, and iii) to propose two mechanical models for predicting the punching capacity of slabs with internal or external FRP.

### 10.2 Punching of Concrete Two-way Flat Plates with Internal FRP Reinforcement

#### 10.2.1 Evaluation of Existing Design Procedures

The literature review presented in chapter 4 showed that most researchers have modified existing punching capacity equations by introducing the elastic moduli ratio  $\frac{E_f}{E_s}$  as a factor. In this section, most of the attention will be centred on the modifications proposed by Matthys and Taerwe (2000c) and El-Ghandour *et al* (1999).

The design equation proposed by Matthys and Taerwe (2000c) is

$$V_{r,Ghent} = 1.36 \frac{\left( 100 \rho_f \frac{E_f}{E_s} f_{cm} \right)^{1/3}}{d^{1/4}} b_o d \quad [10.1]$$

where  $f_{cm}$  is the mean compressive strength of concrete at the time of testing.

El-Ghandour *et al*'s modification to the ACI 318-99 punching shear design equation is

$$V_{r,Sheff} = 0.33 \sqrt{f'_c} \left( \frac{E_f}{E_s} \right)^{1/3} b_o d \quad [10.2]$$



Equations 10.1 and 10.2 will be compared with the test results reported in this study (Series I slabs GFR-1, GFR-2 and NEF-1) as well as with those reported by Matthys and Taerwe (MT Series), El-Ghandour *et al* (EPW Series), Banthia *et al* (BAM Series) and Ahmad *et al* (AZYX Series). The geometric and material properties of test specimens under consideration are given in Appendix E. The test results reported by Ahmad *et al* (1994) are used with caution because these slabs were reinforced with 3-D FRP grids. Since the out-of-plane FRP layer in a 3-D grid acts as shear reinforcement, this may lead to punching shear capacity enhancements that may not be accurately predicted by means of ordinary punching shear design procedures.

Because Matthys and Taerwe's slabs were tested at least 237 days after casting, some account must be made for the aging effect on the mean compressive strength of concrete,  $f_{cm}$ . Based on the recommendations of CEB/FIP MC90, Matthys and Taerwe (2001) use

$$f_{cm}(t) = \beta_{cc}(t) f_{cm} \quad [10.3]$$

where  $\beta_{cc}$  is a time-dependent coefficient, and  $f_{cm}$  is the mean compressive strength of concrete at 28 days, which will be assumed equal to  $f'_c$ . The  $\beta_{cc}$  coefficient is defined as

$$\beta_{cc}(t) = e^{(p(1-\sqrt{28/t}))} \quad [10.4]$$

where  $p$  is a coefficient that depends on the type of cement (assumed equal to 0.25 for normal and rapid hardening cements) and  $t$  is the time in days at which the concrete strength is evaluated.

Figure 10.1 shows the effect of the concrete compressive strength,  $f'_c$ , on the punching shear predictions of slabs with FRP using the format of Eq. 10.1. The points represent the experimental failure loads for each test normalised with respect to Eq. 10.1 without including the term  $f_{cm}$  in the numerator of Eq. 10.1. The solid line represents a best fit of the reported data. The curve is defined by an equation of the form  $y = (k_v f'_c)^{1/3}$ . The constant  $k_v$  is defined so that the average test to predicted ratio for the  $n$  test results reported in the literature calculated according to Eq.10.5 be equal to 1.0.

$$\sum_i^n \frac{(V_{u,test})_i}{\left( \frac{1.36 \left( 100 \rho_f \left( \frac{E_f}{E_s} \right) k_v f'_c \right)^{\frac{1}{3}} b_o d}{d^{\frac{1}{4}}} \right)} = 1.0 \quad [10.5]$$

According to Fig. 10.1, an increase in the concrete compressive strength leads to an increase in the punching capacity. Raising  $f'_c$  to the one-third power, as originally proposed by BS 8110-95, and as has been suggested by Matthys and Taerwe (2000c), adequately describes the trend of the available body of data. It is worth noting however, that there is a lack of experimental results between the 50 and 100 MPa concrete strength range. As a result, the influence of this parameter is tremendously affected by the single test result located in the far right of the plot. This result corresponds to a high strength concrete slab with hybrid Carbon-Glass FRP (slab H1) tested by Matthys and Taerwe (2000c). There is a need to conduct tests on slabs with concrete strengths ranging from 50 to 100 MPa to further validate the observed effect of the compressive strength of concrete. However, the fact that the concrete strength effect on the punching capacity of high-strength concrete slabs with ordinary steel reinforcement is similar to that shown in Fig. 10.1 permits to expect a similar effect for slabs with FRP.

Figure 10.2 shows the effect of the FRP reinforcement ratio,  $\rho_f$ , on the punching capacity of slabs with FRP. The points represent the observed failure load normalised with respect to Eq. 10.1 without including the term  $100 \rho_f$  in Eq. 10.1. The solid line is a best fit for the data. The constant  $k_v$  of the cubic equation is defined according to Eq. 10.6.

$$\sum_i^n \frac{(V_{u,test})_i}{\left( \frac{1.36 \left( 100 k_v \rho_f \left( \frac{E_f}{E_s} \right) f'_c \right)^{\frac{1}{3}} b_o d}{d^{\frac{1}{4}}} \right)} = 1.0 \quad [10.6]$$

According to Fig. 10.2, and consistent with most European Standards for the case of steel-reinforced concrete slabs, the punching capacity of a slab with internal FRP reinforcement increases with the amount of FRP reinforcement. The figure shows that Matthys and Taerwe's assumed effect for the FRP reinforcement ratio (raised to the one-third power) is consistent with the trend displayed by the existing test results.

Figure 10.3 illustrates the slab size effect on the punching capacity predictions of Eq. 10.1 for slabs with FRP. The points indicate values of experimental punching capacities normalised with respect to Eq. 10.1 without accounting for the flexural depth  $d$  in the denominator of Eq. 10.1. The size effect according to the format of Eq. 10.1 is represented by the solid line which is a best fit for the reported data. The constant  $k_v$  is defined so that

$$\sum_i^n \left( \frac{(V_{u,test})_i}{1.36 \left( 100 \rho_f \left( \frac{E_f}{E_s} \right) f'_c \right)^{\frac{1}{3}} b_o d} \cdot \frac{1}{(k_v d)^{\frac{1}{4}}} \right) = 1.0 \quad [10.7]$$

As shown in Fig. 10.3, the effect of the slab size on the punching capacity of slabs reinforced with FRP based on the available body of data is not well defined. This is because the majority of results reported in the figure result from tests conducted on slabs that are relatively thin ( $d < 142$  mm) whereas thicker slabs have not been tested. Based on the available test data reported to date, it will be assumed that the size effect for the punching capacity assessment of slabs with FRP reinforcement is not marked.

The effect of the elastic moduli ratio,  $\frac{E_f}{E_s}$ , on the shear capacity predictions is shown in

Fig. 10.4 according to Eq. 10.2 (El-Ghandour *et al* , 1999) in light of the EPW, MT and series I test results. The ordinates show values of experimental punching capacities

normalised with respect to Eq. 10.2 by isolating the effect of the  $\frac{E_f}{E_s}$  ratio. The assumed

effect of the  $\frac{E_f}{E_s}$  ratio (raised to the one-third power, as proposed by El-Ghandour *et al* ,

1999) is shown as a lower bound. The reinforcement ratios for the lightly reinforced slabs are indicated in the figure. The rest of the slabs have greater reinforcement ratios. These are not shown for neatness. For instance, the four hybrid FRP slabs tested by Matthys and Taerwe (2000c) have reinforcement ratios of either 1.26 or 3.76 %.

The experimental evidence in Fig. 10.4 indicates that an increase in  $\frac{E_f}{E_s}$  leads to greater

test to predicted ratios. However, the predictions based on the assumed lower bound are overly conservative for slabs with greater FRP reinforcement ratios. This occurs because Eq. 10.2 does not account for the effect of the FRP reinforcement ratio on the punching capacity of slabs with FRP. The fact that El-Ghandour *et al*'s proposed modification to the ACI 318 equation penalizes the use of FRP in slabs brings a serious limitation to their proposed design procedure because most real life slabs with FRP need to be over-reinforced to comply with serviceability requirements.

Figure 10.5 shows the effect of the elastic moduli ratio,  $\frac{E_f}{E_s}$  , on the punching capacity

predictions for the available experimental data based on Eq. 10.1. The slabs with GFRP and HFRP are circled. All others have CFRP reinforcement. The points indicate experimental punching capacities normalised with respect to Eq. 10.1 ignoring the term  $\frac{E_f}{E_s}$  in the denominator of Eq. 10.3. The solid line, which is a best fit of reported values,

is of the form  $y = \left( k_v \frac{E_f}{E_s} \right)^{1/3}$  where  $k_v$  is a constant evaluated according with Eq. 10.8.

$$\sum_i^n \frac{(V_{u, test})_i}{\left( \frac{1.36 \left( 100 \rho_f \left( k_v \frac{E_f}{E_s} \right) f'_c \right)^{\frac{1}{3}} b_o d}{d^{\frac{1}{4}}} \right)_i} = 1.0 \quad [10.8]$$

Figure 10.5 shows that the  $\frac{E_f}{E_s}$  effect is now simulated better than it was in Fig. 10.4 because Eq. 10.1 accounts explicitly for the  $\rho_f$  effect. To improve the accuracy of the predictions, an extra curve fit is shown in Fig. 10.5. This curve (shown as a dashed line) varies with the square root of the elastic moduli ratio. This term,  $1.36 \left( \frac{E_f}{E_s} \right)^{\frac{1}{2}}$ , also provides an accurate representation of the trend exhibited by the test results.

### 10.2.2 Proposed Empirical Model

The previous empirical evaluation demonstrates that the effect of intervening variables on the punching capacity of slabs with internal FRP reinforcement is reasonably handled by the design equation proposed by Matthys and Taerwe (2000c). However, since the available experimental data do not strongly support the existence of a size effect, and accounting for the fact that the  $\frac{E_f}{E_s}$  effect can be better represented as shown in Fig.

10.5, the following empirical equation is proposed:

$$V_{r, emp} = 2.77 (\rho_f f'_c)^{\frac{1}{3}} \sqrt{\frac{E_f}{E_s}} b_o d \quad [10.9]$$

where  $\rho_f$  is the FRP reinforcement ratio,  $\rho_f = \frac{A_f}{bd}$ , calculated as in BS 8110-95 and  $b_o$  is the critical perimeter, calculated at 1.5  $d$  away from the column face. As in BS 8110-95, the control surface is rectangular regardless of the column shape.

### 10.2.3 Comparison of the Existing and Proposed Empirical Models

Table 10.1 shows test to predicted ratios for available test results using the following existing or proposed design provisions:

- 1) Current ACI 318-99 design equation.

$$V_r = 0.33 \sqrt{f'_c} b_o d \quad [10.10]$$

- 2) Matthys and Taerwe's Eq. 10.1.
- 3) El-Ghandour *et al*'s Eq. 10.2.
- 4) Proposed Empirical Eq. 10.9.

The properties of the test specimens examined are shown in Appendix F. In the equations expressed in terms of  $f'_c$ , (Eq. 10.2, 10.9 and 10.10), this variable will be interpreted as the mean compressive strength of concrete,  $f_{cm}$ , at the time of slab testing. The modification of the BS equation proposed by El-Ghandour *et al* (1999) has not been included in the analyses because the treatment of influencing variables in this equation is conceptually similar to that in Eq. 10.1. The design provisions in CSA A23.3-94 are not examined because of their conceptual similarity with the ACI 318-99 equation.

Table 10.1 shows that the effect of the FRP reinforcement ratio and the FRP elastic modulus plays a significant role in the punching capacity assessment of two-way slabs with internal FRP reinforcement. The following are the most representative observations associated to each of the design equations under scrutiny.

The predictions according to ACI 318-99 overestimate the punching capacity of lightly FRP-reinforced slabs, e.g. EPW and Series I slabs. Nevertheless, it is worth noting that prototype FRP-reinforced concrete slabs would be rarely under-reinforced. In fact, the ACI predictions for over-reinforced slabs with FRP are more conservative, as indicated by the predictions of the MT slabs with stiffer mats; the predictions, however, are considerably scattered, with a coefficient of variation of 36.8 %. The scattered nature of these predictions is consistent with the trend of the ACI punching shear design equation

applicable to slabs with steel reinforcement, as noted by Regan and Braestrup (1985) and Braestrup (1989). The modification of the ACI equation proposed by El-Ghandour *et al* (1999) leads to much more scatter. This is because the proposed modification considers only the effect of FRP's elastic modulus but disregards that of the FRP reinforcement ratio on shear capacity predictions.

The equation proposed by Matthys and Taerwe (2000c) renders accurate punching capacity predictions. However, it is worth noting that this equation significantly underestimates the capacity of the slabs with CFRP NEFMAC mats tested by Matthys and Taerwe (2000c).

From a statistical viewpoint, Eq. 10.9 is the most accurate of all with a mean test-to-predicted ratio of 1.00 and a coefficient of variation of 12.2 %. It gives more realistic capacity predictions for the slabs with CFRP grids in the MT series compared to Eq. 10.1's predictions. However, Eq. 10.7 tends to be very conservative for slabs with flexible mats, as is the case for all the EPW series. Nevertheless, it is worth noting that slabs with low FRP content will be rarely found in real life.

One important observation from Table 10.1 is that all of the equations that account for  $E_f$  and  $\rho_f$  tend to render slightly unsafe predictions for the slabs with 3-D grids tested by Ahmad *et al* (1993). In particular, Eq. 10.7 gives the most liberal predictions. This seems somewhat misleading because one would expect the vertical grid to act as shear reinforcement and thereby enhance the punching capacity of the slabs. The reasons for this discrepancy are likely related to the particular bond characteristics of the 3-D reinforcing grids. Examination of this aspect falls beyond the scope of this study.

## **10.2.4 Proposed Mechanical Model**

### **10.2.4.1 Fundamentals**

A thorough review of the fundamental concepts behind Alexander and Simmonds' strip model for punching presented in chapter 3 reveals that the model can be modified to predict the punching capacity of concrete slabs with internal FRP reinforcement by duly

accounting for FRP's brittle-elastic behaviour, reduced stiffness and distinctive bond behaviour. In this study, most of the attention will be concentrated on two-way slabs with FRP deformed bars and 2-D grids, placed orthogonally in the slab.

According to the original strip model, the amount of load to be transferred from the slab quadrants to the radial strips strip is constrained by the appropriate limits of shear transfer in one-way slender members. These limits are significantly affected by the ability of the slab reinforcement to develop tensile force gradients. In a slab with internal FRP reinforcement, these gradients are affected by the distinctive material properties associated to FRP.

To complete the load transfer process, the radial strips transfer the load to the supporting column by arching action. In FRP-reinforced slabs, this load transfer mechanism is constrained by either the compressive strength of the joint or the rupture of the through-joint FRP reinforcement. A compressive failure is expected to govern the flexural capacity of the radial strips because, due to the need to comply with serviceability requirements, most FRP-reinforced flat plates will likely be over-reinforced.

The original strip model provides a lower bound estimate for the punching capacity of an interior slab-column connection as

$$P_s = 8 \sqrt{M_s} w \quad [10.11]$$

where  $M_s$  is the total flexural capacity of a radial strip framing into the column and  $w$  is a lower bound estimate of the one-way shear that can be delivered by the adjacent slab quadrant to one side of the strip. Recognizing the elastic-brittle nature, reduced stiffness and inferior bond strength of FRP reinforcement, there is a need to reevaluate  $M_s$  and  $w$  to determine the punching capacity of slabs with internal FRP reinforcement.

#### **10.2.4.2 Calculation of the $M_s$ Term in Slabs with FRP Reinforcement**

The total flexural capacity of a radial strip,  $M_s$ , depends on the amount and stiffness of the FRP reinforcement and the quality of concrete. The evaluation of  $M_s$  is based entirely



on conventional principles of structural concrete design. There is no empiricism whatsoever associated with the equations. The total flexural capacity is the sum of the negative and positive flexural capacities. To calculate the last two, it is necessary to determine whether the strip is under-reinforced or not in both negative and positive moment regions.

Theoretically, a radial strip is considered to be under-reinforced if

$$\rho_{fs} \leq \rho_{f,bal} \quad [10.12]$$

where  $\rho_{fs}$  is the reinforcement ratio of the radial strip,  $\rho_{fs} = A_{fs} / c_w d$ , and  $c_w$  is the column width. Neglecting the contribution of integrity steel acting as compression reinforcement, the balanced FRP reinforcement ratio is given as

$$\rho_{f,bal} = \alpha_1 \beta_1 \frac{f'_c}{f_{fu}} \left( \frac{\epsilon_{cu}}{\epsilon_{cu} + \epsilon_{fu}} \right) \quad [10.13]$$

For under-reinforced conditions, the total nominal flexural capacity of the strip is

$$M_s = M_{s,neg} + M_{s,pos} = \rho_{fs,neg} f_{fu} j d^2 c_w + \rho_{fs,pos} f_{fu} j d^2 c_w \quad [10.14]$$

where  $f_{fu}$  is the ultimate strength of FRP.

To the author's best knowledge, no single punching shear failure among the tests reported in the literature for lightly reinforced slabs with FRP has been reportedly caused by FRP rupture at the face of the column. This may raise some doubts on the adequacy of Eq. 10.14 to estimate the  $M_{s,neg}$  term. However, it seems plausible to assume that the level of FRP stress at punching approaches the tensile strength of FRP. Unfortunately, the measurement of strains in the FRP reinforcement at the face of the column has been rarely reported by researchers.

For over-reinforced radial strips, the strip failure mode is governed by concrete crushing. As a result, both positive and negative flexural strip capacities are calculated as

$$M_{s, pos or neg} = A_f f_f \left( d - \frac{a}{2} \right) \quad [10.15]$$

As shown in chapter 8, the depth of the rectangular compressive stress block,  $a$ , in an over-reinforced section is

$$a = \frac{\phi_s \rho_f E_f \epsilon_{cu} d}{2\phi_c \alpha_1 f'_c} \left( \sqrt{1 + \frac{4\alpha_1 \phi_c f'_c}{\phi_s \rho_f E_f \epsilon_{cu}}} - 1 \right) \quad [10.16]$$

and the FRP stress at punching,  $f_f = f_{fp}$ , is

$$f_{fp} = \left[ \frac{E_f \epsilon_{cu}}{2} \sqrt{1 + \frac{4\alpha_1 \beta_1 \phi_c f'_c}{\rho_f E_f \epsilon_{cu}}} - 1 \right] \quad [10.17]$$

To evaluate the negative flexural capacity of the strip,  $\epsilon_{cu}$  may be assumed to be greater than the 0.0035 value adopted by CSA S806-00 and CSA A23.3-94 depending on the amount of confinement acting on the bottom part of the slab-column joint. For instance, the test results from one-way slabs failing in flexure due to concrete crushing reported by Matthys and Taerwe (2000c) show that the peak compressive strain at failure is in the order of 0.005 mm/mm. This strain limit could be reached in two-way slab-column joints taking into account the greater confinement conditions applied on this type of connections.

Recognizing the reduced confinement conditions in positive moment regions, a value of 0.0035 is recommended at these locations. Note that the assessment of the positive flexural capacity is not required when dealing with isolated slab-column specimens unless there is rotational restraint applied on the slab edges.

#### 10.2.4.3 Calculation of the $w$ Term in Slabs with FRP Reinforcement

In strip model jargon, the  $w$  term controls the amount of shear that can be transferred by beam action from the quadrants to the radial strips. In order for beam action to develop, a force gradient between two points along the FRP reinforcement in the slab quadrant

adjacent to the radial strip needs be developed. Bar force gradients are generated through bond stresses between concrete and the reinforcement.

The description of the mechanics of bond-slip between different FRP types and concrete given in Chapter 7 showed that bond between FRP reinforcement and concrete is usually inferior to that between steel deformed bars and concrete. Since a reduction in bond leads to a reduction in the ability to generate one-way shear, the term  $w$  for slabs reinforced with internal FRP reinforcement becomes

$$w_{f,i} = k_w w = k_w (0.167 \sqrt{f'_c} d) \quad [10.18]$$

where  $k_w$  is a constant less than unity, and  $w$  is that originally derived by Alexander and Simmonds (1991) for steel-reinforced concrete slabs. In accordance with chapter 8, a lower bound for the flexural bond developed by FRP reinforcement is about half of that developed by steel. As a result,  $k_w = 0.5$  provides a lower bound for the amount of shear transferred by beam action by perimeter bars in slabs with internal FRP reinforcement.

The amount of available test results to propose a more accurate definition for the  $w$  term in two-way slabs reinforced internally with FRP is insufficient. It is necessary to conduct experimental tests examining the one-way shear transfer mechanism in i) slabs with AFRP and CFRP, ii) slabs with FRP reinforcement of different texture compared to that of C-bars, and iii) high-strength concrete slabs with FRP. This is just a set of possible case scenarios.

#### **10.2.4.4 Evaluation of Modified Strip Model for Punching of Slabs with Internal FRP Reinforcement**

The last column of Table 10.1 shows test to predicted ratios of punching shear capacity predictions using the modified strip model in light of available tests reported in the literature. The results indicate that the proposed modification leads to safe and accurate punching capacity predictions, with an average mean test to predicted ratio of 1.25 and a coefficient of variation of 14.2 %. The degree of accuracy compares favourably with the empirically derived equation recommended by Matthys and Taerwe. The model gives

much more accurate predictions than the current ACI 318 design provision. It also gives safe predictions for the slabs tested by Ahmad *et al* (1993) and leads to more realistic predictions for the C series slabs tested by Matthys and Taerwe compared to any other procedure.

### **10.3 Punching Shear of Concrete Slabs Strengthened with FRP Sheets**

#### **10.3.1 Proposed Model**

Figure 10.6 shows a plan view of a slab-column connection reinforced externally with orthogonal FRP sheets. The figure shows the slab quadrants and the four radial strips framing into the column. The sheets, of width  $b_f$ , are placed a distance  $g$  away from the column face. According to Fig. 10.6, the FRP strengthening layout used in test ER2-CS1 is defined by  $g = 0$  whereas that in test ER3-CS2 is defined by  $g = 425$  mm. In both tests,  $b_f = 250$  mm.

The proposed mechanical model to predict the punching capacity of slabs with bonded FRP sheets is based on Alexander and Simmonds' strip model for punching. According to this model, the adhesion of FRP sheets in a cruciform array should affect the load transfer from the slab to the column in two major respects: i) the FRP sheets may contribute to both the flexural stiffness and capacity of the radial strips, and ii) the FRP sheets may interact with the internal slab reinforcement in the process of transferring shear from the quadrants to the radial strip by one-way beam-action.

The results of series II slabs reported in Chapter 7 showed that the amount of CFRP used in the tests have a greater influence on the development of force gradients by the internal slab reinforcement than on the flexural capacity of the radial strips. The bar force gradient plots for the internal reinforcing steel bars placed immediately below and adjacent to the sheets show force gradients in the order of 40 % less than those in the virgin slab at similar load levels. The rehabilitation scheme of ER3-CS2 was particularly counterproductive because it affected the force gradient development in all the bars located inside the CFRP banded region around the column. The experimental results also

show that the force gradient provided by the sheets does not compensate for that lost in the internal reinforcement.

To apply the strip model to predict the concentric punching capacity of connections with FRP bands bonded on the top of the slab, it is then necessary to reevaluate the intensity and the distribution of the forces acting on the radial strip.

Figure 10.7 shows free body diagrams of one-half of a single radial strip framing into the column for three cases: i) FRP bands passing by the column face, and ii) FRP bands located away from the column but within the loaded length of the strengthened slab, defined as  $l'$ , and iii) FRP bands away from the column, installed so that their outer edges coincide with  $l'$ . The case of banded sheets located outside the loaded length  $l'$  is not considered in this study.

The non-uniformity of the loads reflects the effect of the FRP bands as a function of their position. For sheets passing by the column face, the load  $w_{fe}$  is assumed to act over a width equal to  $b_f + 0.5d$ . Since bonding of sheets away from the column affects the behaviour of all reinforcing bars located inside the banded region, the load  $w_{fe}$  spreads as shown in Figs. 10.7b and 10.7c.

In the original strip model formulation, the loaded length of the radial strip is dependent on the flexural capacity of the strip,  $M_s$ , and the uniformly distributed load acting on the radial strip,  $w$ . For the case of connections with bonded sheets, the loaded length,  $l'$ , it will be assumed that the FRP contribution to  $M_s$  is negligible. To determine  $w_{fe}$ , results from chapter 7 show that the overall effect of the sheets is more detrimental than beneficial. The reduction in the internal bar force gradients is in the order of 40 % whereas the sheets are able to restore only about 25 % of the gradient that a single bar is capable of supplying. To represent the detrimental effect of the sheets, the term  $w_{fe}$  in slabs with external FRP reinforcement can be conceptually defined as

$$w_{f,e} = k_w w = k_w (0.167 \sqrt{f'_c} d) \quad [10.19]$$

where  $k_w$  is a factor less than unity, that varies depending on the location of the sheets.

For the first case (Fig. 10.7.a), since the sheets reduce the internal force gradient in the bars located within  $b_f + 0.5d$ , the net value of  $w_{f,e}$  acting over this width, expressed as a weighted average of the sheets detrimental and beneficial effects, assuming  $b_f = 250$  mm and an average  $d = 109$  mm, is

$$k_{w,1} = \frac{(b_f + 0.5d) - 0.4(b_f + 0.5d) + 0.25b_f}{b_f + 0.5d} = 0.8 \quad [10.20]$$

For case 2 (Fig. 10.7b) and 3 (Fig. 10.7c), since the sheets affect the behaviour of all the bars located within the distance  $g + b_f + 0.5d$  from the column face, the weighted average assessment leads to  $k_{w,2} = 0.68$  and  $k_{w,3} = 0.68$  as well. Such an equality is fortuitous.

The loaded length,  $l'$ , also varies according to the sheets location. For case 1, from vertical equilibrium of forces, and considering that a single radial strip has two faces,

$$P_s = 2 [l'w - (b_f + 0.5d)(w - w_{f,e})] \quad [10.21]$$

To solve for  $l'$ , it is necessary to consider moment equilibrium and make use of the principle of superposition. This leads to

$$M_s - \frac{2wl'^2}{2} + 2(w - w_{f,e}) \frac{(b_f + 0.5d)^2}{2} = 0 \quad [10.22]$$

Solving for  $l'$  from Eq. 10.22 results in

$$l' = \sqrt{\frac{M_s + (w - w_{f,e})(b_f + 0.5d)^2}{w}} \quad [10.23]$$

Substituting Eq. 10.25 into 10.21, and recognizing that four radial strips frame into an interior column gives the punching capacity of a connection with bonded FRP sheets passing by the column face as

$$P_s = 8 \left[ \sqrt{(M_s + (w - w_{f,e})(b_f + 0.5d)^2)} w - (b_f + 0.5d)(w - w_{f,e}) \right] \quad [10.24]$$

Following the same procedure, for case 2,

$$l' = \sqrt{\frac{M_s + (w - w_{f,e})(g + b_f + 0.5d)^2}{w}} \quad [10.25]$$

and

$$P_s = 8 \left[ \sqrt{(M_s + (w - w_{f,e})(g + b_f + 0.5d)^2)w} - (g + b_f + 0.5d)(w - w_{f,e}) \right] \quad [10.26]$$

For case 3, since the load  $w_{f,e}$  is uniformly distributed over the entire loaded length  $l'$ ,

$$l' = \sqrt{\frac{M_s}{w_{f,e}}} \quad [10.27]$$

and

$$P_s = 8 \sqrt{M_s w_{f,e}} \quad [10.28]$$

Table 10.2 compares the load predictions for series II slabs using the proposed model and ACI 318-99 and BS 8110-95. The strip model for punching has only been used to predict the response of virgin slab ER1-VS. According to the sheet layout, tests ER2-CS1 and ER3-CS2 fall in the first and second cases shown in Fig. 10.7, respectively.

The results show that both ACI 318-99 and BS 8110-95 punching shear capacity predictions are conservative. However, these design provisions do not recognize the effect that the FRP bands had on the behaviour of the internal slab reinforcement. The strip model gives, in turn, a reasonable capacity prediction for ER1-VS. The proposed modification to the strip model yields safe and more accurate predictions for the two slabs with bonded sheets.

Additional test results are required to further validate the proposed design model. Tests of slab panels of realistic size and subjected to realistic boundary conditions are preferred. For the case of bonding FRP bands to the top slab surface in cruciform patterns, bands wider than those used in this study are desired. The effect of bonding FRP sheets on the bottom slab surface needs also be investigated. According to the strip model

fundamentals, this would lead to an increase in the flexural capacity of the radial strips and would therefore lead to an increase in the shear capacity of the connection.



**Table 10.1 Test to Predicted Ratios : Punching Tests on Slabs  
with Internal FRP Reinforcement**

Ref.	Slab	$V_{u, test}$ (kN)	ACI 318-99	Matthys & Taerwe (2000c) (Eq. 10.1)	El-Ghandour <i>et al</i> (1999) (Eq. 10.2)	Eq. 10.9	Modif. Strip Model
AZYX	CFRC-SN1	93	1.30	1.07	1.57	0.96	1.38
	CFRC-SN2	78	1.07	0.88	1.29	0.79	1.13
	CFRC-SN3	96	1.18	1.03	1.43	0.93	1.29
	CFRC-SN4	99	1.26	1.09	1.52	0.98	1.38
BAM	I	65	0.90	1.20	1.13	1.13	1.45
	II	61	0.75	1.04	0.94	0.98	1.28
MT	C1	181	1.22	1.51	1.58	1.25	1.39
	C1'	189	0.95	1.33	1.24	1.10	1.17
	C2	255	1.77	1.36	2.27	1.12	1.54
	C2'	273	1.42	1.22	1.81	1.01	1.32
	C3	347	1.66	1.60	2.15	1.24	1.61
	C3'	343	1.26	1.37	1.63	1.06	1.28
	CS	142	1.03	1.19	1.14	0.91	1.14
	CS'	150	0.81	1.05	0.90	0.81	0.96
	H1	207	0.79	1.19	1.38	1.15	1.17
	H2	231	1.75	1.16	2.98	1.13	1.43
	H2'	171	1.83	1.03	3.11	1.00	1.45
	H3	237	1.22	1.12	2.03	0.99	1.16
	H3'	217	1.50	1.19	2.47	1.04	1.45
EPW	SG1	170	0.46	1.03	0.76	0.87	1.13
	SC1	229	0.61	1.09	0.74	0.79	1.30
	SG2	271	0.62	1.13	1.02	0.96	1.14
	SG3	237	0.67	1.14	1.10	0.97	1.12
	SC2	317	0.91	1.18	1.11	0.86	1.24
Series I	GFR-1	217	0.68	1.17	1.23	1.08	1.03
	GFR-2	260	0.83	1.12	1.49	1.04	1.08
	NEF-1	206	0.58	1.03	1.10	0.98	0.87
Mean :			1.07	1.17	1.52	1.00	1.25
$\sigma$ :			0.397	0.155	0.622	0.122	0.178
CoV (%) :			36.8	13.2	40.8	12.1	14.2

**Table 10.2 Test to Predicted Ratios : Series II Slab Tests**

Test	$V_{u, test}$ (kN)	ACI 318-99 (kN)	BS 8110-95 (kN)	Strip Model (kN)	Prop. Model (kN)	(T/P) ACI	(T/P) BS	(T/P) Strip Model	(T/P) Prop. Model
ER1-VS	540.7	399.8	357.4	495.6	N/A	1.35	1.51	1.09	N/A
ER2-CS1	512.4	430.8	375.7	N/A	475.8	1.19	1.36	N/A	1.08
ER3-CS2	475.9	405.1	360.6	N/A	408.6	1.17	1.32	N/A	1.16

- Notes: 1. Calculations based on  $\rho^- = 0.92\%$  for all slabs, and measured average flexural depths  $d^- = 109$  mm and  $d^+ = 119$  mm.
2. Material properties for the slabs are reported in Table 4.4.
3. For ER2-CS1 and ER3-CS2, the modified strip model calculations rendered values of  $M_s = 38.7$  and  $38.1$  kN.m,  $k_w = 0.8$  and  $0.68$ , and  $l' = 616$  and  $741$  mm, respectively. For the  $M_s$  calculations, the positive moment resistance of the radial strip was evaluated assuming  $A_s = 400$  mm<sup>2</sup> (area of the two integrity steel bars).

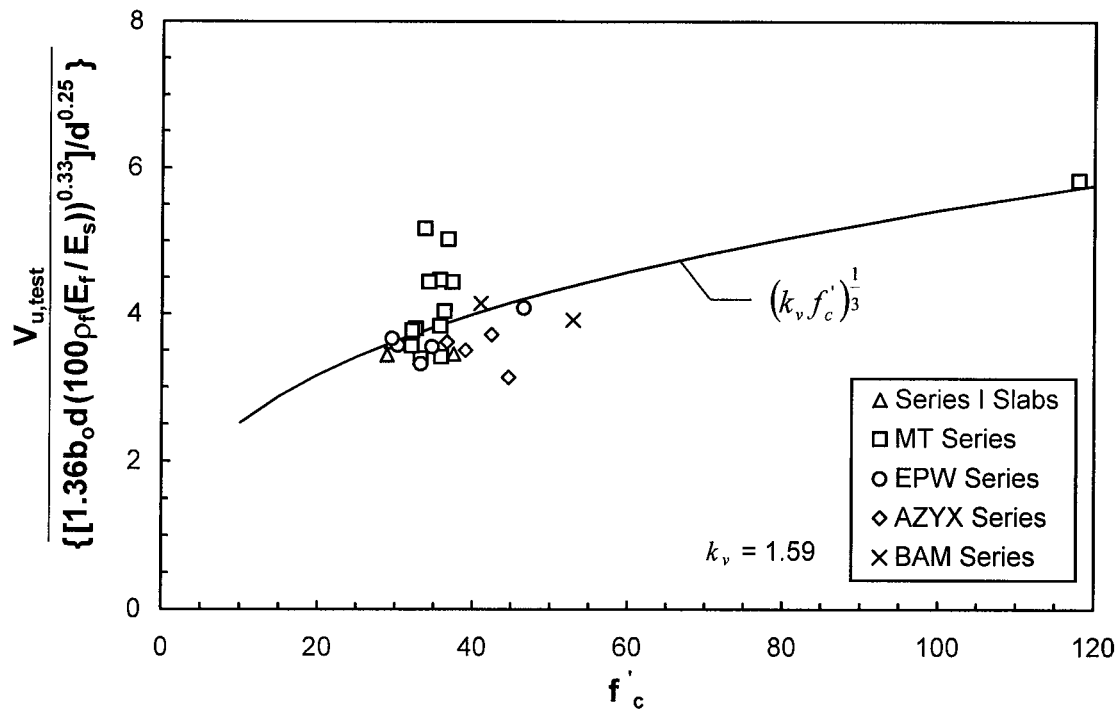


Fig. 10.1 Effect of  $f'_c$  on Eq. 10.1 Predictions

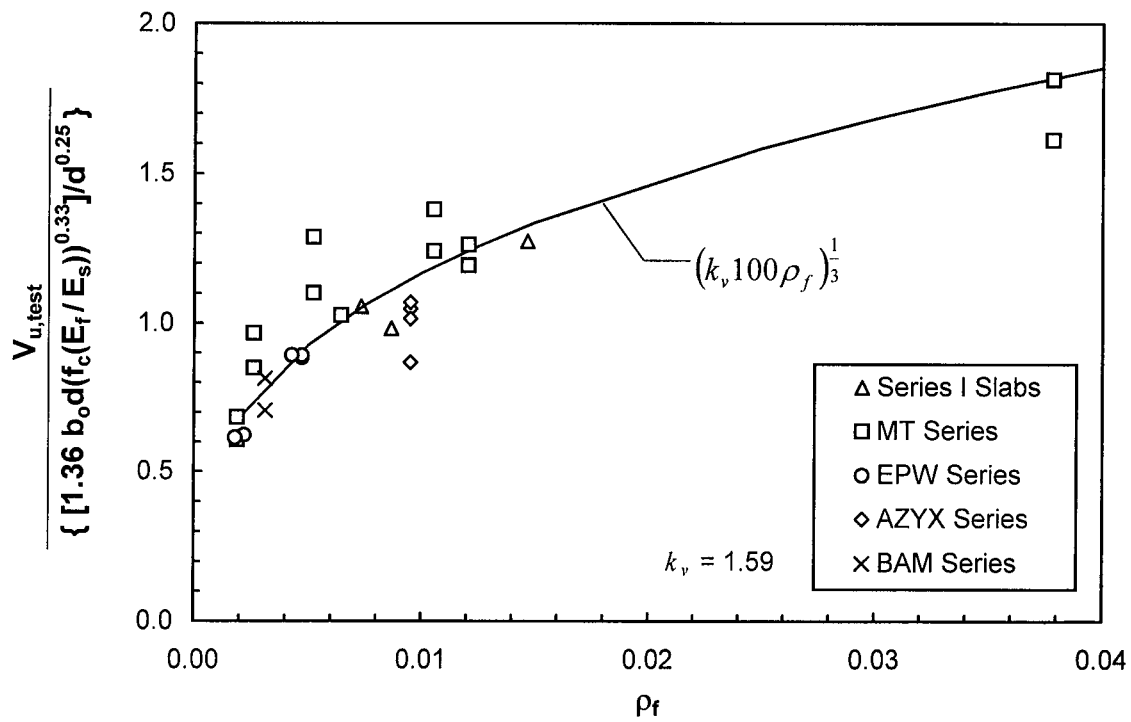


Fig. 10.2 Effect of  $\rho_f$  on Eq. 10.1 Predictions

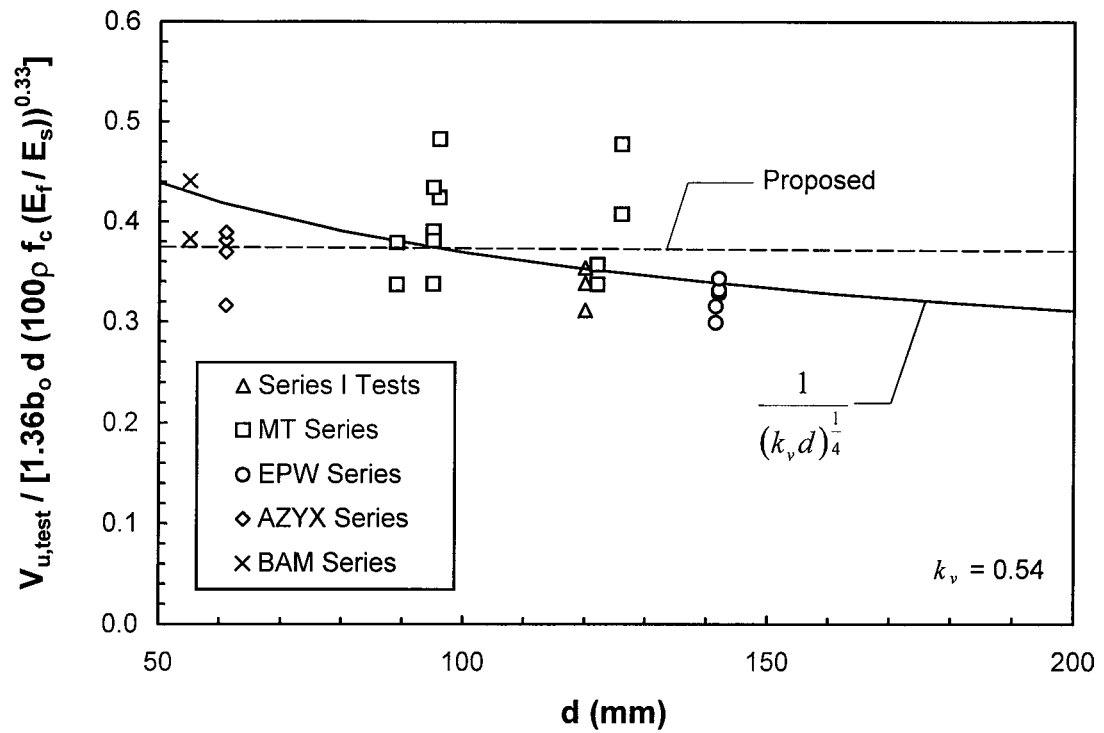


Fig. 10.3 Size Effect on Eq. 10.1 Predictions

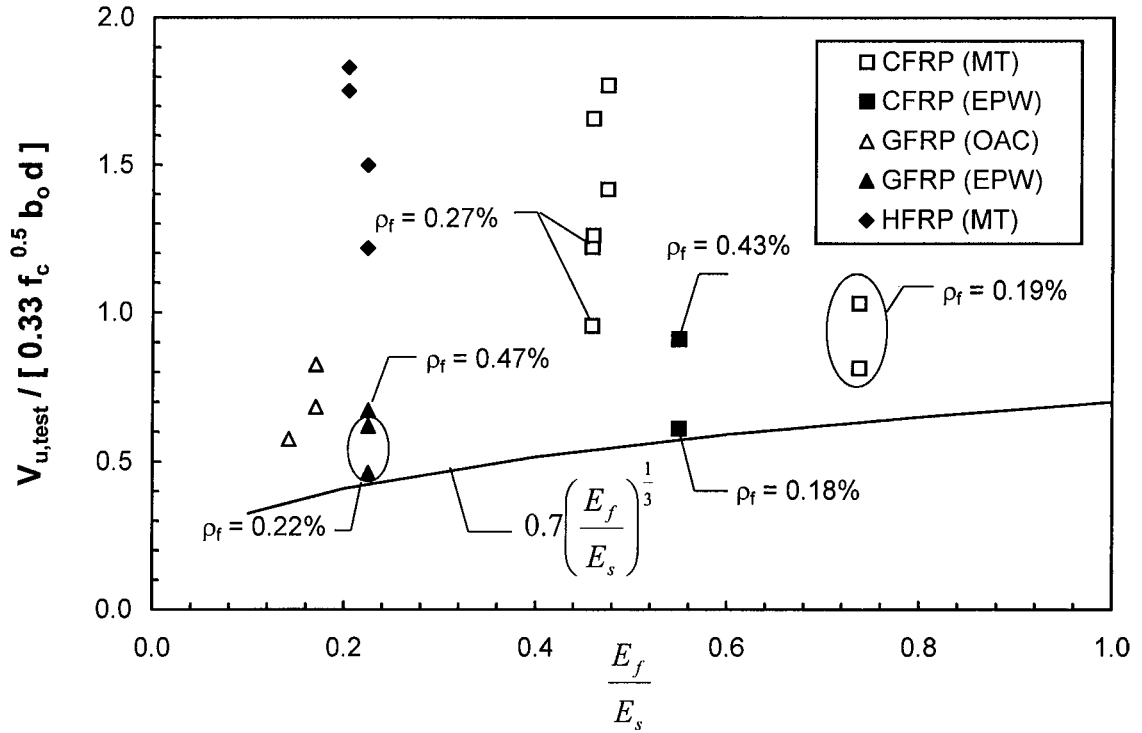


Fig. 10.4 Effect of  $E_f / E_s$  on Eq. 10.2 Predictions

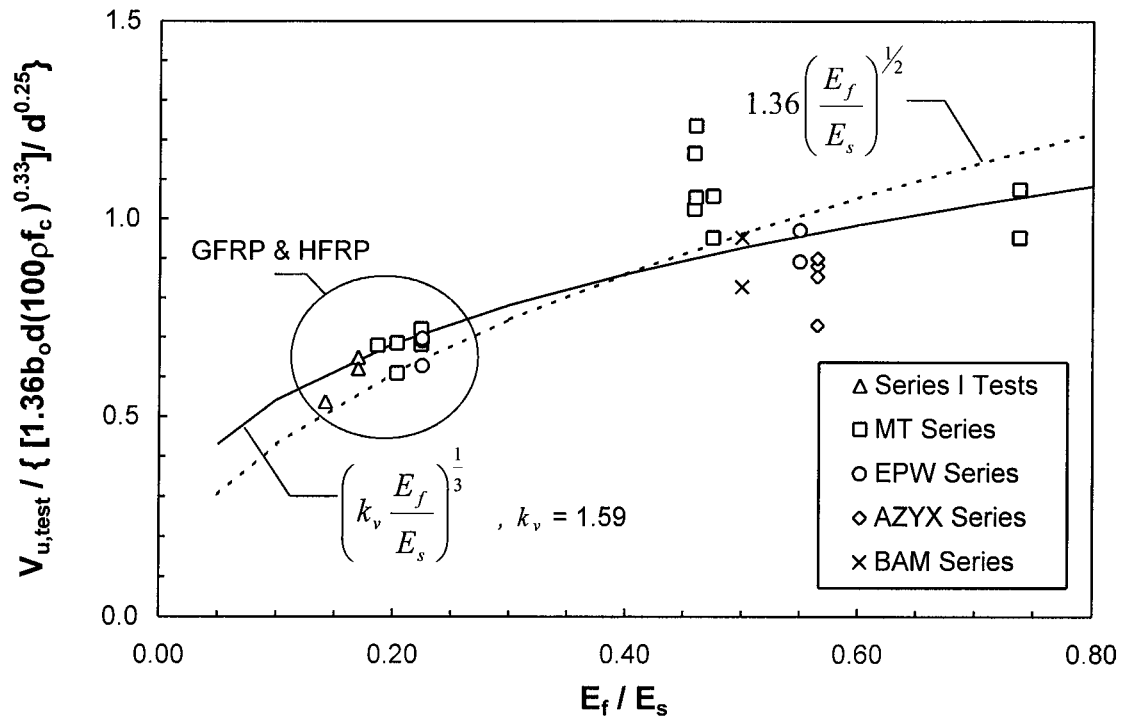


Fig. 10.5 Effect of  $E_f / E_s$  on Eq. 10.1 Predictions

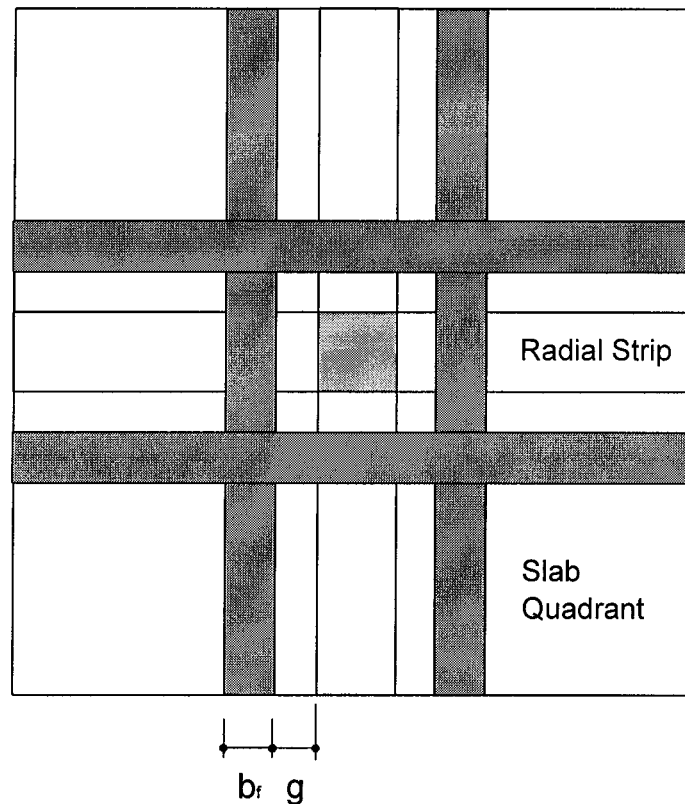
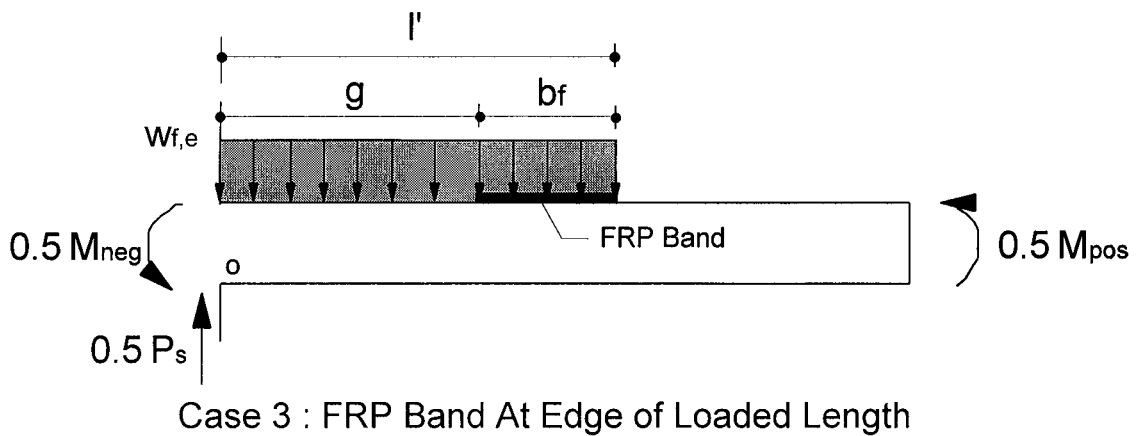
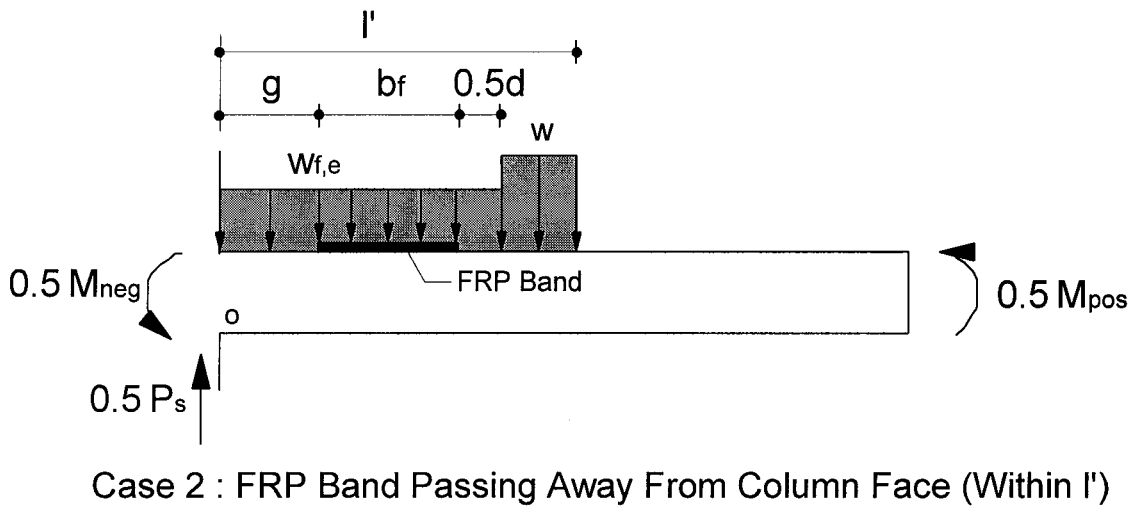
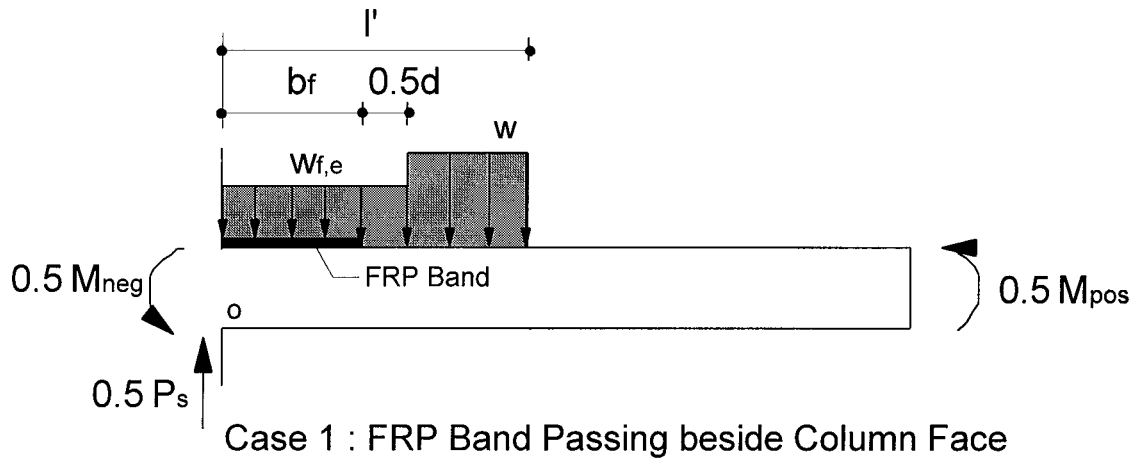


Fig. 10.6 FRP Sheet Strengthening Scheme



**Fig. 10.7 Proposed Model : FBD of Half a Radial Strip with FRP Bands**



# 11 Conclusions and Recommendations

## 11.1 General

In this study, numerous aspects of the behaviour of one and two-way concrete slabs reinforced with FRP bars, grids and sheets have been examined. In the following, conclusions reached regarding the flexural, shear and deformation behaviour of these systems are presented.

## 11.2 Flexural Behaviour

### 11.2.1 Slabs with Internal FRP Reinforcement

1. The tension stiffening effect in one-way concrete slabs reinforced internally with FRP bars is proportionally more significant than that in steel-reinforced concrete slabs. Ignoring this effect may lead to a deflection overestimate.
2. The tension stiffening effect is negligible in one-way concrete slabs reinforced with FRP grids.
3. Crack control in slabs reinforced with FRP bars and grids is as relevant as deflection control. Slabs reinforced with internal FRP rebars and grids exhibit strain localization at cracks for tight reinforcing mats ( $s_f < 100$  mm) and thin slabs ( $h < 200$  mm). The problem is particularly critical in slabs reinforced with GFRP since this material is prone to creep rupture.
4. The strain localization problem increases as the bond strength of the FRP reinforcement increases.
5. The strain localization increases as the slab thickness reduces.
6. To allow wider cracks in slabs reinforced with GFRP simply because of its superior corrosion-resistant nature is not prudent. The appropriateness of a given crack width



limit must be judged by ensuring that the FRP strain at a crack will not exceed a critical limit.

7. The tension chord model provides a comprehensive description of the tension stiffening effect and reasonably models the strain localization effect by reflecting the influence that the properties of FRP reinforcement have on the cracking behaviour of one-way concrete slabs at service load levels.
8. The relationship between crack widths and strains at cracks proposed by Hall (2000) is not independent of the type of reinforcement. Moreover, for the case of FRP-reinforced members, the strain increase in the reinforcement resulting from a crack width increase is not linear relative to the crack width ratio. The relation depends on the elastic modulus, bond strength, and amount of FRP reinforcement.
9. The spacing of flexural cracks is not always governed by bond between the reinforcement and concrete. This applies to both FRP and steel-reinforced concrete members. The disturbing effect of stress raisers such as stirrups or any other form of transverse reinforcement, and the tendency of a member to accommodate deformations due to imposed load are often more dominant than the bond interaction between the reinforcement and concrete.
10. A procedure based on the tension chord model was developed to predict crack widths in members where the crack spacing does not result from the bond interaction between the reinforcement and concrete.
11. For comparable spans, a slab with internal FRP reinforcement needs to be thickened to display a deflection at service level similar to that reached by a slab with steel reinforcement. The slab thickening reduces as the bond strength of the FRP reinforcement increases.

## **11.3 Punching Shear Behaviour**

### **11.3.1 Slabs with Internal FRP Reinforcement**

12. Concrete two-way slabs with non-yielding reinforcement display the same kinematic features that the Kinnunen and Nylander model identifies for steel-reinforced concrete slabs.
13. The punching failure of concrete slabs reinforced with internal FRP bars and grids is significantly affected by the flexural stiffness of the reinforcing mat. For a given slab thickness, the punching capacity increases with the top mat stiffness.
14. The punching capacity of slabs with internal FRP reinforcement is also affected by the quality of bond between FRP and concrete. The use of FRP grids leads to more slip than that associated to GFRP C-bars and, therefore, to a less stiff response in the service life of a structure. At ultimate, a slab with GFRP NEFMAC grid displays a more gradual load drop than does a slab with GFRP C-bars.
15. Test results from series I slabs suggest that concrete crushing does not appear to be a dominant factor in determining the source of punching shear failure in either FRP or steel-reinforced concrete two-way slabs.
16. The strip model for punching proposed by Alexander and Simmonds (1991) for steel-reinforced concrete slabs was modified to predict the punching capacity of slabs reinforced with internal FRP bars or grids. The proposed modification reasonably predicts the punching shear capacity for the totality of tests reported in the literature, to date.

### **11.3.2 Slabs with External FRP Reinforcement**

17. Bonding FRP sheets in cruciform patterns to the slab top surface does not necessarily lead to an increase in the punching shear capacity of two-way concrete slabs. The FRP sheets reduce the force gradients in the internal slab reinforcement and impose

severe shear stresses on the internal reinforcement-concrete cover interface which eventually triggers the punching failure. The sheets' effect becomes more significant the farther away the sheets are bonded relative to the column.

18. The strip model for punching proposed by Alexander and Simmonds (1991) for slabs with internal steel reinforcement was modified to predict the punching capacity of slabs reinforced with bonded FRP sheets in cruciform patterns. The modified model accurately predicts the shear capacity of the two tests reported in this study.

### **11.3.3 Miscellaneous Rehabilitation Techniques**

19. Concrete patching is an inexpensive repair technique that seems feasible for repairing concrete slabs that have experienced punching failures.
20. For the case of interior slab-column connections, the concrete patch may restore the full virgin slab punching capacity and even increase it, if the patch extends at least 200 mm beyond the column face at the lower joint portion and an almost vertical junction with the old concrete is provided.

## **11.4 Design Recommendations**

### **11.4.1 Slabs with Internal FRP Reinforcement**

1. To avoid strain localization problems at cracks, the minimum recommended thickness for concrete flat plates slabs with tight mats of GFRP C-bars and NEFMAC grids is 200 mm. To ensure proper concrete placement, the minimum FRP mat spacing shall be 100 mm.
2. The serviceability design philosophy of ISIS M04-00 and Hall (2000) which ensures that FRP strains at service level remain below a maximum limit relies heavily on an unrealistic crack width limit definition. The selected FRP strain level is, in turn, used later to select the appropriate slab thickness. Crack widths and the FRP strain at the crack can be predicted according to the model proposed in chapter 8.

3. Manufacturers of future generations of FRP deformed bars prone to creep rupture, such as GFRP, should aim at producing reinforcing elements with reduced bond enhancing features in order to attenuate the strain localization effect.
4. This study supports the model presented by Hall (2000) to calculate deflections in flexural members with internal FRP reinforcement.
5. Design equations in ACI 318-99, CSA A23.3-94 and BS 8110-95 evaluating the punching capacity of slabs with internal FRP bars or grids need to be modified to account for both the amount and stiffness of the FRP reinforcing mat. This study proposes an empirical equation and a theoretical procedure that render reasonable punching capacity predictions based on available experimental evidence. The equation proposed by Matthys and Taerwe (2000c) was found to be an accurate predictor as well.
6. The punching capacity of slabs with bonded FRP sheets in cruciform patterns on the top slab surface can be estimated according to the modification of Alexander and Simmonds' strip model presented in chapter 10.

## **11.5 Recommendations for Future Research**

1. Flexural tests on beams and one-way concrete slabs with internal FRP with detailed measurement of strains at cracks, mean crack widths, maximum crack widths and crack spacing are required to further calibrate the proposed model. Tests enforcing bond-induced and bond-independent flexural crack regimes are preferred to further examine Base's "no-slip" crack control theory.
2. There is a need to conduct further flexural tests to better identify the differences between FRP grids and rebars in terms of crack control.

3. There is a need to evaluate more thoroughly the height of the effective concrete area in tension,  $h_{ct}$ , for members with internal FRP reinforcement.
4. Experiments on the flexural behaviour of continuous beams or slabs with internal FRP subjected to uniformly distributed loading are required to further calibrate the indirect deflection control procedures presented in chapter 9.
5. Bond tests under conditions typical of slabs in flexure, representing the effects of reduced covers and bar diameter, are needed to determine the bond strength of the different FRP reinforcement families more accurately.
6. As recommended by Hall (2000), flexural tests assessing long-term effects are also needed.
7. Punching shear tests on slabs with internal FRP reinforcement are required, preferably on: i) slabs with concrete strength greater than 40 MPa, and ii) slabs with thickness greater than 200 mm to better examine the effect of both the concrete strength and the slab size, respectively, on their punching capacity.
8. Punching shear tests on concrete slabs with externally bonded FRP sheets in cruciform patterns are required to further examine this strengthening scheme. For the case of sheets bonded to the top slab surface, FRP bands that are wider than those used in this investigation are preferred.
9. Punching shear tests assessing the effect of bonding sheets on the bottom of the slab are also necessary to explore this strengthening scheme.

## LIST OF REFERENCES

- Achillides, Z., Pilakoutas, K., and Waldron, P., 1997, "Bond Behaviour of FRP Bars to Concrete," *Proceedings, 3<sup>rd</sup> Intl. Symposium on Non-Metallic (FRP) Reinforcement for Concrete Structures*, Sapporo, V. 2, pp. 341-348.
- Achillides, Z., 1998, "Bond Behaviour of FRP Bars in Concrete," Ph.D. Thesis, Centre for Cement and Concrete, Dept. of Civil and Structural Engineering, University of Sheffield.
- ACI Committee 224, 1986, "Cracking of Concrete Members in Direct Tension," *ACI Journal*, Proceedings, V. 83, No. 1, pp. 3-13.
- ACI Committee 318, 1971, "Building Code Requirements for Reinforced Concrete (ACI 318-71)," American Concrete Institute.
- ACI Committee 318, 1999, "Building Code Requirements for Structural Concrete (ACI 318-99) and Commentary (ACI 318R-99)," American Concrete Institute, Farmington Hills.
- ACI Committee 435, 1968, "Allowable Deflections", *ACI Journal*, Proceedings V. 65, No. 6, American Concrete Institute, pp. 433-444.
- ACI Committee 435, 1974, "State-of-the-Art Report, Deflection of Two Way Reinforced Concrete Floor Systems," *ACI SP 43-3, Deflections of Concrete Structures*, pp. 55-81.
- ACI Committee 435, 1978, "Proposed Revisions by Committee 435 to ACI Building Code and Commentary Provisions on Deflections," *ACI Journal*, Proceedings V. 75, No. 6, American Concrete Institute, pp. 229-238.
- ACI Committee 440, 1996, "State-of-the-art Report on Fiber Reinforced Plastic (FRP) Reinforcement for Concrete Structures," American Concrete Institute, Farmington Hills.
- Afhami, S., Alexander, S.D.B., and Simmonds, S.H., 1998, "Strip Model for Capacity of Slab-column Connections," Structural Engineering Report No. 223, Department of Civil and Environmental Engineering, University of Alberta, Edmonton, 231 pp.
- Ahmad, S.H., Zia, P., Yu, T., and Xie, Y., 1993, "Punching Shear Tests of Slabs Reinforced with 3-D Carbon Fiber Fabric," *Concrete International*, V. 16, No. 6, pp. 36-41.
- Aiello, M.A. and Ombres, L., 2000, "Cracking Analysis of FRP-reinforced Concrete Flexural members," *Proceedings, 11<sup>th</sup> International Conference on Mechanics of Composite Materials*, Riga, pp. 645-654.

Alexander, S.D.B., 1999, "Strip Design for Punching Shear," *ACI SP 183, The Design of Two-way Slabs*, T.C. Schaeffer, Ed., American Concrete Institute, Farmington Hills, Michigan, pp. 161-179.

Alexander, S.D.B. and Simmonds, S.H., 1991, "Bond Model for Strength of Slab-column Joints," Structural Engineering Report No. 174, Department of Civil Engineering, University of Alberta, Edmonton, 179 pp.

Alexander, S.D.B. and Simmonds, S.H., 1992, "Bond Model for Concentric Punching Shear," *ACI Structural Journal*, V. 89, No. 3, pp. 325-334.

Alexander, S.D.B., Lu, X., and Simmonds, S.H., 1995, "Mechanism of Shear Transfer in a Column-slab Connection," Annual Conference, Canadian Society for Civil Engineering, Ottawa, pp. 207-216.

Alkhrdaji, T., Ombres, L. and Nanni, A., 2000, "Flexural Behaviour of One-way Slabs Reinforced with Deformed GFRP Bars," *Proceedings, 3<sup>rd</sup> International Conference on Advanced Composite Materials in Bridges and Structures (ACMBS-III)*, Canadian Society for Civil Engineering, Humar, J. and Razaqpur, A.G., Eds., Ottawa, pp. 217-224.

Almeida, F.N., 1972, "Discussion of "Behaviour of Fiber Glass Reinforced Concrete Beams", by Nawy, Neuwerth and Phillips," *ASCE Journal of the Structural Division*, V. 98, No. ST 5, pp. 1207-1208.

Alvarez, M., 1998, "Einfluss des Verbundverhaltens auf das Verformungsvermögen von Stahlbeton (Influence of Bond Behaviour on the Deformation Capacity of Structural Concrete)," Report No. 236, Institute of Structural Engineering, ETH, Zürich.

Anis, N.N., 1970, "Shear Strength of Reinforced Concrete Flat Slabs without Shear Reinforcement," Ph.D. Thesis, Imperial College, London.

ASCE-ACI Committee 426, 1974, "The Shear Strength of Reinforced Concrete Members: Slabs," *ASCE Journal of the Structural Division*, V. 100, No. ST 8, pp. 1543-1591.

Bachmann, H., 1970, "Influence of Shear and Bond on Rotational Capacity of Reinforced Concrete Beams," *IABSE Proceedings*, 30-II, pp. 11-28.

Bakis, Ch.E., 1993, "FRP Reinforcement: Materials and Manufacturing", *Fiber-Reinforced-Plastic (FRP) Reinforcement for Concrete Structures: Properties and Applications*, A. Nanni, Ed., Elsevier Science Publishers, pp. 13-58.

Bakis, Ch.E., Engel, R.S., Nanni, A. and Croyle, M.G., 1997, "FRP Grid Design and Testing," *Proceedings, 3<sup>rd</sup> Intl. Symposium on Non-Metallic (FRP) Reinforcement for Concrete Structures*, Sapporo, V. 2, pp. 591-598.

Balázs, G.L., 1993, "Cracking Analysis Based on Slip and Bond Stresses, *ACI Materials Journal*, V. 90, No. 4, pp. 340-348.

Balázs, G.L., 1999, "Crack Control" in "Structural Concrete, Textbook on Behaviour, Design and Performance, Updated Knowledge of the CEB/FIP Model Code 1990," FIB Bulletin 1, Vol. 2, Fédération Internationale du Béton, Lausanne, pp. 75-99.

Bank, L.C., 1993, "Properties of FRP Reinforcements for Concrete," *Fiber-Reinforced-Plastic (FRP) Reinforcement for Concrete Structures: Properties and Applications*, A. Nanni, Ed., Elsevier Science Publishers, pp. 59-86.

Banthia, N., Al-Asaly, M., and Ma, S., 1995, "Behaviour of Concrete Slabs Reinforced with Fiber-reinforced Plastic Grid," *ASCE Journal of Materials in Civil Engineering*, V. 7, No. 4, pp. 643-652.

Base, G.D., 1982, "Bond and Control of Cracking in Reinforced Concrete," *Bond in Concrete*, P. Bartos, Ed., Applied Science Publishers, London, pp. 446-457.

Base, G.D., Read, J.B., Beeby, A.W., and Taylor, H.P.J., 1966, "Crack Control in Concrete Beams: A Comparison of High Tensile and Mild Steel Reinforcement," CIRIA Research Report No. 18, Parts 1 and 2.

Beeby, A.W., 1970, "An Investigation of Cracking in Reinforced Concrete Slabs Spanning One Way-Static Loading," CIRIA Report No. 21, 48 pp.

Benmokrane, B., Chaallal, O., and Masmoudi, R., 1996, "Flexural Response of Concrete beams Reinforced with FRP Reinforcing Bars," *ACI Structural Journal*, V. 91, No. 2, pp. 46-55.

Benmokrane, B., Tighiouart, B., and Chaalal, O., 1996, "Bond Strength and Load Distribution of Composite GFRP Reinforcing Bars in Concrete," *ACI Materials Journal*, V. 93, No. 3, pp. 246-253.

Braestrup, M.W., 1989, "Punching of Reinforced Concrete Slabs: Code Rules, Plastic Analysis, Test Results," *Nordic Concrete Research*, Publication No. 8, pp. 24-28.

Branson, D.E., 1963, "Instantaneous and Time-dependent Deflections of Simple and Continuous Reinforced Concrete beams," HPR Report No. 7, Part 1, Alabama Highway Department, Bureau of Public Roads, Aug., 78 pp.

Branson, D.E., 1968, "Design Procedures for Computing Deflections," *ACI Journal*, Proceedings V. 65, No. 9, pp. 730-742.

Branson, D.E., 1977, *Deformation of Concrete Structures*, McGraw-Hill, New York, 546 pp.



Bresler, B. and Bertero, V., 1968, "Behavior of Reinforced Concrete Under Repeated Load," *ASCE Journal of the Structural Division*, V. 94, No. ST 6, pp. 1567-1590.

British Standards Association, 1995, "Structural Use of Concrete (BS 8110-95)".

Broms, B.B., 1965, "Crack Width and Crack Spacing in Reinforced Concrete Members," *ACI Journal*, Proceedings V.62, No. 10, Oct., pp. 1237-1256.

Broms, B.B. and Lutz, L.A., 1965, "Effects of Arrangement of Reinforcement on Crack Width and Crack Spacing of Reinforced Concrete Members," *ACI Journal*, Proceedings, V. 62, No. 11, pp. 1395-1410.

Brown, V. and Bartholomew, C.L., 1993, "FRP Reinforcing Bars in Reinforced Concrete Members," *ACI Materials Journal*, V. 90, No. 1, pp. 34-39.

Burgoyne, C. J., 1993, "Should FRP be Bonded to Concrete?" *ACI SP 138 : Fiber Reinforced Plastic Reinforcement for Concrete Structures – International Symposium*, A. Nanni and Ch. Dolan, Eds., American Concrete Institute, pp. 367-380.

Burgoyne, C. J., 1999, "Advanced Composites in Civil Engineering in Europe," *Structural Engineering International*, IABSE, V. 4, pp. 267-273.

Canadian Standards Association, 1994, *CSA A23.3-94, Design of Concrete Structures*, Rexdale, Ontario, 199 pp.

Canadian Standards Association, 2000, *CSA S806-00, Draft 7, Design and Construction of Building Components with Fibre Reinforced Polymers*, Rexdale, Ontario.

Castro, P.F. and Carino, N.J., 1998, "Tensile and Nondestructive Testing of FRP Bars," *ASCE Journal of Composites for Construction*, Vol. 2, No. 1, pp. 17-27.

Chaallal, O. and Benmokrane, B., 1993, "Pullout and bond of glass-fibre rods embedded in concrete and cement grout," *Materials and Structures*, V. 26, pp. 167-175.

Chandrasekhar, S., 1972, "Discussion of "Behaviour of Fiber Glass Reinforced Concrete Beams", by Nawy, Neuwerth and Phillips," *ASCE Journal of the Structural Division*, V. 98, No. ST 2, pp. 538-539.

Chen, Ch-Ch. and Li, Ch-Yan, 2000, "An Experimental Study on the Punching Shear Behaviour of RC Slabs Strengthened by GFRP," *Proceedings of the International Workshop on Punching Shear Capacity of RC Slabs, Dedicated to Professor Sven Kinnunen*, TRITA-BKN Bulletin 57, Silfwerbrand, J. and Hassanzadeh, G., Eds., Stockholm, pp. 415-422.

Cheng, J.J.R. and Lau, D.T., 2000, "Canadian Design Code Provisions for Strengthening of Concrete and Masonry Components with Surface-bonded FRP," *Proceedings, 3<sup>rd</sup>*

*International Conference on Advanced Composite Materials in Bridges and Structures (ACMBS-III)*, Canadian Society for Civil Engineering, Humar, J. and Razaqpur, A.G., Eds., Ottawa, pp. 857-864.

Comité Euro-International du Béton (CEB) / Fédération Internationale de la Précontrainte (FIP), 1990, *Model Code for Concrete Structures, MC-90*, CEB, Thomas Telford House, London.

Corley, W.G. and Hawkins, N.M., 1968, "Shearhead Reinforcement for Slabs," *ACI Journal*, V. 65, No. 10, pp. 811-824.

Cosenza, E., Manfredi, G., and Realfonzo, R., 1997, "behavior and Modeling of Bond of FRP Rebars to Concrete," *ASCE Journal of Composites for Construction*, V. 1, No. 2, pp. 40-51.

Crepps, R.B., 1951, "Glass Fibers as the Tensioning Elements in Prestressed Concrete," *Proceeding, 1<sup>st</sup> U.S.A. Conference on Prestressed Concrete*, pp. 228-230.

Cosenza, E., Pecce, M., and Manfredi, G., 1998, "Experimental Behaviour of Concrete Beams Reinforced with glass FRP Bars," *Proceedings, ECCM-8*, Napoli, pp. 227-238.

Criswell, M., 1974, "Static and Dynamic Response of Reinforced Concrete Slab-column Connections," *ACI SP-42 : Shear in Reinforced Concrete, Vol. 2*, American Concrete Institute, pp. 721-746.

Daniali, S., 1992, "Development Length for Fiber Reinforced Plastic Bars," *Proceedings, 1<sup>st</sup> International Conference on Advanced Composite Materials in Bridges and Structures (ACMBS-I)*, K.W. Neale and P. Labossiere, Eds., pp. 179-188.

Deák, G., Hamza, I., and Visnovitz, G., 1997, "Variability of Deflections and Crack Widths in Reinforced and Prestressed Concrete Elements," CEB Bulletin d'Information No. 235 : Serviceability Models, Lausanne.

Dolan, Ch.W., 1993, "FRP Development in the United States", *Fiber-Reinforced-Plastic (FRP) Reinforcement for Concrete Structures: Properties and Applications*, A. Nanni, Ed., Elsevier Science Publishers, pp. 129-163.

Drucker, D.C., 1960, "On Structural Concrete and the Theorems of Limit Analysis," *IABSE Proceedings*, pp. 49-59.

El-Ghandour, A.W., Pilakoutas, K., and Waldron, P., 1997, "Behaviour of FRP Reinforced Concrete Flat Slabs," *Proceedings, 3<sup>rd</sup> International Symposium on Non-Metallic (FRP) Reinforcement for Concrete Structures*, Sapporo, V. 2, pp. 567-574.

El-Ghandour, A.W., Pilakoutas, K., and Waldron, P., 1999, "New Approach for Punching Shear Capacity Prediction of Fiber Reinforced Polymer Reinforced Concrete Flat Slabs,"

*ACI SP-188 : Fiber Reinforced Polymer Reinforcement for Reinforced Concrete Structures, Fourth Intl. Symposium*, Ch. Dolan, S.H. Rizkalla, A. Nanni, Eds., American Concrete Institute, Farmington Hills, pp. 135-144.

El-Ghandour, A.W., Pilakoutas, K., and Waldron, P., 2000, "Punching Shear Behaviour and Design of FRP RC Flat Slabs," *Proceedings, International Workshop on Punching Shear Capacity of RC Slabs, Dedicated to Professor Sven Kinnunen*, TRITA-BKN Bulletin 57, Silfwerbrand, J. And Hassanzadeh, G., Eds., Stockholm, pp. 359-366.

Eligehausen, R., Popov, E.P., and Bertero, V.V., 1983, "Local Bond Stress-slip Relationships of Deformed Bars Under Generalized Excitations," Report No. UCB/EERC 83-23, University of California, Berkeley.

Erki, M.A. and Heffernan, P.J., 1995, "Reinforced Concrete Slabs Externally Strengthened with Fibre-Reinforced Plastic Materials," *Proceedings, 2<sup>nd</sup> International Symposium on Non-Metallic (FRP) Reinforcement for Concrete Structures*, L. Taerwe, Ed., E & FN Spon, London, pp. 509-516.

Erki, M., (1999), "Fibre-Reinforced Polymers for Structural Engineering in Canada," *Structural Engineering International*, IABSE, V. 4, pp. 278-281.

Faza, S. and GangaRao, H.V.S., 1992a, "Bending and Bond Behaviour of Concrete beams Reinforced with Fiber Reinforced Plastic Bars," WVDORP-83 Phase I Report, West Virginia University, Morgantown, 158 pp.

Faza, S. and GangaRao, H.V.S., 1992b, "Pre- and Post-cracking Deflection Behaviour of Concrete beams Reinforced with Fiber Reinforced Plastic Reinforcing Bars," *Proceedings, 1<sup>st</sup> International Conference on Advanced Composite Materials in Bridges and Structures (ACMBS-I)*, K.W. Neale and P. Labossiere, Eds., pp. 151-160.

Faza, S. and GangaRao, H.V.S., 1993a, "Theoretical and Experimental Correlation of Behaviour of Concrete beams Reinforced with Fiber Reinforced Plastic rebars," *ACI SP 138 : Fiber Reinforced Plastic Reinforcement for Concrete Structures – International Symposium*, A. Nanni and Ch. Dolan, Eds., American Concrete Institute, pp.599-614.

Faza, S. and GangaRao, H.V.S., 1993b, "Glass FRP Reinforcing Bars for Concrete", *Fiber-Reinforced-Plastic (FRP) Reinforcement for Concrete Structures: Properties and Applications*, A. Nanni, Ed., Elsevier Science Publishers, pp. 167-188.

FIB Task Group *Bond Models*, 2000, "Bond of reinforcement in concrete," State-of-art report, FIB Bulletin 10, Fédération Internationale du Béton, Lausanne, 427 pp.

Fujisaki, T., Sekijima, K., Matsuzaki, Y. and Okamura, H., 1987, "New Material for Reinforced Concrete in place of Reinforcing Steel Bar," *IABSE Symposium*, Paris-Versailles, pp. 413-418.

Fukuyama, H. (1999), "Fibre-Reinforced Polymers in Japan," *Structural Engineering International*, IABSE, V. 4, pp. 263-266.

Fürst, A. and Marti, P., 1997, "Robert Maillart's Design Approach for Slabs," *ASCE Journal of Structural Engineering*, V. 123, No. 8, pp. 1102-1110.

Gao, D., Benmokrane, B., and Masmoudi, R., (1998), "A Calculating Method of Flexural Properties of FRP-reinforced Concrete Beam: Part 1: Crack Width and Deflection," Technical Report, Department of Civil Engineering, Université de Sherbrooke, Québec, 24 pp.

Gardner, N., 1990, "Relationship of the Punching Shear Capacity of Reinforced Concrete Slabs with Concrete Strength," *ACI Structural Journal*, V. 87, No. 1, pp. 66-71.

Gergely, P. and Lutz, L.A., 1967, "Maximum Crack Width in Reinforced Concrete Flexural Members," *ACI SP-20 : Causes, Mechanism, and Control of Cracking in Concrete*, American Concrete Institute, pp. 87-117.

Gesund, H. and Kaushik, Y.P., 1970, "Yield Line Analysis of Punching Failures in Slabs," *IABSE Proceedings*, V. 30-I, pp. 41-60.

Ghali, A., 1993, "Deflection of Reinforced Concrete members: A Critical Review," *ACI Structural Journal*, V. 90, No. 4, pp. 364-373.

Ghali, A., Sargious, M.A., and Huizer, A., 1974, "Vertical Prestressing of Flat Plates Around Columns," *ACI SP-42 : Shear in Reinforced Concrete*, American Concrete Institute, pp. 905-920.

Gold, W.J. and Nanni, A., 1998, "In-situ Load Testing to Evaluate New Repair Techniques," *Proceedings, NIST Workshop on Standards Development for the use of Fiber Reinforced Polymers for the Rehabilitation of Concrete and Masonry Structures*," Dat Duthinh, Ed., Tucson, pp. 102-112.

Hall T., 2000, "Deflections of Concrete Members Reinforced with Fibre Reinforced Polymer (FRP) Bars," M.Sc. Thesis, Department of Civil Engineering, The University of Calgary, Calgary, 292 pp.

Hall, T. and Ghali, A., 2000, "Long-term deflection prediction of concrete members reinforced with glass fibre reinforced polymer bars," *Canadian Journal of Civil Engineering*, V. 27, No. 5, pp. 890-898.

Hallgren, M., 1996, "Punching Shear Capacity of Reinforced High Strength Concrete Slabs," Doctoral Thesis, Royal Institute of Technology, TRITA-BKN Bulletin 23, Stockholm, 206 pp.

Hassanzadeh, G.H. and Sundqvist, H., 1999, "Strengthening of Bridge Slabs on Columns," *Nordic Concrete Research*, Publication No. 21.

Hewitt, B.E. and Batchelor, B. de V., 1975, "Punching Shear Strength of Restrained Slabs," *ASCE Journal of the Structural Division*, V. 101, No. ST 9, pp. 1837-1853.

Huang, T., 1972, "Discussion of "Behaviour of Fiber Glass Reinforced Concrete Beams", by Nawy, Neuwerth and Phillips," *ASCE Journal of the Structural Division*, V. 98, No. ST 2, pp. 540-541.

ISIS Canada, 2000, "Reinforcing Concrete Structures with Fibre Reinforced Polymers," Design Guideline ISIS-M04-00, Draft.

Kajfasz, S., 1960, "Some Tests on Beams Prestressed by Fibre-glass Cords," *Magazine of Concrete Research*, V. 12, No. 35, pp. 91-98.

Kaiser, H.P., 1989, "Bewehren von Stahlbeton mit kohlenstoffaserverstärkten Epoxidharzen," Diss. ETH Nr. 8918, CH-8092, Swiss Federal Institute of Technology, ETH, Zürich.

Kanakubo, T., Yonemaru, K., Fukuyama, H., Fujisawa, M., and Sonobe, Y., 1993, *ACI SP 138 : Fiber Reinforced Plastic Reinforcement for Concrete Structures – International Symposium*, A. Nanni and Ch. Dolan, Eds., American Concrete Institute, pp. 767-788.

Karbhari, V.M. and Seible, F., 1999, "Fibre-Reinforced Polymer Composites for Civil Infrastructure in the USA," *Structural Engineering International*, V. 4, pp. 274-277.

Karlsson, M., 1997, "Bond Between C-bar FRP Reinforcement and Concrete," Graduation Thesis E-97:1, Chalmers University of Technology, Division of Building Technology, Göteborg, 71 pp.

Kinnunen, S., 1963, "Punching of Concrete Slabs with Two-way Reinforcement with Special Reference to Dowel Effect and Deviation of Reinforcement from Polar Symmetry," Transactions of the Royal Institute of Technology, No. 198, Stockholm, 108 pp.

Kinnunen, S., and Nylander, H., 1960, "Punching of Concrete Slabs without Shear Reinforcement," Transactions of the Royal Institute of Technology, No. 158, Stockholm, 112 pp.

Kirstein, A.F., 1972, "Discussion of "Behaviour of Fiber Glass Reinforced Concrete Beams", by Nawy, Neuwerth and Phillips," *ASCE Journal of the Structural Division*, V. 98, No. ST 5, pp. 1206-1207.

Leonhardt, F., 1977, "Crack Control in Concrete Structures," *IABSE Surveys No. S-4/77*, International Association for Bridge and Structural Engineering, Zürich, 26 pp.

Leonhardt, F., 1988, "Cracks and Crack Control in Concrete Structures," *PCI Journal*, July-Aug., pp.124-145.

MacGregor, J.G., and Bartlett, F.M., 2000, *Reinforced Concrete: Mechanics and Design*, 1<sup>st</sup> Canadian Ed., Prentice Hall Canada Inc., Scarborough, Ontario, 1042 pp.

Makizumi, T., Sakamoto, Y., and Okada, S., 1993, "Control of Cracking by Use of Carbon Fiber Net as Reinforcement for Concrete," *ACI SP 138 : Fiber Reinforced Plastic Reinforcement for Concrete Structures – International Symposium*, A. Nanni and Ch. Dolan, Eds., American Concrete Institute, pp. 287-299.

Malvar, L.J., 1995, "Tensile and Bond Properties of GFRP Reinforcing Bars," *ACI Materials Journal*, Vol. 92, No. 3, pp. 276-285.

Marti, P., Alvarez, M., Kaufmann, W., and Sigrist, V., 1998, "Tension Chord Model for Structural Concrete," *Structural Engineering International*, IABSE, V.4, pp. 287-298.

Martin, H., 1973, "Zusammenhang zwischen Oberflächenbeschaffenheit, Verbund und Springwirkung von Bewehrungsstählen unter Kurzzeitbelastungen," *Deutscher Ausschuss für Stahlbeton*, Heft 228.

Marzouk, H. and Hussein, A., 1991, "Punching Shear Analysis of Reinforced High-strength Concrete Slabs," *Canadian Journal of Civil Engineering*, V. 18, No. 6, pp. 954-963.

Masicotte, B., Elwi, A.E., and MacGregor, J.G., 1990, "Tension-stiffening Model for Planar Reinforced Concrete Members," *ASCE Journal of Structural Engineering*, V. 116, No. 11, pp. 3039-3058.

Masmoudi, R., Benmokrane, B. and Chaallal, O., 1996, "Cracking behaviour of concrete beams reinforced with fiber reinforced plastic bars," *Canadian Journal of Civil Engineering*, V. 23, No. 6, pp. 1172-1179.

Masmoudi, R., Thériault, M., and Benmokrane, B., 1998, "Flexural Behaviour of Concrete beams Reinforced with Deformed Fiber Reinforced Plastic Reinforcing Rods," *ACI Structural Journal*, V. 95, No. 6, pp. 665-676.

Matthys, S. and Taerwe, L., 1995, "Loading Tests on Concrete Slabs Reinforced with FRP Grids," *Proceedings, 2<sup>nd</sup> International Symposium on Non-Metallic (FRP) Reinforcement for Concrete Structures*, L. Taerwe, Ed., E & FN Spon, London, pp. 287-297.

Matthys, S. and Taerwe, L., 1997, "Punching tests on Concrete Slabs Reinforced with FRP Grids," *Proceedings, 3<sup>rd</sup> International Symposium on Non-Metallic (FRP) Reinforcement for Concrete Structures*, Sapporo, V. 2, pp. 559-566.

Matthys, S. and Taerwe, L., 2000a, "Verification of the Punching resistance of Concrete Slabs Reinforced with FRP Grids," *Proceedings, International Workshop on Punching Shear Capacity of RC Slabs, Dedicated to Professor Sven Kinnunen*, TRITA-BKN Bulletin 57, Silfwerbrand, J. And Hassanzadeh, G., Eds., Stockholm, pp. 475-483.

Matthys, S. and Taerwe, L., 2000b, "Concrete Slabs Reinforced with FRP Grids. I: One-way Bending," *ASCE Journal of Composites for Construction*, V. 4, No. 3, pp. 145-153.

Matthys, S. and Taerwe, L., 2000c, "Concrete Slabs Reinforced with FRP Grids. II: Punching Resistance," *ASCE Journal of Composites for Construction*, V. 4, No. 3, pp. 154-161.

Matthys, S. and Taerwe, L., 2001, Closure to "Concrete Slabs Reinforced with FRP Grids. II: Punching Resistance," Discussion by Ospina, C.E., Alexander, S.D.B. and Cheng, J.J.R., *ASCE Journal of Composites for Construction*, V. 5, No. 4, In press.

Meier, U., 1987, "Bruckensanierungen mit Hochleistungs-Faserverbundwerkstoffen," *Material und Technik*, V. 15, pp. 125-128.

Meier, U., 1992, "Carbon Fiber-Reinforced Polymers: Modern Materials in Bridge Engineering," *Structural Engineering International*, V. 2, pp. 7-12.

Meier, U. and Kaiser, H., 1991, "Strengthening of Structures with CFRP Laminates," *Advanced Composite Materials in Civil Engineering Structures*, ASCE, Las Vegas, pp. 224-232.

Meier, U. and Winistorfer, A., 1995, "Retrofitting of Structures through External Bonding of CFRP Sheets," *Proceedings, 2<sup>nd</sup> International Symposium on Non-Metallic (FRP) Reinforcement for Concrete Structures*, L. Taerwe, Ed., E & FN Spon, London, pp. 465-472.

Menétrey, P., 1996, "Analytical Computation of the Punching Strength of Reinforced Concrete," *ACI Structural Journal*, V. 93, No. 5, pp. 503-511.

Michaluk, C., Rizkalla, S.H., Tadros, G., and Benmokrane, B., 1997, "Flexural Behaviour of One-way Concrete Slabs Reinforced by Fiber Reinforced Plastic Reinforcements," *ACI Structural Journal*, V. 95, No. 3, pp. 353-365.

Miller, B. and Nanni, A., 1999, "Bond Between CFRP Sheets and Concrete," *Proceedings, ASCE 5<sup>th</sup> Materials Congress*, Cincinnati, L.C. Bank, Ed., pp. 240-247.

Mochizuki, S., 1997, "On Slip Strength of Grid Intersection of Two Dimensional Grid Type FRP," *Proceedings, 3<sup>rd</sup> International Symposium on Non-Metallic (FRP) Reinforcement for Concrete Structures*, Sapporo, V. 2, pp. 583-590.

Mochizuki, S. and Udagawa, T., 1995, "On Bond and Anchorage of Two dimensional Grid Type FRP," *Proceedings, 2<sup>nd</sup> International Symposium on Non-Metallic (FRP) Reinforcement for Concrete Structures*, L. Taerwe, Ed., E & FN Spon, London, pp. 200-208.

Mokhtar, A.S., Ghali, A., and Dilger, W., 1985, "Stud Shear Reinforcement for Flat Concrete Plates," *ACI Journal*, V. 82, No. 5, pp. 676-683.

Morita, S. and Fujii, S., 1982, "Bond Capacity of Deformed Bars due to Splitting of Surrounding Concrete," *Bond in Concrete*, P. Bartos, Ed., Applied Science Publishers, London, pp. 331-341.

Nakano, K., Matsuzaki, Y., Fukuyama, H. and Teshigawara, M., 1993, "Flexural Performance of Concrete beams Reinforced with Continuous Fiber Bars," *ACI SP 138 : Fiber Reinforced Plastic Reinforcement for Concrete Structures – International Symposium*, A. Nanni and Ch. Dolan, Eds., American Concrete Institute, pp. 741-766.

Nanni, A., 1993, "Flexural behaviour and Design of RC Members using FRP Reinforcement," *ASCE Journal of Structural Engineering*, Vol. 119, No. 11, pp. 3344-3359.

Nanni, A., Al-Zaharani, M.M., Al-Dulaijan, S.U., Bakis C.E., and Boothby, T.E., 1995, "Bond of FRP Reinforcement to Concrete – Experimental Results," *Proceedings, 2<sup>nd</sup> International Symposium on Non-Metallic (FRP) Reinforcement for Concrete Structures*, L. Taerwe, Ed., E & FN Spon, London, pp. 135-143.

Nawy, E. and Neuwerth, G.E., 1977, "Fiberglass Reinforced Concrete Slabs and beams," *Journal of the Structural Division*, American Society of Civil Engineers, Vol. 103, No. ST 2, pp. 421-440.

Nawy, E., Neuwerth, G.E., and Phillips, C.J., 1971, "Behavior of Fiber Glass Reinforced Concrete Beams," *Journal of the Structural Division*, American Society of Civil Engineers, Vol. 97, No. ST 9, pp. 2203-2215.

Newhook, J.P. and Mufti, A., 1996, "A Reinforcing Steel-free Concrete Deck Slab for the Salmon River Bridge," *Concrete International*, V. 18, No. 6, pp. 30-34.

Olonisakin, A. and Alexander, S.D.B., 1999, "Mechanism of shear transfer in a reinforced concrete beam," *Canadian Journal of Civil Engineering*, V. 26, pp. 810-817.

Park, R. and Paulay, T., 1975, *Reinforced Concrete Structures*, John Wiley and Sons, Toronto, 1975.

Rahman, A.H., Taylor, D.A., and Kingsley, C.Y., 1993, "Evaluation of FRP as Reinforcement for Concrete Bridges," *ACI SP 138 : Fiber Reinforced Plastic*



- Reinforcement for Concrete Structures – International Symposium*, A. Nanni and Ch. Dolan, Eds., American Concrete Institute, pp. 71-86.
- Ramos, A.M.P., Lúcio, V.J.G., and Regan, P.E., 2000, "Repair and Strengthening Methods of Flat Slabs for Punching," *Proceedings, International Workshop on Punching Shear Capacity of RC Slabs, Dedicated to Professor Sven Kinnunen*, TRITA-BKN Bulletin 57, Silfwerbrand, J. And Hassanzadeh, G., Eds., Stockholm, pp. 125-133.
- Rao, 1966, "Umlagerung der Schnittkräfte in Stahlbetonkonstruktionen. Grundlagen der Berechnung bei statisch unbestimmten Tragwerken unter Berücksichtigung der plastischen Verformungen", *Deutscher Ausschuss für Stahlbeton*, Heft 177.
- Razaqpur, A.G., Švecová, D., and Cheung, M.S., 2000, "Rational Method for Calculating Deflection of Fiber-reinforced Polymer Reinforced Beams," *ACI Structural Journal*, V. 97, No.1, pp. 175-184.
- Regan, P.E. and Braestrup, M.W., 1985, "Punching Shear in Reinforced Concrete - A State of Art Report," Bulletin d'Information No. 168, Comité Euro-International du Béton, Lausanne, 232 pp.
- Rizkalla, S.H. and Tadros, G., 1994, "First Smart Bridge in Canada," *Concrete International*, V. 16, No. 6, June, pp. 42-44.
- Rostásy, F.S., Koch, R., and Leonhardt, F., 1976, "Zur Mindestbewehrung für Zwang von Außenwänden aus Stahlleichtbeton," *Deutscher Ausschuss für Stahlbeton*, Heft 267.
- Rubinsky, I.A. and Rubinsky, A.A., 1954, "A Preliminary Investigation of the use of fibre-glass for prestressed concrete," *Magazine of Concrete Research*, V.6, No. 17, pp. 71-78.
- Rüsch, H., 1975, "Die Ableitung der charakteristischen Werte der Beton-zugfestigkeit," *Beton*, Heft, February.
- Scanlon, A., 1999, "Design and Construction of Two-way Slabs for Deflection Control," *ACI SP183 : The Design of Two-way Slabs*, T.C. Schaeffer, Ed., American Concrete Institute, Farmington Hills, pp. 145-160.
- Schmeckpeper, E.R. and Goodspeed, C.H., 1994, "Fiber-Reinforced Plastic Grid for Reinforced Concrete Construction," *Journal of Composite Materials*, V. 28, No. 14, pp. 1288-1304.
- Seible, F., Ghali, A., and Dilger, W.H., 1980, "Pre-assembled Shear Reinforcing Units for Flat Plates," *ACI Journal*, V. 77, No.1, pp. 28-35.
- Sekijima, K. and Hiraga, H., 1990, "Fiber Reinforced Plastics Grid Reinforcement for Concrete Structures," *LABSE Symposium, Brussels*, pp. 593-598.

- Shehata, I.A.E.M, 1990, "Rational Method for Designing RC Slabs to Resist Punching," *ASCE Journal of Structural Engineering*, V. 116, No. 7, pp. 2055-2060.
- Shehata, I.A.E.M. and Regan, P.E., 1989, "Punching in R.C. Slabs," *ASCE Journal of Structural Engineering*, V. 115, No. 7, pp. 1726-1740.
- Sherif, A.G. and Dilger, W.H., 1998, "Critical Review of CSA A23.3-94 Deflection Prediction for Normal and High Strength Concrete Beams," *Canadian Journal of Civil Engineering*, V. 25, No. 3, pp. 474-489.
- Shield, C.K., French, C.W., and Hanus, J.P., 1999, "Bond of Glass Fiber Reinforced Plastic Reinforcing Bar for Consideration in Bridge Decks," *ACI SP-188 : Fiber Reinforced Polymer Reinforcement for Reinforced Concrete Structures, 4th Intl. Symposium*, Ch. Dolan, S.H. Rizkalla, and A. Nanni, Eds., American Concrete Institute, Farmington Hills, pp. 393-406.
- Sigrist, V. and Marti, P., 1994, "Ductility of Structural Concrete: A Contribution," *Proceedings, Workshop on Development of EN 1992 in Relation to New Research Results and to the CEB-FIP Model Code 1990*, Czech Technical University, Prague, pp. 211-223.
- Somes, N.F., "Resin-bonded glass-fibre tendons for prestressed concrete," *Magazine of Concrete Research*, V. 15, No. 45, pp. 151-158.
- Sozen, M. and Siess, C.P., 1963, "Investigation of Multiple-panel Reinforced Concrete Floors Slabs: Design Methods - Their Evolution and Comparison," *ACI Journal*, *Proceedings*, V. 60, No. 8, pp. 999-1027.
- Sugita, M., 1993, "NEFMAC-Grid Type Reinforcement", *Fiber-Reinforced-Plastic (FRP) Reinforcement for Concrete Structures: Properties and Applications*, A. Nanni, Ed., Elsevier Science Publishers, pp. 355-385.
- Švecová, D., 1999, "Flexural Behaviour of Concrete Beams Reinforced with FRP Prestressed Concrete Prisms," Ph.D. Dissertation, Department of Civil and Environmental Engineering, Carleton University, Ottawa.
- Taerwe, L., 1998, "Non-metallic Reinforcement for Concrete Structures: State-of-the-art," *Proceedings of the XIIIth FIP Congress on Challenges for Concrete in the Next Millenium, V.1*, D. Stoelhort & G.P.L. den Boer, Eds., Amsterdam, pp. 13-16.
- Talbot, A.N., 1913, *Reinforced Concrete Wall Footings and Column Footings*, Bulletin 67, University of Illinois Engineering Experiment Station, Urbana, 96 pp.
- Tan, K-H, 2000, "Punching Shear Strength of RC Slabs Bonded with FRP Systems," *Proceedings, 3<sup>rd</sup> International Conference on Advanced Composite Materials in Bridges*

and Structures (ACMBS-III), Canadian Society for Civil Engineering, Humar, J. and Razaqpur, A.G., Eds., Ottawa, pp. 387-394.

Tepfers, R., 1973, "A Theory of Bond Applied to Overlapped Tensile Reinforcement Splices for Deformed Bars," Publ. 73:2, Division of Concrete Structures, Chalmers Tekniska Högskola, Doctoral Thesis, Göteborg, 328 pp.

Tepfers, R., 1997, "Bond of FRP Reinforcement to Concrete - A State-of-the-Art in Preparation," *ACI SP-180 : Bond and Development of Reinforcement, A tribute to Dr. Peter Gergely*, León, R., Ed., American Concrete Institute, Farmington Hills, pp. 493-508.

Tepfers, R., Hedlund, G., and Rosinski, B., 1998, "Pull-out and Tensile Reinforcement Splice Tests with GFRP Bars," *2<sup>nd</sup> International Conference on Composites in Infrastructure, ICCI '98*, H. Saadatmanesh and M.R. Ehsani, Eds., Tucson, V. 2, pp. 37-51.

Tepfers, R. and Karlsson, M., 1997, "Pull-out and tensile reinforcement Splice Tests using FRP C-BARS," *Proceedings, 3<sup>rd</sup> International Symposium on Non-Metallic (FRP) Reinforcement for Concrete Structures*, Sapporo, V. 2, Oct., pp. 357-364.

Thériault, M., 1998, "Flexion, ductilité et design de poutres et de dalles en béton armé de barres en composites," Ph.D. Thesis, Université de Sherbrooke, Québec.

Thériault, M. and Benmokrane, B., 1998, "Effect of FRP Reinforcement Ratio and Concrete Strength on Flexural Behaviour of Concrete Beams," *ASCE Journal of Composites for Construction*, V.2, No. 1, pp. 7-16.

Thippeswamy, H.K., Franco, J.M., and GangaRao, H.V.S., 1998, "FRP Reinforcement in Bridge Deck," *Concrete International*, V. 20, No. 6, pp. 47-50.

Uomoto, T., 2000, "Durability of FRP as Reinforcement for Concrete Structures," *Proceedings, 3<sup>rd</sup> International Conference on Advanced Composite Materials in Bridges and Structures (ACMBS-III)*, Canadian Society for Civil Engineering, Humar, J. and Razaqpur, A.G., Eds., Ottawa, pp. 3-17.

Walraven, J.C., 1999, "Tension Stiffening" and "Moment-Curvature", in "Structural Concrete, Textbook on Behaviour, Design and Performance, Updated Knowledge of the CEB/FIP Model Code 1990," FIB Bulletin 1, Vol. 1, Fédération Internationale du Béton, Lausanne, pp. 189-205.

Wang, C.K. and Salmon, C.G., 1973, *Reinforced Concrete Design*, 2<sup>nd</sup> Ed., Intext Educational Publishers, New York and London, 934 pp.

Watstein, D. and Bresler, B., 1974, "Bond and Cracking in Reinforced Concrete," Chapter 4 of *Reinforced Concrete Engineering, Vol. 1, Materials, Structural Elements, Safety*, B. Bresler, Ed., John Wiley and Sons, New York.

Yamamoto, T. and Kawakubo, M., 1978, "Tests of Shear Strengthened RC Columns with FRP Sheets," *Architectural Institute of Japan*, Tokyo, pp. 1749-1750 (In Japanese).

Yost, J.R., Goodspeed, C.H., and Schmeckpeper, E.R., 2001, "Flexural Performance of Concrete Beams Reinforced with FRP Grids," *ASCE Journal of Composites for Construction*, V. 5, No. 1, pp. 18-25.



## **APPENDIX A**

### **Fibre Reinforced Polymer (FRP) Reinforcement : Description, History, Properties, Landmark Applications**

#### **A.1 Description**

The last decade witnessed an unprecedented growth in the use of the so-called Advanced Composite Materials (ACMs) in the Civil Engineering infrastructure. Fibre Reinforced Polymers (FRPs) form part of this material family. FRPs are composite materials made from thin, high-strength continuous fibres impregnated with a polymeric binder or matrix. The term "polymer" refers to the product of combining a large number of small molecular units called monomers to form long-chain molecules by a chemical process known as polymerization.

The basic component in FRP manufacturing is the single fibre or filament. These terms are often considered as synonymous, although many consider a fibre to be a filament with a length of at least 100 times the diameter (Bakis, 1993). The fibres are the principal source of strength, stiffness and stability. Fibres are very fine, approximately 7 to 12  $\mu\text{m}$  in diameter. In general, the thinner the fibre the higher the strength. A bundle is defined as a bunch of parallel fibres or filaments. A strand or tow, is a straight, untwisted bundle. A yarn is a collection of twisted filament bundles. A roving is a set of strands or yarns collected into a straight or almost straight bundle. The fibres can be natural, such as carbon (CFRP) and glass (GFRP), or synthetic, such as aromatic polyamides, commonly known as Aramid (AFRP).

The matrix binds the fibres together, transfer stresses to them by adhesion and/or friction and protects them from physical and chemical attack from the outside. It is fabricated out of polyester, vinylester, polyimide or epoxy resins, which can be thermoset or thermoplastic. Thermoset resins cannot be softened or remoulded with subsequent reheating. Thermoplastic resins, on the other hand, can be heated and reformed but have weaker mechanical properties.

The resulting product is shaped into rods, flat bars, deformed rounded bars, 2-D grids, 3-D grids, sheets, strips, plates and laminates. The final properties of FRP depend on the design of the composite, which is influenced by the available materials, material shapes and manufacturing techniques available (Bakis, 1993). ACI Committee 440 (1996) presents a very comprehensive description of the properties of FRP's constituent materials.

## **A.2 History**

FRPs have been the centre of attention since the development of lightweight, high-strength and high-stiffness fibres circa World War II. Because of their high costs, the fibres were originally designed for use in high-tech applications where weight was of primary concern, such as the aerospace industry.

The implementation of FRP in the Civil Engineering infrastructure has followed an empirical path plagued by trial-and-error experimentation. Since most of the knowledge on fibre behaviour came from research in the aerospace industry, the performance requirements of the materials needed to produce FRP for concrete reinforcement had to be reassessed. For instance, ensuring that non-prestressed FRP reinforcing bars bond adequately to concrete is unique to the use of FRP in concrete construction.

Schmeckpeper and Goodspeed (1994) report that one of the earliest examples of using FRP bars as reinforcement for concrete is the 1941 Jackson patent application. In the 1950's, the U.S. Army Corps of Engineers were interested in long glass fibres for reinforced and prestressed concrete applications (Dolan, 1993). Crepps (1951) is credited as one of the pioneers behind the use of glass fibre tendons for prestressed concrete. Rubinsky and Rubinsky (1954) noted that creep and shrinkage losses in prestress would be reduced by using glass-fibre tendons instead of conventional steel. Kajfasz (1960) and Somes (1964) also contributed experimental work on the behaviour of concrete beams prestressed with GFRP tendons. Somes (1964) noted that GFRP could be used for prestressing purposes provided that limiting strains were not exceeded at stress transfer.

Wines and Hoff (1966) and Wines, Dietz and Hawley (1966), as reported by Nawy and Neuwerth (1977), successfully tested concrete beams reinforced and prestressed with GFRP rods and tendons. They recognized the FRP merits in terms of energy absorption and recommended that GFRP tendons could be used together with ordinary steel shear reinforcement and that shallow beam depths should be avoided.

In the 1970's, Nawy, Neuwerth and Phillips (1971) and Nawy and Neuwerth (1977) explored the concept of using non-prestressed glass fibre reinforcing bars in concrete beams and two-way slabs. Their research had no immediate or apparent impact within the profession likely because of the intense discussion generated by their 1971 paper. Details about this subject are covered in Chapter 2.

In the mid 70's, corrosion of concrete bridge decks and car parking slabs became a subject of considerable attention among civil engineers. Corrosion may cause or increase cracking in the structure, and over time, may even reduce its safety because of the gradual loss of reinforcement. In North America, this phenomenon is accelerated by the use of deicing salts in parking buildings and bridges and by significant changes in temperature. Millions of dollars were spent in repairs and some initiatives were taken towards the development of strategies to reduce the susceptibility of concrete structures to corrosive environments (Dolan, 1993). Nevertheless, continued high fibre manufacturing costs and the lack of a viable continuous FRP fabrication process hindered the application of FRP in the concrete infrastructure.

By the late 70's and early 80's, the use of FRP reinforcement increased thanks to progress made in enhancing the durability properties of fibres and in reducing production costs. Main applications settled in two major areas: new construction and repair or rehabilitation of existing structures. In Japan, massive research and development began on production techniques for FRP deformed bars, tendons and sheet-type reinforcement for concrete structures. The potential of sheet-type FRP for seismic strengthening of concrete columns was first studied in Japan, by Yamamoto and Kawakubo (1978). In 1978, the German companies Strabag Bau-AG and Bayer AG developed the so-called



“Polystal” cable for stay cable bridge use. The first highway bridge prestressed with “polystal” cables was built in Dusseldorf in 1986 (Taerwe, 1998). In 1983, a composite element known as “Arapree” (Aramid Prestressing Element) was fabricated in Holland by the firms AKZO (chemical producer) and HBG (contractor) with aramid fibres. However, commercial applications were limited to the fabrication of thin elements such as posts, noise barriers and piles. In Switzerland, Maier (1987, 1992), Kaiser (1989) and Maier and Kaiser (1991) pioneered the use of FRP sheets to post-strengthen concrete bridges and slabs. The city hall of Gossau St. Gall, Switzerland was the first building where CFRP strengthening was used (Meier and Winistorfer, 1995).

Structural engineers then embraced FRP as an alternative material to reinforce, prestress, strengthen or repair concrete structures. Applications have long surpassed laboratory limits. Recent landmark applications include: The Beddington Trail/Centre Street bridge in Calgary, Alberta, opened in 1994, the first prestressed concrete highway bridge with some of their girders pre-tensioned by CFRP tendons built in Canada (Rizkalla and Tadros, 1994); The Salmon River bridge, completed in 1995 in Nova Scotia, Canada, the world’s first bridge with a steel free concrete deck (Newhook and Mufti, 1996); The Chalgrove bridge, near Oxford, England, which in 1995 became the first GFRP-reinforced footbridge opened to service (Taerwe, 1998); The Buffalo Creek bridge, opened to service in 1996 in McKinleyville, Brooke County, West Virginia, considered the first vehicular bridge in the U.S. to use FRP reinforcement in its concrete deck (Thippeswamy, Franco and GangaRao, 1998). More examples of recent FRP applications in concrete structures worldwide are reported by Burgoyne (1999), Karbhari and Seible (1999), Erki (1999) and Fukuyama (1999), among others.

The flexibility to shape the composite constituents together with their excellent corrosion resistance, magnetic neutrality, and high stiffness-to-weight and high strength-to-weight ratios are assets that have caught the eye of the construction industry. However, these apparent benefits are accompanied by the necessity of understanding what the bounties and limitations of FRP are and which materials or which shapes are more appealing for a given application.

### **A.3 FRP Forms for the Civil Engineering Infrastructure**

Table A.1, adopted from Fukuyama (1999), presents a classification of FRP reinforcement from a shape viewpoint. The most popular FRP forms for use in civil engineering structures are the deformed bars, rods, tendons, 2-D grids, 3-D grids, strips and sheets. Deformed bars and grids are used as internal reinforcement, rods and tendons for conventionally or externally prestressed concrete structures, and strips for strengthening or repair purposes. Sheets are wrapped around or placed on different types of structural elements to provide strength enhancement or repair. FRP rods or tendons will not be examined in this study.

### **A.4 Fabrication**

#### **A.4.1 FRP Reinforcing Bars and Grids**

FRP bars and grids are fabricated by a process known as the pultrusion method. In this process, indicated schematically in Fig. A.1, the fibres are drawn from creels through a resin bath. Fibre content per volume may range from 40 to 70 %. For the case of bars, as the fibres emerge from the resin, they are pulled through a shaping die, which shapes them into a rounded bar. The bar then passes through a curing chamber to harden the resin. The bar is later cut to the desired length and then stored. To develop a good bond between concrete and the rods, bars are usually sanded or provided with a ribbed surface. Rib deformations are made by wrapping the bar with an additional strand of resin-soaked resin in a 45 degree helical pattern. The shape of the resulting bar resembles that of an epoxy-coated deformed steel bar. The average production output of FRP in the pultrusion method may range from 300 to 1500 mm per minute (Faza and GangaRao, 1993b).

For the case of grids, the fibres are bundled in a pin-winding process forming large cross-sectional or three-dimensional grid shapes. These grids are known as NEFMAC (New Fibre Composite Material for Reinforced Concrete). NEFMAC grids are commonly fabricated with carbon or glass fibres. Carbon NEFMAC grids are more expensive. Sugita (1993) reports that 60 to 180 m<sup>2</sup> of NEFMAC can be produced per hour. A more

detailed description of the pultrusion method for FRP bar manufacturing is given by Faza and GangaRao (1993b), Bakis (1993) and Dolan (1993). Sugita (1993) and Bakis, Engel, Nanni and Croyle (1997) provide a detailed exposition on the FRP grid manufacturing process.

#### **A.4.2 Fibre Reinforced Polymer Sheets**

FRP sheets are planar structures made by arranging fibres, yarns or rovings. Fibres can be aligned in one direction to form strips or tapes, woven to form a fabric, or simply pressed to form a non-woven fabric (Bakis, 1993). Continuous fibres, yarns and rovings can also be arranged randomly in planar forms called mats. Unidirectional strips or tapes are available in various widths. They have the most anisotropic properties of all FRP forms due to the high degree of fibre alignment.

Woven fabrics are designed to be wrapped around complex contours. Woven fabrics are produced by a braiding process. The degree of fibre waving varies according to the application. Unidirectional tapes can be obtained dry or pre-impregnated (prepreg) with resin. Tapes are of variable thickness (usually 0.08 to 0.25 mm) and have fiber approximate volume fractions varying from 50 to 75 % (Bakis, 1993). Commercial woven fabrics have thicknesses of 0.17 to 0.34 mm and fiber volume contents around 60 %. Thin layers of woven or unidirectional tape can be stacked at specific orientations to form laminates. The mechanical properties of a laminate depend on the stacking sequence and fibre orientation. In this study, much of the attention will be focused on unidirectional tapes.

To fabricate an unidirectional tape, the resin is first infiltrated into the reinforcement forming a thin sheet. Resins are usually of the thermoset type because processing temperatures are lower than those associated with thermoplastic prepregs (Bakis, 1993). Later, the resin is cured, the sheet wound onto rolls with interleaved silicone paper to prevent self-adhesion and then the product wound onto cardboard rolls for shipping. Their installation procedure on the concrete surface is described, for instance, by Cheng and Lau (2000) and CSA S806-00.

## **A.5 Mechanical and Durability Properties of FRP**

The mechanical properties of FRP reinforcements are affected by the properties of both constituent fibres and resin, the fibre content, the cross-sectional shape and the method of surface processing, among other other factors. The mechanical properties of available commercial fibres vary widely. In general, carbon fibres have higher stiffness, higher strength and excellent resistance to acidic attack and to freeze-thaw effects. However, they tend to have low toughness and low impact resistance. Glass fibres are usually tougher than CFRP and AFRP, have good freeze-thaw resistance, but they are susceptible to alkaline attack and to creep rupture. In fact, the use of GFRP in prestressed concrete applications is not permitted because of the latter. Aramid fibres are as tough as glass, have excellent freeze-thaw resistance, but have less magnetic permeability than carbon and glass. Their strength may also be reduced due to excessive ultra-violet ray (UVR) exposure. As far as costs are concerned, carbon and aramid are more expensive than glass fibres. Uomoto (2000) provides a comprehensive study on durability properties of FRP.

Figure A.2 shows typical stress-strain relationships for FRP and its constituents. Since the fibres provide the strength of the composite, their rupture governs the response of FRP. In other words, the composite will fail when its longitudinal strain reaches the ultimate tensile strain of the fibre. ACI Committee 440 (1996) recommends that the minimum fibre volume content for the fibres to provide strength to FRP must be 10 %.

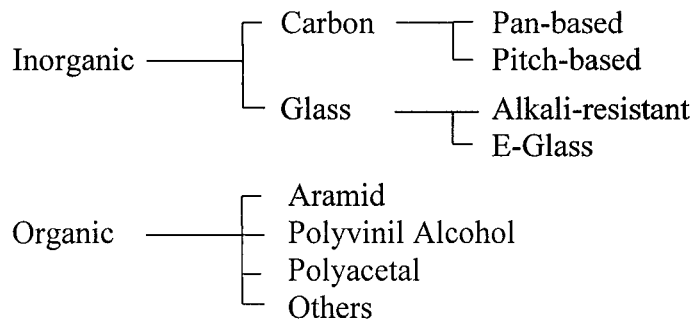
Figure A.3 shows schematic stress-strain curves of CFRP, GFRP and AFRP bars under direct tension compared to that of a conventional steel reinforcing bar. The response of the three fibre types is essentially linear-elastic up to failure. The fibres are less stiff than steel. Tables A.2 and A.3 show typical mechanical and physical properties of commercially available FRP bars, grids and sheets. More details can be found in ISIS M-04-00 or at selected internet websites.

Additional description of material properties of FRP deformed bars is given by ACI Committee 440 (1996), ISIS M04-00, Bank (1993), Faza and GangaRao (1993b) and

Dolan (1993), among others. As far as NEFMAC grids is concerned, Fujisaki, Sekijima, Matsuzaki and Okamura (1987), Sekijima and Hiraga (1990), Sugita (1993) and Mochizuki and Udagawa (1995) provide useful information on NEFMAC's mechanical properties.

**Table A.1 Classification of FRP Reinforcement (After Fukuyama, 1999)**

**Fibre Types**



**Binder Types**

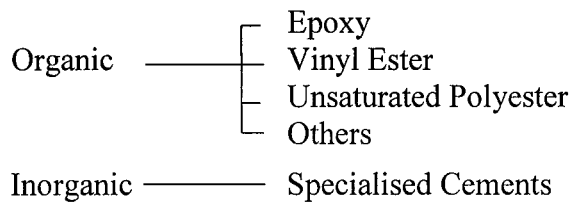


**Table A.2 Typical Mechanical Properties of Some Commercially Available FRP Reinforcing Bars and Grids (After ISIS M04-00)**

Product	Fibre	$f_{fu}$ (MPa)	$E_f$ (GPa)
C-bar®	Glass	680-713	42
Aslan 100 GFRP Rebar	Glass	680	42
ISOROD™	Glass	635-747	37-43
ISOROD™	Carbon	1596	111
NEFMAC™ 2-D Grid	Aramid	1300	54
NEFMAC™ 2-D Grid	Glass	600	30
NEFMAC™ 2-D Grid	Carbon	1200	100
NEFMAC™ 2-D Grid	Hybrid (G-C)	600	37
LEADLINE™ Round	Carbon	2245-2265	147
LEADLINE™ Indented Spiral	Carbon	2245-2255	147
LEADLINE™ Indented Concentric	Carbon	2250-2265	147

- Notes: 1. C-bar® is a Trademark of Marshall Industries Composites Inc.  
2. Aslan 100 GFRP Rebar is produced by Hughes Brothers, Inc.  
3. ISOROD™ is a Trademark of Pultrall, Inc.  
4. ROTAFLEX™ is a Trademark of Rotafix Northern Ltd.  
5. NEFMAC™ is a Trademark of Shimizu Corp.  
6. LEADLINE™ is a Trademark of Mitsubishi Chemical Corp.

**Table A.3 Mechanical Properties of Some Commercial FRP Sheet Systems (After ISIS M04-00)**

Product	Fibre	Thickness (mm)	$f_{fu}$ (MPa)	$E_f$ (GPa)
Mitsubishi Type 20	Carbon	0.111	3400	230
Mitsubishi Type 30	Carbon	0.167	3400	230
MBrace™ CF 530	Carbon	0.165	2940	372
MBrace™ CF 130	Carbon	0.165	3480	80
MBrace™ EG 900	Glass	0.353	1730	26.1
SikaWrap™ Hex 100G	Glass	1.0	600	26.1
SikaWrap™ Hex 103C	Carbon	1.0	960	73.1

- Notes: 1. MBrace is a Trademark of Master Builders Inc.  
2. SikaWrap is a Trademark of Sika.

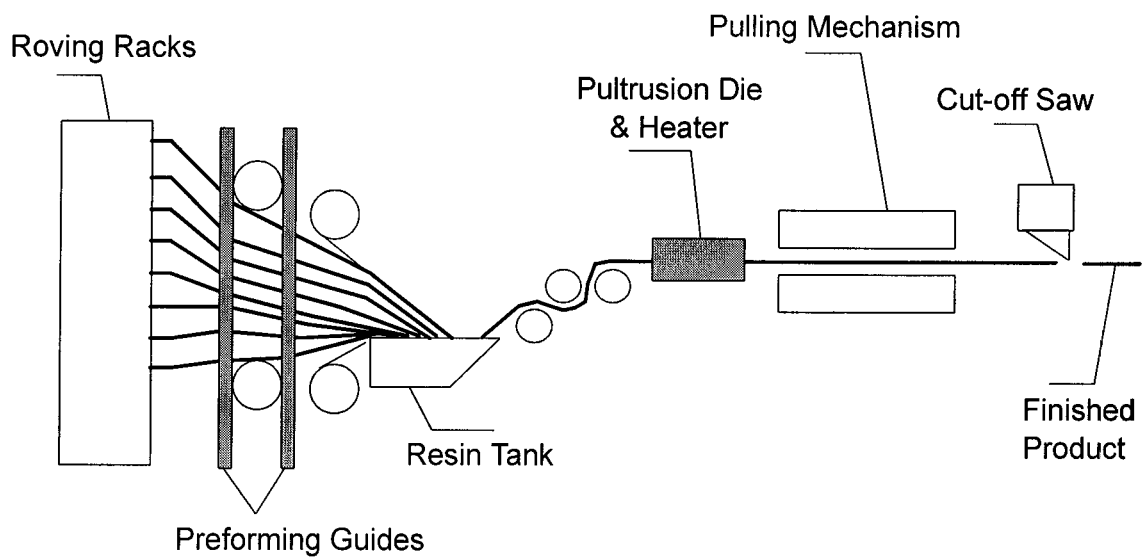


**Fig. A.1 Schematic of Pultrusion Process**

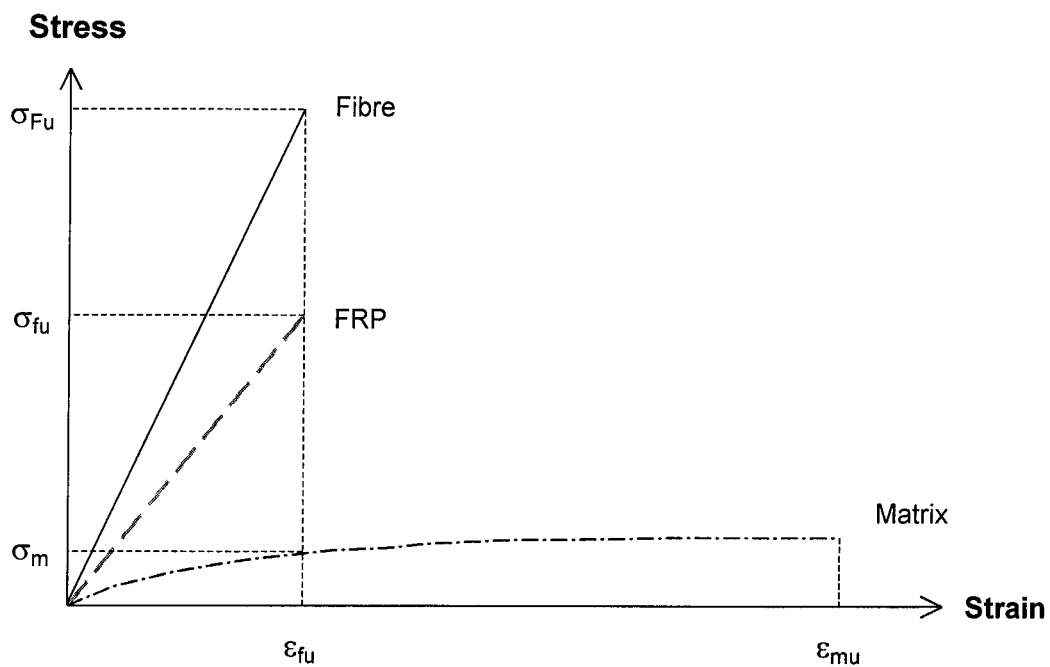


**Fig. A.2 Typical Response in Tension of FRP and Constituents**



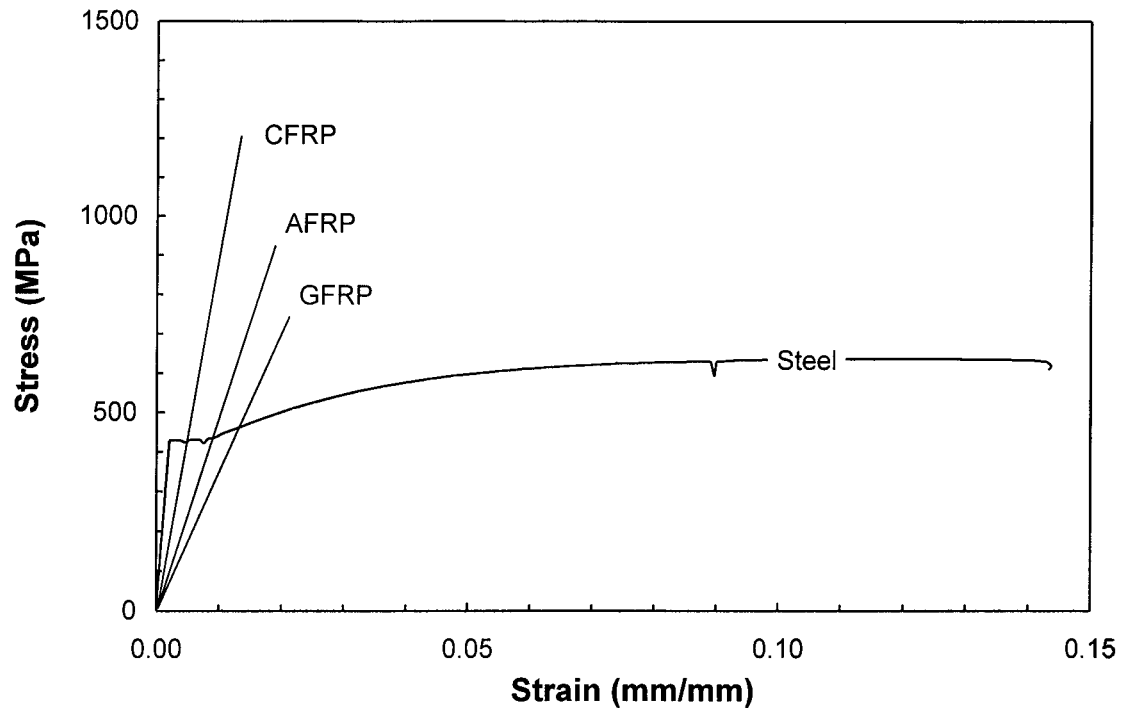


**Fig. A.3 Typical Response in Tension of Rebars**

## APPENDIX B

### Derivation of the Bond-Slip Differential Equation and Formulation of the Tension Chord Model for Linear-Elastic Reinforcement

Consider the differential concrete element of Fig. B.1 reinforced with purely elastic reinforcement subjected to a tensile axial force  $N$ . Let us first define the reinforcement ratio  $\rho_r = A_r / A_g$ . The subscripts “  $r$  ” and “  $c$  ” refer to the “reinforcement” and “concrete”, respectively. The term  $A_g$  refers to the area of the gross cross-section ( $A_g = A_c + A_r$ ).

From equilibrium of forces on the element, the tensile axial load,  $N$ , is equal to

$$N = A_c \sigma_c + A_r \sigma_r \quad [\text{B.1}]$$

From equilibrium of forces on the reinforcement,

$$\tau_b \pi \phi_b dx = d\sigma_r \frac{\pi \phi_b^2}{4} \quad [\text{B.2}]$$

which leads to

$$\frac{d\sigma_r}{dx} = \frac{4\tau_b}{\phi_b} \quad [\text{B.3}]$$

where  $\tau_b$  is the average bond stress and  $\phi_b$  is the diameter of the reinforcement. According to Eq. B.3, the sign of the bond stress diagram is determined by the slope of the reinforcement stress distribution.

Likewise, from equilibrium of forces in the concrete element,

$$\frac{d\sigma_c}{dx} = -\frac{4\tau_b}{\phi_b} \left( \frac{\rho_r}{1 - \rho_r} \right) \quad [\text{B.4}]$$

The slip,  $\delta$ , between the reinforcement and concrete is defined as the difference between the reinforcement and the concrete displacements.

$$\delta = u_r - u_c \quad [\text{B.5}]$$

The change of slip along the length  $dx$  is the difference between the reinforcement and concrete strains.

$$\frac{d\delta}{dx} = \frac{d}{dx}(u_r - u_c) = \varepsilon_r - \varepsilon_c \quad [\text{B.6}]$$

Differentiating Eq. B.6 once more results in

$$\frac{d^2\delta}{dx^2} = \frac{d\varepsilon_r}{dx} - \frac{d\varepsilon_c}{dx} \quad [\text{B.7}]$$

Assuming linear elastic behaviour in both the reinforcement and concrete, and substituting Eqs. B.3 and B.4 into B.7, one obtains the differential equation for the slip.

$$\frac{d^2\delta}{dx^2} = \frac{4\tau_b}{\phi_b E_r} + \frac{4\tau_b}{\phi_b E_c} \left( \frac{\rho_r}{1 - \rho_r} \right) \quad [\text{B.8}]$$

which can be further re-arranged as

$$\frac{d^2\delta(x)}{dx^2} = \frac{4\tau_b(\delta(x))}{\phi_b E_r} \left( 1 + \frac{n\rho_r}{1 - \rho_r} \right) \quad [\text{B.9}]$$

The solution of this differential equation gives the slip on each crack side. The crack width at the reinforcement level is simply the sum of the slips on each side. To facilitate the estimation of crack widths, the bond stress will be assumed independent of the slip. Assuming  $\tau_b = \tau_{bo}$ , and integrating Eq. B.10 once results in

$$\frac{d\delta(x)}{dx} = \frac{4\tau_{bo}}{\phi_b E_r} \left( \frac{1 + \rho_r(n-1)}{1 - \rho_r} \right) x + C_1 \quad [\text{B.10}]$$

The constant  $C_1$  is the initial value for the difference between the reinforcement strain and the concrete strain. For a member in the single crack formation phase, this value is

zero. To simplify the integration procedure for the stabilised cracking phase, let us assume that  $C_I$  is equal to zero.

Integrating Eq. B.10 once more gives the slip

$$\delta(x) = \frac{2\tau_{bo}}{\phi_b E_r} \left( \frac{1 + \rho_r(n-1)}{1 - \rho_r} \right) x^2 \quad [\text{B.11}]$$

For a member in the single crack formation stage, the independent variable  $x$  is equivalent to the transfer length,  $l_o$ , on each side of the crack.

Taking into account that concrete tensile stresses cannot exceed the tensile strength of concrete,  $f_{ct}$ , the following restriction for a stabilised crack pattern (Alvarez, 1998) needs be applied to Eq. B.4.

$$\frac{4}{\phi_b} \left( \frac{\rho_r}{1 - \rho_r} \right) \int_0^{s_{\max}/2} \tau_{bo} dx \leq f_{ct} \quad [\text{B.12}]$$

where  $s_{\max}$  is the maximum crack spacing. Performing the integration and re-arranging terms, one obtains the maximum crack spacing as

$$s_{\max} = \frac{f_{ct} \phi_b}{2\tau_{bo}} \left( \frac{1 - \rho_r}{\rho_r} \right) \quad [\text{B.13}]$$

Since bond stresses are assumed slip-independent, the stresses in the reinforcement and concrete vary linearly from the crack location to a point located midway between two cracks, as shown in Fig. B.2.

In Fig. B.2a, the dotted lines show the mean stresses in both the reinforcement and concrete. If the concrete stress reaches  $f_{ct}$  a new crack will form midway between those spaced at  $s_{\max}$ . This means that the minimum crack spacing,  $s_{\min}$ , is equal to  $s_{\max}/2$ . Stress distributions in the reinforcement and concrete for this condition are shown in Fig. B.2b.

Consequently, the mean crack spacing in a fully developed crack pattern is bounded by the following limits:

$$\left( s_{\min} = \frac{s_{\max}}{2} \right) \leq s_m \leq s_{\max} \quad [\text{B.14}]$$

or

$$0.5 \leq \left( \lambda = \frac{s_m}{s_{\max}} \right) \leq 1.0 \quad [\text{B.15}]$$

where  $\lambda$  is essentially an statistical parameter that relates the mean crack spacing to the maximum crack spacing.

Combining Eqs. B.13 and B.15, the mean crack spacing,  $s_m$ , is

$$s_m = \frac{\lambda f_{ct} \phi_b}{2 \tau_{bo}} \left( \frac{1 - \rho_r}{\rho_r} \right), \quad 0.5 \leq \lambda \leq 1.0 \quad [\text{B.16}]$$

Substituting  $x = 0.5 s_m$  into Eq. B.11 gives the slip for the single crack formation phase as

$$\delta(x) = \frac{2 \tau_{bo}}{\phi_b E_r} \left( \frac{1 + \rho_r (n-1)}{1 - \rho_r} \right) \left( \frac{\lambda s_{\max}}{2} \right)^2 \quad [\text{B.17}]$$

which can be re-arranged as

$$\delta(x) = \frac{\lambda^2 \phi_b f_{ct}^2}{4 \tau_{bo} E_r} \left( \frac{1 + \rho_r (n-1)}{\rho_r^2} \right) (1 - \rho_r) \quad [\text{B.18}]$$

Figure B.3 shows a free body diagram of a tension chord immediately after first cracking. From equilibrium, the reinforcement stress at the crack immediately after the formation of the first crack,  $\sigma_{rro}$ , is

$$\sigma_{rro} = \frac{A_c}{A_r} f_{ct} + n f_{ct} \quad [\text{B.19}]$$

Since  $\rho_r = A_r / (A_c + A_r)$ , the reinforcement stress at the crack is related to the tensile strength of concrete as

$$f_{ct} = \frac{\sigma_{rro} \rho_r}{1 + \rho_r (n - 1)} \quad [\text{B.20}]$$

Substituting Eq. B.20 into B.18 and recognizing that the mean crack width is twice the slip which develops on either side of the crack, results in

$$w_m = 2\delta = \frac{\lambda^2 \phi_b f_{ct} (1 - \rho_r)}{4 \tau_{bo} E_r \rho_r} \sigma_{rro} \quad [\text{B.21}]$$

This equation applies only for the single crack formation stage. To calculate crack widths in the stabilised crack formation phase, i.e., for  $\sigma_{rr} > \sigma_{rro}$ , it is necessary to examine the axial stress-strain response of the tension chord in full detail.

Figure B.4 shows the variation of the stress in the reinforcement as a function of both the average chord strain and the strain at the reinforcement. The figure has been adapted from Alvarez (1998). The dashed line represents the response of the naked reinforcement. The solid and dotted lines represent the reinforcement stress-average chord strain response for both maximum and minimum crack spacings.

The strain  $\varepsilon_{rr} = \frac{f_{ct}}{E_r}$  signals first flexural cracking. At this instant, all the stresses taken by concrete are suddenly transferred to the reinforcement, resulting in a reinforcement stress  $\sigma_{rro}$ , which can be determined from Eq. B.20.

At this level, the single crack formation stage starts. In theory, any increase in strain beyond this stress level under imposed load conditions should be accompanied by a slight increase in stress. For simplicity, the model treats the crack formation phase as a flat line. The model assumes that the mean strain of the cracked chord increases up to a point defined by the degree of tension stiffening offered by the cracked concrete.

The tension stiffening effect can be evaluated based on the stress distributions of Fig. B.2. For a fully developed crack pattern, with average crack spacing  $s_m$ , the reinforcement stress at a crack can be expressed as

$$\sigma_{rr} = \sigma_{rm} + \frac{\tau_{bo} \left( \frac{s_m}{4} \right) \pi \phi_b}{\frac{\pi}{4} \phi_b^2} \quad [\text{B.22}]$$

or

$$\sigma_{rr} = \sigma_{rm} + \frac{\tau_{bo} s_m}{\phi_b} \quad [\text{B.23}]$$

where  $\sigma_{rm}$  is the mean stress in the reinforcement,  $s_m$  is the average crack spacing in the stabilised cracking stage, and  $\phi_b$  is the bar diameter.

Substituting Eq. B.16 into Eq. B.23 and dividing the reinforcement stress by the modulus of elasticity of the reinforcement, the reinforcement strain at the crack, for the stabilised cracking stage, i.e.  $\sigma_r$  greater than  $\sigma_{rro}$ , becomes

$$\varepsilon_{rr} = \varepsilon_{rm} + \Delta\varepsilon_{ts} = \varepsilon_{rm} + \frac{\lambda f_{ct} (1 - \rho_r)}{2 E_r \rho_r} \quad [\text{B.24}]$$

The term  $\Delta\varepsilon_{ts}$  represents the strain correction due to concrete's tension stiffening effect in the stabilised cracking stage. As illustrated in Fig. B.4, the tension stiffening effect becomes greater when the crack spacing is maximum, i.e.  $\lambda = 1$ , and becomes minimum when the crack spacing is minimum, i.e.  $\lambda = 0.5$ . Since the tension chord model formulation is based on a constant slip-independent bond strength, the slope of the reinforcement stress-average strain curve in the stabilised cracking phase matches that of the naked FRP bar, i.e. the tension stiffening effect is constant.

Following the philosophy of CEB/FIP MC90, the mean crack width in the stabilised cracking phase can be calculated as

$$w_m = s_m (\varepsilon_{rm} - \varepsilon_{cm}) \quad [\text{B.25}]$$

where  $s_m$  is the mean crack spacing,  $\varepsilon_{rm}$  is the mean reinforcement strain at the given load level and  $\varepsilon_{cm}$  is the mean concrete strain at the end of the single crack formation phase. According to Fig. B.2, the mean concrete strain can be evaluated as

$$\varepsilon_{cm} = \frac{\lambda}{2} \frac{f_{ct}}{E_c} \quad [\text{B.26}]$$

Substituting Eqs. B.24 and B.26 into B.25 results in

$$w_m = s_m \left( \varepsilon_{rr} - \frac{\lambda}{2} \frac{f_{ct}}{E_r} \frac{(1 + \rho_r(n-1))}{\rho_r} \right) \quad [\text{B.27}]$$

Since the mean crack width is bounded by the minimum and maximum crack spacing limits, Eq. B.27 can be expanded out as

$$\begin{aligned} \frac{\phi_b f_{ct}}{4\tau_{bo}} \left( \frac{1 - \rho_r}{\rho_r} \right) \left( \varepsilon_{rr} - \frac{f_{ct}}{4E_r} \frac{(1 + \rho_r(n-1))}{\rho_r} \right) &\leq w_m \\ &\leq \frac{\phi_b f_{ct}}{2\tau_{bo}} \left( \frac{1 - \rho_r}{\rho_r} \right) \left( \varepsilon_{rr} - \frac{f_{ct}}{2E_r} \frac{(1 + \rho_r(n-1))}{\rho_r} \right) \end{aligned} \quad [\text{B.28}]$$



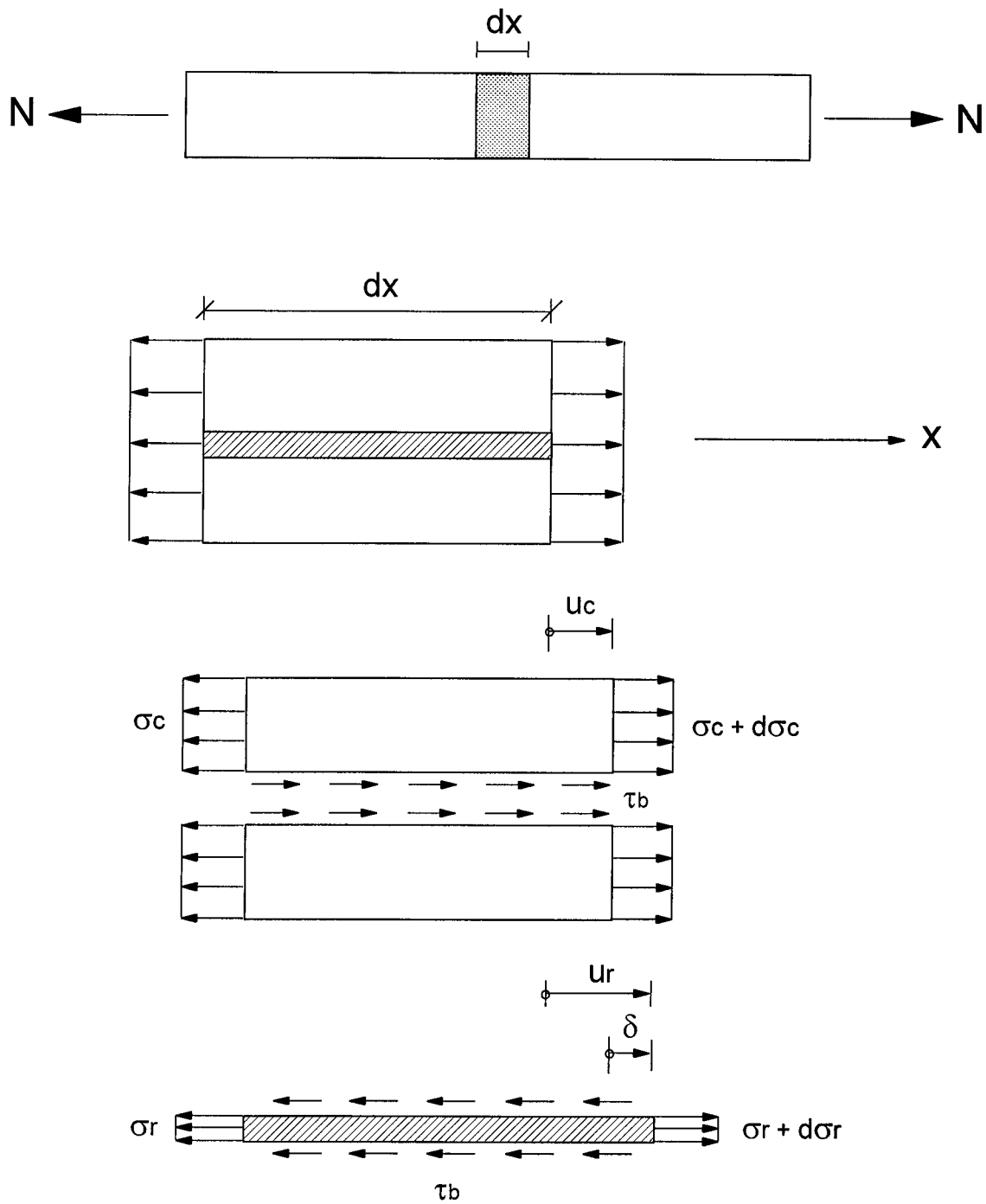
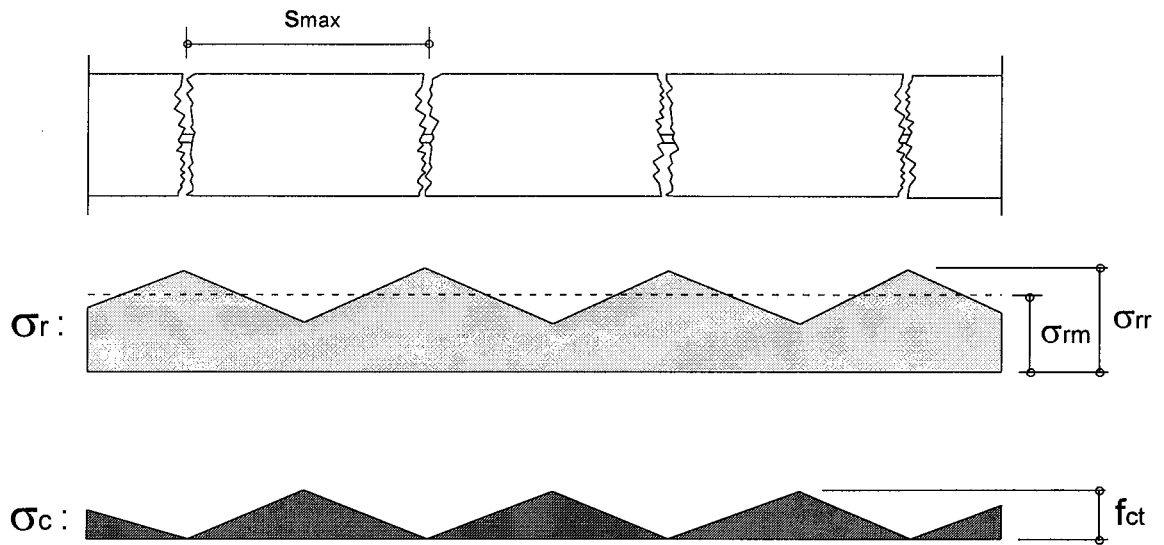
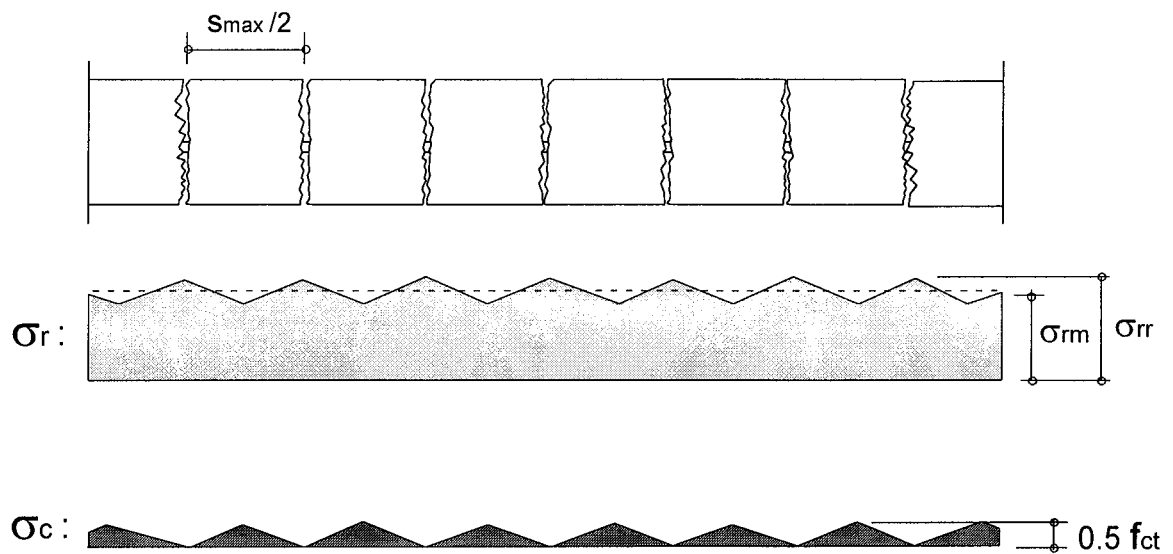


**Fig. B.1 Differential Element for Derivation of Tension Chord Model Formulation**



a) Assumed Stress Distributions at Maximum Crack Spacing



b) Assumed Stress Distributions at Minimum Crack Spacing

**Fig. B.2 Crack Spacing-dependent Stress Distributions According to Tension Chord Model (After Alvarez, 1998)**

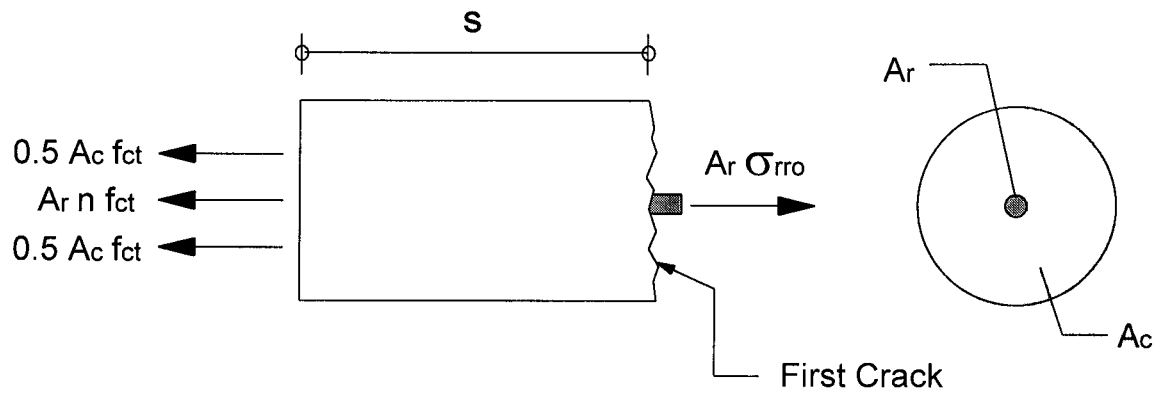


**Fig. B.3 Tension Chord Forces After First Cracking**

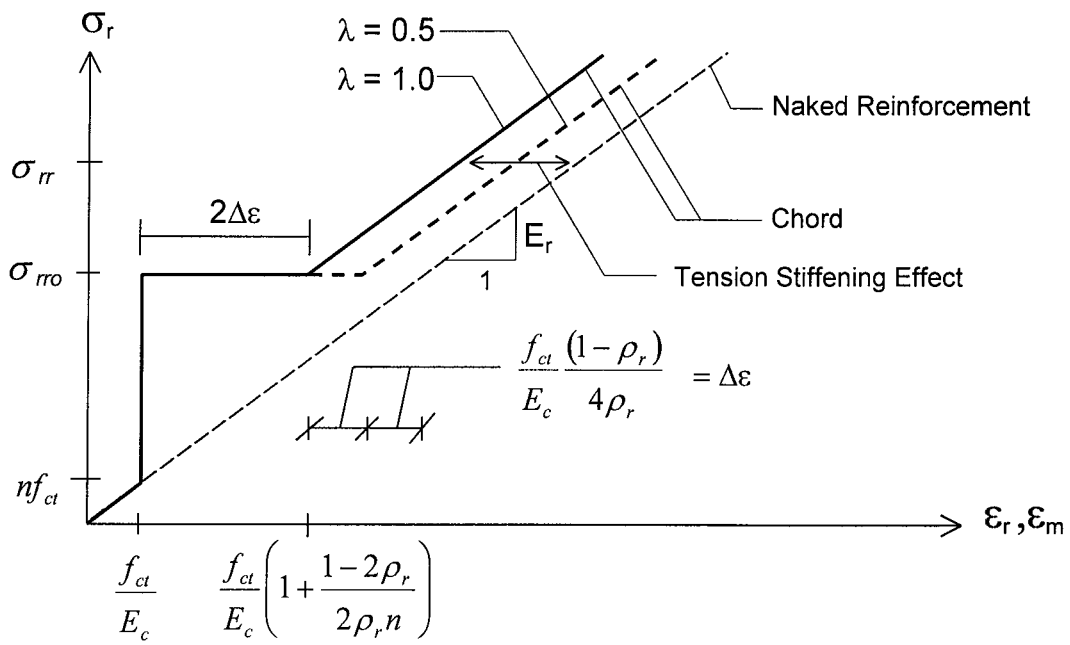


**Fig. B.4 Stress-Strain Response of Tension Chord  
(After Alvarez, 1998)**

## APPENDIX C

### Selected Pictures of Experimental Program

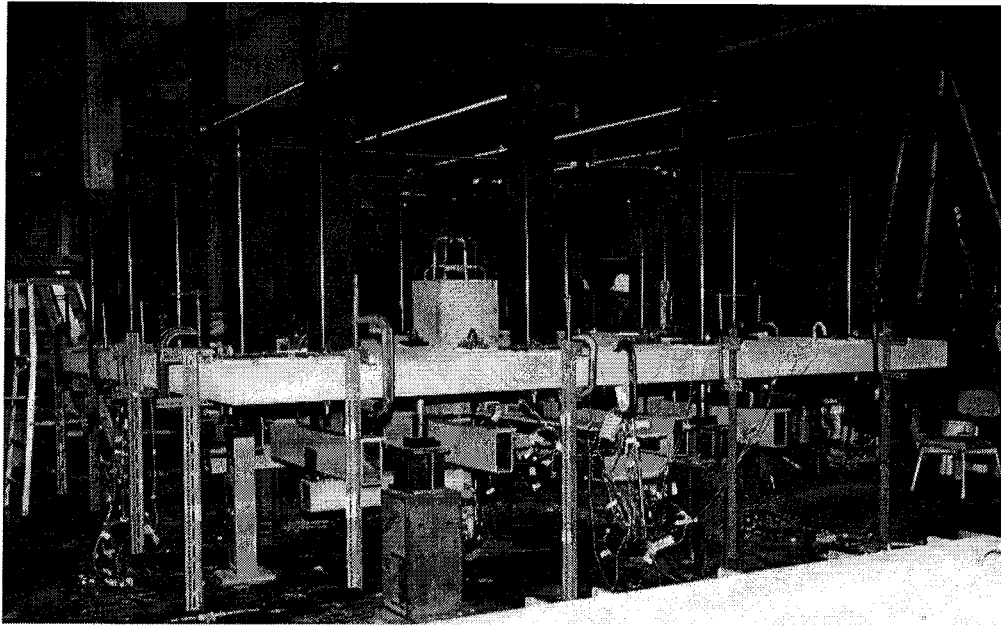


**Fig. C.1 Typical Test Set-up (Virgin Slab)**

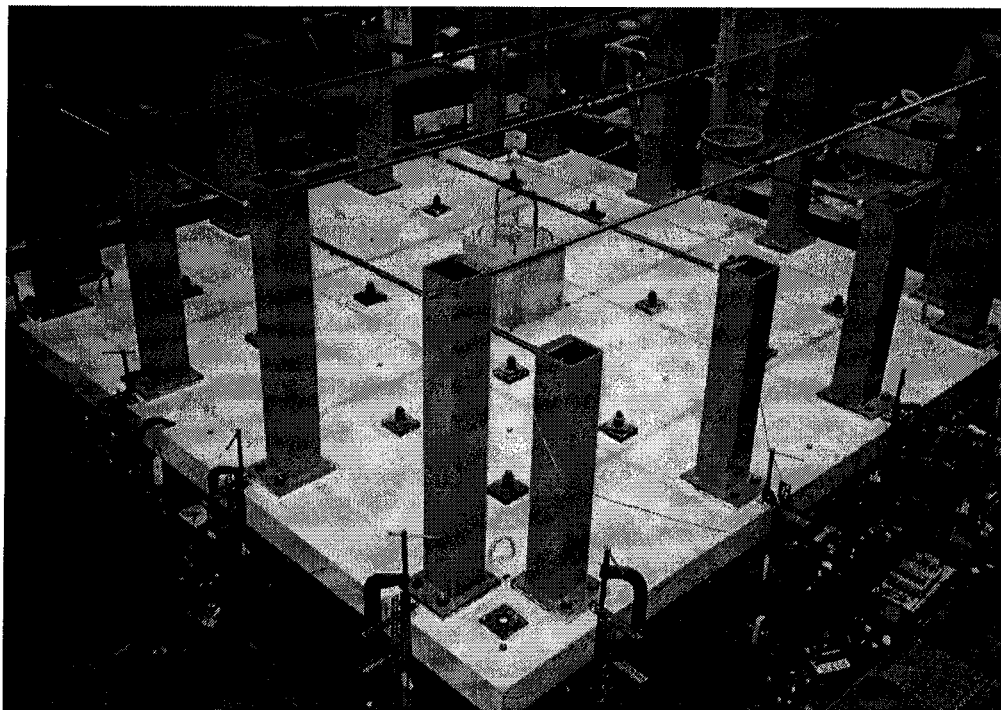


**Fig. C.2 Typical Test Set-up (Virgin Slab)**

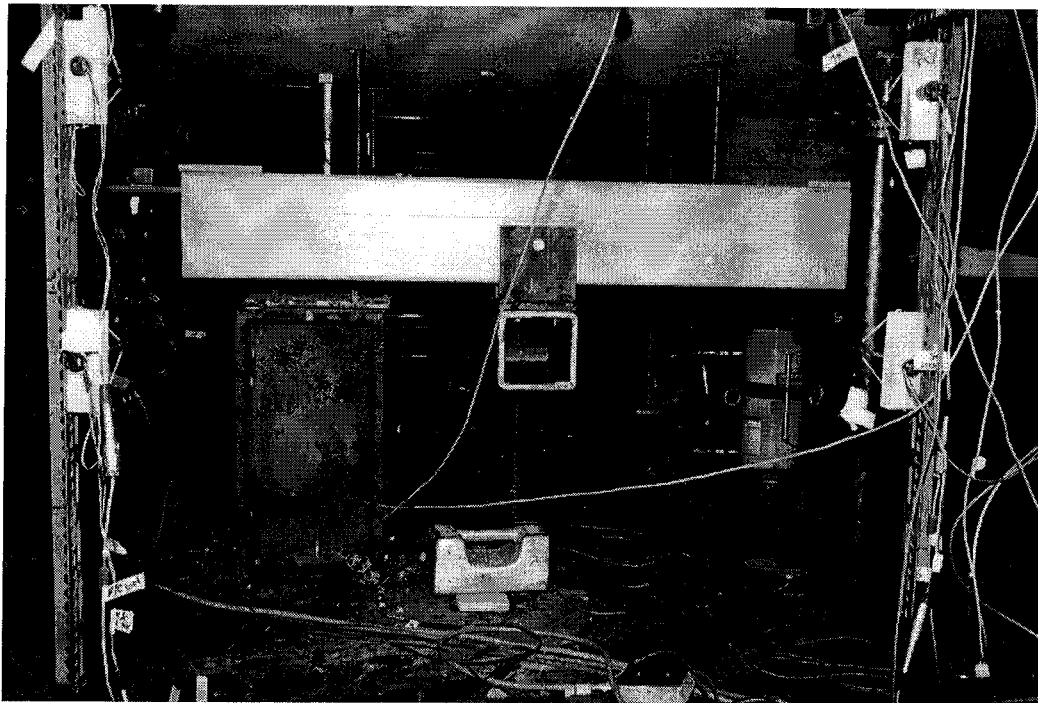


**Fig. C.3 Whiffle Tree Detail**

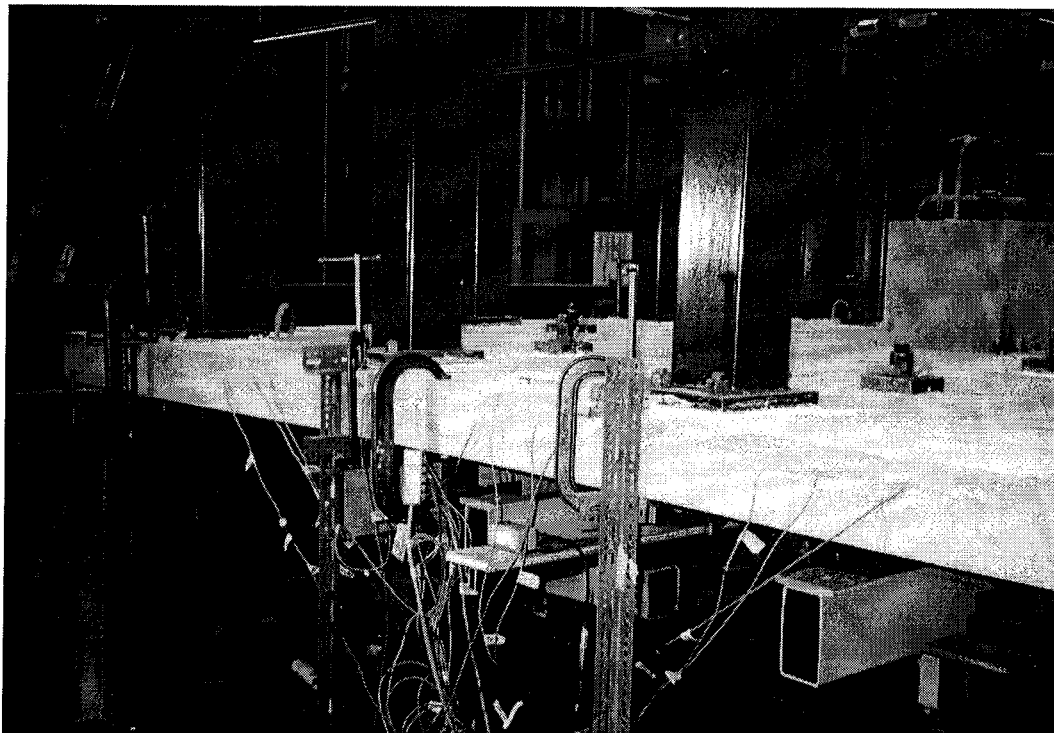


**Fig. C.4 Edge Restraint System Effect**

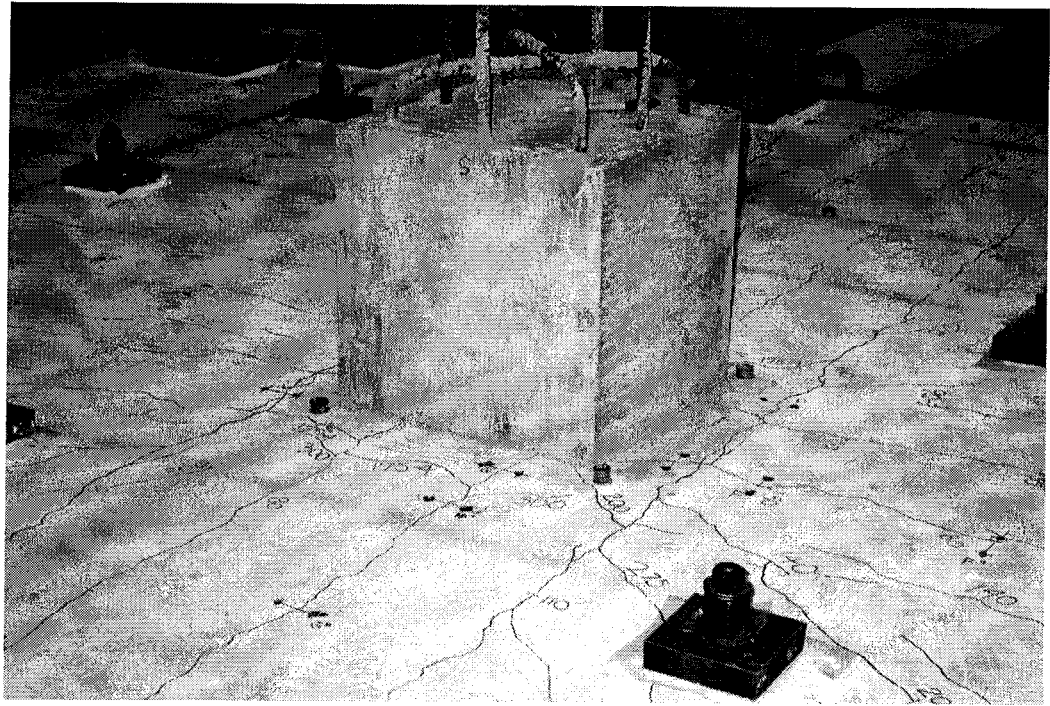


**Fig. C.5 Test ER1-VS (Before Punching)**

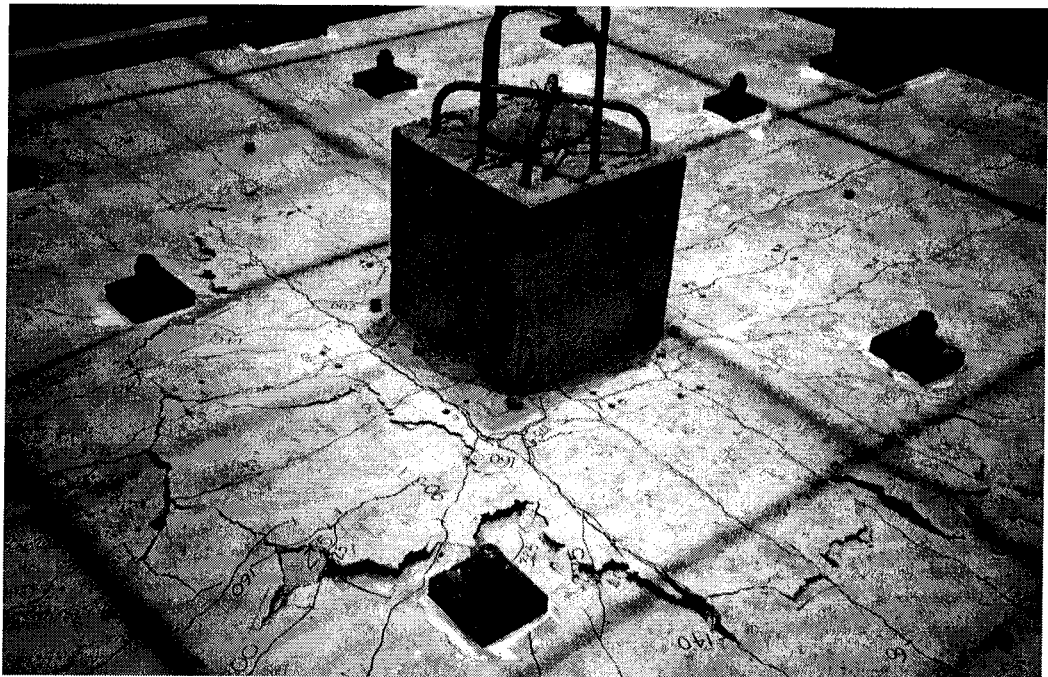


**Fig. C.6 Test ER1-VS (After Punching)**

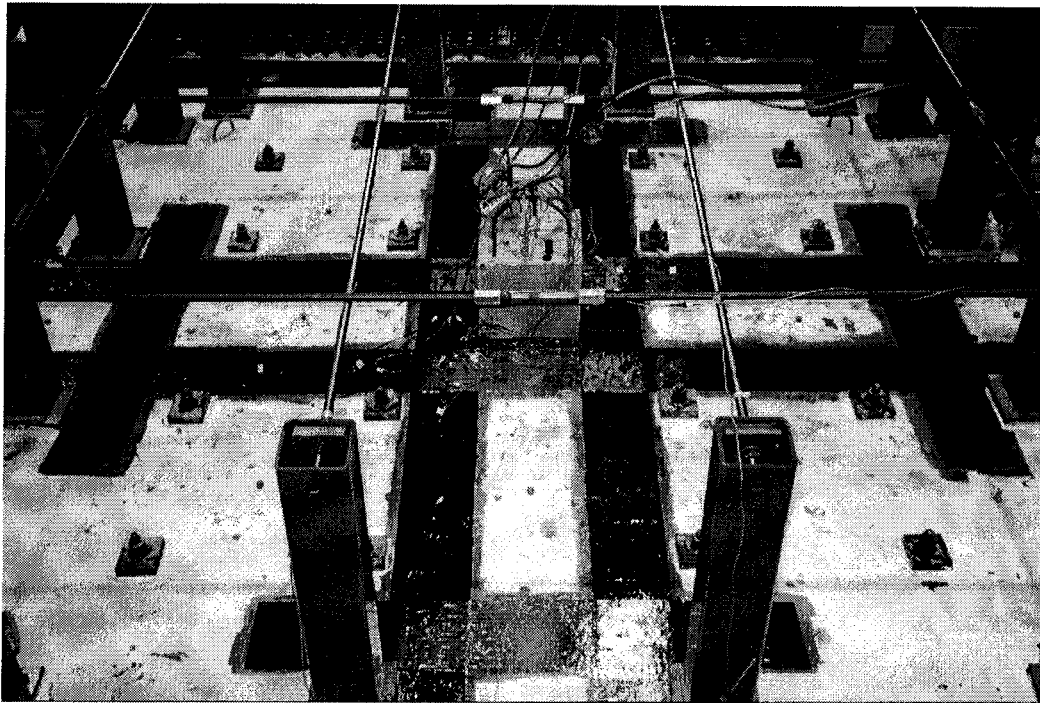


**Fig. C.7 Test ER2-CS1 : Strengthening Layout**

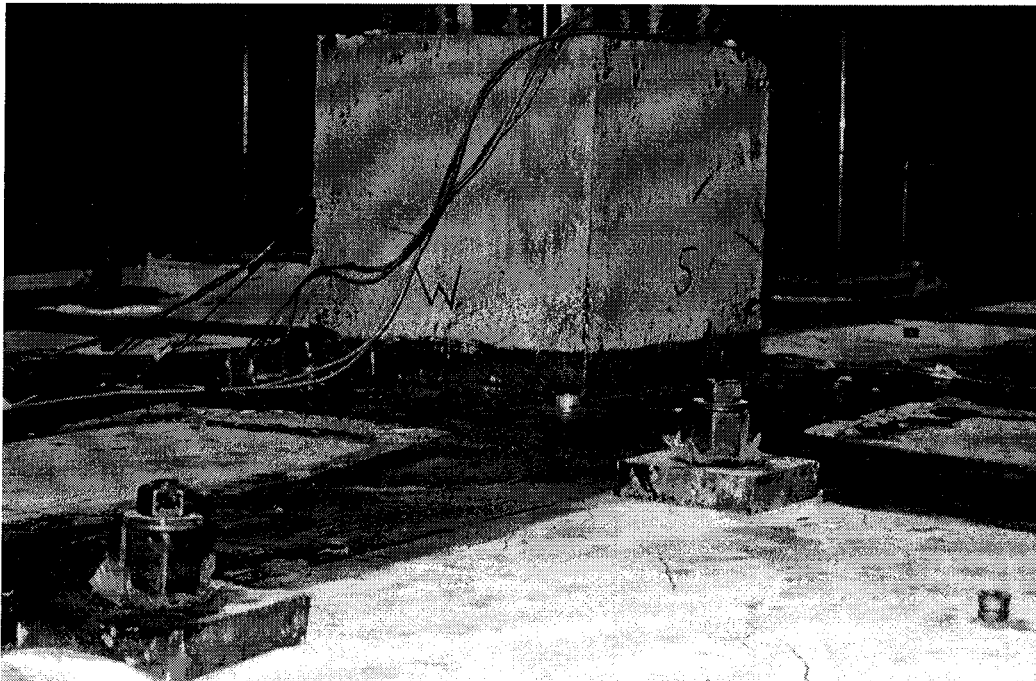


**Fig. C.8 Test ER2-CS1 : Slab Punching**

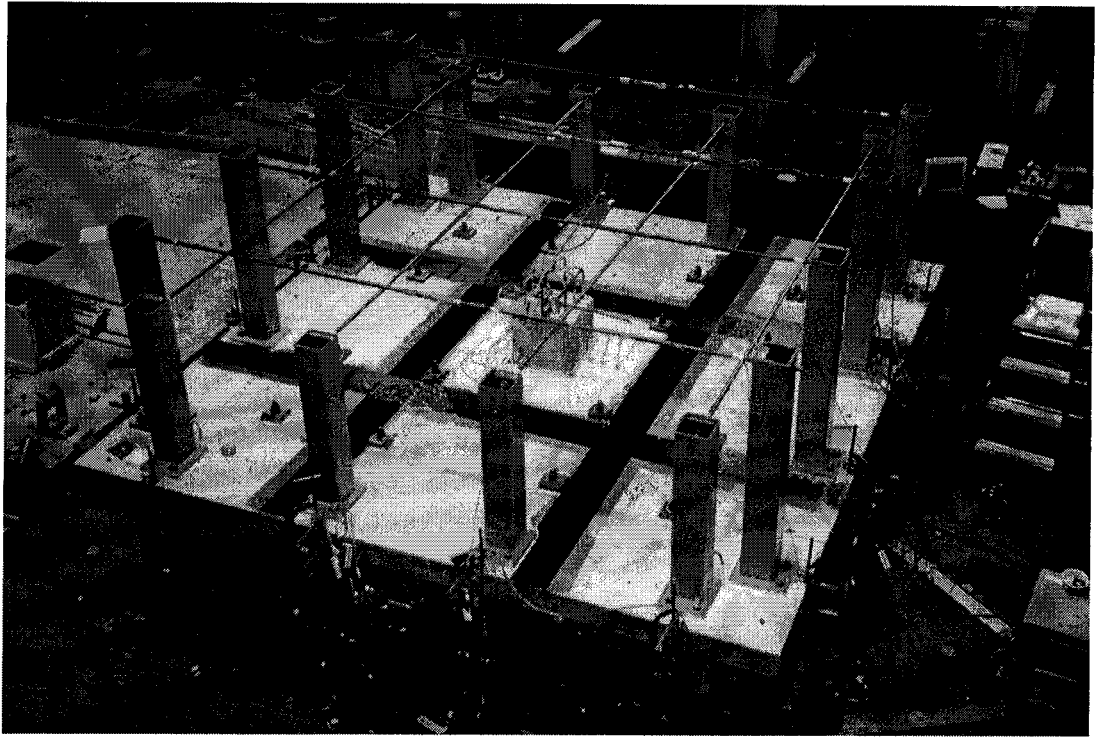


**Fig. C.9 Test ER3-CS2 : Strengthening Layout**

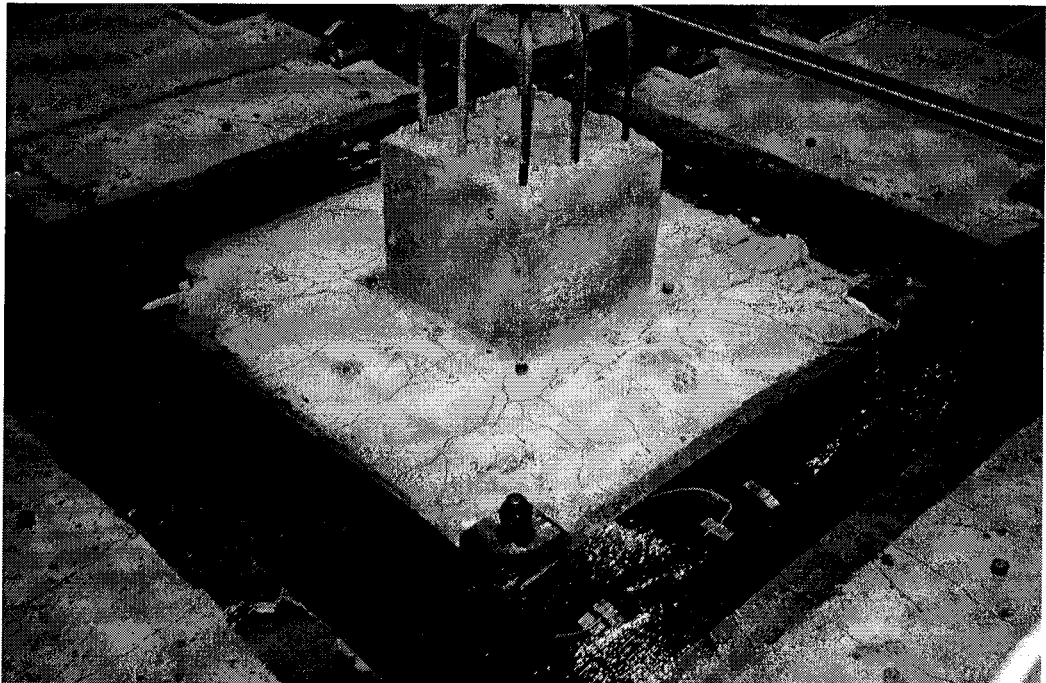


**Fig. C.10 Test ER3-CS2 : Slab Punching**



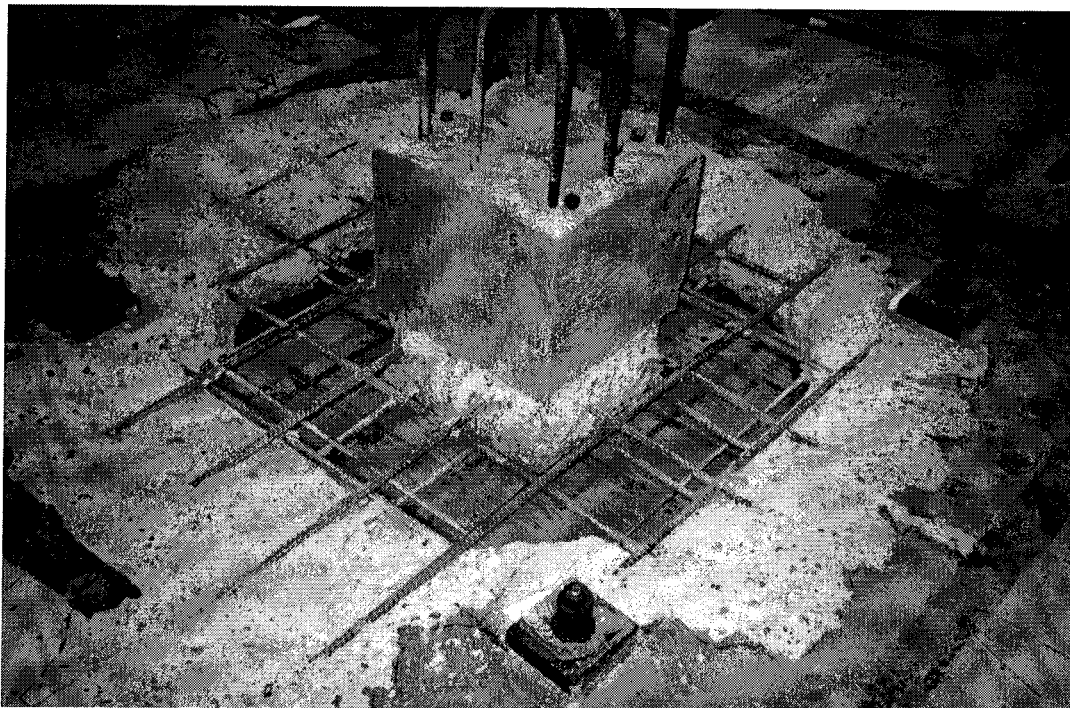


**Fig. C.11 Slab Repair (Test ER3-CP2)**

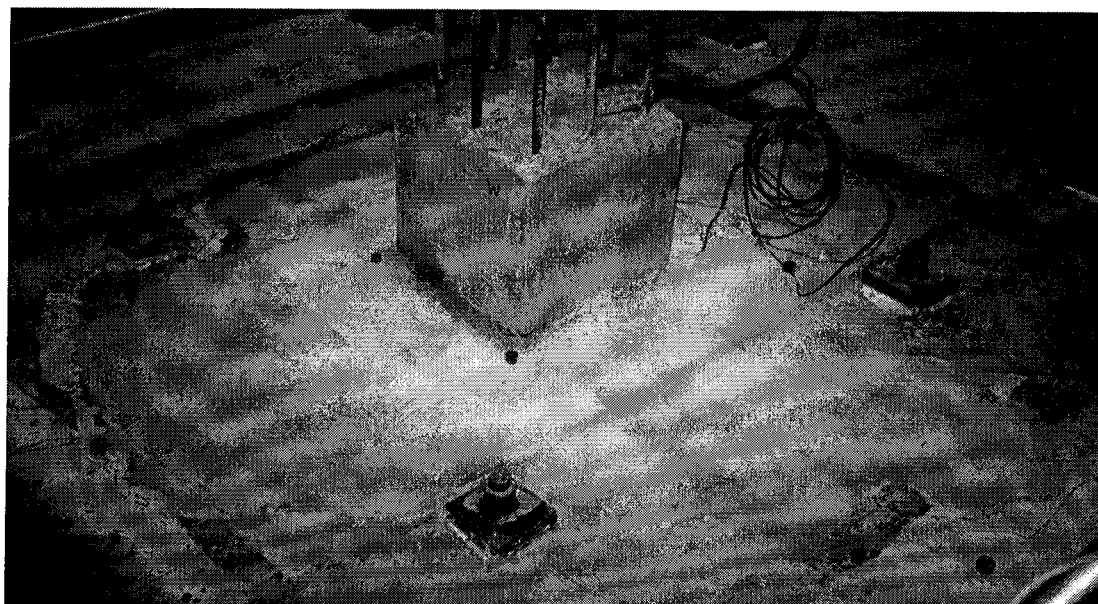


**Fig. C.12 Concrete Patch (Test ER3-CP2)**

## APPENDIX D

### Properties of Flexural Test Beam Specimens with Internal FRP Bars or Grids

Table D.1 Properties of Flexural Test Beam Specimens with Internal FRP Bars or Grids

Ref.-Specimen	$L$ mm	$a_v$ mm	$b$ mm	$h$ mm	$d^*$ mm	$f_{cm}$ MPa	FRP Type	$\phi_b$ mm	$\rho_f$ (%)	$E_f$ GPa	$f_{fu}$ MPa
MBC IS2B1	3000	1250	200	300	263.7	39	GFRP	12.7	0.5	42	689
MBC K2B1	3000	1250	200	300	263.7	40	GFRP	12.7	0.5	45.5	689
MBC IS3B1	3000	1250	200	300	263.7	39	GFRP	12.7	0.75	42	689
MBC KD3B1	3000	1250	200	300	263.7	40	GFRP	12.7	0.75	45.5	689
MBC IS4B1	3000	1250	200	300	241.3	45	GFRP	12.7	1.07	42	689
MBC KD4B1	3000	1250	200	300	241.3	40	GFRP	12.7	1.07	45.5	689
TB BC2NA	1500	500	130	180	153.9	30	GFRP	12.3	1.13	38	773
TB BC2HA	1500	500	130	180	153.9	57.2	GFRP	12.3	1.13	38	773
TB BC2VA	1500	500	130	180	153.9	97.4	GFRP	12.3	1.13	38	773
TB BC4NA	1500	500	130	180	135.2	46.2	GFRP	12.3	2.77	38	773
TB BC4VA	1500	500	130	180	135.2	93.5	GFRP	12.3	2.77	38	773
MTB CB2B-1	3000	1250	200	300	262.6	52	GFRP	14.9	0.67	41.4	773
MTB CB3B-1	3000	1250	200	300	262.6	52	GFRP	14.9	1.01	41.4	773
MTB CB4B-1	3000	1250	200	300	240.1	45	GFRP	14.9	1.47	41.4	773
MTB CB6B-1	3000	1250	200	300	240.1	45	GFRP	14.9	2.20	41.4	773
NMFT RC-A3	2400	900	200	300	245	29.4	AFRP	8	0.82	64.5	1467
NMFT RC-A4	2400	900	200	300	245	29.4	AFRP	12	1.63	58.2	1314
NMFT RC-A5	2400	900	200	300	245	29.4	AFRP	16	3.27	59.4	1314
NMFT RC-C1	2400	900	200	300	245	29.4	CFRP	8	0.82	112.1	1518
MRTB I-200-C	3000	1000	1000	200	154.1	66	GFRP	15.9	0.77	41.3	692
MRTB LL-200-C	3000	1000	1000	200	158	66	CFRP	8	0.3	147	2250
NN BF6	3048	1067	127	305	286	35.2	GFRP	12.7	1.4	26.2	724
NN BF7	3048	1067	127	305	276	32.4	GFRP	12.7	1.8	26.2	724
NN BF9	3048	1067	127	305	273	29.6	GFRP	12.7	2.2	26.2	724
NN BF11	3048	1067	127	305	274	39.3	GFRP	12.7	2.5		

**Notes:** MBC (Masmoudi, Benmokrane & Chaalal, 1995), TB (Thériault & Benmokrane, 1998), MTB (Masmoudi, Thériault & Benmokrane, 1998), NMFT (Nakano, Matsuzaki, Fukuyama & Teshigawara, 1993), MRTB (Michalak, Rizkalla, Tadros & Benmokrane, 1997), NN (Nawy & Neuwarth, 1977).

**Conventions:**  $L$  = Span,  $a_v$  = Shear span,  $b$  = width,  $h$  = height,  $d$  = effective flexural depth,  $\phi_b$  = bar diameter



## APPENDIX E

### Derivation of Indirect Deflection Control Procedure for Concrete Beams and One-way Slabs with Internal FRP Reinforcement Using Branson's Concept, According with Thériault's Definition of $I_e$

The maximum span-depth ratio for a member subjected to a uniformly distributed load associated to a maximum allowable deflection-span ratio, using Branson's  $I_e$  concept, is

$$\frac{L}{d} \leq \frac{\alpha}{2} \frac{\Delta_m}{L} \left( \frac{E_c}{f_r K_1} \right) \left( \frac{M_{cr}}{M_{\max}} \right) \left( \frac{I_e}{I_g} \right) \quad [\text{E.1}]$$

According to Thériault (1998),

$$I_e = \frac{I_t I_{cr}}{I_{cr} + \left( 1 - 0.5 \left( \frac{M_{cr}}{M_{\max}} \right)^2 \right) (I_t - I_{cr})} \quad [\text{E.2}]$$

Assuming that  $I_t = I_g$  and dividing both sides of Eq. E.2 by  $I_g$  results in

$$\frac{I_e}{I_g} = \frac{I_{cr}}{I_g} \left( \frac{I_g}{I_{cr} + \left( 1 - 0.5 \left( \frac{M_{cr}}{M_{\max}} \right)^2 \right) (I_t - I_{cr})} \right) \quad [\text{E.3}]$$

The moment of inertia of an elastic cracked rectangular cross-section with FRP is

$$I_{cr} = \frac{b(xd)^3}{3} + n\rho_f b d^3 (1-x)^2 \quad [\text{E.4}]$$

Setting  $\alpha = \frac{h}{d}$  and dividing Eq. E.4 by  $I_g$  results in

$$\frac{I_{cr}}{I_g} = \frac{4}{\alpha^3} \left[ \frac{x^3}{3} + 3n\rho_f (1-x)^2 \right] \quad [\text{E.5}]$$

$$\text{where } x = \sqrt{(\rho_f n)^2 + 2\rho_f n} - \rho_f n \quad [\text{E.6}]$$

Substituting Eq. E.3 into E.1 and rearranging terms, results in

$$\frac{L}{d} \leq \frac{\alpha}{2} \frac{\Delta_m}{L} \left( \frac{E_c}{f_r K_1} \right) \left( \frac{M_{cr}}{M_{\max}} \right) \frac{\frac{I_{cr}}{I_g}}{\frac{I_{cr}}{I_g} + \left( 1 - 0.5 \left( \frac{M_{cr}}{M_{\max}} \right)^2 \left( 1 - \frac{I_{cr}}{I_g} \right) \right)} \quad [\text{E.7}]$$

with  $\frac{I_{cr}}{I_g}$  defined according to Eq. E.5.

## APPENDIX F

### Properties of Punching Test Two-way Slab Specimens with Internal FRP Bars or Grids

**Table F.1 Properties of Punching Test Two-way Slab Specimens with Internal FRP Bars or Grids**

Ref.	Slab	c * (mm)	d (mm)	$f_{cm}^{\dagger}$ (MPa)	FRP Type §	$\rho_f$ (%)	$E_f$ (GPa)	$f_{fu}$ (MPa)
AZYX	CFRC-SN1	S 75	61	42.4	3-D C Grid	0.95	113.0	1330
	CFRC-SN2	S 75	61	44.6	3-D C Grid	0.95	113.0	1330
	CFRC-SN3	S 100	61	39.0	3-D C Grid	0.95	113.0	1330
	CFRC-SN4	S 100	61	36.6	3-D C Grid	0.95	113.0	1330
BAM	I	C 100	55	41.0	C NEF	0.31	100.0	1200
	II	C 100	55	52.9	C NEF	0.31	100.0	1200
MT	C1	C 150	96	30.4/36.7	C NEF	0.26	91.8	1690
	C1'	C 230	96	30.4/37.3	C NEF	0.26	91.8	1690
	C2	C 150	95	29.6/35.7	C NEF	1.05	95.0	1340
	C2'	C 230	95	29.6/36.3	C NEF	1.05	95.0	1340
	C3	C 150	126	28.0/33.8	C NEF	0.52	92.0	1350
	C3'	C 230	126	28.0/34.3	C NEF	0.52	92.0	1350
	CS	C 150	95	27.2/32.6	CS Rods	0.19	147.6	2300
	CS'	C 230	95	27.2/33.2	CS Rods	0.19	147.6	2300
	H1	C 150	95	96.7/118.0	GC NEF	0.64	37.3	665
	H2	C 150	89	29.3/35.8	GC NEF	3.78	40.7	555
	H2'	C 80	89	29.3/35.9	GC NEF	3.78	40.7	555
	H3	C 150	122	26.3/32.1	GC NEF	1.21	44.8	640
	H3'	C 80	122	26.3/32.1	GC NEF	1.21	44.8	640
EPW	SG1	S 200	142	33.3	G Rebars	0.22	45.0	600
	SC1	S 200	142	34.7	C Rebars	0.18	110.0	100
	SG2	S 200	142	46.6	G Rebars	0.47	45.0	600
	SG3	S 200	142	30.3	G Rebars	0.47	45.0	600
	SC2	S 200	142	29.6	C Rebars	0.43	110.0	1000
Series I	GFR-1	S 250	120	29.5	G Rebars	0.73	34.0	660
	GFR-2	S 250	120	28.9	G Rebars	1.46	34.0	660
	NEF-1	S 250	120	37.5	G NEF	0.87	28.4	570

**Notes:** AZYW : Ahmad, Zia, Yu & Xie (1993), BAM : Bantia, Al-Asaly & Ma (1995),  
MT : Matthys & Taerwe (2000c), EPW : El-Ghandour, Pilakoutas & Waldron (1997, 2000).

\* Shape of column stub / load patch and corresponding diameter or width.

C = circular, S = square.

§ NEF = NEFMAC Grid, G = Glass, C = Carbon, S = Sanded.

†  $f_{cm}$  values for EPW slabs were obtained from cube test results, assuming  $f_{cm} = 0.8 f_{cube}$ .  
The two  $f_{cm}$  values for MT slabs are those at 28 days and at testing time, respectively.